Springer Series in Solid-State Sciences 180

Adolfo Avella
Ferdinando Mancini *Editors*

Strongly Correlated Systems

Experimental Techniques

Springer

Springer Series in Solid-State Sciences

Volume 180

The Springer Series in Solid-State Sciences consists of fundamental scientific books prepared by leading researchers in the field. They strive to communicate, in a systematic and comprehensive way, the basic principles as well as new developments in theoretical and experimental solid-state physics.

More information about this series at http://www.springer.com/series/682

Adolfo Avella · Ferdinando Mancini
Editors

Strongly Correlated Systems

Experimental Techniques

With 117 Figures

Springer

Editors
Adolfo Avella
Dipartimento di Fisica "E.R. Caianiello"
Università degli Studi di Salerno
Fisciano (SA)
Italy

Ferdinando Mancini
Dipartimento di Fisica "E.R. Caianiello"
Università degli Studi di Salerno
Fisciano (SA)
Italy

ISSN 0171-1873 ISSN 2197-4179 (electronic)
ISBN 978-3-662-44132-9 ISBN 978-3-662-44133-6 (eBook)
DOI 10.1007/978-3-662-44133-6

Library of Congress Control Number: 2013930016

Springer Heidelberg New York Dordrecht London

Printed on acid-free paper

Springer is part of Springer Science+Business Media (www.springer.com)

Preface

This volume "Experimental Techniques for Strongly Correlated Systems", together with the set "Methods and Techniques for Strongly Correlated Systems" it belongs to, builds upon the long-standing experience we have acquired in organizing the "Trainings Course in the Physics of Strongly Correlated Systems" in Vietri sul Mare (Salerno, Italy) since 1996 and our scientific working experience in the field. Running a school for advanced graduate students and junior postdocs, we have realized that this field of condensed matter and solid-state physics lacked in adequate textbooks and that the whole strongly correlated systems community would benefit from a systematic exposition of the field. The present volume consists of a series of monographs on the most relevant experimental techniques currently used to tackle the hoary problem of correlations. The authors have been selected, the major experts in the field have been consulted, among the most world-wide famous scientists who have invented or greatly helped improve/spread the specific technique in the community. Each chapter presents the method in a pedagogical way and contains at least one case study where the method has proved to give a substantial leap forward in the knowledge and a very rich bibliography. The book is mainly intended for neophytes, who will find in one single volume all the pieces of information necessary to choose and start learning an experimental technique. Also more experienced researchers would benefit from this volume as they would gain a deeper understanding of what any single technique can really tell them and what cannot. Accordingly, the accent is more on the ideas behind (origins, pros/cons, perspectives, ...) than on the technical details, which are left to the comprehensive bibliography.

We wish to thank all the authors of this volume as they all joined this editorial project with enthusiasm and provided the whole community with what we hope will become a relevant resource for any researcher in the field as a comprehensive and extended reference.

Salerno, Italy
June 2014

Adolfo Avella
Ferdinando Mancini

Contents

Contributors

Riccardo Comin Department of Physics and Astronomy, University of British Columbia, Vancouver, BC, Canada

Nicholas J. Curro Department of Physics, University of California, Davis, CA, USA

Andrea Damascelli Quantum Matter Institute, Department of Physics and Astronomy, University of British Columbia, Vancouver, BC, Canada

J. C. Davis LASSP, Department of Physics, Cornell University, Ithaca, NY, USA; CMPMS Department, Brookhaven National Laboratory, Upton, NY, USA; Kavli Institute at Cornell for Nanoscience, Cornell University, Ithaca, NY, USA; School of Physics and Astronomy, University of St. Andrews, Scotland, UK

Guy Deutscher School of Physics and Astronomy, Tel Aviv University, Ramat Aviv, Tel Aviv, Israel

Hiroshi Eisaki National Institute of Advanced Industrial Science and Technology (AIST), Tsukuba, Ibaraki, Japan

Inês Firmo LASSP, Department of Physics, Cornell University, Ithaca, NY, USA; CMPMS Department, Brookhaven National Laboratory, Upton, NY, USA

Kazuhiro Fujita LASSP, Department of Physics, Cornell University, Ithaca, NY, USA; CMPMS Department, Brookhaven National Laboratory, Upton, NY, USA

Mohammad Hamidian LASSP, Department of Physics, Cornell University, Ithaca, NY, USA; CMPMS Department, Brookhaven National Laboratory, Upton, NY, USA

Stephen R. Julian Department of Physics, University of Toronto, Toronto, ON, Canada

Chung Koo Kim CMPMS Department, Brookhaven National Laboratory, Upton, NY, USA

Sourin Mukhopadhyay LASSP, Department of Physics, Cornell University, Ithaca, NY, USA; Kavli Institute at Cornell for Nanoscience, Cornell University, Ithaca, NY, USA

Michael Nicklas Max Planck Institute for Chemical Physics of Solids, Nöthnitzer Str. 40, Dresden, Germany

Hans R. Ott Laboratory for Solid State Physics, Department of Physics, ETH Zurich, Zurich, Switzerland

John M. Tranquada Brookhaven National Laboratory, Upton, NY, USA

Shin-ichi Uchida Department of Physics, University of Tokyo, Bunkyo-ku, Tokyo, Japan

Yasutomo J. Uemura Department of Physics, Columbia University, New York, NY, USA

Dirk van der Marel Département de Physique de la Matière Condensée, Université de Genève, Genève 4, Switzerland

Igor A. Zaliznyak Brookhaven National Laboratory, Upton, NY, USA

Foreword

Hans R. Ott

1 Introduction

This volume is intended to give an overview of various important experimental methods and techniques for studying correlation and many-body effects in solids. Naturally, the content of the chapters concentrates on the modern, i.e., state-of-the-art situation of these aspects. In order to put these contributions in relation to the developments in studies of correlations in solids, the first section of this foreword aims at briefly reviewing the history of corresponding investigations, emphasizing the interplay between experiment and theory.

An early experimental or rather observational evidence for correlation effects among electrons in solids, but certainly not identified as such at the time, is the phenomenon of persistent magnetization in ferrous materials found in nature. A much more recent but in this context also early and then unexplained indication of the same was the discovery of superconductivity via experiments probing the electrical resistance of Mercury (Hg) at low temperatures in 1911 [1]. In 1933, simple experiments [2], again probing the temperature dependence of the electrical resistivity $\rho(T)$ of a metal, at this time Gold (Au), marked the beginning of a new direction in the slow development of understanding the role of electron correlations that was to bloom only much later. At these early times, electronic transport in metals was considered to be adequately described by the motion of free or quasifree electrons in the crystal lattice. Hence the observed increase of $\rho(T)$ with decreasing T at low temperatures was registered as a not understood anomaly which, eventually but much later, was shown to be due to transition-metal (TM) impurities in common metals such as Cu and Au [3]. The first theory-based link between magnetism and electronic conduction in solids was provided by Bloch [4].

H.R. Ott (✉)
Laboratory for Solid State Physics, Department of Physics
ETH Zurich Zurich, Switzerland
e-mail: ott@phys.ethz.ch

Yet another experimental fact concerning the electronic conduction in solids, namely the insulating behavior of NiO, initiated new ideas on how correlation effects among electrons are decisive for solids to turn out to be either metals, i.e., electrical conductors, or insulators. Following conventional wisdom, NiO is expected to be a metal and not an insulator as verified experimentally. In 1949, based on a comparison of the Heitler-London approach [5] with Blochs [6] approximation in dealing with electronic states in solids, Mott [7] argued that the NiO puzzle was a result of correlation effects. Already in this first discussion of his ideas, known data on the magnetic susceptibility and the specific heat of transition-metal elements were used to support the conjectures.

Subsequently, experimental and theoretical investigations on the stability of magnetic moments and the occurrence of magnetic order in metals, launched a development of activities that continue to be a major part of contemporary condensed matter physics research. The behavior of magnetic moments in, and their influence on a metallic environment was first treated by considering a single magnetic moment as an impurity in an itinerant-electron system by Friedel [8], Blandin [9] and others around 1956. Experiments employing the still young experimental technique of nuclear magnetic resonance (NMR) provided information on the polarization of conduction electrons by the spins of more localized electrons on atoms of d-transition-metal elements [10]. Accompanying theoretical investigations [11–13] finally provided a scheme for describing the onset of magnetic order induced by the interaction between itinerant and more localized core electrons, the Ruderman-Kittel-Kasuya-Yosida (RKKY) interaction.

Magnetization measurements probing the influence of magnetic moments on the normal state of metals, mainly by Matthias, Suhl, Clogston, and others [14, 15], revealed unexpected complications. This prompted Anderson to extend the then existing model by creating what is now known as the Anderson Hamiltonian [16], aiming at explaining why a magnetic moment due to localized electrons is stable in one metal but not in another. At the same time, with the same simple experiments, again Matthias and co-workers, noted detrimental effects of magnetic moments on the superconducting state of selected materials [17]. In this case it was Abrikosov and Gorkov [18] who provided an explanation by considering the particular correlated superconducting ground state put forward a few years earlier by Bardeen, Cooper, and Schrieffer (BCS) [19].

Not much later, in 1963, another model Hamiltonian, attempting to capture correlation effects among narrow-band d-electrons in transition metals (TM), was introduced and analyzed by Hubbard [20]. Although formally quite simple, rigorous solutions are difficult to obtain. The model and variations of it are, however, still very popular and, as mentioned below, often used in numerical investigations of correlated electron systems. Almost in parallel, an explanation of the above-mentioned experimental observation of the minimum in $\rho(T)$ was given by Kondo [21]. He argued that a single localized magnetic moment embedded in a metallic environment is shielded by oppositely oriented spins in a cloud of conduction electrons

in the neighborhood of the impurity. The resulting partial rearrangement of the excitation spectrum of the conduction electrons is then responsible for the observed increase of $\rho(T)$ with decreasing temperature below a material-specific temperature T_K, the Kondo temperature.

New aspects of electronic correlations in metals were soon discovered via experiments probing thermal, transport, and magnetic properties of rare-earth and actinide compounds. It was expected and confirmed that the corresponding 4f- and 5f-electrons are even more localized than the d-electrons in the above-mentioned d-transition metals and their compounds. As expected, Curie-Weiss type magnetic susceptibility data below room temperature indicated the presence of well localized, weakly interacting f-electron moments occupying regular lattice sites. A particularly intriguing result was the observation that a Curie-Weiss type magnetic susceptibility at elevated temperatures does not necessarily imply the onset of magnetic order at low temperatures [22]. In other cases, the established magnetic order was among moments, in magnitude much reduced below the values indicated by the Curie-Weiss effective moment at elevated temperatures [23]. A particular case in this respect is $CeAl_3$ with Ce^3+ ions carrying a significant localized magnetic moment and occupying a regular crystalline sublattice. Results of measurements of the temperature dependences of the specific heat, the electrical resistivity and the magnetic susceptibility were interpreted as being due to conduction electrons with extremely large effective masses [24] or, equivalently, very low Fermi velocities v_F. In a first approximation, these features obviously imply that the involved itinerant electrons occupy energy states in very narrow bands and may be regarded as forming a very strongly renormalized Fermi liquid, a situation that was discussed in detail by Landau 20 years earlier [25]. In some sense, the magnetic degrees of freedom appear to be transferred to the subsystem of the itinerant electrons at low temperatures. The resulting anomalously large effective masses mimic the tendency to localization and the local ionic moments are substantially reduced. An interesting toy model describing the situation of order among much reduced moments or eventually no order at all was put forward by Doniach [26]. He suggested that a competition between different correlations, those of Kondo type and those of RKKY type, might cause this anomalous electronic many-body state. Not surprisingly and early indicated by results of thermal expansion [24] and elastic-constant measurements [27], the properties of these narrow-band electron systems are easily influenced by the application of external pressure. Subsequently and as also mentioned below, some spectacular transitions from magnetic order to superconductivity were discovered in later studies [28].

In view of the above-mentioned previously observed detrimental effect of magnetic moments in superconducting materials, the discovery of superconductivity [29] in these materials with narrow bands and strong electronic correlations, was really unexpected. Experimental data, mainly invoking thermal (specific heat) and spectroscopic (NMR) properties, soon prompted first claims of the identification of unconventional superconductivity in metallic solids [30].

Research on electronic correlations in solids received an unprecedented boost by the again completely unexpected discovery of superconductivity in a particular class of copper-oxide compounds with critical temperatures T_c between 30 and 40 K [31]. Efforts to enhance the critical temperature T_c in the same and various other cuprate materials were soon successful in raising the onset of superconductivity to above the boiling point of liquid nitrogen and finally to temperatures up to 134 K [32]. Considering the onset of superconductivity in such materials at all and the magnitude of T_c seemed to violate conventional wisdom to an extent that conjectures of unconventional superconductivity also in these cases, were to be expected. Experimental efforts employing a variety of methods probing the phase of the superconducting order parameter indeed confirmed the occurrence of nodes in the k-dependent energy gap of the electronic excitation spectrum in the superconducting state [33, 34]. In another experimental approach to directly verify such gap nodes, a new experimental method with a rapid development in technical perfection, namely angular-resolved photoemission spectroscopy (ARPES), encountered its first real success [35]. The increasing importance of this method was naturally based on the growing availability of intense light sources in the form of large electron synchrotrons. The mapping of $E(k)$ spectra of cuprate superconductors was widely used in many ARPES-based investigations, hoping that this type of information would help to understand the reasons for the instability of the electronic subsystem leading to superconductivity at unusually high temperatures in these compounds.

Similar progresses in instrumentations of this and other experimental techniques provided new ways for investigating the influence of electronic correlations in solids. With respect to access narrow bands of electronic excitations, the energy resolution in photoemission methods was greatly improved and finally resulted in commercially available detectors for this purpose [36]. A similar but less rigorous development took place in using elastic and inelastic neutron diffraction. In particular, the method of small-angle neutron scattering [37], primarily used for studies of macromolecules and polymers, gained in importance for studies of (H, T) phase diagrams of superconductors [38]. In parallel to these improvements of the instrumentation at large-scale facilities, the methods employing scanning-tunneling techniques such as based on electron-tunneling (STM) and atomic-force microscopy (AFM) provided new ways of probing electronic and magnetic properties at a local, i.e., atomically resolved level [39].

It turned out that the electronic conductivity in these materials is the result of specifically doping initially insulating and magnetically ordering compounds. The aims to provide a theoretical basis for explaining the observations concerning the normal state of these substances led to a revival of the above-mentioned models of Mott and Hubbard and extensions thereof [40]. Yet another model, earlier devised by Anderson by reviving Paulings resonant-valence-bond concept [41], was considered as a possible approach to solve the problem. An early account of strong correlation and superconductivity is given in [42]. Some of these models implied the formation of a ground state that would not be consistent with the Fermi liquid type description of the metallic, i.e., $\partial\rho/\partial T > 0$, state and a number of the available experimental data seemed to support this view [43]. The anomalous electronic

properties of the normal state of cuprates encouraged detailed experiments investigating the electronic properties of TM oxides and related materials. An early review of the results of these efforts, concentrating on the phenomenon of externally controlled metal-insulator transitions was provided by Imada and co-workers [44].

Because of the very high upper critical fields H_{c2} of these cuprate superconductors, the low-temperature electronic structure of the normal state of these materials was, at the time, not accessible by employing the usual magneto-oscillatory effects on the resistivity and the magnetisation. The already mentioned progresses in ARPES experiments made it possible to investigate these features also at elevated temperatures above T_c, previously not accessible by conventional means [45]. Much more recently, improved sample quality and progress in the technical handling of high-field magnets and measuring devices made it possible to observe the long sought field-induced oscillatory features of transport coefficients [46]. New insights into the correlations in electronic subsystems, mainly in cuprates and other TM compounds close to metal-insulator transitions were achieved via measurements of optical properties and using advanced photoelectron spectroscopy techniques.

Inspired by earlier results and to some extent encouraged by the experimental results indicating the anomalous features of the normal state of the cuprate compounds and noting the perspectives of new aspects in the understanding of metallic conductivity, more detailed experimental investigations, mostly probing thermal, transport, and magnetic properties, were made on compounds featuring heavy electrons. Data from specific heat experiments at very low temperatures indicated significant deviations from the behavior expected for Fermi liquids [47]. Other studies revealed that the properties of this low-temperature electronic state can be significantly altered by changing externally controlled parameters, such as variations of the chemical composition, external pressure, or magnetic fields. Again, some of the results of the corresponding experiments indicated properties not compatible with Landaus original Fermi-liquid model; others suggested the occurrence of so-called quantum phase transitions (QPT) [48], a concept [49] with a bright future, as will be seen below.

Structural investigations of the cuprate superconductors, mostly by employing X-ray and neutron diffraction [50], revealed that the arrangement of atoms in the crystallographic unit cells may be viewed as a stacking of planes of atoms. It turned out that the essential physical properties of these compounds are determined by planes consisting of copper and oxygen atoms; additional planes, occupied by atoms of the other constituent chemical elements, are regarded as mostly inactive spacer blocks and charge reservoirs [51]. This insight triggered new and extensive efforts in synthesizing other similar oxide materials based on Cu and other TM elements with low-dimensional (low-D) structural subunits, such as planes, multileg ladders, and chains. These included both electrical conductors and insulators. Since the Cu and other TM ions, depending on their charge configuration, carry a definite electronic spin, the cited subunits may be regarded as spin chains, ladders, and planes. In special cases, the interactions between the low-D spin subunits in insulators turn out to be weak. For this reason, these particular materials were and

still are considered as assemblies of quasi-individual low-D objects, serving as model systems for testing rigorous theoretical predictions concerning the properties of ensembles of spins which accumulated over many years up to present.

With respect to theory, low-D spin arrangements have a long history, starting with Isings model of individual magnets on a chain in his contribution to the theory of ferromagnetism [52]. The more general approach of Heisenberg to consider the exchange phenomenon in the quantum-mechanical description of indistinguishable particles for the description of ferromagnetism was the next step [53]. It was taken up by Bloch who concluded that planar arrangements of magnetic moments would not support ferromagnetism [4]. Next it was Bethe who calculated the eigenfunctions and eigenvalues of a linear chain of atoms, each with a single valence electron and its spin [54]. With this method he aimed at establishing the magnetic and transport properties of such systems, also in higher dimensions.

General aspects of phase transitions in low-D systems were first discussed by Onsager [55]. He considered a 2D model which exhibits an order–disorder transition. Later, Griffiths [56] as well as Mermin and Wagner [57] discussed the possibility of magnetic order in low-dimensional systems. Based on earlier work of Bloch [58], the features of low-D electronic systems were also studied, first by Tomonaga [59] and later by Luttinger [60]. From still later work by Haldane [61] and Affleck [62] it was concluded that the above-mentioned Fermi-liquid model, describing the electronic properties of common metals so well, was not applicable in treating 1D conductors. These authors saw a more suitable treatment with a concept that they termed Luttinger-liquid model, the 1D equivalent of the Fermi-liquid model. It turns out that quite generally the physical properties of low-D systems are characteristically different from those usually observed in common 3D objects. The 1D physics is strongly influenced by quantum effects, defects, and fluctuations which are usually masked in standard 3D materials. For unraveling these effects, systems with chains (1D) of spins with $S = 1/2$ and antiferromagnetic couplings are the most favorable choice. The low-energy excitations were shown to be objects carrying a spin $S = 1/2$ and the spectrum of these Fermions, termed spinons, turns out to be gapless [63]. A rather unexpected theoretical result was Haldanes conjecture that the excitation spectrum of the same type of chains but with $S = 1$ ought to exhibit a gap [64]. Follow-up studies by Affleck and co-workers [65] demonstrated that the theoretical reasoning for explaining this difference is far from trivial. Later, a very fruitful development originated in interpreting the low-energy excitations of low-D spin systems as particles. To see this it is useful to note that in the considered spin systems, spin dimers with a singlet ground state and $S = 1$ excitations to a triplet excited state may form. Apart from regarding the above-mentioned spinons as Fermions, an analogy between these $S = 1$ excitations termed triplons and Bosons was established [66]. As a consequence, a Bose-Einstein condensation (BEC) of such excitations in the form of magnetic order was predicted to occur under the influence of an external magnetic field [67]. It also turned out that some of these systems are show cases for studying the properties of a Luttinger liquid [68].

First experiments for testing some of the theoretical predictions were made with TM bronzes and some organic compounds, both of which exhibit considerable anisotropies in electronic conduction. Early results are reviewed in [69]. Soon it was found that some of the low-D organic compounds exhibit a variety of ground states from insulating and magnetically ordered to metallic and superconducting; varying by applications of external pressure and/or magnetic field. An up-to-date review can be found in [70]. Later, the research interests began to focus on materials containing the mentioned weakly coupled low-D spin systems in an electrically insulating environment. The physics of these spin systems is often assumed to be captured by relatively simple Hamiltonians of the Heisenberg type; complications are to be expected from the unavoidable anisotropies and spin-orbit coupling. The interactions in each individual spin chain are based on the exchange phenomenon. Naturally, they depend on the bond strength and directions between the atomic sites. Therefore, they may be varied by applying external pressure and introducing selected defects. Likewise, the application of external magnetic fields which softens the above-mentioned triplon excitations is expected to induce phase transitions. This offers new opportunities for studies of the physical behavior of these systems if links between the theoretical concepts and really existing materials can be made. Many new compounds with spin-carrying cations (Cu, V, Ni) were synthesized. Based on first structural and magnetic characterisations, some of them were indeed identified to serve as model compounds for experimental tests under varying external conditions as outlined above. Both bulk and microscopic experimental probes, such as magnetization measurements as well as neutron-scattering and NMR techniques are being used to identify the magnetic properties of these systems. A good part of corresponding efforts and the achieved results up to 2003 are summarized in [71]. More recent results, mainly in connection with the BEC phenomenon in quantum magnets are presented and discussed in [72]. The model Hamiltonians offer a playground for analytical as well as numerical studies of the influence of correlations in solids; the current status of both these activities is documented in detail in two other, recently published volumes of this series [73, 74].

As mentioned at the beginning, the third volume of this series is devoted to reviewing current experimental methods and techniques that play an essential role in contemporary studies of correlation effects in solids. Below, brief summaries of the content of each chapter are given.

2 Nuclear Magnetic Resonance

As mentioned in the introduction, nuclear magnetic resonance (NMR) experiments were already employed in early studies of correlation effects in metals. A highlight was the experimental confirmation of the NMR-related coherence effect in superconductors as predicted by the BCS theory.

In the first section, Nicholas Curro covers the basic theoretical background of the method. It includes the density-matrix approach, the introduction of the concept of the rotating frame and Blochs equations. The latter defines two important parameters representing the characteristic times of the decay of the transverse magnetization (T_2) and of the recovery of the longitudinal equilibrium magnetization (T_1). A section on pulse techniques explains the principles of the free induction decay and the spin-echo technique, including some practical technical details concerning the detection of the response signals and briefly recalling the role of spin-lattice relaxation.

Since many probed nuclei possess spins $I_n > 1/2$, quadrupolar effects due to the interaction between the nuclear quadrupole moments and the local electric potential at the site of the nucleus, complicate the response and hence the spectra. The corresponding section summarizes the essentials of these complications and the resulting spectra and their dependence on the angle between the magnetic field orientation and the principal axes of the crystalline lattice. The case where the external magnetic field is set to zero, i.e., the nuclear quadrupole resonance (NQR), is also briefly addressed.

The usually dominating interaction in correlated electron systems is the hyperfine coupling between the spins of the probed nuclei and the spins of electrons in the local environment. In metals the latter includes conduction electrons and localized electrons on ions occupying neighboring lattice sites; in insulators the so-called transferred hyperfine interaction couples to spins of localized electrons. These interactions lead to resonance shifts which are summarized under the term Knight shifts. While simple and usually temperature independent in simple metals, these shifts are more complex in cases where different hyperfine couplings contribute to the total shift or correlation effects influence the local susceptibilities. These interactions not only influence the position of the corresponding resonance but also affect the dynamics of the above-mentioned spin-lattice relaxation process.

The last section is devoted to a case study of field-induced magnetism in superconducting $CeCoIn_5$, demonstrating the power of NMR-based methods in studies of the strongly correlated electron system in this compound. It is demonstrated that the available microscopic information may correct seemingly solid interpretations of data obtained from measurements of bulk thermal properties. The NMR data reveal a static antiferromagnetic order in the superconducting phase close to H_{c2} at $T << T_c$. Although coexistence of antiferromagnetic order and superconductivity has been observed before in several cases, the phenomenon in $CeCoIn_5$ is most likely of different nature and still awaits a sound theoretical interpretation.

3 Angle-Resolved Photoemission

Before the authors, Riccardo Comin and Andrea Damascelli, address the technical aspects of angle-resolved photoemission (ARPES) experiments, they offer an overview on correlation-dominated materials in the form of d-electron transition-

metal oxides (TMOs). In view of correlation effects the chosen classification scheme of these systems includes (i) Mott-Hubbard insulators, (ii) charge-transfer insulators and (iii) relativistic Mott insulators. As usual, this choice is based on the relative magnitudes of the on-site Coulomb repulsion U, the band width W and the spin-orbit interaction λ.

Angle-resolved photoelectron spectroscopy is the experimental dream tool for those interested in exploring the electronic structure of materials. Its application requires the availability of both intense photon sources which are provided by, e.g., electron synchrotrons, and detectors with sufficient energy and angular resolution for harvesting the escaping photoelectron as a function of their energy and momentum. A section of the chapter is devoted to discuss technical aspects of state-of-the-art photoemission with respect to both radiation sources and electron detectors and their current performance parameters. Also briefly addressed are specific aspects of the geometrical configuration of the incoming light beam and the detector in ARPES experiments.

Starting with the basics, the authors first explain the kinematics of photoemission and continue by summarizing the essentials of the three-step model and the sudden approximation which they use to model the photoemission process. As the interpretation of the collected photoelectron spectra requires solid theoretical guidelines, the authors discuss the routinely employed Green's function formalism to obtain the one-particle spectral function $A(\omega, k)$ which is directly probed by ARPES. For extracting quantitative information from the spectra, matrix element effects and the influence of the unavoidable limited resolutions and the extrinsic background have to be considered.

The discussion of rather generic aspects of photoemission experiments is followed by a longer section emphasizing the physics of correlations probed by ARPES. It starts with describing spectral functions of small many-body systems such as molecules, in this case H_2. Considering solids, electron-phonon correlations and the corresponding quasiparticle, the polaron, are described first and illustrated with existing results. Naturally, the electronic structure of Cu oxides is a primary example for illustrating correlation effects in solids and corresponding work and results are summarized under the heading: doping controlled coherence. For temperature-controlled coherence manganese oxide (Mn-O) compounds are chosen as examples. A particular feature of the ARPES technique, namely to exploit the dependence of matrix elements that determine the spectral intensity on the light polarization, is exemplified in a discussion of relevant work on cobaltates where contributions of different electron bands to the spectra need to be unraveled. Further subsections deal with the influence of relativistic effects due to enhanced spin-orbit coupling in 4d and 5d electron TMO materials, including a novel type of insulating state due to correlations in an Ir oxide material, termed relativistic Mott insulator.

4 Spectroscopic Imaging Scanning-Tunneling Microscopy (SI-STM)

This chapter, co-authored by 8 contributors affiliated with various institutions, concentrates on efforts to visualize the electronic structure and its symmetry of a particular compound series of cuprate superconductors with scanning-tunneling microscopy in the spectroscopic imaging mode. First, a brief and rather general review of the low-temperature phase diagram and related electronic structures of hole-doped cuprate superconductors summarizes the principal features reported in the literature. The two distinct energy scales, Δ_0 and Δ_1, related to two distinct phases, are introduced. While the first is clearly identified as being related to excitations across the gap that forms upon the onset of the superconducting state, the cause and significance of the second, characterizing the so-called pseudogap phase, is judged to be still rather obscure. The investigated system is based on the parent compound $Bi_2Sr_2CaCu_2O_{8+\delta}$. The doping parameter δ is chosen such that the system is in the underdoped regime where both the superconducting and the pseudogap phase can be probed.

The technique is based on measuring the voltage dependence of the tunneling current $\partial I/\partial T$ as a function of the tunneling site and the energy of the tunneling electrons. The authors prefer to describe the theoretical background of the method rather than its technical realization. For the latter, they refer to information existing in the literature. Probably led by previous experience, some of the most serious and in practice often overlooked systematic errors that may occur in such investigations are described and some guidance of how to avoid or at least minimize them is given. The next section is devoted to describing how magnetic and nonmagnetic impurity atoms can serve as indicators for the pairing mechanism and/or symmetry in superconductors. It is pointed out that the corresponding spectra change appreciably upon varying the degree of doping. The doping itself introduces electronic disorder at the nanoscale. The influence of these defects on spectra, especially related to the pseudogap phase are discussed. Information on quasiparticle scattering can be obtained from Bogoliubov-quasiparticle interference imaging. In particular, the evolution of the electronic structure in k-space in the form of Fermi arcs with varying degree of doping can be studied. This type of experiments is believed to clarify whether the pseudogap phase may be regarded as a state of incoherent d-wave superconductivity. In the strongly underdoped regime, the experimental results reveal ungapped Fermi arcs, a gap of a phase-incoherent superconductor and local symmetry-breaking excitations that are the same in the superconducting and pseudogap regime. The final two sections deal with observing symmetry-broken electronic states in the pseudogap regime. The simultaneous observation of two different broken symmetries in the form of nematic and smectic fluctuations allows to study their interactions. In spite of all this new information on local details of the electronic structure, the relation between the pseudogap phase and the superconducting phase are admitted to be not yet understood. There is no doubt, however, that the two phenomena are linked in some way. This type of

studies also reveals a characteristic difference between the electronic structures in the under and overdoped regime, respectively. The question of what is causing this transition is also still unanswered.

5 Point-Contact Spectroscopy

Although physically and technically quite different, point-contact spectroscopy (PCS) has at least one similarity with the above-mentioned STM technique. Both methods basically involve a transfer of electronic quasiparticles from one electrode to another. As it is explained in the introduction of this chapter, PCS is an extension of early experiments which employed point contacts for locally studying electron trajectories in a metal which is exposed to an external magnetic field.

In this chapter, Guy Deutscher concentrates on the use of PCS between a sharply pointed normal electrode and a laterally extended superconducting electrode. In the introduction he emphasizes the pros and cons of the method with respect to electron-tunneling methods, including scanning-tunneling techniques. Concerning the physical realization of PC, its concept invented by Sharvin and the parameters that govern the electronic transport through such a contact are discussed. The dominating factor is the Sharvin resistance which depends on the lateral extension d of the contact and the electron mean-free path in the electrode. Although simple in concept, various sources of complications in real contacts have to be considered. These include scattering effects if the mean-free path is smaller or similar in length as the contact diameter, which may lead to a local heating of the contact. Similar heating effects due to exceeding critical velocities determined by parameters of the probed superconductor may falsify the observed properties. At any rate, the most reliable results using PCS are obtained at low temperatures. An important parameter is the effective transparency coefficient of the contact, crucial in the determination of the contact size. A short review of practical realizations of PCs is presented in the next section. The controlled fabrication of a contact of desired quality is still a major problem. In so-called break junctions, both electrodes are of the same material, thus eliminating the usually unknown mismatch of the Fermi velocities between both sides of the junction.

The interpretation of PCS data on conventional superconductors is usually based on the theory of Blonder, Tinkham and Klapwijk (BTK) and a short overview on this approach is given in the next section and various aspects that have to be considered in practice are discussed. Next it is explained how extensions of the BTK theory in connection with the phase sensitivity can be used to establish the order parameter symmetry, an important aspect in connection with studies of unconventional superconductors for which the gap configuration exhibits nodes.

The well-known quasiparticle reflection effects at the contact interface, in particular the Andreev-Saint James reflections under special circumstances, are the topic of the next section. In it, the importance of retardation effects which open the possibility to evaluate the effective masses of quasiparticles in metals with very

strong correlations, is emphasized. In order to demonstrate how this approach can be used in the fitting procedure of conductance data, typical examples of superconductors with different causes of mass enhancement are discussed in detail. These include Nb, MgB_2, high-T_c Copper-oxide, and Fe-pnictide superconductors as well as intermetallics with moderate and strong enhancements of the quasiparticles' masses. It is concluded that effective masses due to strong correlations established in this way are in very good agreement with values that have been obtained from data that were acquired with other experimental techniques. Quite remarkably, the method also allows for a relatively easy access to determine the electron–phonon mass enhancement in conventional superconductors.

A brief account on some PCS data obtained with contacts between an inhomogeneously magnetic material and a conventional superconductor is given in the short final section.

6 Quantum Oscillation Measurements

Studies of the electronic structure of metals via measurements employing the de Haas-van Alphen (dHvA) effect and other magneto-oscillatory techniques had their first high in the 1960s and early 1970s of the last century. With the growing interest in metals with strongly correlated electrons, the corresponding methods experienced a revival and new experimental data revealed detailed insights into the behavior of such systems which are not accessible by other means.

After describing some of the advantages but also limits of employing this type of probing the electronic structure in comparison with other experimental methods, Stephen Julian gives a brief but fairly complete account of the theoretical basis of the dHvA effect, starting from the Landau quantization and a derivation of the Onsager relation for a cylindrical Fermi surface (FS) which relates the frequencies of the observed quantum oscillations with, in this case only one, extremal cross-sections of the FS. What follows are descriptions of various aspects that have to be considered when interpreting the recorded data. First, the influence of temperature and scattering on the amplitude of the quantum oscillations is discussed. It is recalled that while band-structure calculations employing the local density approximation (LDA) are adequate to predict the topology of FS, they usually underestimate the correlation effects which, to a large extent, determine the effective masses of the electronic quasiparticles. Julian's discussion of the influence of many-body effects on the Landau levels is original and clear. The resulting amplitude damping factors due to nonzero temperature and quasiparticle scattering at impurities can be used to obtain information on the effective mass and the mean-free path of the quasiparticles. The spin damping factor arises from the magnetic field-induced splitting of the FS into a spin-up and a spin-down part. It turns out that probing these split parts in strongly correlated systems reveals different amplitudes for each part. This difference can be traced back to spin dependent effective masses reflecting the electron-electron interactions. Mapping 3D Fermi surfaces requires

measurements of the angular dependence of the oscillations by varying the angle between the crystal orientation with respect to the direction of the applied magnetic field. Julian's description of how this is done in principle, is followed by a brief presentation of the Lifshitz-Kosevitch equation which governs the oscillatory magnetisation of common metals. Julian ends this section with number of comments on how this basic equation needs to be modified if strong correlations have to be taken into account.

Very helpful for prospective users is the section in which it is explained how measurements of the dHvA effect can actually be done. It includes the description and possible realization of measurements involving either the field modulation technique or using torque magnetometry. Briefly mentioned are measurements of all the other physical properties that are affected by the Landau quantisation of the energy levels of the itinerant quasiparticles, and therefore exhibit magneto-oscillatory behaviour. The section ends with a comparison of DC- versus pulsed-field applications and a short discussion on the information that can be gained from a detailed analysis of the dHvA signals.

These preparatory parts are complemented with an extensive case study on the compound Sr_2RuO_4 whose electronic subsystem is clearly influenced by strong correlation effects and exhibits unconventional superconductivity. It is shown that the topology and size of the Fermi surface obtained from the dHvA data is in very good agreement with those predicted by band-structure calculations. It is pointed out, however, that the dHvA analysis provides much more details concerning the form of the different FS parts as well as, from the temperature dependence of the oscillation amplitudes, the effective masses and their anisotropies. Finally, it is shown how the parameters obtained from the dHvA investigations can be tested with respect to their compatibility with measured bulk properties. It turns out that the correct, often not straightforward, analyses of the data and their combination provide very satisfactory results in this respect. This confirms that experimental methods under the heading of this chapter are particularly well suited to enhance the understanding of correlation effects in metals.

7 Pressure Probes

External pressure, often relatively moderate in magnitude, has been shown to be one of the versatile control parameters for studies of physical properties of materials that are dominated by correlation effects. Many examples of pressure-induced quantum phase transitions (QPT) are described in the literature. It is therefore quite natural that one chapter in this series, authored by Michael Nicklas, is devoted to an overview of currently employed methods for pressure generation and of experimental techniques to perform measurements of different physical properties under impeding conditions, including very low temperatures.

Pressure generation is the first topic that is addressed. First, two types of pressure cells are considered and described in some detail; piston-cylinder type and opposed

anvil type. The performance of these cells with respect to achieved pressures depends on the choice of materials for the different components of the cells. In many cases, very low magnetic susceptibilities of the chosen materials are required, which usually limits their mechanical strength. With piston-cylinder cells, pressures of 3–4 GPa have been achieved. For higher pressures, anvil-type cells are required; the highest static pressures, up to 30 GPa are achieved with diamond anvils. Other forms of pressure cells, including the indenter-type configuration, and solutions for contacting samples inside the cell with electrical leads are briefly discussed at the end of the same section.

The distribution of pressure within the cell's sample volume, i.e., hydrostatic or anisotropic, depends on the choice of the pressure-transmitting medium. Once the pressure is generated, its value needs to be measured independently under the conditions of the primary measurement, often at low temperatures. These two aspects are discussed in a subsequent section.

Very informative is the next section where it is shown that a wealth of different physical properties can in principle be measured under external pressure, although often only with difficulties and by taking into account a number of complications. For obvious reasons, thermal properties, where measuring constant small temperature differences is an important part of the experiment, are notoriously difficult to determine with accuracies that are achieved under ambient conditions. Nevertheless, possible ways to resolve the experimental difficulties for measurements of thermal conductivity, thermopower, specific heat and thermal expansion are discussed. Equally difficult are experiments probing magnetostriction. More feasible are measurements where monitoring an induction signal with a simple coil is the essential part of the experiment. This is the case for measurements of magnetic susceptibilities, magnetizations and de Haas-van Alphen oscillations, as well as resonance experiments such as NMR and ESR. Also experiments involving particle beams at large facilities, such as muon spin rotation/resonance and neutron scattering are routinely done for probing samples under pressure. For optical experiments where access of visible light to and from the sample is required, the use of diamond anvil cells is inevitable.

The chapter ends with a presentation of examples where pressure tuning of metals with strong electron correlations leads to phase transitions of various kinds. Well documented are the examples of 122 Ce compounds such as $CeCu_2Si_2$, $CeCu_2Ge_2$ and other $CeTM_2Si_2$ compounds as well as $CeIn_3$. For all of them, antiferromagnetic and superconducting phases are the competing ground states. More recent are the observations of pressure-induced phase changes in compounds of the type $CeTMIn_5$.

8 Neutron Scattering

As Igor Zaliznyak and John Tranquada point out, magnetic phenomena in solids are the result of correlation effects and different varieties of neutron-scattering techniques are the experimental tool of choice for investigating magnetic correlations in

condensed matter. In the introduction, they mention a few pros and cons for using these methods and they provide useful references to existing literature that cover the topic in more detail.

They continue with describing the basic properties of the neutron as a particle and briefly summarize the use of different energy scales for practical purposes. Using neutrons for scattering experiments of course requires that they are available in sufficient quantities and the authors offer a brief account on existing reactor-based and spallation-type neutron sources, including their performance characteristics.

Next they discuss the two fundamental scattering processes of neutrons in matter, namely the nuclear and the magnetic scattering which both are exploited in different scattering techniques. They then explain the notions of the scattering lengths and cross-sections relevant in neutron-scattering experiments. Subsequently, two subsections deal with nuclear scattering in more detail. The authors distinguish between nuclear scattering in condensed matter per se and in condensed matter in crystalline form. For the first case, they present the energy versus momentum dispersion curve of superfluid ^4He as a prime example of the usefulness of neutrons for studying elementary excitations in quantum-dominated systems. In the section on nuclear scattering in crystalline matter, aspects of experimentally establishing atomic order and the energy-momentum relations of lattice excitations are briefly discussed.

The context of correlations in solids the magnetic interactions of neutrons with magnetic moments due to electron's spins and orbital motion are of primary interest. First the authors stress the importance of the detailed-balance constraint and the fluctuation–dissipation theorem in interpreting corresponding neutron-scattering experiments. Static magnetization can be accessed by elastic neutron scattering while information on its motion may be obtained from inelastic scattering. The subsequent sections deal with magnetic Bragg peaks indicating magnetic order, the magnetic form factor and spin correlations, spin waves and anisotropy effects.

The content of the sections explaining the theoretical background for performing and analyzing neutron-scattering experiments prepare for a brief review of results on structural and magnetic properties of cuprate superconductors obtained by employing neutron-scattering techniques in the concluding section of the chapter.

9 Muon Spin Relaxation (μSR) Studies

In the first section of this chapter, Yasutomo Uemura briefly describes the particle-physics history of muons and their importance in the experimental verification of parity violation in weak interactions. He continues by explaining the very basic principles of μ^+SR experiments, based on implanting positively charged muons μ^+ into a specimen and monitoring the time evolution of their spin polarization via observing the ejection direction of the positrons that result from the decay of the muons. Also mentioned are the most versatile external-field configurations that are

employed for extracting different informations on the internal field distributions at the sites adopted by the muons at the time of their decay into positrons.

In the second section, the role of μ^+SR in investigations of magnetic phase diagrams of unconventional superconductors is described. Examples of the interplay between magnetic order and superconductivity are presented for different families of superconductors, such as heavy-fermion and Cu–O compounds, organic materials, and fullerides as well as Fe-based chalcogenides.

Since μ^+SR is a very sensitive probe for detecting small internal magnetic fields, it has been employed in searches for time-reversal-symmetry (TRS)-breaking phases in unconventional superconductors. Following the early cases of corresponding evidence in U-based heavy-fermion superconductors, other materials were investigated in this respect. The phenomenon of TRS has been reported to occur in the superconducting state of Sr_2RuO_4 and filled skutterudites. The corresponding evidence for TRS is much less convincing, however, in data obtained from studies of cuprate superconductors in the pseudogap regime.

Early experiments to determine the penetration depth λ of magnetic fields of cuprate superconductors were made by employing the μSR technique. Section IV is a summary of such efforts to provide evidence for unconventional pairing in the superconducting state of cuprate superconductors by measuring the temperature dependence of λ and comparing it with corresponding theoretical predictions. Based on the fact that the value of λ at low temperatures is related to the pair density n_s, it was established that the critical temperature T_c of cuprate superconductors is, quite generally, controlled by *ns* such that T_c varies linearly with n_s. Section V describes how from n_s, an effective Fermi energy in the excitation spectrum can be extracted and be compared with trends in the variation of T_c in cuprate- and other types of superconductors.

The following sections VI, VII, and VIII cover a wide range of efforts, not necessarily based on μSR experiments, to establish correlations between different key parameters that might determine the critical temperature of superconductors. In particular, efforts to clarify the interrelation between antiferromagnetic order and superconductivity, often competing phases in unconventional superconductors, are described and illustrated. Phase boundaries and the physical properties in their vicinity are discussed. The last section is a brief outlook into the future with some ideas for future investigations of unconventional superconductors, including a comprehensive understanding of the driving mechanisms that induce these unusual condensates of charge carriers.

10 Optical Properties

This chapter, authored by Dirk van der Marel, offers a step-by-step introduction to the field of optical conductivity of correlated electrons. He focusses on the theoretical background for treating many-body effects influencing the optical

conductivity of interacting electrons, including the methodology of corresponding measurements and their analyses. For introductions to experimental optical techniques, he refers to the existing literature.

He starts with describing general aspects of the two commonly used experimental configurations for measuring optical parameters of matter, i.e., the reflection of electromagnetic waves at the interface between the vacuum and the probed substance, or the transmission through a sample under investigation. The discussion is based on Maxwell's equations and their solutions invoking macroscopic parameters of the investigated material. It focusses on the influence of the interface on the incoming and reflected radiation; the transmission process through the sample is not treated.

After introducing the basic relations between current and electric field, in this case the optical conductivity $\sigma(\mathbf{k}, \omega)$, the terms longitudinal and transverse dielectric function are explained. Next, the quantum description of the electrodynamics of electrons in a crystal lattice is outlined and the relevant Hamilton operators are introduced. In order to calculate the linear response of the current density to the electric field, the vector potential $\mathbf{A}$ needs to be invoked. Due to the noncommuting operators, the calculation is complicated and is explained in detail in three subsections. It is shown that the optical conductivity is given by two contributions. The diamagnetic part $\sigma^d(q, \omega)$, reflecting the response of a plasma of freely moving electrons, is complemented by the so-called regular part $\sigma^1(q, \omega)$ which is the response of the interacting electrons confined in the potential exerted by the crystal lattice and is proportional to the current-current correlation function. In the subsequent section it is shown how to calculate the response for a system with defined many-body states. Explicit results are compared with experimental data for a series of Si-based compounds that exhibit correlation effects in their physical properties. At the end of this section, the Drude-Lorentz concept of ascribing the response to a combined action of independent oscillators which represent the principal optical transitions is introduced. In practice, this approach is successfully used to fit experimental data, even for multi-component materials such as high-T_c cuprates.

In the final section, the significance of spectral weight sum rules in many-body physics is emphasized. Spectral weights are again divided into two parts, a diamagnetic part W^d and a regular part W^r. It turns out that after integration over frequencies, $W^r\ (q) = 1$. In addition, the delta functions in W^d and W^r cancel exactly for normal metals but not for superconductors. Of particular practical importance is the so-called F-sum rule which relates the integrated optical conductivity to the density of charged particles and the ratio of their charges and effective mass. In a rather detailed discussion of the regular part of $\sigma(q)$, the author concludes that new experimental techniques for probing $\sigma(q \neq 0)$ can provide information on the integrated spectral weight at nonzero frequencies and hence the free-carrier optical-response intensity of correlated electrons.

11 Summary

It turns out that establishing the physical properties of materials which are dominated by correlation effects requires the application of many different experimental techniques and methods, often under extreme conditions such as very low temperatures as well as high magnetic fields or pressure. The content of this volume covers a major part of such endeavors. Prominently represented are spectroscopic techniques and local probes. Unfortunately, experiments probing thermal and transport properties are much less well represented. This is particularly regretful because many new aspects or phenomena are actually discovered by measurements probing the bulk of the material of interest.

References

1. H. Kamerlingh-Onnes, Commun. Leiden 122b and 124c (1911)
2. W. de Haas, J. de Boer, G. van den Berg, Phys. **1**, 1115 (1933)
3. J. Franck, F. Manchester, D. Martin, Proc. Roy. Soc. (London) A**263**, 494 (1961)
4. F. Bloch, Z. Phys. **57**, 545 (1929)
5. W. Heitler, F. London, Z. Phys. **44**, 455 (1927)
6. F. Bloch, Z. Phys. **52**, 553 (1928)
7. N. Mott, Proc. Phys. Soc. A **62**, 416 (1949)
8. J. Friedel, Can. J. Phys. **34**, 1190 (1956)
9. A. Blandin, J. Friedel, J. Phys. Radium **19**, 573 (1958)
10. N. Bloembergen, T. Rowland, Acta Metall. **1**, 731 (1953)
11. M. Rudermann, C. Kittel, Phys. Rev. **96**, 99 (1954)
12. T. Kasuya, Progr. Theoret. Phys. **16**, 58 (1956)
13. K. Yosida, Phys. Rev. **107**, 396 (1957)
14. B. Matthias et al., Phys. Rev. Lett. **5**, 542 (1960)
15. A. Clogstonet al., Phys. Rev. **125**, 541 (1962)
16. P. Anderson, Phys. Rev. **124**, 41 (1961)
17. B. Matthias, H. Suhl, E. Corenzwit, Phys. Rev. Lett. **1**, 92 (1958)
18. A. Abrikosov, L. Gorkov, Zh. Eksp. Teor. Fiz. **39**, 1781 (1960)
19. J. Bardeen, L. Cooper, J. Schrieffer, Phys. Rev. **108**, 1175 (1957)
20. J. Hubbard, Proc Roy. Soc. A **276**, 238 (1963)
21. J. Kondo, Progr. Theoret. Phys. (Kyoto) **32**, 37 (1964)
22. D. Wohlleben, B. Coles, *Magnetism* (Academic Press, New York, 1973)
23. H.R. Ott, J. Kjems, F. Hulliger, Phys. Rev. Lett. **42**, 1378 (1979)
24. K. Andres, J. Graebner, H.R. Ott, Phys. Rev. Lett. **35**, 1779 (1975)
25. L. Landau, Zh. Eksp. Teor. Fiz. **30**, 1058 (1956)
26. S. Doniach, Physica B **91**, 231 (1977)
27. R. Takke et al., Z. Phys. B **44**, 33 (1981)
28. N. Mathur et al., Nature **394**, 39 (1998)
29. F. Steglich et al., Phys. Rev. Lett. **43**, 1892 (1979)
30. H.R. Ott et al., Phys. Rev. Lett. **52**, 1915 (1984)
31. J. Bednorz, K. Muller, Z. Phys. B **64**, 189 (1986)
32. A. Schilling et al., Nature (London) **363**, 56 (1993)
33. D.V. Harlingen, Rev. Mod. Phys. **67**, 515 (1995)
34. C. Tsuei, J. Kirtley, Rev. Mod. Phys. **72**, 969 (2000)

35. J. Campuzano et al., *The Gap Symmetry and Fluctuations in high-Tc Superconductors, NATO-ASI, Series B,* vol. 371, (Plenum, New York, 1998), p.229
36. A. Damascelli, Z. Hussain, Z. Shen, Rev. Mod. Phys. **75**, 473 (2003)
37. G. Zaccaï, B. Jacrot, Ann. Rev. Biophys. Bioeng. **12**, 139 (1983)
38. V. Geshkenbein, (World Scientific, Singapore, 1998)
39. Ø. Fischer et al., Rev. Mod. Phys. **79**, 354 (2007)
40. T. Rice, in *The Los Alamos Symposium 1993*, ed. by K. Bedell, Z. Wang, D. Meltzer, A. Balatsky, E. Abrahams. *The Los Alamos Symposium 1993* (Addison-Wesley, Reading 1994, 1993), p. 494
41. P. Anderson, Mat. Res. Bull **8**, 153 (1973)
42. H. Fukuyamam, S. Maekawa, A. Malozemoff, *Strong Correlations and Superconductivity, Springer Series in Solid-State Sciences*, vol. 89 (Springer, Berlin, 1989)
43. P. Anderson, Phys. Rev. Lett. **67**, 2092 (1991)
44. M. Imada, A. Fujimori, Y. Tokura, Rev. Mod. Phys. **70**, 1039 (1998)
45. M. Norman et al., Nature (London) **392**, 157 (1998)
46. N. Doiron-Leyraud et al., Nature **447**, 565 (2007)
47. B. Andraka, A. Tsvelik, Phys. Rev. Lett. **67**, 2886 (1991)
48. H.V. Löhneysen et al., Rev. Mod. Phys. **79**, 1015 (2007)
49. S. Sachdev, *Quantum Phase Transitions* (Cambridge University Press, New York, 1999)
50. A. Hewat, in *NATO ASI*, *Series E*, vol. 263, ed. by E. Kaldis (Kluwer Academic Publishers, Dordrecht, 1994), p. 17
51. M. Marezio, C. Chaillout, *Materials and Crystallographic Aspects of HTcsuperconductivity, NATO ASI series 263* (Kluwer Academic, Dordrecht, 1994), p. 3
52. E. Ising, Z. Phys. **31**, 253 (1925)
53. W. Heisenberg, Z. Phys. **49**, 619 (1928)
54. H. Bethe, Z. Phys. **71**, 205 (1931)
55. L. Onsager, Phys. Rev. **65**, 117 (1944)
56. R. Griffth, Phys. Rev. **136**, 437 (1964)
57. N. Mermin, H. Wagner, Phys. Rev. Lett. **17**, 1133 (1966)
58. F. Bloch, Helv. Phys. Acta 7, **385** (1934)
59. S. Tomonaga, Progr. Theor. Phys. **5**, 544 (1950)
60. J. Luttinger, J. Math. Phys. **4**, 1154 (1963)
61. F. Haldane, J. Phys. C: Solid State Phys. **14**, 2585 (1981)
62. I. Affleck, J. Phys.: Condens. Matter **1**, 3047 (1989)
63. L. Fadeev, L. Takhtajan, Phys. Lett. A **85**, 375 (1981)
64. F. Haldane, Phys. Lett. A **93**, 464 (1983)
65. I. Affleck et al., Phys. Rev. Lett. **59**, 799 (1987)
66. E. Batyev, L. Braginski, Sov. Phys. JETP **60**, 781 (1984)
67. T. Giamarchi, A. Tsvelik, Phys. Rev. B **59**, 11398 (1999)
68. K. Schönhammer, in *Strong Interactions in Low Dimensions*, vol. 25, ed. by D. Baeriswyl, L. Degiorgi (Kluwer Academic Publishers, Dordrecht, 2004), p. 93
69. D. Jerome, H. Schulz, Adv. Phys. **31**, 299 (1982)
70. D. Jerome, in *Superconductivity in New Materials*, vol. 4, ed. by Z. Fisk, H. Ott (Elsevier, Amsterdam, 2011), p. 149
71. T. Giamarchi, *Quantum Physics in One Dimension* (Oxford University Press, 2003)
72. T. Giamarchi, C. Rüegg, O. Tchernyshyov, Nat. phys. **4**, 198 (2008)
73. A. Avella, F. Mancini, *Strongly Correlated Systems: Theoretical Methods*, *Springer Series in Solid-State Sciences*, vol. 171 (Springer, Berlin, Heidelberg, 2012). doi:10.1007/978-3-642-21831-6
74. A. Avella, F. Mancini, *Strongly Correlated Systems: Numerical Methods*, *Springer Series in Solid-State Sciences*, vol. 176 (Springer, Berlin, Heidelberg, 2013). doi:10.1007/978-3-642-35106-8

Chapter 1
Nuclear Magnetic Resonance as a Probe of Strongly Correlated Electron Systems

Nicholas J. Curro

Abstract Beginning with the pioneering NMR experiments of Hebel and Slichter in superconducting Aluminum, nuclear magnetic resonance (NMR) has played a central role in the study of strongly correlated electron matter. The relatively small energies associated with the nuclear spin degrees of freedom guarantee that the experimental probes of the nuclear spin behavior have little or no effect on the electronic degrees of freedom. On the other hand, the hyperfine coupling between the electronic and nuclear spins enables one to probe the static and dynamic properties of the electron spins through their effect on the nuclei. NMR offers detailed microscopic information about homogeneity, dynamics, and novel phases of electron matter and can probe under extreme conditions of high magnetic field, ultra low temperature, and high pressures. This chapter discusses the basics of NMR in condensed matter solids, including basic measurements such as the Knight shift, the hyperfine field, and the relaxation rates. To illustrate these concepts we discuss the case of field-induced antiferromagnetism and the exotic superconducting phase in $CeCoIn_5$.

1.1 Basics of Nuclear Magnetic Resonance

1.1.1 NMR Spectra

The energy of a nuclear magnetic moment in a magnetic field is given by the Zeeman Hamiltonian:

$$\begin{aligned}\mathcal{H}_Z &= \boldsymbol{\mu} \cdot \boldsymbol{H}_0 \\ &= \gamma\hbar \hat{\boldsymbol{I}} \cdot \boldsymbol{H}_0 \\ &= \hbar\omega_L \hat{I}_z,\end{aligned} \tag{1.1}$$

N.J. Curro (✉)
Department of Physics, University of California, Davis, CA 95616, USA
e-mail: curro@physics.ucdavis.edu

A. Avella and F. Mancini (eds.), *Strongly Correlated Systems*,
Springer Series in Solid-State Sciences 180, DOI 10.1007/978-3-662-44133-6_1

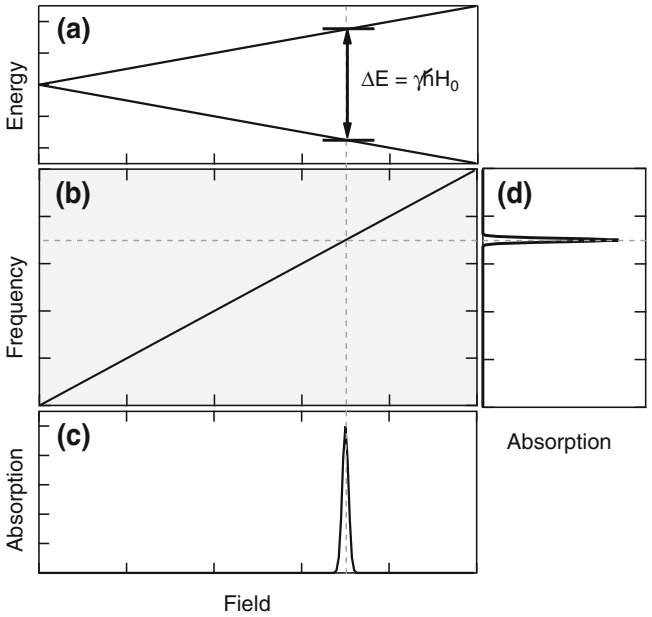

Fig. 1.1 **a** Energy levels for a spin $\frac{1}{2}$ in a magnetic field, **b** resonance frequency versus field, **c** field-swept spectrum at constant frequency, and **d** frequency-swept spectrum at constant field

where γ is the gyromagnetic ratio, $\hbar$ is Planck's constant, $\hat{\boldsymbol{I}} = \hat{I}_x\hat{x} + \hat{I}_y\hat{y} + \hat{I}_z\hat{z}$ is the nuclear spin operator, $\boldsymbol{H}_0 = H_0\hat{z}$ is the magnetic field and $\omega_L = \gamma H_0$ is the Larmor frequency. For a spin $I = \frac{1}{2}$ nucleus we have:

$$\mathcal{H}_Z = \begin{pmatrix} \frac{\hbar\omega_L}{2} & 0 \\ 0 & -\frac{\hbar\omega_L}{2} \end{pmatrix} \tag{1.2}$$

The solution of this equation is straightforward: the eigenstates are $|\phi_m\rangle = |m\rangle$ with energy $E_m = \hbar\omega_L m$, where $m = \pm\frac{1}{2}$ and the splitting is $\Delta E = \hbar\omega_L$. The energy levels are shown in Fig. 1.1 as a function of magnetic field. There is a single resonance at the Larmor frequency. For higher spin nuclei there are $2I$ separate resonances, and depending on other terms in the Hamiltonian there can be considerable more structure in the spectra.

Nuclei transition between levels by absorbing or emitting a photon of energy $\hbar\omega_L$. In a typical NMR experiment, an ensemble of $\sim 10^{23}$ nuclei is located in a tuned radiofrequency coil that generates an electromagnetic field oscillating at the Larmor frequency, and power will be transferred between the nuclear spin system and the electromagnetic field. The spectrum is a measure of the absorbed power as a function of either the field, H_0, or the frequency, ω, of the resonant circuit. Both approaches

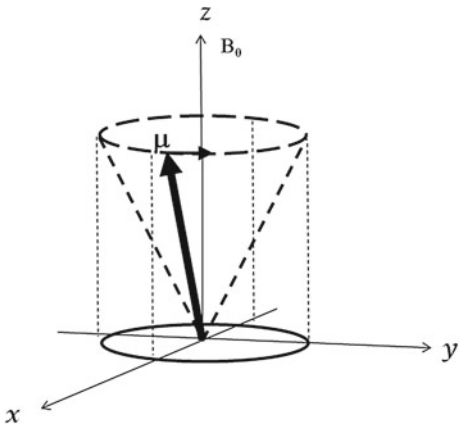

Fig. 1.2 Precession of a magnetic moment, $\boldsymbol{M}$ around a magnetic field, $\boldsymbol{H}_0$ oriented along the z-axis. The precession frequency is given by $\omega_L = \gamma H_0$, where γ is the gyromagnetic ratio

are complementary, and correspond to cuts across the frequency-field diagram in Fig. 1.1 along the vertical and horizontal axes, respectively. The absorption of power can be measured by detecting the response of a resonant circuit, such as a change in the quality factor of the resonance. Alternatively, the nuclei can be perturbed by resonant pulses of radiofrequency fields, and their response observed as a function of either field or frequency. This latter approach forms the basis of modern pulsed NMR and requires a detailed understanding of the time dependent response of the quantum mechanical system.

1.1.2 Density Matrix Solution

The wavefunction of the Hamiltonian in (1.2) is given by:

$$|\psi\rangle = ae^{i\omega_L t/2}|\uparrow\rangle + be^{-i(\omega_L t/2+\phi)}|\downarrow\rangle, \tag{1.3}$$

where the real constants a, b, and the phase factor ϕ depend on the initial conditions. Alternatively the solution can be expressed in terms of the density matrix:

$$\rho = \begin{pmatrix} a^2 & abe^{i(\omega_L t+\phi)} \\ abe^{-i(\omega_L t+\phi)} & b^2 \end{pmatrix}. \tag{1.4}$$

The diagonal elements are time independent and the off-diagonal elements oscillate at the Larmor frequency. The expectation values of the nuclear magnetization $\langle M_\alpha \rangle = \gamma\hbar \mathrm{Tr}[\rho(t)\hat{I}_\alpha]$ are given by:

$$\langle I_x \rangle = ab\cos(\omega_L t + \phi) \tag{1.5}$$

$$\langle I_y \rangle = ab\sin(\omega_L t + \phi) \tag{1.6}$$

$$\langle I_z \rangle = \frac{1}{2}(a^2 - b^2). \tag{1.7}$$

These equations describe the magnetization vector $\langle \boldsymbol{M} \rangle$ precessing around the magnetic field $\boldsymbol{H}_0$ at frequency ω_L (Fig. 1.2). Of course, if we start the system off in an eigenstate of $\mathcal{H}_Z$, then either a or b is zero, $\langle I_x \rangle = \langle I_y \rangle = 0$, and there is no time dependence of the expectation value. In order for the spins to precess, they must be in a superposition of the eigenstates of $\mathcal{H}_Z$.

1.1.2.1 Statistical Ensemble

The density matrix (1.4) is valid for a single spin-$\frac{1}{2}$ in a magnetic field. In real solids, there are $N \sim 10^{23}$ nuclei, each with it's own phase, ϕ_j. The Hilbert space has dimensions of $(2I+1)^N \times (2I+1)^N$, which is intractable for anything more than a few spins. However, it turns out that for most cases of interest we can treat the spins as independent particles. Of course, the nuclei do interact with both the surrounding electrons and with one another, but these interactions are small compared with the Zeeman interaction and can be introduced perturbatively. In practice this is a very good assumption, since the nuclei in a solid sit far apart from one another (the typical spacing between nuclei in a solid is $\sim 10^{-10}$ m, whereas the nuclei have radii $\sim 10^{-15}$ m). On the other hand, it is exactly these interactions both with one another and their environment that renders magnetic resonance such a powerful technique to probe the behavior of solids.

For N independent spins the density matrix has the form:

$$\hat{\rho}_N = \begin{pmatrix} a_1^2 & a_1 b_1 f(t) e^{i\phi_1} & \cdots & 0 & 0 \\ a_1 b_1 f(t) e^{i\phi_1} & b_1^2 & \cdots & 0 & 0 \\ \vdots & \vdots & \ddots & \vdots & \vdots \\ 0 & 0 & \cdots & a_N^2 & a_N b_N f(t) e^{i\phi_N} \\ 0 & 0 & \cdots & a_N b_N f(t) e^{i\phi_N} & b_N^2 \end{pmatrix}, \tag{1.8}$$

where $f(t) = e^{i\omega_L t}$. The statistical ensemble density matrix is obtained by a partial trace over the N degrees of freedom:

$$\langle \hat{\rho} \rangle = \begin{pmatrix} \langle a^2 \rangle & \langle ab \rangle e^{i\omega_L t} \sum_N e^{-i\phi_j}/N \\ \langle ab \rangle e^{-i\omega_L t} \sum_N e^{i\phi_j}/N & \langle b^2 \rangle \end{pmatrix}, \tag{1.9}$$

where $\langle a^2 \rangle = \frac{1}{N}\sum_n^N a_n^2$, $\langle b^2 \rangle = \frac{1}{N}\sum_n^N b_n^2$, and $\langle ab \rangle = \frac{1}{N}\sum_n^N a_n b_n$. In equilibrium each spin will have a different phase and these phases will be uncorrelated, thus the average of the phase factors $e^{i\phi_j}$ vanishes:

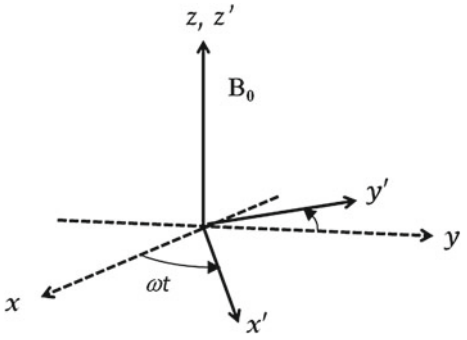

Fig. 1.3 The rotating frame rotates around the z-axis at angular frequency ω

$$\lim_{N\to\infty} \frac{1}{N} \sum_{j=1}^{N} e^{i\phi_j} = 0. \tag{1.10}$$

The off-diagonal matrix elements of the ensemble average density matrix, $\langle\rho\rangle$, are zero in thermal equilibrium. If the system is disturbed from thermal equilibrium (for example by pulsed NMR techniques), then these off-diagonal elements become finite and time dependent. The diagonal elements $\langle a^2\rangle$ and $\langle b^2\rangle$ for the ensemble average are simply the statistical probabilities of finding the spin in either the up or down state: $\langle a^2\rangle$, $\langle b^2\rangle = \frac{1}{Z} e^{\pm\beta\hbar\omega_L/2}$, where $\beta = 1/k_B T$, k_B is the Boltzmann constant, T is the temperature, and $Z = e^{-\hbar\omega_L/2k_B T} + e^{-\hbar\omega_L/2k_B T}$ is the partition function. Since $\pm\frac{1}{2}\hbar\omega_L$ are the eigenvalues of $\mathcal{H}_Z$, we can write the thermal equilibrium ensemble average density matrix as:

$$\rho_{EQ} = \frac{1}{Z} e^{-\beta\mathcal{H}_Z}, \tag{1.11}$$

where $\beta = 1/k_B T$. One can then calculate various thermodynamic quantities of interest associated with the nuclei using this formalism, such as the nuclear magnetization, M, the specific heat, C_n, and the magnetic susceptibility, χ_n. It is important to note that there are two types of density matrices: ρ, the density matrix for a single particle, and $\langle\rho\rangle$, the statistical ensemble density matrix for a system of N spins. In most cases we will consider the statistical ensemble average density matrix, drop the bracket notation and simply refer to it as the "density matrix". Care should be taken, however, to not confuse the case for a single spin.

1.1.2.2 The Rotating Frame

Modern NMR spectrometers detect the coherent precession of an ensemble of nuclear spins, which give rise to a time dependent magnetization that couples to the NMR circuit. In this case, the ensemble average density matrix is not in equilibrium, and off-diagonal elements are created by radiofrequency pulses. During such a

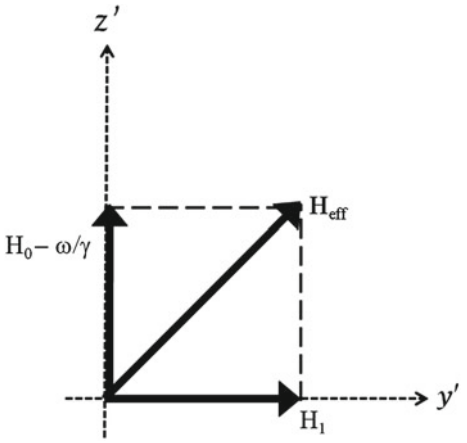

Fig. 1.4 In the rotating frame, the moments precess around the effective field, $\boldsymbol{H}_{\text{eff}}$, which lies perpendicular to $\boldsymbol{H}_0$ when the irradiation frequency, ω is equal to the Larmor frequency, $\omega_L = \gamma H_0$

pulse, the Hamiltonian becomes: $\mathcal{H} = \gamma\hbar[\hat{I}_z B_0 + \hat{I}_y H_1 \cos(\omega t)]$, where $\boldsymbol{H}_1$ is the radiofrequency field generated by the solenoid oscillating at ω along the coil direction (taken here to lie along $\hat{y}$) perpendicular to the external field $\boldsymbol{H}_0$. Typically $H_1 \sim 10 - 100\,\text{Oe}$, whereas $H_0 \sim 10 - 100\,\text{kOe}$. In order to solve for the time dependence of the magnetization, it is useful to transform to the rotating frame, which is equivalent to the interaction picture (see Fig. 1.3). In the rotating frame, the state vector, Hamiltonian, and density matrix transform as:

$$|\psi\rangle_R = \hat{U}|\psi\rangle \tag{1.12}$$

$$\mathcal{H}_R = \hat{U}\mathcal{H}\hat{U}^\dagger - i\hbar\frac{\partial \hat{U}}{\partial t}\hat{U}^\dagger \tag{1.13}$$

$$\rho_R = \hat{U}\rho\hat{U}^\dagger, \tag{1.14}$$

where $\hat{U} = e^{i\omega t \hat{I}_z}$, and the subscript R corresponds to the rotating frame. The Hamiltonian can be written as $\mathcal{H}_R = \gamma\hbar H\hat{\boldsymbol{I}} \cdot \boldsymbol{H}_{\text{eff}}$, where $\boldsymbol{H}_{\text{eff}} = (H_0 - \omega/\gamma)\hat{z} + H_1\hat{y}$ is the effective field in the rotating frame (Fig. 1.4). When the rf frequency ω is equal to the natural resonance frequency of the nuclei in the magnetic field, ω_L, then $\boldsymbol{H}_{\text{eff}}$ has no component along the $\hat{z}$ direction—only along $\hat{y}$. In other words, at resonance in the rotating frame the spins process around $\boldsymbol{H}_1$, not $\boldsymbol{H}_0$. By selectively turning pulses on and off along different directions, one can therefore manipulate the spins to point in any direction and create off-diagonal resonances in the density matrix.

The time dependence of $\rho_R(t)$ is given by:

$$i\hbar\frac{\partial \rho_R}{\partial t} = [\mathcal{H}_R, \rho_R], \tag{1.15}$$

and since $\mathcal{H}_R$ is time independent this equation can be solved to give:

$$\rho_R(t) = e^{i\mathcal{H}_R t/\hbar}\rho_R(0)e^{-i\mathcal{H}_R t/\hbar}. \tag{1.16}$$

This expression enables one to calculate the density matrix, and hence the expectation values of the magnetization, following a series of pulses of varying power and duration by realizing that the pulses act as unitary transformations on the density matrix.

Consider, for example, a radiofrequency pulse exactly on resonance ($\omega = \omega_L$) with intensity $H_1 = \Omega_1/\gamma$ for a time $t_p \ll 1/\omega_L$. In this case $\hat{U} = e^{i\Omega_1 t\hat{I}_y}$. Immediately following the pulse the density matrix is given by:

$$\rho(t_p) = e^{i\Omega_1 t_p\hat{I}_y}\rho_R(0)e^{-i\Omega_1 t_p\hat{I}_y}. \tag{1.17}$$

If we assume that we start off in thermal equilibrium, then $\rho_R(0) = \rho(0) = \rho_{\mathrm{EQ}}$. Furthermore, for temperatures $T > \hbar\omega_L/k_B \sim 10^{-6}$ K it is reasonable to use the high temperature approximation:

$$\rho_{\mathrm{EQ}} = \frac{1}{Z}e^{\beta\hat{\mathcal{H}}_Z} \approx \frac{1}{N}\left(\hat{1} + \beta\hbar\omega_L\hat{I}_z + \cdots\right). \tag{1.18}$$

We shall be interested in calculating observables such as $\langle M_z\rangle = \gamma\hbar\mathrm{Tr}\{\hat{\varrho}\hat{I}_z\}$, in which case the first term of this expansion will vanish, and we can safely ignore it. Therefore, in the rotating frame the equilibrium density matrix is identical to that in the laboratory frame:

$$\rho_R(0) = \varepsilon e^{i\omega t\hat{I}_z}\hat{I}_z e^{-i\omega t\hat{I}_z} = \varepsilon\hat{I}_z, \tag{1.19}$$

where $\varepsilon = \beta\hbar\omega_L/N \ll 1$.

In order to determine the effect of the radiofrequency pulse, it is important to consider the effect of the unitary rotation transform $\hat{U}_y = e^{i\theta\hat{I}_y}$ on the operator $\hat{I}_z$. It can be shown that [1]:

$$e^{i\theta\hat{I}_y}\hat{I}_z e^{-i\theta\hat{I}_y} = \hat{I}_z\cos(\theta) - \hat{I}_x\sin(\theta). \tag{1.20}$$

Therefore the density matrix immediately following the pulse is given by:

$$\rho_R(t_p) = \varepsilon\left(\hat{I}_z\cos(\Omega_1 t_p) - \hat{I}_x\sin(\Omega_1 t_p)\right) \tag{1.21}$$

$$= \frac{\varepsilon}{2}\begin{pmatrix} -\cos(\Omega_1 t_p) & \sin(\Omega_1 t_p) \\ \sin(\Omega_1 t_p) & \cos(\Omega_1 t_p)\end{pmatrix}, \tag{1.22}$$

and for times following the pulse in the laboratory frame the density matrix is:

$$\rho(t) = \frac{\varepsilon}{2}\begin{pmatrix} -\cos(\Omega_1 t_p) & \sin(\Omega_1 t_p)e^{i\omega_L t/2} \\ \sin(\Omega_1 t_p)e^{-i\omega_L t/2} & \cos(\Omega_1 t_p)\end{pmatrix}. \tag{1.23}$$

By turning on the H_1 field for a time of length $t_p = \frac{\pi}{2\Omega_1}$ the diagonal elements can be completely converted to *off-diagonal* elements, which then give rise to a time dependent magnetization $\boldsymbol{M}(t)$ precessing perpendicular to $\boldsymbol{H}_0$.

1.1.2.3 Bloch Equations

The effect of a pulse is identical both for an individual spin-1/2 nucleus and an ensemble of independent nuclei. In the latter case, the density matrix describes an ensemble average, and it is important to note that the pulse creates a *coherent* precession of the spins. In other words, all of the nuclei start off with the same phase following the pulse. For $\Omega_1 t_p = \pi/2$ (1.23) describes finite off-diagonal coherence indefinitely. This result cannot be correct, however, since $\rho(t)$ must decay to $\rho_{\rm EQ}$, a *time-independent* result, for sufficiently long times. Eventually all of the precessing spins will lose their coherence and relax back to a time independent equilibrium Boltzmann distribution. These relaxation processes are due to interactions between the spins themselves and with their environment. The *Bloch equations* describe the time dependence of the spins with relaxation by including two phenomenological parameters:

$$\frac{dM_x}{dt} = \gamma(\boldsymbol{M} \times \boldsymbol{H})_x - \frac{M_x}{T_2} \tag{1.24}$$

$$\frac{dM_y}{dt} = \gamma(\boldsymbol{M} \times \boldsymbol{H})_y - \frac{M_y}{T_2} \tag{1.25}$$

$$\frac{dM_z}{dt} = \gamma(\boldsymbol{M} \times \boldsymbol{H})_z - \frac{M_0 - M_z}{T_1}. \tag{1.26}$$

Here $\boldsymbol{M} = \gamma\hbar\langle \boldsymbol{I} \rangle / V$ is the magnetization density, the constant $M_0 = \chi_n H_0$ is the equilibrium magnetization, and $\chi_n = N\gamma^2\hbar^2 I(I+1)/3k_B T$ is the nuclear spin susceptibility. The time constant T_2 is the transverse relaxation, or spin-spin decoherence time, and T_1 is the longitudinal relaxation, or spin-lattice relaxation time. The first terms in the Bloch equations describe precession, and the second set of terms describe relaxation of the spins to equilibrium. T_2 describes the relaxation of the off-diagonal terms in the ensemble average density matrix, and T_1 describes the relaxation of the diagonal terms. The spin-lattice relaxation time is the time scale for the ensemble of spins to acquire thermal equilibrium. The spin-decoherence time, which generally is *not* equivalent to T_1, describes the decay of the off-diagonal terms in the density matrix. Alternatively, if we consider the expectation value $\langle \boldsymbol{M} \rangle = \gamma\hbar {\rm Tr}\{\rho \hat{\boldsymbol{I}}\}$, then T_1 describes the relaxation of the z component of the magnetization and T_2 describes the relaxation of the x- and y-components. Following a pulse along the $\hat{y}$ direction of duration $t_p = \pi/2\Omega_1$, the time dependence of the ensemble average density matrix is given by:

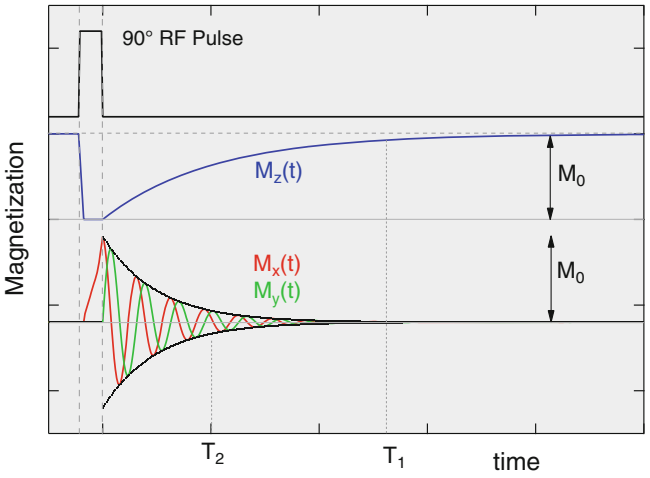

Fig. 1.5 Time dependence of the three components of the nuclear magnetization in the laboratory frame following a 90° radiofrequency pulse in the $y-$direction. In this case, $T_1 \gg T_2$, and $M_0 = \chi_n H_0$ is the equilibrium magnetization

$$\rho(t) = \frac{\varepsilon}{2}\begin{pmatrix} -\left(1 - e^{-t/T_1}\right) & e^{i\omega_L t/2} e^{-t/T_2} \\ e^{-i\omega_L t/2} e^{-t/T_2} & \left(1 - e^{-t/T_1}\right) \end{pmatrix}, \tag{1.27}$$

and the magnetization $\langle \boldsymbol{M} \rangle$ is:

$$\begin{aligned} M_x(t) &= \frac{1}{4}\gamma\hbar\varepsilon e^{-t/T_2}\cos(\omega_L t) \\ M_y(t) &= \frac{1}{4}\gamma\hbar\varepsilon e^{-t/T_2}\sin(\omega_L t) \\ M_z(t) &= \frac{1}{4}\gamma\hbar\varepsilon\left(1 - e^{-t/T_1}\right). \end{aligned} \tag{1.28}$$

These equations are plotted in Fig. 1.5. Note that T_2 describes the decay of the envelope of the transverse magnetization, and over a time scale T_1 the magnetization returns to equilibrium along the z-axis.

1.1.3 Pulse Techniques

The response of the magnetization following a pulse described by (1.28) is known as a Free Induction Decay or FID. The spectrum is given by the complex Fourier transform of the FID,

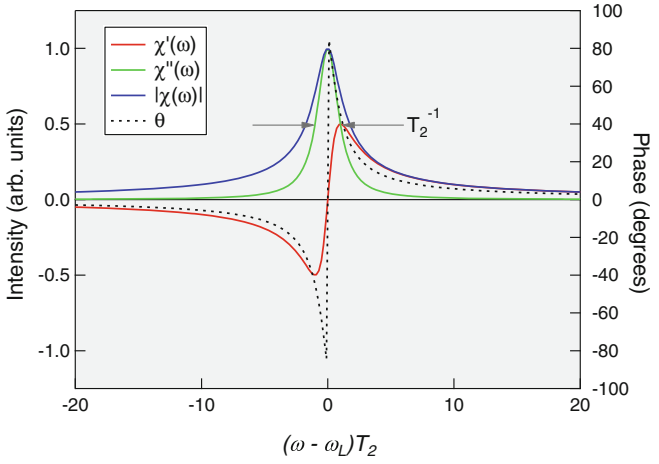

Fig. 1.6 Frequency dependence of the absorptive (*red*) and dispersive (*green*) components of the magnetization. Also shown are the magnitude (*blue*) and phase angle θ. The full width at half maximum of the resonance is given by T_2^{-1}. In a pulsed experiment, these correspond to the magnetization components along the two planar directions, where θ is defined relative to the phase of the original H_1 pulse

$$S(\omega) = \frac{1}{\sqrt{2\pi}} \int_{-\infty}^{\infty} M_+(t) e^{i\omega t} dt, \tag{1.29}$$

where $M_\pm = M_x \pm i M_y$. In this case it is given by:

$$S(\omega) = \frac{M_0}{2\pi} \frac{\omega_L T_2}{1 + i(\omega - \omega_L)T_2}. \tag{1.30}$$

The real and imaginary parts of $S(\omega)$ are the absorptive and dispersive parts of the spectrum, and are shown in Fig. 1.6. The spectrum is centered at ω_L and has a FWHM linewidth of $2T_2^{-1}$. $S(\omega)$ is measured usually by detecting the magnetization in real time and then taking the Fourier transform of the data. The components of the magnetization precessing perpendicular to $\boldsymbol{H}_0$ give rise to a voltage signal $V(t)$ across an NMR coil that is proportional to dM_y/dt. A typical phase sensitive spectrometer splits the detected signal $V(t)$ into two channels, then mixes it with internally generated signal $s_1(t) = s_0 \cos(\omega t)$ and $s_2(t) = s_0 \sin(\omega t)$. After mixing the signals in the two channels become:

$$s_1(t) \sim M_0 \omega_L [\sin((\omega - \omega_L)t) - \sin((\omega + \omega_L)t)] \tag{1.31}$$

$$s_2(t) \sim M_0 \omega_L [-\cos((\omega - \omega_L)t) + \cos((\omega + \omega_L)t)] \tag{1.32}$$

If $\omega \approx \omega_L$ then the first term will oscillate at very low frequency, and the second high frequency component can be eliminated by a low pass filter. Thus $s_1(t) \sim M_y(t)$ and $s_2(t) \sim M_x(t)$ are direct measures of the magnetization in the rotating frame. This is the basic operation of a *homodyne* quadrature receiver, and enables one to measure both the magnitude and phase of the magnetization.

There are several more complex types of receivers. For example a *heterodyne* receiver mixes $V(t)$ down to an intermediate frequency $\omega_I < \omega_L$. At this point, the signal could be passed through a narrow band-pass filter to reduce noise and then mixed down to DC in two channels which can then be digitized. However, modern data acquisition cards can digitize at rates up to several hundred MHz, which enables one to digitize either the intermediate signal at ω_I or even the original signal at ω_L. After digitization at these high frequencies, the signal can then be processed digitally to extract the magnitude and phase independently.

A serious problem with the detection of FIDs is that the voltage signal $V(t)$ in the NMR coil will ring for several time constants following a large rf pulse. Typical rf pulses induce voltages on the order of a hundred volts, whereas the precessing magnetization signal is often only μV in magnitude. Consequently there is a dead time of several ms during which the sensitive low-noise preamplifiers must be turned off in order to avoid saturation of the response. If T_2 is sufficiently short then it is possible that the FID will have decayed before the spectrometer can detect it. Quadrature detection is helpful in this regard because it enables one to vary the phase of the H_1 pulses in such a manner that the transient decay of the pulse ringing in the circuit can be canceled out, thus partially reducing the dead time.

1.1.3.1 Spin Echoes

In 1950, Erwin Hahn discovered a second magnetization signal in an NMR coil at a time $t = 2\tau$ if second 180° pulse is applied at a time τ after the first 90° pulse [2]. An NMR spin-echo arises because the ensemble of precessing spins that dephases during an FID can be refocused, and has the same time dependence as the FID itself. This enables one to detect the signal at a time τ after the end of the second pulse, during which time the voltage ringing can die down.

In order to understand the spin-echo, it is important to understand the origin of the decay of the FID signal. Equation (1.28) implies that the time dependence of the FID decay is determined by the time constant T_2. T_2 was introduced as a phenomenological parameter, but what determines this quantity? The answer depends on details of the measuring equipment and the substance being measured. If the nuclei experience a distribution $P(H_{\rm loc})$ of local magnetic fields, then there will be a distribution $P(\omega_L)$ of precession frequencies. If we assume a normal distribution $P(\omega_L) = \frac{1}{\sqrt{2\pi}\delta} \exp\left[(\omega_L - \omega_L^0)^2/2\delta^2\right]$, then in the time domain the signal is proportional to $e^{-\delta t}\cos(\omega_L^0 t)$. In other words, the measured decay time is $\delta^{-1} \equiv T_2^*$, which is equivalent to the *second moment of the local magnetic field distribution*. In the ensemble of $\sim 10^{23}$ spins, each one precesses at a slightly larger or slightly

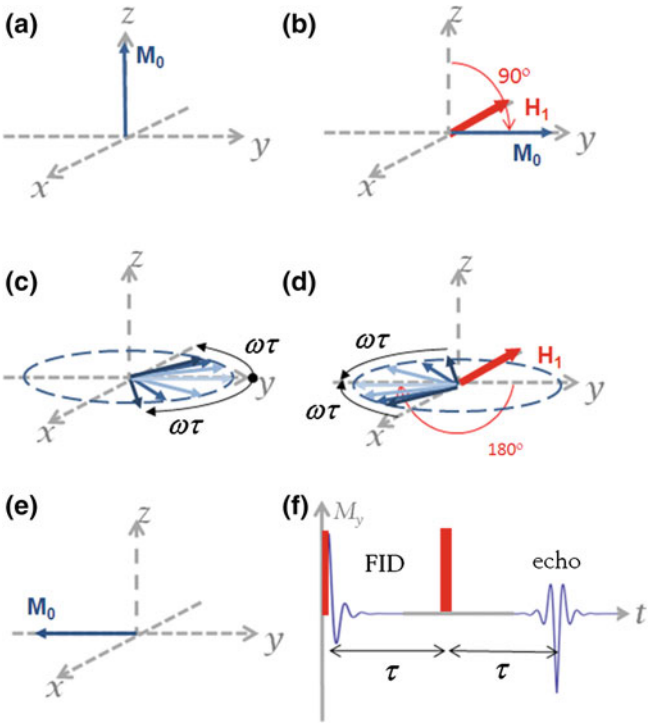

Fig. 1.7 A spin echo is formed by a two-pulse sequence. In this case, the sequence in panels (**a**)–(**e**) is $90_{\bar{x}} - \tau - 180_{\bar{x}} - \tau -$echo. The FID forms along the $+y$-direction in the rotating frame. Since M is the vector sum of all the individual spins, each with a slightly different precession frequency, the FID signal decays with time constant T_2^* as seen in panel (**f**). The second 180° pulse refocuses these spins a time 2τ after the first pulse. In this case, the echo forms along the $-y$-direction

smaller rate than the average precession rate ω_L^0 so that in the rotating frame of ω_L^0, the ensemble of spins will spread out around the plane over time. Eventually the net sum of these spins along the original axis will average to zero and the FID signal will decay with time constant $T_2^* \cdot T_2^*$ is often much smaller than the intrinsic T_2 of a a material. This phenomenon is demonstrated in Fig. 1.7.

Two important sources of local magnetic field distributions are magnet inhomogeneity and dipole couplings between nuclei in a rigid lattice. Typically $\delta/\gamma \sim 0.01 - 10$ G for NMR magnets, and $\delta/\gamma \sim 100 - 1{,}000$ G for dipole couplings in solid materials. FIDs typically decay much faster in solids, in which case spin echoes are particularly important. Alternatively, the Fourier transform of the FID in a solid will be much broader than in a liquid. In both cases, however, the linewidth of the Fourier transform is given by $1/T_2^*$, which is not necessarily the intrinsic spin-decoherence time of the density matrix.

A classic analogy for the formation of a spin echo is a set of runners on a track. Initially all the runners are gathered in a pack at the starting line. When the gun

blows and the runners start racing, some will run faster and other will run slower. Eventually the pack of runners spreads out around the track. If the gun were shot a second time at which point each runner turns around and races backwards, then the pack of runners would return to the starting line exactly twice the time difference between the two gun shots. The fastest runners would have run the farthest and the slowest runners run the shortest distance, but the time to return to the starting line is the same for all the runners.

One apparent failure of this analogy is that the runners would tire after sufficient time, so that the longer time the run, the slower they become. If the second gun shot were to occur only 10 s after the start of the race, then the entire pack would return simultaneously to the starting line 10 s later. However if the second gun shot were to occur 10 min after the start, it is doubtful that all the runners would return exactly 10 min later in a well defined pack. The same effect occurs for the ensemble of nuclear spins, and is due to the loss of coherence in the density matrix. In other words, if $T_2^* \ll T_2$, then the FID signal (or the envelope of the echo) decays quickly, but echoes can still be formed as long as $\tau \lesssim T_2$. In fact, the intrinsic T_2 can be measured directly by measuring the echo size as a function of pulse spacing τ. In this case, the echo amplitude will decay as $e^{-2\tau/T_2}$.

1.1.3.2 Spin Lattice Relaxation

Any spin system that does not exhibit a Boltzmann population distribution among the energy levels is out of thermal equilibrium and will eventually return to equilibrium, in which all off-diagonal elements of the density matrix vanish and only the diagonal terms remain. This process is known as spin lattice relaxation, and can be measured with a sequence of three pulses:

$$180_x - t_1 - 90_x - \tau - 180_x - \tau - \text{echo}. \tag{1.33}$$

The first 180° pulse will invert the magnetization such that $M_z = -M_0$. The system then will return to equilibrium according to (1.24). The size of the magnetization at a time t_1 is measured by applying a two-pulse echo sequence to inspect $M_z(t_1)$. In this case, the magnetization is reversed by the first pulse, however other initial configurations are possible. For example, one could apply a 90° pulse, or a series of multiple 90° pulses known as a "comb" sequence. A comb sequence is intended to prepare the initial state such that $\langle M_x \rangle = \langle M_y \rangle = \langle M_z \rangle = 0$. Both types of preparatory pulses or pulse sequences simply change the initial conditions. For a spin 1/2 nucleus the recovery is single exponential, but for higher spin systems the recovery function is more complex, determined by a system of coupled differential equations.

1.2 Quadrupolar Nuclei

Approximately 71 % of all the isotopes with nuclear spins have $I > \frac{1}{2}$, and such nuclei manifest the full breadth and versatility of NMR as an experimental probe of the solid state. These isotopes are often referred to as quadrupolar nuclei since they experience an interaction between their electric quadrupolar moments and the local electrostatic potential in addition to any spin interactions. For $I > \frac{1}{2}$ there are multiple resonances corresponding to transitions between different nuclear spin levels. The spectra of such nuclei can be rich, complex, and challenging to interpret, but containing a wealth of information about the local electronic environment of the nuclei.

The quadrupolar interaction originates from the shape of a nucleus and its preferential orientation in the surrounding electrostatic environment usually created by the electrons. This interaction is given by:

$$\mathcal{H}_Q = \frac{1}{6}\sum_{\alpha\beta} \hat{Q}_{\alpha\beta} V_{\beta\alpha}, \tag{1.34}$$

where

$$Q_{\alpha\beta} = \int \rho_n(\boldsymbol{r})(3r_\alpha r_\beta - r^2\delta_{\alpha\beta})d^3r \tag{1.35}$$

are the elements of a quadrupolar tensor, where α and β are direction indices, and $\rho_n(\boldsymbol{r})$ is the nuclear charge density. The elements $V_{\beta\alpha} = \frac{\partial^2 V(0)}{\partial x_\alpha \partial x_\beta}$, where $V(\boldsymbol{r})$ is the electrostatic potential created by the electrons. $V_{\beta\alpha}$ form a second rank tensor in real space known as the Electric Field Gradient, or EFG tensor. The EFG is determined by the electronic system, and $Q_{\alpha\beta}$ is a property of the nucleus. Equation (1.34) describes the interaction between the nuclear quadrupolar moment and the EFG, but in this case the $Q_{\alpha\beta}$ are quantum mechanical operators that depend on the shape and orientation of the nucleus in the ground state manifold of I. By taking advantage of various quantum mechanical theorems and nuclear symmetries, this interaction can be written entirely in terms of spin operators and parameters of the EFG:

$$\mathcal{H}_Q = \frac{e^2 Qq}{4I(2I-1)}\left[(3\hat{I}_z^2 - \hat{I}^2) + \eta(\hat{I}_x^2 - \hat{I}_y^2)\right]. \tag{1.36}$$

Here Q is the quadrupolar moment of the nucleus, $eq \equiv V_{zz}$ is the largest eigenvalue of the EFG tensor, $\eta \equiv \left(V_{xx} - V_{yy}\right)/V_{zz}$ is the asymmetry parameter of the EFG. Q, like I, is an intrinsic parameter of the nucleus, and typically is on the order of a barn ($10^{-24}\,\mathrm{cm}^2$). This expression is only valid in the basis which diagonalizes the EFG tensor, so that V_{xx}, V_{yy} and V_{zz} are the principal eigenvalues of the EFG tensor. For arbitrary directions the operators $\hat{I}_\alpha$ must be rotated using rotation operators. Usually the direction associated with the largest eigenvalue is notated $\boldsymbol{q}$ and corresponds to $|V_{zz}| > |V_{xx}| > |V_{yy}|$.

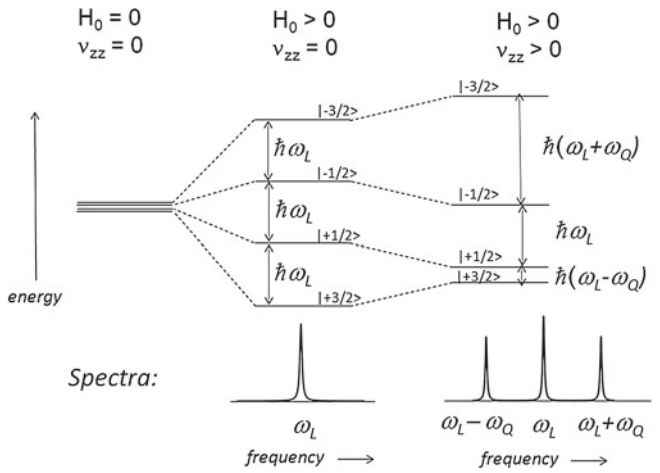

Fig. 1.8 A spin $I = 3/2$ nucleus in an external magnetic field $\boldsymbol{H}_0$ with an axial field gradient parallel to $\boldsymbol{H}_0$ has Hamiltonian $\mathcal{H} = \hbar\omega_L \hat{I}_z + \hbar\omega_Q(3\hat{I}_z^2 - \hat{I}^2)/6$. This system has three resonances split by the EFG

1.2.1 Quadrupolar Nuclei in Field

For a quadrupolar nucleus in a magnetic field the $2I + 1$ eigenstates are determined by $\mathcal{H}_Z + \mathcal{H}_Q$. In general $\boldsymbol{H}_0$ may not be in the same direction as one of the principal directions of the EFG tensor, in which case the Hamiltonian can quickly become difficult to diagonalize analytically. We will consider a simple case that captures the essential features of the spectrum of a quadrupolar nucleus and can still be solved analytically. Here $\boldsymbol{H}_0$ is parallel to $\boldsymbol{q}$ and the EFG has axial symmetry ($\eta = 0$), so the total Hamiltonian is given by:

$$\mathcal{H} = \hbar\omega_L \hat{I}_z + \frac{\hbar\omega_Q}{6}\left(3\hat{I}_z^2 - \hat{I}^2\right), \tag{1.37}$$

where $\hbar\omega_Q \equiv \frac{3e^2qQ}{2I(2I-1)}$. Since $\hat{I}_z$ commutes with $\mathcal{H}$, the Hamiltonian is diagonal in the $\hat{I}_z$ basis. For $I = 3/2$ the eigenstates are given by:

$$|\phi_m\rangle = |m\rangle \tag{1.38}$$

$$\epsilon_m/\hbar = m\omega_L + \frac{4m^2 - 5}{8}\omega_Q = \begin{cases} -\frac{3}{2}\omega_L + \frac{1}{2}\omega_Q \text{ for } m = -\frac{3}{2} \\ -\frac{1}{2}\omega_L - \frac{1}{2}\omega_Q \text{ for } m = -\frac{1}{2} \\ +\frac{1}{2}\omega_L - \frac{1}{2}\omega_Q \text{ for } m = +\frac{1}{2} \\ +\frac{3}{2}\omega_L + \frac{1}{2}\omega_Q \text{ for } m = +\frac{3}{2}. \end{cases} \tag{1.39}$$

The transition frequencies (given by the selection rule $\Delta m = \pm 1$) are: $\omega_L - \omega_Q, \omega_L$, and $\omega_L + \omega_Q$. The energy levels and the spectrum are shown in Fig. 1.8. Usually these three transitions are referred to the central $(-\frac{1}{2} \leftrightarrow \frac{1}{2})$ transition, and the satellites transitions $(\pm\frac{1}{2} \leftrightarrow \pm\frac{3}{2})$. The transition frequencies of each transition are linear in field:

$$\omega = \gamma H_0 \pm n\omega_Q, \tag{1.40}$$

where $n = -1, 0 + 1$. This behavior can be seen in the left panel of Fig. 1.9.

It is instructive to consider the behavior of the density matrix in this case. Previously we considered a spin-1/2 nucleus and found that the off diagonal terms of the density matrix oscillate at the Larmor frequency. For a higher spin nucleus, the off diagonal terms oscillate at a frequency $\omega_{\alpha\beta} = (\epsilon_\alpha - \epsilon_\beta)/\hbar$, where ϵ_α is the energy of the ith eigenstate and corresponds to the $i \leftrightarrow j$ transition. Each one of these off-diagonal elements corresponds to one of the possible nuclear spin transitions.

Consider such a system initially in equilibrium that experiences a 90° rotation about the y-axis. Following the rotation, the density matrix will evolve as:

$$\hat{\rho} = \begin{pmatrix} \frac{3}{2} & 0 & 0 & 0 \\ 0 & \frac{1}{2} & 0 & 0 \\ 0 & 0 & -\frac{1}{2} & 0 \\ 0 & 0 & 0 & -\frac{3}{2} \end{pmatrix} \xrightarrow{90^\circ_y} \begin{pmatrix} 0 & \frac{\sqrt{3}}{2} & 0 & 0 \\ \frac{\sqrt{3}}{2} & 0 & 1 & 0 \\ 0 & 1 & 0 & \frac{\sqrt{3}}{2} \\ 0 & 0 & \frac{\sqrt{3}}{2} & 0 \end{pmatrix} \xrightarrow{e^{i\mathcal{H}t/\hbar}}$$

$$\begin{pmatrix} 0 & \frac{\sqrt{3}}{2}e^{i(\omega_L+\omega_Q)t} & 0 & 0 \\ \frac{\sqrt{3}}{2}e^{-i(\omega_L+\omega_Q)t} & 0 & e^{i\omega_L t} & 0 \\ 0 & e^{-i\omega L t} & 0 & \frac{\sqrt{3}}{2}e^{i(\omega_L-\omega_Q)t} \\ 0 & 0 & \frac{\sqrt{3}}{2}e^{-i(\omega_L-\omega_Q)t} & 0 \end{pmatrix}. \tag{1.41}$$

In this case, the off-diagonal elements oscillate at one of the three transition frequencies. The expectation value for the magnetization is:

$$\langle M_x \rangle = \frac{3}{2}\cos\left((\omega_L - \omega_Q)t\right) + 2\cos\left(\omega_L t\right) + \frac{3}{2}\cos\left((\omega_L + \omega_Q)t\right). \tag{1.42}$$

(Note that the spectrum $S(\omega)$ is the Fourier transform of $\langle M_x \rangle$.) This equation indicates that there will be three resonances at $\omega_L - \omega_Q$, ω_L and $\omega_L + \omega_Q$, with relative intensities given by the ratio 3 : 4 : 3. The intensity of the transition between the $|m\rangle$ and $|m+1\rangle$ level is given by the square of the matrix element $(\hat{I}_+)^2_{m,m+1} = I(I+1) - m(m+1)$. For higher spin nuclei there will be more transitions, each with relative intensity given by this formula.

The 90° rotation needed to generate these off-diagonal elements must be generated by an H_1 pulse. If this pulse has components of frequency at each of the three transitions, then each off-diagonal matrix element will be generated as shown above. This is possible if the pulse length is short enough such that the frequency bandwidth of the pulse is wider than the difference between the resonances; in other words, if

$t_p < (2\omega_Q)^{-1}$. This condition may not be possible in general, since ω_Q can vary anywhere from a few kHz to several MHz whereas t_p is typically on the order of a microsecond or longer. The broadest coverage of a resonance is typically less than about 1 MHz, so if $\omega_Q > 500$ kHz, then not all of the transitions can be excited simultaneously. In some cases, one can use special frequency-swept excitation pulses, or special pulse sequences to excite all of the transitions [3]. Alternatively, one can excite and detect each resonance independently of one another.

Consider the effect of a 90° pulse at the lower satellite transition of the spin $\frac{3}{2}$ case discussed above. The Hamiltonian in the rotating frame is:

$$\begin{aligned}\mathcal{H}_R &= \hbar(\omega_L - \omega)\hat{I}_z + \hbar\frac{\omega_Q}{6}(3\hat{I}_z^2 - I^2) + \hbar\Omega_1\hat{I}_y \\ &= \hbar\begin{pmatrix} \frac{(3\omega_L+\omega_Q-3\omega)}{2} & -\frac{1}{2}i\sqrt{3}\Omega_1 & 0 & 0 \\ \frac{1}{2}i\sqrt{3}\Omega_1 & \frac{(\omega_L-\omega_Q-\omega)}{2} & -i\Omega_1 & 0 \\ 0 & i\Omega_1 & \frac{(\omega-\omega_L-\omega_Q)}{2} & -\frac{1}{2}i\sqrt{3}\Omega_1 \\ 0 & 0 & \frac{1}{2}i\sqrt{3}\Omega_1 & \frac{(3\omega-3\omega_L+\omega_Q)}{2} \end{pmatrix}.\end{aligned} \tag{1.43}$$

In principle we can compute the solution to the density matrix by using the operator $\hat{T}(t) = e^{i\mathcal{H}_R t/\hbar}$ since $\mathcal{H}_R$ is independent of time. However, this quickly becomes intractable even when ω matches one of the three resonance frequencies because there is no closed form expression for the operator $\hat{T}(t)$.

In order to make headway, note that we only really care about the first off diagonal elements of the density matrix, not the entire density matrix itself. Furthermore, we only are interested in one particular transition at a time. In this case, we can focus on the subspace of Hilbert space corresponding to the two eigenstates of the transition in question:

$$\begin{pmatrix} \boxed{\begin{matrix} \frac{1}{2}\left(3\omega_L + \omega_Q - 3\omega\right) & -\frac{1}{2}i\sqrt{3}\Omega_1 \\ \frac{1}{2}i\sqrt{3}\Omega_1 & \frac{1}{2}\left(\omega_L - \omega_Q - \omega\right) \end{matrix}} & \begin{matrix} 0 & 0 \\ -i\Omega_1 & 0 \end{matrix} \\ \begin{matrix} 0 & i\Omega_1 \\ 0 & 0 \end{matrix} & \begin{matrix} \frac{1}{2}\left(\omega - \omega_L - \omega_Q\right) & -\frac{1}{2}i\sqrt{3}\Omega_1 \\ \frac{1}{2}i\sqrt{3}\Omega_1 & \frac{1}{2}\left(3\omega - 3\omega_L + \omega_Q\right) \end{matrix} \end{pmatrix}.$$

We can consider the two upper levels as an effective spin-$\frac{1}{2}$ system, with Hamiltonian:

$$\mathcal{H}_{\text{eff}} = \hbar\begin{pmatrix} \frac{1}{2}\left(3\omega_L + \omega_Q - 3\omega\right) & -\frac{1}{2}i\sqrt{3}\Omega_1 \\ \frac{1}{2}i\sqrt{3}\Omega_1 & \frac{1}{2}\left(\omega_L - \omega_Q - \omega\right) \end{pmatrix}. \tag{1.44}$$

If $\omega = \omega_L + \omega_Q$, then

$$\mathcal{H}_{\text{eff}} = \hbar\begin{pmatrix} -\omega_Q & -\frac{1}{2}i\sqrt{3}\Omega_1 \\ \frac{1}{2}i\sqrt{3}\Omega_1 & -\omega_Q \end{pmatrix} = -\hbar\omega_Q\hat{\mathbb{I}} + \hbar\frac{\sqrt{3}}{2}\Omega_1\hat{I}_y. \tag{1.45}$$

The first term is just a constant offset, and the second term indicates that the effective field lies along the y axis, with amplitude $\frac{\sqrt{3}}{2}\Omega_1/\gamma$. This means that the magnetization of the effective spin-$\frac{1}{2}$ will precess around H_1 in the rotating frame, but at an enhanced precession rate. A 90° rotation would be enabled with a pulse width such that $\frac{\sqrt{3}}{2}\Omega_1 t_p = \frac{\pi}{2}$. The other transitions remain unaffected, so the density matrix evolves as:

$$\hat{\rho} = \begin{pmatrix} \frac{3}{2} & 0 & 0 & 0 \\ 0 & \frac{1}{2} & 0 & 0 \\ 0 & 0 & -\frac{1}{2} & 0 \\ 0 & 0 & 0 & -\frac{3}{2} \end{pmatrix} \overset{90^\circ_y(\omega_L+\omega_Q)}{\longrightarrow} \begin{pmatrix} 0 & \frac{\sqrt{3}}{2} & 0 & 0 \\ \frac{\sqrt{3}}{2} & 0 & 1 & 0 \\ 0 & 0 & -\frac{1}{2} & 0 \\ 0 & 0 & 0 & -\frac{3}{2} \end{pmatrix} \overset{e^{i\mathcal{H}t/\hbar}}{\longrightarrow} \tag{1.46}$$

$$\begin{pmatrix} 0 & \frac{\sqrt{3}}{2}e^{i(\omega_L+\omega_Q)t} & 0 & 0 \\ \frac{\sqrt{3}}{2}e^{-i(\omega_L+\omega_Q)t} & 0 & 0 & 0 \\ 0 & 0 & -\frac{1}{2} & 0 \\ 0 & 0 & 0 & -\frac{3}{2} \end{pmatrix}.$$

This example demonstrates that each of the quadrupolar satellites can be observed independently from one another, and that each transition has a particular resonance amplitude and effective H_1 field that depends on the transition and the spin of the nucleus.

1.2.1.1 Nuclear Quadrupolar Resonance

The simple relationship between the field H_0 and the resonance frequency for a spin 1/2 system becomes more complex for higher spin nuclei. Equation (1.40) expresses this relationship for the simple case discussed above, and is shown in Fig. 1.9. There are clearly three sets of transitions, and even at $H_0 = 0$ there is a finite frequency. This zero field resonance corresponds to Nuclear Quadrupolar Resonance (NQR). In this case the two sets of states $|\pm\frac{3}{2}\rangle$ and $|\pm\frac{1}{2}\rangle$ are both degenerate, with an splitting given by $\hbar\omega_Q$. NQR is essentially identical to NMR except with the absence of a magnetic field. ω_Q is determined by the parameters of the crystal, and often one cannot determine the EFG a priori. In practice ω_Q is determined by measuring the spectrum in field prior to doing an NQR experiment. A significant advantage of NQR is that the absence of an external field means that there are no alignment issues for the crystal. In fact, NQR is often performed on a powder sample. Nuclei in any crystallites in the powder oriented such $\boldsymbol{q} \perp \boldsymbol{H}_1$ will be excited. NQR is particularly useful for measuring the internal field of magnetically ordered materials. In this case, the development of long range magnetic order generally gives rise to a static internal magnetic field, which shifts or splits the NQR resonance, as seen in Fig. 1.9 and in (1.40).

1.2.1.2 Angular Dependence

In cases where the Hamiltonian cannot be diagonalized analytically, it can often be solved either by perturbation theory or via numerical methods. This is the case for arbitrary orientation of $\boldsymbol{H}_0$ with respect to the EFG, and for $\eta \neq 0$. The frequency versus field relationship is shown in Figs. 1.9 and 1.10. In these plots, the intensity of the line is proportional to the intensity

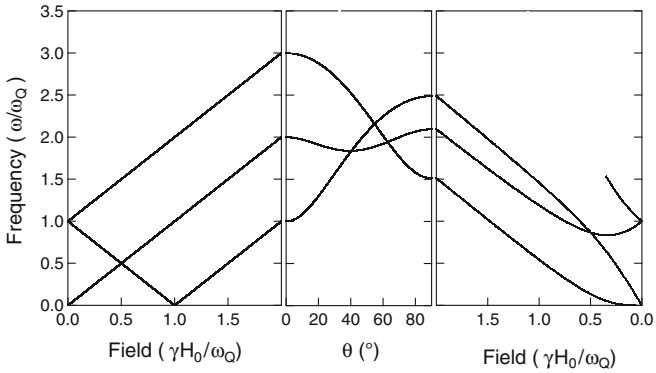

Fig. 1.9 The resonance frequencies of the Hamiltonian (1.37) for $I = 3/2$ and $\eta = 0$ as a function of field and angle. The normalized resonance frequency ω/ω_Q is plotted on the vertical axis, and the field is normalized as $\gamma H_0/\omega_Q$. The *left panel* shows the frequency versus field for $\theta = 0$ ($\boldsymbol{H}_0 \parallel \boldsymbol{q}$), the *center panel* shows the frequencies versus angle θ, and the *right panel* shows the frequencies versus field for $\theta = 90°$

of the transition. The intensity of a transition between the states $|j\rangle$ and $|k\rangle$ is given by the square of the matrix element $|\langle j|\hat{I}_x|k\rangle|^2$. For most cases, this matrix element vanishes. If the eigenstates are given by the $|m\rangle$ states (such that $\hat{I}_z$ is diagonal) then $\langle j|\hat{I}_x|k\rangle = 0$ unless $j = k \pm 1$ or $\Delta m = \pm 1$. This rule implies that there should be only $2I$ transition in the spectrum—for example Figs. 1.9 and 1.10 show three transitions for $I = \frac{3}{2}$. The only allowed transitions are those between adjacent levels because the field $\boldsymbol{H}_1$ couples to the $\hat{I}_+$ and $\hat{I}_-$ operators, which can only raise or lower the state by one level. However, when $[\mathcal{H}, \hat{I}_z] \neq 0$ the eigenstates $|j\rangle$ are superpositions of the $|m\rangle$ states and it is possible that $\langle j|\hat{I}_x|k\rangle > 0$ for states that are not adjacent in energy and $\Delta m \neq \pm 1$ for such a transition. These are so-called "forbidden" transitions, and generally have weaker transition intensities because the matrix element $\langle j|\hat{I}_x|k\rangle$ is smaller. An example is seen in Fig. 1.9. For $\theta = 90°$, $[\mathcal{H}_Q, \mathcal{H}_Z] \neq 0$, and for low fields ($H_0 \ll \omega_Q/\gamma$) there are more than just $2I$ transitions possible. In this case a fourth weaker transition is evident, as seen on the right hand side of the Figure. The same phenomenon is visible for $\eta \neq 0$ in Fig. 1.10. For sufficiently large fields H_0, the matrix element $|\langle j|\hat{I}_x|k\rangle|^2$ becomes too small to detect the transition.

Plots of frequency versus field such as Figs. 1.9 and 1.10 are critical to understanding the spectra of single crystals with high spin nuclei. In practice it can be difficult to identify a particular resonance, which depends on both the orientation as well as the EFG parameters eq and η. Careful measurements at either constant frequency or constant field, as well as angle rotational studies, are key to identifying the various NMR quantities such as the EFG and the magnetic shift (discussed below).

1.3 Hyperfine Couplings

In the previous discussion of the Bloch equations, the parameters T_1 and T_2 were introduced as phenomenological parameters to take into account the effect of interactions among nuclear spins and their environment. These interactions can include magnetic dipolar interactions

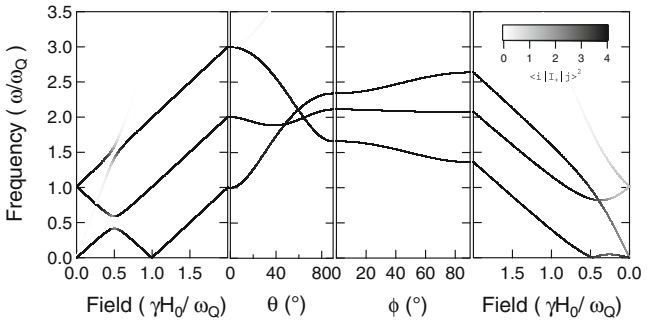

Fig. 1.10 The resonance frequencies of the Hamiltonian (1.34) for $I = 3/2$ and $\eta = 0.3$ as a function of field and angle. The normalized resonance frequency ω/ω_Q is plotted on the vertical axis, and the field is normalized as $\gamma H_0/\omega_Q$. The *left panel* shows the frequency versus field for $\theta = 0$ ($\boldsymbol{H}_0 \parallel \boldsymbol{q}$), the two *center panels* shows the frequencies versus the angles θ and ϕ, respectively, and the *right panel* shows the frequencies versus field for $\theta = \phi = 90°$. The square of the matrix element of the transition is shown on the gray scale legend. For some range of parameters, the transitions "fade out"—these are "forbidden" transitions

among neighboring nuclei or with nearby electrons. In fact, one of of the most important interaction for nuclei in condensed matter and strongly correlated systems is the hyperfine interaction, coupling the nuclear spins to the electron spins:

$$\begin{aligned}\mathcal{H}_{\rm hyp} &= A\hat{\boldsymbol{I}} \cdot \mathbf{S} \\ &= A\hat{I}_z S_z + \frac{1}{2}A(\hat{I}_+ S_- + \hat{I}_- S_+),\end{aligned} \tag{1.47}$$

where A is the hyperfine constant, typically on the order of 10^{-8} eV. This constant is often expressed as $A/\gamma\hbar\mu_B$ in units of Oe/μ_B. Typical values are on the order of 10 kOe/μ_B. This unit is often more useful since it gives an estimate of the size of the hyperfine field that the electron spin creates at the nucleus. This coupling allows the nuclei to probe both the static susceptibility, χ_0, and the dynamical susceptibility, $\chi(\mathbf{q}, \omega)$, of the electronic degrees of freedom. The diagonal term $A\hat{I}_z\hat{S}_z$ gives rise to a static shift of the resonance frequency.

1.3.1 Knight Shift

The Hamiltonian for a nucleus in an external field that experiences a hyperfine interaction is given by:

$$\mathcal{H} = \hbar\omega_L \hat{I}_z + A\hat{I}_z S_z. \tag{1.48}$$

For temperatures $T \gg A/k_B \sim 10^{-4}$ K, the electron and nuclear spins do not develop any coherence and therefore we can replace S_z with its thermal averaged value $\langle S_z \rangle = \chi H_0$, where χ is the magnetic susceptibility of the electronic system. The Hamiltonian can be rewritten then as:

$$\mathcal{H} = \hbar\omega_L(1+K)\hat{I}_z, \tag{1.49}$$

where the Knight shift, K, measures the percent shift of the resonance frequency from that of an isolated nucleus ($\omega_0 = \gamma H_0$). The Knight shift is given by: $K = A\chi_0/\hbar\gamma\mu_B$. In a Fermi liquid, χ_0 is given by the Pauli susceptibility, so $K \sim AN(0)$ is temperature independent.

This scenario works well for simple metals such as Li and Na, yet there are many cases where the Knight shift is more complex. In Pt, for example, there are multiple hyperfine couplings to the d- and sp- bands, and hence several contributions to the total shift [4]. In many-electron atoms, there is also a core-polarization term, in which the core s electrons acquire a population difference between the up- and down-spin states. This difference arises because the orthogonal eigenstates of the many-electron atom get mixed by the perturbing influence of the external field. In practice, it is difficult to estimate the contribution of a core-polarization term versus a purely contact term [5]. As a result, hyperfine couplings are usually taken to be material dependent parameters.

In metals with local moments, such as rare-earth and d-electron systems, there is also a second hyperfine coupling to these moments that give rise to a strong temperature dependence of the total shift [6]. In heavy fermion systems the hyperfine coupling is given by:

$$\hat{\mathcal{H}}_{\text{hyp}} = \gamma\hbar\hat{\boldsymbol{I}}\cdot\left(\mathbb{A}\cdot\mathbf{S}_c + \mathbb{B}\cdot\mathbf{S}_f\right), \tag{1.50}$$

where $\mathbb{A}$ is an on-site hyperfine tensor interaction to the conduction electron spin, and $\mathbb{B}$ is a transferred hyperfine tensor to the f spins [7]. Note that we consider here nuclear spins on the ligand sites, i.e., not on the f atom nucleus.

Given the two spin species, S_c and S_f, there are three different spin susceptibilities: $\chi_{cc} = \langle S_c S_c\rangle$, $\chi_{cf} = \langle S_c S_f\rangle$, and $\chi_{ff} = \langle S_f S_f\rangle$. The full expression for the Knight shift is given by:

$$K(T) = A\chi_{cc}(T) + (A+B)\,\chi_{cf}(T) + B\chi_{ff}(T). \tag{1.51}$$

where we have absorbed the g-factors into the definition of the hyperfine constants and dropped the tensor notation for notational simplicity [7]. The bulk susceptibility is given by:

$$\chi(T) = \chi_{cc}(T) + 2\chi_{cf}(T) + \chi_{ff}(T). \tag{1.52}$$

Note that if $A = B$, then $K \propto \chi$ for all temperatures. However, if $\chi_{cc}(T)$, $\chi_{cc}(T)$, and $\chi_{cc}(T)$ have different temperature dependences, then the Knight shift will not be proportional to susceptibility, leading to a Knight shift anomaly at a temperature T^*. This phenomenon is illustrated in Fig. 1.11. In this case both χ_{ff} and χ_{cf} have different temperature dependences, thus K and χ stop scaling with one another below $T^* \sim$60 K. This temperature corresponds to the coherence temperature of the Kondo lattice in this compound [8, 9].

1.3.2 Spin Lattice Relaxation

The off diagonal terms of the hyperfine interaction couple neighboring transitions through the $\hat{I}_\pm$ operators. This perturbation corresponds to a spin-flip exchange between the electron spin and the nuclear spin. These processes do not shift the resonance frequency, but do affect the dynamics of the nuclei. In fact, this process is crucial to bring about an equilibrium population

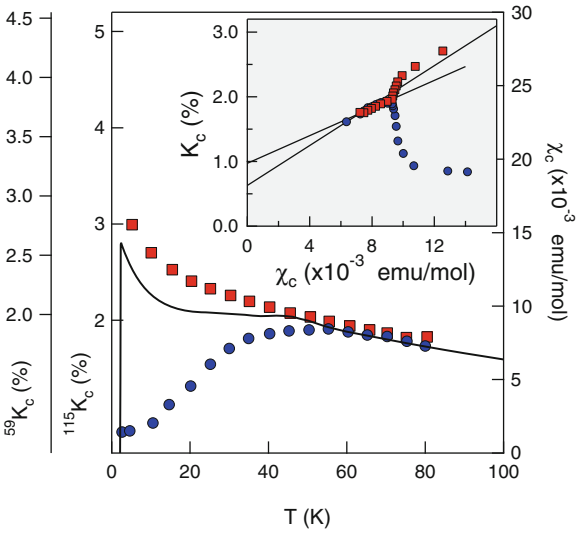

Fig. 1.11 The Knight shift of the In(1) (*red squares*) and the Co (*blue circles*) in $CeCoIn_5$, compared with the bulk susceptibility, $\chi(T)$ (*solid line*), in the c-direction. INSET: K_c[(In(1)] and K_c(Co) versus χ_c with temperature as an implicit parameter. The *solid lines* are linear fits to the data for $T > T^*$. T^*, the temperature where K and χ diverge, is approximately 50 K in this case

distribution among the nuclear spin levels. Consider a Fermi liquid with a simple contact interaction give by (1.50). As the quasiparticles scatter from one nucleus to another, they maintain essentially the same energy since the nuclear Zeeman energy is orders of magnitude lower than the Fermi level, and the quasiparticle Zeeman energy can be absorbed by states within $k_B T$ of E_F. By using Fermi's Golden Rule one can show that the spin-lattice-relaxation rate can be written as:

$$T_1^{-1} = \gamma^2 A^2 \int_0^\infty \langle \hat{S}_+(t)\hat{S}_-(0)\rangle e^{i\omega_0 t} dt, \tag{1.53}$$

where the brackets indicate a thermal averaged correlation function. In a Fermi liquid, the states available for scattering the quasiparticles are those at the Fermi surface, and by a simple counting argument one can show that (1.53) can be written as:

$$T_1^{-1} = \frac{\gamma^2 A^2}{2} \int_0^\infty N(E_i)N(E_f)f(E_i)(1 - f(E_f))dE_i \tag{1.54}$$

where $E_f - E_i = \hbar\omega_0$. Since $f(E)(1 - f(E)) \approx k_B T\delta(E - E_F)$, we find that $T_1^{-1} \sim TA^2N^2(0)$. In other words, measurements of T_1^{-1} yield information about the square of the density of quasiparticle states at the Fermi level. Any changes to the Fermi surface as a function of temperature, such as the development of a superconducting gap, will be reflected in T_1^{-1}. It is also immediately obvious that $T_1 T K^2 \equiv \mathcal{K}$ is constant in a Fermi liquid. This Korringa

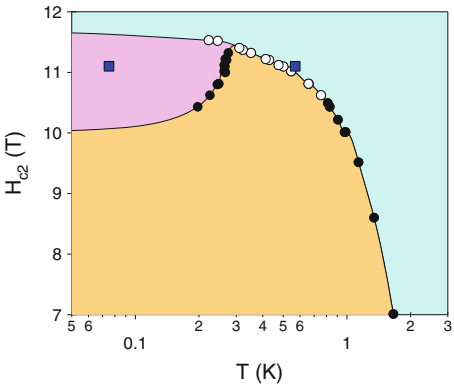

Fig. 1.12 The phase diagram of $CeCoIn_5$ in high field as determined by specific heat [11]. *Solid points* represent second order phase transitions and *open points* are first order transitions. The *solid blue squares* are the points at which the spectra in Figs. 1.14 and 1.15 were obtained

constant, $\mathcal{K} = \pi^2\hbar\gamma^2/\mu_B^2$, is valid for non-interacting systems. In practice $\mathcal{K}$ is found often to deviate from unity, which is usually taken as a measure of the strength of the quasiparticle interactions [10].

The expression (1.53) can be rewritten also in terms of the dynamical susceptibility:

$$T_1^{-1} = \gamma^2 k_B T \lim_{\omega\to 0} \sum_{\mathbf{q}} A^2(\mathbf{q}) \frac{\chi''(\mathbf{q},\gamma)}{\hbar\omega}, \tag{1.55}$$

where the form factor $A^2(\mathbf{q})$ is the square of the Fourier transform of the hyperfine interaction, and the sum over $\mathbf{q}$ is over the first Brillouin zone [12]. For a contact interaction, $A^2(\mathbf{q})$ is constant, but for more complex situations involving transferred couplings between neighboring sites, $A^2(\mathbf{q})$ can have structure and may vanish at particular wavevectors. A $\mathbf{q}$-dependent form factor can have profound consequences for the behavior of T_1^{-1} in materials. A notorious example is the difference in T_1^{-1} observed for the planar Cu and planar O in the cuprates [13]. Each nucleus has a different form factor and the dynamical susceptibility of this material is dominated by fluctuations at a particular wavevector, $\mathbf{Q}$. Since $A^2(\mathbf{q})$ vanishes for the O site but not for the Cu site, the two spin-lattice-relaxation rates have very different temperature dependences, even though they are coupled to the same degree of freedom, the Cu $3d^9$ $S = 1/2$ spins.

1.4 Case Study: Field Induced Magnetism

The heavy-fermion superconductor $CeCoIn_5$ has attracted considerable attention since its discovery in 2001, and NMR has played a central role in elucidating the novel physics of this strongly correlated electron system [14]. Of particular interest is a magnetic field induced phase (the Q phase) that emerges close to the upper critical field H_{c2} (see Fig. 1.12). This material is an unconventional d-wave superconductor that also exhibits non-Fermi liquid behavior associated with proximity to an antiferromagnetic quantum critical point. The normal state quasiparticles have an enhanced mass and a large magnetic susceptibility, and

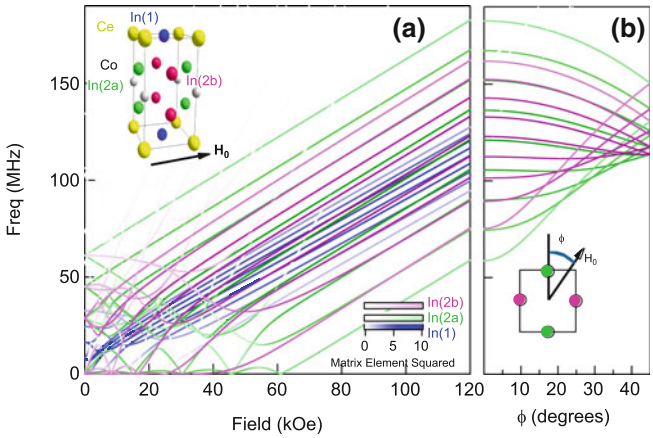

Fig. 1.13 **a** The frequency versus field relationship for the In(1) and In(2) sites in $CeCoIn_5$ for the field located in the *ab* plane. There are two distinct In(2) sites in this orientation because the field can point either parallel or perpendicular to the principal EFG axis, $\boldsymbol{q}$. The *inset* shows the unit cell. **b** The position of the two In(2) resonances as a function of the angle, ϕ in the *ab* plane

consequently the superconducting state is Pauli limited [15]. This means that for sufficiently large magnetic fields the superconductivity is destroyed by breaking apart the Cooper pair singlets rather than by orbital currents as in more common orbital limited superconductors. In Pauli limited superconductors the condensate is expected theoretically to form long wavelength modulations in which the Cooper pairs develop finite momenta in certain limits [16–18]. This so-called Fulde-Ferrell-Larkin-Ovchinnikov (FFLO) superconducting phase was first predicted to exist in Pauli-limited superconductors several decades ago, but an experimental realization has proved elusive. The field-induced phase of $CeCoIn_5$ was identified initially as an FFLO phase based on bulk thermodynamic measurements [11, 19–21].

Subsequent NMR work, however, revealed a much more complex picture [22]. This material is ideal for NMR studies because there are multiple NMR active sites in the unit cell. There are two In sites per unit cell (^{115}In has spin $I = 9/2$), and one Co site (^{59}Co has spin $I = 7/2$). The In(1) site has axial symmetry and is located in the Ce-In plane, and the In(2) site has lower symmetry and is located on the lateral faces of the unit cell (see inset of Fig. 1.13). The EFG parameters of both sites are well known ($\nu_Q = 8.173\,\text{MHz}$, $\eta = 0$ for the In(1) and $\nu_{zz} = 15.489\,\text{MHz}$, $\eta = 0.386$ for the In(2), and the frequency versus field relationship for this material is shown in Fig. 1.13 [8]. In this case there are two In(2) sites since the external magnetic field can point either parallel or perpendicular to the unit cell face, and the principal axis of the EFG ($\boldsymbol{q}$) points towards the center of the unit cell. These two sites are sometimes referred to In(2a) ($\boldsymbol{H}_0 \parallel \boldsymbol{q}$) and In(2b) ($\boldsymbol{H}_0 \perp \boldsymbol{q} \perp \hat{c}$). Thus there are four unique crystallographic sites that can be probed with NMR in the Q phase.

Initial NMR studies focused solely on the In(1) site and found dramatic changes to the Knight shift that were interpreted as evidence for the FFLO phase [21, 23, 24]. A more careful study looking at all four NMR sites revealed the presence of incommensurate antiferromagnetic order in contrast to the standard predictions for the FFLO phase [18, 22, 25]. Figures 1.14 and 1.15 show the In and Co spectra at constant field as a function of temperature. Each site clearly exhibits a different response in the Q phase. There is a discontinuity in the Knight shift

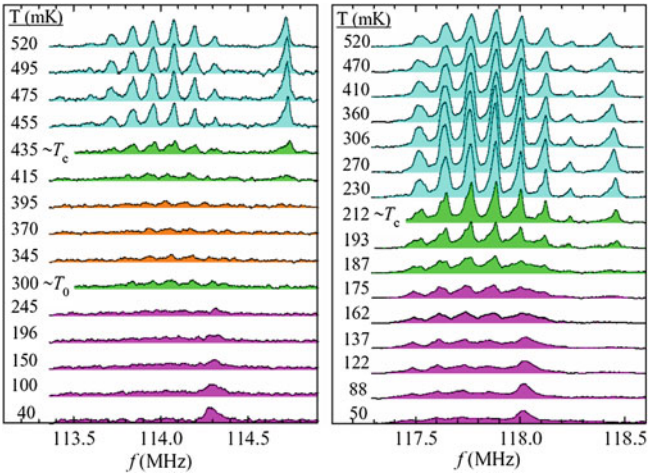

Fig. 1.14 NMR spectra of the Co and the In(1) site in $CeCoIn_5$ acquired in a field of 11.1 T (*left*) and 11.485 T (*right*). The *light blue spectra* are in the normal state, the *green* are within 20 mK of a phase transition, the *orange* are in the mixed (vortex) phase, and the *purple* are in the field induced antiferromagnetic phase. Reproduced from [22]

(and hence the resonance frequency) due to the first order nature of the phase transition as the temperature is lowered through T_c. Deep within the Q phase, the In(1) and Co resonances are somewhat broadened and shifted, but remain relatively unaffected. For the In(2b) site the spectrum broadens by several MHz and develops a two-peaked pattern consistent with the presence of long range antiferromagnetic order. Several subsequent NMR and neutron scattering experiments confirmed the presence of this static antiferromagnetism [26–29].

The lack of splitting in the spectra of the In(1) and Co sites coupled with the broad double-peak structure of the In(2b) spectra place strong constraints on the possible magnetic structure. The spectrum is split into two peaks because the hyperfine field at the In(2b) site is either parallel or perpendicular to the applied field. However the relationship between the direction of the ordered Ce moments and that of the hyperfine field is non-trivial. Young et al. proposed a minimal model where the magnetic structure consists of ordered local Ce spins with moments $\mathbf{S}_0$ along the applied magnetic field direction (along [100]), with an ordering wavevector of the form $\mathbf{Q} = \pi(\frac{1+\delta}{a}, \frac{1}{a}, \frac{1}{c})$. The structure of the NMR spectra revealed the incommensurate nature, but the value of the modulation δ remained undetermined since the hyperfine field at the In(2) site depends on the product of the size of the ordered moment and the incommensuration. A more complete analysis of the static hyperfine fields that develop at each of these sites for different magnetic structures and orientations of the ordered Ce moments suggested that for $\mathbf{H} \parallel [100]$ the spins are oriented as $\mathbf{S}_0 \parallel [001]$ and the incommensurate wavevector is $\mathbf{Q}_i \perp \mathbf{S}_0$, as summarized in Fig. 1.16 [30]. Recent detailed studies of the evolution of the In(2b) spectrum as a function of temperature and field have revealed a continuous growth of the antiferromagnetic order parameter in this phase (see Fig. 1.17). The antiferromagnetic order parameter vanishes above H_{c2}, indicating that the physical origin of the Q phase is tied closely to the presence of the superconductivity.

Neutron diffraction experiments confirmed the presence of static long range incommensurate antiferromagnetism in the Q phase, both for the field along [100] and along [110], as well

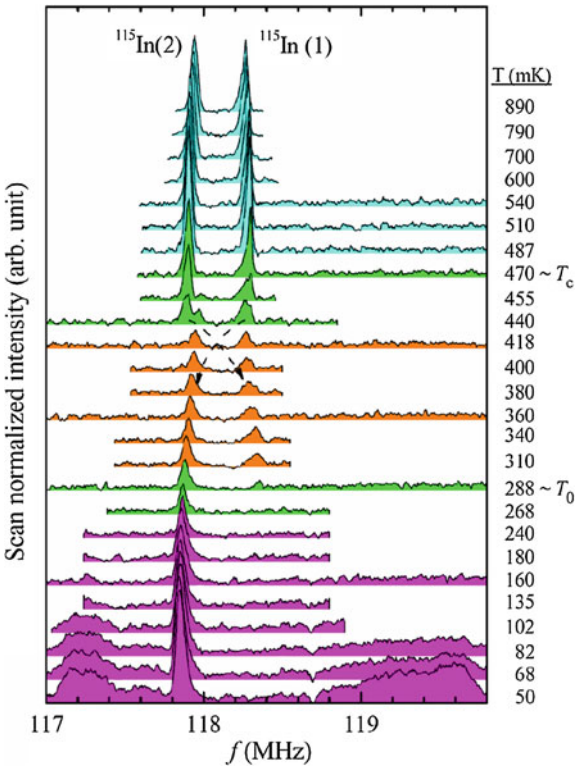

Fig. 1.15 Spectra of the In(1) and In(2b) in $CeCoIn_5$ acquired at 11.1 T. The In(1) transition at shifts down in frequency below T_c, and the In(2b) shifts up due to the first order normal to superconducting phase transition. The In(2b) spectra develop two split peaks at low temepartures due to the antiferromagnetic ordering. Reproduced from [22]

as directly measured δ [31, 32]. A crucial observation was that δ is *independent of the applied field*, in contrast to the predictions for the FFLO phase. In an FFLO phase, the incommensurate wavevector of the superconducting order parameter is field dependent.

The discovery of static antiferromagnetism in this field induced phase has spurred considerable theoretical interest. A key question is whether the magnetic order is a consequence of an instability of the superconductivity that gives way to a more complex form of coexisting FFLO and antiferromagnetism, or whether the magnetism is tied to the proximity to a quantum critical point. A Ginzburg-Landau analysis of the coupled superconducting and antiferromagnetic order parameters, $\Delta(\mathbf{r})$ and $M(\mathbf{r})$, indicates that if the superconductivity develops modulations as prescribed by the FFLO scenario, then M can also develop such modulations [27]. Such a state may be described by pair density wave (PDW) condensate, which may also carry a small spin-triplet component [33–35]. An alternative description is that the antiferromagnetism develops as a spin density wave (SDW) between the Fermi pockets that emerge at the d-wave nodes of the superconducting order parameter [36]. In a magnetic field the Zeeman interaction shifts the quasiparticle spectrum such that the nodes develop into pockets. These pockets are nested, and since the normal state of this material already has strong

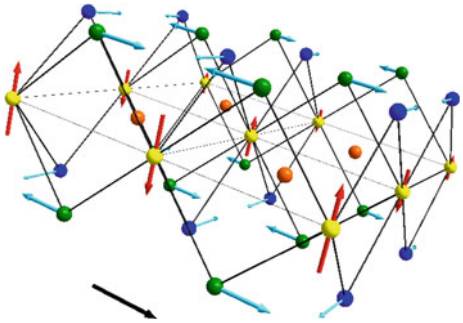

Fig. 1.16 Hyperfine fields and ordered moments in the field induced phase of $CeCoIn_5$. The in-plane tetragonal structure is outlined in *gray*. The Ce atoms are *yellow*, and their moments are indicated by *red arrows* pointing along [100]. The In(1) atoms are *orange*, and the Co are not shown. The In(2a) are *blue* and the In(2b) are *green*. The hyperfine fields are indicated by *blue arrows*, and the direction of $\mathbf{B}_0$ is shown by the *black arrow*. Reproduced from [30]

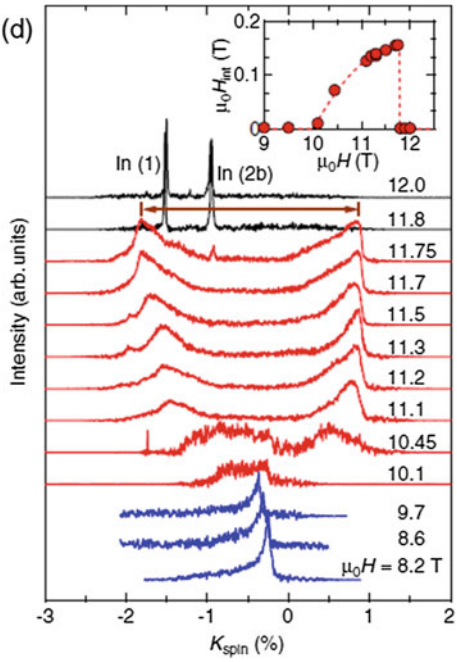

Fig. 1.17 Spectra of the In(1) and In(2b) at several different fields at 50 mK. The *inset* shows the temperature dependence of the internal field at the In(2b) site. Reproduced from [29]

antiferromagnetic fluctuations at the wavevector $\boldsymbol{Q} = (\pi/a, \pi/a)$ the quasiparticles can form an SDW. In this picture the superconducting order parameter is not modulated. Furthermore this scenario is consistent with the observation that the ordering wavevector $\mathbf{Q}$ is independent of the orientation of the field in the plane [32].

In summary, NMR has played a crucial role in the discovery and subsequent characterization of the field induced phase of $CeCoIn_5$, illustrating a fascinating example of correlated

electron behavior in condensed matter. At present there remains no consensus as to the origin of the antiferromagnetism, which emerges in a region of parameter space where the Zeeman energy of the electrons, the superconducting condensate energy, and the Kondo exchange between the local moments and the conduction electrons are all on the same order of magnitude. Furthermore, recent detailed NMR studies of the In(1) and In(2a) sites suggest that the superconducting order parameter $\Delta(\mathbf{r})$ may also be spatially modulated [29]. It is unclear, however, that the length scale of such a modulation is tied with that of the antiferromagnetism, or if this behavior reflects a more complex FFLO state. In addition, recent NMR data has suggested an unusual behavior of the vortex lattice phase in fields $H_{c1} < H < H^*$, where $H^* \approx 10$ T low field boundary of the Q phase [28]. For moderate fields the NMR linewidth is significantly broader than that expected for a conventional Abrikosov vortex lattice, and it has been suggested that there is yet another phase present in this field range. It remains unclear whether these observations are consistent with a true thermodynamic phase or are a manifestation of slow spin fluctuations close to the phase boundary. Undoubtedly further NMR work will continue to reveal new information about this exotic new phase of strongly correlated electron matter.

References

1. C.P. Slichter, *Principles of Nuclear Magnetic Resonance*, 3rd edn. (Springer, New York, 1992)
2. E.L. Hahn, Phys. Rev. **80**, 580 (1950)
3. J. Haase, M.S. Conradi, Chem. Phys. Lett. **209**(3), 287 (1993)
4. A.M. Clogston, V. Jaccarino, Phys. Rev. **121**(5), 1357 (1961)
5. R.E. Walstedt, R.F. Bell, L.F. Schneemeyer, J.V. Waszczak, G.P. Espinosa, Phys. Rev. B **45**(14), 8074 (1992)
6. N.J. Curro, Rep. Prog. Phys. **72**(2), 026502 (24pp) (2009)
7. N.J. Curro, B.L. Young, J. Schmalian, D. Pines, Phys. Rev. B **70**(23), 235117 (2004)
8. N.J. Curro, B. Simovic, P.C. Hammel, P.G. Pagliuso, J.L. Sarrao, J.D. Thompson, G.B. Martins, Phys. Rev. B **64**(18), 180514 (2001)
9. Y.F. Yang, Z. Fisk, H.O. Lee, J.D. Thompson, D. Pines, Nature **454**, 611 (2008)
10. D. Pines, Phys. Rev. **95**(4), 1090 (1954)
11. A. Bianchi, R. Movshovich, C. Capan, P.G. Pagliuso, J.L. Sarrao, Phys. Rev. Lett. **91**(18), 187004 (2003)
12. T. Moriya, J. Phys. Soc. Jpn. **18**(4), 516 (1963)
13. S.E. Barrett, J.A. Martindale, D.J. Durand, C.H. Pennington, C.P. Slichter, T.A. Friedmann, J.P. Rice, D.M. Ginsberg, Phys. Rev. Lett. **66**(1), 108 (1991)
14. C. Petrovic, R. Movshovich, M. Jaime, P.G. Pagliuso, M.F. Hundley, J.L. Sarrao, Z. Fisk, J.D. Thompson, Europhys. Lett. **53**(3), 354 (2001)
15. K. Maki, T. Tsuneto, Prog. Theor. Phys. **31**, 945 (1964)
16. P. Fulde, R.A. Ferrell, Phys. Rev. **135**, A550 (1964)
17. A.I. Larkin, Y.N. Ovchinnikov, Sov. Phys. JETP **20**, 762 (1965)
18. A.B. Vorontsov, M.J. Graf, Phys. Rev. B **74**, 172504 (2006)
19. A. Bianchi, R. Movshovich, N. Oeschler, P. Gegenwart, F. Steglich, J.D. Thompson, P.G. Pagliuso, J.L. Sarrao, Phys. Rev. Lett. **89**(13), 137002 (2002)
20. H.A. Radovan, N.A. Fortune, T.P. Murphy, S.T. Hannahs, E.C. Palm, S.W. Tozer, D. Hall, Nature **425**, 51 (2003)
21. K. Kakuyanagi, M. Saitoh, K. Kumagai, S. Takashima, M. Nohara, H. Takagi, Y. Matsuda, Phys. Rev. Lett. **94**(4), 047602 (2005)
22. B.L. Young, R.R. Urbano, N.J. Curro, J.D. Thompson, J.L. Sarrao, A.B. Vorontsov, M.J. Graf, Phys. Rev. Lett. **98**, 036402 (2007)

23. V.F. Mitrović, G. Koutroulakis, M. Klanjšek, M. Horvatić, C. Berthier, G. Knebel, G. Lapertot, J. Flouquet, Phys. Rev. Lett. **101**(3), 039701 (2008)
24. V.F. Mitrovic, M. Horvatic, C. Berthier, G. Knebel, G. Lapertot, J. Flouquet, Phys. Rev. Lett. **97**(11), 117002 (2006)
25. A.B. Vorontsov, M.J. Graf, in AIP Conference Proceedings LT24 850, 729 (2006)
26. G. Koutroulakis, V.F. Mitrović, M. Horvatić, C. Berthier, G. Lapertot, J. Flouquet, Phys. Rev. Lett. **101**(4), 047004 (2008)
27. M. Kenzelmann, T. Strassle, C. Niedermayer, M. Sigrist, B. Padmanabhan, M. Zolliker, A.D. Bianchi, R. Movshovich, E.D. Bauer, J.L. Sarrao, J.D. Thompson, Science **321**(5896), 1652 (2008)
28. G. Koutroulakis, M.D. Stewart, V.F. Mitrović, M. Horvatić, C. Berthier, G. Lapertot, J. Flouquet, Phys. Rev. Lett. **104**, 087001 (2010)
29. K. Kumagai, H. Shishido, T. Shibauchi, Y. Matsuda, Phys. Rev. Lett. **106**, 137004 (2011)
30. N.J. Curro, B.L. Young, R.R. Urbano, M.J. Graf, J. Low Temp. Phys. **2010**, 635 (2009)
31. A.D. Bianchi, M. Kenzelmann, L. DeBeer-Schmitt, J.S. White, E.M. Forgan, J. Mesot, M. Zolliker, J. Kohlbrecher, R. Movshovich, E.D. Bauer, J.L. Sarrao, Z. Fisk, C. Petrovic, M.R. Eskildsen, Science **319**, 177 (2008)
32. M. Kenzelmann, S. Gerber, N. Egetenmeyer, J.L. Gavilano, T. Strässle, A.D. Bianchi, E. Ressouche, R. Movshovich, E.D. Bauer, J.L. Sarrao, J.D. Thompson, Phys. Rev. Lett. **104**, 127001 (2010)
33. D.F. Agterberg, M. Sigrist, H. Tsunetsugu, Phys. Rev. Lett. **102**(20), 207004 (2009)
34. A. Aperis, G. Varelogiannis, P.B. Littlewood, Phys. Rev. Lett. **104**, 216403 (2010)
35. Y. Yanase, M. Sigrist, J. Phys. Soc. Jpn. **78**(11), 114715 (2009)
36. Y. Kato, C.D. Batista, I. Vekhter, Phys. Rev. Lett. **107**, 096401 (2011)

Chapter 2
ARPES: A Probe of Electronic Correlations

Riccardo Comin and Andrea Damascelli

Abstract Angle-resolved photoemission spectroscopy (ARPES) is one of the most direct methods of studying the electronic structure of solids. By measuring the kinetic energy and angular distribution of the electrons photoemitted from a sample illuminated with sufficiently high-energy radiation, one can gain information on both the energy and momentum of the electrons propagating inside a material. This is of vital importance in elucidating the connection between electronic, magnetic, and chemical structure of solids, in particular for those complex systems which cannot be appropriately described within the independent-particle picture. Among the various classes of complex systems, of great interest are the transition metal oxides, which have been at the center stage in condensed matter physics for the last four decades. Following a general introduction to the topic, we will lay the theoretical basis needed to understand the pivotal role of ARPES in the study of such systems. After a brief overview on the state-of-the-art capabilities of the technique, we will review some of the most interesting and relevant case studies of the novel physics revealed by ARPES in 3*d*-, 4*d*- and 5*d*-based oxides.

2.1 Introduction

Since their original discovery, correlated oxides have been extensively studied using a variety of experimental techniques and theoretical methods, thereby attracting an ever-growing interest by the community. It was soon realized that the low-energy electronic degrees of freedom were playing a key role in determining many of their unconventional properties, with the concepts of "correlations" and "many-body

A. Damascelli (✉) · R. Comin
Department of Physics and Astronomy, University of British Columbia,
Vancouver, BC V6T 1Z1, Canada
e-mail: damascelli@physics.ubc.ca

R. Comin
e-mail: r.comin@utoronto.ca

A. Avella and F. Mancini (eds.), *Strongly Correlated Systems*,
Springer Series in Solid-State Sciences 180, DOI 10.1007/978-3-662-44133-6_2

physics" gradually becoming part of the everyday dictionary of many condensed-matter physicists. It was only around the mid 90's that a series of considerable technological advancements, allowing for unprecedentedly high momentum- and energy-resolutions, made ARPES one of the prime techniques for the study of correlated materials. We will show, by discussing the required theoretical basis in conjunction with a few selected case studies, how the experimental information directly accessible using ARPES provides a unique and rich perspective towards the understanding of the electronic properties of these materials at the microscopic level.

The correlated materials treated here belong to the ample (and growing) class of transition metals oxides (TMOs). Despite giving rise to a rich variety of distinctive unconventional phenomena, these systems all share the same basic structural elements: TM-O_6 (near) octahedral units, where a central transition metal (TM) cation TM^{n+} is coordinated to 6 neighboring O^{2-} anions, sitting at positions $\boldsymbol{\delta} = \{(\pm a_x, \pm a_y, \pm a_z)\}$, a_i being the TM-O nearest neighbor bond length (along the axis $\hat{\mathbf{i}}$). Most TMOs possess either cubic ($a_x = a_y = a_z$) or tetragonal ($a_x = a_y \neq a_z$) TM-O_6 units, although deviations from these two local symmetries are also present in some compounds. The remaining elements in the structure primarily serve the purpose of completing the stoichiometry and also, in most cases, to help controlling certain material parameters (e.g. doping, bandwidth, structure, magnetism). The delicate interplay between the *localized* physics taking place *within* these building blocks, and the *delocalized* behaviour emerging when such local units are embedded in a crystalline matrix, is what makes these systems so complex and fascinating.

We will discuss the emerging physics in this class of materials, as one goes from the row of 3*d* to that of 5*d* transition metals. This is schematically illustrated in Fig. 2.1, where the relevant elements are highlighted (see caption). The phenomenology of correlated oxides can be understood in terms of the competition between charge fluctuation (favored by the O-2*p* electrons) and charge localization (driven by the TM-*d* electrons). The peculiarity of 3*d* and 4*f* shells is that the radial part of the wave functions has an extension which is small compared to typical interatomic distances, as opposed to the oxygen 2*p* orbitals which are more extended. This follows from the fact that the average squared radius $\langle r^2 \rangle_{nl}$ of the atomic wavefunctions decreases with increasing angular quantum number l. As a results, the localized 3*d* and 4*f* electrons are not well described within the independent particle picture, where electrons are assumed to interact with the average (electronic) charge density, which is hardly affected by the motion of a single electron. In reality, for the tightly confined 3*d* and 4*f* electrons, the addition of an extra electron in the same shell entails a large energy cost given by the strong increase in Coulomb repulsion U. This is at the heart of what is referred to as *strongly-correlated electron behavior*, and it underlies most of the spectacular phenomena observed in these materials. As a result, all the relevant degrees of freedom—charge, spin, orbital and lattice—are deeply entangled, and their mutual interplay is what governs the low-energy physics.

Over time experimentalists have learned how to tune this delicate interplay by means of selected control parameters—bandwidth, band filling, and dimensionality. All of these parameters are primarily tuned chemically (e.g. via the choice of the

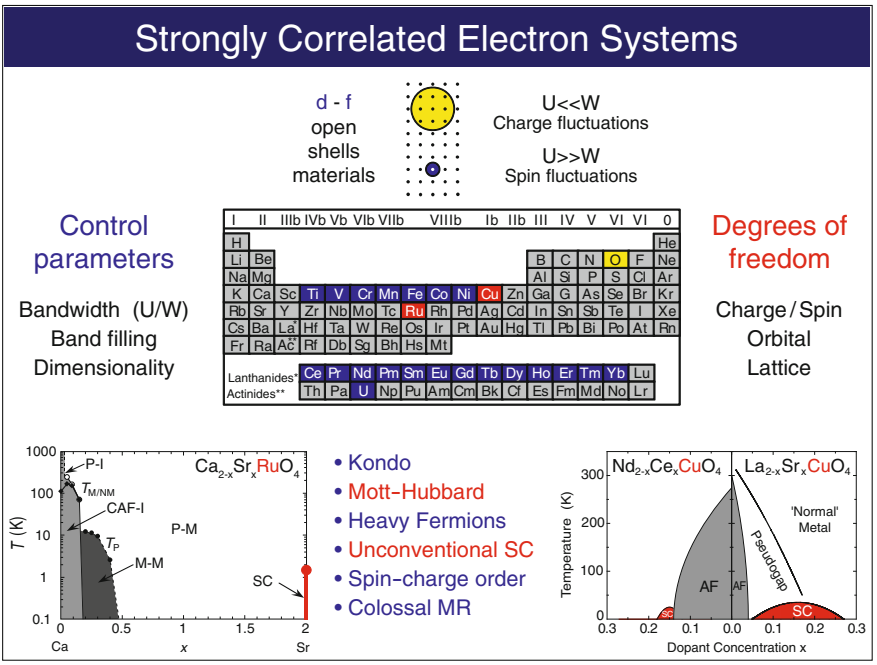

Fig. 2.1 Building blocks of correlated materials and related control parameters. U refers to the on-site Coulomb repulsion, whereas W indicates the bandwidth of the valence band, proportional to the electron hopping amplitude in the lattice. The *yellow* and *blue* circles pictorially represent the two extreme cases for an atomic wavefunction having $U \ll W$ and $U \gg W$, respectively. *Blue boxes* indicate those elements exhibiting strongly localized physics ($U \gg W$), due to the presence of localized $3d$ (transition metals) and $4f$ (rare earths) orbitals. Correlated physics emerges when these species form oxide compounds, and the localized d orbitals mix with the delocalized O $2p$ states. In this chapter we will review: $3d$-based materials, such as manganites, cobaltates, and cuprates, the $4d$-based ruthenates and rhodates, and the $5d$-based iridates. The phase diagrams for the special cases of Cu-based (from [1]) and Ru-based (from [2]) oxides, which exhibit unconventional superconductivity, are expanded in the *bottom right* and *left* panels, respectively

specific TM ion, or by carrier doping) but they can also be controlled experimentally (e.g. by means of pressure, EM fields, or in-situ doping). The resulting novel phenomena and materials include Kondo physics [3] and heavy fermion systems [4] (found especially in—but not limited to—$4f$-based materials), Mott-Hubbard/charge-transfer insulators [5] (e.g. CuO, NiO, CoO, MnO), unconventional superconductivity [6–8] (cuprates, such as e.g. La_2CuO_4, and also Sr_2RuO_4), spin-charge ordering phenomena [9, 10] (e.g. La_2CoO_4, La_2NiO_4, $La_{1-x}Ca_xMnO_3$), and colossal magnetoresistance [11] ($La_{2-x}Sr_xMn_2O_7$). Remarkably, some of these phenomena can be found in the very same phase diagram, as is the case of Cu- and Ru-oxides (see bottom-right and bottom-left phase diagrams in Fig. 2.1, respectively).

To better elucidate the origin and nature of correlated behaviour, we will first discuss one of the most fascinating manifestations of the novel, correlated physics

arising from the spatial extent of p- and d-orbitals: the *Mott insulator*. In order to understand the origin of this concept, it is useful to start from classical band theory. One of the fundamental paradigms of band theory affirms that the nature of the electronic ground state in a single-band material is entirely determined by the band filling, which is directly related to the number of electrons N_{UC} in the unit cell: if N_{UC} is odd (even), the system *must be* metallic (insulating). For this reason, the discovery of insulating TMOs having odd N_{UC} came as a surprise. The breakdown of single-particle physics, and consequently of band theory (where electrons are assumed to interact only with the lattice ionic potential and the average electronic density), was originally suggested by Sir. Neville Mott [12]. This new category of correlated insulators is the manifestation of the dominant role of on-site interactions in 3d oxides: at half-filling (1 electron per site), the large on-site Coulomb repulsion (parametrized by the Hubbard parameter U) between the strongly localized 3d electrons makes hopping processes unfavourable, thus leading to charge localization and subsequent insulating behaviour, with a gap in the electronic spectrum opening up at the chemical potential. When the lowest occupied and the first unoccupied bands both have mainly TM-d orbital character, as in Fig. 2.2a, we use the term *Mott insulator*. The presence of a *Mott gap*, with its characteristic scale of order U, is therefore a hallmark of correlated behaviour in these systems. The lowest electron removal and addition states (bands) are respectively termed *lower Hubbard band* (*LHB*) and *upper Hubbard band* (*UHB*). This is sketched in Fig. 2.2a, where a gap at the chemical potential is separating the LHB and UHB (both having mainly 3d-character).

The stability of a Mott-Hubbard insulating ground state against a delocalized metallic behavior lies in the fulfilment of the *Mott criterion*, i.e. $U > W$, which establishes the condition for the localizing energy scale (U) to overcome the delocalizing ones (the bandwidth W, proportional to intersite hopping). This criterion is based on the prerequisite that the correlated d-states are the lowest-lying ones, i.e. those closest to E_F. While this is in most cases true, it fails to hold for the late 3d transition metals [5, 13], where $\epsilon_{3d} < \epsilon_{2p}$ instead, ϵ being the orbital on-site energy (or the band center-of-mass in a delocalized picture). In such cases we talk of *charge-transfer insulators* [5], the denomination following from the fact that the lowest-energy excitation involves the transfer of one electron from the last occupied band, of O-2p character, onto the first unoccupied band, of TM-3d character. This is depicted in Fig. 2.2b, where now the *charge-transfer gap* separates the 3d-derived UHB and the O 2p-derived valence band. A comprehensive classification can be found in [5].

The bandwidth W and Coulomb repulsion U are not the only relevant energy scales in the field of correlated materials. More recently, a new class of materials has appeared on the stage, that are based on the late 5d transition metals (osmium, iridium), and whose electronic states have to be treated within a relativistic framework, due to the heavier nuclear mass. This results in a new energy scale making its way into the problem: *spin-orbit* (SO) *interaction*, whose strength will be indicated by ζ_{SO}. This new element in the Hamiltonian, despite being a single-particle term (coming from the expansion of the single-fermion Dirac Hamiltonian), strongly affects

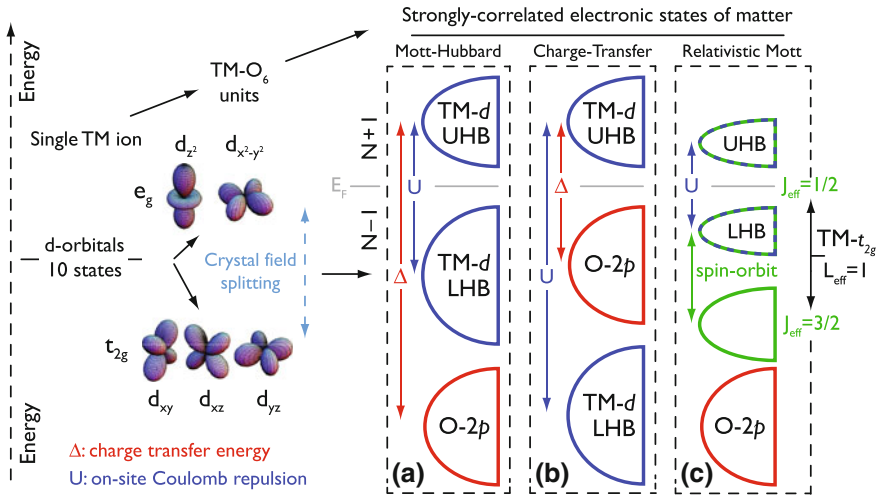

Fig. 2.2 Different types of correlated quantum states of matter discovered in transition metal oxides. The energy axis refers to spectrum of many-body excitations, with the Fermi Energy E_F separating the electron addition part ($N+1$, above E_F) from the electron removal part ($N-1$, below E_F). **a** when d-states are close to E_F (i.e., they are the *lowest-ionization states*), the partially-filled d-band is split into a lower (LHB) and an upper Hubbard band (UHB) by the action of U. Whenever $U > W$ a gap opens up at E_F. **b** same as (a), but now the last occupied band has O-2p character, since U is larger than the Cu-O charge-transfer energy Δ; the corresponding gap is a *charge-transfer gap*. **c** the action of *spin-orbit* (SOC) *interaction* splits the t_{2g} manifold into $J_{eff} = 3/2$ and 1/2 submanifolds. The latter is higher in energy and lies close to E_F. Again, the action of U can open a Mott-like gap, but this hinges on the previous SOC-induced splitting of the t_{2g} band

the balance governing the interplay between W and U, making the previously introduced Mott criterion not sufficient. This results in the emergence of a new class of correlated quantum states of matter, the *relativistic Mott insulator*, in which on-site Coulomb repulsion and spin-orbit interaction have to be treated on equal footing. The idea behind the existence of such a state is sketched in Fig. 2.2c. To summarize, we have introduced three different classes of correlated TMOs:

1. Mott-Hubbard insulators—Fig. 2.2a.
2. Charge-transfer insulators—Fig. 2.2b.
3. Relativistic Mott insulators—Fig. 2.2c.

Please note that the 4d-based oxides have been left out of this overview, as the presence of Mott physics in such systems is still debated, although they host a variety of different many-body phenomena, including relativistic correlated metallic behavior and unconventional superconductivity.

It is then clear how, as one goes down from 3d to 5d materials, U progressively decreases whereas a new energy scale, spin-orbit coupling, gains importance and thus has to be accounted on equal footing. The evolution of U/W and the interplay

with SO from 3*d* to 5*d* will be the focus of this review. In the last section of this chapter we will present a few selected examples which illustrate the different flavors of correlated electrodynamics in various TMOs (cuprates, manganites, cobaltates, ruthenates, rhodates, and iridates), and discuss the role of ARPES for quantitative and qualitative estimates of correlation effects in these systems.

2.2 The ARPES Technique[1]

Photoelectron spectroscopy is a general term that refers to all those techniques based on the application of the photoelectric effect originally observed by Hertz [15] and later explained as a manifestation of the quantum nature of light by Einstein [16], who recognized that when light is incident on a sample an electron can absorb a photon and escape from the material with a maximum kinetic energy $E_{kin} = h\nu - \phi$ (where ν is the photon frequency and ϕ, the material work function, is a measure of the potential barrier at the surface that prevents the valence electrons from escaping, and is typically 4–5 eV in metals). In the following, we will show how the photoelectric effect also provides us with deep insights into the quantum description of the solid state. In particular, we will give a general overview of angle-resolved photoemission spectroscopy (ARPES), a highly advanced spectroscopic method that allows the direct experimental study of the momentum-dependent electronic band structure of solids. For a further discussion of ARPES and other spectroscopic techniques based on the detection of photoemitted electrons, we refer the reader to the extensive literature available on the subject [1, 17–47].

As we will see in detail throughout the paper and in particular in Sect. 2.4, due to the complexity of the photoemission process in solids the quantitative analysis of the experimental data is often performed under the assumption of the *independent-particle picture* and of the *sudden approximation* (i.e., disregarding the many-body interactions as well as the relaxation of the system during the photoemission itself). The problem is further simplified within the so-called *three-step model* (Fig. 2.3a), in which the photoemission event is decomposed in three independent steps: optical excitation between the initial and final *bulk* Bloch eigenstates, *travel* of the excited electron to the surface, and escape of the photoelectron into vacuum after transmission through the *surface* potential barrier. This is the most common approach, in particular when photoemission spectroscopy is used as a tool to map the electronic band structure of solids. However, from the quantum-mechanical point of view photoemission should not be described in terms of several independent events but rather as a *one-step* process (Fig. 2.3b): in terms of an optical transition (with probability given by 2.10) between initial and final states consisting of many-body wave functions that obey appropriate boundary conditions at the surface of the solid. In particular (see Fig. 2.4), the initial state should be one of the possible N-electron eigenstates of the semi-infinite crystal, and the final state must be one of the eigenstates of the ionized $(N-1)$-electron semi-infinite crystal; the latter has also to include

[1] Parts of the following sections have been readapted from our previous publications, [1, 14].

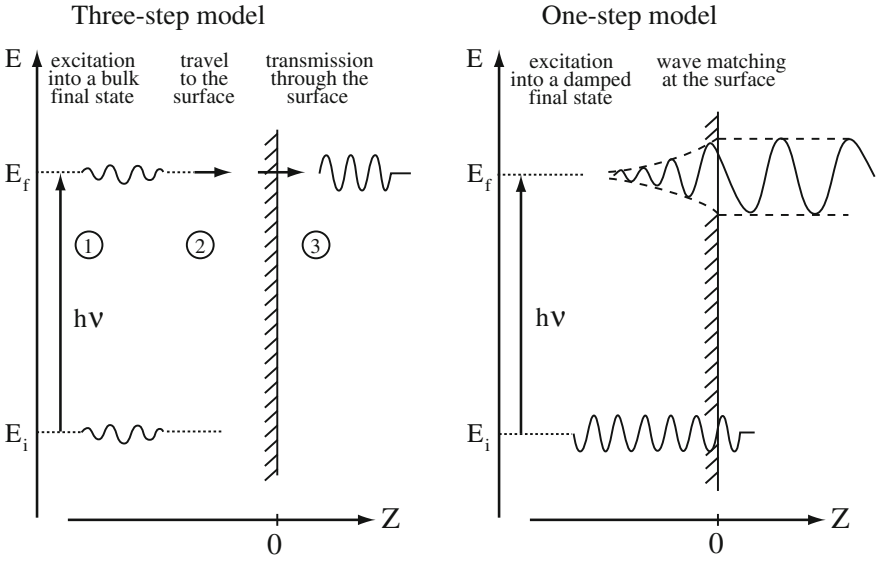

Fig. 2.3 Pictorial representation of three-step and one-step model description of the photoemission process (from [30])

a component consisting of a propagating plane-wave in vacuum (to account for the escaping photoelectron) with a finite amplitude inside the crystal (to provide some overlap with the initial state). Furthermore, as expressed by 2.10, which represents a complete one-step description of the problem, in order for an electron to be photoemitted in vacuum not only there must be a finite overlap between the amplitude of initial and final states, but the following energy and momentum conservation laws for the impinging photon and the N-electron system as a whole must also be obeyed:

$$E_f^N - E_i^N = h\nu \tag{2.1}$$

$$\mathbf{k}_f^N - \mathbf{k}_i^N = \mathbf{k}_{h\nu}\,. \tag{2.2}$$

Here the indexes i and f refer to initial and final state, respectively, and $\mathbf{k}_{h\nu}$ is the momentum of the incoming photon. Note that, in the following, when proceeding with the more detailed analysis of the photoemission process as well as its application to the study of the momentum-dependent electronic structure of solids (in terms of both conventional band mapping as well as many-body effects), we will mainly restrict ourselves to the context of the three-step model and the sudden approximation.

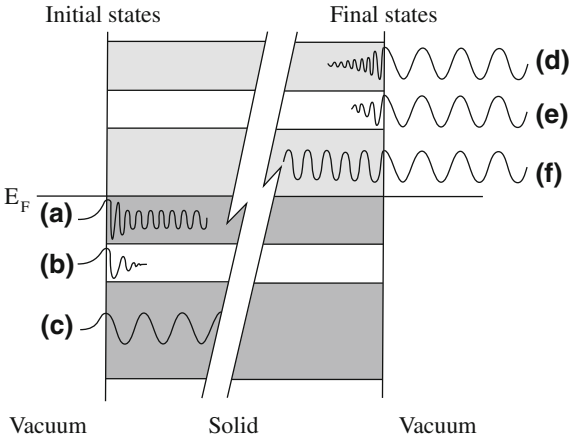

Fig. 2.4 Initial (*left*) and final (*right*) eigenstates for the semi-infinite crystal. *Left* **a** surface resonance; **b** surface Shockley state situated in a gap of the bulk band structure; **c** bulk Bloch state. *Right* **d** surface resonance; **e** in gap evanescent state; **f** bulk Bloch final state (from [48])

2.3 Kinematics of Photoemission

The energetics and kinematics of the photoemission process are shown in Figs. 2.5 and 2.6, while the geometry of an ARPES experiment is sketched in Fig. 2.7a. A beam of monochromatized radiation supplied either by a gas-discharge lamp, a UV laser, or a synchrotron beamline is incident on a sample (which has to be a properly aligned single crystal in order to perform *angle*- or, equivalently, *momentum*-resolved measurements). As a result, electrons are emitted by photoelectric effect and escape into the vacuum in all directions. By collecting the photoelectrons with an electron energy analyzer characterized by a finite acceptance angle, one measures their kinetic energy E_{kin} for a given emission direction. This way, the wave vector or momentum $\mathbf{K} = \mathbf{p}/\hbar$ of the photoelectrons *in vacuum* is also completely determined: its modulus is given by $K = \sqrt{2mE_{kin}}/\hbar$ and its components parallel ($\mathbf{K}_{||} = K_x\hat{\mathbf{u}}_x + K_y\hat{\mathbf{u}}_y$) and perpendicular ($\mathbf{K}_{\perp} = K_z\hat{\mathbf{u}}_z$) to the sample surface are obtained in terms of the polar (ϑ) and azimuthal (φ) emission angles defined by the experiment:

$$K_x = \frac{1}{\hbar}\sqrt{2mE_{kin}}\sin\vartheta\cos\varphi \tag{2.3}$$

$$K_y = \frac{1}{\hbar}\sqrt{2mE_{kin}}\sin\vartheta\sin\varphi \tag{2.4}$$

$$K_z = \frac{1}{\hbar}\sqrt{2mE_{kin}}\cos\vartheta\,. \tag{2.5}$$

The goal is then to deduce the electronic dispersion relations $E(\mathbf{k})$ for the solid left behind, i.e. the relation between binding energy E_B and momentum $\mathbf{k}$ for the electrons propagating *inside* the solid, starting from E_{kin} and $\mathbf{K}$ measured for the

photoelectrons *in vacuum*. In order to do that, one has to exploit the total energy and momentum conservation laws ((2.1) and (2.2), respectively). Within the non-interacting electron picture, it is particularly straightforward to take advantage of the energy conservation law and relate, as pictorially described in Fig. 2.5, the kinetic energy of the photoelectron to the binding energy E_B of the electronic-state inside the solid:

$$E_{kin} = h\nu - \phi - |E_B| \,. \tag{2.6}$$

More complex, as we will discuss below, is to gain full knowledge of the crystal electronic momentum $\mathbf{k}$. Note, however, that the photon momentum can be neglected in (2.2) at the low photon energies most often used in ARPES experiments ($h\nu < 100\,\text{eV}$), as it is much smaller than the typical Brillouin-zone dimension $2\pi/a$ of a solid (see Sect. 2.7 for more details). As shown in Fig. 2.6, within the three-step model description (see also Sect. 2.4), the optical transition between the bulk initial and final states can be described by a vertical transition in the *reduced-zone scheme* ($\mathbf{k}_f - \mathbf{k}_i = 0$), or equivalently by a transition between momentum-space points connected by a reciprocal-lattice vector $\mathbf{G}$ in the *extended-zone scheme* ($\mathbf{k}_f - \mathbf{k}_i = \mathbf{G}$). In regard to (2.1) and (2.2) and the deeper meaning of the reciprocal-lattice vector $\mathbf{G}$ note that, as emphasized by Mahan in his seminal paper on the theory of photoemission in simple metals [49], "*in a nearly-free-electron gas, optical absorption may be viewed as a two-step process. The absorption of the photon provides the electron with the additional energy it needs to get to the excited state. The crystal potential imparts to the electron the additional momentum it needs to reach the excited state. This momentum comes in multiples of the reciprocal-lattice vectors* $\boldsymbol{G}$. *So in a reduced zone picture, the transitions are vertical in wave-vector space. But in photoemission, it is more useful to think in an extended-zone scheme.*" On the contrary in an infinite crystal with no periodic potential (i.e., a truly free-electron gas scenario lacking of any periodic momentum structure), no $\mathbf{k}$-conserving transition is possible in the limit $\mathbf{k}_{h\nu} = 0$, as one cannot go from an initial to a final state along the same unperturbed free-electron parabola without an external source of momentum. In other words, direct transitions are prevented because of the lack of appropriate final states (as opposed to the periodic case of Fig. 2.6). Then again the problem would be quite different if the surface was more realistically taken into account, as in a one-step model description of a semi-infinite crystal. In fact, while the surface does not perturb the translational symmetry in the x–y plane and $\mathbf{k}_\parallel$ is conserved to within a reciprocal lattice vector $\mathbf{G}_\parallel$, due to the abrupt potential change along the z axis the perpendicular momentum $\mathbf{k}_\perp$ is not conserved across the sample surface (i.e., $\mathbf{k}_\perp$ is not a good quantum number except for deeply into the solid, contrary to $\mathbf{k}_{||}$). Thus, the surface can play a direct role in momentum conservation, delivering the necessary momentum for indirect transitions even in absence of the crystal potential (i.e., the so-called *surface photoelectric effect*; see also (2.10) and the related discussion).

Reverting to the three-step model *direct-transition* description of Fig. 2.6, the transmission through the sample surface is obtained by matching the bulk Bloch eigenstates inside the sample to free-electron plane waves in vacuum. Because of the translational symmetry in the x–y plane across the surface, from these match-

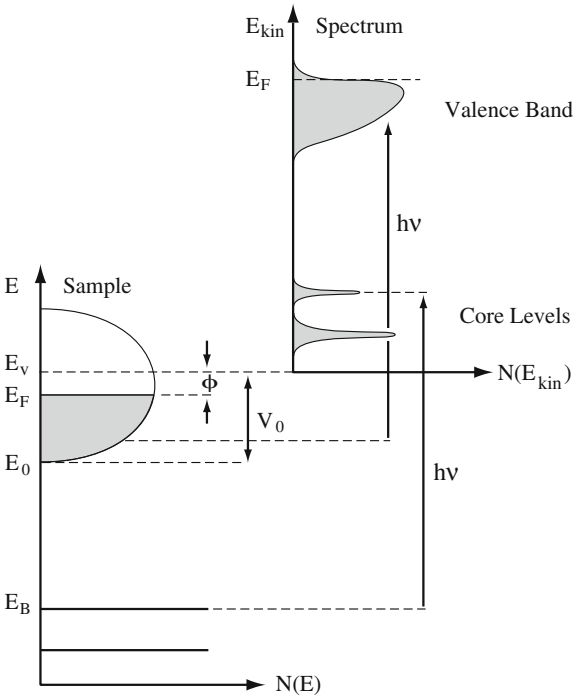

Fig. 2.5 Energetics of the photoemission process (from [30]). The electron energy distribution produced by the incoming photons, and measured as a function of the kinetic energy E_{kin} of the photoelectrons (*right*), is more conveniently expressed in terms of the binding energy E_B (*left*) when one refers to the density of states in the solid ($E_B = 0$ at E_F)

ing conditions it follows that the parallel component of the electron momentum is conserved in the process:

$$|\mathbf{k}_\parallel| = |\mathbf{K}_\parallel| = \frac{1}{\hbar}\sqrt{2mE_{kin}} \cdot \sin\vartheta \tag{2.7}$$

where $\mathbf{k}_\parallel$ is the component parallel to the surface of the electron crystal momentum in the *extended-zone scheme* (upon going to larger ϑ angles, one actually probes electrons with $\mathbf{k}_\parallel$ lying in higher-order Brillouin zones; by subtracting the corresponding reciprocal-lattice vector $\mathbf{G}_\parallel$, the *reduced* electron crystal momentum in the first Brillouin zone is obtained). As for the determination of $k_\perp$, which is not conserved but is also needed in order to map the electronic dispersion $E(\mathbf{k})$ versus the total crystal wave vector $\mathbf{k}$, a different approach is required. As a matter of fact, several specific experimental methods for absolute three dimensional band mapping have been developed [30, 50, 51]; however, these are rather complex and require additional and/or complementary experimental data. Alternatively, the value of $k_\perp$ can be determined if some *a priori* assumption is made for the dispersion of the electron final states involved in the photoemission process; in particular, one can either use the results of band structure calculations, or adopt a nearly-free-electron description for the final bulk Bloch states:

$$E_f(\mathbf{k}) = \frac{\hbar^2\mathbf{k}^2}{2m} - |E_0| = \frac{\hbar^2(\mathbf{k}_\parallel{}^2 + k_\perp{}^2)}{2m} - |E_0| \tag{2.8}$$

where once again the electron momenta are defined in the *extended-zone scheme*, and E_0 corresponds to the bottom of the valence band as indicated in Fig. 2.6 (note that both E_0 and E_f are referenced to the Fermi energy E_F, while E_{kin} is referenced to the vacuum level E_v). Because $E_f = E_{kin} + \phi$ and $\hbar^2\mathbf{k}_\parallel^2/2m = E_{kin}\sin^2\vartheta$, which follow from Fig. 2.6 and (2.7), one obtains from (2.8):

$$k_\perp = \frac{1}{\hbar}\sqrt{2m(E_{kin}\cos^2\vartheta + V_0)}\,. \tag{2.9}$$

Here $V_0 = |E_0| + \phi$ is the *inner potential*, which corresponds to the energy of the bottom of the valence band referenced to vacuum level E_v. From (2.9) and the measured values of E_{kin} and ϑ, if V_0 is also known, one can then obtain the corresponding value of $\mathbf{k}_\perp$. As for the determination of V_0, three methods are generally used: (i) optimize the agreement between theoretical and experimental band mapping for the occupied electronic state; (ii) set V_0 equal to the theoretical zero of the muffin tin potential used in band structure calculations; (iii) infer V_0 from the experimentally observed periodicity of the dispersion $E(\mathbf{k}_\perp)$. The latter is actually the most convenient method as the experiment can be realized by simply detecting the photoelectrons emitted along the surface normal (i.e., $\mathbf{K}_\parallel = 0$) while varying the incident photon energy and, in turn, the energy E_{kin} of the photoelectrons and thus K_z (see (2.5)). Note that the nearly-free electron approximation for the final states is expected to work well for materials in which the Fermi surface has a simple spherical (free-electron-like) topology such as in the alkali metals, and for high-energy final states in which case the crystal potential is a small perturbation (eventually the final-state bands become so closely spaced in energy as to form a continuum, and the details of the final states become unimportant). However this approximation is also often used for more complicated systems, even if the initial states are not-free electron-like.

A particular case in which the uncertainty in $k_\perp$ is less relevant is that of the low-dimensional systems characterized by an anisotropic electronic structure and, in particular, a negligible dispersion along the z axis (i.e., the surface normal, see Fig. 2.7a). The electronic dispersion is then almost exclusively determined by $\mathbf{k}_\parallel$ (as in the case of many transition metal oxides, such as for example the two-dimensional copper oxide superconductors [1]). As a result, one can map out in detail the electronic dispersion relations $E(\mathbf{k})$ simply by tracking, as a function of $\mathbf{K}_\parallel$, the energy position of the peaks detected in the ARPES spectra for different take-off angles (as in Fig. 2.7b, where both direct and inverse photoemission spectra for a single band dispersing through the Fermi energy E_F are shown). Furthermore, as an additional bonus associated with the lack of a z dispersion, one can directly identify the width of the photoemission peaks as the lifetime of the photohole [53], which contains information on the intrinsic correlation effects of the system and is formally described by the imaginary part of the electron self energy (see Sect. 2.5). On the contrary, in 3D

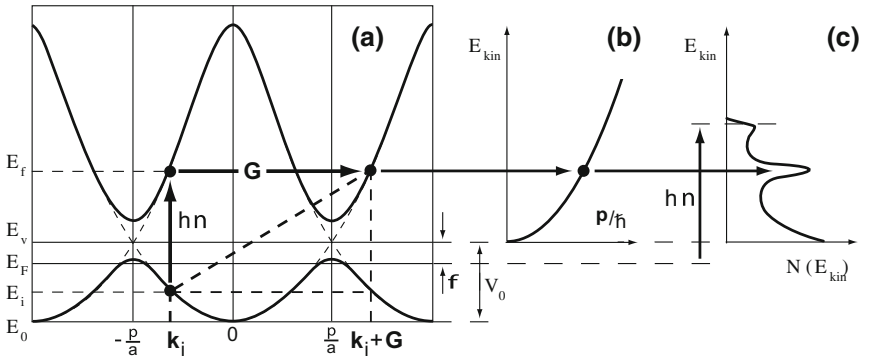

Fig. 2.6 Kinematics of the photoemission process within the three-step nearly-free-electron final state model. **a** direct optical transition in the solid (the lattice supplies the required momentum, given by the **G** vector); **b** free-electron final state in vacuum; **c** corresponding photoelectron spectrum, with a background due to the scattered electrons ($E_B = 0$ at E_F). From [52]

systems the linewidth contains contributions from both photohole and photoelectron lifetimes, with the latter reflecting final state scattering processes and thus the finite probing depth; as a consequence, isolating the intrinsic many-body effects becomes a much more complicated problem.

2.4 Three-Step Model and Sudden Approximation

To develop a formal description of the photoemission process, one has to calculate the transition probability w_{fi} for an optical excitation between the N-electron ground state Ψ_i^N and one of the possible final states Ψ_f^N. This can be approximated by Fermi's golden rule:

$$w_{fi} = \frac{2\pi}{\hbar}|\langle\Psi_f^N|H_{int}|\Psi_i^N\rangle|^2\delta(E_f^N - E_i^N - h\nu) \tag{2.10}$$

where $E_i^N = E_i^{N-1} - E_B^{\mathbf{k}}$ and $E_f^N = E_f^{N-1} + E_{kin}$ are the initial and final-state energies of the N-particle system ($E_B^{\mathbf{k}}$ is the binding energy of the photoelectron with kinetic energy E_{kin} and momentum $\mathbf{k}$). The interaction with the photon is treated as a perturbation given by:

$$H_{int} = \frac{e}{2mc}(\mathbf{A}\cdot\mathbf{p} + \mathbf{p}\cdot\mathbf{A}) = \frac{e}{mc}\,\mathbf{A}\cdot\mathbf{p} \tag{2.11}$$

where $\mathbf{p}$ is the electronic momentum operator and $\mathbf{A}$ is the electromagnetic vector potential (note that the gauge $\Phi = 0$ was chosen for the scalar potential Φ, and the quadratic term in $\mathbf{A}$ was dropped because in the linear optical regime it is typically negligible with respect to the linear terms). In (2.11) we also made use of the com-

mutator relation $[\mathbf{p}, \mathbf{A}] = -i\hbar\nabla \cdot \mathbf{A}$ and dipole approximation (i.e., $\mathbf{A}$ constant over atomic dimensions and therefore $\nabla \cdot \mathbf{A} = 0$, which holds in the ultraviolet). Although this is a routinely used approximation, it should be noted that $\nabla \cdot \mathbf{A}$ might become important at the *surface* where the electromagnetic fields may have a strong spatial dependence. This surface photoemission contribution, which is proportional to $(\varepsilon - 1)$ where ε is the medium dielectric function, can interfere with the bulk contribution resulting in asymmetric lineshapes for the bulk direct-transition peaks [27, 54–56]. At this point, a more rigorous approach is to proceed with the so-called *one-step model* (Fig. 2.3b), in which photon absorption, electron removal, and electron detection are treated as a single coherent process [49, 57–70]. In this case bulk, surface, and vacuum have to be included in the Hamiltonian describing the crystal, which implies that not only bulk states have to be considered but also surface and evanescent states, as well as surface resonances (see Fig. 2.4). Note that, under the assumption $\nabla \cdot \mathbf{A} = 0$, from (2.11) and the commutation relation $[H_0, \mathbf{p}] = i\hbar\nabla V$ (where $H_0 = \mathbf{p}^2/2m + V$ is the unperturbed Hamiltonian of the semi-infinite crystal) it follows that the matrix elements appearing in (2.10) are proportional to $\langle \Psi_f^N | \mathbf{A} \cdot \nabla V | \Psi_i^N \rangle$. This explicitly shows that for a true free-electron like system it would be impossible to satisfy simultaneously energy and momentum conservation laws inside the material because there $\nabla V = 0$. The only region where electrons could be photoexcited is at the surface where $\partial V/\partial z \neq 0$, which gives rise to the so-called *surface photoelectric effect*. However, due to the complexity of the one-step model, photoemission data are usually discussed within the three-step model (Fig. 2.3a), which, although purely phenomenological, has proven to be rather successful [61, 71, 72]. Within this approach, the photoemission process is subdivided into three independent and sequential steps:

(i) Optical excitation of the electron in the *bulk*.
(ii) Travel of the excited electron to the surface.
(iii) Escape of the photoelectron into vacuum.

The total photoemission intensity is then given by the product of three independent terms: the total probability for the optical transition, the scattering probability for the travelling electrons, and the transmission probability through the surface potential barrier. Step (i) contains all the information about the intrinsic electronic structure of the material and will be discussed in detail below. Step (ii) can be described in terms of an effective mean free path, proportional to the probability that the excited electron will reach the surface without scattering (i.e., with no change in energy and momentum). The inelastic scattering processes, which determine the surface sensitivity of photoemission (see Sect. 2.7), give rise to a continuous background in the spectra which is usually ignored or subtracted. Step (iii) is described by a transmission probability through the surface, which depends on the energy of the excited electron and the material work function ϕ (in order to have any finite escape probability the condition $\hbar^2 k_\perp^2/2m \geq |E_0| + \phi$ must be satisfied).

In evaluating step (i), and therefore the photoemission intensity in terms of the transition probability w_{fi}, it would be convenient to factorize the wavefunctions in (2.10) into photoelectron and $(N-1)$-electron terms, as we have done for the corresponding energies. The final state Ψ_f^N then becomes:

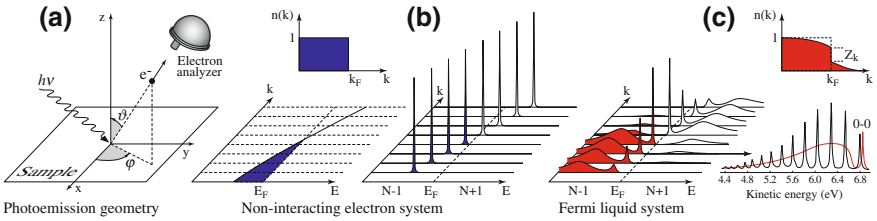

Fig. 2.7 **a** Geometry of an ARPES experiment; the emission direction of the photoelectron is specified by the polar (ϑ) and azimuthal (φ) angles. Momentum resolved one-electron removal and addition spectra for: **b** a non-interacting electron system (with a single energy band dispersing across the Fermi level); **c** an interacting Fermi liquid system. The corresponding ground-state ($T = 0$ K) momentum distribution function $n(\mathbf{k})$ is also shown. **c** *Bottom right* photoelectron spectrum of gaseous hydrogen (*black*) and the ARPES spectrum of solid hydrogen developed from the gaseous one (*red*). Adapted from [1]

$$\Psi_f^N = \mathcal{A}\,\phi_f^{\mathbf{k}}\,\Psi_f^{N-1} \tag{2.12}$$

where $\mathcal{A}$ is an antisymmetric operator that properly antisymmetrizes the N-electron wavefunction so that the Pauli principle is satisfied, $\phi_f^{\mathbf{k}}$ is the wavefunction of the photoelectron with momentum $\mathbf{k}$, and Ψ_f^{N-1} is the final state wavefunction of the $(N-1)$-electron system left behind, which can be chosen as an excited state with eigenfunction Ψ_m^{N-1} and energy E_m^{N-1}. The *total* transition probability is then given by the sum over *all* possible excited states m. This derivation, which originated from writing the transition probability using Fermi's golden rule, (2.10), implicitly assumes the validity of the so-called *sudden approximation*, which is extensively used in many-body calculations of the photoemission spectra from interacting electron systems, and is in principle applicable only to high kinetic-energy electrons. In this limit, the photoemission process is assumed to be *sudden*, with no post-collisional interaction between the photoelectron and the system left behind (in other words, an electron is instantaneously removed and the effective potential of the system changes discontinuously at that instant).[2] Note, however, that the sudden approximation is inappropriate for low kinetic energy photoelectrons, which may need longer than the system response time to escape into vacuum. In this case, the so-called *adiabatic limit*, one can no longer use the instantaneous transition amplitudes w_{fi} and the detailed screening of photoelectron and photohole has to be taken into account [74].

For the initial state, let us first assume for simplicity that Ψ_i^N is a single Slater determinant (i.e., Hartree-Fock formalism), so that we can write it as the product of a one-electron orbital $\phi_i^{\mathbf{k}}$ and an $(N-1)$-particle term:

[2] In particular, this implies that the wavefunction for the (N−1)-electron system at time t_1 (when the interaction H_{int} is switched on) remains unchanged when H_{int} is switched off at t_2, thus allowing to use Fermi's golden rule and the instantaneous transition probabilities w_{fi}. This approximation is only valid when $t_2 - t_1 \ll \frac{\hbar}{\Delta E}$, ΔE being the characteristic energy separation of the (N−1) system [73].

$$\Psi_i^N = \mathcal{A}\,\phi_i^{\mathbf{k}}\,\Psi_i^{N-1}\,. \tag{2.13}$$

More generally, however, Ψ_i^{N-1} should be expressed as $\Psi_i^{N-1} = c_{\mathbf{k}}\Psi_i^N$, where $c_{\mathbf{k}}$ is the annihilation operator for an electron with momentum $\mathbf{k}$. This also shows that Ψ_i^{N-1} is *not* an eigenstate of the (N−1) particle Hamiltonian, but is just what remains of the N-particle wavefunction after having pulled out one electron. At this point, we can write the matrix elements in (2.10) as:

$$\langle\Psi_f^N|H_{int}|\Psi_i^N\rangle = \langle\phi_f^{\mathbf{k}}|H_{int}|\phi_i^{\mathbf{k}}\rangle\langle\Psi_m^{N-1}|\Psi_i^{N-1}\rangle \tag{2.14}$$

where $\langle\phi_f^{\mathbf{k}}|H_{int}|\phi_i^{\mathbf{k}}\rangle \equiv M_{f,i}^{\mathbf{k}}$ is the one-electron dipole matrix element, and the second term is the $(N-1)$-electron overlap integral. Here, we replaced Ψ_f^{N-1} with an eigenstate Ψ_m^{N-1}, as discussed above. The total photoemission intensity measured as a function of E_{kin} at a momentum $\mathbf{k}$, namely $I(\mathbf{k}, E_{kin}) = \sum_{f,i} w_{f,i}$, is then proportional to:

$$\sum_{f,i} |M_{f,i}^{\mathbf{k}}|^2 \sum_m |c_{m,i}|^2 \delta(E_{kin} + E_m^{N-1} - E_i^N - h\nu) \tag{2.15}$$

where $|c_{m,i}|^2 = |\langle\Psi_m^{N-1}|\Psi_i^{N-1}\rangle|^2$ is the probability that the removal of an electron from state i will leave the $(N-1)$-particle system in the excited state m. From here we see that, if $\Psi_i^{N-1} = \Psi_{m_0}^{N-1}$ for one particular $m = m_0$, the corresponding $|c_{m_0,i}|^2$ will be unity and all the others $c_{m,i}$ zero; in this case, if also $M_{f,i}^{\mathbf{k}} \neq 0$, the ARPES spectra will be given by a delta function at the Hartree-Fock orbital energy $E_B^{\mathbf{k}} = -\varepsilon_{\mathbf{k}}^b$, as shown in Fig. 2.7b (i.e., non-interacting particle picture). In the strongly correlated systems, however, many of the $|c_{m,i}|^2$ terms will be different from zero because the removal of the photoelectron results in a strong change of the system effective potential and, in turn, Ψ_i^{N-1} will have an overlap with many of the eigenstates Ψ_m^{N-1}. Therefore, the ARPES spectra will not consist of single delta functions but will show a main line and several satellites according to the number of excited states m created in the process (Fig. 2.7c).

2.5 One-Particle Spectral Function

In the discussion of photoemission on solids, and in particular on the correlated electron systems in which many $|c_{m,i}|^2$ in (2.15) are different from zero, the most powerful and commonly used approach is based on the Green's function formalism [75–80]. In this context, the propagation of a single electron in a many-body system is described by the *time-ordered* one-electron Green's function $\mathcal{G}(\mathbf{k}, t - t')$, which can be interpreted as the probability amplitude that an electron added to the system in a Bloch state with momentum $\mathbf{k}$ at a time zero will still be in the same state

after a time $|t - t'|$. By taking the Fourier transform, $\mathcal{G}(\mathbf{k}, t - t')$ can be expressed in energy-momentum representation resulting in $\mathcal{G}(\mathbf{k}, \omega) = G^+(\mathbf{k}, \omega) + G^-(\mathbf{k}, \omega)$, where $G^+(\mathbf{k}, \omega)$ and $G^-(\mathbf{k}, \omega)$ are the one-electron addition and removal Green's function, respectively. At $T = 0$:

$$G^{\pm}(\mathbf{k}, \omega) = \sum_m \frac{|\langle \Psi_m^{N\pm1} | c_{\mathbf{k}}^{\pm} | \Psi_i^N \rangle|^2}{\omega - E_m^{N\pm1} + E_i^N \pm i\eta} \tag{2.16}$$

where the operator $c_{\mathbf{k}}^+ = c_{\mathbf{k}\sigma}^\dagger$ ($c_{\mathbf{k}}^- = c_{\mathbf{k}\sigma}$) creates (annihilates) an electron with energy ω, momentum $\mathbf{k}$, and spin σ in the N-particle initial state Ψ_i^N; the summation runs over all possible $(N \pm 1)$-particle eigenstates $\Psi_m^{N\pm1}$ with eigenvalues $E_m^{N\pm1}$, and η is a positive infinitesimal (note also that from here on we will take $\hbar = 1$). In the limit $\eta \to 0^+$ one can make use of the identity $(x \pm i\eta)^{-1} = \mathcal{P}(1/x) \mp i\pi\delta(x)$, where $\mathcal{P}$ denotes the principle value, to obtain the *one-particle spectral function* $A(\mathbf{k}, \omega) = A^+(\mathbf{k}, \omega) + A^-(\mathbf{k}, \omega) = -(1/\pi)\mathrm{Im}\, G(\mathbf{k}, \omega)$, with:

$$A^{\pm}(\mathbf{k}, \omega) = \sum_m |\langle \Psi_m^{N\pm1} | c_{\mathbf{k}}^{\pm} | \Psi_i^N \rangle|^2 \delta(\omega - E_m^{N\pm1} + E_i^N) \tag{2.17}$$

and $G(\mathbf{k}, \omega) = G^+(\mathbf{k}, \omega) + [G^-(\mathbf{k}, \omega)]^*$, which defines the *retarded* Green's function. Note that $A^-(\mathbf{k}, \omega)$ and $A^+(\mathbf{k}, \omega)$ define the one-electron removal and addition spectra which one can probe with direct and inverse photoemission, respectively. This is evidenced, for the direct case, by the comparison between the expression for $A^-(\mathbf{k}, \omega)$ and (2.15) for the photoemission intensity (note that in the latter $\Psi_i^{N-1} = c_{\mathbf{k}} \Psi_i^N$ and the energetics of the photoemission process has been explicitly accounted for). Finite temperatures effect can be taken into account by extending the Green's function formalism just introduced to $T \neq 0$ (see, e.g., [78]). In the latter case, by invoking once again the sudden approximation, the intensity measured in an ARPES experiment on a 2D single-band system can be conveniently written as:

$$I(\mathbf{k}, \omega) = I_0(\mathbf{k}, \nu, \mathbf{A}) f(\omega) A(\mathbf{k}, \omega) \tag{2.18}$$

where $\mathbf{k} = \mathbf{k}_\parallel$ is the in-plane electron momentum, ω is the electron energy with respect to the Fermi level, and $I_0(\mathbf{k}, \nu, \mathbf{A})$ is proportional to the squared one-electron matrix element $|M_{f,i}^{\mathbf{k}}|^2$ and therefore depends on the electron momentum, and on the energy and polarization of the incoming photon. We also introduced the Fermi function $f(\omega) = (e^{\omega/k_B T} + 1)^{-1}$, which accounts for the fact that direct photoemission probes only the occupied electronic states. Note that in (2.18) we neglected the presence of any extrinsic background and the broadening due to the energy and momentum resolution, which however have to be carefully considered when performing a quantitative analysis of the ARPES spectra [see Sect. 2.6 and (2.25)].

The corrections to the Green's function originating from electron-electron correlations can be conveniently expressed in terms of the electron *proper self energy* $\Sigma(\mathbf{k}, \omega) = \Sigma'(\mathbf{k}, \omega) + i\Sigma''(\mathbf{k}, \omega)$. Its real and imaginary parts contain all the infor-

mation on the energy renormalization and lifetime, respectively, of an electron with band energy $\varepsilon^b_{\mathbf{k}}$ and momentum $\mathbf{k}$ propagating in a many-body system. The Green's and spectral functions expressed in terms of the self energy are then given by:

$$G(\mathbf{k},\omega) = \frac{1}{\omega - \varepsilon^b_{\mathbf{k}} - \Sigma(\mathbf{k},\omega)} \tag{2.19}$$

$$A(\mathbf{k},\omega) = -\frac{1}{\pi}\frac{\Sigma''(\mathbf{k},\omega)}{[\omega - \varepsilon^b_{\mathbf{k}} - \Sigma'(\mathbf{k},\omega)]^2 + [\Sigma''(\mathbf{k},\omega)]^2}\,. \tag{2.20}$$

Because $G(t,t')$ is a linear response function to an external perturbation, the real and imaginary parts of its Fourier transform $G(\mathbf{k},\omega)$ have to satisfy causality and, therefore, also Kramers-Kronig relations. This implies that if the full $A(\mathbf{k},\omega) = -(1/\pi)\mathrm{Im}\,G(\mathbf{k},\omega)$ is available from photoemission and inverse photoemission, one can calculate $\mathrm{Re}\,G(\mathbf{k},\omega)$ and then obtain both the real and imaginary parts of the self energy directly from (2.19). However, due to the lack of high-quality inverse photoemission data, this analysis is usually performed using only ARPES spectra by taking advantage of certain approximations (such as, e.g., particle-hole symmetry near E_F; for a more detailed discussion, see also [81, 82] and references therein).

In general, the exact calculation of $\Sigma(\mathbf{k},\omega)$ and, in turn, of $A(\mathbf{k},\omega)$ is an extremely difficult task. In the following, as an example we will briefly consider the interacting FL case [83–85]. Let us start from the trivial $\Sigma(\mathbf{k},\omega)=0$ non-interacting case. The N-particle eigenfunction Ψ^N is a single Slater determinant and we always end up in a single eigenstate when removing or adding an electron with momentum $\mathbf{k}$. Therefore, $G(\mathbf{k},\omega) = 1/(\omega - \varepsilon^b_{\mathbf{k}} \pm i\eta)$ has only one pole for each $\mathbf{k}$, and $A(\mathbf{k},\omega) = \delta(\omega - \varepsilon^b_{\mathbf{k}})$ consists of a single line at the band energy $\varepsilon^b_{\mathbf{k}}$ [as shown in Fig. 2.7b]. In this case, the occupation numbers $n_{\mathbf{k}\sigma} = c^\dagger_{\mathbf{k}\sigma}c_{\mathbf{k}\sigma}$ are good quantum numbers and for a metallic system the *momentum distribution* [i.e., the expectation value $n(\mathbf{k}) \equiv \langle n_{\mathbf{k}\sigma}\rangle$, quite generally independent of the spin σ for nonmagnetic systems], is characterized by a sudden drop from 1 to 0 at $\mathbf{k} = \mathbf{k}_F$ [Fig. 2.7b, top], which defines a sharp Fermi surface. If we now switch on the electron-electron correlation adiabatically, (so that the system remains at equilibrium), any particle added into a Bloch state has a certain probability of being scattered out of it by a collision with another electron, leaving the system in an excited state in which additional electron-hole pairs have been created. The momentum distribution $n(\mathbf{k})$ will now show a discontinuity smaller than 1 at $\mathbf{k}_F$ and a finite occupation probability for $\mathbf{k} > \mathbf{k}_F$ even at $T = 0$ (Fig. 2.7c, top). As long as $n(\mathbf{k})$ shows a finite discontinuity $Z_{\mathbf{k}} > 0$ at $\mathbf{k} = \mathbf{k}_F$, we can describe the correlated Fermi sea in terms of well defined *quasiparticles*, i.e. electrons *dressed* with a manifold of excited states, which are characterized by a pole structure similar to the one of the non-interacting system but with renormalized energy $\varepsilon^q_{\mathbf{k}}$, mass m^*, and a finite lifetime $\tau_{\mathbf{k}} = 1/\Gamma_{\mathbf{k}}$. In other words, the properties of a FL are similar to those of a free electron gas with damped quasiparticles. As the bare-electron character of the quasiparticle or pole strength (also called coherence factor) is $Z_{\mathbf{k}} < 1$ and the

total spectral weight must be conserved (see (2.23)), we can separate $G(\mathbf{k},\omega)$ and $A(\mathbf{k},\omega)$ into a *coherent* pole part and an *incoherent* smooth part without poles [86]:

$$G(\mathbf{k},\omega) = \frac{Z_{\mathbf{k}}}{\omega - \varepsilon^q_{\mathbf{k}} + i\Gamma_{\mathbf{k}}} + G_{incoh} \tag{2.21}$$

$$A(\mathbf{k},\omega) = Z_{\mathbf{k}} \frac{\Gamma_{\mathbf{k}}/\pi}{(\omega - \varepsilon^q_{\mathbf{k}})^2 + \Gamma^2_{\mathbf{k}}} + A_{incoh} \tag{2.22}$$

where $Z_{\mathbf{k}} = (1 - \frac{\partial \Sigma'}{\partial \omega})^{-1}$, $\varepsilon^q_{\mathbf{k}} = Z_{\mathbf{k}}(\varepsilon^b_{\mathbf{k}} + \Sigma')$, $\Gamma_{\mathbf{k}} = Z_{\mathbf{k}}|\Sigma''|$, and the self energy and its derivatives are evaluated at $\omega = \varepsilon^q_{\mathbf{k}}$. It should be emphasized that the FL description is valid only in proximity to the Fermi surface and rests on the condition $\varepsilon^q_{\mathbf{k}} - \mu \gg |\Sigma''|$ for small $(\omega - \mu)$ and $(\mathbf{k} - \mathbf{k}_F)$. Furthermore, $\Gamma_{\mathbf{k}} \propto [(\pi k_B T)^2 + (\varepsilon^q_{\mathbf{k}} - \mu)^2]$ for a FL system in two or more dimensions [86, 87], although additional logarithmic corrections should be included in the two-dimensional case [88]. By comparing the electron removal and addition spectra for a FL of quasiparticles with those of a non-interacting electron system (in the lattice periodic potential), the effect of the self-energy correction becomes evident [see Figs. 2.7c and 2.7b, respectively]. The quasiparticle peak has now a finite lifetime and width (due to Σ''), but sharpens rapidly as it emerges from the broad incoherent component and approaches the Fermi level, where the lifetime is infinite corresponding to a well defined quasiparticle [note that the coherent and incoherent part of $A(\mathbf{k},\omega)$ represent the main line and satellite structure discussed in the previous section and shown in Fig. 2.7c, bottom right]. Furthermore, the peak position is shifted with respect to the bare band energy $\varepsilon^b_{\mathbf{k}}$ (due to Σ'): as the quasiparticle mass is larger than the band mass because of the dressing ($m^* > m$), the total dispersion (or bandwidth) will be smaller ($|\varepsilon^q_{\mathbf{k}}| < |\varepsilon^b_{\mathbf{k}}|$). We note here, as later discussed in more detail in relation to Fig. 2.13, that the continuum of excitations described by the incoherent part of $A(\mathbf{k},\omega)$ in general does still retain a $\mathbf{k}$ and ω-dependent structure with spectral weight distributed predominately along the non-interacting bare band. This, however, is usually characterized by remarkably broad lineshapes (see e.g. Figs. 2.12c and 2.15) and should not be mistaken for a quasiparticle dispersion.

Among the general properties of the spectral function there are also several sum rules. A fundamental one, which in discussing the FL model was implicitly used to state $\int d\omega A_{coh} = Z_{\mathbf{k}}$ and $\int d\omega A_{incoh} = 1 - Z_{\mathbf{k}}$ (where A_{coh} and A_{incoh} refer to coherent and incoherent parts of the spectral function), is:

$$\int_{-\infty}^{+\infty} d\omega A(\mathbf{k},\omega) = 1 \tag{2.23}$$

which reminds us that $A(\mathbf{k},\omega)$ describes the probability of removing/adding an electron with momentum $\mathbf{k}$ and energy ω to a many-body system. However, as it also requires the knowledge of the electron addition part of the spectral function, it

is not so useful in the analysis of ARPES data, unless particle-hole symmetry holds. A sum rule more relevant to this task is:

$$\int_{-\infty}^{+\infty} d\omega\, f(\omega) A(\mathbf{k}, \omega) = n(\mathbf{k}) \tag{2.24}$$

which solely relates the one-electron removal spectrum to the momentum distribution $n(\mathbf{k})$. When electronic correlations are important and the occupation numbers are no longer good quantum numbers, the discontinuity at $\mathbf{k}_F$ is reduced (as discussed for the FL case), but a drop in $n(\mathbf{k})$ is usually still observable even for strong correlations [89]. By tracking the *loci* of steepest descent of the experimentally determined $n(\mathbf{k})$ in $\mathbf{k}$-space, i.e. maxima in $|\nabla_{\mathbf{k}}\, n(\mathbf{k})|$, one may thus identify the Fermi surface even in those correlated systems exhibiting particularly complex ARPES features. However, great care is necessary in making use of (2.24), because the integral of (2.18) does not give just $n(\mathbf{k})$, but rather $I_0(\mathbf{k}, \nu, \mathbf{A}) n(\mathbf{k})$ [1, 90]. A more detailed discussion of this point with specific relevance to undoped Mott insulating cuprates can be found in [91, 92].

2.6 Matrix Elements and Finite Resolution Effects

As discussed in the previous section and summarized by (2.18), ARPES directly probes the one-particle spectral function $A(\mathbf{k}, \omega)$. However, in extracting quantitative information from the experiment, not only the effects of the matrix element term $I_0(\mathbf{k}, \nu, \mathbf{A})$ have to be taken into account, but also the finite experimental resolution and the extrinsic continuous background due to the secondaries (those electrons which escape from the solid after having suffered inelastic scattering events and, therefore, with a reduced E_{kin}). The latter two effects may be explicitly accounted for by considering a more realistic expression for the photocurrent $I(\mathbf{k}, \omega)$:

$$\int d\tilde{\omega} d\tilde{\mathbf{k}} \left[I_0(\tilde{\mathbf{k}}, \nu, \mathbf{A}) f(\tilde{\omega}) A(\tilde{\mathbf{k}}, \tilde{\omega}) R(\omega - \tilde{\omega}) Q(\mathbf{k} - \tilde{\mathbf{k}}) \right] + B \tag{2.25}$$

which consists of the convolution of (2.18) with energy (R) and momentum (Q) resolution functions [R is typically a Gaussian, Q may be more complicated], and of the background correction B. Of the several possible forms for the background function B [30], two are more frequently used: (i) the step-edge background (with three parameters for height, energy position, and width of the step-edge), which reproduces the background observed all the way to E_F in an unoccupied region of momentum space; (ii) the Shirley background $B_{Sh}(\omega) \propto \int_{\omega}^{\mu} d\omega' P(\omega')$, which allows to extract from the measured photocurrent $I(\omega) = P(\omega) + c_{Sh} B_{Sh}(\omega)$ the contribution $P(\omega)$ of the unscattered electrons (with the only parameter c_{Sh} [93]).

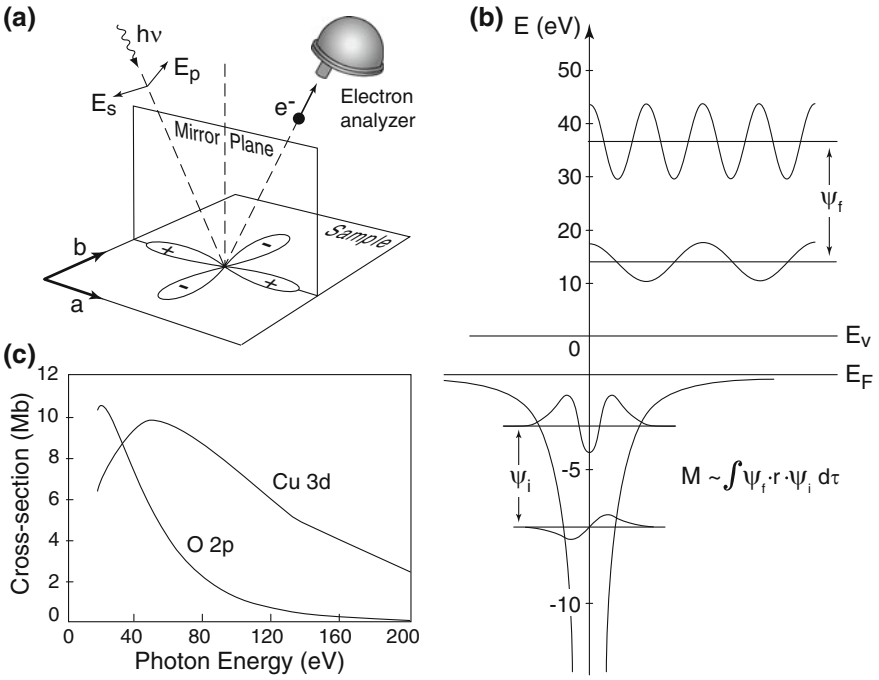

Fig. 2.8 **a** Mirror plane emission from a $d_{x^2-y^2}$ orbital. **b** Sketch of the optical transition between atomic orbitals with different angular momenta (the harmonic oscillator wavefunctions are here used for simplicity) and free electron wavefunctions with different kinetic energies (from [14]). **c** Calculated photon energy dependence of the photoionization cross-sections for Cu $3d$ and O $2p$ atomic levels

Let us now very briefly illustrate the effect of the matrix element term $I_0(\mathbf{k}, \nu, \mathbf{A}) \propto |M^{\mathbf{k}}_{f,i}|^2$, which is responsible for the dependence of the photoemission data on photon energy and experimental geometry, and may even result in complete suppression of the intensity [94–97]. By using the commutation relation $\hbar\mathbf{p}/m = -i[\mathbf{x}, H]$, we can write $|M^{\mathbf{k}}_{f,i}|^2 \propto |\langle\phi^{\mathbf{k}}_f|\varepsilon \cdot \mathbf{x}|\phi^{\mathbf{k}}_i\rangle|^2$, where ε is a unit vector along the polarization direction of the vector potential $\mathbf{A}$. As in Fig. 2.8a, let us consider photoemission from a $d_{x^2-y^2}$ orbital, with the detector located in the mirror plane (when the detector is out of the mirror plane, the problem is more complicated because of the lack of an overall well defined even/odd symmetry). In order to have non vanishing photoemission intensity, the whole integrand in the overlap integral must be an even function under reflection with respect to the mirror plane. Because odd parity final states would be zero everywhere on the mirror plane and therefore also at the detector, the final state wavefunction $\phi^{\mathbf{k}}_f$ itself must be even. In particular, at the detector the photoelectron is described by an even parity plane-wave state $e^{i\mathbf{k}\cdot\mathbf{r}}$ with momentum in the mirror plane and fronts orthogonal to it [96]. In turn, this implies that $(\varepsilon\cdot\mathbf{x})|\phi^{\mathbf{k}}_i\rangle$ must be even. In the case depicted in Fig. 2.8a, where $|\phi^{\mathbf{k}}_i\rangle$ is also even, the photoemission

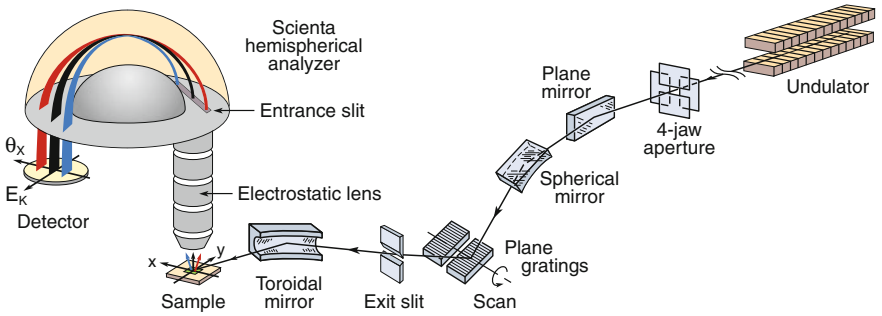

Fig. 2.9 Beamline equipped with a plane grating monochromator and a 2D position-sensitive electron analyzer (from [1])

process is symmetry allowed for **A** even or in-plane (i.e., $\varepsilon_p \cdot \mathbf{x}$ depends only on in-plane coordinates and is therefore even under reflection with respect to the plane) and forbidden for **A** odd or normal to the mirror plane (i.e., $\varepsilon_s \cdot \mathbf{x}$ is odd as it depends on normal-to-the-plane coordinates). For a generic initial state of either even or odd symmetry with respect to the mirror plane, the polarization conditions resulting in an overall even matrix element can be summarized as:

$$\left\langle \phi_f^{\mathbf{k}} \middle| \mathbf{A}\cdot\mathbf{p} \middle| \phi_i^{\mathbf{k}} \right\rangle \begin{cases} \phi_i^{\mathbf{k}}\ even & \langle + | + | + \rangle \ \Rightarrow\ \mathbf{A}\ even \\ \phi_i^{\mathbf{k}}\ odd & \langle + | - | - \rangle \ \Rightarrow\ \mathbf{A}\ odd \end{cases} \tag{2.26}$$

In order to discuss the photon energy dependence, from (2.11) and by considering a plane wave $e^{i\mathbf{kr}}$ for the photoelectron at the detector, one may more conveniently write $|M_{f,i}^{\mathbf{k}}|^2 \propto |(\varepsilon \cdot \mathbf{k})\langle \phi_i^{\mathbf{k}} | e^{i\mathbf{kr}} \rangle|^2$. The overlap integral, as sketched in Fig. 2.8b, strongly depends on the details of the initial state wavefunction (peak position of the radial part and its oscillating character), and on the wavelength of the outgoing plane wave. Upon increasing the photon energy, both E_{kin} and $\mathbf{k}$ increase, and $M_{f,i}^{\mathbf{k}}$ changes in a fashion which is not necessarily monotonic (see Fig. 2.8c, for the Cu-3d and the O 2p atomic case). In fact, the photoionization cross section is usually characterized by one minimum in free atoms, the so-called Cooper minimum [98], and a series of them in solids [99].

2.7 State-of-the-Art Photoemission

The configuration of a generic angle-resolved photoemission beamline is shown in Fig. 2.9. A beam of radiation peaked about a specific photon energy is produced in a wiggler or an undulator (these so-called 'insertion devices' are the straight sections of the electron storage ring where radiation is produced). The light is then monochromatized at the desired photon energy by a grating monochromator and

focused on the sample. Alternatively, a UV-laser or a gas-discharge lamp can be used as a radiation source (the latter has to be properly monochromatized to avoid complications due to the presence of different satellites, and refocused to a small spot size, essential for high angular resolution). However, synchrotron radiation offers important advantages: it covers a wide spectral range (from the visible to the X-ray region) with an intense and highly polarized continuous spectrum; lasers and discharge lamps provide only a few resonance lines at discrete energies.

Photoemitted electrons are then collected by the electron analyzer, where kinetic energy and emission angle are determined (the whole system is in ultra-high vacuum at pressures lower than 5×10^{-11} torr). A conventional hemispherical analyzer consists of a multi-element electrostatic input lens, a hemispherical deflector with entrance and exit slits, and an electron detector (i.e. a channeltron or a multi-channel detector). The heart of the analyzer is the deflector which consists of two concentric hemispheres (of radius R_1 and R_2). These are kept at a potential difference ΔV, so that only those electrons reaching the entrance slit with kinetic energy within a narrow range centered at $E_{pass} = e\Delta V/(R_1/R_2 - R_2/R_1)$ will pass through this hemispherical capacitor, thus reaching the exit slit and then the detector. This way it is possible to measure the kinetic energy of the photoelectrons with an energy resolution given by $\Delta E_a = E_{pass}(w/R_0 + \alpha^2/4)$, where $R_0 = (R_1 + R_2)/2$, w is the width of the entrance slit, and α is the acceptance angle. The role of the electrostatic lens is that of decelerating and focusing the photoelectrons onto the entrance slit. By scanning the lens retarding potential one can effectively record the photoemission intensity versus the photoelectron kinetic energy.

One of the innovative characteristics of a state-of-the-art analyzer is the two-dimensional position-sensitive detector consisting of two micro-channel plates and a phosphor plate in series, followed by a CCD camera. In this case, no exit slit is required: the electrons, spread apart along the Y axis of the detector (Fig. 2.9) as a function of their kinetic energy due to the travel through the hemispherical capacitor, are detected simultaneously. In other words, a range of electron energies is dispersed over one dimension of the detector and can be measured in parallel; scanning the lens voltage is in principle no longer necessary, at least for narrow energy windows (a few percent of E_{pass}). Furthermore, contrary to a conventional electron spectrometer in which the momentum information is averaged over all the photoelectrons within the acceptance angle (typically $\pm1°$), state-of-the-art 2D position-sensitive electron analyzers can be operated in angle-resolved mode, which provides energy-momentum information not only at a single k-point but along an extended cut in k-space. In particular, the photoelectrons within a variable angular window as wide as $\sim 30°$ along the direction defined by the analyzer entrance slit can be focused on different X positions on the detector (Fig. 2.9). It is thus possible to measure multiple energy distribution curves simultaneously for different photoelectron angles, obtaining a 2D snapshot of energy versus momentum. Such snapshots, for differing sample orientations, can be combined to form a 3D volume (Fig. 2.10), and then cut at constant energy to generate a material's Fermi surface when done at $\omega = E_F$ on a metal, or along any k-space path to generate a band mapping versus energy and momentum. State-of-the-art spectrometers typically allow for energy and angular resolutions of

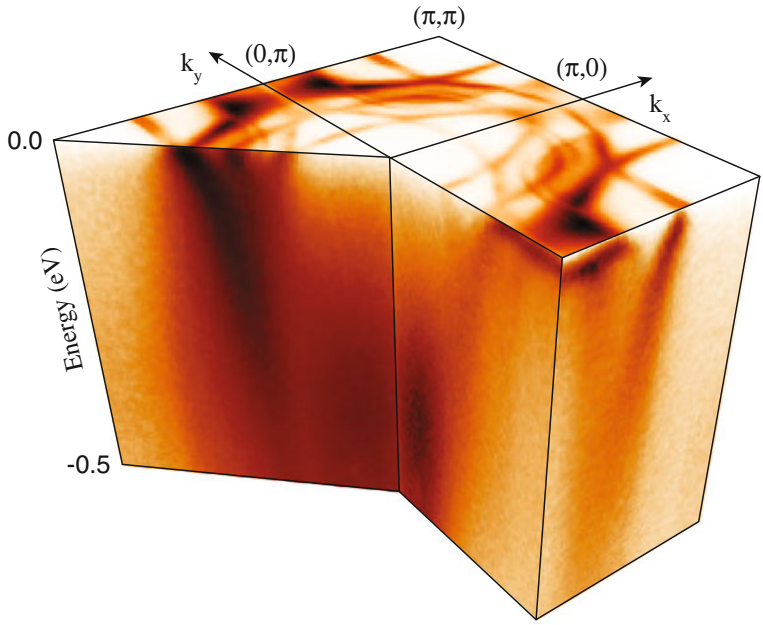

Fig. 2.10 3D plot of the ARPES intensity from Sr_2RuO_4 versus energy (ω) and momentum (k_x and k_y), in the first Brillouin zone. The *top* plane shows the Fermi surface $A(\mathbf{k}, \omega = 0)$, while the side cuts show the spectral function along certain high-symmetry directions. The multiple features that are visible in dispersion and Fermi surface, in addition to the three Ru-t_{2g} bands expected for this material, arise from near-surface structural instabilities, and associated structural reconstruction and band-folding [100]. Note that these data differ from those in Fig. 2.17, which were measured under different conditions intended to suppress the contribution from the surface top-most layers and are thus representative of the bulk of Sr_2RuO_4 [101]

less than approximately 1 meV and 0.1–0.2°, respectively. Taking as example the transition metal oxides and in particular the cuprate superconductors (for which $2\pi/a \simeq 1.6$ Å^{-1}), one can see from (2.7) that 0.2° corresponds to ∼0.5 % of the Brillouin zone size for the 21.2 eV photons of the He-Iα line typically used in ARPES systems equipped with a gas-discharge lamp. In the case of a beamline, in order to estimate the total energy resolution one has to take into account also the ΔE_m of the monochromator, which can be adjusted with entrance and exit slits (the ultimate resolution a monochromator can deliver is given by its resolving power $R = E/\Delta E_m$ and in general worsens upon increasing the photon energy). The current record in energy resolution is of 360 μeV obtained on an ARPES spectrometer equipped with a Scienta R4000 electron analyzer and a UV laser operating in continuous-wave mode at ∼ 6.994 eV (see Figs. 2.11). One should note however that while the utilization of UV lasers allows superior resolutions, it also leads to some important shortcomings: (i) access to a limited region of k-space, often smaller than the first Brillouin zone, due to the reduced kinetic energy of photoelectrons; (ii) extreme sensitivity to

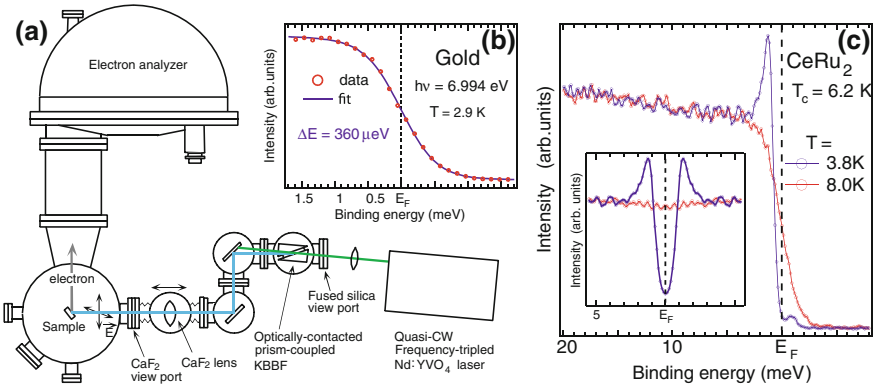

Fig. 2.11 **a** Schematics of a laser-ARPES setup, with **b** sub-meV resolution on a Au target ($\Delta E = 360\,\mu$eV). This enables **c** the detection of a $\Delta = 500\,\mu$eV superconducting gap in the heavy fermion system $CeRu_2$ (from [102])

final state effects, with the detailed energy-momentum structure of the final states becoming important, since at low photon energies one cannot reach the high-energy continuum (the kinematic constraints of energy and momentum conservation may be satisfied only for a limited set of momenta, and as a result the photoemission intensity might be completely suppressed in certain regions of the Brillouin zone); (iii) breakdown of the sudden approximation, in which case the photoemission intensity would all be found in the "0-0" transition between the initial and final ground states (see discussion of Fig. 2.7 and especially (2.12)), providing no information on the excited states of the system left behind, and in turn on the strength and nature of the underlying many-body interactions (the crossover from sudden to adiabatic regime in TMOs is still being debated, see e.g. [103], and depends on the specific relaxation processes of a given material).

2.8 Physics of Correlations—The ARPES Perspective

The sensitivity of ARPES to correlation effects is deeply connected to its corresponding observable, which is the one-particle spectral function previously introduced in Sect. 2.5. This physical quantity conveys information not only on the single-particle excitations, but also on the many-body final states which can be reached in the photoemission process. However, the distinction between single-particle and many-body features in $A(\mathbf{k}, \omega)$ at the experimental level is often subtle. In order to disentangle the nature of the underlying excitations it is common practice to decompose the spectral function into a coherent, $A_{coh}(\mathbf{k}, \omega)$, and an incoherent part, $A_{incoh}(\mathbf{k}, \omega)$, as explained in Sect. 2.5.

Whereas in a purely non-interacting system all single-electron excitations are coherent, since they are insensitive to the behavior of the other particles, things can be quite different when *electron-electron* interactions, and therefore quantum-mechanical correlation effects, are turned on. For these reasons, the redistribution of spectral weight between the coherent and incoherent part in $A(\mathbf{k}, \omega)$ is commonly regarded as a distinct signature of correlations at work. In particular, the integrated spectral intensity of the coherent part, the *quasiparticle strength* $Z_{\mathbf{k}}$ that can be extracted from ARPES, is a relatively direct measure of the correlated behavior of a given system. Following its definition given in (2.19), $Z_{\mathbf{k}}$ can vary from 1 (non-interacting case) to 0 (strongly correlated case, no coherent states can be excited).

In the following subsections we will explain how the concept of correlation already emerges in simple molecular-like systems (i.e. few-body) and evolves into the complex structures found in solid-state materials (i.e. many-body). Different types of correlation effects will be reviewed, with particular emphasis on those stemming from *electron-phonon* and *electron-electron* interactions. We will then discuss different aspects of correlated electron behavior in a few selected transition metal oxides, and show how correlations evolve with—and to some degree can be controlled by—the external control parameters introduced in Sect. 2.1 and Fig. 2.1.

2.8.1 Origin of Correlations in Photoelectron Spectroscopy

In general, the connection between the one-particle spectral function and correlations is not immediately obvious and might look mysterious to the reader. It is useful and instructive to clarify what the photoelectron spectrum for a correlated system looks like, beginning with an example from molecular physics. In Fig. 2.12 we show the photoionization spectrum of the molecular gas H_2 which, at variance with a simpler atomic gas (e.g., He or Ne), exhibits a fine structure made of a series of peaks almost evenly separated in energy. The underlying physical explanation for these spectral features relates to the Franck-Condon principle, which is explained in Fig. 2.12a. This is best understood if we write down the equation for the photoionization cross section, which will involve: (i) an initial state wavefunction ψ_i, assumed to be the ground state for the neutral molecule; and (ii) a final state wavefunction ψ_f, which can be a linear combination of eigenstates for the ionized, positively charged molecule H_2^+. The possible eigenstates we consider here can be separated into an electronic part (the hydrogen-like 1 s orbital ϕ_{1s}) and a nuclear part, which in a diatomic molecule like H_2 can be vibrationally excited. The latter is given, to a good approximation, by one of the eigenfunctions of the harmonic oscillator, $\phi_n(R_{eq})$, which depend on the interatomic equilibrium distance R_{eq}. Combining together electronic and nuclear (i.e., vibrational) components we obtain a basis set for the molecular Hamiltonian in the form $\psi_n = \phi_{1s}\phi_n(R_{eq})$. We can then use this set of functions in the matrix element governing the photoionization process:

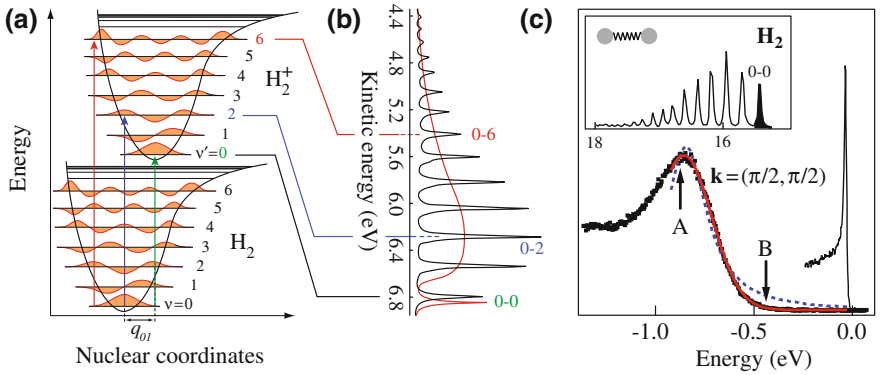

Fig. 2.12 **a** Franck-Condon effect and its relation to the single-particle spectral function in atomic physics. **b** Photoionization spectrum of gaseous H_2 (from [104]), featuring a comb of lines corresponding to the various accessible excited (vibrational) final states of the H_2^+ system left behind; the *red line* is an abstraction to what would happen in solid-state H_2 (from [105]). **c** $A(\mathbf{k}=(\pi/2,\pi/2),\omega)$ from $Ca_2CuO_2Cl_2$, showing the broad incoherent Zhang-Rice peak, with the sharp Sr_2RuO_4 lineshape superimposed for comparison (from [106])

$$I_{H_2\rightarrow H_2^+} \propto \sum_m \langle \psi_m^{H_2^+} | \mathbf{p}\cdot\mathbf{A} | \psi_{n=0}^{H_2} \rangle \propto \sum_m \langle \phi_{\mathbf{k},m} | \mathbf{p}\cdot\mathbf{A} | \phi_{1s} \rangle \langle \phi_m(R_{eq}^{H_2^+}) | \phi_0(R_{eq}^{H_2}) \rangle \,. \tag{2.27}$$

Here $\mathbf{p}\cdot\mathbf{A}$ is the dipole interaction operator and the initial state is the ground state for H_2, or $\psi_{GS}^{H_2} = \psi_{n=0}$. The term $\langle \phi_{\mathbf{k},m} | \mathbf{p}\cdot\mathbf{A} | \phi_{1s} \rangle = M_m^{\mathbf{k}}$ is the *matrix element* previously introduced in Sect. 2.6, representing the overlap between the initial-state electronic wavefunction ϕ_{1s} and the final state plane-wave $\phi_{\mathbf{k},m}$. It is readily seen that, if $R_{eq}^{H_2^+} = R_{eq}^{H_2}$, then $I_{H_2\rightarrow H_2^+} \propto \sum_m \delta_{m,0}$ and the photoionization spectrum would be composed of a single peak, corresponding to the "0–0" transition between the initial and final ground states. In reality, the neutral and ionized molecule will see a different charge distribution (thus leading to a different electrostatic potential), due to the missing Coulomb interaction term for the 1*s* electrons in the Hamiltonian for H_2^+. As a consequence, the molecule before and after photoexcitation will have a different interatomic equilibrium distance, and many of the terms in (2.27) will be different from zero resulting in multiple transitions in the experimental spectrum (corresponding to the vertical excitations in Fig. 2.12a and to the various peaks in Fig. 2.12b). The lowest energy peak (labeled "0–0" in Fig. 2.12b) still corresponds to a transition into the ground state of the ionized molecule, but it only contains a fraction of the total photoemission intensity, or *spectral weight*. At this point it is useful to introduce an alternative definition (but equivalent to the one given in Sect. 2.5) of *coherent* and *incoherent* spectral weight:

- The *coherent* spectral weight is a measure of the probability to reach the *ground state* of the final-state Hamiltonian ($\mathcal{H}_{H_2^+}$) in the photoexcitation process. In exper-

imental terms, it is represented by the total area of the 0–0 transition shown in Fig. 2.12b.
- The *incoherent* spectral weight is a measure the probability to leave the ionized system in any of its *excited states*. It can be therefore calculated from the integrated intensity of all the 0–m ($m \neq 0$) peaks in the ionization spectrum, as shown in Fig. 2.12b.

In solid-state, many-body systems, both molecular vibrations and electronic levels are no longer discrete but have an energy dispersion (turning into phonons and electronic bands, respectively). This is what gives a continuum of excitations when many body interactions are at play, as opposed to the sharp excitation lines of the H_2 case. However, these concepts remain valid, although we shall now restate them within a many-body framework:

- The *coherent* spectral weight corresponds to the probability of reaching, via the electron addition/removal process ($\Delta N = \pm 1$, where N is the initial number of electrons), the *many-body* ground-state for the $(N \pm 1)$-particle Hamiltonian ($\mathcal{H}^{\mp}_{N\pm1}$).
- The *incoherent* spectral weight gives the cumulative probability that the $(N \pm 1)$-particle system is instead left in an excited state.

A photoelectron spectrum for a solid-state many-body system will look like the dashed curve in Fig. 2.12b, due to the multitude of final states that can be reached as a result of the photoemission process. The well-defined features characterizing $A(\mathbf{k}, \omega)$ in the molecular case will then broaden out into a continuum of excitations. This was experimentally found to occur in the strongly-coupled cuprate material $Ca_2CuO_2Cl_2$ [see Fig. 2.12c], which will be discussed in more detail in the next section. We also note that for the incoherent part of the spectral function two cases are possible in a solid:

1. $A_{incoh}(\boldsymbol{k}, \omega)$ is composed of gapless many-body excitations, e.g. creation of electron-hole pairs in a metal; this typically produces an asymmetric lineshape, as in the case of the Doniach-Sunjic model [107].
2. $A_{incoh}(\boldsymbol{k}, \omega)$ originates from gapped excitations, e.g. coupling between electrons and optical phonons; in this case, the coherent part is well separated from the incoherent tail, and a quasiparticle peak can be more properly identified.

What we have just seen for the H_2 molecule stems from the interaction between the electronic and the nuclear degrees of freedom. In the absence of such interplay, there would be no fine structure in the corresponding spectral function. This is a very important concept, which is deeply connected to the idea of correlations. The Hamiltonian of a given (few-body or many-body) system, in the absence of interaction terms, can be decomposed into a sum of single particle terms (non-interacting case). Correspondingly, the system is unperturbed by the addition or removal of a particle during the photoexcitation process; due to the orthonormality of the involved eigenstates, the $(N \pm 1)$-system left behind will not be found in a superposition of excited states but rather left unperturbed in its ground state (at zero temperature). Single-particle spectroscopy would then detect a single transition (e.g., the 0–0 peak

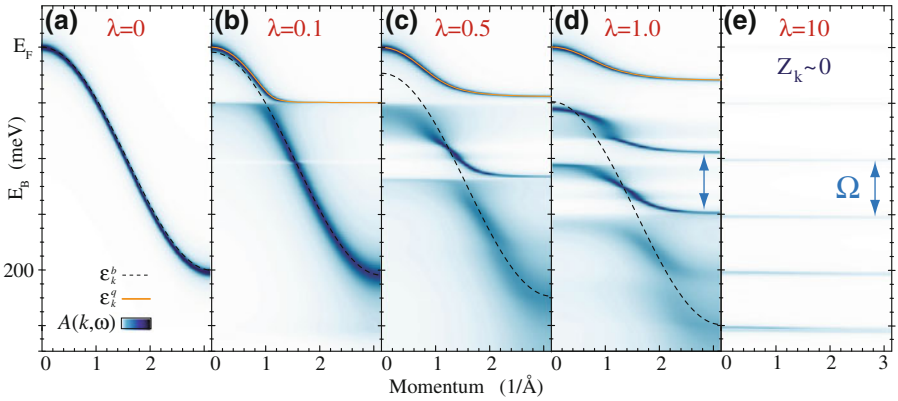

Fig. 2.13 $A(\mathbf{k}, \omega)$ for the Holstein model, showing the quasiparticle band and the 0-, 1- and n-phonon dispersing poles in the spectral function for increasing values of the electron-phonon coupling $\lambda = 0$, 0.1, 0.5, 1.0 and 10 (panels a, b, c, d and e, respectively). The *dashed black*, and the *orange lines* represent the bare band $\varepsilon^b_{\mathbf{k}}$, and the renormalized quasiparticle band $\varepsilon^q_{\mathbf{k}}$, respectively. The Fermi energy E_F has been set at the top of the quasiparticle band (from [82])

in Fig. 2.12); the spectral weight is *fully coherent*. Conversely, when the electron-nucleus and/or electron-lattice interaction are switched on, addition/removal of a single electron perturbs the molecular/lattice potential to some degree and this can trigger creation or annihilation of one or multiple vibrational modes in the process. As we will see in the following section for electron-phonon coupling in solids, the effect at the level of spectral function can be very different according to the strength of the interaction.

2.8.2 *Electron-Phonon Correlations in Solids: The Polaron*

The interaction of the mobile charges with the static ionic lattice is what underlies the formation of electronic bands in all crystalline materials. However, the lattice is never really static and its low-energy excitations, the *phonons*, are present even at very low temperatures. As they hop around in the lattice, electrons can interact (through the ionic Coulomb potential) with—or become "dressed" by—phonons, thereby slowing their quantum motion. These new composite entities, known as *polarons*, represent the true quasiparticles of the coupled electron-lattice system: the properties of the "bare" electrons, *in primis* bandwidth and mass, are now renormalized in a fashion which directly depends on the strength of the *electron-phonon* coupling. Here we show two examples of polaronic physics, one experimental and the other theoretical, which exhibit different features but relate to the same underlying interactions.

The first case is that of $Ca_2CuO_2Cl_2$ (CCOC). This compound is the undoped *parent* compound of the high-T_c superconducting cuprates, where the low-energy

physics originates from the hybridized Cu $3d-$O $2p$ states of the CuO_2 planes. In Fig. 2.12c, the ARPES spectrum of CCOC at $\mathbf{k} = (\pi/2, \pi/2)$ is shown [106]. This value of electron momentum corresponds to the lowest ionization state of the Zhang-Rice singlet (ZRS) band [108]. The latter is a 2-particle state, made of a combination of one O $2p$ and one Cu $3d$ hole in a total spin-zero state (singlet). Hence the nature of such a state is intrinsically correlated, and cannot be described within a single-particle framework. While this feature was originally recognized as the quasiparticle pole of the same Cu–O band that is also found in the doped compounds [109], the Gaussian lineshape, together with the broad linewidth ($\Gamma \sim 0.5\,\mathrm{eV}$), suggest that this feature might instead be identified as the incoherent part of the spectral function. It follows that the spectral function has no actual quasiparticle weight $Z_{\mathbf{k}}$ because the intensity of the lowest energy excitation [the "0–0" line marked by the "B" arrow in Fig. 2.12c] approaches zero.

While the previous example illustrates a case where the strong electron-boson interaction entirely washes away the coherent spectral weight, in different physical systems it is possible to have sizeable weight in the quasiparticle pole. This is illustrated with the second example discussed here, the one-dimensional (1D) Holstein model [82], shown in Fig. 2.13 and represented by the Hamiltonian:

$$\mathcal{H}^{1D}_{\mathrm{Holstein}} = \sum\nolimits_{\mathrm{k}} \varepsilon^{b}_{\mathrm{k}} c^{\dagger}_{\mathrm{k}} c_{\mathrm{k}} + \Omega \sum\nolimits_{\mathrm{Q}} b^{\dagger}_{\mathrm{Q}} b_{\mathrm{Q}} + \frac{g}{\sqrt{n}} \sum\nolimits_{\mathrm{k,Q}} c^{\dagger}_{\mathrm{k-Q}} c_{\mathrm{k}} (b^{\dagger}_{\mathrm{Q}} + b_{\mathrm{-Q}}) \,. \quad (2.28)$$

The evolution of the associated spectral function as a function of the dimensionless electron-phonon coupling parameter $\lambda = g^2/2t\Omega$ (in this calculation $\Omega = 50\,\mathrm{meV}$) is shown in Fig. 2.13. The case $\lambda = 0$ (no coupling), shown in Fig. 2.13a, yields a spectral function which exactly follows the bare electronic band $\varepsilon^{b}_{\mathrm{k}}$ (indicated by the black dashed line in Fig. 2.13), i.e. $A(\mathrm{k}, \omega) = \delta(\omega - \varepsilon^{b}_{\mathrm{k}})$, where the δ-function is here broadened into a Lorentzian for numerical purposes. Already in the small coupling limit $\lambda = 0.1$, a quasiparticle band branches off the original band, with a k-dependent spectral weight (see Fig. 2.13b). The latter is substantially redistributed, with the spectral weight at binding energies higher than the quasiparticle band belonging to the incoherent part of the spectral function, which forms a continuum of many-body excitations for $E_B > \Omega$. As the electron-phonon coupling is further increased, it can be noted from Fig. 2.13c,d how: (i) there is a progressive renormalization of the quasiparticle band ($\varepsilon^{q}_{\mathrm{k}}$), which implies a reduction in the total bandwidth and a change in the slope $\partial\varepsilon^{q}_{\mathrm{k}}/\partial\mathrm{k}$ (quasiparticle velocity); (ii) the spectral weight is redistributed between the quasiparticle band $\varepsilon^{q}_{\mathrm{k}}$ and the incoherent features at higher binding energy, corresponding to a photohole co-propagating with, or "dressed" by, one or multiple phonons. In the strong-coupling regime $\lambda = 10$, the quasiparticle band and its n-phonon replicas are nondispersive (i.e., corresponding to a diverging quasiparticle mass), and the coherent spectral weight $Z_{\mathbf{k}}$ has almost completely vanished (Fig. 2.13d). Having discussed quasiparticle renormalization due to electron-phonon coupling, in the following we will turn our focus onto electron-electron interaction effects, which are particularly pronounced in $3d$-TMOs, and dominate the low-energy electrodynamics in these systems.

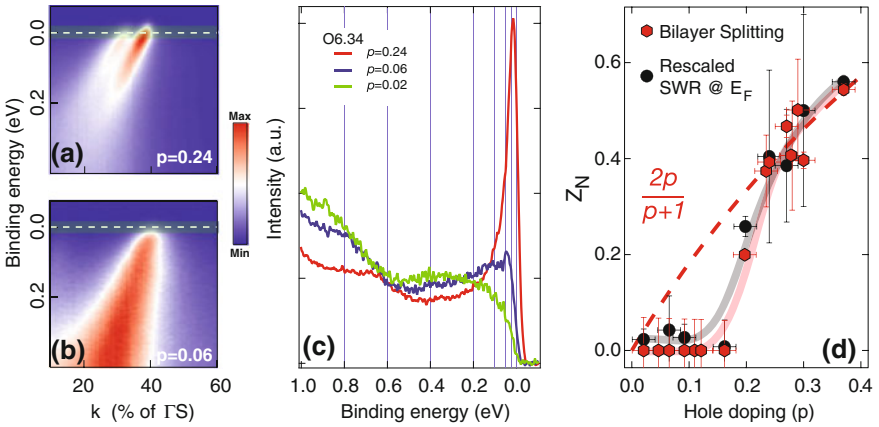

Fig. 2.14 **a, b**: ARPES dispersion in YBCO, along the nodal cut $[\Gamma \rightarrow (\pi, \pi)]$ for $p = 0.24$ and 0.06, respectively, showing the lack of bonding-antibonding (B-AB) bilayer splitting and the spectral function being mostly incoherent for $p = 0.06$. **c** $A(\mathbf{k} = \mathbf{k}_{F,N}, \omega)$ as a function of doping for the bonding Cu-O band, showing the progressive suppression of the quasiparticle peak. **d** Z_N as determined from the B-AB splitting and the spectral-weight ratio SWR (see text). Also shown are guides-to-the-eye and the $2p/(p+1)$ Gutzwiller projection relation (from [112])

2.8.3 Doping-Controlled Coherence: The Cuprates

As anticipated, copper-based oxide superconductors exhibit a rich phase diagram, encompassing a variety of unconventional phases (Fig. 2.1), which include: high-temperature superconductivity, Mott insulating behavior, pseudogap phase, strange metal (non-conventional Fermi liquid), and possibly electronic liquid crystal (nematic phase), to name a few. In particular, their remarkable peculiarity lies in the possibility of realizing these different phases simply by controlling the charge carriers doped into the CuO_2 planes.

A manifestation of the underlying correlated nature of these materials can be found in the doping-dependent evolution of coherent behavior in the low-energy electrodynamics. This is the case of the ARPES results on $YBa_2Cu_3O_{6+x}$ (YBCO), one of the most studied within the family of cuprates owing to its superior purity. In this and similar materials, hole-doping is usually controlled at the chemical level, by tuning the stoichiometric ratio between the O and Cu content. As for the study of the low-energy electronic structure by ARPES, this has been hampered by the lack of a natural cleavage plan and especially the polarity of the material, which leads to the self doping of the cleaved surfaces [110–112]. As a result, while the bulk of YBCO cannot be doped beyond 20 % by varying the oxygen content, the surfaces appear to be overdoped up to almost 40 % (the highest overdoping value reached on any cuprate [112]). An approach devised to resolve this problem involves the control of the carrier concentration at the surface [111, 112] by in-situ potassium deposition on the cleaved crystals, which enables the investigation of the surface electronic

structure all the way from the overdoped ($p \sim 0.37$) to the very underdoped region of the phase diagram ($p \sim 0.02$).

Concurrent with a modification of the Fermi surface, which evolves from large hole-like cylinders to Fermi arcs [111, 112], there is also a pronounced change in the ARPES spectral lineshape [see Fig. 2.14c, where the corresponding energy distribution curves have been extracted from the ARPES maps in panels (a, b), for $\mathbf{k} = \mathbf{k}_F$]. In particular, two major effects are observed going from the over- to the under-doped surface: (i) the progressive loss of the nodal coherent weight with no quasiparticle peak being detected at $p = 0.02$ (Fig. 2.14c), accompanied by an increase in the incoherent tail, and consistent with conservation of the total spectral weight; (ii) the suppression of the nodal bilayer splitting $\Delta\epsilon_N^{B,AB}$ shown in the ARPES intensity maps of Fig. 2.14a, b (an even more pronounced suppression can be observed at the antinodes), which goes hand-in-hand with the redistribution of spectral weight from the coherent to the incoherent part of the spectral function. Since correlation effects suppress hopping within and between planes in a similar fashion, the renormalization of the measured bilayer splitting with respect to the prediction of density functional theory can be used as an equivalent measure of the coherent weight $Z_{\mathbf{k}} = \Delta\epsilon_N^{B,AB}/2t_\perp^{LDA}(N)$, with $t_\perp^{LDA}(N) \simeq 120\,\text{meV}$. This is a more quantitative and more accurate method than estimating the spectral weight ratio between quasiparticle and many-body continuum, $\text{SWR} = \int_{E_F}^{-\infty} I(\text{k}_{F,N}, \omega)\text{d}\omega / \int_{0.8eV}^{-\infty} I(\text{k}_{F,N}, \omega)\text{d}\omega$, since in this case the coherent and incoherent parts of $A(\mathbf{k}, \omega)$ are not well separated. Using both methods, it is possible to observe a suppression of the coherent weight as one goes underdoped, with $Z_{\mathbf{k}}$ vanishing around $p = 0.1 - 0.15$ (Fig. 2.14d), which is consistent with the observation that the underdoped ($p < 0.1$) ARPES spectra are mostly incoherent, $A(\mathbf{k}, \omega) \sim A_{incoh}(\mathbf{k}, \omega)$. The proximity of the Mott phase ($p = 0$), with its strongly correlated behavior, is believed to be the reason underlying the loss of coherent behavior as hole doping is progressively reduced, and forces a departure from the Fermi liquid description much more rapidly than predicted by the mean field Gutzwiller projection $Z = 2p/(p + 1)$.

2.8.4 Temperature-Controlled Coherence: The Manganites

Another family of $3d$-based oxides characterized by a rich phase diagram is that of the manganites. These materials, which exhibit the fascinating phenomenon known as colossal magnetoresistance, have been extensively studied by ARPES [113–119]. In one of these compounds, $La_{1.2}Sr_{1.8}Mn_2O_7$, the high temperature spectra ($T > 120\,\text{K}$) do not qualitatively differ from those seen for undoped cuprates, previously presented in Fig. 2.12c. As shown in Fig. 2.15d, there is no spectral weight at the Fermi energy, and the lowest-energy excitation is a broad peak dispersing between -1 and -0.5 eV [113]. This finding suggests that we are again looking at a strongly correlated system, where all the spectral weight is pushed into a broad and incoherent structure away from E_F. Surprisingly, when the temperature is lowered through the Curie value $T_C \sim 120\,\text{K}$, a sharp feature emerges at the chemical potential, with an intensity

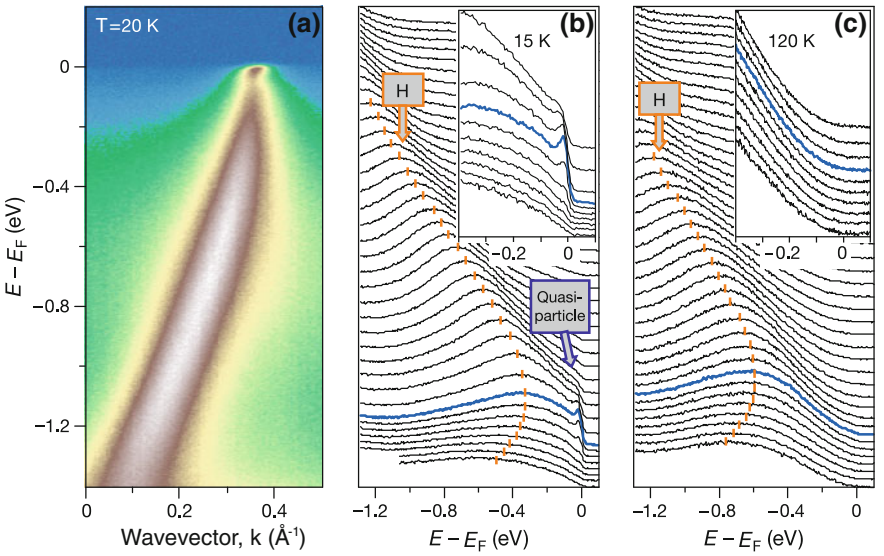

Fig. 2.15 **a** ARPES image plot of the Mn-e_g valence band along the $(0, 0)$–(π, π) direction in $La_{1.2}Sr_{1.8}Mn_2O_7$ ($T = 20$ K); note the quasiparticle band ε_k^q branching off the bare band near E_F, in analogy to the case of the Holstein model (Fig. 2.13b). **b**, **c** Stack of low-energy EDCs for $T = 15$ and 120 K, respectively, emphasizing the emergence of the quasiparticle peak below T_C (from [113])

progressively increasing as the sample is cooled down to 15 K (see Fig. 2.15a, b, and c and related insets). This is a remarkable example of how temperature can lead to a transfer of spectral weight from A_{incoh} to A_{coh}, in this case associated with the ferromagnetic transition occurring at T_C. Note the large ratio A_{incoh}/A_{coh}, i.e. a incoherent-to-coherent transition, and the subsequently small $Z_{\mathbf{k}}$: this is an indication of the fact that we are still in a regime where electronic correlations are very strong, similar to the case of undoped and underdoped cuprates and, as we will see in the following section, also of cobaltates [120]. In addition, it is important to note how the coherent spectral weight does not necessarily appear throughout the entire Brillouin zone, but might instead be limited to a reduced momentum range, where electronic excitations can propagate in a coherent manner.

2.8.5 *Probing Coherence with Polarization: The Cobaltates*

As discussed in the previous sections, the distinction between coherent and incoherent parts of $A(\mathbf{k}, \omega)$—and thus the determination of the quasiparticle strength $Z_{\mathbf{k}}$—although conceptually well defined, is often not easy to estimate from ARPES experiments. An additional complication is encountered whenever more overlapping bands contribute to the low energy electronic structure in the same region of momentum. In such instances, there is one characteristic of the ARPES technique which

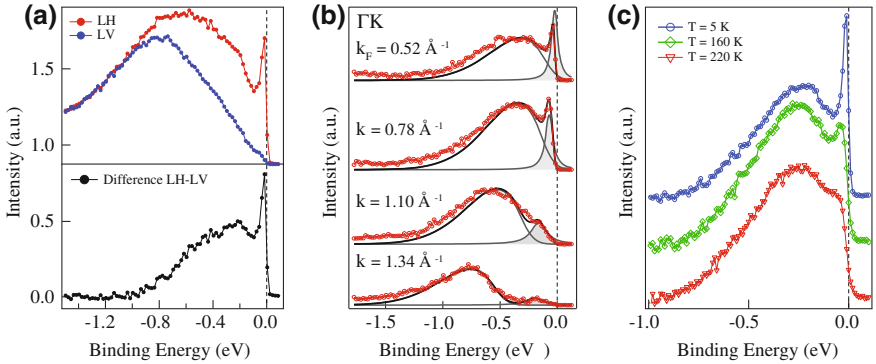

Fig. 2.16 **a** *top panel*: $A(\mathbf{k}=\mathbf{k}_F, \omega)$ from the misfit cobaltate $[Bi_2Ba_2O_4][CoO_2]$ for two different polarizations—*red curve* is linear horizontal (LH), *blue curve* is linear vertical (LV); **a** *bottom panel*: linear dichroism $A_{LD} = A_{LH} - A_{LV}$. **b** momentum-dependence of A_{LD} near $\mathrm{k}=\mathrm{k}_F$ (from [121]). **c** temperature-dependence of A_{LD} [122]

can be exploited, namely the explicit dependence on light polarization of the photoemission intensity from a band of specific symmetry, as a result of matrix-element effects (see Sect. 2.6). For a single band system, changing any of the experimental parameters would change the ARPES intensity as a whole, thus preserving the shape of the spectral function and in particular the ratio between $A_{coh}(\mathbf{k}, \omega)$ and $A_{incoh}(\mathbf{k}, \omega)$, since these terms are weighted by an identical matrix element. The situation is very different in a multiband system since, whenever the quasiparticle peaks and the many-body continua originate from different single-particle bands, they will be characterized by a different overall symmetry. In this case, one may use the polarization dependence of the single-particle matrix elements to disentangle the different spectral functions contributing to the total ARPES intensity. This approach, shown in Fig. 2.16 and discussed in more detail in [121], has been used in the study of misfit cobaltates, a family of layered compounds, where the low-energy electronic states reside in the CoO_2 planes. These compounds all have 3 bands crossing the chemical potential and, while detecting A_{coh} is relatively simple due to its sharpness in proximity to E_F, evaluating the ratio between A_{coh} and A_{incoh} is complicated due to the overlap of contributions stemming from different orbitals.

Two close-lying bands, of respectively a_{1g} and $e_g{}'$ orbital character, have different symmetries and can thus be selected using polarization, as described in Sect. 2.6 (see top panel in Fig. 2.16a). Taking the difference between spectra measured with different polarization (linear dichroism), one can isolate the full spectral function for the a_{1g} band (Fig. 2.16a, bottom panel). The momentum- and temperature-dependence are then displayed in Fig. 2.16b,c, respectively, evidencing a very similar behavior to the one found in the manganites [122]. With this approach it is thus possible to track the quasiparticle weight $Z_{\mathbf{k}}$ as a function of temperature and doping, even in multiband systems and in those regions of momentum space where bands overlap.

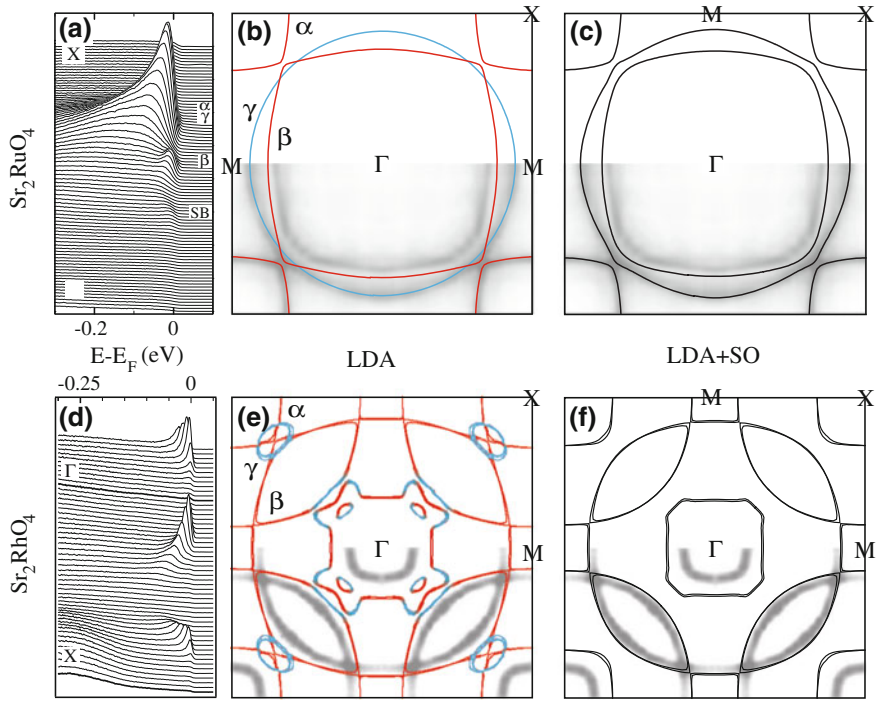

Fig. 2.17 **a–c** Stack of experimental ARPES EDCs in Sr_2RuO_4, along the high-symmetry direction $\rightarrow$ X (**a**), with LDA (**b**) and LDA+SO (**c**) predictions for the Fermi surface (from [101, 123]). **d–f** same as (**a–c**), for the case of Sr_2RhO_4 (from [123–125])

2.8.6 Correlated Relativistic Metals: Spin-Orbit Coupled 4d-TMOs

Stepping down one row in the periodic table we find the 4*d* transition metal oxides. Based on simple arguments, one would expect correlations to play a less important role in these materials. This is due to the larger spatial extent of the 4*d* orbitals, as compared to the 3*d* case, which at the same time favors delocalization (larger W) and reduces on-site electron-electron interactions (smaller U), thus positioning these systems away from the *Mott criterion*. Following such intuitive expectations, one indeed finds an evident suppression of correlation effects, which is accompanied by the emergence of coherent charge dynamics even in undoped (i.e., stoichiometric) compounds. However, marking the difference from 3*d* oxides, a new important term has to be considered for 4*d* materials: the spin-orbit (SO) interaction. The associated energy scale ζ_{SO} becomes increasingly important for heavier elements (with an approximate $\zeta_{SO} \propto Z^4$ dependence on the atomic number Z), which then have to be treated within a relativistic framework. Whereas these effects are largely neglected in cuprates, where $\zeta_{SO}(Cu^{2+}) \sim 20$–$30$ meV, they are important in ruthenates and rhodates (and even more in 5*d* materials, as we will see later), where $\zeta_{SO}(Ru^{4+}) =$

161 meV and $\zeta_{SO}(Rh^{4+}) = 191$ meV [126]. Furthermore, in 4*d* systems correlation effects continue to play a role, hence these systems are commonly classified as *correlated relativistic metals*.

ARPES results on two of the most studied 4*d*-based oxides, namely Sr_2RuO_4 and Sr_2RhO_4 [101, 123–125] are shown in Fig. 2.17, together with predictions for the Fermi surface from density functional theory in the local density approximation (LDA). While one indeed finds intense and sharp quasiparticle peaks in the energy distribution curves (EDCs)—and consequently large values of $Z_{\mathbf{k}}$ supporting the strongly reduced relevance of many-body correlations—the matching between experimental and predicted Fermi surfaces is not perfect for Sr_2RuO_4 and is actually poor for the even more covalent Sr_2RhO_4. Experiments and theory are almost fully reconciled when SO coupling is included in the single-particle methods used to describe the low-energy electronic structure of 4*d*-oxides; on the other hand, the experimental bands still appear renormalized with respect to the calculations, by approximately a factor of 2 similar to overdoped cuprates [112, 127], which indicates that electronic correlations cannot be completely neglected. This ultimately qualifies Sr_2RuO_4 and Sr_2RhO_4 as *correlated relativistic metals*.

2.8.7 Mott Criterion and Spin-Orbit Coupling: 5d TMOs

Based on the reduced correlation effects observed in 4*d*-oxides, a progressive evolution into an even less correlated physics in 5*d* materials would be expected. For this reason, the discovery of an insulating state in Sr_2IrO_4, a compound isostructural and chemically similar to cuprates and ruthenates, came as a big surprise. The first resistivity profiles to be measured in this iridate [128] showed an insulating behavior, as also later confirmed by optical spectroscopy [129]. ARPES data on this material, showing the low-energy dispersions of the Ir 5*d*-t_{2g} states, consistently found no spectral weight at E_F (see Fig. 2.18a). Furthermore, and most importantly, there is a significant disagreement between experimental data and LDA(+SO) calculations that, as displayed in Fig. 2.18b, c, would predict the system to be metallic, with a Fermi surface corresponding to a large Luttinger counting. This is a situation reminiscent of the 3*d*-oxides, where fulfilment of the *Mott criterion* would yield a correlated $S = 1/2$ insulating state at variance with band theory. This novel underlying physics emerges because of the prominent role of the SO interaction, whose strength is $\zeta_{SO} \sim 500$ meV for Ir^{4+}, and which now acts in concert with the other relevant energy scales (W and U). In the atomic limit, the action of SO would split the otherwise degenerate t_{2g} orbitals into two submanifolds with the total angular momentum $J^2_{eff} = L^2_{eff} + S^2$, and its projection J^z_{eff}, as new quantum numbers. Within such a framework, local correlations would then split the $J_{eff} = 1/2$ manifold into lower and upper Hubbard bands, thus opening a Mott gap, provided $U > W_{J_{eff}=1/2}$. This mechanism, sketched in Fig. 2.18f, g, yields a novel type of correlated ground state, the so-called *relativistic Mott-insulator*. One should note that the validity of such *pseudospin-1/2* approximation is still debated, and alternative

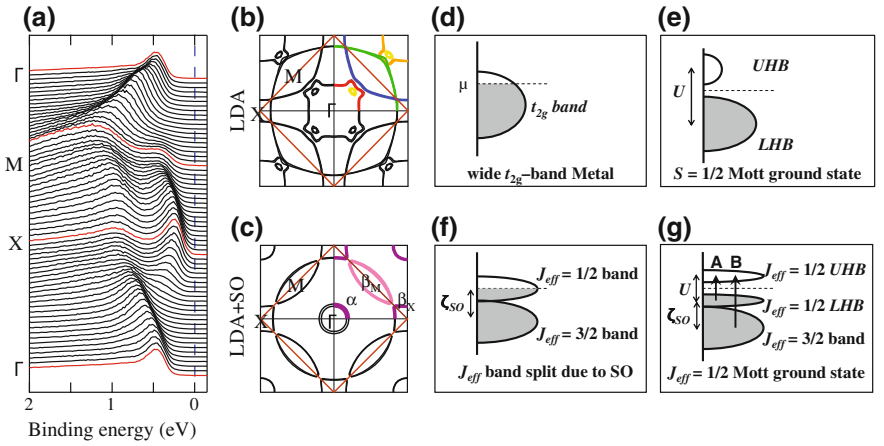

Fig. 2.18 **a** ARPES data along high-symmetry directions (EDCs at high-symmetry points are marked in *red*), showing no spectral weight at E_F. **b**, **c**: density-functional calculations within the LDA and LDA+SO approximations, respectively. **d**, **e** Possible low-energy scenarios in a $5d^5$ system: **d** $U = 0$, $\zeta_{SO} = 0$, yielding an uncorrelated metallic ground state; **e** $U > W$, $\zeta_{SO} = 0$, yielding a $S = 1/2$ Mott-insulating state; **f** $U = 0$, $\zeta_{SO} \sim W$, giving a spin-orbit coupled metal; **g** $\zeta_{SO} \sim W$, $U \sim W_{J_{eff}=1/2}$, producing a $J_{eff} = 1/2$ Mott-insulating ground state (from [129])

mechanisms are being discussed. Also, recent works have questioned the Mott-like nature of the electronic ground state in Sr_2IrO_4 and suggested that this system could be closer to a *Slater-type* (thus, non-correlated) insulator [130, 131]. In the latter case, the insulating gap would result from the onset of long-range magnetic ordering and not from strong electron correlations of the Mott type, i.e. the metal-insulator transition would coincide with the magnetic ordering transition. In the next section, we will present an unambiguous experimental realization of relativistic Mott physics in iridates and highlight similarities and differences with respect to Sr_2IrO_4.

2.8.8 Relativistic Mott Insulating Behavior: Na_2IrO_3

After the original discovery and proposal of a Mott-insulating state in Sr_2IrO_4, new systems were predicted, both on theoretical and experimental grounds, to exhibit similar physics. Na_2IrO_3 is one of these compounds, which has been the subject of early theoretical speculations [133–135], and was later synthesized and found to behave in a correlated manner. Early transport and magnetization measurements [136] provided evidence for an insulating behavior characterized by local spin moments, therefore pointing to a Mott scenario (charge localization). Further spectroscopic evidence for such a scenario has been provided by a combination of ARPES, optics and LDA calculations [132]. ARPES data for the Ir $5d$-t_{2g} bands from a pristine surface are shown in Fig. 2.19a, and highlight few primary aspects: no spectral weight is found at E_F and the band dispersions are surprisingly narrow

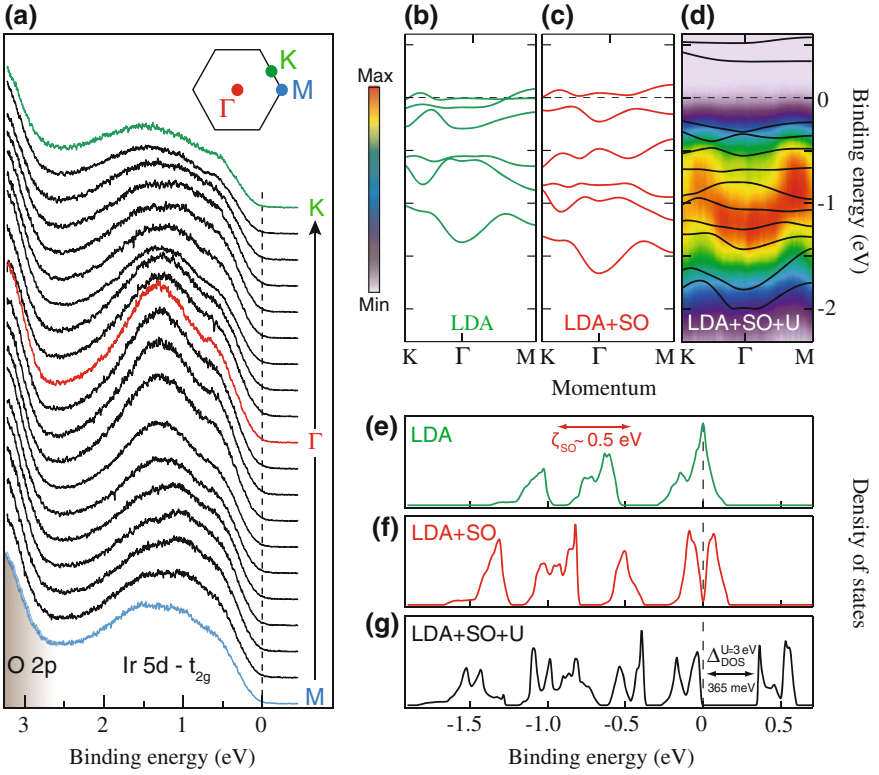

Fig. 2.19 **a** Experimental EDCs from ARPES, along the high-symmetry directions M → γ → K (as defined in the hexagonal surface-Brillouin zone, top-right corner). Ir 5*d* states populate the range 0–2 eV, whereas the O 2*p* states are found at $E_B > 2$ eV. **b**, **c**, **d** DFT band structure from LDA, LDA+SO, and LDA+SO+U [with ARPES intensity map superimposed in (d)]. **e**, **f**, **g** Corresponding theoretical densities of states (DOS) for the various LDA methods (from [132])

($W \sim 0.15$ eV). Moreover, the energy distribution curves are very broad, with no evidence of sharp quasiparticles, perhaps as a result of a vanishing $Z_{\mathbf{k}}$, at variance with Sr_2IrO_4. While this is unexpected for a system possessing the more extended 5*d* orbitals, it also brings us closer to fulfilment of the Mott criterion $U > W$ and therefore to a correlated, Mott-Hubbard-like physics. LDA predicts this system to be metallic with a density of states peaking at E_F (see Fig. 2.19b, e). The disagreement with the ARPES data implies that the charge dynamics cannot be explained within a simple band-model. When also accounting for the SO interaction, it is found that this is sufficient to turn the system insulating within the LDA calculations (Fig. 2.19c), although with a 0-gap at E_F (Fig. 2.19f). It is only with the further inclusion of the Coulomb term U that the correct gap size $\Delta_{gap} \sim 340$ meV, as found from optics and ARPES with potassium evaporation [132], can finally be reproduced (see Fig. 2.19d, g, where values of $U = 3$ eV and $J_H = 0.6$ eV have been used). The presence of a

sizeable on-site electron-electron interaction also explains the presence of local moments well above the long-range antiferromagnetic ordering temperature $T_N \sim 13$ K (i.e., in the paramagnetic phase). These findings reveal that the expectation of correlation-free physics in 5*d* oxides is in general unrealistic, and that spin-orbit coupling has a primary role in making these systems unstable even against small correlation effects. This indicates that many-body and spin-orbit interactions cannot be fully disentangled, thus conclusively establishing Na_2IrO_3—and possibly other members of the iridates family—as *relativistic Mott insulators*: a novel type of correlated insulator in which many-body (Coulomb) and relativistic (spin-orbit) effects have to be treated on an equal footing.

References

1. A. Damascelli, Z. Hussain, Z.X. Shen, Rev. Mod. Phys. **75**, 473 (2003)
2. S. Nakatsuji, Y. Maeno, Phys. Rev. Lett. **84**, 2666 (2000)
3. J. Kondo, Prog. Theor. Phys. **32**(1), 37 (1964)
4. Z. Fisk, D.W. Hess, C.J. Pethick, D. Pines, J.L. Smith, J.D. Thompson, J.O. Willis, Science **239**(4835), 33 (1988)
5. J. Zaanen, G.A. Sawatzky, J.W. Allen, Phys. Rev. Lett. **55**, 418 (1985)
6. E. Dagotto, Rev. Mod. Phys. **66**, 763 (1994)
7. P.A. Lee, N. Nagaosa, X.G. Wen, Rev. Mod. Phys. **78**, 17 (2006)
8. A.P. Mackenzie, Y. Maeno, Rev. Mod. Phys. **75**, 657 (2003)
9. M. Imada, A. Fujimori, Y. Tokura, Rev. Mod. Phys. **70**, 1039 (1998)
10. M.B. Salamon, M. Jaime, Rev. Mod. Phys. **73**, 583 (2001)
11. P.A. Grünberg, Rev. Mod. Phys. **80**, 1531 (2008)
12. N.F. Mott, Proc. Phys. Soc. London A **62**, 416 (1949)
13. G.A. Sawatzky, J.W. Allen, Phys. Rev. Lett. **53**, 2339 (1984)
14. A. Damascelli, Physica Scripta **T109**, 61 (2004)
15. H. Hertz, Ann. Phys. **17**, 983 (1887)
16. A. Einstein, Ann. Phys. **31**, 132 (1905)
17. R.Z. Bachrach, *Synchrotron Radiation Research, Advances in Surface and Interface Science*, vol. 1 (Plenum Press, New York, 1992)
18. J. Braun, Rep. Prog. Phys. **59**, 1267 (1996)
19. C.R. Brundle, A.D. Baker, *Electron Spectroscopy: Theory, Techniques, and Applications*, vol. 1 (Academic Press, New York, 1977)
20. C.R. Brundle, A.D. Baker, *Electron Spectroscopy: Theory, Techniques, and Applications*, vol. 2 (Academic Press, New York, 1978)
21. M. Cardona, L. Ley, *Photoemission in Solids*, vol. 1 (Springer, Berlin, 1978)
22. T.A. Carlson, *Photoelectron and Auger Spectroscopy* (Plenum Press, New York, 1975)
23. R. Courths, S. Hüfner, Phys. Rep. **112**, 53 (1984)
24. A. Damascelli, D.H. Lu, Z.X. Shen, J. Electron Spectr. Relat. Phenom. **117–118**, 165 (2001)
25. D.E. Eastman, in Techniques of Metal Research, vol. VI, part I, ed. by E. Passaglia (Interscience Publisher, New York, 1972), vol. VI, part I.
26. B. Feuerbacher, R.F. Willis, J. Phys. Solid State Phys. **9**, 169 (1976)
27. B. Feuerbacher, B. Fitton, R.F. Willis, *Photoemission on the Electronic Properties of Surfaces* (Wiley, New York, 1978)
28. M. Grioni, J. Electron Spectr. Relat. Phenom. 117–118 (2001). Special issue on Strongly Correlated Systems.
29. F.J. Himpsel, Adv. Phys. **32**, 1 (1983)

30. S. Hüfner, *Photoelectron Spectroscopy* (Springer, Berlin, 1995)
31. J.E. Inglesfield, B.W. Holland, in *The Chemical Physics of Solid Surfaces and Heterogeneous Catalysis*, ed. by D.A. King, D.P. Woodruff (Elsevier, Amsterdam, 1981)
32. S.D. Kevan, *Angle Resolved Photoemission-Theory and Current Applications* (Elsevier, Amsterdam, 1992)
33. R.C.G. Leckey, Appl. Surf. Sci. **13**, 125 (1982)
34. L. Ley, M. Cardona, *Photoemission in Solids*, vol. II (Springer, Berlin, 1979)
35. I. Lindau, W.E. Spicer, in *Synchrotron Radiation Research*, ed. by H. Winick, S. Doniach (Plenum Press, New York, 1980)
36. D.W. Lynch, C.G. Olson, *Photoemission Studies of High-Temperature Superconductors* (Cambridge University Press, Cambridge, 1999)
37. G.D. Mahan, in *Electron and Ion Spectroscopy of Solids*, ed. by L. Fiermans, J. Vennik, W. Dekeyser (Plenum Press, New York, 1978)
38. G. Margaritondo, J.H. Weaver, in *Methods of Experimental Physics: Surfaces*, ed. by M.G. Legally, R.L. Park (Academic Press, New York, 1983)
39. V.V. Nemoshkalenko, V.G. Aleshin, *Electron Spectroscopy of Crystals* (Plenum Press, New York, 1979)
40. E.W. Plummer, W. Eberhardt, in *Advances in Chemical Physics*, ed. by I. Prigogine, S.A. Rice (Wiley, New York, 1982)
41. Z.X. Shen, D.S. Dessau, Phys. Rep. **253**, 1 (1995)
42. N.V. Smith, Crit. Rev. Solid State Sci. **2**, 45 (1971)
43. N.V. Smith, F.J. Himpsel, in *Handbook on Synchrotron Radiation*, ed. by E.E. Koch (North-Holland, Amsterdam, 1983)
44. K.E. Smith, S.D. Kevan, Prog. Solid State Chem. **21**, 49 (1991)
45. G. Wendin, *Breakdown of the One-Electron Pictures in Photoelectron Spectroscopy* (Springer, Berlin, 1981)
46. G. Wertheim, in *Electron and Ion Spectroscopy of Solids*, ed. by L. Fiermans, J. Vennik, W. Dekeyser (Plenum Press, New York, 1978)
47. R.H. Williams, G.P. Srivastava, I.T. McGovern, Rep. Prog. Phys. **43**, 1357 (1980)
48. M.B.J. Meinders, Ph.D. Thesis, University of Groningen, The Netherlands, 1994
49. G.D. Mahan, Phys. Rev. B **2**, 4334 (1970)
50. V.N. Strocov, H.I. Starnberg, P.O. Nilsson, H.E. Brauer, L.J. Holleboom, Phys. Rev. Lett. **79**, 467 (1997)
51. V.N. Strocov, R. Claessen, G. Nicolay, S. Hüfner, A. Kimura, A. Harasawa, S. Shin, A. Kakizaki, P.O. Nilsson, H.I. Starnberg, P. Blaha, Phys. Rev. Lett. **81**, 4943 (1998)
52. T. Pillo, Ph.D. Thesis, University of Freiburg, Switzerland, 1999
53. N.V. Smith, P. Thiry, Y. Petroff, Phys. Rev. B **47**, 15476 (1993)
54. T. Miller, W.E. McMahon, T.C. Chiang, Phys. Rev. Lett. **77**, 1167 (1996)
55. E.D. Hansen, T. Miller, T.C. Chiang, Phys. Rev. B **55**, 1871 (1997)
56. E.D. Hansen, T. Miller, T.C. Chiang, Phys. Rev. Lett. **78**, 2807 (1997)
57. K. Mitchell, Proc. Roy. Soc. London A **146**, 442 (1934)
58. R.E.B. Makinson, Phys. Rev. **75**, 1908 (1949)
59. M.J. Buckingham, Phys. Rev. **80**, 704 (1950)
60. W.L. Schaich, N.W. Ashcroft, Phys. Rev. B **3**, 2452 (1971)
61. P.J. Feibelman, D.E. Eastman, Phys. Rev. B **10**, 4932 (1974)
62. J.B. Pendry, Surf. Sci. **57**, 679 (1976)
63. J.B. Pendry, J. Phys. Solid State Phys. **8**, 2413 (1975)
64. A. Liebsch, Phys. Rev. B **13**, 544 (1976)
65. A. Liebsch, in *Electron and Ion Spectroscopy of Solids*, ed. by L. Fiermans, J. Vennik, W. Dekeyser (Plenum Press, New York, 1978)
66. M. Lindroos, A. Bansil, Phys. Rev. Lett. **75**, 1182 (1995)
67. M. Lindroos, A. Bansil, Phys. Rev. Lett. **77**, 2985 (1996)
68. A. Bansil, M. Lindroos, J. Phys. Chem. Solids **56**, 1855 (1995)
69. A. Bansil, M. Lindroos, J. Phys. Chem. Solids **59**, 1879 (1998)

70. A. Bansil, M. Lindroos, Phys. Rev. Lett. **83**, 5154 (1999)
71. H.Y. Fan, Phys. Rev. **68**, 43 (1945)
72. C.N. Berglund, W.E. Spicer, Phys. Rev. **136**, A1030 (1964)
73. J. Sakurai, *Modern Quantum Mechanics* (Pearson Education, New Jersey, 2006)
74. J.W. Gadzuk, M. Šunjić, Phys. Rev. B **12**, 524 (1975)
75. A.A. Abrikosov, L.P. Gor'kov, I.E. Dzyaloshinskii, *Quantum Field Theoretical Methods in Statistical Physics* (Pergamon Press, Oxford, 1965)
76. L. Hedin, S. Lundqvist, in *Solid State Physics: Advances in Research and Applications*, ed. by H. Ehrenreich, F. Seitz, D. Turnbull (Academic Press, New York, 1969)
77. A.L. Fetter, J.D. Walecka, *Quantum Theory of Many-Particle Systems* (McGraw-Hill, New York, 1971)
78. G.D. Mahan, *Many-Particle Physics* (Plenum Press, New York, 1981)
79. E.N. Economou, *Green's Functions in Quantum Physics, Springer Series in Solid State Science*, vol. 7 (Springer, Berlin, 1983)
80. G. Rickayzen, *Green's Functions and Condensed Matter in Techniques of Physics, vol*, vol. 7 (Academic Press, London, 1991)
81. C.N. Veenstra, G.L. Goodvin, M. Berciu, A. Damascelli, Phys. Rev. B **82**, 012504 (2010)
82. C.N. Veenstra, G.L. Goodvin, M. Berciu, A. Damascelli, Phys. Rev. B **84**, 085126 (2011)
83. L.D. Landau, Sov. Phys. JETP **3**, 920 (1956)
84. L.D. Landau, Sov. Phys. JETP **5**, 101 (1957)
85. L.D. Landau, Sov. Phys. JETP **8**, 70 (1959)
86. D. Pines, P. Noziéres, *The Theory of Quantum Liquids* (Benjamin, New York, 1966)
87. J.M. Luttinger, Phys. Rev. **121**, 942 (1961)
88. C. Hodges, H. Smith, J.W. Wilkins, Phys. Rev. B **4**, 302 (1971)
89. P. Nozières, *Theory of Interacting Fermi Systems* (Benjamin, New York, 1964)
90. A. Damascelli, D. Lu, Z. Shen, J. Electron Spectr. Relat. Phenom. **117–118**, 165 (2001)
91. F. Ronning, C. Kim, D.L. Feng, D.S. Marshall, A.G. Loeser, L.L. Miller, J.N. Eckstein, L. Bozovic, Z.X. Shen, Science **282**, 2067 (1998)
92. F. Ronning, C. Kim, K.M. Shen, N.P. Armitage, A. Damascelli, D.H. Lu, D.L. Feng, Z.X. Shen, L.L. Miller, Y.J. Kim, F. Chou, I. Terasaki, Phys. Rev. B **67**, 035113 (2003)
93. D.A. Shirley, Phys. Rev. B **5**, 4709 (1972)
94. G.W. Gobeli, F.G. Allen, E.O. Kane, Phys. Rev. Lett. **12**, 94 (1964)
95. E. Dietz, H. Becker, U. Gerhardt, Phys. Rev. Lett. **36**, 1397 (1976)
96. J. Hermanson, Solid State Commun. **22**, 9 (1977)
97. W. Eberhardt, F.J. Himpsel, Phys. Rev. B **21**, 5572 (1980)
98. J.W. Cooper, Phys. Rev. **128**, 681 (1962)
99. S.L. Molodtsov, S.V. Halilov, V.D.P. Servedio, W. Schneider, S. Danzenbächer, J.J. Hinarejos, M. Richter, C. Laubschat, Phys. Rev. Lett. **85**, 4184 (2000)
100. C. Veenstra, Z.H. Zhu, B. Ludbrook, M. Capsoni, G. Levy, A. Nicolaou, J.A. Rosen, R. Comin, S. Kittaka, Y. Maeno, I.S. Elfimov, A. Damascelli, Phys. Rev. Lett. **110**, 097004 (2013)
101. A. Damascelli, D.H. Lu, K.M. Shen, N.P. Armitage, F. Ronning, D.L. Feng, C. Kim, Z.X. Shen, T. Kimura, Y. Tokura, Z.Q. Mao, Y. Maeno, Phys. Rev. Lett. **85**, 5194 (2000)
102. T. Kiss, F. Kanetaka, T. Yokoya, T. Shimojima, K. Kanai, S. Shin, Y. Onuki, T. Togashi, C. Zhang, C.T. Chen, S. Watanabe, Phys. Rev. Lett. **94**, 057001 (2005)
103. J.D. Koralek, J.F. Douglas, N.C. Plumb, Z. Sun, A.V. Fedorov, M.M. Murnane, H.C. Kapteyn, S.T. Cundiff, Y. Aiura, K. Oka, H. Eisaki, D.S. Dessau, Phys. Rev. Lett. **96**, 017005 (2006)
104. L. Åsbrink, Chem. Phys. Lett. **7**, 549 (1970)
105. G.A. Sawatzky, Nature **342**, 480 (1989)
106. K.M. Shen, F. Ronning, D.H. Lu, W.S. Lee, N.J.C. Ingle, W. Meevasana, F. Baumberger, A. Damascelli, N.P. Armitage, L.L. Miller, Y. Kohsaka, M. Azuma, M. Takano, H. Takagi, Z.X. Shen, Phys. Rev. Lett. **93**, 267002 (2004)
107. S. Doniach, M. Sunjic, J. Phys. C: Solid State Phys. **3**, 285 (1970)
108. F.C. Zhang, T.M. Rice, Phys. Rev. B **37**, 3759 (1988)

109. B.O. Wells, Z.X. Shen, A. Matsuura, D.M. King, M.A. Kastner, M. Greven, R.J. Birgeneau, Phys. Rev. Lett. **74**, 964 (1995)
110. V.B. Zabolotnyy, S.V. Borisenko, A.A. Kordyuk, J. Geck, D.S. Inosov, A. Koitzsch, J. Fink, M. Knupfer, B. Büchner, S.L. Drechsler, H. Berger, A. Erb, M. Lambacher, L. Patthey, V. Hinkov, B. Keimer, Phys. Rev. B **76**, 064519 (2007)
111. M.A. Hossain, J.D.F. Mottershead, D. Fournier, A. Bostwick, J.L. McChesney, E. Rotenberg, R. Liang, W.N. Hardy, G.A. Sawatzky, I.S. Elfimov, D.A. Bonn, A. Damascelli, Nat. Phys. **4**, 527 (2008)
112. D. Fournier, G. Levy, Y. Pennec, J.L. McChesney, A. Bostwick, E. Rothenberg, R. Liang, W.N. Hardy, D.A. Bonn, I. Elfimov, A. Damascelli, Nat. Phys. **6**, 905 (2010)
113. N. Mannella, W.L. Yang, X.J. Zhoe, H. Zheng, J.F. Mitchell, J. Zaanen, T.P. Devereaux, N. Nagaosa, Z. Hussain, Z.-X. Shen, Nature **438**, 474 (2005)
114. Y.D. Chuang, A.D. Gromko, D.S. Dessau, T. Kimura, Y. Tokura, Science **292**, 1509 (2001)
115. Z. Sun, Y.D. Chuang, A.V. Fedorov, J.F. Douglas, D. Reznik, F. Weber, N. Aliouane, D.N. Argyriou, H. Zheng, J.F. Mitchell, T. Kimura, Y. Tokura, A. Revcolevschi, D.S. Dessau, Phys. Rev. Lett. **97**, 056401 (2006)
116. Z. Sun, J.F. Douglas, A.V. Fedorov, Y.D. Chuang, H. Zheng, J.F. Mitchell, D.S. Dessau, Nat. Phys. **3**, 248 (2007)
117. S. de Jong, Y. Huang, I. Santoso, F. Massee, R. Follath, O. Schwarzkopf, L. Patthey, M. Shi, M.S. Golden, Phys. Rev. B **76**, 235117 (2007)
118. S. de Jong, F. Massee, Y. Huang, M. Gorgoi, F. Schaefers, J. Fink, A.T. Boothroyd, D. Prabhakaran, J.B. Goedkoop, M.S. Golden, Phys. Rev. B **80**, 205108 (2009)
119. F. Massee, S. de Jong, Y. Huang, W.K. Siu, I. Santoso, A. Mans, A.T. Boothroyd, D. Prabhakaran, R. Follath, A. Varykhalov, L. Patthey, M. Shi, J.B. Goedkoop, M.S. Golden, Nat. Phys. **7**, 978 (2011)
120. Z. Yusof, B.O. Wells, T. Valla, P.D. Johnson, A.V. Fedorov, Q. Li, S.M. Loureiro, R.J. Cava, Phys. Rev. B **76**, 165115 (2007)
121. A. Nicolaou, V. Brouet, M. Zacchigna, I. Vobornik, A. Tejeda, A. Taleb-Ibrahimi, P. Le Fèvre, F. Bertran, S. Hébert, H. Muguerra, D. Grebille, Phys. Rev. Lett. **104**, 056403 (2010)
122. V. Brouet, A. Nicolaou, Publication in progress
123. M.W. Haverkort, I.S. Elfimov, L.H. Tjeng, G.A. Sawatzky, A. Damascelli, Phys. Rev. Lett. **101**, 026406 (2008)
124. F. Baumberger, N.J.C. Ingle, W. Meevasana, K.M. Shen, D.H. Lu, R.S. Perry, A.P. Mackenzie, Z. Hussain, D.J. Singh, Z.X. Shen, Phys. Rev. Lett. **96**, 246402 (2006)
125. B.J. Kim, J. Yu, H. Koh, I. Nagai, S.I. Ikeda, S.J. Oh, C. Kim, Phys. Rev. Lett. **97**, 106401 (2006)
126. A. Earnshaw, B.N. Figgis, J. Lewis, R.D. Peacock, J. Chem. Soc. pp. 3132–3138 (1961) Please provide volume number for [126].
127. M. Platé, J.D.F. Mottershead, I.S. Elfimov, D.C. Peets, R. Liang, D.A. Bonn, W.N. Hardy, S. Chiuzbaian, M. Falub, M. Shi, L. Patthey, A. Damascelli, Phys. Rev. Lett. **95**, 077001 (2005)
128. G. Cao, J. Bolivar, S. McCall, J.E. Crow, R.P. Guertin, Phys. Rev. B **57**, R11039 (1998)
129. B.J. Kim, H. Jin, S.J. Moon, J.Y. Kim, B.G. Park, C.S. Leem, J. Yu, T.W. Noh, C. Kim, S.J. Oh, J.H. Park, V. Durairaj, G. Cao, E. Rotenberg, Phys. Rev. Lett. **101**, 076402 (2008)
130. R. Arita, J. Kuneš, A.V. Kozhevnikov, A.G. Eguiluz, M. Imada, Phys. Rev. Lett. **108**, 086403 (2012)
131. D. Hsieh, F. Mahmood, D.H. Torchinsky, G. Cao, N. Gedik, Phys. Rev. B **86**, 035128 (2012)
132. R. Comin, G. Levy, B. Ludbrook, Z.H. Zhu, C.N. Veenstra, J.A. Rosen, Y. Singh, P. Gegenwart, D. Stricker, J.N. Hancock, D. van der Marel, I.S. Elfimov, A. Damascelli, Phys. Rev. Lett. **109**, 266406 (2012)
133. A. Shitade, H. Katsura, J. Kuneš, X.L. Qi, S.C. Zhang, N. Nagaosa, Phys. Rev. Lett. **102**, 256403 (2009)
134. H. Jin, H. Kim, H. Jeong, C.H. Kim, J. Yu, arXiv:0907.0743v1 2009
135. J. Chaloupka, G. Jackeli, G. Khaliullin, Phys. Rev. Lett. **105**, 027204 (2010)
136. Y. Singh, P. Gegenwart, Phys. Rev. B **82**, 064412 (2010)

Chapter 3
Spectroscopic Imaging STM: Atomic-Scale Visualization of Electronic Structure and Symmetry in Underdoped Cuprates

Kazuhiro Fujita, Mohammad Hamidian, Inês Firmo, Sourin Mukhopadhyay, Chung Koo Kim, Hiroshi Eisaki, Shin-ichi Uchida and J.C. Davis

Abstract Atomically resolved spectroscopic imaging STM (SI-STM) has played a pivotal role in visualization of the electronic structure of cuprate high temperature superconductors. In both the *d*-wave superconducting (*d*SC) and the pseudogap (PG) phases of underdoped cuprates, two distinct types of electronic states are observed

K. Fujita (✉) · M. Hamidian · I. Firmo · S. Mukhopadhyay · J.C. Davis
LASSP, Department of Physics, Cornell University, Ithaca, NY 14853, USA
e-mail: fujita@cornell.edu

M. Hamidian
e-mail: m.hamidian@gmail.com

I. Firmo
e-mail: inesfirmo@gmail.com

S. Mukhopadhyay
e-mail: sourin.mukhopadhyay@gmail.com

J.C. Davis
e-mail: jcdavis@ccmr.cornell.edu

K. Fujita · M. Hamidian · I. Firmo · C. Kim · J.C. Davis
CMPMS Department, Brookhaven National Laboratory, Upton, NY 11973, USA

C. Kim
e-mail: ckkim@bnl.gov

S. Mukhopadhyay · J.C. Davis
Kavli Institute at Cornell for Nanoscience, Cornell University, Ithaca, NY 14850, USA

H. Eisaki
National Institute of Advanced Industrial Science and Technology (AIST),
Tsukuba, Ibaraki 305-8568, Japan
e-mail: h-eisaki@aist.go.jp

S. Uchida
Department of Physics, University of Tokyo, Bunkyo-ku, Tokyo 113-0033, Japan
e-mail: uchida@phys.s.u-tokyo.ac.jp

J.C. Davis
School of Physics and Astronomy, University of St. Andrews, Scotland KY16 9SS, UK

A. Avella and F. Mancini (eds.), *Strongly Correlated Systems*,
Springer Series in Solid-State Sciences 180, DOI 10.1007/978-3-662-44133-6_3

when using SI-STM. The first consists of the dispersive Bogoliubov quasiparticles of a homogeneous d-wave superconductor existing in an energy range $|E| \leq \Delta_0$ and only upon an arc in momentum space (**k**-space) that terminates close to the lines connecting $\mathbf{k} = \pm(\pi/a_0, 0)$ to $\mathbf{k} = \pm(0, \pi/a_0)$. This 'nodal' arc shrinks continuously as electron density increases towards half filling. In both phases, the only broken symmetries detected in the $|E| \leq \Delta_0$ states are those of a d-wave superconductor. The second type of electronic state occurs near the pseudogap energy scale $|E| \sim \Delta_1$ or equivalently near the 'antinodal' regions $\mathbf{k} = \pm(\pi/a_0, 0)$ and $\mathbf{k} = \pm(0, \pi/a_0)$. These states break the expected 90°-rotational (C_4) symmetry of electronic structure within each CuO_2 unit cell, at least down to 180°-rotational (C_2), symmetry. This intra-unit-cell symmetry breaking is interleaved with the incommensurate conductance modulations locally breaking both rotational and translational symmetries. Their wavevector **S** is always found to be determined by the **k**-space points where Bogoliubov quasiparticle interference terminates along the line joining $\mathbf{k} = (0, \pm\pi/a_0)$ to $\mathbf{k} = (\pm\pi/a_0, 0)$, and thus diminishes continuously with doping. The symmetry properties of these $|E| \sim \Delta_1$ states are indistinguishable in the dSC and PG phases. While the relationship between the $|E| \sim \Delta_1$ broken symmetry states and the $|E| \leq \Delta_0$ Bogoliubov quasiparticles of the homogeneous superconductor is not yet fully understood, these two sets of phenomena are linked inextricably because the **k**-space locations where the latter disappears are always linked by the modulation wavevectors of the former.

3.1 Electronic Structure of Hole-doped Cuprates

The CuO_2 plane electronic structure is dominated by Cu $3d$ and O $2p$ orbitals [1]. Each Cu $d_{x^2-y^2}$ orbital is split energetically into singly and doubly occupied configurations by on-site Coulomb interactions. This results in a 'charge-transfer' Mott insulator [1, 2] that is also strongly antiferromagnetic due to inter-copper superexchange [3, 4]. So called 'hole-doping', a process distinct from the eponymous one in semiconductors, is achieved by removing electrons from the 2p6 orbitals of the O atoms [5–7].

The phase diagram [8] as a function of the number of holes per CuO_2 measured from half-filling, p, is shown schematically in Fig. 3.1a. Antiferromagnetism exists for $p <$ 2–5 %, superconductivity appears in the range 5–10 % $< p <$ 25–30 %, and a likely Fermi liquid state appears for $p >$ 25–30 %. The highest superconducting critical temperature T_c occurs at 'optimal' doping $p \sim 16\%$ and the superconductivity exhibits d-wave symmetry. With reduced p, an unexplained electronic excitation with energy $|E| \sim \Delta_1$ and that is anisotropic in **k**-space, [8–13] appears at $T^* > T_c$. This phase is so called 'pseudegap' (PG) because the energy scale Δ_1 could be the energy gap of a distinct electronic phase [9, 10]. Explanations for the PG phase include (i) that it occurs via hole-doping an antiferromagnenic Mott insulator to create a spin-liquid [4, 14–18] or, (ii) that it is a d-wave superconductor but without

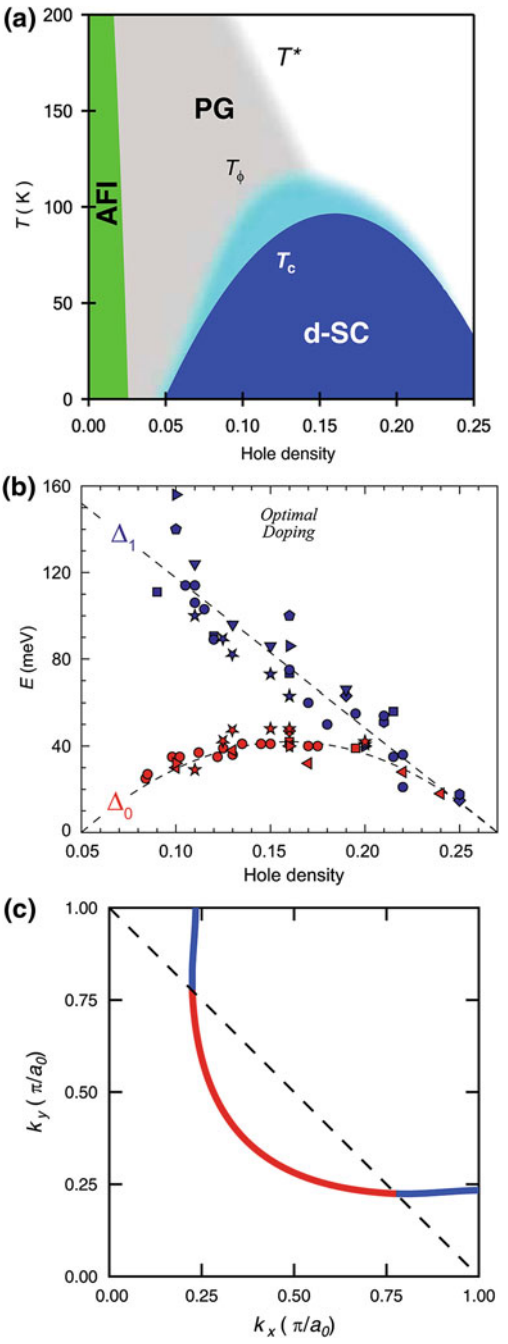

Fig. 3.1 **a** Schematic cuprate phase diagram. Here T_c is the critical temperature circumscribing a 'dome' of superconductivity, T_ϕ is schematic of the maximum temperature at which superconducting phase fluctuations are detectable within the pseudogap phase, and T^* is the approximate temperature at which the pseudogap phenomenology first appears. **b** The two classes of electronic excitations in cuprates. The separation between the energy scales associated with excitations of the superconducting state (dSC, denoted by Δ_0) and those of the pseudogap state (PG, denoted by Δ_1) increases as p decreases (reproduced from [10]). The different symbols correspond to the use of different experimental techniques. **c** A schematic diagram of electronic structure within the 1st Brillouin zone of hole-doped CuO_2. The *dashed lines* joining $\mathbf{k} = (0, \pm\pi/a_0)$ to $\mathbf{k} = (\pm\pi/a_0, 0)$ are found, empirically, to play a key role in the doping-dependence of electronic structure. The hypothetical Fermi surface (as it would appear if correlations were suppressed) is labeled using two colors, red for the 'nodal' regions bounded by the *dashed lines* and *blue* for the 'antinodal' regions near $\mathbf{k} = (0, \pm\pi/a_0)$ to $\mathbf{k} = (\pm\pi/a_0, 0)$

long range phase coherence [19–24] or, (iii) that it is a distinct electronic ordered phase [25–39].

The energy scales Δ_1 and Δ_0 are associated with two distinct types of electronic excitations [8–11, 40–43] and are observed in underdoped cuprates by many techniques. Further, Δ_1 and Δ_0 deviate continuously from one another with diminishing p (Fig. 3.1b from [10]). Transient grating spectroscopy shows that the $|E| \sim \Delta_1$ excitations propagate very slowly without recombination into Cooper pairs, while the lower energy 'nodal' excitations propagate freely and pair as expected [40]. Andreev tunneling identifies two distinct excitation energy scales which diverge as $p \rightarrow 0$: the first is identified with the pseudogap energy Δ_1 and the second Δ_0 with the maximum pairing gap energy of Cooper pairs [41]. Raman spectroscopy finds that only the scattering near the d-wave node is consistent with delocalized Cooper pairing [42]. The superfluid density from muon spin rotation evolves with hole-density as if the whole Fermi surface is unavailable for Cooper pairing [43]. Figure 3.1c shows a schematic depiction of the Fermi surface and distinguishes the 'nodal' from 'antinodal' regions of **k**-space on red and blue. Momentum-resolved studies of cuprate electronic structure using angle resolved photoemission spectroscopy (ARPES) in the PG phase reveals that excitations with $E \sim -\Delta_1$ occur near the antinodal regions $\mathbf{k} \cong (\pi/a_0, 0)$; $(0, \pi/a_0)$, and that $\Delta_1(p)$ increases rapidly as $p \rightarrow 0$ [9–12], while the nodal region of **k**-space exhibits an ungapped 'Fermi Arc' [44] in the PG phase upon which a momentum- and temperature-dependent energy gap opens in the dSC phase [44–50].

Density-of-states measurements report an energetically particle-hole symmetric excitation energy $|E| = \Delta_1$ that is unchanged in the PG and dSC phases [51, 52]. Figure 3.2b shows the evolution of spatially-averaged differential tunneling conductance $g(E)$ for $Bi_2Sr_2CaCu_2O_{8+\delta}$ [53–55] with the evolution of the pseudogap energy $E = \pm\Delta_1$ indicated by a blue dashed curve, while that of Δ_0 is shown by red dashed curves (Sect. 3.6). SI-STM uses spatially mapped tunneling spectroscopy to visualize the spatial structure and symmetry of these distinct types of states. For energies $|E| \leq \Delta_0$, the dispersive Bogoliubov quasiparticles of a spatially homogeneous superconductor are always observed [56–62] while the states near $|E| \sim \Delta_1$ are highly disordered [53–55, 63–70] and exhibit distinct broken symmetries [7, 53, 60–62, 71, 72].

3.2 $Bi_2Sr_2CaCu_2O_8$ Crystals

We have studied a sequence of $Bi_2Sr_2CaCu_2O_{8+\delta}$ samples with $p \cong 0.19, 0.17, 0.14, 0.10, 0.08, 0.07, 0.06$ or with $T_c(\mathrm{K}) = 86, 88, 74, 64, 45, 37, 20$ respectively, and many of these samples were studied in both the dSC and PG phases [53–58, 60–64, 71, 72]. Each sample is inserted into the cryogenic ultra high vacuum of the SI-STM [76] and cleaved to reveal an atomically clean BiO surface. All measurements were made between 1.9 and 65 K using three different cryogenic SI-STMs. These samples were derived from large single crystals with very high quality of $Bi_{2.1}Sr_{1.9}CaCu_2O_{8+\delta}$

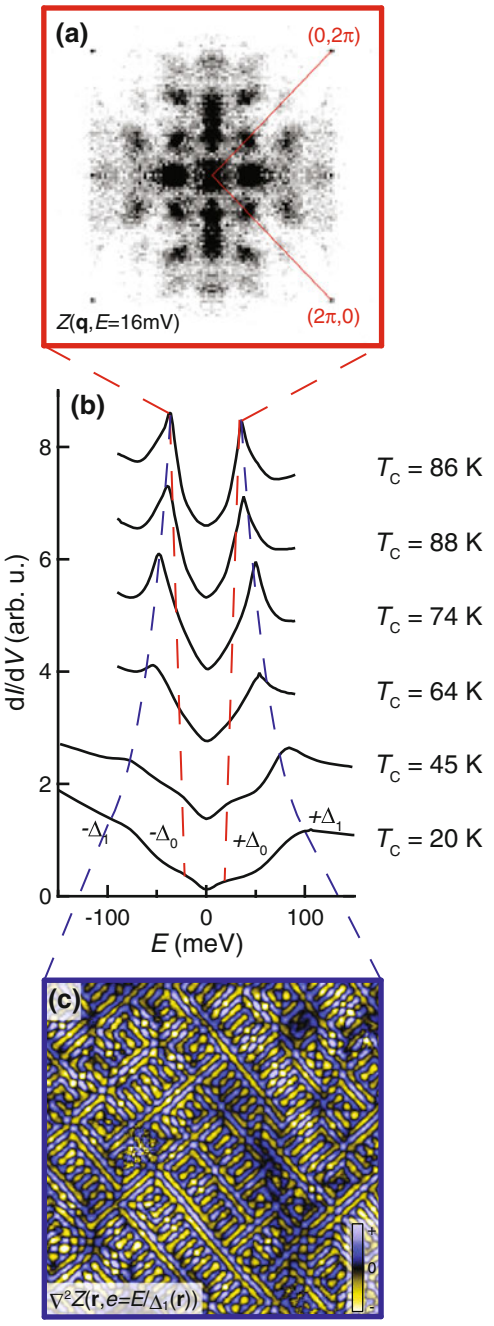

Fig. 3.2 **a** Fourier transform of the conductance ratio map $Z(\mathbf{r}, E)$ at a representative energy below Δ_0 for $T_c = 45$K $Bi_2Sr_2Ca_{0.8}Dy_{0.2}Cu_2O_{8+\delta}$, which only exhibits the patterns characteristic of homogenous d-wave superconducting quasiparticle interference. **b** Evolution of the spatially averaged tunneling spectra of $Bi_2Sr_2CaCu_2O_{8+\delta}$ with diminishing p, here characterized by $T_c(p)$. The energies $\Delta_1(p)$ (*blue dashed line*) are detected as the pseudogap edge while the energies $\Delta_0(p)$ (*red dashed line*) are more subtle but can be identified by the correspondence of the "kink" energy with the extinction energy of Bogoliubov quasiparticles, following the procedures in [57] and [61]. **c** Laplacian (or equivalent high pass filter) of the conductance ratio map $Z(\mathbf{r})$ at the pseudogap energy $E = \Delta_1$, emphasizing the local symmetry breaking of these electronic states

and $Bi_{2.2}Sr_{1.8}Ca_{0.8}Dy_{0.2}Cu_2O_{8+\delta}$. The crystal growth was carried out in air and at growth speeds of 0.15–0.2 mm/h. Annealing was used to vary the critical temperature of each sample. Oxidation annealing is performed in air or under oxygen gas flow, and deoxidation annealing is done in vacuum or under nitrogen gas flow for the systematic study at different hole-densities [77].

3.3 Spectroscopic Imaging Scanning Tunneling Microscopy

The spectroscopic imaging STM technique consists of making atomically resolved and registered measurements of the STM tip-sample differential tunneling conductance $\mathrm{d}I/\mathrm{d}V(\mathbf{r}, E = eV) \equiv g(\mathbf{r}, E = eV)$ which is a function of both location $\mathbf{r}$ and electron energy E. It can simultaneously determine the real space ($\mathbf{r}$-space) and momentum space ($\mathbf{k}$-space) electronic structure both above and below E_F. Successful implementation of this approach requires quite specialized STM techniques and facilities [76].

SI-STM does suffer from some common systematic errors, the most important and most widely ignored of which emerges from the tunneling current equation itself. The tunneling current is given by

$$I(\mathbf{r}, z, V) = C(\mathbf{r})e^{-\frac{z(\mathbf{r})}{z_0}} \int_0^{eV} [f(E,T)N(\mathbf{r},E)][1 - f(E,T)]\, N_{\mathrm{Tip}}(E)dE \quad (3.1)$$

Here $z(\mathbf{r})$ is the tip-surface distance, V the tip-sample bias voltage, $N(\mathbf{r}, E)$ the sample's local-density-of-electronic-states, $N_{\mathrm{Tip}}(E)$ the tip density-of-electronic-states, $C(\mathbf{r})e^{-\frac{z(\mathbf{r})}{z_0}}$ contains effects of tip elevation, of work function based tunnel-barrier, and of tunneling matrix elements, $f(E, T)$ is the Fermi function. Therefore, as $T \to 0$ and with N_{Tip} and $C(\mathbf{r})$ both equal to constants (3.1) can be simplified as,

$$I_s = Ce^{-\frac{z(\mathbf{r})}{z_0}} \int_0^{eV_s} N(\mathbf{r}, E)dE \Rightarrow Ce^{-\frac{z(\mathbf{r})}{z_0}} = I_s / \int_0^{eV_s} N(\mathbf{r}, E)dE \quad (3.2)$$

Here V_s and I_s are the (constant but arbitrary) junction 'set-up' bias voltage and current respectively that are used in practice to fix $z(\mathbf{r})$. Taking the energy derivative of (3.1) as $T \to 0$ and with N_{Tip} and $C(\mathbf{r})$ both equal to constants, and then substituting from (3.2), the measured $g(\mathbf{r}, E) \equiv \mathrm{d}I/\mathrm{d}V(\mathbf{r}, E = eV)$ data are then related to $N(\mathbf{r}, E)$ by [58, 60–62]

$$g(\mathbf{r}, E = eV) = \frac{eI_s}{\int_0^{eV_s} N(\mathbf{r}, E')dE'} N(\mathbf{r}, E) \quad (3.3)$$

Equation (3.3) shows that when $\int_0^{eV_s} N(\mathbf{r}, E')dE'$ is heterogeneous at the atomic scale as it invariably is in $Bi_2Sr_2CaCu_2O_{8+\delta}$ [53–55, 59–71], the $g(\mathbf{r}, E = eV)$ data can never be used to measure the spatial arrangements of $N(\mathbf{r}, E)$. Mitigation [58, 60–62] of these systematic errors can be achieved by using

$$Z(\mathbf{r}, E) \equiv \frac{g(\mathbf{r}, E = +eV)}{g(\mathbf{r}, E = -eV)} = \frac{N(\mathbf{r}, +E)}{N(\mathbf{r}, -E)} \tag{3.4}$$

which cancels the unknown 'setup effect' errors. This approach allows energy magnitudes, distances, wavelengths and spatial symmetries to be measured correctly but at the expense of mixing information derived from states at $\pm E$.

A second very important and frequently overlooked systematic error is the 'thermal broadening' which results in an unavoidable energy uncertainty δE in the energy argument of all types of tunneling spectroscopy. This thermal broadening effect is caused by the convolution of the tip and sample Fermi-Dirac distributions $f(E)(1-f(E))$ in (3.1). As the maximum of this product is $f(0)(1-f(0)) = \frac{1}{4}$, the observed FWHM in tunneling conductance due to a delta-function in $N(E)$ at $T = 0$ is determined implicitly from

$$\left(e^{\frac{E}{k_BT}} + 1\right)^{-1}\left[1 - \left(e^{\frac{E}{k_BT}} + 1\right)^{-1}\right] = \frac{1}{8} \tag{3.5}$$

to be $\delta E > 3.53k_BT$ (or $\delta E > 1.28\,\text{meV}$ at $T = 4.2\text{K}$). This FWHM is the lower limit of meaningful energy resolution in tunneling spectroscopy, and features in tunnelling spectra whose energy width grows linearly with T with this slope, are due merely to the form of the Fermi function.

A third important systematic error limits **k**-space resolution when using $\tilde{g}(\mathbf{q}, E)$ and $\tilde{Z}(\mathbf{q}, E)$, the power spectral density Fourier transforms of $g(\mathbf{r}, E)$ and $Z(\mathbf{r}, E)$. Because **q**-space resolution during Fourier analysis is inverse to the **r**-space field-of-view size, to achieve sufficient precision in $|\mathbf{q}(E)|$ for discrimination of a non-dispersive ordering wavevector $\mathbf{q}^*$ due to an electronic ordered phase from the dispersive wavevectors $\mathbf{q}(E)$ due to quantum interference patterns of delocalized states, requires that $g(\mathbf{r}, E)$ or $Z(\mathbf{r}, E)$ be measured in large fields-of-view and with energy resolution at or below ~2 meV for cuprates. Using a smaller FOV or poorer energy resolution in $g(\mathbf{r}, E)$ studies inexorably generates the erroneous impression of non-dispersive modulations. For example, in $Bi_2Sr_2CaCu_2O_{8+\delta}$, no deductions distinguishing between dispersive and non-dispersive excitations can or should be made using Fourier transformed $g(\mathbf{r},E)$ data from a FOV smaller than ~45nm-square [57, 62].

A final subtle but important systematic error derives from the slow picometer scale distortions in rectilinearity of the image over the continuous and extended period (of up to a week or more) required for each $g(\mathbf{r}, E)$ data set to be acquired. This is particularly critical in research requiring a precise knowledge of the spatial phase of the crystal lattice [71, 72]. To address this issue, we recently introduced a

post-measurement distortion correction technique that is closely related to an approach we developed earlier to address incommensurate crystal modulation effects [78] in $Bi_2Sr_2CaCu_2O_{8+\delta}$. We identify a slowly varying field $\mathbf{u}(\mathbf{r})$ [79] that measures the displacement vector $\mathbf{u}$ of each location $\mathbf{r}$ in a topographic image of the crystal surface $T(\mathbf{r})$, from the location $\mathbf{r}$-$\mathbf{u}(\mathbf{r})$ where it should be if $T(\mathbf{r})$ were perfectly periodic. Therefore, we consider an atomically resolved topograph $T(\mathbf{r})$ with tetragonal symmetry. In SI-STM, the $T(\mathbf{r})$ and its simultaneously measured $g(\mathbf{r}, E)$ are specified by measurements on a square array of pixels with coordinates labeled as $\mathbf{r} = (x, y)$. The power-spectral-density (PSD) Fourier transform of $T(\mathbf{r})$, $|\tilde{T}(\mathbf{q})|^2$—where, $\tilde{T}(\mathbf{q}) = \mathrm{Re}\tilde{T}(\mathbf{q}) + i\,\mathrm{Im}\tilde{T}(\mathbf{q})$, then exhibits two distinct peaks representing the atomic corrugations; these are centered at the first reciprocal unit cell Bragg wavevectors $\mathbf{Q}_a = (Q_{ax}, Q_{ay})$ and $\mathbf{Q}_b = (Q_{bx}, Q_{by})$ with a and b labeling the unit cell vectors. Next $T(\mathbf{r})$ is multiplied by reference cosine and sine functions with periodicity set by the wavevectors $\mathbf{Q}_a$ and $\mathbf{Q}_b$, and whose origin is chosen at an apparent atomic location in $T(\mathbf{r})$. The resulting four images are filtered to retain $\mathbf{q}$-regions within a radius $\delta q = \frac{1}{\lambda}$ of the four Bragg peaks; the magnitude of λ is chosen to capture only the relevant image distortions. This procedure results in four new images which retain the local phase information $\Theta_a(\mathbf{r})$, $\Theta_b(\mathbf{r})$ that quantifies the local displacements from perfect periodicity:

$$X_a(\mathbf{r}) = \cos\Theta_a(\mathbf{r}),\ Y_a(\mathbf{r}) = \sin\Theta_a(\mathbf{r}) \tag{3.6}$$

$$X_b(\mathbf{r}) = \cos\Theta_b(\mathbf{r}),\ Y_b(\mathbf{r}) = \sin\Theta_b(\mathbf{r}) \tag{3.7}$$

Dividing the appropriate pairs of images then allows one to extract

$$\Theta_a(\mathbf{r}) = \tan^{-1}\frac{Y_a(\mathbf{r})}{X_a(\mathbf{r})} \tag{3.8}$$

$$\Theta_b(\mathbf{r}) = \tan^{-1}\frac{Y_b(\mathbf{r})}{X_b(\mathbf{r})} \tag{3.9}$$

Of course, in a perfect lattice the $\Theta_a(\mathbf{r})$, would be independent of $\mathbf{r}$. However, in the real image $T(\mathbf{r})$, $\mathbf{u}(\mathbf{r})$ represents the distortion of the local maxima away from their expected perfectly periodic locations, with the identical distortion occurring in the simultaneous spectroscopic data $g(\mathbf{r}, E)$. Considering only the components periodic with the lattice, the measured topograph can therefore be represented by

$$T(\mathbf{r}) = T_0\left[\cos\left(\mathbf{Q}_a \cdot (\mathbf{r} + \mathbf{u}(\mathbf{r}))\right) + \cos\left(\mathbf{Q}_b \cdot (\mathbf{r} + \mathbf{u}(\mathbf{r}))\right)\right] \tag{3.10}$$

Correcting this for the spatially dependent phases $\Theta_a(\mathbf{r})$, $\Theta_b(\mathbf{r})$ generated by $\mathbf{u}(\mathbf{r})$ requires an affine transformation at each point in (x,y) space. We see that the actual local phase of each of cosine component at a given spatial point $\mathbf{r}$, $\varphi_a(\mathbf{r})$, $\varphi_b(\mathbf{r})$ can be written as

$$\varphi_a(\mathbf{r}) = \mathbf{Q}_a \cdot \mathbf{r} + \Theta_a(\mathbf{r}) \tag{3.11}$$

$$\varphi_b(\mathbf{r}) = \mathbf{Q}_b \cdot \mathbf{r} + \Theta_b(\mathbf{r}) \tag{3.12}$$

where $\Theta_i(\mathbf{r}) = \mathbf{Q}_i \cdot \mathbf{u}(\mathbf{r})$; $i = a, b$ is the additional phase generated by the displacement field $\mathbf{u}(\mathbf{r})$. This simplifies (3.10) to

$$T(\mathbf{r}) = T_0 \left[\cos\left(\varphi_a(\mathbf{r})\right) + \cos\left(\varphi_b(\mathbf{r})\right)\right] \tag{3.13}$$

which is defined in terms of its local phase fields only, and every peak associated with an atomic local maximum in the topographic image has the same φ_a and φ_b. We then need to find a transformation, using the given phase information $\varphi_{a,b}(\mathbf{r})$, to map the distorted lattice onto a perfectly periodic one. This is equivalent to finding a set of local transformations which makes $\Theta_{a,b}$ take on constant values, Θ_a and Θ_b, over all space. Thus, let $\mathbf{r}$ be a point on the unprocessed (distorted) $T(\mathbf{r})$, and let $\tilde{\mathbf{r}} = \mathbf{r} - \mathbf{u}(\mathbf{r})$ be the point of equal phase on the 'perfectly' lattice-periodic image which needs to be determined. This produces a set of equivalency relations

$$\begin{aligned} \mathbf{Q}_a \cdot \mathbf{r} + \Theta_a(\mathbf{r}) &= \mathbf{Q}_a \cdot \tilde{\mathbf{r}} + \bar{\Theta}_a \\ \mathbf{Q}_b \cdot \mathbf{r} + \Theta_b(\mathbf{r}) &= \mathbf{Q}_b \cdot \tilde{\mathbf{r}} + \bar{\Theta}_b \end{aligned} \tag{3.14}$$

Solving for the components of $\tilde{\mathbf{r}}$ and then re-assigning the $T(\mathbf{r})$ values measured at $\mathbf{r}$, to the new location $\tilde{\mathbf{r}}$ in the (x,y) coordinates produces a topograph with virtually perfect lattice periodicity. To solve for $\tilde{\mathbf{r}}$ we rewrite (3.14) in matrix form:

$$\mathbf{Q}\begin{pmatrix} \tilde{\mathrm{r}}_1 \\ \tilde{\mathrm{r}}_2 \end{pmatrix} = \mathbf{Q}\begin{pmatrix} \mathrm{r}_1 \\ \mathrm{r}_2 \end{pmatrix} - \begin{pmatrix} \bar{\theta}_a - \theta_a(\mathbf{r}) \\ \bar{\theta}_b - \theta_b(\mathbf{r}) \end{pmatrix} \tag{3.15}$$

where

$$\mathbf{Q} = \begin{pmatrix} Q_{ax} & Q_{ay} \\ Q_{bx} & Q_{by} \end{pmatrix} \tag{3.16}$$

Because $\mathbf{Q}_a$ and $\mathbf{Q}_b$ are orthogonal, $\mathbf{Q}$ is invertible allowing one to solve for the displacement field $\mathbf{u}(\mathbf{r})$ which maps $\mathbf{r}$ to $\tilde{\mathbf{r}}$ as

$$\mathbf{u}(\mathbf{r}) = \mathbf{Q}^{-1}\begin{pmatrix} \bar{\theta}_a - \theta_a(\mathbf{r}) \\ \bar{\theta}_b - \theta_b(\mathbf{r}) \end{pmatrix} \tag{3.17}$$

with the convention $\bar{\Theta}_i = 0$ that generates a 'perfect' lattice with an atomic peak at the origin; this is equivalent to ensuring that there are no imaginary (sine) components to the Bragg peaks in the Fourier transform. Then, by using this technique, one can estimate $\mathbf{u}(\mathbf{r})$ and thereby undo distortions in the raw $T(\mathbf{r})$ data with the result that it is transformed into a distortion-corrected topograph $T'(\mathbf{r})$ exhibiting the known periodicity and symmetry of the termination layer of the crystal. The key step for electronic-structure symmetry determination is then that the identical geometrical

transformations to undo $\mathbf{u}(\mathbf{r})$ in $T(\mathbf{r})$ yielding $T'(\mathbf{r})$, are also carried out on every $g(\mathbf{r}, E)$ acquired simultaneously with the $T(\mathbf{r})$ to yield a distortion corrected $g'(\mathbf{r}, E)$. The $T'(\mathbf{r})$ and $g'(\mathbf{r}, E)$ are then registered to each other and to the lattice with excellent periodicity. This procedure can be used quite generally with SI-STM data, provided it exhibits appropriately high resolution in both $\mathbf{r}$-space and $\mathbf{q}$-space.

3.4 Effect of Magnetic and Non-magnetic Impurity Atoms

Substitution of magnetic and non-magnetic impurity atoms can probe the microscopic electronic structure of an unconventional superconductor including whether there are sign changes on the order parameter [80–83]. For a BCS superconductor, if the order parameter exhibits s-wave symmetry, then non-magnetic impurity atoms should have little effect because time reversed pairs of states which can undergo Cooper pairing are not disrupted. Magnetic impurity atoms, on the other hand should be quite destructive since they break time reversal symmetry. For unconventional superconductors (non s-wave) this simple situation does not pertain and both magnetic and non-magnetic impurities produce strong pair breaking effects. However, the spatial/energetic structure of the bound and resonant states [80, 84] can be highly revealing of the microscopic order parameter symmetry. These theoretical ideas as summarized in [80] were the basis for SI-STM studies of non-magnetic Zn impurity atoms and magnetic Ni impurity atoms substituted on the Cu sites of $Bi_2Sr_2CaCu_2O_{8+\delta}$ [85–87].

For Zn-doped $Bi_2Sr_2CaCu_2O_{8+\delta}$ near optimal doping, a typical $g(\mathbf{r}, E)$ of a 50 nm square region at $V = -1.5$ mV is shown in Fig. 3.3a with the expected overall white background being indicative of a very low $g(\mathbf{r}, E)$ near the Fermi level. However there are many randomly distributed dark sites corresponding to areas of high $g(\mathbf{r}, E)$, each with a distinct four-fold symmetric shape and the same relative orientation as clearly seen in Fig. 3.3b. In Fig. 3.3c we show a comparison between spectra taken at their centers and at usual superconducting regions of the sample. The spectrum at the center of a dark site has a very strong intra-gap conductance peak at energy $\Omega = -1.5 \pm 0.5$ meV. And, at these sites, the superconducting coherence peaks are strongly diminished, indicating the suppression of superconductivity. All of these phenomena are among the theoretically predicted characteristics of a ∼unitary quasiparticle scattering resonance at a single potential-scattering impurity atom in a d-wave superconductor [80].

Studies of Ni-doped samples near optimal doping revealed more intriguing results. Figure 3.4 shows two simultaneously acquired $g(\mathbf{r}, E = eV)$ maps taken on Ni-doped $Bi_2Sr_2CaCu_2O_{8+\delta}$ at sample bias $V_{\text{bias}} = \pm 10$mV. At $+10$ mV in Fig. 3.4b '+-shaped' regions of higher $g(\mathbf{r}, E)$ are observed, whereas at -10mV in Fig. 3.4a the corresponding higher $g(\mathbf{r}, E)$ regions are 'X-shaped'. $g(\mathbf{r}, E)$ maps at $V_{\text{bias}} = \pm 19$mV show the particle-like and hole-like components of a second impurity state at Ni whose spatial structure is very similar to that at $V_{\text{bias}} = \pm 10$ mV. Figure 3.4c shows the typical spectra taken at the Ni atom site in which there are two clear particle-like $g(\mathbf{r}, E)$ peaks. The average magnitudes of these on-site impurity-state

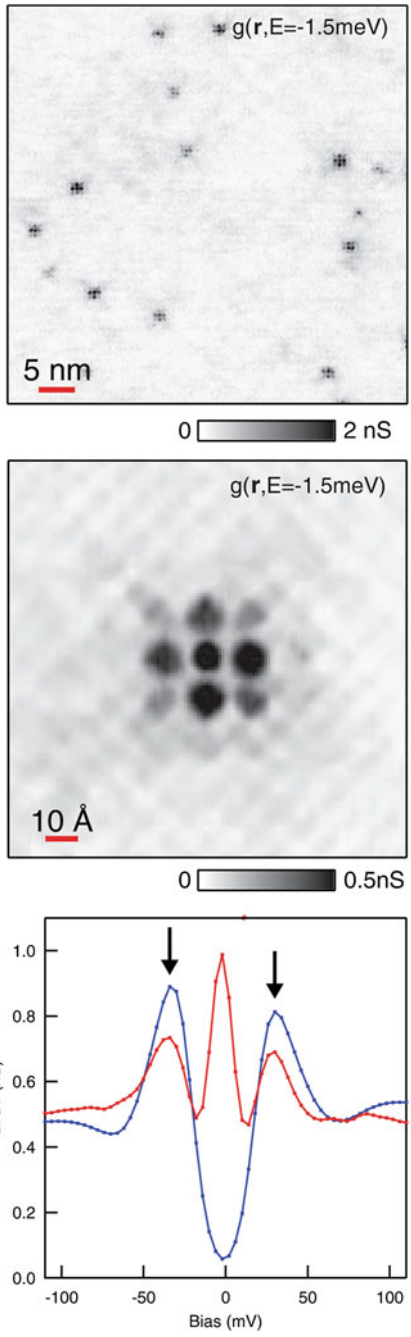

Fig. 3.3 **a** $g(\mathbf{r}, E = -1.5\,\mathrm{mV})$ showing the random dark 'crosses' which are the resonant impurity states of a d-wave superconductor, at each Zn impurity atom site. **b** High resolution $g(\mathbf{r}, E = -1.5\,\mathrm{mV})$. The dark center of scattering resonance in (b) coincides with the position of a Bi atom. The inner dark cross is oriented with the nodes of the d-wave gap. The weak outer features, including the ∼30 Å- long "quasiparticle beams" at 45° to the inner cross, are oriented with the gap maxima. **c** The spectrum of a usual superconducting region of the sample, where Zn scatterers are absent (*white region* in a, b), is shown in blue. The arrows indicate the superconducting coherence peaks that are suppressed near Zn. The data shown in *red*, with an interpolating fine *solid line*, are the spectrum taken exactly at the *center* of a dark Zn scattering site. It shows both the intense scattering resonance peak centered at $\Omega = -1.5\,\mathrm{mV}$, and the very strong suppression of both the superconducting coherence peaks and gap magnitude at the Zn site

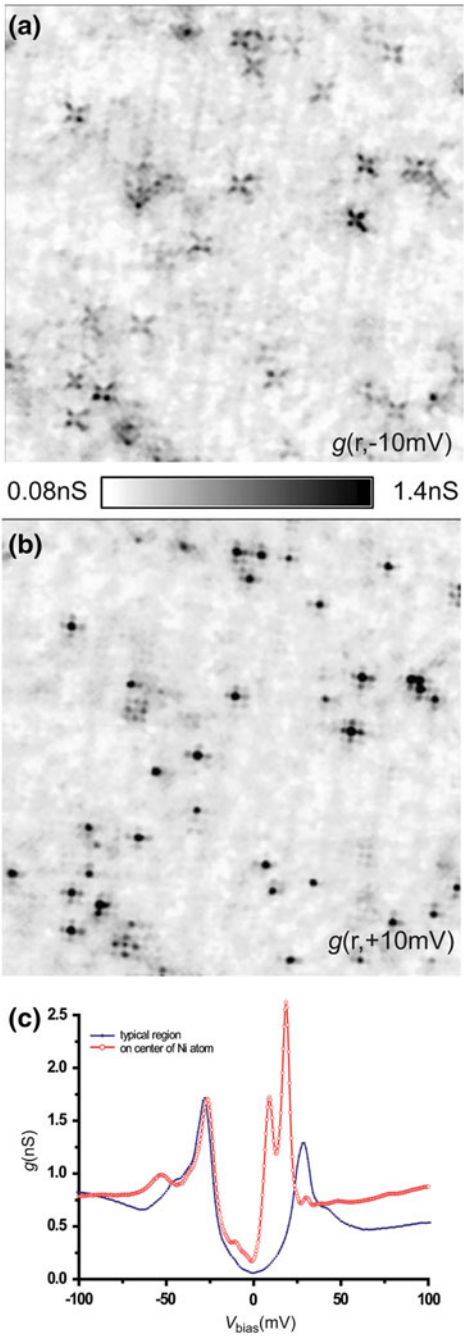

Fig. 3.4 a, b $g(\mathbf{r}, E = \pm 10\,\mathrm{mV})$ revealing the impurity states at locations of the Ni impurity atoms in this 128 Å × 128 Å square FOV. At $V_{\mathrm{bias}} = +10\,\mathrm{mV}$, showing the '+-shaped' regions of high local density of states associated with the Ni atoms. At $V_{\mathrm{bias}} = -10\,\mathrm{mV}$, showing the 45° spatially rotated 'X-shaped' pattern. **c** $g(\mathbf{r},E)$ spectra above a Ni atom (*red*) and away from the Ni atom (*blue*).

energies are $\Omega_1 = 9.2 \pm 1.1$meV and $\Omega_2 = 18.6 \pm 0.7$ meV. The existence of two states is as expected for a magnetic impurity in a d-wave superconductor [80]. Perhaps most significant, however, is that the magnetic impurity does not appear to suppress the superconductivity (as judged by the coherence peaks) at all, as if magnetism is non destructive to the pairing interaction locally. This is not as expected within BCS-based models of the pairing mechanism.

One of the most interesting observations made during these impurity atom studies, and one which was not appreciated at the time of the original experiments, was that the vivid, clear and theoretically reasonable d-wave impurity states at Zn and Ni disappear as hole density p is reduced below optimal doping in $Bi_2Sr_2CaCu_2O_{8+\delta}$ [64, 88, 89]. Thus, even though the density of Zn or Ni impurity atoms is the same, the response of the CuO_2 electronic structure to them is quite different approaching half-filling. In fact, the Zn and Ni impurity states (Figs. 3.3 and 3.4) quickly diminish in intensity and eventually become undetectable at low hole-density [88, 89]. One possible explanation for this strong indication of anomalous electronic structure in underdoped $Bi_2Sr_2CaCu_2O_{8+\delta}$ could be that the **k**-space states which contribute to Cooper pairing on the whole Fermi surface at optimal doping, no longer do so at lower p (Sect. 3.6). In this situation, all the Bogoliubov eigenstates necessary for scattering resonances to exist [80, 84] would no longer be available. This hypothesis is quite consistent with the discovery of restricted regions of **k**-space supporting coherent Bogoliubov quasiparticles that diminish in area with falling hole-density [61] as discussed in Sect. 3.6.

3.5 Nanoscale Electronic Disorder in $Bi_2Sr_2CaCu_2O_{8+\delta}$

Nanoscale electronic disorder is pervasive in images of $\Delta_1(\mathbf{r})$ measured on $Bi_2Sr_2CaCu_2O_{8+\delta}$ samples [53–55, 57, 60–71]. The magnitude of $|\Delta_1|$ ranges from above 130 meV to below 10 meV as p ranges from 0.06 to 0.22. Equivalent nanoscale $\Delta_1(\mathbf{r})$ disorder is found in $Bi_2Sr_2CuO_{6+\delta}$ [59, 68] and in $Bi_2Sr_2Ca_2Cu_3O_{10+\delta}$ [90].

Figure 3.5a shows a typical $Bi_2Sr_2CaCu_2O_{8+\delta}$ $\Delta_1(\mathbf{r})$ image—upon which the sites of the non-stoichiometric oxygen dopant ions are overlaid as white dots [54]. Figure 3.5b shows the typical $g(E)$ spectrum associated with each different value of $\pm\Delta_1$ [53]. It also reveals quite vividly how the electronic structure becomes homogeneous [53–55, 58, 59, 61, 62] for $|E| \leq \Delta_0$ as indicated by the arrows. Samples of $Bi_2Sr_2CuO_{6+\delta}$ and $Bi_2Sr_2Ca_2Cu_3O_{10+\delta}$ show virtually identical effects [59, 68, 90] and imaging $\Delta_1(\mathbf{r})$ in the PG phase reveals highly similar [62, 67–69] electronic disorder.

One component of the explanation for these phenomena is that electron-acceptor atoms must be introduced [91] to generate hole doping. This almost always creates random distributions of differently charged dopant ions near the CuO_2 planes [92]. The dopants in $Bi_2Sr_2CaCu_2O_{8+\delta}$ are $-2e$ oxygen ions charged interstitials and may cause a range of different local effects. For example, electrostatic screening may cause holes to congregate surrounding the dopant locations thereby reducing

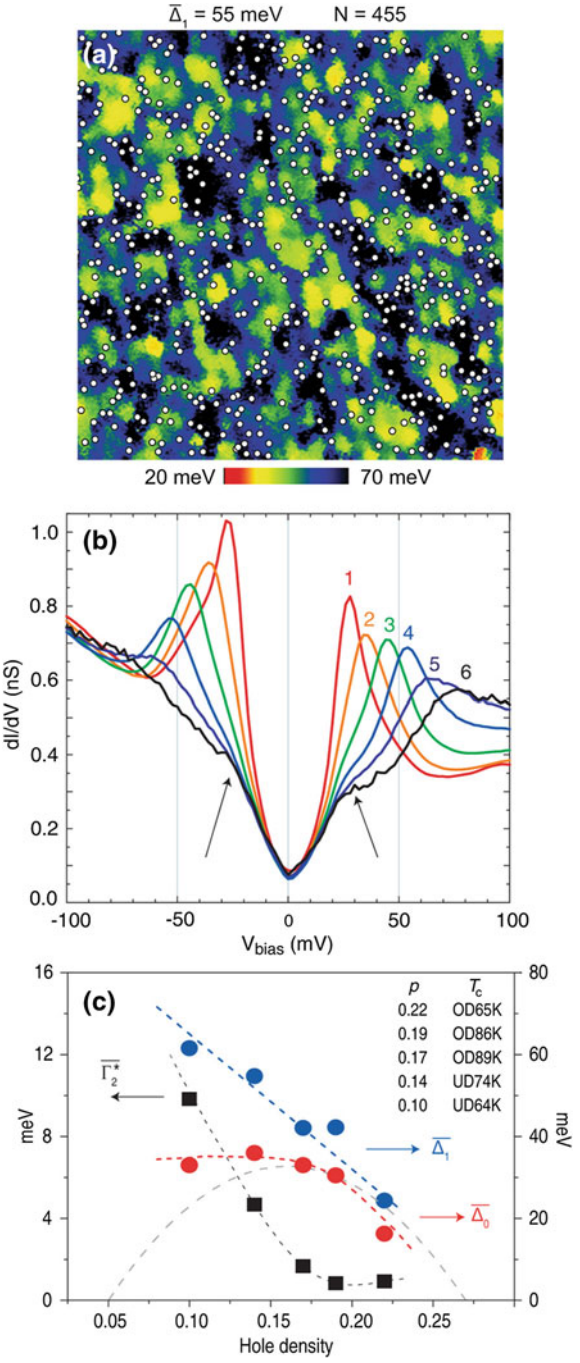

Fig. 3.5 **a** Map of the local energy scale $\Delta_1(\mathbf{r})$ from a 49 nm field of view (corresponding to $\sim$16, 000 CuO_2 plaquettes) measured on a sample with $T_c = 74$ K. Average gap magnitude Δ_1 is at the top, together with the values of N, the total number of dopant impurity states (shown as *white circles*) detected in the local spectra. **b** The average tunneling spectrum, $g(E)$, associated with each gap value in the field of view in a. The arrows locate the "kinks" separating homogeneous form heterogeneous electronic structure and which occur at energy $\sim\Delta_0$. **c** The doping dependence of the average Δ_1 (*blue circles*), average Δ_0 (*red circles*) and average antinodal scattering rate Γ_2* (*black squares*), each set interconnected by *dashed guides* to the eye. The higher-scale Δ_1 evolves along the pseudogap line whereas the lower-scale Δ_0 represents segregation in energy between homogeneous and heterogeneous electronic structure

the energy-gap values nearby [93, 94]. Or the dopant ions could cause nanoscale crystalline stress/strain [95–99] thereby disordering hopping matrix elements and electron-electron interactions within the CuO_2 unit cell. In $Bi_2Sr_2CaCu_2O_{8+\delta}$ the locations of interstitial dopant ions are identifiable because an electronic impurity state occurs at $E = -0.96$ V nearby each ion [54]. Significant spatial correlations are observed between the distribution of these impurity states and $\Delta_1(\mathbf{r})$ maps implying that dopant ion disorder is responsible for much of the $\Delta_1(\mathbf{r})$ electronic disorder. The principal effect near each dopant is a shift of spectral weight from low to high energy, with Δ_1 increasing strongly. Simultaneous imaging of the dopant ion locations and $g(\mathbf{r}, E< \Delta_0)$ reveals that the dispersive $g(\mathbf{r},E)$ modulations due to scattering of Bogoliubov quasiparticles are well correlated with dopant ion locations meaning that the dopant ions are an important source of such scattering (Sect. 3.6) [53, 54, 56–59, 61, 62].

The microscopic mechanism of the Δ_1-disorder is not yet fully understood. Hole-accumulation surrounding negatively charged oxygen dopant ions does not appear to be the explanation because the modulations in integrated density of filled states are observed to be weak [54]. More significantly, Δ_1 is actually strongly increased nearby the dopant ions [54] that is diametrically opposite to the expected effect from hole-accumulation there. Atomic substitution at random on the Sr site by Bi or by some other trivalent lanthanoid is known to suppress superconductivity strongly [92, 100] possibly due to geometrical distortions of the unit cell and associated changes in the hopping matrix elements. It has therefore been proposed that the interstitial dopant ions might act similarly, perhaps by displacing the Sr or apical oxygen atoms [92, 95, 96, 100] and thereby distorting the unit cell geometry. Direct support for this point of view comes from the observation that quasi-periodic distortions of the crystal unit-cell geometry yield virtually identical perturbations in $g(E)$ and $\Delta_1(\mathbf{r})$ but now are unrelated to the dopant ions [78]. Thus it seems that the Δ_1-disorder is not caused primarily by carrier density modulations but by geometrical distortions to the unit cell dimensions with resulting strong local changes in the high energy electronic structure. One could also expect the presence of such disorder in $Ca_{2-x}Na_xCuO_2Cl_2$ as Ca is substituted by Na since indeed similar Δ_1 disorder is also observed in this material [60].

Underdoped cuprate $g(E)$ spectra always exhibit "kinks" [53–55, 58, 59, 61, 63–66, 68–70] close to the energy scale where electronic homogeneity is lost. They are weak perturbations to $N(E)$ near optimal doping, becoming more clear as p is diminished [53, 55]. Figure 3.5b demonstrates how, in Δ_1-sorted $g(E)$ spectra, the kinks are universal but become more obvious for $\Delta_1 > 50$ meV [53, 55]. Each kink can be identified and its energy is labeled by $\Delta_0(\mathbf{r})$. By determining $\bar{\Delta}_0$ as a function of p (Fig. 3.5c), we find that it always divides the electronic structure into two categories [55]. For $|E| < \bar{\Delta}_0$ the excitations are spatially coherent in $\mathbf{r}$-space and therefore represent well defined Bogoliubov quasiparticle eigenstates in $\mathbf{k}$-space (Sect. 3.6). By contrast, the pseudogap excitations at $|E| \sim \Delta_1$ are heterogeneous in $\mathbf{r}$-space and ill defined in $\mathbf{k}$-space (Sect. 3.7).

To summarize: the Δ_1-disorder of $Bi_2Sr_2CaCu_2O_{8+\delta}$ is strongly influenced by the random distribution of dopant ions [54] and oxygen vacancies [101]. It occurs

through an electronic process in which geometrical distortions of the crystal unit cell appear to play a prominent role [97–102]. While the electronic disorder is most strongly reflected in the states near the pseudogap energy $|E| \sim \Delta_1$, the states with $|E| \leq \Delta_0$ are homogeneous when studied using direct imaging [53–55, 64] or from quasiparticle interference as described in Sect. 3.6. Therefore this intriguing phenomenon is clearly not heterogeneity of the superconductivity or superconducting energy gap, because in all simultaneously determined images the spatial coherence of Bogoliubov scattering interferences shows the superconducting energy gap to be homogeneous.

3.6 Bogoliubov Quasiparticle Interference Imaging

Bogoliubov quasiparticle interference (QPI) occurs when quasiparticle de Broglie waves are scattered by impurities and the scattered waves undergo quantum interference. In a d-wave superconductor with a single hole-like band of uncorrelated electrons as sometimes used to describe $Bi_2Sr_2CaCu_2O_{8+\delta}$, the Bogoliubov quasiparticle dispersion $E(\mathbf{k})$ would exhibit constant energy contours which are 'banana-shaped'. The d-symmetry superconducting energy gap would then cause strong maxima to appear for a given E, in the joint-density-of-states at the eight banana-tips $\mathbf{k}_j(E)$; $j = 1, 2,\ldots, 8$. Elastic scattering between the $\mathbf{k}_j(E)$ should produce $\mathbf{r}$-space interference patterns in $N(\mathbf{r},E)$. The resulting $g(\mathbf{r},E)$ modulations should exhibit 16 $\pm\mathbf{q}$ pairs of dispersive wavevectors in $\tilde{g}(\mathbf{q}, E)$ (Fig. 3.6a).

The set of these wavevectors characteristic of d-wave superconductivity consists of seven: $\mathbf{q}_i(E)$ $i = 1,\ldots,7$ with $\mathbf{q}_i(-E) = \mathbf{q}_i(+E)$. By using the point-group symmetry of the first CuO_2 Brillouin zone and this 'octet model', [102–104] the locus of the banana tips $\mathbf{k}_B(E) = (k_x(E),k_y(E))$ can be determined from:

$$\begin{aligned} 2k_x &= q_1, q_{4x}, q_{2x} - q_{2y}, q_{6y} + q_{6x}, (q_3 + q_7)/\sqrt{2}, q_5 - \sqrt{2}q_7 \\ 2k_y &= q_5, q_{4y}, q_{2x} + q_{2y}, q_{6y} - q_{6x}, (q_3 - q_7)/\sqrt{2}, \sqrt{2}q_7 - q_1 \end{aligned} \tag{3.18}$$

The $\mathbf{q}_i(E)$ are measured from $|\tilde{Z}(\mathbf{q}, E)|$, the Fourier transform of spatial modulations seen in $Z(\mathbf{r}, E)$ and the $\mathbf{k}_B(E)$ are then determined by using (3.18) within the requirement that all its independent solutions be consistent at all energies. The superconductor's Cooper-pairing energy gap $\Delta(\mathbf{k})$ is then determined directly by inverting the empirical data $\mathbf{k}_B(E = \Delta)$.

Near optimal doping in $Bi_2Sr_2CaCu_2O_{8+\delta}$, measurements from QPI of $\mathbf{k}_B(E)$ and $\Delta(\mathbf{k})$ (Fig. 3.6b inset) are consistent with ARPES [57, 105]. And, in $Ca_{2-x}Na_xCuO_2Cl_2$ this octet model yields $\mathbf{k}_B(E)$ and $\Delta(\mathbf{k})$ equally well [58, 59] as indeed the equivalent 'octet' approach does in iron-pnictide high temperature superconductors [106]. Therefore, Fourier transformation of $Z(\mathbf{r},E)$ in combination with the octet model of d-wave Bogoliubov QPI yields the two branches of the Bogoliubov excitation spectrum $\mathbf{k}_B(\pm E)$ plus the superconducting energy gap magnitude $\pm\Delta(\mathbf{k})$ along the

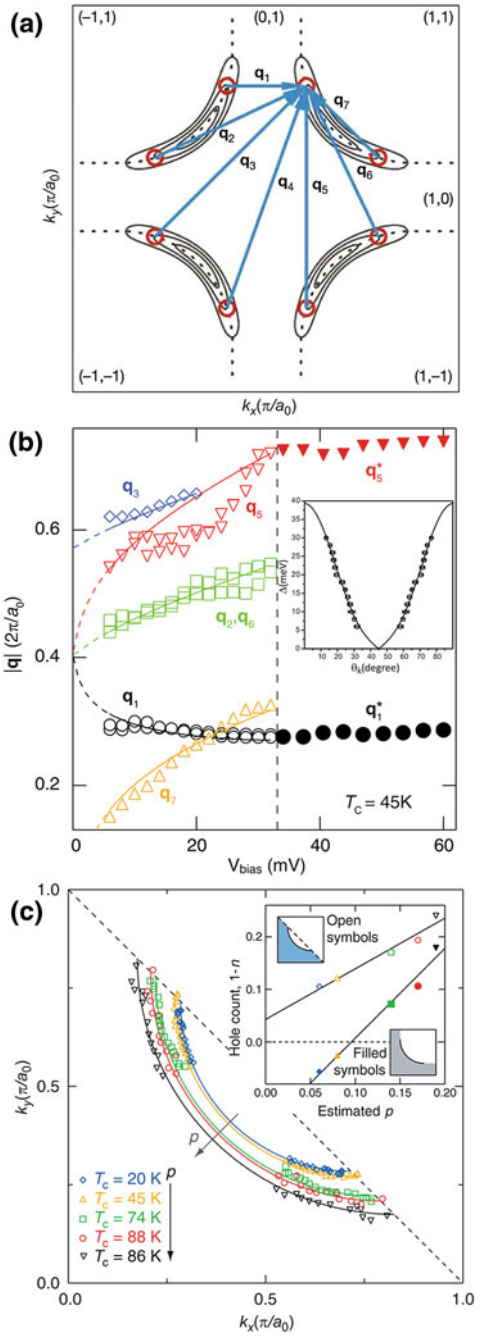
(a)
(−1,1)
(0,1)
(1,1)
(1,0)
(−1,−1)
(1,−1)
q1
q2
q3
q4
q5
q6
q7
ky(π/a0)
kx(π/a0)
(b)
q3
q5
q5*
q2,q6
q1
q1*
q7
Δ (meV)
θk(degree)
|q| (2π/a0)
Vbias (mV)
Tc = 45K
(c)
Open symbols
Filled symbols
Hole count, 1 - n
Estimated p
p
Tc = 20 K
Tc = 45 K
Tc = 74 K
Tc = 88 K
Tc = 86 K
ky(π/a0)
kx(π/a0)

◀**Fig. 3.6** **a** The 'octet' model of expected wavevectors of quasiparticle interference patterns in a superconductor with electronic band structure like that of $Bi_2Sr_2CaCu_2O_{8+\delta}$. Solid lines indicate the **k**-space locations of several banana-shaped quasiparticle contours of constant energy as they increase in size with increasing energy. As an example, at a specific energy, the octet of regions of high JDOS are shown as *red circles*. The seven primary scattering **q**-vectors interconnecting elements of the octet are shown in *blue*. **b** The magnitude of various measured QPI vectors, plotted as a function of energy. Whereas the expected energy dispersion of the octet vectors $\mathbf{q}_i(E)$ is apparent for $|E| < 32$mV, the peaks which avoid extinction ($\mathbf{q}_1^*$ and $\mathbf{q}_5^*$) shows ultra-slow or zero dispersion above Δ_0 (*vertical dashed line*). Inset: A plot of the superconducting energy gap $\Delta(\theta_k)$ determined from octet model inversion of quasiparticle interference measurements, shown as (*open circles*) [57]. **c** Locus of the Bogoliubov band minimum $\mathbf{k}_B(E)$ found from extracted QPI peak locations $\mathbf{q}_i(E)$, in five independent $Bi_2Sr_2CaCu_2O_{8+\delta}$ samples with increasing hole density. Fits to quarter-circles are shown and, as p decreases, these curves enclose a progressively smaller area. The BQP interference patterns disappear near the perimeter of a **k**-space region bounded by the lines joining $\mathbf{k} = (0, \pm\pi/a_0)$ and $\mathbf{k} = \pm(\pi/a_0, 0)$. The spectral weights of $\mathbf{q}_2$, $\mathbf{q}_3$, $\mathbf{q}_6$ and $\mathbf{q}_7$ vanish at the same place (*dashed line*; see also [61]). *Filled symbols* in the inset represent the hole count $p = 1- n$ derived using the simple Luttinger theorem, with the fits to a large, hole-like Fermi surface indicated schematically here in *grey*. *Open symbols* in the inset are the hole counts calculated using the area enclosed by the Bogoliubov arc and the lines joining $\mathbf{k} = (0, \pm\pi/a_0)$ and $\mathbf{k} = (\pm\pi/a_0, 0)$, and are indicated schematically here in *blue*

specific **k**-space trajectory $\mathbf{k}_B$ for both filled and empty states in a single experiment. And, since only the Bogoliubov states of a d-wave superconductor could exhibit such a set of 16 pairs of interference wavevectors with $\mathbf{q}_i(-E) = \mathbf{q}_i(+E)$ and all dispersions internally consistent within the octet model, the energy gap $\pm\Delta(\mathbf{k})$ determined by these procedures is definitely that of the delocalized Cooper-pairs.

These Bogoliubov QPI imaging techniques are used to study the evolution of **k**-space electronic structure with diminishing p in $Bi_2Sr_2CaCu_2O_{8+\delta}$. In the SC phase, the expected 16 pairs of **q**-vectors are always observed in $|\tilde{Z}(\mathbf{q}, E)|$ and are found consistent with each other within the octet model (Fig. 3.6a). However, in underdoped $Bi_2Sr_2CaCu_2O_{8+\delta}$ the dispersion of octet model **q**-vectors always stops at the same weakly doping-dependent [53, 59, 61] excitation energy Δ_0 and at **q**-vectors indicating that the relevant **k**-space states are still far from the boundary of the Brillouin zone (Fig. 3.6c). These observations are quite unexpected in the context of the d-wave BCS octet model. Moreover, for $|E| > \Delta_0$ the dispersive octet of **q**-vectors disappears and three ultra-slow dispersion **q**-vectors become predominant. They are the reciprocal lattice vector **Q** along with $\mathbf{q}_1^*$ and $\mathbf{q}_5^*$ (see Fig. 3.7a).

The ultra-slow dispersion incommensurate modulation wavevectors equivalent to $\mathbf{q}_1^*$ and $\mathbf{q}_5^*$ has also been detected by SI-STM in $Ca_{2-x}Na_xCuO_2Cl_2$ [58] and $Bi_2Sr_2CuO_{6+\delta}$ [59].

We show in Fig. 3.6c the locus of Bogoliubov quasiparticle states $\mathbf{k}_B(E)$ determined as a function of p using QPI. Here we discovered that when the Bogoliubov QPI patterns disappear at Δ_0, the **k**-states are near the diagonal lines between $\mathbf{k} = (0, \pi/a_0)$ and $\mathbf{k} = (\pi/a_0, 0)$ within the CuO_2 Brillouin zone. These **k**-space Bogoliubov arc tips are defined by both the change from clearly dispersive states to those whose dispersion is extremely slow or non existent, and by the disappearance of the $\mathbf{q}_2$, $\mathbf{q}_3$, $\mathbf{q}_6$ and $\mathbf{q}_7$ modulations. Thus, the QPI signature of delocalized Cooper pairing is con-

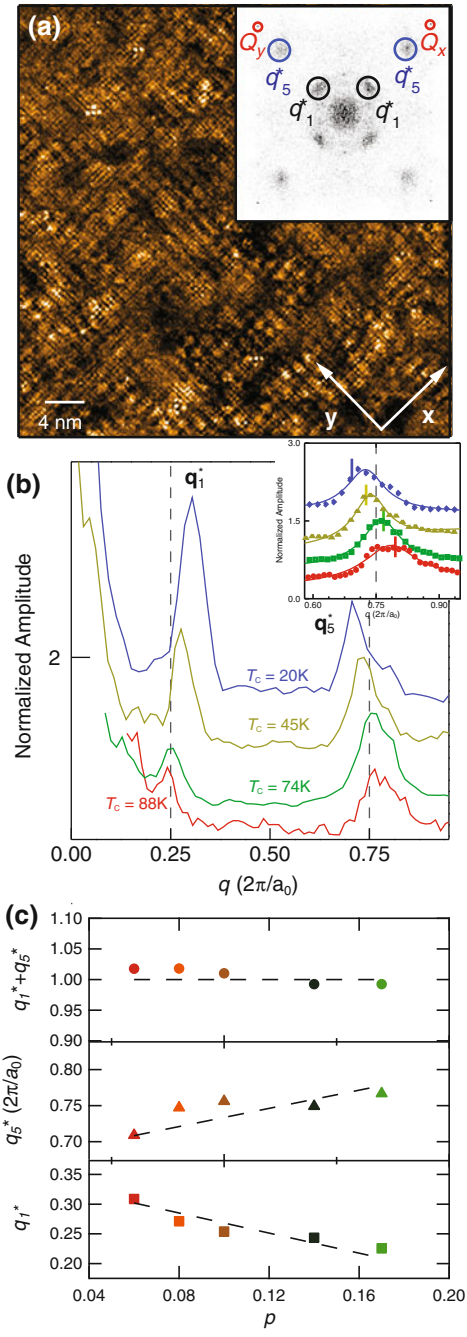

Fig. 3.7 **a** A large FOV $Z(\mathbf{r}, E = 48\,\text{mV})$ image from a strongly underdoped sample showing the full complexity of the electronic structure modulations. Inset: $|\tilde{Z}(\mathbf{q}, E = 48\,\text{mV})|$ for underdoped $T_c = 50\,\text{K}$ $Bi_2Sr_2CaCu_2O_{8+\delta}$. The (*circles*) label the location of the wavevectors $\mathbf{q}_1^*$, $\mathbf{q}_5^*$ (or $\mathbf{S}_x$, $\mathbf{S}_y$ at $E \sim \Delta_1$) and $\mathbf{Q}_x$, $\mathbf{Q}_y$ as described in the text. **b** Doping dependence of line-cuts of $|\tilde{Z}(\mathbf{q}, E = 48\,\text{mV})|$ extracted along the Cu-O bond direction $\mathbf{Q}_x$. Inset: The peak is $\mathbf{q}_5^*$, and the lines over the data are fits used to extract its location. The short *vertical lines* indicate the terminating $2k_y$ values derived from lower bias data. The *vertical dashed lines* demonstrate that the $\mathbf{q}$-vectors at energies between Δ_0 and Δ_1 are not commensurate harmonics of a $4a_0$ periodic modulation, but instead evolve in a fashion directly related to the extinction point of the Fermi arc. **c** $\mathbf{q}_1^*$, $\mathbf{q}_5^*$, and their sum $\mathbf{q}_1^* + \mathbf{q}_5^*$ as a function of p demonstrating that, individually, these modulations evolve with doping while their sum does not change and is equal to the reciprocal lattice vector defining the first Brillouin zone. This indicates strongly that these modulations are primarily a $\mathbf{k}$-space phenomenon

fined to an arc that shrinks with falling p [61]. This observation has been supported directly by ARPES studies [43, 50] and by QPI studies, [58, 59] and indirectly by analyses of $g(\mathbf{r}, E)$ by fitting to a multi-parameter model for $\mathbf{k}$-space structure of a dSC energy gap [70].

The minima (maxima) of the Bogoliubov bands $\mathbf{k}_B(\pm E)$ should occur at the $\mathbf{k}$-space location of the Fermi surface of the non-superconducting state. One can therefore ask if the carrier-density count satisfies Luttinger's theorem, which states that twice the $\mathbf{k}$-space area enclosed by the Fermi surface, measured in units of the area of the first Brillouin zone, equals the number of electrons per unit cell, n. In Fig. 3.7c we show as fine solid lines hole-like Fermi surfaces fitted to our measured $\mathbf{k}_B(E)$. Using Luttinger's theorem with these $\mathbf{k}$-space contours extended to the zone face would result in a calculated hole-density p for comparison with the estimated p in the samples. These data are shown by filled symbols in the inset showing how the Luttinger theorem is violated at all doping below $p \sim 10\,\%$ if the large hole-like Fermi surface persists in the underdoped region of the phase diagram.

Figure 3.7 provides a doping-dependence analysis of the locations of the ends of the arc-tips at which Bogoliubov QPI signature disappears and where the $\mathbf{q}_1^*$ and $\mathbf{q}_5^*$ modulations appear. Figure 3.7a shows a typical $Z(\mathbf{r},E=48\text{mV})$ where $\Delta_0 < E < \Delta_1$ and its $|\tilde{Z}(\mathbf{q}, E)|$ as an inset. Here the vectors $\mathbf{q}_1^*$ and $\mathbf{q}_5^*$ are labeled along with the Bragg vectors $\mathbf{Q}_x$ and $\mathbf{Q}_y$. Figure 3.7b shows the doping dependence for $Bi_2Sr_2CaCu_2O_{8+\delta}$ of the location of both $\mathbf{q}_1^*$ and $\mathbf{q}_5^*$ measured from $|\tilde{Z}(\mathbf{q}, E)|$ [61]. The measured magnitude of $\mathbf{q}_1^*$ and $\mathbf{q}_5^*$ versus p are then shown in Fig. 3.7c along with the sum $\mathbf{q}_1^* + \mathbf{q}_5^*$ which is always equal to $1(2\pi/a_0)$. This demonstrates that, as the Bogoliubov QPI extinction point travels along the line from $\mathbf{k} = (0,\ \pi/a_0)$ and $\mathbf{k} = (\pi/a_0, 0)$, the wavelengths of incommensurate modulations $\mathbf{q}_1^*$ and $\mathbf{q}_5^*$ are controlled by its $\mathbf{k}$-space location [61]. Equivalent phenomena have also been reported for $Bi_2Sr_2CuO_{6+\delta}$ [59]. A natural speculation is that "hot spot" scattering related to antiferromagnetic fluctuations is involved in *both* the disappearance of the Bogoliubov QPI patterns and the appearance of the incommensurate quasi-static modulations at $\mathbf{q}_1^*$ and $\mathbf{q}_5^*$ at the diagonal lines between $\mathbf{k} = (0, \pi/a_0)$ and $\mathbf{k} = (\pi/a_0, 0)$ within the CuO_2 Brillouin zone [107].

If the PG state of underdoped cuprates is a phase incoherent d-wave superconductor, these Bogoliubov-like QPI octet interference patterns could continue to exist above the transport T_c. This is because, if the quantum phase $\phi(\mathbf{r}, t)$ is fluctuating while the energy gap magnitude $\Delta(\mathbf{k})$ remains largely unchanged, the particle-hole symmetric octet of high joint-density-of-states regions generating the QPI should continue to exist [108–110]. But any gapped $\mathbf{k}$-space regions supporting Bogoliubov-like QPI in the PG phase must then occur beyond the tips of the ungapped Fermi Arc [44]. Evidence for phase fluctuating superconductivity is detectable for cuprates in particular regions of the phase diagram [111–116] as indicated by the region $T_c < T < T_\phi$ (Fig. 3.1a). The techniques involved include terahertz transport studies, [111] the Nernst effect, [112, 113] torque-magnetometry measurements, [114] field dependence of the diamagnetism, [115] and zero-bias conductance enhancement [116]. Moreover, because cuprate superconductivity is quasi-two-dimensional,

the superfluid density increases from zero approximately linearly with p, and the superconducting energy gap $\Delta(\mathbf{k})$ exhibits four $\mathbf{k}$-space nodes, fluctuations of phase $\phi(\mathbf{r}, t)$ could strongly impact the superconductivity at low p [19–24].

To explore these issues, the temperature evolution of the Bogoliubov octet in $|\tilde{Z}(\mathbf{q}, E)|$ was studied as a function of increasing temperature from the dSC phase into the PG phase using 48 nm square FOV. Representative $|\tilde{Z}(\mathbf{q}, E)|$ for six temperatures are shown in Fig. 3.8.

Clearly, the $\mathbf{q}_i(E)$ ($i = 1,2,\ldots,7$) characteristic of the superconducting octet model are observed to remain unchanged upon passing above T_c to at least $T \sim 1.5T_c$. This demonstrates that the Bogoliubov-like QPI octet phenomenology exists in the cuprate PG phase. Thus for the low-energy ($|E| < 35$ mV) excitations in the PG phase, the $\mathbf{q}_i(E)$ ($i = 1, 2, \ldots, 7$) characteristic of the octet model are preserved unchanged upon passing above T_c. All seven $\mathbf{q}_i(E)$ ($i = 1, 2, \ldots, 7$) modulation wavevectors which are dispersive in the dSC phase remain dispersive into the PG phase still consistent with the octet model [62]. The octet wavevectors also retain their particle-hole symmetry $\mathbf{q}_i(+E) = \mathbf{q}_i(-E)$ in the PG phase and the $g(\mathbf{r}, E)$ modulations occur in the same energy range and emanate from the same contour in $\mathbf{k}$-space as those observed at lowest temperatures [62]. Thus the Bogoliubov QPI signatures detectable in the dSC phase survive virtually unchanged into the underdoped PG phase—up to at least $T \sim 1.5T_c$ for strongly underdoped $Bi_2Sr_2CaCu_2O_{8+\delta}$ samples. Additionally, for $|E| \leq \Delta_0$ all seven dispersive $\mathbf{q}_i(E)$ modulations characteristic of the octet model in the dSC phase remain dispersive in the PG phase. These observations rule out the existence for all $|E| \leq \Delta_0$ of non-dispersive $g(E)$ modulations at finite ordering wavevector $\mathbf{Q}^*$ which would be indicative of a static electronic order which breaks translational symmetry, a conclusion which is in agreement with the results of ARPES studies. In fact the excitations observable using QPI are indistinguishable from the dispersive $\mathbf{k}$-space eigenstates of a phase incoherent d-wave superconductor [62].

Our overall picture of electronic structure in the strongly underdoped PG phase from SI-STM contains three elements: (i) the ungapped Fermi arc, [44] (ii) the particle-hole symmetric gap $\Delta(\mathbf{k})$ of a phase incoherent superconductor, [62] and (iii) the locally symmetry breaking excitations at the $E \sim \Delta_1$ energy scale [53, 60–62, 71, 72] (which remain completely unaltered upon the transition between the dSC and the PG phases [62, 71]). This three-component description of the electronic structure of the cuprate pseudogap phase has recently been confirmed in detail by ARPES studies [49].

3.7 Broken Spatial Symmetries of $E \sim \Delta_1$ Pseudogap States

The electronic excitations in the pseudogap energy range $|E| \sim \Delta_1$ are associated with a strong antinodal pseudogap in $\mathbf{k}$-space: [11, 12] they exhibit slow dynamics without recombination to form Cooper pairs, [40] their Raman characteristics appear distinct from expectations for a d-wave superconductor, [42] and they appear not to contribute to superfluid density [43]. As described on Sects. 3.4, 3.5 and

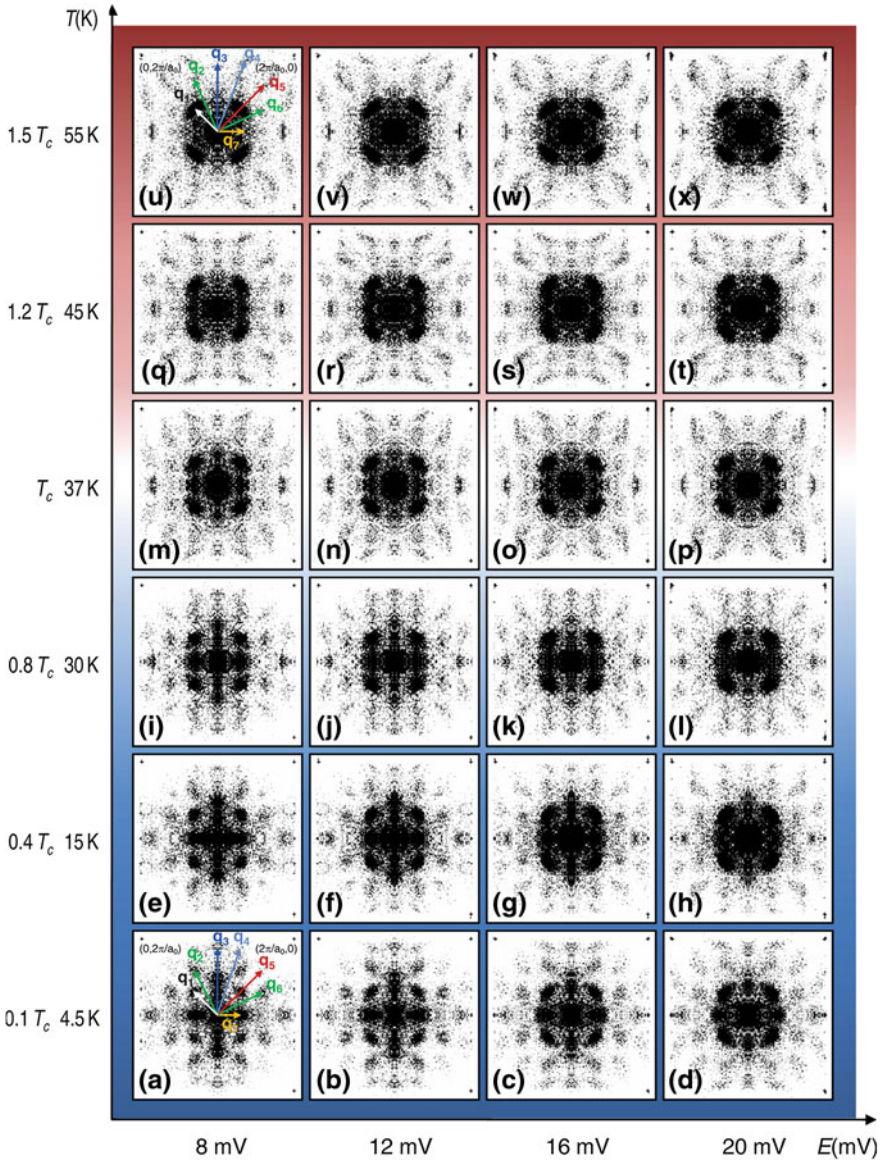

Fig. 3.8 (**a** to **x**) Differential conductance maps $g(\mathbf{r}, E)$ were obtained in an atomically resolved and registered FOV $> 45 \times 45\,\mathrm{nm}^2$ at six temperatures. Each panel shown is the $|\tilde{Z}(\mathbf{q}, E)|$ for a given energy and temperature. The QPI signals evolve dispersively with energy along the horizontal energy axis. The temperature dependence of QPI for a given energy evolves along the vertical axis. The octet-model set of QPI wave vectors is observed for every E and T as seen, for example, by comparing (a) and (u), each of which has the labeled octet vectors. Within the basic octet QPI phenomenology, there is no particular indication in these data of where the superconducting transition T_c, as determined by resistance measurements, occurs

especially Sect. 3.6, underdoped cuprates exhibit an octet of dispersive Bogoliubov QPI wavevectors $\mathbf{q}_i(E)$, but only upon a limited and doping-dependent arc in $\mathbf{k}$-space. Surrounding the pseudogap energy $E \sim \Delta_1$, these phenomena are replaced by a spectrum of states whose dispersion is extremely slow (Fig. 3.6b) [53, 59–62, 71].

Remarkably, for underdoped cuprates the atomically resolved $\mathbf{r}$-space images of the phenomena in $Z(\mathbf{r}, E \sim \Delta_1(\mathbf{r}))$ show highly similar spatial patterns. By changing to the reduced energy variables $e(\mathbf{r}) = E/\Delta_1(\mathbf{r})$ and imaging $Z(\mathbf{r}, e)$ it becomes clearer that these modulations exhibit a strong maximum in intensity at $e = 1$ [61, 62] and that they both break translational symmetry, and reduce the expected C_4 symmetry of states within the unit cell to at least to C_2 symmetry [60–62, 71, 72]. Theoretical concerns [117] about a possibly spurious nature to the spatial symmetry breaking in these images were addressed by carrying out a sequence of identical experiments on two very different cuprates: strongly underdoped $Ca_{1.88}Na_{0.12}CuO_2Cl_2$ ($T_c \sim 21K$) and $Bi_2Sr_2Ca_{0.8}Dy_{0.2}Cu_2O_{8+\delta}$ ($T_c \sim 45K$). These materials have completely different crystallographic structures, chemical constituents, dopant-ion species, and inequivalent dopant sites within the crystal-termination layers [60]. Images of the $|E| \sim \Delta_1$ states for these two systems demonstrate statically indistinguishable electronic structure arrangements [60]. As these virtually identical phenomena at $|E| \sim \Delta_1$ in these two materials must occur due to the common characteristic of these two quite different materials, the spatial characteristics of $Z(\mathbf{r}, e = 1)$ images [60–62, 71] are due to the intrinsic electronic structure of the CuO_2 plane.

To examine the broken spatial symmetries of the $|E| \sim \Delta_1$ states within the CuO_2 unit cell, we use high-resolution $Z(\mathbf{r}, e)$ imaging performed in a sequence of underdoped $Bi_2Sr_2CaCu_2O_{8+\delta}$ samples with T_c's between 20 and 55 K. The necessary registry of the Cu sites in each $Z(\mathbf{r}, e)$ is achieved by the picometer scale transformation that renders the topographic image $T(\mathbf{r})$ perfectly a_0-periodic (Sect. 3.3). The same transformation is then applied to the simultaneously acquired $Z(\mathbf{r}, e)$ to register all the electronic structure data to this ideal lattice.

The topograph $T(\mathbf{r})$ is shown in Fig. 3.9a; the inset compares the Bragg peaks of its real (in-phase) Fourier components $\mathrm{Re}\tilde{T}(\mathbf{Q}_x)$, $\mathrm{Re}\tilde{T}(\mathbf{Q}_y)$ showing that $\mathrm{Re}\tilde{T}(\mathbf{Q}_x)/\mathrm{Re}\tilde{T}(\mathbf{Q}_y) = 1$. Therefore $T(\mathbf{r})$ preserves the C_4 symmetry of the crystal lattice. In contrast, Fig. 3.9b shows that the $Z(\mathbf{r}, e = 1)$ determined simultaneously with Fig. 3.9a breaks various crystal symmetries [60–62]. The inset shows that since $\mathrm{Re}\tilde{Z}(\mathbf{Q}_x, e = 1)/\mathrm{Re}\tilde{Z}(\mathbf{Q}_y, e = 1) \neq 1$ the pseudogap states break C_4 symmetry. We therefore defined a normalized measure of intra-unit-cell nematicity as a function of e:

$$O_N^Q(e) \equiv \frac{\mathrm{Re}\tilde{Z}(\mathbf{Q}_y, e) - \mathrm{Re}\tilde{Z}(\mathbf{Q}_x, e)}{\bar{Z}(e)} \tag{3.19}$$

where $\bar{Z}(e)$ is the spatial average of $Z(\mathbf{r}, e)$. The plot of $O_N^Q(e)$ in Fig. 3.9c shows that the magnitude of $O_N^Q(e)$ is low for $e \ll \Delta_0/\Delta_1$, begins to grow near $e \sim \Delta_0/\Delta_1$, and becomes well defined as $e \sim 1$ or $E \sim \Delta_1$.

Within the CuO_2 unit cell itself we directly imaged $Z(\mathbf{r}, e)$ [60, 71] to explore where the symmetry breaking stems from. Figure 3.9d shows the topographic image

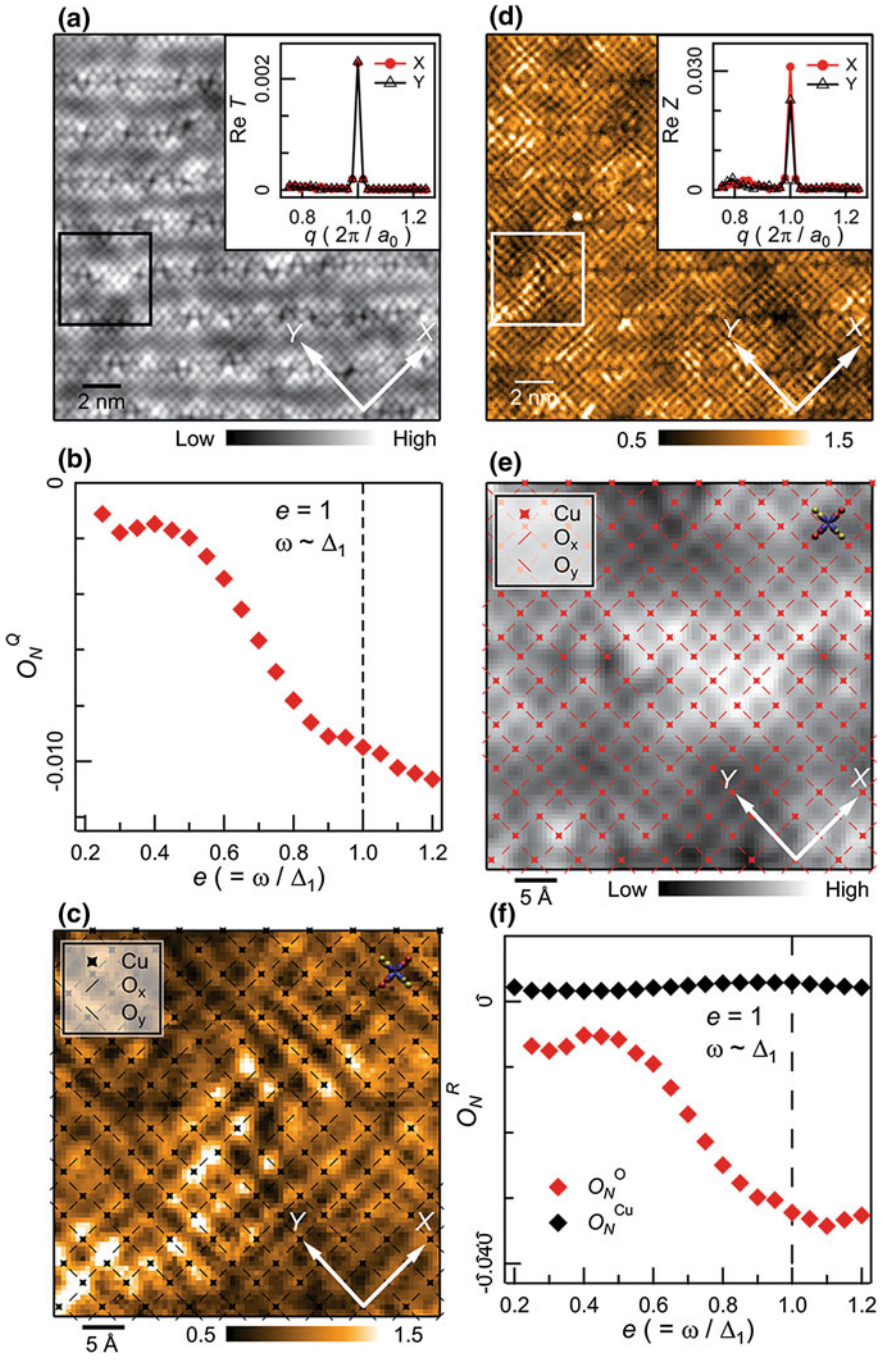
(a)
Re T
0.002
0
X
Y
0.8 1.0 1.2
q (2π / a0)
2 nm
Y
X
Low
High
(d)
Re Z
0.030
0
X
Y
0.8 1.0 1.2
q (2π / a0)
2 nm
Y
X
0.5
1.5
(b)
0
-0.010
e = 1
ω ~ Δ1
ON Q
0.2 0.4 0.6 0.8 1.0 1.2
e (= ω / Δ1)
(e)
Cu
Ox
Oy
Y
X
5 Å
Low
High
(c)
Cu
Ox
Oy
Y
X
5 Å
0.5
1.5
(f)
e = 1
ω ~ Δ1
ON R
ON O
ON Cu
0.2 0.4 0.6 0.8 1.0 1.2
e (= ω / Δ1)

◀**Fig. 3.9** **a** Topographic image $T(\mathbf{r})$ of the $Bi_2Sr_2CaCu_2O_{8+\delta}$ surface. The inset shows that the real part of its Fourier transform Re $\tilde{T}(\mathbf{q})$ does not break C_4 symmetry at its Bragg points because plots of $\tilde{T}(\mathbf{q})$ show its values to be indistinguishable at $\mathbf{Q}_x = (1, 0)2\pi/a_0$ and $\mathbf{Q}_y = (0, 1)2\pi/a_0$. Thus neither the crystal nor the tip used to image it (and its $Z(\mathbf{r}, E)$ simultaneously) exhibits C_2 symmetry. **b** The $Z(\mathbf{r}, e = 1)$ image measured simultaneously with $T(\mathbf{r})$ in **(a)**. The inset shows that the Fourier transform $|\tilde{Z}(\mathbf{q}, e = 1)|$ does break C_4 symmetry at its Bragg points because $\mathrm{Re}\tilde{Z}(\mathbf{Q}_x, e \sim 1) \neq \mathrm{Re}\tilde{Z}(\mathbf{Q}_y, e \sim 1)$. **c** The value of $O_N^Q(e)$ computed from $Z(\mathbf{r}, e)$ data measured in the same FOV as (**a**) and (**b**). Its magnitude is low for all $E < \Delta_0$ and then rises rapidly to become well established near $e \sim 1$ or $E \sim \Delta_1$. Thus the pseudogap states in underdoped $Bi_2Sr_2CaCu_2O_{8+\delta}$ break the expected C_4 symmetry of CuO_2 electronic structure. **d** Topographic image $T(\mathbf{r})$ from the region identified by a small *white box* in (**a**). It is labeled with the locations of the Cu atom plus both the O atoms within each CuO_2 unit cell (labels shown in the inset). Overlaid is the location and orientation of a Cu and four surrounding O atoms. **e** The simultaneous $Z(\mathbf{r}, e = 1)$ image in the same FOV as (**d**) (the region identified by small *white box* in (**b**)) showing the same Cu and O site labels within each unit cell (see inset). Thus the physical locations at which the nematicity measure $O_N^R(e)$ is evaluated are labeled by the *dashes*. Overlaid is the location and orientation of a Cu atom and four surrounding O atoms. **f** The value of $O_N^R(e)$ computed from $Z(\mathbf{r}, e)$ data measured in the same FOV as (**a**) and (**b**). As in (**c**), its magnitude is low for all $E < \Delta_0$ and then rises rapidly to become well established at $e \sim 1$ or $E \sim \Delta_1$

of a representative region from Fig. 3.9a; the locations of each Cu site $\mathbf{R}$ and of the two O atoms within its unit cell are indicated. Figure 3.9e shows $Z(\mathbf{r}, e)$ measured simultaneously with Fig. 3.9d with same Cu and O site labels. An $\mathbf{r}$-space measure of intra-unit-cell nematicity can also be defined

$$O_N^R(e) = \sum_{\mathbf{R}} \frac{Z_x(\mathbf{R}, e) - Z_y(\mathbf{R}, e)}{\bar{Z}(e)N} \tag{3.20}$$

where $Z_x(\mathbf{R}, e)$ is the magnitude of $Z(\mathbf{r}, e)$ at the O site $a_0/2$ along the x-axis from $\mathbf{R}$ while $Z_y(\mathbf{R}, e)$ is the equivalent along the y-axis, and N is the number of unit cells. This estimates intra-unit-cell nematicity similarly to $O_N^Q(e)$ but counting only O site contributions. Figure 3.9f contains the calculated value of $O_N^R(e)$ from the same FOV as Fig. 3.9a, b showing good agreement with $O_N^Q(e)$. Thus the intra-unit-cell C_4 symmetry breaking is specific to the states at $|E| \sim \Delta_1$, manifestly, because of inequivalence, on the average, of electronic structure at this energy at the two oxygen atom sites within each cell.

Atomic-scale imaging of electronic structure evolution from the insulator through the emergence of the pseudogap to the superconducting state in $Ca_{2-x}Na_xCuO_2Cl_2$ also reveals how the intra-unit-cell C_4 symmetry breaking emerges from the C_4 symmetric antiferromagnetic insulator existing at zero hole-doping. Quite remarkably, at lowest finite dopings, nanoscale regions appear exhibiting pseudogap-like spectra and 180°-rotational (C_{2v}) symmetry, and form unidirectional clusters within a weakly insulating and the C_{4v}-symmetric matrix [7]. Therefore 'hole doping' in cuprates seems to proceed by the appearance of nanoscale clusters of localized holes within which the intra-unit-cell broken-symmetry pseudogap state is stabilized. A fundamentally two-component electronic structure then exists until these C_{2v}-symmetric

clusters touch each other at higher doping at which point the long-range high-T_c superconductivity emerges in $Ca_{2-x}Na_xCuO_2Cl_2$.

There are also strong incommensurate electronic structure modulations (density waves) in $Bi_2Sr_2CaCu_2O_{8+\delta}$, $Ca_{2-x}Na_xCuO_2Cl_2$ and $Bi_2Sr_2CuO_{6+\delta}$, for $\Delta_0 < |E| < \Delta_1$ states. They exhibit two ultra-slow dispersion $\mathbf{q}$-vectors, $\mathbf{q}_1^*$ and $\mathbf{q}_5^*$. We find that they evolve with p as shown in Fig. 3.7b, c. The $\mathbf{q}_1^*$ modulations appear as the energy transitions from below to above Δ_0 but disappear quickly leaving only two primary electronic structure elements of the pseudogap-energy electronic structure in $Z(\mathbf{q}, E \cong \Delta_1)$. These occur at the incommensurate wavevector $\mathbf{S}_x, \mathbf{S}_y$ representing phenomena that locally break translational and rotational symmetry at the nanoscale. The doping evolution of $|\mathbf{S}_x| = |\mathbf{S}_y|$ indicates that these modulations are directly and fundamentally linked to the doping-dependence of the extinction point of the arc of Bogoliubov QPI in Sect. 3.6. The rotational symmetry breaking of these incommensurate smectic modulations can be examined by defining a measure analogous to (3.19) of C_4 symmetry breaking, but now focused only upon the modulations with $\mathbf{S}_x, \mathbf{S}_y$:

$$O_S^Q(e) \equiv \frac{\mathrm{Re}\tilde{Z}(\mathbf{S}_y, e) - \mathrm{Re}\tilde{Z}(\mathbf{S}_x, e)}{\bar{Z}(e)} \tag{3.21}$$

Low values found for $|O_S^Q(e)|$ at low e occur because these states are dispersive Bogoliubov quasiparticles [56, 57, 61, 62] and cannot be analyzed in term of any static electronic structure, smectic or otherwise, but $|O_S^Q(e)|$ shows no tendency to become well established at the pseudogap or any other energy and its correlation lengths are always on the nanometer scale [71].

There is growing interest in possible procedures for measurement of nematic order in STM expeirments as discussed in [74] which identified some challenges inherent in specific approaches. It is important to note that while as they apply to the data presented therein the conclusions of [74] may be true, they are of no relevance for those presented in this section or in [71, 72]. This is because [74] defines "nematicity" by the ratio of the *magnitudes* measured at the $\mathbf{Q}_x = [100]$ and $\mathbf{Q}_y = [010]$ Bragg peaks of $g(\mathbf{q})$,-the Fourier transform of $g(\mathbf{r})$ in the following fashion

$$\frac{|g(\mathbf{Q}_y)| - |g(\mathbf{Q}_x)|}{|g(\mathbf{Q}_y)| + |g(\mathbf{Q}_x)|}, \tag{3.22}$$

as is also described in [39]. This is profoundly and essentially different from the definition of nematic order given in (3.19) above; that nematic order parameter O_N^Q is lattice-phase sensitive (and thus atomic site selective) and characterizes the contribution primarily from the oxygen atoms in the CuO_2 plane. In contrast, (3.22) as defined in [74] mixes both real and imaginary Fourier Bragg components indiscriminately in a fashion that renders CuO_2 intra-unit-cell symmetry breaking extremely difficult, if no impossible, to detect.

At a more practical level, the approaches in [74] and in (3.19) are also highly distinct. In order to obtain O_N^Q given by (3.19), one has first to correct for sub-angstrom

scale distorsions in rectilinearity throughout the images of $g(\mathbf{r}, E)$ using the Fujita-Lawler algorithms [71] or similar procedure, and then establish the correct lattice phase with high precision (2 % of 2π), as described in Sect. 3.3. This allows establishment and analysis of the complex elements of the Fourier transform, $\mathrm{Re}T(\mathbf{q})$ and $\mathrm{Im}T(\mathbf{q})$, in order to yield a well defined $\mathrm{Re}g(\mathbf{q})$ and $\mathrm{Im}g(\mathbf{q})$ only from which O_N^Q can be calculated correctly. We emphasize that this technique not only requires the mathematical steps described in Sect. 3.3, but it also requires spectroscopic measurements using many pixels inside each CuO_2 unit-cell. If these measurement specifications, the above lattice-phase definition procedures, and the resulting determination of $\mathrm{Re}g(\mathbf{q})$ and $\mathrm{Im}g(\mathbf{q})$ are not all achieved demonstrably, no deductions about the validity of C_{4v} symmetry breaking in the STM data using (3.19) can or should be made. Therefore, whether the (3.22) is valid (or invalid) measure of nematicity as discussed in [74] has no relevance whatsoever for our measurements throughout this section because we use (3.19) along with the procedures described in Sect. 3.3.

In any case, there are simple practical tests for the capability to correctly measure nematicity: observation of adjacent domains with opposite nematic order when using same tip, or the direct detection of the intra-unit-cell symmetry breaking in a characteristic energy associated with the electronic states therein.

In summary: electronic structure imaging in underdoped $Bi_2Sr_2CaCu_2O_{8+\delta}$ and $Ca_{2-x}Na_xCuO_2Cl_2$ reveal compelling evidence for intra-unit-cell C_4 sysmetry breaking specific to the states at the $|E| \sim \Delta_1$ pseudogap energy. These effects exist because of inequivalence, when averaged over all unit cells in the image, of electronic structure at the two oxygen atom sites within each CuO_2 cell. This intra-unit-cell nematicity coexists with finite $\mathbf{q} = \mathbf{S}_x, \mathbf{S}_y$ smectic electronic modulations, but they can be analyzed separately by using Fourier filtration techniques. The wavevector of smectic electronic modulations is controlled by the point of $\mathbf{k}$-space where the Bogoliubov interference signature disappears when the arc supporting delocalized Cooper pairing approaches the lines between $\mathbf{k} = \pm(0, \pi/a_0)$ and $\mathbf{k} = \pm(\pi/a_0, 0)$ (Fig. 3.6b, c). This appears to indicate that the $\mathbf{q} = \mathbf{S}_x, \mathbf{S}_y$ smectic effects are dominated by the same $\mathbf{k}$-space phenomena which restrict the regions of Cooper pairing [61] and are not a characteristic of $\mathbf{r}$-space ordering.

3.8 Interplay of Intra-unit-cell and Incommensurate Broken Symmetry States

The distinct properties of the $|E| \sim \Delta_1$ smectic modulations can be examined independently of the $|E| \sim \Delta_1$ intra-unit-cell C_4-symmetry breaking, by focusing in $\mathbf{q}$-space only upon the incommensurate modulation peaks $\mathbf{S}_x$ and $\mathbf{S}_y$. A coarse grained image of the local smectic symmetry breaking reveals the very short correlation length of the strongly disordered smectic modulations [60, 71, 72]. The amplitude and phase of two unidirectional incommensurate modulation components measured in each $Z(\mathbf{r}, e = 1)$ image (Fig. 3.10a, b) can be further extracted by denoting the local contribution to the $\mathbf{S}_x$ modulations at position $\mathbf{r}$ by a complex field

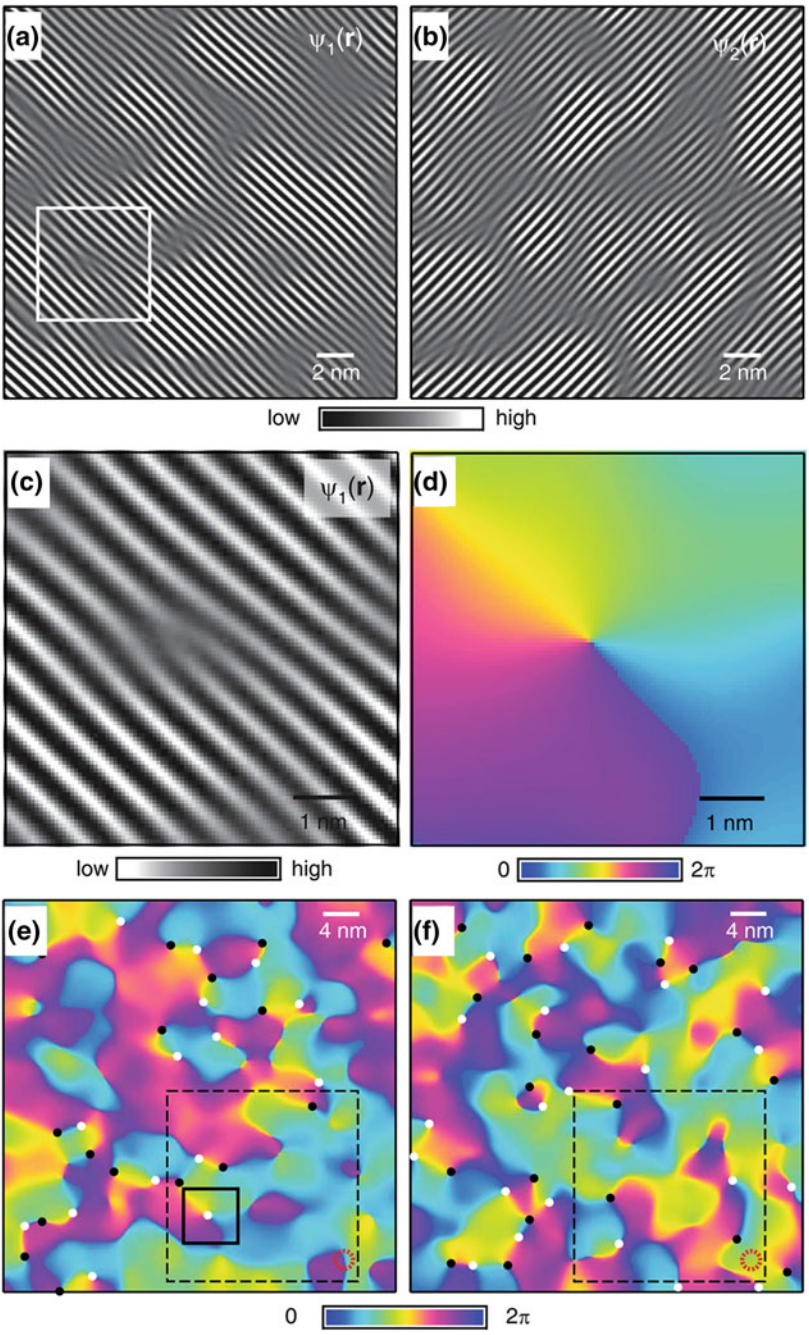
(a)
$\psi_1(\mathbf{r})$
2 nm
(b)
$\psi_2(\mathbf{r})$
2 nm
low
high
(c)
$\psi_1(\mathbf{r})$
1 nm
(d)
1 nm
low
high
0
2π
(e)
4 nm
(f)
4 nm
0
2π

◀**Fig. 3.10** **a** Smectic modulations along x-direction are visualized by Fourier filtering out all the modulations in $Z(\mathbf{r}, e = 1)$ of the underdoped $Bi_2Sr_2CaCu_2O_{8+\delta}$ except those at $\mathbf{S}_x$. **b** Smectic modulations along y-direction are visualized by Fourier filtering out all the modulations of $Z(\mathbf{r}, e = 1)$ except those at $\mathbf{S}_y$. **c** Smectic modulation around the single topological defect in the same FOV showing that the dislocation core is indeed at the center of the topological defect and that the modulation amplitude tends to zero there. This is true for all the 2π topological defects identified in (e) and (f). **d** Phase field around the single topological defect in the FOV in (c). **e f** Phase field $\phi_1(\mathbf{r})(\phi_2(\mathbf{r}))$ for smectic modulations along $x(y)$—direction exhibiting the topological defects at the points around which the phase winds from 0 to 2π. Depending on the sign of phase winding, the topological defects are marked by either *white* or *black* dots. The *broken red circle* is the measure of the spatial resolution determined by the cut-off length (3σ) in extracting the smectic field from $\tilde{Z}(\mathbf{q}, e = 1)$

$\Psi_1(\mathbf{r})$. This contributes to the $Z(\mathbf{r}, e = 1)$ data as $\Psi_1(\mathbf{r})e^{i\mathbf{S}_x\cdot\mathbf{r}} + \Psi_1^*(\mathbf{r})e^{-i\mathbf{S}_x\cdot\mathbf{r}} \equiv 2|\Psi_1(\mathbf{r})|\cos(\mathbf{S}_x \cdot \mathbf{r} + \phi_1(\mathbf{r}))$ thus allowing the local phase $\phi_1(\mathbf{r})$ of $\mathbf{S}_x$ modulations to be mapped; similarly for the local phase $\phi_2(\mathbf{r})$ of $\mathbf{S}_y$ modulations.

A typical example of an individual topological defect (within solid white box in Fig. 3.10a) is shown in Fig. 3.10c, d. The dislocation core (Fig. 3.10c) and its associated 2π phase winding (Fig. 3.10d) are clear. We find that the amplitude of $\Psi_1(\mathbf{r})$ or $\Psi_2(\mathbf{r})$ always goes to zero near each topological defect. In Fig. 3.10e, f we show the large FOV images of $\phi_1(\mathbf{r})$ and $\phi_2(\mathbf{r})$ derived from $Z(\mathbf{r}, e = 1)$ in Fig. 3.10a, b. They show that the smectic phases $\phi_1(\mathbf{r})$ and $\phi_2(\mathbf{r})$ take on all values between 0 and $\pm 2\pi$ in a complex spatial pattern. Large numbers of topological defects with 2π phase winding are observed; these are indicated by black ($+2\pi$) and white (-2π) circles and occur in approximately equal numbers. These data are all in agreement with the theoretical expectations for quantum smectic dislocations [35].

Simultaneous imaging of two different broken symmetries in the electronic structure provides an unusual opportunity to explore their relationtship empirically, and to develop a Ginzburg-Landau style description of their interactions. The local nematic fluctuation $\delta O_n(\mathbf{r}) \equiv O_n(\mathbf{r}) - < O_n >$ (Fig. 3.11a) is the natural small quantity to enter the GL functional. In all cases we then focus upon the phase fluctuations of the smectic modulations (meaning that $\delta O_n(\mathbf{r})$ couples to local shifts of the incommensurate wavectors) we find that $\delta O_n(\mathbf{r}) = \mathbf{l} \cdot \nabla\phi$ surrounding each topological defect [72] where the vector $\mathbf{l} \propto (\alpha_x, \alpha_y)$ lies along the line where $\delta O_n(\mathbf{r}) = 0$. The resulting prediction is that $\delta O_n(\mathbf{r})$ will vanish along the line in the direction of $\mathbf{l}$ that passes through the core of the topological defect with $\delta O_n(\mathbf{r})$ becoming greater on one side and less on the other (Fig. 3.11b), and this is what is observed throughout data sets.

Both nematic and smectic broken symmetries have been reported in the electronic/magnetic structure of different cuprate compounds [73, 117–119]. This approach may provide a good starting point to address the interplay between the

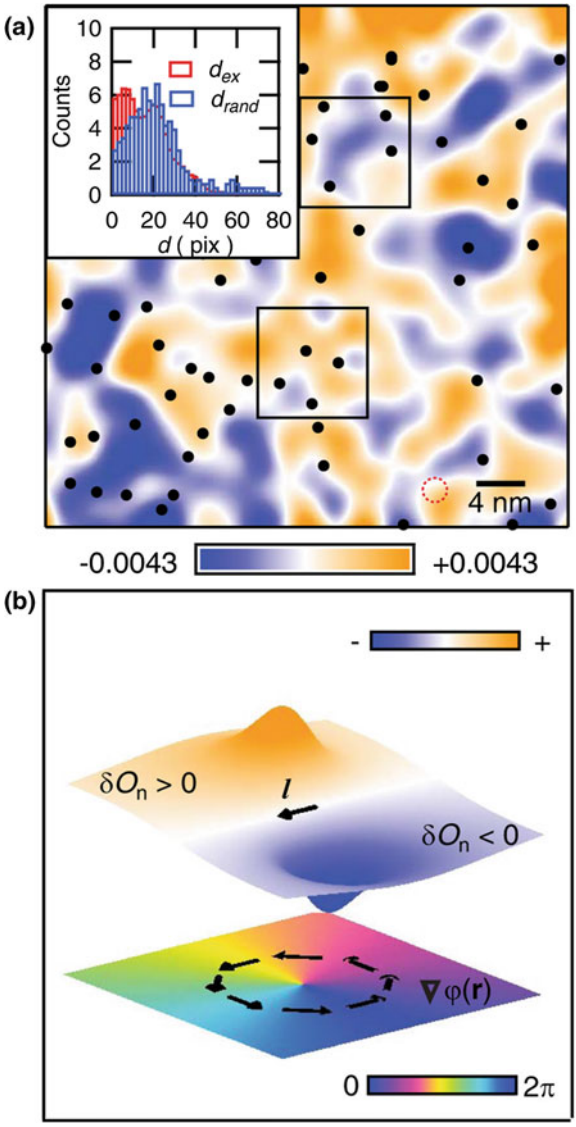

Fig. 3.11 **a** Fluctuations of electronic nematicity $\delta O_n(\mathbf{r}, e=1)$ obtained by subtracting the spatial average $< O_n(\mathbf{r}, e=1) >$ from $O_n(\mathbf{r}, e = 1)$. The locations of all 2π topological defects measured simultaneously are indicated by *black dots*. They occur primarily near the lines where $\delta O_n(\mathbf{r}, e = 1) = 0$. Inset shows the distribution of distances between the nearest $\delta O_n(\mathbf{r}, e = 1) = 0$ contour and each topological defect; it reveals a strong tendency for that distance to be far smaller than expected at random. **b** Theoretical $\delta O_n(\mathbf{r}, e = 1)$ from the Ginzburg Landau functional in the [72] at the site of a single topological defect (bottom). The vector **l** lies along the zero-fluctuation line of $\delta O_n(\mathbf{r}, e = 1)$

different broken electronic symmetries and the superconductivity near the cuprate Mott insulator state.

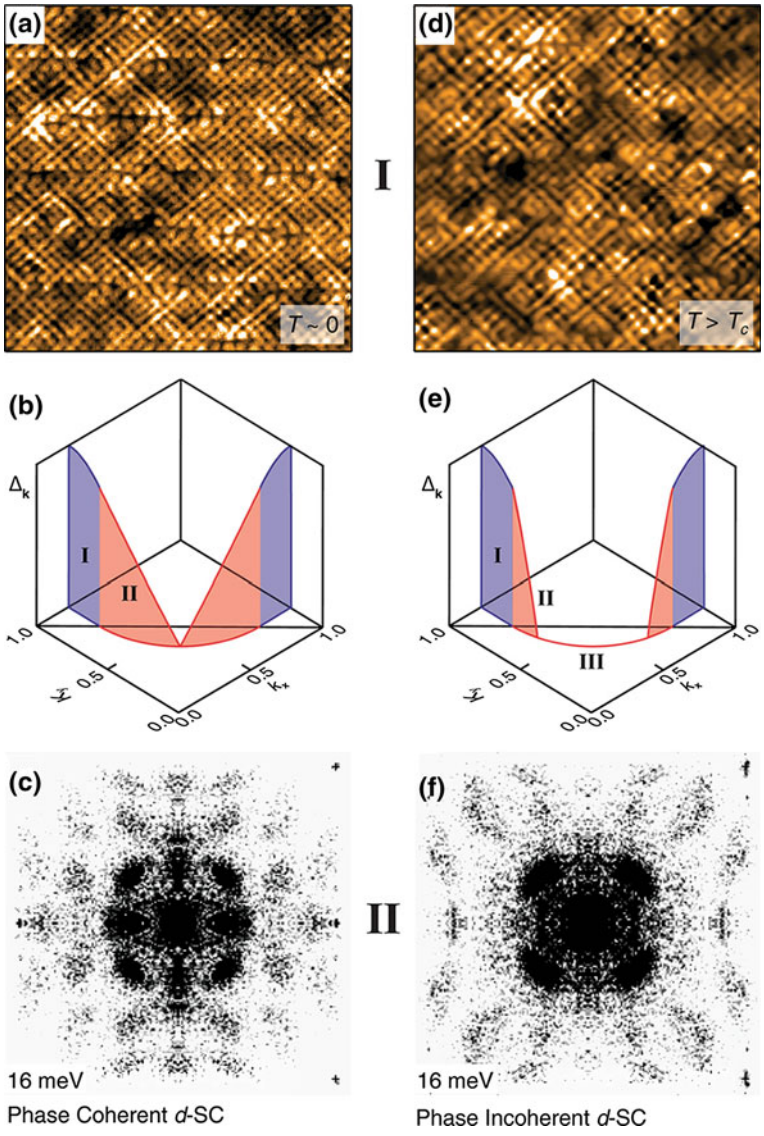
(a)
T ~ 0
I
(d)
T > T_c
(b)
Δ_k
I
II
1.0
0.5
0.0
k_y
k_x
(e)
III
(c)
16 meV
Phase Coherent d-SC
II
(f)
16 meV
Phase Incoherent d-SC

◀**Fig. 3.12** **a** Image typical of the broken spatial symmetries in electronic structure as measured in the dSC phase at the pseudogap energy $E \sim \Delta_1$ in underdoped cuprates (both $Bi_2Sr_2CaCu_2O_{8+\delta}$ and $Ca_{2-x}Na_xCuO_2Cl_2$). **b** A schematic representation of the electronic structure in one quarter of the Brillouin zone at lowest temperatures in the dSC phase. The region marked II in front of the line joining $\mathbf{k} = (\pi/a_0, 0)$ and $\mathbf{k} = (0, \pi/a_0)$ is the locus of the Bogoliubov QPI signature of delocalized Cooper pairs. **c** An example of the characteristic Bogoliubov QPI signature of sixteen pairs of interference wavevectors, all dispersive and internally consistent with the octect model as well as particle-hole symmetric $\mathbf{q}_i(+E) = \mathbf{q}_i(-E)$, here measured at lowest temperatures. **d** An example of the broken spatial symmetries which are concentrated upon pseudogap energy $E \sim \Delta_1$ as measured in the PG phase; they are indistinguishable from measurements at $T \sim 0$. **e** A schematic representation of the electronic structure in one quarter of the Brillouin zone at $T \sim 1.5T_c$ in the PG phase. The region marked III is the Fermi arc, which is seen in QPI studies as a set of interference wavevectors $\mathbf{q}_i(E = 0)$ indicating that there is no gap-node at $E = 0$. Region II in front of the line joining $\mathbf{k} = (\pi/a_0, 0)$ and $\mathbf{k} = (0, \pi/a_0)$ is the locus of the phase incoherent Bogoliubov QPI signature. Here all 16 pairs of wavevectors of the octet model are detected and found to be dispersive. Thus although the sample is not a long-range phase coherent superconductor, it does give clear QPI signatures of d-wave Cooper pairs. **f** An example of the characteristic Bogoliubov QPI signature of sixteen pairs of interference wavevectors, all dispersive and internally consistent with the octet model as well as particle-hole symmetric $\mathbf{q}_i(+E) = \mathbf{q}_i(-E)$, but here measured at $T \sim 1.5T_c$

3.9 Conclusions

We summarize our empirical understanding of underdoped cuprate electronic structure as derived from SI-STM studies in Fig. 3.12.

In the dSC phase (Fig. 3.12a–c) the Bogoliubov QPI signature of delocalized Cooper pairs exhibiting a spatially homogenous pairing energy gap (Sect. 3.6) exists upon the arc in $\mathbf{k}$-space labeled by region II in Fig. 3.12b. States of this type have energy $|E| \leq \Delta_0$. The Bogoliubov QPI disappears near the lines connecting $\mathbf{k} = (0, \pm\pi/a_0)$ to $\mathbf{k} = (\pm\pi/a_0, 0)$—thus defining a $\mathbf{k}$-space arc which supports the delocalized Cooper pairing. This arc shrinks rapidly towards the $\mathbf{k} = (\pm\pi/2a_0, \pm\pi/2a_0)$ points with falling hole-density in a fashion which could satisfy Luttinger's theorem if it were actually a hole-pocket bounded from behind by the $\mathbf{k} = \pm(\pi/a_0, 0) - \mathbf{k} \pm (0, \pi/a_0)$ lines. The $|E| \sim \Delta_1$ pseudogap excitations (Sect. 3.7) are labeled schematically by region I and exhibit a radically different $\mathbf{r}$-space phenomenology locally breaking the expected C_4 symmetry of electronic structure at least down to C_2, by rendering the two oxygen sites electronically inequivalent within each CuO_2 unit cell (Fig. 3.12a). These intra-unit-cell broken C_4-symmetry states coexist with incommensurate modulations that break translational and rotational symmetry locally. The wavelengths of these incommensurate modulations $\mathbf{q} = \mathbf{S}_x, \mathbf{S}_y$ are controlled by the $\mathbf{k}$-space locations at which the Bogoliubov QPI signatures disappear; this is the empirical reason why $\mathbf{S}_x, \mathbf{S}_y$ evolve continuously with doping along the line joining $\mathbf{k} = \pm(\pi/a_0, 0) - \mathbf{k} \pm (0, \pi/a_0)$ (Sect. 3.6). In the PG phase (Figs. 3.12d–f), the Bogoliubov QPI signature (Fig. 3.12f) exists upon a smaller part of the same arc in $\mathbf{k}$-space as it did in the dSC phase. This is labeled as region II while the ungapped Fermi-arc (region III) predominates. The $E \sim \Delta_1$ excitations

in the PG phase, (Sect. 3.7) are again labeled by region I and exhibit intra-unit-cell C_4 breaking and $\mathbf{q} = \mathbf{S}_x, \mathbf{S}_y$ incommensurate smectic modulations indistinguishable from those in the dSC phase (Fig. 3.12e). One further point must be reemphasized: the spatially disordered and symmetry breaking states with $E \sim \Delta_1$ are obviously not due to heterogeneity (granularity) of the superconductivity, because the Bogoliubov scattering interference patterns exhibit ∼long range spatial coherence, for all dopings and materials studied.

The relationship between the $|E| \sim \Delta_1$ broken symmetry states (Sects. 3.5, 3.7, 3.8) and the $|E| \leq \Delta_0$ Bogoliubov quasiparticles indicative of Cooper pairing (Sects. 3.4 and 3.6), and thus the relationship between quantum states associated with the heterogeneous pseudogap and those with the homogeneous superconductivity, is not yet understood. However, these two sets of phenomena appear to be linked inextricably. The reason is that the **k**-space location where the latter disappears always occurs where the Fermi surface touches the lines connecting $(0, \pm\pi/a_0)$ to $(\pm\pi/a_0, 0)$, while the wavevectors $\mathbf{q}_1^*$ and $\mathbf{q}_5^*$ close to this intersection are those of the incommensurate modulations at $|E| \sim \Delta_1$.

Finally, site-specific measurements within each CuO_2 unit-cell that are segregated into three separate electronic structure images (containing only the Cu sites ($Cu(\mathbf{r})$) and only the x/y-axis O sites ($O_x(\mathbf{r})$ and $O_y(\mathbf{r})$)) allows sublattice phase resolved Fourier analysis. This has recently revealed directly that the modulations in the $O_x(\mathbf{r})$ and $O_y(\mathbf{r})$ sublattice electronic structure images consistently exhibit a relative phase of π. These observations demonstrate by direct sublattice phase-resolved visualization that the cuprate smectic state (density wave) with wavevector **S**, is in fact a d-form factor density wave [120].

Acknowledgments We acknowledge and thank all our collaborators: E.-A. Kim, M.J. Lawler, J.W. Alldredge, T. Hanaguri, P.J. Hirschfeld, J.E. Hoffman, E.W. Hudson, Y. Kohsaka, K.M. Lang, C. Lupien, Jhinhwan Lee, Jinho Lee, V. Madhavan, K. McElroy, J. Orenstein, S.H. Pan, R. Simmonds, A. Schmidt, J. Sethna, J. Slezak, H. Takagi, C. Taylor, P. Wahl and M. Wang. Preparation of this manuscript was supported by the Center for Emergent Superconductivity, an Energy Frontier Research Center funded by the U.S. Department of Energy, Office of Basic Energy Sciences under Award Number DE-2009-BNL-PM015. We also acknowledge support during the writing of this article by US DOE under contract DEAC02-98CH10886, as well as by a Grant-in-Aid for Scientific Research from the Ministry of Science and Education (Japan) and the Global Centers of Excellence Program for Japan Society for the Promotion of Science. C.K.K. was supported under the FlucTeam program at Brookhaven National Laboratory under contract DE-AC02-98CH10886. M.H. acknowledges funding the Office of Naval Research under Award N00014-13-1-0047. S.M. acknowledges support from NSF Grant DMR-1120296 to the Cornell Center for Materials Research.

References

1. J. Zaanen, G.A. Sawatzky, J.W. Allen, Phys. Rev. Lett. **55**, 418 (1985)
2. C. Weber, C. Yee, K. Haule, G. Kotliar, Euro. Phys. Lett. **100**, 37001 (2012)
3. P.W. Anderson, Phys. Rev. **79**, 350 (1950)
4. P.W. Anderson, Sci. **235**, 1196 (1987)

5. C.T. Chen, F. Sette, Y. Ma, M.S. Hybertsen, E.B. Stechel, W.M.C. Foulkes, M. Schulter, S.W. Cheong, A.S. Cooper, L.W. Rupp Jr, B. Batlogg, Y.L. Soo, Z.H. Ming, A. Krol, Y.H. Kao, Phys. Rev. Lett. **66**, 104 (1991)
6. Y. Sakurai, M. Itou, B. Barbiellini, P.E. Mijnarends, R.S. Markiewicz, S. Kaprzyk, J.M. Gillet, S. Wakimoto, M. Fujita, S. Basak, Y.J. Wang, W. Al-Sawai, H. Lin, A. Bansil, K. Yamada, Science **332**, 698 (2011)
7. Y. Kohsaka, T. Hanaguri, M. Azuma, M. Takano, J.C. Davis, H. Takagi, Nat. Phys. **8**, 534 (2012)
8. J. Orenstein, A.J. Millis, Science **288**, 468 (2000)
9. T. Timusk, B. Statt, Rep. Prog. Phys. **62**, 61 (1999)
10. S. Hüefner, M.A. Hossain, A. Damascelli, G.A. Sawatzky, Rep. Prog. Phys. **71**, 062501 (2008)
11. A. Damascelli, Z. Hussain, Z.X. Shen, Rev. Mod. Phys. **75**, 473 (2003)
12. J.C. Campuzano, M.R. Norman, M. Randeria, *The Physics of Superconductors* (Springer, New York, 2004)
13. M.R. Norman, C. Pépin, Rep. Prog. Phys. **66**, 1547 (2003)
14. F.C. Zhang, C. Gros, T.M. Rice, H. Shiba, Super. Sci. Tech. **1**, 36 (1988)
15. G. Kotliar, Phys. Rev. B **37**, 3664 (1988)
16. A. Paramekanti, M. Randeria, N. Trivedi, Phys. Rev. Lett. **87**, 217002 (2001)
17. P.W. Anderson, P.A. Lee, M. Randeria, T.M. Rice, N. Trivedi, F.C. Zhang, J. Phys. Cond. Matt. **16**, R755 (2004)
18. K.Y. Yang, T.M. Rice, F.C. Zhang, Phys. Rev. B **73**, 174501 (2006)
19. M. Randeria, N. Trivedi, A. Moreo, R.T. Scalettar, Phys. Rev. Lett. **69**, 2001 (1999)
20. V.J. Emery, S.A. Kivelson, Nature **374**, 434 (1995)
21. M. Franz, A.J. Millis, Phys. Rev. B **58**, 14572 (1998)
22. E.W. Carlson, S.A. Kivelson, V.J. Emery, E. Manousakis, Phys. Rev. Lett. **83**, 612 (1999)
23. H.J. Kwon, A.T. Dorsey, P.J. Hirschfeld, Phys. Rev. Lett. **86**, 3875 (2001)
24. E. Berg, E. Altman, Phys. Rev. Lett. **99**, 247001 (2007)
25. C.M. Varma, Phys. Rev. B **73**, 155113 (2006)
26. P.A. Lee, N. Nagaosa, X.G. Wen, Rev. Mod. Phys. **78**, 17 (2006)
27. S. Chakravarty, R.B. Laughlin, D.K. Morr, C. Nayak, Phys. Rev. B **63**, 094503 (2001)
28. C. Honerkamp, H.C. Fu, D.H. Lee, Phys. Rev. B **75**, 014503 (2007)
29. D.M. Newns, C.C. Tsuei, Nat. Phys. **3**, 184 (2007)
30. J. Zaanen, O. Gunnarsson, Phys. Rev. B **40**, 7391 (1989)
31. V.J. Emery, S.A. Kivelson, J.M. Tranquada, Proc. Natl. Acad. Sci. **96**, 8814 (1999)
32. S.R. White, D.J. Scalapino, Phys. Rev. Lett. **80**, 1272 (1998)
33. S.A. Kivelson, E. Fradkin, V.J. Emery, Nature **393**, 550 (1998)
34. M. Vojta, S. Sachdev, Phys. Rev. Lett. **83**, 3916 (1999)
35. S.A. Kivelson, I.P. Bindloss, E. Fradkin, V. Oganesyan, J.M. Tranquada, A. Kapitulnik, C. Howald, Rev. Mod. Phys. **75**, 1201 (2003)
36. S. Sachdev, Rev. Mod. Phys. **75**, 913 (2003)
37. M. Vojta, Adv. Phys. **58**, 699 (2009)
38. E.A. Kim, M.J. Lawler, P. Oreto, S. Sachdev, E. Fradkin, S.A. Kivelson, Phys. Rev. B **77**, 184514 (2008)
39. E. Fradkin, S.A. Kivelson, M.J. Lawler, J.P. Eisenstein, A.P. Mackenzie, Annu. Rev. Condens. Matter Phys. **1**, 153 (2010)
40. N. Gedik, J. Orenstein, R. Liang, D.A. Bonn, W.N. Hardy, Science **300**, 1410 (2003)
41. G. Deutscher, Nature **397**, 410 (1999)
42. M.L. Tacon, A. Sacuto, A. Georges, G. Kotliar, Y. Gallais, D. Colson, A. Forget, Nat. Phys. **2**, 537 (2006)
43. R. Khasanov, T. Kondo, M. Bendele, Y. Hamaya, A. Kaminski, S.L. Lee, S.J. Ray, T. Takeuchi, Phys. Rev. B **82**, 020511(R) (2010)
44. M.R. Norman, H. Ding, M. Randeria, J.C. Campuzano, T. Yokoya, T. Takeuchi, T. Takahashi, T. Mochiku, K. Kadowaki, P. Guptasarma, D.G. Hinks, Nature **392**, 157 (1998)

45. K.M. Shen, F. Ronning, D.H. Lu, F. Baumberger, N.J.C. Ingle, W.S. Lee, W. Meevasana, Y. Kohsaka, M. Azuma, M. Takano, H. Takagi, Z.X. Shen, Science **307**, 901 (2005)
46. K. Tanaka, W.S. Lee, D.H. Lu, A. Fujimori, T. Fujii, Risdiana, I. Terasaki, D.J. Scalapino, T.P. Devereaux, Z. Hussain. Science **314**, 1910 (2006)
47. A. Kanigel, M.R. Norman, M. Randeria, U. Chatterjee, S. Souma, A. Kaminski, H.M. Fretwell, S. Rosenkranz, M. Shi, T. Sato, T. Takahashi, Z.Z. Li, H. Raffy, K. Kadowaki, D. Hinks, L. Ozyuzer, J.C. Campuzano, Nat. Phys. **2**, 447 (2006)
48. A. Kanigel, U. Chatterjee, M. Randeria, M.R. Norman, S. Souma, M. Shi, Z.Z. Li, H. Raffy, J.C. Campuzano, Phys. Rev. Lett. **99**, 157001 (2007)
49. T. Kondo, R. Khasanov, T. Takeuchi, J. Schmalian, A. Kaminski, Nature **457**, 296 (2009)
50. H.B. Yang, J.D. Rameau, Z.H. Pan, G.D. Gu, P.D. Johnson, H. Claus, D.G. Hinks, T.E. Kidd, Phys. Rev. Lett. **107**, 047003 (2011)
51. Ch. Renner, B. Revaz, J.Y. Genoud, K. Kadowaki, Ø. Fischer, Phys. Rev. Lett. **80**, 149 (1998)
52. Ø. Fischer, M. Kugler, I. Maggio-Aprile, C. Berthod, Ch. Renner, Rev. Mod. Phys. **79**, 353 (2007)
53. K. McElroy, D.H. Lee, J.E. Hoffman, K.M. Lang, J. Lee, E.W. Hudson, H. Eisaki, S. Uchida, J.C. Davis, Phys. Rev. Lett. **94**, 197005 (2005)
54. K. McElroy, J. Lee, J.A. Slezak, D.H. Lee, H. Eisaki, S. Uchida, J.C. Davis, Sci. **309**, 1048 (2005)
55. J.W. Alldredge, J. Lee, K. McElroy, M. Wang, K. Fujita, Y. Kohsaka, C. Taylor, H. Eisaki, S. Uchida, P.J. Hirschfeld, J.C. Davis, Nat. Phys. **4**, 319 (2008)
56. J.E. Hoffman, K. McElroy, D.H. Lee, K.M. Lang, H. Eisaki, S. Uchida, J.C. Davis, Sci. **297**, 1148 (2002)
57. K. McElroy, R.W. Simmonds, J.E. Hoffman, D.H. Lee, J. Orenstein, H. Eisaki, S. Uchida, J.C. Davis, Nature **422**, 592 (2003)
58. T. Hanaguri, Y. Kohsaka, J.C. Davis, C. Lupien, I. Yamada, M. Azuma, M. Takano, K. Ohishi, M. Ono, H. Takagi, Nat. Phys. **3**, 865 (2007)
59. W.D. Wise, K. Chatterjee, M.C. Boyer, T. Kondo, T. Takeuchi, H. Ikuta, Z. Xu, J. Wen, G.D. Gu, Y. Wang, E.W. Hudson, Nat. Phys. **5**, 213 (2009)
60. Y. Kohsaka, C. Taylor, K. Fujita, A. Schmidt, C. Lupien, T. Hanaguri, M. Azuma, M. Takano, H. Eisaki, H. Takagi, S. Uchida, J.C. Davis, Science **315**, 1380 (2007)
61. Y. Kohsaka, C. Taylor, P. Wahl, A. Schmidt, J. Lee, K. Fujita, J.W. Alldredge, K. McElroy, J. Lee, H. Eisaki, S. Uchida, D.H. Lee, J.C. Davis, Nature **454**, 1072 (2008)
62. J. Lee, K. Fujita, A.R. Schmidt, C.K. Kim, H. Eisaki, S. Uchida, J.C. Davis, Science **325**, 1099 (2009)
63. S.H. Pan, J.P. O'neal, R.L. Badzey, C. Chamon, H. Ding, J.R. Engelbrecht, Z. Wang, H. Eisaki, S. Uchida, A.K. Gupta, K.W. Ng, E.W. Hudson, K.M. Lang, J.C. Davis, Nature **413**, 282 (2001)
64. K.M. Lang, V. Madhavan, J.E. Hoffman, E.W. Hudson, H. Eisaki, S. Uchida, J.C. Davis, Nature **415**, 412 (2002)
65. T. Cren, D. Roditchev, W. Sacks, J. Klein, Euro. Phys. Lett. **54**, 84 (2001)
66. C. Howald, P. Fournier, A. Kapitulnik, Phys. Rev. B **64**, 100504 (2001)
67. A. Matsuda, T. Fujii, T. Watanabe, Phys. C **388**, 207 (2003)
68. M.C. Boyer, W.D. Wise, K. Chatterjee, M. Yi, T. Kondo, T. Takeuchi, H. Ikuta, E.W. Hudson, Nat. Phys. **3**, 802 (2007)
69. K.K. Gomes, A.N. Pasupathy, A. Pushp, S. Ono, Y. Ando, A. Yazdani, Nature **447**, 569 (2007)
70. A. Pushp, C.V. Parker, A.N. Pasupathy, K.K. Gomes, S. Ono, J.S. Wen, Z. Xu, G.D. Gu, A. Yazdani, Science **324**, 1689 (2009)
71. M.J. Lawler, K. Fujita, J. Lee, A.R. Schmidt, Y. Kohsaka, C.K. Kim, H. Eisaki, S. Uchida, J.C. Davis, J.P. Sethna, E.A. Kim, Nature **466**, 347 (2010)
72. A. Mesaros, K. Fujita, H. Eisaki, S. Uchida, J.C. Davis, S. Sachdev, J. Zaanen, M.J. Lawler, E.A. Kim, Science **333**, 426 (2011)
73. E.H.S. Neto, P. Aynajian, R.E. Baumbach, E.D. Bauer, J. Mydosh, S. Ono, A. Yazdani, Phys. Rev. B **87**, 161117(R) (2013)

74. S.H. Pan, E.W. Hudson, J.C. Davis, Rev. Sci. Instrum. **70**, 1459 (1999)
75. H. Hobou, S. Ishida, K. Fujita, M. Ishikado, K.M. Kojima, H. Eisaki, S. Uchida, Phys. Rev. B **79**, 064507 (2009)
76. J.A. Slezak, J. Lee, M. Wang, K. McElroy, K. Fujita, B.M. Andersen, P.J. Hirschfeld, H. Eisaki, S. Uchida, J.C. Davis, Proc. Natl. Acad. Sci. **105**, 3203 (2008)
77. P.M. Chaikin, T.C. Lubensky, *Principles of condensed matter physics* (Cambridge University Press, Cambridge, 2010)
78. A.V. Balatsky, I. Vekhter, J.X. Zhu, Rev. Mod. Phys. **78**, 373 (2006)
79. A.A. Abrikosov, L.P. Gor'kov, Sov. Phys. JETP **12**, 1243 (1961)
80. Y. Fukuzumi, K. Mizuhashi, K. Takenaka, S. Uchida, Phys. Rev. Lett. **76**, 684 (1996)
81. A.P. Mackenzie, R.K.W. Haselwimmer, A.W. Tyler, G.G. Lonzarich, Y. Mori, S. Nishizaki, Y. Maeno, Phys. Rev. Lett. **80**, 161 (1998)
82. H. Shiba, Prog. Theor. Phys. **40**, 435 (1968)
83. S.H. Pan, E.W. Hudson, K.M. Lang, H. Eisaki, S. Uchida, J.C. Davis, Nature **403**, 746 (2000)
84. M.H. Hamidian, I.A. Firmo, K. Fujita, S. Mukhopadhyay, J.W. Orenstein, H. Eisaki, S. Uchida, M.J. Lawler, E.A. Kim, J.C. Davis, New J. Phys. **14**, 053017 (2012)
85. E.W. Hudson, K.M. Lang, V. Madhavan, S.H. Pan, H. Eisaki, S. Uchida, J.C. Davis, Nature **411**, 920 (2001)
86. T. Machida, T. Kato, H. Nakamura, M. Fujimoto, T. Mochiku, S. Ooi, A.D. Thakur, H. Sakata, K. Hirata, Phys. Rev. B **82**, 180507(R) (2010)
87. J. E. Hoffman, A search for alternative electronic order in the high temperature superconductor $Bi_2Sr_2CaCu_2O_{8+\delta}$ by scanning tunneling microscopy. Ph.D. thesis, University of California, Berkeley (2003).
88. N. Jenkins, Y. Fasano, C. Berthod, I. Maggio-Aprile, A. Piriou, E. Giannini, B.W. Hoogenboom, C. Hess, T. Cren, Ø. Fischer, Phys. Rev. Lett. **103**, 227001 (2009)
89. S. Maekawa, *Physics of Transition Metal Oxides* (Springer, Berlin, 2004)
90. H. Eisaki, N. Kaneko, D.L. Feng, A. Damascelli, P.K. Mang, K.M. Shen, Z.X. Shen, M. Greven, Phys. Rev. B **69**, 064512 (2004)
91. Q.H. Wang, J.H. Han, D.H. Lee, Phys. Rev. B **65**, 054501 (2001)
92. I. Martin, A.V. Balatsky, Phys. C **357**, 46 (2001)
93. J.X. Zhu, K.H. Ahn, Z. Nussinov, T. Lookman, A.V. Balatsky, A.R. Bishop, Phys. Rev. Lett. **91**, 057004 (2003)
94. E. Kaneshita, I. Martin, A.R. Bishop, J. Phys. Soc. Jpn. **73**, 3223 (2004)
95. T.S. Nunner, B.M. Andersen, A. Melikyan, P.J. Hirschfeld, Phys. Rev. Lett. **95**, 177003 (2005)
96. Y. He, T.S. Nunner, P.J. Hirschfeld, H.P. Cheng, Phys. Rev. Lett. **96**, 197002 (2006)
97. M. Mori, G. Khaliullin, T. Tohyama, S. Maekawa, Phys. Rev. Lett. **101**, 247003 (2008)
98. K. Fujita, T. Noda, K.M. Kojima, H. Eisaki, S. Uchida, Phys. Rev. Lett. **95**, 097006 (2005)
99. I. Zeljkovic, Z. Xu, J. Wen, G. Gu, R.S. Markiewicz, J.E. Hoffman, Science **337**, 320 (2012)
100. Q.H. Wang, D.H. Lee, Phys. Rev. B **67**, 020511 (2003)
101. L. Capriotti, D.J. Scalapino, R.D. Sedgewick, Phys. Rev. B **68**, 014508 (2003)
102. T.S. Nunner, W. Chen, B.M. Andersen, A. Melikyan, P.J. Hirschfeld, Phys. Rev. B **73**, 104511 (2006)
103. J. Mesot, M.R. Norman, H. Ding, M. Randeria, J.C. Campuzano, A. Paramekanti, H.M. Fretwell, A. Kaminski, T. Takeuchi, T. Yokoya, T. Sato, T. Takahashi, T. Mochiku, K. Kadowaki, Phys. Rev. Lett. **83**, 840 (1999)
104. M.P. Allan, A.W. Rost, A.P. Mackenzie, Y. Xie, J.C. Davis, K. Kihou, C.H. Lee, A. Iyo, H. Eisaki, T.M. Chuang, Science **336**, 563 (2012)
105. B.M. Andersen, P.J. Hirschfeld, Phys. Rev. B **79**, 144515 (2009)
106. T. Pereg-Barnea, M. Franz, Phys. Rev. B **68**, 180506 (2003)
107. S. Misra, M. Vershinin, P. Phillips, A. Yazdani, Phys. Rev. B **70**, 220503 (2004)
108. D. Wulin, Y. He, C.C. Chien, D.K. Morr, K. Levin, Phys. Rev. B **80**, 134504 (2009)
109. J. Corson, R. Mallozzi, J. Orenstein, J.N. Eckstein, I. Bozovic, Nature **398**, 221 (1999)
110. Z.A. Xu, N.P. Ong, Y. Wang, T. Kakeshita, S. Uchida, Nature **406**, 486 (2000)
111. Y. Wang, L. Li, N.P. Ong, Phys. Rev. B **73**, 024510 (2006)

112. Y. Wang, L. Li, M.J. Naughton, G.D. Gu, S. Uchida, N.P. Ong, Phys. Rev. Lett. **95**, 247002 (2005)
113. L. Li, Y. Wang, M.J. Naughton, S. Ono, Y. Ando, N.P. Ong, Europhys. Lett. **72**, 451 (2005)
114. N. Bergeal, J. Lesueur, M. Aprili, G. Faini, J.P. Contour, B. Lerido, Nat. Phys. **4**, 608 (2008)
115. Y. Chen, T.M. Rice, F.C. Zhang, Phys. Rev. Lett. **97**, 237004 (2006)
116. J.M. Tranquada, B.J. Sternlieb, J.D. Axe, Y. Nakamura, S. Uchida, Nature **375**, 561 (1995)
117. J.M. Tranquada, H. Woo, T.G. Perring, H. Goka, G.D. Gu, G. Xu, M. Fujita, K. Yamada, Nature **429**, 534 (2004)
118. P. Abbamonte, A. Rusydi, S. Smadici, G.D. Gu, G.A. Sawatzky, D.L. Feng, Nat. Phys. **1**, 155 (2005)
119. Y.J. Kim, G.D. Gu, T. Gog, D. Casa, Phys. Rev. B **77**, 064520 (2008)
120. K. Fujita, M.H. Hamidian, S.D. Edkins, C. Kim, Y. Kohsaka, M. Azuma, M. Takano, H. Takagi, H. Eisaki, S. Uchida, A. Allais, M.J. Lawler, E.A. Kim, S. Sachdev, J.C. Davis, Proc. Nat'l. Acad. Sci. **111**, E3026 (2014)

Chapter 4
Point Contact Spectroscopy in Strongly Correlated Systems

Guy Deutscher

Abstract The application of Point Contact Spectroscopy to strongly correlated materials is reviewed. Results obtained on MgB_2, high T_c cuprates, heavy fermions, pnictides and spin-active interfaces are reviewed, with an emphasis on the quantitative determination of the mass enhancement factor. The method of analysis presented is particularly useful when low temperature heat capacity measurements cannot be performed due to very high superconducting critical fields.

4.1 Introduction

The development of Point Contact Spectroscopy can be traced back to an early paper by Sharvin [1]. In this paper, Sharvin pointed out that when electrons cross a small aperture without undergoing any collision, which occurs if its size d is smaller than the electron mean free path, this contact will nevertheless have a finite resistance. However he did not himself use point contacts for spectroscopic investigations. Instead, his idea was to use devices incorporating two point contacts to study electron orbits under applied magnetic fields: electrons injected through one contact could be collected in the second one if the field would bend over the electron beam so that it would hit back the surface at the location of the second contact. It is interesting to note that at the same time Andreev [2] had predicted that electrons hitting a normal metal to superconductor interface should be reflected back as holes at biases below the gap. It turned out later that the Point Contact invented by Sharvin was in fact the perfect tool to study these reflections, also predicted at the same time independently by de Gennes and Saint-James [3] and by Saint James [4]. In what follows, I will call these reflections Andreev–Saint James, or ASJ, as has now been accepted [5].

The first observation of ASJ reflections at a normal metal/superconductor interface was reported by Pankove [6], who noticed that the conductance of small Nb/Al contacts decreased abruptly at a bias of the order of the superconducting gap. As we

G. Deutscher (✉)
School of Physics and Astronomy, Tel Aviv University, 690978 Ramat Aviv, Tel Aviv, Israel
e-mail: guyde@post.tau.ac.il

A. Avella and F. Mancini (eds.), *Strongly Correlated Systems*,
Springer Series in Solid-State Sciences 180, DOI 10.1007/978-3-662-44133-6_4

shall see below, this sudden decrease is a basic characteristic of ASJ reflections. However, Pankove did not relate his observations to the predicted electron-hole reflections below the gap. In fact it was only in 1980 that Zaitsev [7] showed explicitly that the conductance of a Sharvin contact between a normal metal and a superconductor is enhanced below the gap. Shortly thereafter Blonder, Tinkham and Klapwijk [8] produced a full theory of the I(V) characteristics of such contacts, covering the full range between Sharvin (ballistic) contacts and tunneling junctions whose resistance is mostly due to a barrier at the interface.

However, in the case of conventional superconductors Point Contact Spectroscopy does not present much of an advantage over the well established Giaever tunneling spectroscopy [9]. In addition to the determination of the gap, Giaever tunneling also allows the determination of the detailed interaction with the bosons (here phonons) that provide the glue for pair formation.

I believe that the justification for the present review is the discovery of many new superconductors (strongly correlated systems such as heavy fermions, cuprates, pnictides, and also MgB_2). While tunneling was the tool of choice for the study of conventional superconductors, it has turned out to be basically inapplicable to these new superconductors, which are complex materials that do not allow the preparation of high quality tunnel barriers. To some extent the development of Scanning Tunneling Spectroscopy has replaced conventional tunneling, but it has its own limitations. It requires a very smooth and clean surface, and few materials can be easily cleaved to produce them. Besides it investigates the density of states at the surface, and may not necessarily be trusted to always reflect bulk properties. By contrast, Point Contact Spectroscopy does not require perfect surfaces, and investigates the properties of the material over a depth of the order of the coherence length. These are I believe the experimental reasons why there has been in recent years strong renewed interest in this technique for the study of complex materials, particularly strongly correlated systems.

Besides, there has also been progress in the theoretical understanding of the properties of contacts with materials where interactions are strong. It has been shown that the effective transparency of these contacts is not affected by retardation effects [10]. This result has allowed the development of a new method for the quantitative determination of mass enhancement due for instance to strong correlation effects. The mass enhancement factor is obtained by comparing the effective Fermi velocity of the strongly correlated material that enters into the contact resistance, and that which determines the superconducting coherence length. In this way it has become possible to establish a classification of strongly correlated systems in terms of their mass enhancement factors.

Another reason for recent successes in the use of Point Contact Spectroscopy for the study of unconventional superconductors is that, contrary to tunneling spectroscopy, it is phase sensitive. For instance, in the case of the high Tc cuprates, it has been possible to make a quantitative fit of I(V) characteristics to theory by taking into account the d-wave symmetry of the order parameter.

Overall, the quality of the fits of Point Contact data is today comparable to that which had been achieved in the past by tunneling spectroscopy on conventional superconductors.

4.2 Experimental Realization of Point Contacts

4.2.1 Resistance of a Sharvin Contact

Sharvin considered the transport of electrons through a small aperture connecting two electrodes in the case where the size d of this aperture is smaller than the electrons mean free path l (Fig. 4.1). He remarked that in spite of the absence of scattering this contact has a finite resistance. His argument is that when a difference of potential V is applied between the two electrodes, electrons crossing the aperture acquire an additional kinetic energy equal to eV as compared to their Fermi kinetic energy. Denoting the additional velocity by δv and the Fermi velocity by v_F one has to first order $mv_F \cdot \delta v = eV$. The net current resulting from the excess velocity is $I = ned^2 \cdot \delta v$ and therefore the resistance of the contact is equal to:

$$R_{sh} = \frac{mv_F}{nd^2e^2}. \tag{4.1}$$

This result is easily transformed into $R_{sh} = \rho l/d^2$ where ρ is the resistivity of the metallic electrodes. A more precise calculation taking into account the three dimensional character of the electron gas gives:

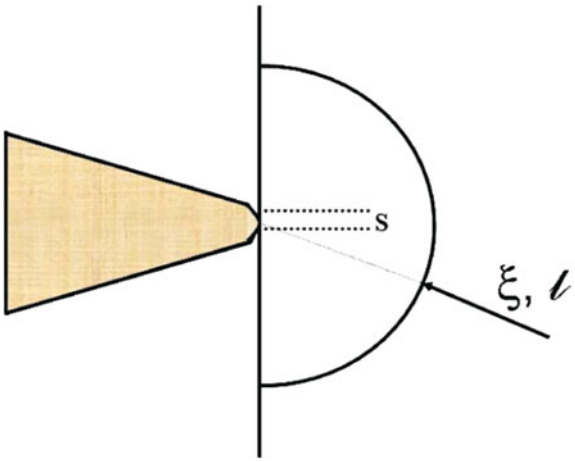

Fig. 4.1 A contact between a normal tip, on the *left*, and a superconducting electrode on the *right hand side*. The physical size of the contact, s, should be smaller than the mean free path l to avoid heating effects, and than the coherence length ξ to avoid the proximity effect that may weaken locally the superconducting gap

$$R_{sh} = \frac{16\rho l}{3\pi d^2} \tag{4.2}$$

or equivalently:

$$R_{sh} = \frac{16\hbar}{(k_F d)^2 2e^2} \tag{4.3}$$

where the universal resistance $h/2e^2 = 12.9\,\mathrm{k}\Omega$ appears. This last expression has a simple physical meaning: the Sharvin resistance is equal to the universal resistance divided by the number of quantum channels across the contact.

In most metals the product ρl is of the order of $1 \times 10^{-11}\ \Omega\,\mathrm{cm}^2$. In a relatively clean metal the mean free path will be of the order of 100 nm or more. In order to qualify as a Sharvin contact a point contact resistance should therefore be of the order of 1 Ω or more. This is a useful number to remember. It is in fact a lower limit as the resistance will often be increased by the presence of a physical barrier or a mismatch of the Fermi velocities of the two electrodes, if we have a heterogeneous contact as will in general be the case.

The above expressions give the resistance of a Sharvin contact in the low bias limit. But in fact in what follows we shall be mainly interested in the behavior of the contact at finite biases, where interactions can modify the I(V) characteristic. For instance, electrons can interact with phonons and be scattered back, thus reducing the net flow of electrons at a given bias. More generally inelastic scattering will generate heating, which in some instances such as a contact with a superconductor can strongly modify the conductivity. In the next section we briefly consider these possibilities and the limitation they imply for point contact spectroscopy.

4.2.2 Scattering Effects

Elastic scattering in the contact area results in an additional diffusive term in its resistance, basically equal to ρ/d. Here ρ is the resistivity in the region of the contact, and it is assumed that $l \ll d$. A useful interpolation expression given by Wexler [11] is:

$$R = \frac{16\rho l}{3\pi d^2} + \frac{\rho\,(T)}{d} \tag{4.4}$$

which is just the sum of the Sharvin resistance and of the diffusive term. Temperature dependence of a contact resistance is therefore a sign that it is not in the Sharvin limit.

Joule heating *inside* the constriction arises if the inelastic mean free path—in addition to the elastic mean free path—is smaller than the size of the constriction. This results in an elevation of its temperature T_{PC}, which is bias dependent. If it rises substantially above that of the bath, it is given by [12]:

$$eV = 3.63 k_B T_{PC} \tag{4.5}$$

In the case of a normal metal to superconductor contact, spectroscopy involves biases of the order of the superconducting gap $\Delta = 1.75 k_B T_c$ for a BCS superconductor. Spectroscopy is typically performed at temperatures well below the critical temperature T_c. As can be seen from the above expression, at such bias the temperature of the constriction can in fact easily reach values of the order of T_c. The measured gap will then be significantly smaller than its low temperature value.

4.2.3 Critical Velocity Effects

In the case of a normal metal to superconductor point contact, heating is not an issue as long as the superconducting state is maintained since there is zero dissipation. However, when $eV \geq \Delta$, the velocity that pairs acquire is of the order of the critical velocity at which massive depairing occurs:

$$v_c = \frac{\Delta}{p_F} \tag{4.6}$$

where p_F is the Fermi momentum. Quasi-particles are then produced at the expense of the superconducting condensate. If the contact is not in the Sharvin limit, heating will immediately occur, the temperature will rise substantially and possibly above T_c. At that point the (I/V) characteristic will reverse to that in the normal state, instead of following the behavior predicted in the superconducting state, where above the gap the production of quasi-particles occurs gradually. This results in a dip in the dynamical conductance dI/dV at a bias of the order of the gap. Such a signature of heating effects is often seen, see Fig. 4.2. Vice-versa, the absence of such a dip at the gap bias is a strong indication that the contact is in the Sharvin limit.

When pairs are reaching the critical velocity, heat will be dissipated inside the superconducting material within a radius l_{in} of the contact. The longer this inelastic scattering length, the smaller the temperature rise: away from the contact the pair velocity will decrease as r^{-2} and heat will be dissipated in a larger volume. Therefore the condition $l_{in} \gg d$ is of ultimate importance. At high temperatures scattering occurs mostly through the electron-phonon interaction, the elastic and inelastic scattering lengths are close to each other. But at low temperatures the inelastic length grows as T^{-p} where the exponent p ranges from 1 to 3 depending on the scattering process and the dimensionality. It can easily reach values of the order of one micron in the liquid Helium temperature range. This is a large length scale compared to the typical contact size of the order of 10 nm. Point contact spectroscopy is therefore best conducted at low temperatures.

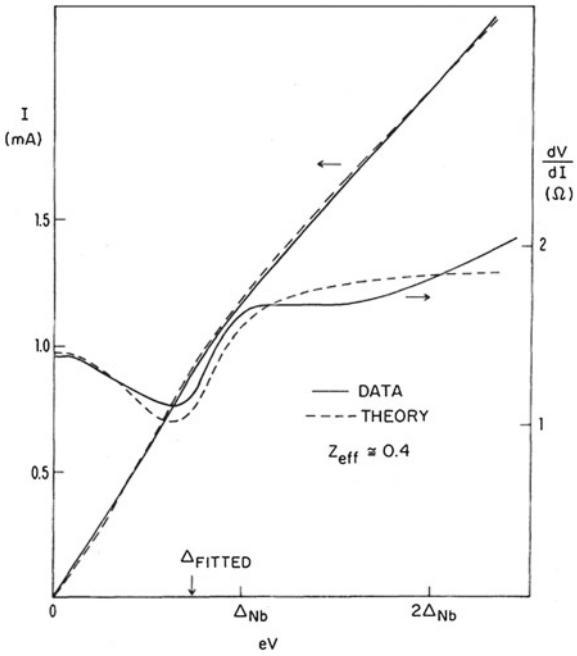

Fig. 4.2 Characteristic of a low resistance Cu/Nb point contact (about 0.1 Ω) showing heating effects. A fit to theory is possible, but the dip in dV/dI occurs at a bias smaller than the gap of the bulk superconductor and the resistance rises at high voltages. After Blonder and Tinkham [13]

4.2.4 Contact Size

Determining the contact size through a measurement of the contact resistance using the Sharvin relation gives only a rough estimate. This is because it assumes that the contact is perfectly transparent, while it in fact never is. Transparency of the contact is limited for two reasons: the possible existence of a physical barrier at the interface, and a mismatch of the Fermi velocities, as already mentioned.

Blonder et al. [8] have modeled the barrier through a delta function $V = H\delta(x)$ and have introduced a transparency coefficient $Z = H/\hbar v_F$. In addition they have taken into account the ratio r between the Fermi velocities of the two electrodes. The effective transparency coefficient Z_{eff} is given by:

$$Z_{eff}^2 = Z^2 + \frac{(1-r)^2}{4r} \tag{4.7}$$

and the actual resistance of the contact is:

$$R = R_{sh}\left(1 + Z_{eff}^2\right). \tag{4.8}$$

An independent determination of Z_{eff} is therefore necessary to obtain the value of the Sharvin resistance, and therefore of the contact size. This is in general not possible in the normal state, but as we shall see in the next section it is possible for

a normal metal to superconductor contact. By itself, a measurement of the contact resistance only gives an upper bound for R_{sh} and therefore a lower bound for the contact size.

4.2.5 Practical Realization of Point Contacts

A commonly used technique to produce a point contact is to prepare a sharp normal metal tip and to bring in into contact with the surface of the material under study. Tip preparation can be done for instance by cutting the edge of a gold wire with a sharp razor. The typical radius of curvature achieved is of about one micron. Although this size is by itself much too large to fabricate a Sharvin contact, one can make one by bringing delicately the tip into contact through a micro-screw device. At first, the contact resistance is usually of the order of several kΩ, in general due to the presence of some insulating material on the surface. The (I/V) characteristic is then structure-less. But by moving the tip down slowly, and sometimes by adding some small lateral movement, this resistance can be brought down into the desired range of 10–100 Ω. A useful characteristic can then be recorded.

How the small point contact is actually achieved is not obvious. One possibility is that by moving the tip one scratches the surface of the material under study, and that contact with the tip is actually through a pinhole. Existence of pinholes is a non-desired but common feature in thin insulating oxides used to produce tunnel junctions.

A different technique consists indeed in creating pinholes in a thin oxide barrier by applying a voltage pulse across a small area junction between two thin wires at right angle. This has been done for instance to study ferromagnetic to superconductor contacts. Here the ferromagnet (Ni or Co) was evaporated first and let to oxidize in air for some limited time. In a second stage the superconductor (for instance In) was evaporated and prepared in a cross-wire geometry. Resistance of the contact is at first high but can be brought down into the desired range by the application of series of voltage pulses [14].

Mechanically controlled break junctions have also been used to produce point contacts [15, 16]. Here both electrodes are identical, the advantage being that one unknown parameter—the mismatch between the Fermi velocities between the two electrodes—is eliminated.

4.3 Point Contact Spectroscopy of Conventional Superconductors

The theory of Blonder et al. [8] still constitutes the basis of our understanding of point contact spectroscopy of superconductors. Although it was developed for conventional superconductors—by which we mean *s*-wave order parameter symmetry and weakly

correlated systems—its application to unconventional superconductors has proven to be extraordinarily useful for reasons that will become clear below. Therefore a brief overview will be helpful here for the reader actually interested in strong correlation effects.

In a pure Sharvin contact an electron coming from the normal side at an energy ε (counted from the Fermi energy) smaller than the gap cannot penetrate into the superconductor. It can however be reflected as a hole of opposite spin at an energy $-\varepsilon$. Recombination into a Cooper pair occurs in S over the length scale of the superconducting coherence length ξ. At biases smaller than the gap a charge of $2e$ flows through the interface, as compared to a charge e in the normal state. This increase in conductance below the gap, by a factor of 2, can be understood intuitively by noting that the resistance of the contact in the normal state comes for half from each side, and that the contribution of one half disappears when one electrode becomes superconducting. Above the gap voltage quasi-particles progressively reduce this enhanced conductance until it returns to its normal state value.

If the contact is not perfectly transparent, the incoming electron can undergo several processes. It can still be reflected as a hole along the incident trajectory with probability $A(\varepsilon)$ (ASJ reflection); it can be reflected as a normal electron (normal specular reflection) with probability $B(\varepsilon)$ even at bias below the gap; it can be transmitted as an electron with a wave vector $k > k_F$ (no branch crossing) with probability $C(\varepsilon)$; or it can be transmitted as an electron with a wave vector $k < k_F$ (branch crossing) with probability $D(\varepsilon)$. The sum of these probabilities is equal to unity. The current across the contact is the same on both sides of the contact, knowledge of two coefficients for instance $A(\varepsilon)$ and $B(\varepsilon)$ is sufficient to calculate it:

$$I = J_0 \int_{-\infty}^{+\infty} [1 + A(\varepsilon) - B(\varepsilon)] [f(\varepsilon - eV) - f(\varepsilon) d\epsilon] \tag{4.9}$$

where J_0 depends on the geometry of the contact and $f(\varepsilon)$ is the Fermi function.

The shape of the dynamical conductance characteristic dI/dV(V) is a sensitive function of the effective barrier parameter Z_{eff}. As shown in Fig. 4.3, when Z (read Z_{eff}) is smaller than 0.5, the zero bias conductance is enhanced compared to the normal state one (the conductance well above the gap). In other terms, ASJ reflections still dominate. For Z values increasing from zero to 0.5, a conductance peak progressively develops at the gap bias. For $Z > 0.5$, the zero bias conductance is reduced and for $Z > 2$, the characteristic is basically tunneling like, with sharp coherence peaks developing at the gap.

Experimentalists often present dV/dI characteristics, like that shown in Fig. 4.3. Instead of a peak, a dip is seen at the gap bias.

For a normal to superconducting contact a further restriction to the contact size applies, in addition to $d \ll l_{in}$. In spite of the desire for good contact between the normal metal (for instance a tip) and the superconducting electrode, the value of the gap in S should not be affected by this contact as it normally is because of the proximity effect [17]. Lack of a proximity effect can be achieved if the size of the

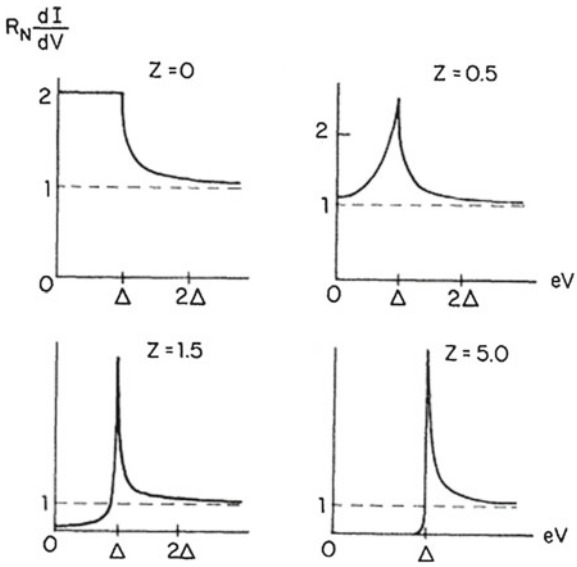

Fig. 4.3 Typical dynamical conductances of point contacts for values of the transparency parameter Z ranging from 0 (pure Sharvin limit) to 5 (tunneling like characteristic). After Blonder et al. [8]

contact is much smaller than the superconducting coherence length, $d \ll \xi$, since ξ is the length scale over which the conversion of quasi-particles to Cooper pairs occurs. At low temperatures this condition is more stringent than $d \ll l_{in}$, because as mentioned above the inelastic scattering lengthdiverges at low temperatures, while the coherence length reaches a finite value. For a clean, low temperature superconductor ξ is of the order of one micron, which poses no problems. But the coherence length of clean Nb is already down to 40 nm, a value further reduced in the dirty limit $l < \xi$. As can be seen in Fig. 4.4, for intermediate resistance contacts the condition $d \ll \xi$ is met. But it is not for a low resistance contact, see Fig. 4.2 where the gap "seen" at the contact is evidently reduced precisely by the proximity effect.

4.4 Fitting the Symmetry of the Superconductor Order Parameter

Like ARPES, point contact spectroscopy is sensitive to gap anisotropy. But it has in addition the unique property to be phase sensitive, namely it can distinguish between a strongly anisotropic order parameter and a d-wave order parameter for which there is a change in phase by π at nodes between neighboring lobs. Extensions of the BTK theory to include unconventional order parameter symmetries by Tanaka and Kashiwaya [18] have been successfully used to fit point contact spectroscopy data obtained on high T_c cuprates [5, 19].

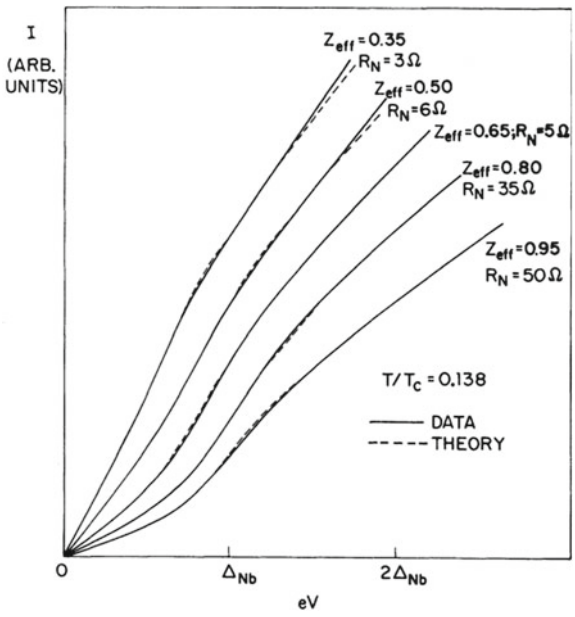

Fig. 4.4 Characteristic of a Cu/Nb point contact of intermediate resistance (about 4 Ω) showing no heating effects. The only adjustable parameter is Z, the value of the gap is that of bulk Nb. The fit is not perfect but the dip in dV/dI occurs at the bulk gap bias, and the resistance is almost flat at high bias (actually a small rise above the theory fit can be seen). After Blonder and Tinkham [13]

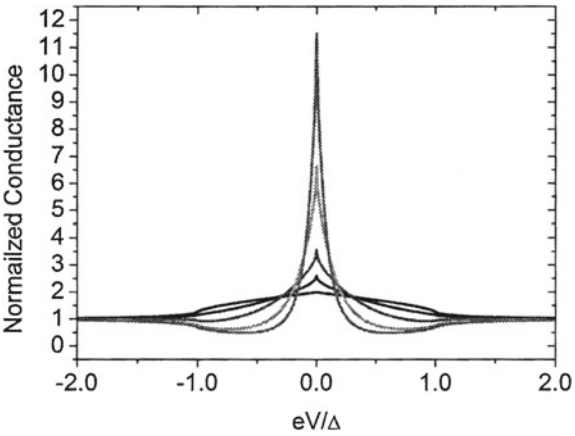

Fig. 4.5 Conductance of a point contact with a d-wave superconductor in a nodal direction for the following Z values: 0; 0.5; 1.0; 2.0; 3.0. The surface zero energy bound states are better defined for less transparent contacts, resulting in a higher and narrower peak a zero bias

Zero energy bound states are formed at the surface of a d-wave superconductor oriented perpendicular to a node direction [20]. These zero energy states are formed because during a Saint-James cycle [4] involving two successive specular reflections at the surface, excitations explore successively lobes of the order parameter having phases that differ by π. These zero energy states result in a sharp conductance peak at zero bias. The height of this peak is twice the normal state conductance for a perfectly transparent Sharvin contact. As the transparency reduces, the conductance peak narrows and its height increases (Fig. 4.5).

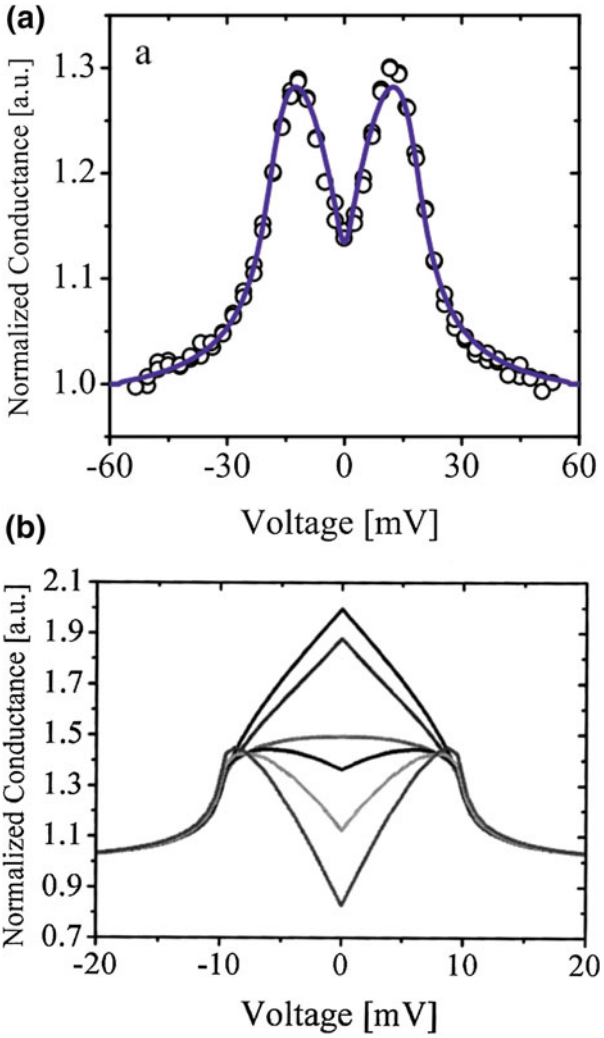

Fig. 4.6 **a** Conductance of a Au/YBCO point contact on a (100) oriented facet (anti-nodal direction). The continuous curve is a fit to theory with $Z = 0.6$ and $\Delta_d = 18.6$ meV. After Kohen et al. [19]. **b** Theoretical conductance curves calculated for a contact along a (100) direction between a normal metal and a d-wave superconductor having a gap of 10 meV for the following Z values: 0;0.2;0.3;0.5;07;1.0

Characteristics are quite different when the surface is oriented perpendicular to an anti-node direction. In that orientation they are sensitive to the gap anisotropy rather than to its phase because during a Saint-James cycle quasi-particles are reflected by lobs having the same phase, before and after a specular reflection at the surface. Figure 4.6a shows data obtained on a (100) oriented facet of an optimally doped

$YBa_2Cu_3O_{7-\delta}$ film [19], together with a fit to the theory of Tanaka and Kashiwaya with $Z = 0.68$ and $\Delta_d = 18.6\,\text{meV}$.

As shown Fig. 4.6b, the shape of the theoretical curves is very sensitive to the value of the Z parameter in the range from 0 to 1. A quick comparison between the data shown Fig. 4.6a and the theoretical curves shown Fig. 4.6b immediately tells that the value of the Z parameter must fall for this contact between 0.5 and 0.7. As said above, a more refined fit gives the value 0.68.

An interesting feature of the theoretical curves in the case of a d-wave symmetry is that for Z values larger than about 0.5 they present a weak coherence peak about 1.4 times higher than the normal state conductance at the gap bias. This was already observed in the early data obtained by Hass et al. [21], but at the time it was not understood that the origin of this weak coherence peak was the d-wave symmetry of the order parameter.

A surprising fact also noted in this early data was the relatively small value of the Z parameter, immediately obvious because of the enhanced conductance below the gap. Compared to normal metals, cuprates have a small Fermi velocity of about 1.5×10^7 cm/s, as determined for instance by ARPES measurements. This is about 10 times smaller that the Fermi velocity in the Au tip. According to the BTK expression for a perfectly clean interface $Z_{eff} = [(1-r)^2/4r]^{1/2}$, which gives $Z_{eff} \approx 2$. The actual value of Z_{eff} can only be larger than this. Instead, fits to the characteristics of contacts to cuprates give typically $Z_{eff} \approx 0.5$ or less. In other terms, point contacts to cuprates should always give Giaever like characteristics, while they are in fact commonly Sharvin like, see Fig. 4.3. It will turn out that a high transparency is a key property of point contacts to strongly correlated metals, in spite of their short Fermi velocity.

Another surprise is that in spite of the very short coherence length of the cuprates, which is typically of the order of 1–2 nm, an excellent quantitative fit to the BTK theory can be achieved, see Fig. 4.6a. Such contacts have resistances of about 10 Ω, and therefore do not meet the condition $d \ll \xi$ since they must have a minimum size of about 1 nm—of the same order as the coherence length.

The high transparency of contacts to heavy fermions as well as their "point contact character" raise questions regarding their effective Fermi velocity and quasi-particles to Cooper pairs effective recombination length. We deal with them in the next section.

4.5 Theory of ASJ Reflections in the Presence of Retardation Effects

As will be reviewed below, normal metal/heavy fermion interfaces are characterized by a high transparency. This is at first view surprising since according to the BTK theory the large mismatch of the Fermi velocities, which can reach values of the order of 100, should lead to a low transparency. This apparent contradiction between experiment and theory was resolved in 1994 by Deutscher and Nozières [10]. However their argument seems not to have been fully appreciated [22]. We shall therefore

review it here and show how well it applies to a wide range of interfaces with materials showing various degrees of electronic correlations. It turns out that their theory can be used to determine quantitatively the mass enhancement factor by combining the experimental determination of the value of Z_{eff} and that of the coherence length.

The origin of the short Fermi velocity and short coherence length in the cuprates and heavy fermions lies in the large electron mass enhancement typical of strongly correlated materials. However, this mass enhancement cancels out from the boundary condition determining the transparency of contacts with normal metals.

Corrections to the free electron approximation come from the potential of the lattice periodic crystal and from interaction terms such as electron-phonon, electron-electron of various kinds. If one uses the electrons wave functions in the periodic lattice as the basis, the other interactions are included in a self-energy term $\Sigma(k, \omega)$. The wave vector dependence of this self-energy is usually small and can often be neglected, contrary to the wave vector dependence due to the potential of the periodic lattice.

The finite transparency resulting from a mismatch of the Fermi velocities is a well-known effect in optics. When light strikes an interface between two media having different refraction indices, in which the velocities of propagation are different, a fraction of the incoming wave is reflected. The same applies to electron waves at an interface between two lattices where the velocities of *propagation* are different due to different interactions with the potentials of their respective lattices. By contrast, one may guess that the frequency dependence of the self-energy does not affect the transparency of the contact because this is a retarded and *local* effect.

One must distinguish between three different velocities: the bare velocity v_{F_0} of the electron's wave in the potential of the lattice, this velocity corrected for the wave vector dependence of the self-energy $\overline{v_F}$, and the fully renormalized velocity v_F:

$$\overline{v_F} = v_{F_0}\left(1 - \frac{\partial \Sigma}{\partial k}\right) \tag{4.10}$$

$$v_F = \frac{\overline{v_F}}{1 + \frac{\partial \Sigma}{\partial \omega}} \tag{4.11}$$

where appears the renormalization factor z:

$$z = \frac{1}{1 + \frac{\partial \Sigma}{\partial \omega}} \tag{4.12}$$

in the above expressions the derivatives are taken at the Fermi level.

It is the ratio r between the velocity $\overline{v_F}$ in the heavy fermion and the velocity in the normal metal v_{F_N} (for which self energy corrections are negligible) that determines the minimum value of Z_{eff}. As we have seen in the above section, barring heating effects, the value of Z_{eff} at a normal/superconducting contact can be determined

by fitting the conductance characteristic to the BTK theory for the appropriate order parameter symmetry. This value can then be used to obtain that of $\overline{v_F}$, if v_{F_N} is known (which is the case if N is a conventional normal metal). In this way we can calibrate the Fermi velocity in the superconducting electrode, corrected for the wave vector dependence of the self-energy, against the known Fermi velocity of the normal metal electrode.

On the other hand, the superconducting coherence length ξ involves the fully renormalized Fermi velocity v_F:

$$\xi = \frac{\hbar v_F}{\pi \Delta} \tag{4.13}$$

where Δ is the renormalized (measured) gap.

If ξ and Δ are known, v_F can be calculated and the mass enhancement factor obtained as the ratio between $\overline{v_F}$ and v_F. This will give a lower bound for this factor since the presence of a physical barrier at the N/S interface will increase the measured value of Z_{eff}.

In the following section we show how this method can be applied to obtain the mass enhancement factor in conventional superconductors, MgB_2, f electron heavy fermions, high T_c cuprates, and some pnictides.

4.6 Experimental Determination of the Mass Enhancement Factor: From Conventional Superconductors to Heavy Fermions

4.6.1 A Conventional Superconductor: Nb

In their pioneering work Blonder and Tinkham [13] studied Nb/Cu contacts and fitted well their data using the then accepted bulk gap value of Nb (1.47 meV), when contacts had a normal state resistance of more than a few Ω. Contacts were in the Sharvin limit, with a size estimated to be about 100 Å. The most transparent contacts they produced had $Z_{eff} = 0.3$, corresponding to $r = 1.75$. Cu has a Fermi velocity of 1.36×10^8 cm/s, from which we obtain $\overline{v_F} = 0.77 \times 10^8$ cm/s. The coherence length of Nb, equal to 380 Å, is larger as requested than the contact size. Using their gap value and this coherence length, we get for the fully renormalized velocity $v_F = 0.3 \times 10^8$ cm/s. Finally we have for Nb a mass enhancement factor:

$$\frac{\partial \Sigma}{\partial \omega} = 2.5 \tag{4.14}$$

Assuming that the mass enhancement is entirely due to the electron-phonon interaction, $\frac{\partial \Sigma}{\partial \omega} = 1 + \lambda_{e-p}$, we get $\lambda_{e-p} = 1.5$.

This method of evaluation of the electron-phonon interaction is much easier to apply than the McMillan-Rowell [23] method of inversion of the tunneling

characteristic, which requires very high quality tunnel junctions. Those are in general not available for d-band metals such as Nb. For instance, Bostock et al. [24] give $\lambda_{e-p} = 0.39$, clearly much to small.

Based on an analysis of their critical field measurements Kerchner et al. [25] have given for Niobium a mass enhancement factor of 2.2, not too far from the value we have calculated.

This is the place to remember that the mass enhancement factor is only equal to $(1 + \lambda_{e-p})$ in the case it is entirely due to the electron-phonon interaction. If the electron-electron interaction (correlation) also contributes, this is no longer true: the mass enhancement factor is then larger than $(1 + \lambda_{e-p})$. This will appear more clearly when we describe results obtained on heavy fermions.

4.6.2 MgB_2: A Weakly Correlated High Temperature Superconductor

With a critical temperature of 39 K, MgB_2 stands out as being in the same range as many High T_c cuprates, known to be strongly correlated materials. It is therefore important to establish the degree of electron correlation in this superconductor.

Several groups have published converging point contact results for normal state contact resistances of the order of 10 Ω and estimated contact sizes below 100 Å. The mean free path in good samples is quoted as being equal to 800 Å [26], the contacts are thus well in the Sharvin limit. The contact size is of the order of the coherence length, see below. Daghero and Gonnelli [26], Szabó et al. [27], Kohen and Deutscher [28] have reported $Z_{eff} = 0.5$ in their most transparent contacts. This gives for r the lower bound 2.6, and for $\overline{v_F}$ the lower bound 5×10^7 cm/s.

It has been shown that MgB_2 has a lamellar structure and is a two band, two gap superconductor (for a review see [26]). To calculate the values of the renormalized Fermi velocity we have used the very accurate STM gap measurements of Giubileo et al. [29], $\Delta_1 = 3.8$ meV and $\Delta_2 = 7.8$ meV, and the coherence lengths deduced from the in-plane and out-of-plane critical fields (3.5 and 17 T respectively), $\xi_{parallel} = 100$ Å and $\xi_\perp = 44$ Å. We remark that the products $\Delta\xi$ are very close to each other and use their average to calculate the normalized Fermi velocities, for which we get 1.8×10^7 cm/s.

This gives an average mass enhancement factor of 2.8. If we attribute it entirely to the electron-phonon interaction, we obtain the $\lambda_{e-p} = 1.8$. This value is close to but somewhat larger than that found for Pb for which $\lambda_{e-p} = 1.55$ [30], (Fig. 4.7).

Nicol and Carbotte [31] have calculated strong coupling effects in MgB_2 in a two band model characterized by four interaction parameters, one for each band and two for inter-band coupling. They characterize the degree of strong coupling by the ratio of the critical temperature to a characteristic phonon frequency. They conclude that this parameter is somewhat larger for MgB_2 than for Pb. This is in line with the average effective value we have obtained for λ_{e-p}.

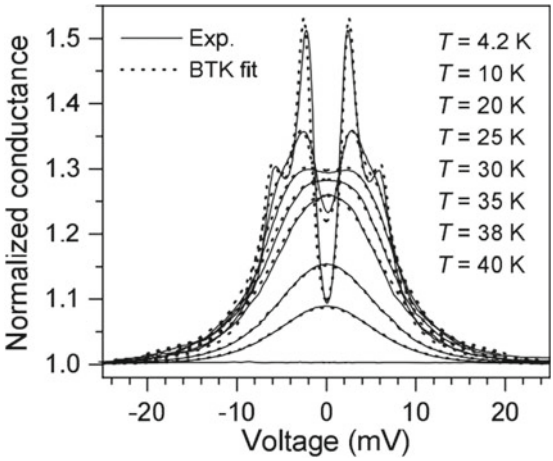

Fig. 4.7 Conductance of a Cu/MgB_2 contact showing a two-gap structure well resolved at low temperature. The fit to the BTK theory involves in principle 7 parameters: two gap values, two barrier parameters, two broadening parameters, and a parameter giving the respective weight of the two bands. All curves have been fitted here with a single $Z = 0.5$ (after Szabó et al. [27]). The values of the broadening parameters used in this particular fit were not given. They are often of the order of one half or one third of the gap. After Daghero et al. [26]

Based on point contact spectroscopy results, we may conclude that MgB_2 is a conventional superconductor in the sense that the mass enhancement factor is due entirely to the electron-phonon interaction. Strong coupling effects are similar to but somewhat stronger than in Pb. Two-band superconductivity certainly contributes to getting a relatively high T_c, but strong coupling effects are also essential.

4.6.3 High T_c Cuprates

Kohen et al. [19] have fitted their conductance data to the BTK theory for Au/YBCO contacts having Z parameter values ranging from 0.3 to 0.7 (one of them is shown Fig. 4.6a). Contact resistances were in the range of 5–40 Ω, indicating contact sizes ranging from 150 to 50 Å. The results were obtained on nearly optimally doped YBCO films with contacts in the anti-nodal direction. They found that for contact with the lowest Z values it was necessary to add to the main d-wave pair potential an id_{xy} component, which they proposed is due to a proximity effect. The authors propose that this additional component occurs because the size of low Z contacts is substantially larger than the coherence length. The value of the Dynes broadening parameter Γ used in their fits was in every case much smaller than the main pair potential $\Delta_{d_{x^2-y^2}}$. This is in contrast with many point contact conductance data, for

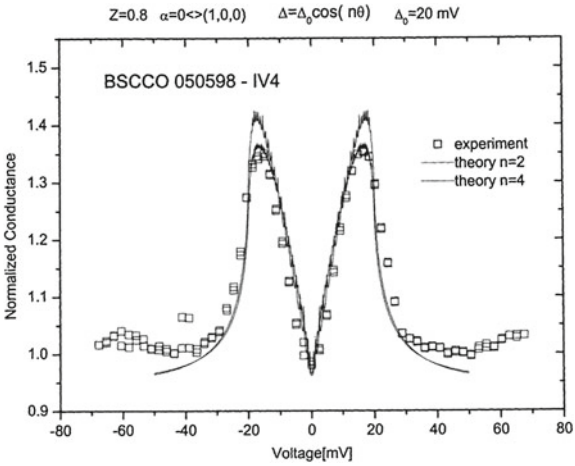

Fig. 4.8 Point contact conductance of a Au/BSCCO 2212 contact. Note the good agreement with the theoretical curves shown Fig. 4.6b. The height of the normalized conductance peaks is close to its maximum theoretical value, and the shape of the characterisitic around zero bias displays the V shape predicted for the anti-nodal direction. No broadening parameter has been used in the fit to the BTK theory. After D'Gorno and Kohen quoted in [5]

which a smearing parameter of the order of the gap is often required, and shows that such a large broadening parameter when found has probably an extrinsic origin.

Using the above described procedure, with $Z = 0.3$, a coherence length of 18 Å (corresponding to an estimated upper critical field of 100 T), a gap of 18 meV (as obtained from the fits), the mass enhancement factor comes out to be of about 5 for optimally doped YBCO.

For LSCO Hass et al. [32] fitted their data with $Z = 0.3$, $\overline{v_F} = 6\times10^7$ cm/s and $v_F = 1.5\times10^7$ cm/s, giving a mass enhancement factor of 4 at optimum doping. For BSCCO there is not enough point contact data available, and the upper critical field value is not known well enough to give a reliable value of the mass enhancement factor. We nevertheless show Fig. 4.8 point contact data with a high quality fit achieved without a Dynes broadening parameter.

A mass enhancement factor of 4–5 is probably typical of optimally doped cuprates. The moderate value of the $2\Delta/k_BT_c$ ratio [33] excludes a very strong electron-phonon coupling as do isotope effect, transport and tunneling experiments.

It is more likely that the mass enhancement factor in the cuprates is mostly due to correlation effects. Several theories of superconductivity in the cuprates consider that it is due to electron-electron interactions. Experimental determination of the mass enhancement factor could be useful for a quantitative test of these theories. Such a discussion is however beyond the scope of this review.

4.6.4 An Example of Moderate Heavy Fermion: $PuCoGa_5$

$PuCoGa_5$ has the highest critical temperature amongst heavy fermions, 18 K. It is considered a moderate heavy fermion because the value of its electronic specific heat

coefficient γ is of the order of 77–95 mJ/mole K^2, compared for instance to UBe_{13} for which it is of the order of 1 J/mole K^2 [34, 35]. $PuCoGa_5$ is of particular interest because it is iso-structural to $CeCoIn_5$, a well researched superconducting heavy fermion for which $\gamma = 350$ mJ/mole K^2 [35].

Daghero et al. [36] studied Au/$PuCoGa_5$ single crystal point contacts having resistances of 6 Ω. The contact size can be estimated to be of at least 100 Å. It is certainly larger than the superconducting coherence length, see below.

In spite of this, Daghero et al. achieved good fits to the BTK theory with a moderate broadening parameter, about one order of magnitude smaller than the gap. For certain contacts the conductance characteristic as shown in Fig. 4.9 had the shape predicted for a d-wave order parameter in a nodal direction as seen in Fig. 4.5. It has a sharp peak at zero bias, with the conductance returning to its normal state value at the gap voltage. The fitted gap value is 5 meV, and the broadening parameter 0.6 meV.

Daghero et al. could follow the temperature dependence of the gap, see Fig. 4.10. It has the general BCS shape, with a sharp onset at T_c. The strong coupling ratio $2\Delta/k_B T_c$ was found to be equal to 6.4, as compared to 4.28 for a weak coupling d-wave superconductor. They analyze their results in terms of the Eliashberg strong coupling theory, which allows to calculate the critical temperature and the gap in terms of a characteristic boson frequency, the electron boson interaction parameter λ, and the renormalized Coulomb interaction parameter μ^*. Since none of these parameters is known a priori, the authors could only arrive at a range of likely values, assuming that $0 < \mu^* < 0.2$. Their conclusion is that $2.2 < \lambda < 3.7$, and

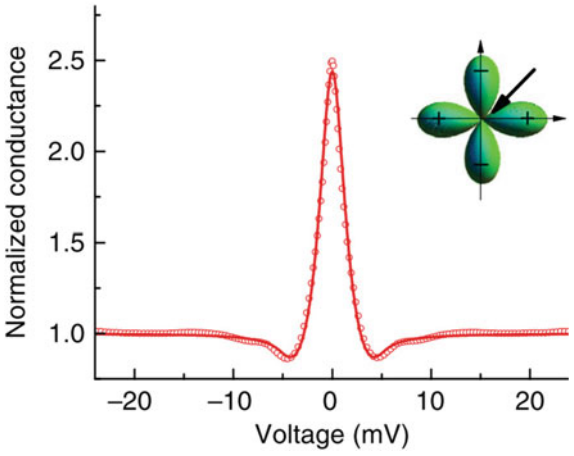

Fig. 4.9 Fit of point contact data obtained on a $PuCoGa_5$ single crystal to the BTK theory for a d-wave order parameter in a nodal direction. The fit parameters are $\Delta = 4.85$ meV and $Z = 0.84$. Note that as predicted by theory the peak height at zero bias is larger than 2, and that there is a slight undershoot below the normal state conductance that ends about at the gap bias. After Daghero et al. [36]

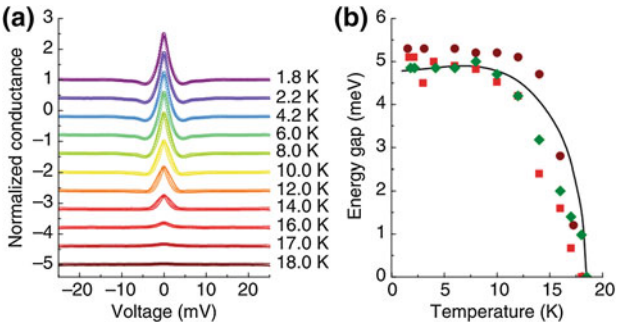

Fig. 4.10 Temperature dependence of Au/ $PuCoGa_5$ point contact characteristics. Note that in **a** the zero bias peak remains sharp up to T_c, and that in **b** the fitted gap has a sharp onset at T_c, as predicted by the BCS/Eliashberg theory. After Daghero et al. [36]

that the characteristic boson frequency is in the range 5.3–8 meV, which would fit a spin fluctuation spectrum.

Using the method described above, it is now possible to obtain directly the value of the mass enhancement parameter and to compare it to the range of values of the electron-boson interaction parameter given by Daghero et al. Using $\Delta = 5$ meV, $Z = 0.84$ and $\xi = 20$ Å (from the value of $H_{c2} = 74$ T given by [34]), we get $\overline{v_F} = 3 \times 10^7$ cm/s and $v_F = 0.53 \times 10^7$ cm/s, for a mass enhancement factor of 5.6 and $\lambda = 4.6$. This is somewhat out of the range of the electron-boson interaction parameter given by Daghero et al., but not by a lot considering that their gap value of 5 meV may be somewhat underestimated as values as high 6.3 meV from other authors have been cited by them.

4.6.5 Strong Heavy Fermions: UBe_{13} and $CeCoIn_5$

The first determination of the gap in UBe_{13} by point contact was performed by Nowack et al. [37]. Below $T_c = 0.9$ K they observed a V shape drop of the dynamical resistance around zero bias, by almost a factor of 3 at the lowest temperature achieved T = 0.53 mK, followed by a flat part beyond roughly 0.300 meV. They estimated the gap value as the half width at mid-height of this peak, and gave $2\Delta/k_B T_c = 10$. In a later work Wälti et al. [38] observed a very sharp conductance peak having a height 10 times the normal state conductance, followed by an undershoot ending up at 0.250 meV. This behavior is roughly what would be expected for a high Z contact to a d-wave superconductor in a nodal direction. Wälti et al. give $2\Delta/k_B T_c = 6$. Neither the Nowack nor the Wälti data can be fitted quantitatively to the BTK theory.

Qualitatively the results of Nowack et al. indicate that a rather high transparency contact is possible. Both sets of data give close gap values. With $Z = 0.3$,

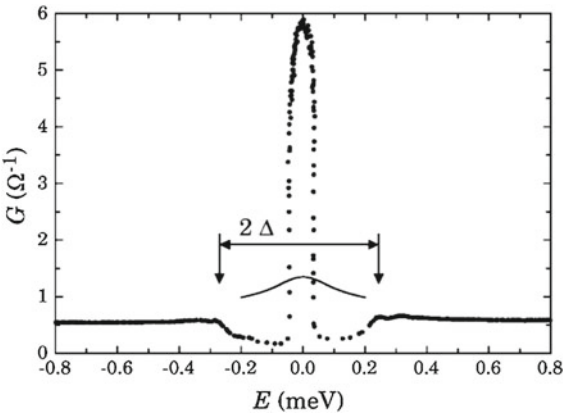

Fig. 4.11 Conductance of a Au/UBe_13 point contact having a normal state resistance of about 2 Ω. The high peak at zero bias and the undershoot at 0.3 meV are in rough agreement with a nodal contact to a *d*-wave superconductor. After Wälti et al. [38]

$\Delta = 0.25$ meV and $\xi = 60$ Å (from $H_{c2} = 7$ T [39]), we calculate a mass enhancement factor of 90.

Although the large electronic heat capacity of UBe_{13} ($\gamma = 1.1$ J/mole K^2) clearly establishes that the mass enhancement factor is large, the heat capacity data is not by itself sufficient to calculate it precisely. This is because in these complex materials the number of free electrons per atom is not known a priori, and must be evaluated from additional data. Stewart has reviewed various methods used in the literature, based on resistivity, upper critical field and heat capacity data, usually making the assumption of a spherical Fermi surface [40]. These various methods give for UBe_{13} mass enhancement factors of up to about 200. In view of the uncertainties involved, the agreement with the result we have obtained here is reasonable and in a sense remarkable since the methods used are so different (Fig. 4.11).

Discovered later the heavy fermion $CeCoIn_5$ has been much researched owing to its relatively high critical temperature $T_c = 2.3$ K. The value of its electronic heat capacity coefficient has been determined to be $\gamma = 35$ mJ/mole K^2 [41]. Park et al. [42] reported detailed measurements on Au/$CeCoIn_5$ single crystal point contacts down to 400 mK, having normal state resistances of about 1 Ω. They estimated the contact size to be at most 460 Å, and established that it is certainly smaller than the elastic and inelastic mean free paths, respectively 800 and 6,500 Å (at least). Therefore they rightly claim that these contacts are in the Sharvin limit, so that their characteristics should not be affected by heating effects. However the contact size is substantially larger than the coherence length values given by Thompson [43] $\xi_{ab} = 82$ Å and $\xi_c = 53$ Å. ξ_c is presumably the relevant length scale since the point contacts were oriented along the *c* axis of the crystal. Since this coherence length is almost one order of magnitude smaller than the contact size, proximity effects at the contact cannot be excluded.

Figure 4.12 reproduces the results of Park et al. It shows the temperature dependence of the gap and of the broadening parameter resulting from a fit to the data assuming an *s*-wave order parameter. At the lowest temperature Δ approaches

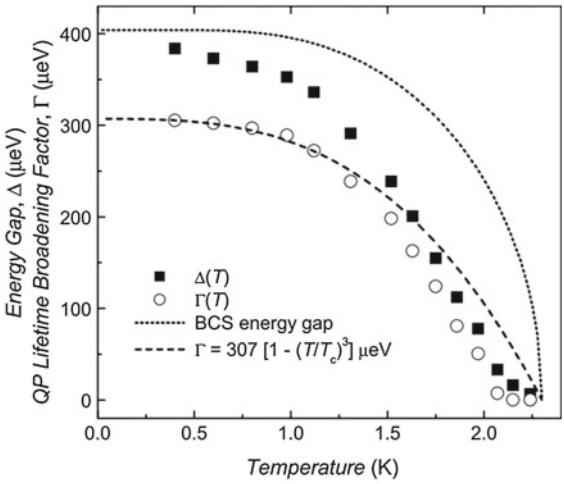

Fig. 4.12 The gap Δ and the broadening parameter Γ of point contact data to $CeCoIn_5$ fitted to an *s*-wave order parameter. After Park et al. [44]

the value 0.4 meV and Γ the value 0.3 meV. Both have an anomalous temperature dependence, Δ rising much too slowly below T_c and Γ approaching zero at T_c, while it should be temperature independent. The fits use a temperature independent $Z = 0.3$. Fits assuming a *d*-wave order parameter are preferred by the authors, and give a slightly higher value $\Delta = 0.46$ meV.

The large contact size compared to the coherence length as well as the slow rise of the gap below T_c makes one consider the possibility of a proximity effect that reduces the measured gap value compared to the bulk. It may also induce a surface *s*-wave component, which would explain the difficulty the authors had in differentiating between *s*-wave and *d*-wave symmetries fits, see Kohen et al. [19]. Recent STM measurements have indeed given a somewhat larger gap value $\Delta = 0.55$ meV and have confirmed that the order parameter symmetry is likely to be *d*-wave [45].

Taking $\Delta = 0.55$ meV, $\xi = 53$ Å and $\overline{v_F} = 8 \times 10^7$ cm/s from $Z = 0.3$, we get for the mass enhancement factor the value of 35. This is about 5–6 times larger than its value for $PuCoGa_5$ and 3 times smaller than for UBe_{13}, values that are in line with the respective electronic heat capacity coefficients of these heavy fermions.

4.6.6 Pnictides

Point contact results on pnictides have been recently reviewed by Daghero et al. [46]. An enhanced conductance at zero bias is generally observed, with a double peak for the 1111 (like SmFeAsO) and 122 (like BaFeAs) compounds indicating in both cases a *s*-wave symmetry order parameter. Fits to the BTK theory often give two distinct gaps, similar to MgB_2.

For instance, for SmFeAs(OF) compounds having critical temperatures of up to 52 K, Z parameters of about 0.5 have been shown to fit the data, with a low gap around 6 meV and a large gap around 15–18 meV. The upper critical field is anisotropic, the extrapolation of the lower one to $T = 0$ (corresponding to the (*ab*) orientation) being of the order of 100 T. We associate the lower gap to the larger coherence length (lower critical field), and take $\Delta = 7$ meV, $\xi = 20$ Å, $Z = 0.5$ and obtain for the mass enhancement factor a value of about 5. This is similar to the values obtained for $PuGaIn_5$ and YBCO.

4.7 Spin Active Interfaces

An interesting area of investigation that has been barely touched upon is that of nano-scale contacts between a conventional superconductor and a spin-active magnetic material. While a contact between a superconductor and a homogeneous ferromagnet has for main effect to destroy superconductivity as soon as the exchange field is larger than the superconducting gap, more interesting effects can take place if the magnetization of the magnetic material can be made in some way to be inhomogeneous near the interface. In that case it has been predicted that an order parameter having an equal-spin *p*-wave component can be induced in the superconductor near the interface [47].

The conductance of nano-scale Co/CoO/In contacts [48] having resistances of the order of the universal resistance (from 7 to 13 kΩ) is shown in Fig. 4.13. An enhanced ASJ conductance is seen at low bias in the least resistive contact J24. It must therefore be composed of a very small number of quantum channels, likely

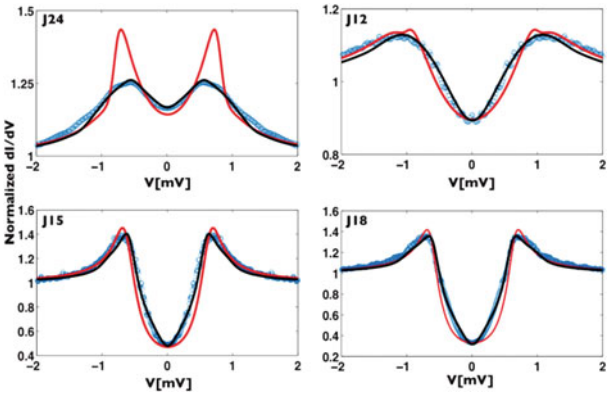

Fig. 4.13 Conductance of Co/CoO/In nano-scale contacts having normal state resistances of the order of the universal resistance. A *p*-wave component of the order parameter gives the characteristics their V shape, best seen in sample J18. Fits to a pure *s*-wave order parameter give instead the usual U shape (*red lines*). After Hacohen-Gourgy et al. [48]

pinholes in the CoO interface layer. Fits of the data have been made to a pure *s*-wave order parameter (red lines) and to a mixed *s* and *p* order parameter (dark line). Nodes in the *p* component give the characteristics of V shape, most clearly visible in the higher resistances contacts J18 and J15 for which the fitted transparency parameter Z is about 2 (poorly transparent interface). The combination Co/CoO provides the magnetic inhomogeneity that allows the presence of a *p*-wave component of the order parameter at the interface.

4.8 Conclusions

In spite of some uncertainties mainly due to a contact size often somewhat larger than the coherence length, it appears that reliable values of the gap and of the barrier parameter can be safely obtained from conductance data of point contacts to practically every superconductor, going from simple metals to heavy fermions and related materials. The mass enhancement factor can then be derived using coherence length values obtained from critical field measurements. In addition, point contact measurements provide reliable information on the symmetry of the order parameter.

For metals such as Nb the mass enhancement factor is essentially due to the electron-phonon interaction, which so far could not be established from tunneling experiments using the McMillan and Rowell inversion method, because of the lack of sufficiently high quality tunnel junctions.

The high effective transparency of contacts between noble metals and heavy fermions, as determined by fits to the BTK theory, is well explained by the theory presented in Sect. 4.5, for mass enhancement factors ranging from moderate to very high values. This theory allows one to obtain the mass enhancement factor for heavy fermions. Good agreement with values derived from electronic heat capacity measurement on heavy fermions validates this method. It can then be used for cases where low temperature heat capacity measurements are not available, because the normal state cannot be restored due to a very high critical field. In this way, the mass enhancement factor could be determined for the high Tc cuprates, for the heavy fermion PuCoIn5 and for the pnictides. These values should be useful for a quantitative comparison between theories and experiments concerning the normal and superconducting states in these strongly correlated materials.

Acknowledgments I am indebted to Philippe Nozières for many illuminating conversations on boundary conditions with heavy fermions and their application to point contact spectroscopy. I also wish to thank warmly Nimrod Bachar for his careful reading of the manuscript.

References

1. Y. Sharvin, Zh. Eksp. Teor. Fiz. **48**, 984 (1965) [Sov. Phys. JETP **21**, 655 (1965)]
2. A. Andreev, Zh. Eksp. Teor. Fiz. **46**, 1823 (1964) [Sov. Phys. JETP **19**, 1228 (1964)]
3. P. de Gennes, D. Saint-James, Phys. Lett. **4**(2), 151 (1963). doi: 10.1016/0031-9163(63)90148-3
4. D. Saint-James, J. Phys. Fr. **25**(10), 899 (1964). doi:10.1051/jphys:019640025010089900
5. G. Deutscher, Rev. Mod. Phys. **77**, 109 (2005). doi:10.1103/RevModPhys.77.109
6. J. Pankove, Phys. Lett. **21**(4), 406 (1966). doi:10.1016/0031-9163(66)90506-3
7. A. Zaitsev, Sov. Phys. JETP **51**, 111 (1980)
8. G.E. Blonder, M. Tinkham, T.M. Klapwijk, Phys. Rev. B **25**, 4515 (1982). doi:10.1103/PhysRevB.25.4515
9. I. Giaever, Phys. Rev. Lett. **5**, 147 (1960). doi:10.1103/PhysRevLett.5.147
10. G. Deutscher, P. Nozières, Phys. Rev. B **50**, 13557 (1994). doi:10.1103/PhysRevB.50.13557
11. G. Wexler, Proc. Phys. Soc. **89**(4), 927 (1966)
12. Y.G. Naidyuk, I.K. Yanson, J. Phys. Condens. Matter **10**(40), 8905 (1998)
13. G.E. Blonder, M. Tinkham, Phys. Rev. B **27**, 112 (1983). doi:10.1103/PhysRevB.27.112
14. B. Almog, S. Hacohen-Gourgy, A. Tsukernik, G. Deutscher, Phys. Rev. B **84**, 054514 (2011). doi:10.1103/PhysRevB.84.054514
15. C. Muller, J. van Ruitenbeek, L. de Jongh, Phys. C Supercond. **191**(3–4), 485 (1992). doi:10.1016/0921-4534(92)90947-B
16. Y.G. Naidyuk, K. Gloos, A.A. Menovsky, J. Phys. Condens. Matter **9**(29), 6279 (1997)
17. G. Deutscher, P.G. de Gennes, *Proximity Effects in Superconductivity* (Dekker, New York, 1969)
18. Y. Tanaka, S. Kashiwaya, Phys. Rev. Lett. **74**, 3451 (1995). doi:10.1103/PhysRevLett.74.3451
19. A. Kohen, G. Leibovitch, G. Deutscher, Phys. Rev. Lett. **90**, 207005 (2003). doi:10.1103/PhysRevLett.90.207005
20. C.R. Hu, Phys. Rev. Lett. **72**, 1526 (1994). doi:10.1103/PhysRevLett.72.1526
21. N. Hass, D. Ilzycer, G. Deutscher, G. Desgardin, I. Monot, M. Weger, J. Supercond. **5**(2), 191 (1992). doi:10.1007/BF00618066
22. J.E. Kloeppel, Point-Contact Spectroscopy Deepens Mystery Of Heavy-Fermion Superconductors.
23. W.L. McMillan, J.M. Rowell, Phys. Rev. Lett. **14**, 108 (1965). doi:10.1103/PhysRevLett.14.108
24. J. Bostock, V. Diadiuk, W.N. Cheung, K.H. Lo, R.M. Rose, M.L.A. Mac Vicar, Phys. Rev. Lett. **36**, 603 (1976). doi:10.1103/PhysRevLett.36.603
25. H.R. Kerchner, D.K. Christen, S.T. Sekula, Phys. Rev. B **24**, 1200 (1981). doi:10.1103/PhysRevB.24.1200
26. D. Daghero, R.S. Gonnelli, Supercond. Sci. Technol. **23**(4), 043001 (2010). http://stacks.iop.org/0953-2048/23/i=4/a=043001
27. P. Szabó, P. Samuely, J. Kačmarčík, T. Klein, J. Marcus, D. Fruchart, S. Miraglia, C. Marcenat, A. Jansen, Phys. Rev. Lett. **87**(13), 137005 (2001). doi:10.1103/PhysRevLett.87.137005
28. A. Kohen, G. Deutscher, Phys. Rev. B **64**, 060506 (2001). doi:10.1103/PhysRevB.64.060506
29. F. Giubileo, D. Roditchev, W. Sacks, R. Lamy, D.X. Thanh, J. Klein, S. Miraglia, D. Fruchart, J. Marcus, P. Monod, Phys. Rev. Lett. **87**, 177008 (2001). doi:10.1103/PhysRevLett.87.177008
30. P.B. Allen, R.C. Dynes, Phys. Rev. B **12**, 905 (1975). doi:10.1103/PhysRevB.12.905. http://link.aps.org/doi/10.1103/PhysRevB.12.905
31. E.J. Nicol, J.P. Carbotte, Phys. Rev. B **71**, 054501 (2005). doi:10.1103/PhysRevB.71.054501
32. G. Deutscher, N. Hass, Y. Yagil, A. Revcolevschi, G. Dhalenne, J. Supercond. **7**(2), 371 (1994). doi:10.1007/BF00724571
33. G. Deutscher, Nature **397**, 410 (1999). doi:10.1038/17075
34. J.L. Sarrao, L.A. Morales, J.D. Thompson, B.L. Scott, G.R. Stewart, F. Wastin, J. Rebizant, P. Boulet, E. Colineau, G.H. Lander, Nature **420**(6913), 297 (2002). doi:10.1038/nature01212

35. E.D. Bauer, J.D. Thompson, J.L. Sarrao, L.A. Morales, F. Wastin, J. Rebizant, J.C. Griveau, P. Javorsky, P. Boulet, E. Colineau, G.H. Lander, G.R. Stewart, Phys. Rev. Lett. **93**, 147005 (2004). doi:10.1103/PhysRevLett.93.147005
36. D. Daghero, M. Tortello, G.A. Ummarino, J.C. Griveau, E. Colineau, R. Eloirdi, A.B. Shick, J. Kolorenc, A.I. Lichtenstein, R. Caciuffo, Nat. commun. **3**, 786 (2012). doi:10.1038/ncomms1785
37. A. Nowack, A. Heinz, F. Oster, D. Wohlleben, G. Güntherodt, Z. Fisk, A. Menovsky, Phys. Rev. B **36**, 2436 (1987). doi:10.1103/PhysRevB.36.2436
38. C. Wälti, H.R. Ott, Z. Fisk, J.L. Smith, Phys. Rev. Lett. **84**, 5616 (2000). doi:10.1103/PhysRevLett.84.5616. http://link.aps.org/doi/10.1103/PhysRevLett.84.5616
39. Y. Shimizu, Y. Haga, K. Tenya, T. Yanagisawa, H. Hidaka, H. Amitsuka, J. Phys. Conf. Ser. **391**(1), 012065 (2012)
40. G.R. Stewart, Rev. Mod. Phys. **56**, 755 (1984). doi:10.1103/RevModPhys.56.755
41. C. Petrovic, P.G. Pagliuso, M.F. Hundley, R. Movshovich, J.L. Sarrao, J.D. Thompson, Z. Fisk, P. Monthoux, J. Phys. Condens. Matter **13**(17), L337 (2001)
42. W.K. Park, L.H. Greene, J.L. Sarrao, J.D. Thompson, Phys. Rev. B **72**, 052509 (2005). doi:10.1103/PhysRevB.72.052509
43. J. Thompson, M. Nicklas, A. Bianchi, R. Movshovich, A. Llobet, W. Bao, A. Malinowski, M. Hundley, N. Moreno, P. Pagliuso, J. Sarrao, S. Nakatsuji, Z. Fisk, R. Borth, E. Lengyel, N. Oeschler, G. Sparn, F. Steglich, Phys. B Condens. Matter 329-333, Part 2(0), 446 (2003). doi:10.1016/S0921-4526(02)01987-7
44. W.K. Park, L.H. Greene, J.L. Sarrao, J.D. Thompson, Proc. SPIE **5932**, 59321Q (2005). doi:10.1117/12.622251
45. M.P. Allan, F. Massee, D.K. Morr, J. van Dyke, A. Rost, A.P. Mackenzie, C. Petrovic, J.C. Davis, arxiv:1303.4416v1 pp. 1–14 (2013)
46. D. Daghero, M. Tortello, G.A. Ummarino, R.S. Gonnelli, Rep. Prog. Phys. **74**(12), 124509 (2011)
47. F. Bergeret, A. Volkov, K. Efetov, Appl. Phys. A **89**(3), 599 (2007). doi:10.1007/s00339-007-4184-5
48. S. Hacohen-Gourgy, B. Almog, G. Deutscher, Phys. Rev. B **84**(1), 014532 (2011). doi:10.1103/PhysRevB.84.014532

Chapter 5
Quantum Oscillation Measurements Applied to Strongly Correlated Electron Systems

Stephen R. Julian

Abstract The de Haas-van Alphen effect and related quantum oscillation measurements are powerful tools for studying the behaviour of electron quasiparticles in conducting strongly correlated electron systems. Using them, one can: measure the size and shape of Fermi surfaces; determine quasiparticle effective masses on a Fermi-surface-specific basis; determine mean-free paths on a Fermi-surface-specific basis; and obtain information about quasiparticle g-factors. This chapter first gives an outline of the theory of quantum oscillations, and then reviews experimental methods, focusing on aspects that are of particular relevance to strongly correlated electron systems. The chapter concludes by describing, as a 'case study', quantum oscillation measurements on the p-wave superconductor Sr_2RuO_4, a material that is of great current interest, and that illustrates many aspects of quantum oscillation measurements that are applicable across a broad range of strongly correlated electron systems.

5.1 Introduction

L.D. Landau predicted in 1930 that the conduction electrons in a metal can, in principle, show a diamagnetism that oscillates as a function of applied magnetic field [29]. Almost simultaneously, de Haas and Van Alphen first observed such oscillations in the magnetism of bismuth [14]. Over the subsequent decades the investigation of Fermi surface topologies with the de Haas-van Alphen (dHvA) effect and related "quantum oscillation" techniques, notably by David Shoenberg and his collaborators, was primarily responsible for our modern conception of the Fermi surface as a geometrical object in momentum space.

By the 1970s, however, dHvA measurements were regarded as somewhat routine, an experimental tool primarily useful for confirming the accuracy of computer generated band-structures of the elements. There remained, however, some mysteries

S.R. Julian (✉)
Department of Physics, University of Toronto, 60 St. George Street,
Toronto, ON M5S 1A7, Canada
e-mail: sjulian@physics.utoronto.ca

A. Avella and F. Mancini (eds.), *Strongly Correlated Systems*,
Springer Series in Solid-State Sciences 180, DOI 10.1007/978-3-662-44133-6_5

associated with magnetic metals, and the advent of strongly correlated electron systems in the form of heavy fermions [58], followed by superconducting oxides, led to a renaissance of the technique. Its unique power to measure not just Fermi surfaces—which turned out to be much less predictable in these new materials than in the elemental metals—but also many-body mass enhancements reaching up to 100 times the bare electron mass [59] played a key role in our developing understanding of strongly correlated systems. In recent years the technique has continued to have a high impact in such diverse areas as cuprate superconductivity [15] and graphene [66].

The key to understanding strongly correlated electron matter is to understand the many-body quantum states of the electrons. Essentially all of the theoretical work in the field is devoted to theories of electronic states that lie at or beyond the extreme limits of the standard approximations that are employed to describe conventional metals and magnetic insulators. For the experimentalist, there are a number of probes of electronic structure available, ranging from macroscopic probes such as resistivity, Hall effect, specific heat, magnetic susceptibility, optical conductivity, etc., to microscopic probes of k-space states, such as Angle Resolved Photoemission (ARPES) and Quasiparticle Interference (QPI) using scanning tunneling microscopy, techniques described in Chaps. 2 and 3 of this volume. This chapter is devoted to a technique—the de Haas-van Alphen effect—that plays an essential role in elucidating the properties of quasiparticles at the Fermi surface in strongly correlated electron metals. An unusual aspect of the dHvA effect is that it straddles the macroscopic and microscopic: one measures bulk properties—the magnetization in the de Haas-van Alphen effect, the resistivity in the Shubnikov-de Haas effect, etc.—yet the information that is obtained is microscopic in k-space.

The dHvA effect is important because it can be employed in conditions where others methods cannot, such as at millikelvin temperatures, and in very high magnetic fields, and moreover it probes some quantities, such as the effective mass of quasiparticles, with much greater accuracy than can be achieved by other techniques. In strongly correlated electron systems having complex, three-dimensional Fermi surfaces, quantum oscillations have proven to be more useful for mapping the Fermi surface than surface based probes of electronic structure, such as ARPES, which are most reliable when applied to quasi-two-dimensional systems.

On the other hand, quantum oscillation measurements are limited to low temperatures, one obtains information only about states in the immediate vicinity of the Fermi energy, and in general one requires very high quality crystals in order to observe the oscillations.

In the first part of this chapter we outline the theory of the dHvA effect, emphasizing that it can be used to test Fermi liquid theory, and that in principle quantum oscillations can be observed in non-Fermi-liquids. We motivate the discussion of each theoretical capability by listing some significant results, on a variety of strongly correlated electron systems, that have been obtained using quantum oscillation measurements.

We follow with a brief overview of experimental methods. These have developed rapidly in the past decade with the development of ever-higher-field pulsed magnets with increasingly sensitive detection systems.

We conclude by showing how these methods have been employed to study one particular material, Sr_2RuO_4. This p-wave superconductor is a somewhat rare example in which the electronic structure can be understood in fairly simple terms, and in which there is good agreement between the theoretical and experimental Fermi surfaces. There is also good agreement between measured bulk properties such as the specific heat, electrical conductivity and Hall coefficient, and estimates based on quantum oscillation measurements of quasiparticle properties such as effective masses, mean-free-paths and Fermi surface size.

5.2 Theory of the de Haas-van Alphen Effect

In this section we will gradually build up the theory of quantum oscillations, beginning with a two-dimensional non-interacting Fermi gas at $T = 0$ K, and ending with a theory that can be applied to three-dimensional non-Fermi-liquids with spin-dependent masses at arbitrary temperature.

5.2.1 Landau Quantization and the Onsager Relation

In a quantum oscillation measurement some property, such as the diamagnetism of the conduction electrons, or the resistivity, oscillates as a function of applied magnetic field B. The oscillations are periodic in $1/B$, with frequency F, and in this section we sketch the derivation of the famous Onsager result, $F = \hbar\mathcal{A}/2\pi e$, in which $\mathcal{A}$ is an extremal area of the Fermi surface.

Through the Onsager relation, the three-dimensional shape of a Fermi surface can be determined in detail, and this capability has been important to our understanding of strongly correlated electron systems. For example, in UPt_3 [44, 59] dHvA measurements showed that local-density-approximation electronic-structure calculations can give a reasonably accurate picture of the Fermi surface of heavy fermion metals. This permits dHvA measurements to address a central issue in heavy fermion physics, which is whether the f-electrons are 'localized' or 'itinerant', that is: do they contribute to the Fermi volume? Early work suggested that in magnetically ordered systems the f-electrons are localized [32, 50], while in paramagnetic heavy fermions they contribute to the Fermi volume [2, 32]. Recently, in a classic paper, [56], it was shown that in $CeRhIn_5$ the Fermi volume jumps from f-localized to f-itinerant when the ground state changes from antiferromagnetic to paramagnetic as a function of applied pressure. Similarly, quantum oscillations reveal that in the cuprates there is a drastic reconstruction of the Fermi surface between the underdoped and the overdoped sides of the phase diagram [15, 61]. In the p-wave superconductor Sr_2RuO_4,

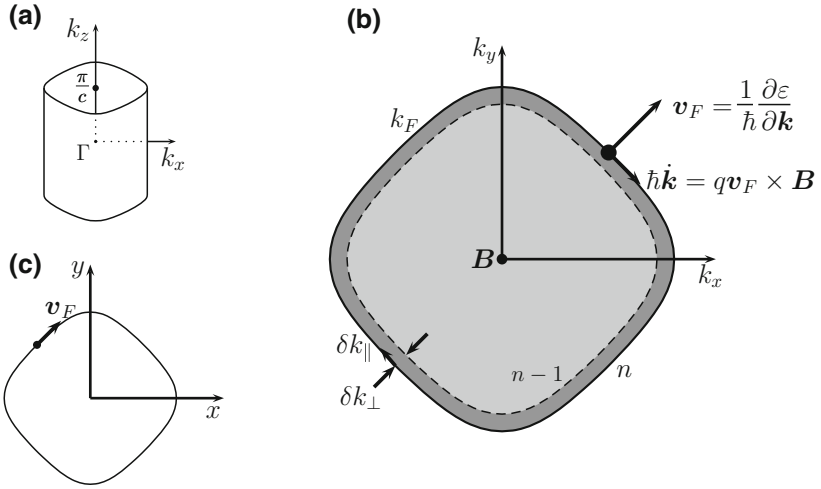

Fig. 5.1 The semiclassical orbit of a wave packet on a two-dimensional Fermi surface, in the presence of an applied field $\boldsymbol{B} = B\hat{z}$. **a** shows a Fermi surface having no dispersion along the c-axis. **b** is a top view of a slice of k-space perpendicular to $\boldsymbol{B}$. The *shaded region* shows occupied states, and the *dark region* shows the area of k-space between two adjacent Landau levels. The *large dot* indicates the center of a semi-classical wave-packet located at the Fermi surface. **c** shows a cyclotron orbit of the semiclassical packet in real-space, with x and y measured from the center of the orbit. (Note that the Landau levels are highly degenerate, and the classical orbit shown in (**c**) is just one of many possible orbits that can be constructed [11].)

which we discuss in detail in Sect. 5.4, dHvA measurements can be used to fix the parameters of a tight-binding fit to the electronic structure. In general this can place strong constraints on model Hamiltonians for a strongly correlated electron system, providing important input to theories of exotic electronic states. In the iron-pnictide superconductors, quantum oscillation measurements have been very prominent in this role [10].

To simplify subsequent mathematics, it is useful to start by considering an energy band with no dispersion along the z-axis, such as would arise in a quasi-two-dimensional metal composed of decoupled two-dimensional sheets. The Fermi surface then consists of tubes parallel to the z-axis, such as that shown in Fig. 5.1a.

A semi-classical wave-packet on a two-dimensional Fermi surface, moving under the influence of a uniform magnetic field as shown in Fig. 5.1, moves with velocity $\boldsymbol{v}_F(\mathrm{k})$ and has equation of motion

$$\hbar\dot{\boldsymbol{k}} = -e\boldsymbol{v}_F(\boldsymbol{k}) \times \boldsymbol{B}, \quad \text{where } \boldsymbol{v}_F(\boldsymbol{k}) = \frac{1}{\hbar}\frac{\partial \varepsilon(\boldsymbol{k})}{\partial \boldsymbol{k}}, \tag{5.1}$$

and $\hbar\boldsymbol{k}$ is the crystal momentum. Since the Lorentz force is perpendicular to the gradient of the energy, the wave-packet moves on a surface of constant energy, which

in this case is the Fermi surface, so in the absence of scattering the wave-packet will orbit periodically on the Fermi surface.

The resulting semiclassical orbit is quantized according to the Bohr-Sommerfeld rule (for details see [57], pp. 32–33)

$$\oint \boldsymbol{p} \,.\, d\boldsymbol{r} = (n + \gamma)\, 2\pi\hbar \tag{5.2}$$

where n is an integer, $\boldsymbol{p} = (\hat{\boldsymbol{p}} - e\boldsymbol{A})$ with $\hat{\boldsymbol{p}}$ the canonical momentum, $\nabla \times \boldsymbol{A} = \boldsymbol{B}$, and γ is a constant phase factor. Integrating (5.1) with respect to time to relate the real and $\boldsymbol{k}$-space orbits then leads to the famous result that the magnetic flux enclosed by the real-space orbit is quantized: $\Phi = B_z a_r = (n + \gamma)2\pi\hbar/e$. The area of the k-space orbit is related to that of the real-space orbit by $a_r = a_k\hbar^2/e^2B^2$, thus we finally obtain

$$a_k = (n + \gamma)\frac{2\pi e B}{\hbar}, \tag{5.3}$$

which tells us that the area of the k-space orbits is quantized. In a non-interacting, free-electron system, where the area is πk^2 and the energy is $\hbar^2k^2/2m$, this gives the more familiar result that the energy is quantized in units of $\hbar\omega_c$, where $\omega_c = eB/m$ is the classical cyclotron frequency.

The k-space area between neighbouring Landau orbits can be simply found by considering the difference in area swept out by electrons orbiting on adjacent orbits labelled n and $n - 1$ in Fig. 5.1b. The element of area δA between orbits at $\mathbf{k}$ and $\mathbf{k} + \delta\mathbf{k}$ can be calculated by writing (5.1) as

$$\hbar\,\frac{\delta k_\perp}{\delta t} \;=\; \frac{e}{\hbar}\,\frac{\delta\varepsilon}{\delta k_\parallel}\;B, \tag{5.4}$$

where $\delta k_\perp$ and $\delta k_\parallel$ are defined in Fig. 5.1, so that

$$\delta A \;=\; \delta k_\perp\,\delta k_\parallel \;=\; \frac{eB}{\hbar^2}\,\delta\varepsilon\,\delta t. \tag{5.5}$$

Integrating δA around a single orbit, with the period and the difference in energy between adjacent Landau tubes $\delta t = \tau = 2\pi/\omega_c$ and $\delta\varepsilon = \hbar\omega_c$, gives

$$A_n - A_{n-1} = \frac{2\pi e B}{\hbar}. \tag{5.6}$$

The angular velocity of the quasiparticle is of the classical form $\omega_c = eB/m$, however in a crystal we need to use $\omega_c = eB/m^*(\varepsilon)$, with renormalised effective mass m^* defined from the orbital period:

$$\tau \;=\; \frac{2\pi}{\omega_c} \;=\; \frac{\hbar^2}{eB}\,\frac{\partial A(\varepsilon)}{\partial\varepsilon} \;\;\Rightarrow\;\; m^*(\varepsilon) \;=\; \frac{\hbar^2}{2\pi}\,\frac{\partial A(\varepsilon)}{\partial\varepsilon}. \tag{5.7}$$

Consider now the passage of successive Landau levels through the Fermi surface of area $\mathcal{A}$ as the magnitude of the magnetic field, B_z, changes. If at a given field, B_n say, level n coincides with the Fermi energy so that, from (5.3), $B_n = \hbar\mathcal{A}/2\pi e(n+\gamma)$, then level $(n-1)$ will have the same area when the field has increased to $B_{n-1} = \hbar\mathcal{A}/2\pi e(n-1+\gamma)$. From this we see that

$$\Delta\left(\frac{1}{B}\right) \equiv \frac{1}{B_n} - \frac{1}{B_{n-1}} = \frac{2\pi e}{\hbar\mathcal{A}}. \tag{5.8}$$

At $T = 0$ K, the Fermi function dictates that only those states with energy less than the Fermi energy can be occupied. Thus, with increasing magnetic field, as each Landau level crosses the Fermi energy it will empty into states below ε_F. The passage of consecutive Landau levels through ε_F will cause the density of states at the Fermi surface to vary periodically as a function of $1/B$. Consequently, all properties of the system dependent on the density of states, such as the diamagnetic moment of the conduction electrons in the de Haas-van Alphen effect, will oscillate. The oscillations are periodic in $1/B$, with corresponding frequency given by the Onsager equation

$$F = \frac{\hbar\mathcal{A}}{2\pi e}. \tag{5.9}$$

5.2.2 The Effect of Temperature and Scattering

Another powerful capability of quantum ocillation measurements is the determination of quasiparticle effective masses and scattering rates on a Fermi surface specific basis. When applied to heavy fermion systems, such measurements have revealed that, although LDA band-structure calculations can predict Fermi surface topologies that are approximately correct, they typically predict effective masses that are much too small [59], because they fail to account for many-body mass enhancements. In some systems, the mass enhancement is found to be radically different on different sheets of the Fermi surface [2, 32], and even to vary by a large amount over a single sheet of Fermi surface [16], information which cannot be obtained from bulk measurements such as specific heat which average over all of the Fermi surfaces in a material. In other cases, the mass enhancement at high magnetic field has been found to be spin-dependent [40, 55]. In strongly correlated oxide metals, Fermi-surface-specific mass enhancements again provide an important guide to the nature of many-body effects, e.g. [35].

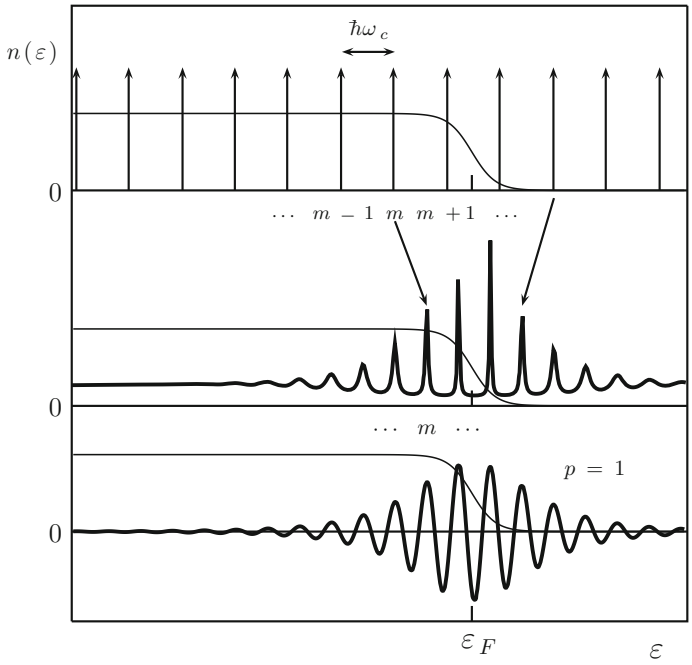

Fig. 5.2 The effect of electron-electron interactions and scattering on quantum oscillations. The occupancy of the Landau levels is determined by the Fermi-Dirac function. The *top panel* shows this function superposed on the Landau levels of a Fermi gas, which are a set of equally spaced delta functions. When interactions are turned on, each Landau level is shifted by the real part of the self-energy, and broadened to a Lorentzian by the imaginary part of the self energy (*middle panel*), as described in the text. The set of Lorentzians can be analyzed into "harmonics": the *bottom panel* shows the $p = 1$ term. Integrating the product of this term with the Fermi function gives the $p = 1$ term in (5.17)

Here we give a simplified, intuitive, derivation of the temperature dependence of the quantum oscillation amplitude that goes beyond the standard textbook treatment to allow for both Fermi-liquid and weakly non-Fermi-liquid states [18, 42]. The main steps in the calculation are illustrated in Fig. 5.2.

We start from a two-dimensional Fermi gas at constant chemical potential in an applied magnetic field, for which the electrons condense onto Landau levels with energies $(n + 1/2)\hbar\omega_c + \gamma$, where n is an integer, $\omega_c = eB/m_e$, and γ is a constant phase factor [30]. The Landau levels are shown, superposed on the Fermi-Dirac distribution function, in the top panel of Fig. 5.2. As the magnetic field increases, $\hbar\omega_c$ increases and successive Landau levels cross the Fermi energy. We calculate the temperature dependence of the electron number N for the energy band of interest at constant chemical potential which for the Fermi gas is:

$$N = D(B) \int_0^\infty d\varepsilon \, \frac{\sum_{n=0}^{\infty} \delta(\varepsilon - (n+1/2)\hbar\omega_c - \gamma)}{e^{(\varepsilon-\mu)/k_BT} + 1}, \tag{5.10}$$

where $D(B)$, the degeneracy per Landau level [57], does not enter into the temperature dependence.

The effect of electron-electron interactions is to shift each Landau level by the real part of the self-energy, and broaden it by the imaginary part. The sum over delta functions becomes a sum over Lorentzians,

$$N = \frac{D(B)}{\pi} \int_0^\infty d\varepsilon \, \frac{1}{e^{(\varepsilon-\mu)/k_BT} + 1} \times \sum_{n=0}^{\infty} \frac{-\Sigma_n''(\varepsilon)}{(\varepsilon - (n+1/2)\hbar\omega_c - \gamma - \Sigma_n'(\varepsilon))^2 + \Sigma_n''(\varepsilon)^2}. \tag{5.11}$$

This equation is illustrated in the middle panel of Fig. 5.2 where we have assumed a Fermi liquid state so that the real part of the self energy varies as $\Sigma(\varepsilon) \propto |\varepsilon - \varepsilon_F|$ and the imaginary part as $\Sigma''(\varepsilon) \propto -(\varepsilon - \varepsilon_F)^2$. The sum over Lorentzians is next re-expressed as a sum over their Fourier transforms:

$$\mathrm{Re} \int_0^\infty d\tau \sum_{n=0}^{\infty} e^{i(\varepsilon-(n+1/2)\hbar\omega_c-\gamma-\Sigma_n'(\varepsilon))\tau+\Sigma_n''(\varepsilon)\tau}. \tag{5.12}$$

Since $\sum_n (e^{-i\hbar\omega_c\tau})^n = \sum_p \delta(\tau - 2p\pi/\hbar\omega_c)$ where the p's are integers, the integral over τ can be carried out to obtain

$$N \propto \mathrm{Re} \int_0^\infty d\varepsilon \, \frac{\sum_{p=0}^{\infty} e^{i(\varepsilon-\hbar\omega_c/2-\gamma-\Sigma'(\varepsilon)-i\Sigma''(\varepsilon))2p\pi/\hbar\omega_c}}{e^{(\varepsilon-\mu)/k_BT} + 1}. \tag{5.13}$$

In Fig. 5.2, at energies far from ε_F, the Landau levels are broadened out of existence by $\Sigma''(\varepsilon)$, thus distinct Landau levels are only identifiable in the vicinity of $\varepsilon_F = \mu$.

This means that the oscillatory terms in the sum (those with $p > 0$) vanish everywhere except very close to ε_F, as shown in the lower panel of Fig. 5.2, allowing the lower limit of integration to be extended to $-\infty$. Each integral in the sum (except $p = 0$, which is not of interest) can then be evaluated by contour integration. From Cauchy's theorem, this corresponds to evaluating the numerator at the poles of the Fermi function, $(\varepsilon - \mu) = i\omega_n = i(2n+1)\pi k_BT$, which gives

$$N \propto \mathrm{Re} \sum_{p,\omega_m} (-1)^p \exp\left[\frac{2p\pi i}{\hbar\omega_c}\{\mu + i\omega_m - \Sigma(i\omega_m) - \gamma\}\right]. \tag{5.14}$$

Thus, to within some constants, the oscillatory part of the pth harmonic can be expressed as

$$\sum_{\omega_m} (-1)^p \, \mathrm{e}^{-\frac{2p\pi}{\hbar\omega_c}\{\omega_m - \Sigma''(i\omega_m)\}} \cos\left[\frac{2p\pi}{\hbar\omega_c}(\mu - \Sigma'(i\omega_m) - \gamma)\right]. \tag{5.15}$$

This corresponds to equation 58 of [62], which gives a more rigorous, but abstract, derivation that includes the effect of a three-dimensional band structure—in the presence of a lattice the self-energy in this formula becomes an average around the quasiparticle orbit, and the bare electron mass in ω_c, m_e, is replaced by m_b, the average of the band mass around the quasiparticle orbit.

The cosine term in (5.15) produces the oscillations. It is normal to expand the self-energy around the Fermi energy, in which case $\Sigma'(i\omega_m) = 0$, and the cosine term may be brought in front of the sum over ω_m. At low temperature, $\mu = \varepsilon_F$ and the argument of the cosine function can be cast into the familiar form for quantum oscillations. Consider for example the simple case of a cylindrical Fermi surface, for which $\varepsilon_F/\hbar\omega_c = (\hbar^2 k_F^2/2m^*)/(\hbar eB/m^*) = (\hbar\pi k_F^2/2\pi e)/B = \hbar\mathcal{A}/2\pi eB$, so that the oscillatory term can be written

$$\cos\left(2\pi p\frac{\hbar\mathcal{A}}{2\pi eB} + \phi\right) = \cos\left(2\pi p\frac{F}{B} + \phi\right), \tag{5.16}$$

where ϕ is a phase factor that is independent of B to a good approximation, and F is the Onsager frequency derived in the previous section.

Our interest here is in the non-oscillatory part of (5.15). These are damping terms that affect the amplitude of the oscillations, so we write

$$a(T) \propto \sum_{\omega_m} (-1)^p \exp\left[-\frac{2p\pi}{\hbar\omega_c}\{\omega_m - \Sigma''(i\omega_m)\}\right]. \tag{5.17}$$

The damping is controlled by the imaginary part of the self-energy on the imaginary axis.

It is interesting to consider various forms of the self-energy. Firstly, for the Fermi gas, $\Sigma(\omega) = 0$, so the series sums to a thermal damping factor

$$R_{p,T} = \sum_{n=0}^{\infty} \exp(-2p\pi\omega_n/\hbar\omega_c) = \frac{pX}{\sinh pX}, \quad \text{where} \quad X \equiv \frac{2\pi^2 k_B T}{\hbar\omega_c}. \tag{5.18}$$

The function $X/\sinh X$ is the famous Lifshitz-Kosevich temperature dependence [31]. One of the classic equations of the physics of metals, this equation can be shown

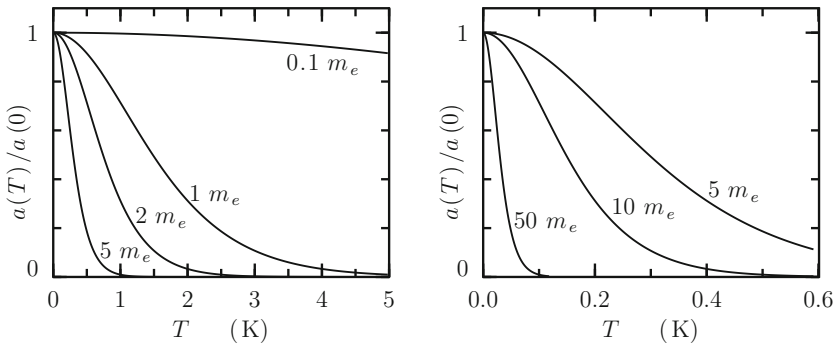

Fig. 5.3 Calculated temperature damping factor $X/\sinh X$ for different quasiparticle masses at a magnetic field of 10 T. Effective masses can vary enormously, from much less than $1\,m_e$ in semiconductors and in topological insulators, to over $100\,m_e$ in heavy fermion systems. The temperature dependence of the quantum oscillation signal enables effective masses to be measured with high accuracy. In materials with multiple extremal orbits (see below) the effective mass on different orbits can be measured

to be the Fourier transform of the Fermi-Dirac distribution. If impurity damping is included, all levels are broadened equally, so $\Sigma''(i\omega_n) = -\hbar/2\tau$, where τ is the scattering lifetime (including all scattering, with no preferential weight given to large-angle scattering, so in general the quantum oscillation τ is shorter than the transport τ) giving the famous exponential "Dingle factor" damping

$$R_{p,D} \equiv \mathrm{e}^{-2\pi p 2/\tau\hbar\omega_c} = \mathrm{e}^{-p\pi r_c/l_\circ} \tag{5.19}$$

where $r_c = \hbar k_F/eB$ is the cyclotron radius, and $l_\circ$ is the mean-free-path.

In a Fermi liquid, the frequency-dependent part of the self-energy (which adds to the constant impurity scattering part) is $\Sigma(\omega) = -\lambda\omega - i\,\Gamma\omega^2$, so that the imaginary part of the self-energy on the imaginary axis is $\Sigma''(i\omega_n) = -\lambda\omega_n + \Gamma\omega_n^2$. To leading order this is the same dependence on ω_n as in the Fermi gas, so the oscillations still follow an $X/\sinh X$ behaviour, but with a modified cyclotron frequency $\omega_c = eB/(1+\lambda)m_b$, equivalent to an enhanced mass $m^* = (1+\lambda)m_b$, as was first shown by Bychkov and Gork'ov in 1962 [9]. The $X/\sinh X$ temperature dependence thus allows quasiparticle effective masses to be obtained from the temperature dependence of the amplitude, as illustrated in Fig. 5.3.

Equation (5.17) also allows for non-Fermi-liquid forms of the self-energy, as explored in [41, 42, 62].

5.2.3 The Spin Damping Factor

In addition to producing quantized cyclotron motion, the applied magnetic field B polarizes the Fermi surface, via Pauli paramagnetism, into a spin-up part whose area $\mathcal{A}_\uparrow$ grows with increasing field, and a spin-down part whose area $\mathcal{A}_\downarrow$ shrinks with increasing field. As a result, each quantum oscillation signal is a superposition of two oscillations with field dependent frequencies $F_\uparrow(B)$ and $F_\downarrow(B)$. This allows quantum oscillations to be used to determine quasiparticle g-factors on a Fermi-surface specific basis. As shown below, however, there are subtleties both in the measurement and its interpretation, so this capability is somewhat neglected. Nevertheless, there are important recent examples in the strongly correlated electron literature: in the heavy fermion system URu_2Si_2 quantum oscillation measurements [45] reveal a highly anisotropic g-factor that may yield important insights into the famous hidden order phase of this material [1]; in other heavy fermion systems, interference between oscillations from the spin-up and spin-down branches of the Fermi surface show that the effective mass has a marked dependence on spin [17, 40, 55, 60]; in the strongly correlated oxide Sr_2RuO_4, described in the last section of this chapter, g-factor measurements uncover important aspects of spin-orbit interactions; and recent measurements of the g-factor of quasiparticles in underdoped cuprates [48] show that the g-factor is free-electron-like, which excludes some forms of spin-density wave order.

In conventional metals it is assumed that the spin-up and spin-down oscillations have identical amplitudes, but in strongly correlated systems this is not always so, so we write the pth harmonic term in the dHvA signal as

$$\tilde{M}_p(T) \propto a_{p,\uparrow}(T)\sin\left(2\pi p\frac{F_\uparrow(B)}{B}+\phi_o\right) + a_{p,\downarrow}(T)\sin\left(2\pi p\frac{F_\downarrow(B)}{B}+\phi_o\right) \tag{5.20}$$

where $a_{p,\uparrow}$ and $a_{p,\downarrow}$ are the spin-dependent amplitudes:

$$a_{p,\sigma} = \frac{1}{m_\sigma} R_{p,D_\sigma} R_{p,T_\sigma}, \tag{5.21}$$

with the impurity and thermal damping factors given in (5.19) and (5.18).

If the splitting is linear, then the field dependent frequencies $F_\uparrow(B)$ and $F_\downarrow(B)$ can be written as

$$F_\uparrow(B) = F_o + B\frac{\partial F}{\partial B} \qquad F_\downarrow(B) = F_o - B\frac{\partial F}{\partial B} \tag{5.22}$$

where F_o is the frequency at $B = 0$, and (5.20) becomes

$$\tilde{M}_p(T) \propto a_{p,\uparrow}(T)\sin\left(2\pi p\frac{F_\mathrm{o}}{B}+\phi_\mathrm{o}+2\pi p\frac{\partial F}{\partial B}\right) + a_{p,\downarrow}(T)\sin\left(2\pi p\frac{F_\mathrm{o}}{B}+\phi_\mathrm{o}-2\pi p\frac{\partial F}{\partial B}\right). \tag{5.23}$$

Setting $\phi_{p,s}=2\pi p(\partial F/\partial B)$ allows this to be re-expressed as

$$\tilde{M}_p(T) \propto \sin\left(2\pi p\frac{F_\mathrm{o}}{B}+\phi_\mathrm{o}\right)\,[a_{p,\uparrow}(T)+a_{p,\downarrow}(T)]\cos\phi_{p,s} + \cos\left(2\pi p\frac{F_\mathrm{o}}{B}+\phi_\mathrm{o}\right)[a_{p,\uparrow}(T)-a_{p,\downarrow}(T)]\sin\phi_{p,s}. \tag{5.24}$$

Note that, although the spin-up and spin-down Fermi surface areas are field dependent, the measured dHvA frequency is $F_\circ$, the so-called "back-projected" frequency, which is the intercept at $B=0$ of the tangent of $F(B)$ at $B_\circ$. This back-projection effect is the main subtlety involved in the interpretation of dHvA oscillations from magnetically polarized Fermi surfaces. Note in particular that linear spin-splitting effects only the quantum oscillation *amplitude*, not its measured frequency.

If the spin-up and spin-down amplitudes are equal, (5.24) reduces to

$$\tilde{M}_p(T) \propto \frac{1}{m^*}R_{p,D}R_{p,T}R_{p,S}\sin\left(2\pi p\frac{F_\mathrm{o}}{B}+\phi_\mathrm{o}\right). \tag{5.25}$$

with the spin damping factor

$$R_{p,S}=\cos\phi_{p,s}\ \text{ where }\ \phi_{p,s}=2\pi\frac{\partial F}{\partial B}=\frac{\pi p g m_s^*}{2m_e}. \tag{5.26}$$

The latter expression comes from combining the Onsager relation with the expression for the Pauli susceptibility, and m_s^* includes only electron-electron enhancement of the mass, not the electron-phonon enhancement which does not contribute to the magnetic susceptibility.

When $a_\uparrow \neq a_\downarrow$, the overall amplitude is

$$a_p(T) \propto \Big[(a_{p,\uparrow}(T)+a_{p,\downarrow}(T))^2\cos^2\phi_{p,s}(B) + (a_{p,\uparrow}(T)-a_{p,\downarrow}(T))^2\sin^2\phi_{p,s}(B)\Big]^{1/2}. \tag{5.27}$$

The amplitude has a minimum when the spin-up and spin-down oscillations are out of phase with each other, i.e. when

$$\phi_{p,s}=n\pi+\frac{\pi}{2},\quad \text{where } n \text{ is an integer.} \tag{5.28}$$

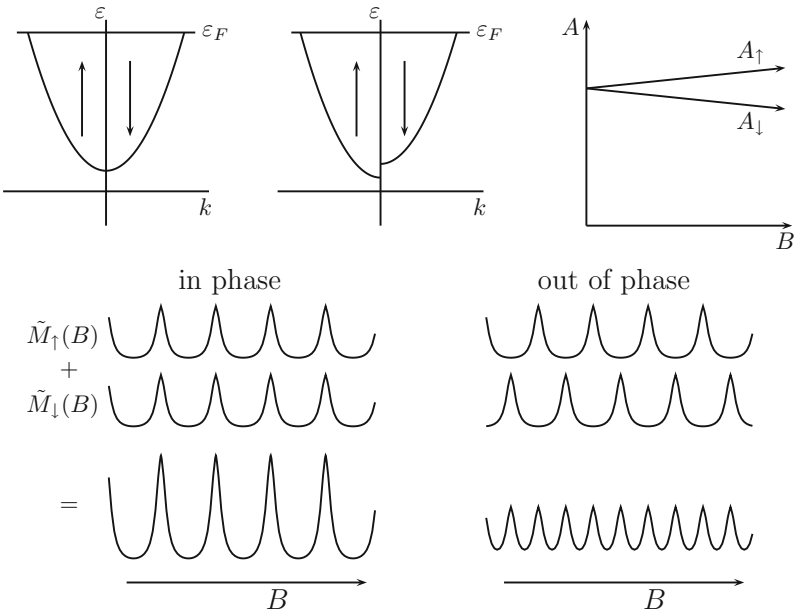

Fig. 5.4 Spin splitting in a paramagnetic metal. In an applied field $\boldsymbol{B}$, the Fermi surface splits into a shrinking spin-down surface and a growing spin-up surface (*top left*), so that a net spin-up magnetization arises in the material. The spin splitting of the Fermi surface areas produces oscillations that range from in-phase (*bottom left*) to out-of-phase (*bottom-right*) depending on the value of the g-factor. The latter case, a so-called *spin-zero*, in which the fundamental ($p = 1$) amplitude is zero while the second harmonic ($p = 2$) is enhanced, is the strongest signature arising from interference of the spin-up and spin-down Fermi surface. In other cases, careful measurement of the relative amplitude of harmonics can be used to determine the g-factor [24]

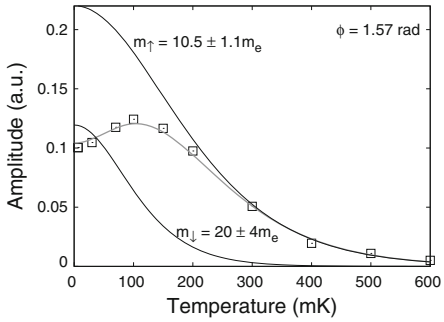

Fig. 5.5 Amplitude versus temperature for a quantum oscillation in $CeCoIn_5$, illustrating spin-dependent masses. In this case the spin-up and spin-down signals are out-of-phase ($\phi_{p,1} = \pi/2$). At high temperature only the lighter-mass signal contributes, but below 300 mK, as the heavier-mass amplitude becomes significant, the oscillation amplitude (squares) actually falls at low temperature [40]

If $a_\uparrow = a_\downarrow$ and $m_\uparrow = m_\downarrow$ then this produces a *spin zero*, because then $a_p(T) = 0$. This is illustrated in the bottom-right panel of Fig. 5.4. If however the effective mass is spin-dependent, then unusual temperature dependence of the signal can result. Figure 5.5 shows such a situation in $CeCoIn_5$ at high magnetic field. Here the spin-up and spin-down oscillations are out-of-phase, and one mass is significantly heavier than the other. Above 300 mK the dHvA signal looks normal, because only the lighter spin direction is contributing. Below 300 mK however the heavier spin signal starts to rise, partially cancelling the light-spin signal so that the overall amplitude actually falls at low temperature.

5.2.4 Three-Dimensional Fermi Surfaces

As a final but important generalization, we relax the assumption of pure two-dimensionality, by which the Fermi surfaces were simple tubes. The Fermi surface is now to be considered an arbitrary three-dimensional geometrical object, and it produces quantum oscillations with frequencies determined by the "extremal" orbit areas, which are the semiclassical orbits in k-space whose area is a local maximum or minimum, as illustrated by the shaded ellipses in Fig. 5.6. The variation of quantum oscillation frequencies with the angle of the applied magnetic field allows the Fermi surface shape and size to be mapped out in detail. This capability is very powerful, allowing detailed comparison with theoretical Fermi surfaces from either LDA band-structures or tight-binding effective Hamiltonians. Some examples were listed earlier, to motivate our derivation of the Onsager expression at the start of this section.

Figure 5.6 shows the simplest generalization of a Fermi surface for a quasi-two-dimensional metal, consisting of a cylindrical Fermi surface with warping along the vertical axis. When the field $\boldsymbol{B}$ is tilted the cyclotron orbits also tilt, remaining always perpendicular to $\boldsymbol{B}$ in k-space.

We can apply our earlier results by slicing such a Fermi surface into short tubular slices, of height dk_z, that are perpendicular to $\boldsymbol{B} = B\hat{z}$. A slice has cross-sectional area $\mathcal{A}(k_z)$, and the total signal is the sum of the oscillations from the slices:

$$\int dk_z \, \cos\left[2\pi p\left(\frac{\hbar \mathcal{A}(k_z)}{2\pi e B} - \gamma\right)\right]. \tag{5.29}$$

$\mathcal{A}(k_z)$ is an extremum when $d\mathcal{A}/dk_z = 0$. It is usually the case that the curvature of the Fermi surface is large, in the sense that that many Landau levels simultaneously intersect ε_F. In this case, as illustrated by the zoomed regions in Fig. 5.6, it is only when $\mathcal{A}(k_z)$ is at an extremum (i.e. a turning point) that the oscillatory signals from many adjacent slices add coherently to give a finite contribution to the integral. Away from an extremum the integrand oscillates rapidly as we move from one slice to the next, and thus there is no net contribution to the integral. The integral can be approximated, (for details see [57], pp. 53–55) and the result is

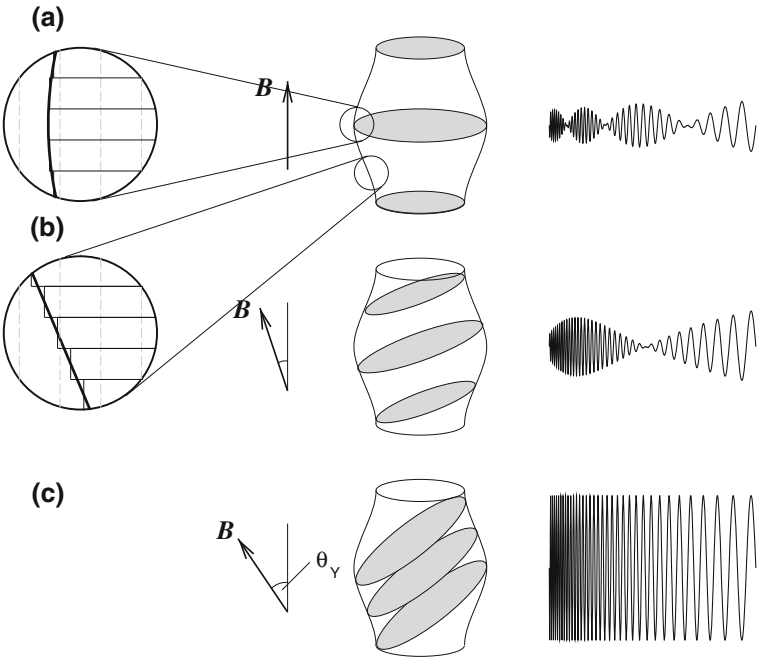

Fig. 5.6 Extremal orbits for a warped cylindrical Fermi surface. The quantum oscillations can be approximated as a sum of oscillations from short cylindrical sections that are perpendicular to the applied field (*zoomed regions on the left*). At the "extremal orbits" (*the gray ellipses*) the oscillations from adjacent cylinders are nearly in phase (*upper zoomed section*, with the Landau levels shown as *dashed gray lines*), so there is a large contribution. At a non-extremal region (*lower zoomed region*) the oscillations from nearby cylindrical sections all have different phase, so there is no net contribution. For a warped cylinder there are in general two extremal orbits, at the maximum and minimum cross-sectional areas perpendicular to the applied field, so the resulting oscillations have two contributions that beat against each other, as in **a** and **b**. At certain 'magic angles', as in **c**, the maximum and minimum orbits are identical in area, and the oscillations interfere constructively over the whole surface, giving rise to a large amplitude signal with no beats. From [7]

$$\frac{1}{\left|\frac{\partial^2 A_{\text{ext}}}{\partial k_z{}^2}\right|^{\frac{1}{2}}} \sum_{p=1}^{\infty} \cos\left[2\pi p\left(\frac{F}{B}-\gamma\right)\pm\frac{\pi}{4}\right] \tag{5.30}$$

where F is the frequency of the extremal orbit, $F = \hbar\mathcal{A}_{\text{ext}}/2\pi e$, and the $\pm$ in the argument of the cosine is $+$ when A_{ext} is a minimum and $-$ when it is a maximum. The prefactor is the inverse of the curvature of the Fermi surface at the extremal orbit, and this makes intuitive sense: lower warping means that more slices near the extremal orbit contribute coherently before the oscillations de-phase.

If the Fermi surface has more than one extremal cross-section, as in Fig. 5.6, the signal measured experimentally will be a superposition of oscillations with frequencies corresponding to each extremal area.

If only a few Landau levels intersect a quasi-two-dimensional Fermi surface then the full integration must be carried out [64]. We can describe a simple warped cylinder like the one shown in Fig. 5.6 with two parameters, an average radius k_{00}, plus warping described by k_{01}, such that $\mathcal{A}(k_z)$ varies as

$$\mathcal{A}(k_z) = \pi k_{00}^2 / \cos\theta_\circ + \frac{2\pi k_{00} k_{01} J_0(\kappa_F \tan\theta_\circ)}{\cos\theta_\circ} \cos\kappa_z, \tag{5.31}$$

where $\kappa_z \equiv k_z c$, $\theta_\circ$ is the angle between $\boldsymbol{B}$ and the cylinder axis, and J_0 is the zero-order Bessel function. Then

$$\tilde{\boldsymbol{M}} \propto \sin\left(\frac{2\pi F(\theta_\circ)}{B}\right) J_0\left(\frac{\pi \Delta F(\theta_\circ)}{B}\right), \tag{5.32}$$

where ΔF is the difference between the maximum and minimum extremal orbit dHvA frequencies at angle θ_0. Because the amplitude of the oscillations is modified by the Bessel function, the change in amplitude with angle can be used to determine ΔF, and thus the warping of the Fermi surface.

Reference [6] shows how the angle dependence of the amplitude can also be used to determine higher-order warpings of tubular Fermi surfaces in great detail.

5.2.5 The Full Lifshitz-Kosevich Equation

In a conventional metal the quantum oscillatory magnetisation is given by the Lifshitz-Kosevich (LK) equation (we continue to ignore a number of numerical factors that can be found in [57]):

$$\tilde{M} \propto \frac{F B^{\frac{1}{2}}}{m^* \left|\frac{\partial^2 A_{\rm ext}}{\partial k_z^2}\right|^{\frac{1}{2}}} \sum_{p=1}^{\infty} R_{p,T} R_{p,D} R_{p,S}\, p^{-\frac{3}{2}} \sin\left[2\pi p\left(\frac{F}{B} - \gamma\right) \pm \frac{\pi}{4}\right], \tag{5.33}$$

where $R_{p,D}$ is the Dingle factor, (5.19), $R_{p,S}$ is the spin-damping factor, (5.26), and $R_{p,T}$ is the thermal damping factor, (5.18). We have seen, however that in strongly correlated electron systems this equation may need to be modified in qualitatively important ways: if the effective mass is spin dependent (in which case the scattering rate is probably spin dependent as well) then we must use (5.24), in which each spin direction has a separate thermal and impurity scattering factor (5.21); if the self-energy of the electron fluid has a non-Fermi-liquid form then the product of the Dingle and thermal damping factors must generalized to (5.17); and if the system is so two dimensional that only a few Landau levels intersect the Fermi surface at a time, then the curvature factor cannot be used, and we must generalize to (5.32), which sums the oscillatory contribution of the entire Fermi surface, rather than keeping only the part near the extremal orbits. The lesson is that, although the conventional expression

may often be applied, and useful information derived thereby, in strongly correlated systems there are effects beyond the simple LK expression that firstly require caution to be exercised in interpreting measurements, but secondly allow substantially more information to be derived from a quantum oscillation measurement.

5.3 Measuring the de Haas-van Alphen Effect

In this section we give an overview of some of the key measurement techniques for the de Haas-van Alphen effect, focusing on field modulation, torque, and pulsed field techniques. Each has its advantages and disadvantages, and each requires more or less specialized apparatus. Brief mention is made of other quantum oscillation techniques of importance in strongly correlated systems.

5.3.1 The Field Modulation Technique

Figure 5.7 illustrates the field modulation technique. A sample, measuring typically $0.5 \times 0.5 \times 2$ mm^3, is placed in one coil of an astatic pair which will have on the order of 1,000 turns of wire on each coil. The pair of coils is carefully wound so that, in the absence of the sample, the pickup of the two coils cancels. The coil and sample are placed in a rotation mechanism that can change the angle of the sample with respect to the magnetic field.

A superconducting magnet supplies a quasi-static magnetic field that is slowly swept, while a specially constructed modulation coil, built into the bore of the magnet, supplies an alternating magnetic field with amplitude up to 0.005 T and frequency up to 50 Hz. The magnetic induction, due to the time varying magnetization of the sample, is measured using lock-in detection techniques. Note that the modulation field amplitude is large compared to a value of <0.0001 T typically used to measure ac-susceptibility. The applied magnetic field $H(t) = H + \tilde{h}(t)$ will induce a time-varying voltage V

$$V = \mu_o \mathcal{V} n_\phi \frac{N}{l} \frac{dM}{dt} \tag{5.34}$$

where n_ϕ is the filling factor, N/l is the turns density, and M and $\mathcal{V}$ are respectively the magnetisation and volume of the sample. The magnetisation is made up of non-oscillatory contributions from the Pauli and van Vleck spin susceptibilities $\chi_o H$ plus a static contribution $M_\circ$ if the sample is ferromagnetic, plus an oscillatory part $\tilde{M}_o(F)$, assumed for simplicity to have only a single dHvA frequency F, so that

$$M = M_\circ + \frac{\chi_o B}{\mu_o} + \tilde{M}_o(F) \sin\left(\frac{2\pi F}{B} + \phi\right), \tag{5.35}$$

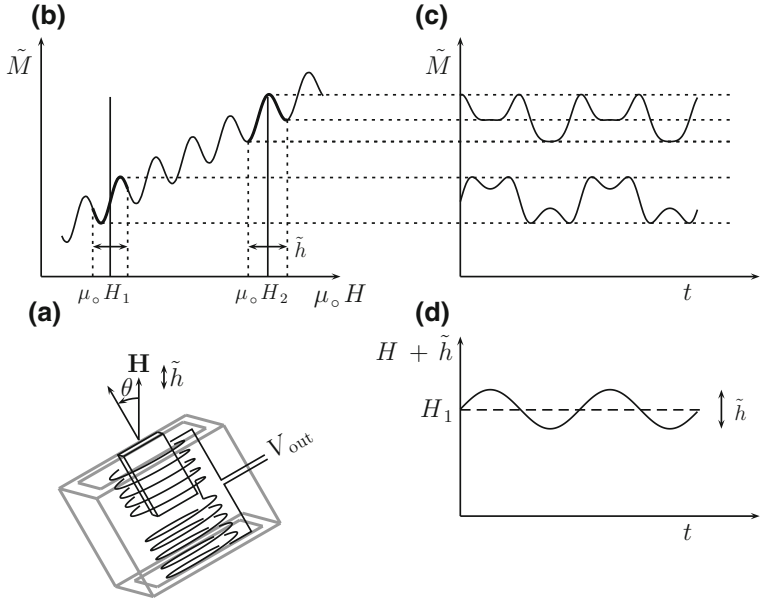

Fig. 5.7 Illustration of the field modulation technique. **a** The sample is placed in one of a pair of coils with opposed windings, so that direct pickup of the alternating field $\tilde{h}$ is eliminated. **b** The alternating field amplitude can be chosen to be comparable to the period of the quantum oscillations, as shown in the *upper-left* with the oscillatory magnetization greatly exaggerated. **c** This produces a time-varying magnetization that has considerable harmonic distortion. Focusing on the second-harmonic, at a field H_1 that is centred on a zero of $\tilde{M}$, the second harmonic distortion is zero, but at H_2 centered on a maximum the second harmonic is maximal, thus we see that the $2f$ signal oscillates as the quasistatic field H is swept

where $B(t) = \mu_\circ(H+M)$. An expression for the time-variation of the magnetisation can be obtained by replacing B with $B(t)$ in (5.35) and linearly expanding the sine for $b = \mu_\circ(\tilde{h} + \tilde{M}) \ll B_\mathrm{o}$:

$$M(t) = M_\circ + \frac{\chi_\mathrm{o} B_\mathrm{o}}{\mu_\mathrm{o}} + \frac{\chi_\mathrm{o} b}{\mu_\mathrm{o}} \cos\omega t + \tilde{M}_\mathrm{o}(F) \times \left[\sin\left(\frac{2\pi F}{B_\mathrm{o}} + \phi\right) \cos(\lambda \cos\omega t) - \cos\left(\frac{2\pi F}{B_\mathrm{o}} + \phi\right) \sin(\lambda \cos\omega t) \right] \tag{5.36}$$

where

$$\lambda = \frac{2\pi F b}{B_\mathrm{o}^2} = \frac{2\pi F \mu_\circ(\tilde{h} + \tilde{M})}{\mu_\circ^2 (H + M_\circ)^2}. \tag{5.37}$$

The presence of $M_\circ$ in the denominator can be important for ferromagnets at low fields, but normally it can be ignored; the presence of $\tilde{M}$ in the numerator can create

extreme non-linearities if $\tilde{M}$ is comparable to $\tilde{h}$, a problem known as "magnetic interaction" (see Chap. 6 of [57]), but usually this too can be ignored. The $\cos(\lambda \cos \omega t)$ and $\sin(\lambda \cos \omega t)$ terms in (5.36) can be expanded as Fourier series whose coefficients are Bessel functions, $J_\nu(\lambda)$. Applying (5.34) then leads to an expression for the pick-up voltage as a Fourier series of harmonics:

$$V = -\mu_o \mathcal{V} n_\phi \frac{N}{l} \omega \left[\chi_o b \sin \omega t - 2\omega \tilde{M}_o \sum_{\nu=1}^{\infty} \nu J_\nu(\lambda) \sin\left(\frac{2\pi F}{B_o} + \phi - \frac{k\pi}{2} \right) \sin \nu\omega t \right]. \quad (5.38)$$

From (5.38) it can be seen why setting the lock-in amplifier to detect at the second or higher harmonics (i.e. $\nu \geq 2$) is advantageous. Firstly, the static susceptibility χ_o contributes only to the $\nu = 1$ fundamental, thus by detecting on a harmonic, $\nu > 1$, the static susceptibility is removed. In the actual experiment, a notch filter is placed at the fundamental frequency, removing the χ_o signal and any direct pickup of the modulation field if the coils are unbalanced. Secondly, the amplitude of the oscillatory signal can be tuned, through the Bessel function dependence on the modulation field amplitude, allowing the experimenter to focus on the particular quantum oscillation of interest.

The advantages of the field modulation technique are as follows: (1) provided that suitably large single crystals are available and one is working in a superconducting magnet, it is the most sensitive measurement technique—moment sensitivities down to $\mu_{\min} \sim 10^{-11}$ Am^2 can be achieved if low-temperature transformers and low-noise pre-amplifiers are used; (2) lower temperatures can be achieved with this technique than with torque or pulsed-field methods—the sample is typically heat-sunk through high-conductivity wires directly to the mixing chamber of a dilution refrigerator, and thus temperatures in the low mK range can be achieved [41]; (3) the filtering effect of harmonic detection can eliminate the signal due to the static susceptibility and large quantum oscillations that are not of primary interest; and (4) it is possible to have such a setup in a laboratory, which allows much longer measurement times than are possible at user facilities.

The main disadvantages are: (1) you need fairly large single crystals to achieve very high sensitivity; (2) the maximum field is limited by superconducting magnet technology to below ~20 T (at present); and (3) you need a specially constructed magnet, with the modulation coils built into the bore of the magnet, to achieve the the required modulation field amplitude.

5.3.2 Torque Magnetometry

Compared with the field modulation method, torque magnetometry has a number of advantages. It is easy to measure, typically requiring only simple capacitance

or resistance bridges. Also, it is readily scaled to very small samples, for example piezoresistive cantilevers can be applied to crystals as small as $10 \times 100 \times 100\ \mu m^3$. This a huge advantage when, as is often the case, only small single crystals are available. It is quicker to set up, requiring only that the sample be fixed on the end of a flexible foil or cantilever. Finally, because it does not employ a pick-up coil, it is more immune to magnetic field noise than the field modulation technique, and thus is appropriate for resistive or even pulsed field magnets. For these reasons, torque is probably the most popular method of measuring de Hass-van Alphen oscillations.

However, there are some disadvantages. If large, mm sized crystals available, then the field modulation method is more sensitive. Also, it is more difficult to heat sink samples than in field modulation, so if the measurement requires going to very low temperatures then torque does not work well. With some measurement methods, for example the popular piezoresistive cantilever technique, the measurement itself generates enough heat that it is not possible to cool the sample below several 10's of millikelvin. Finally, many samples have a large, anisotropic non-oscillatory magnetic signal (e.g. $YbRh_2Si_2$ [28]) so a cantilever that is sufficiently sensitive to detect quantum oscillations will flex so much that it breaks. The method chosen has to be adapted to the available apparatus, the requirements of the measurement, and the properties of the material studied.

The physical basis of the technique is straightforward. We intially considered a quasi-two-dimensional metal with a tubular Fermi surface. The Lorentz force equation $\hbar d\mathbf{k}/dt = ev \times \boldsymbol{B}$ requires that the k-space orbit be perpendicular to the applied magnetic field $\boldsymbol{B}$. However in real space, a tubular Fermi surface means that there is no component of velocity perpendicular to the conducting planes, thus the electron quasiparticles are confined to orbits in real space that are perpendicular to the out-of-plane direction. The orbital diamagnetism is thus always parallel to the out-of-plane direction, and there will be a torque, $\tilde{M}_o \times \boldsymbol{B}$. Although the torque vanishes when $\mathbf{B}$ is perpendicular to the planes, in practice the angle between $\boldsymbol{B}$ and the perpendicular can be as small as a few degrees, in order to produce a strong torque signal.

The previous paragraph describes the limiting case of a purely two-dimensional Fermi surface, however unless the Fermi surface is perfectly spherical there is usually sufficient anisotropy of the Fermi velocity to generate a torque signal, and the torque method has been applied to many three-dimensional metals, e.g. [57].

Figure 5.8 illustrates the torque method of detection using piezo-resistive cantilevers.

Detection of the torque signal is quite straightforward. The High Magnetic Field Laboratory in Tallahassee for example has a standard setup with cantilevers cut out of beryllium-copper foil, and the deflection is monitored capacitively using commercially available capacitance bridges. Or, with commercially available piezoresistive cantilevers (illustrated schematically in Fig. 5.8) intended for scanning-AFM use, a simple Wheatstone bridge can be used to monitor the signal. An essential component of any measurement system is a rotating stage, so that the angle between the principal axes of the sample and the applied field can be adjusted. But in general such stages are required in order to map out the Fermi surface, so this is not a limitation of the method.

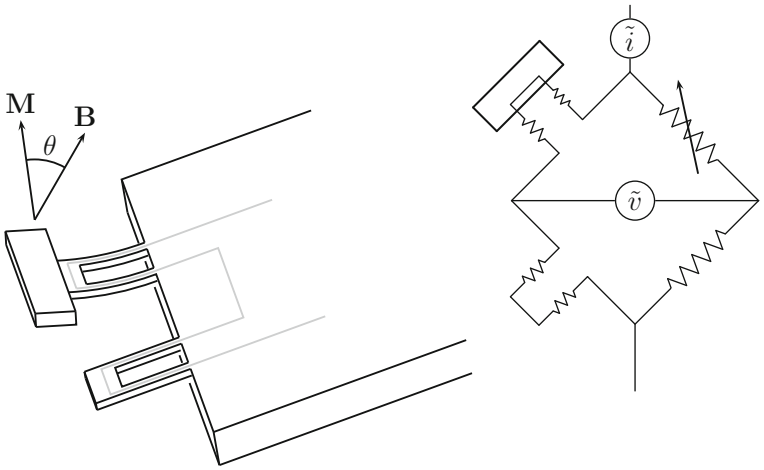

Fig. 5.8 The torque method of detection. *Left* a schematic of a piezoresistive torque measurement. Two cantilevers are used, one for a balance signal, the other carrying the sample. The resistivity of the conducting path changes as the cantilever bends. *Right* Wheatstone bridge setup for measuring the deflection of the cantilever. Alternatively, the sample can be mounted on a foil that makes one half of a capacitor, and the deflection monitored capacitively

Wiegers et al. [63] describe perhaps the most sensitive torque magnetometer constructed to date, having a rotor/stator arrangement with deflection measured capacitively. With this they were able to observe quantum oscillations in a two-dimensional electron gas.

5.3.3 Transport and Other Measurements

In principle, quantum oscillations can be observed in all thermodynamic and transport properties that involve quasiparticles at the Fermi surface. The Nernst effect has been shown recently to be a very effective probe of oscillations in semi-metals [5]. Quantum oscillations in the specific heat have contributed to the ongoing debate about the nature of the pseudogap phase of underdoped cuprates [52], although these measurements are quite specialized. Quantum oscillations in the magnetoresistance, known as the Shubnikov-de Haas (SdH) effect, and also in the Hall voltage, are commonly employed. These methods have traditionally been regarded as most effective to observe small Fermi surfaces, for example in graphene and in two-dimensional electron gases. Resonant rf circuits using tunnel diode oscillators [12] allow contactless measurement of SdH oscillations via changes in the skin-depth of a sample.

5.3.4 Pulsed Versus DC Field

Aside from detection technique, the choice of magnet is important. In general a high field is advantageous. The Dingle damping factor, $R_D = e^{-\pi r_c/l_\circ}$, (5.19), where $l_\circ$ is the mean free path and $r_c = \hbar k_F/eB$ is the cyclotron radius, means that quantum oscillations may grow *exponentially* with increasing magnetic field, depending on sample purity. Particularly where there are moderate levels of disorder, there can be many orders of magnitude improvement in signal by going to the highest available fields. Also, a long sweep range can help to resolve overlapping dHvA frequencies, although in general it is better (and cheaper) to get purer samples and sweep to lower fields, than to get a bigger magnet and sweep to higher fields.

Laboratory scale superconducting magnets have some advantages. Fields up to 20 T are sufficient to overcome the Dingle factor in materials that can be produced with mean free paths of around 100's of nm. As a rough rule of thumb, this corresponds typically to a residual resitivity of 1 $\mu\Omega$ cm, although if the Fermi surface is small then higher resistivity crystals can reasonably be attempted. These magnets have very low flux noise, and they can have a modulation coil installed in the bore of the magnet if the magnet is to be devoted to dHvA measurements. Also, it is only with these magnets that very low temperatures (in the low mK range) can be achieved, because they can have a canceled field region that allows a metal dilution refrigerator to be employed. A further advantage is unlimited measurement time, allowing detailed studies as a function of angle and temperature.

Fields up to 37 T are now available with resistive magnets at high magnetic field laboratories. These magnets are not as quiet as superconducting magnets, and access time is more restricted, so detailed studies of the angular dependence, or the temperature dependence, of oscillations can be difficult, and may require multiple visits to the facility. However, these magnets are well set up and more likely to produce successful results for non-experts who have high quality cyrstals, and 30 + T can produce sufficiently large improvements in signal, for mildly disordered samples, that the additional flux noise of the magnet is overcome.

In the next highest field range, with even more restricted access, is the 45 T hybrid magnet at the National High Magnetic Field Laboratory in Tallahassee. Torque and transport measurements have been carried out successfully, and a recent measurement in $Tl_2Ba_2CuO_{6+\delta}$ [53] illustrates the power of such high fields: at some dopings in this cuprate superconductor the quantum oscillations show up only the last few tesla.

Non-destructive pulsed field magnets have recently reached 100 T at the National High Magnetic Field Laboratory in Los Alamos, and fields above 60 T can be reached in a number of laboratories. They have been used to study quantum oscillations in organic metals, heavy fermion systems and, most importantly, underdoped cuprates, e.g. [4, 15, 23, 61, 65], where such high fields are required to overcome impurity scattering and to suppress superconductivity to reach the normal state.

The measurement methods for pulsed fields are highly specialized, and great care must be taken to eliminate sources of vibration, minimize eddy currents, and reduce indirect pickup of electromagnetic signals from the pulses, however the plused-

field facilities at Toulouse, Los Alamos and Dresden have developed very effective methods that yield suprisingly good signal-to-noise ratios. Quantum oscillations in pulsed-field measurements are often observed through oscillations in the magnetoresistance (Shubnikov-de Haas, SdH, oscillations) or the Hall signal [15]. The Los Alamos laboratory specializes in measuring SdH oscillations through changes in the skin-depth of a sample via changes in the resonant frequency of high-frequency circuits (e.g. [65]). In a recent application, a tunnel-diode-oscillator circuit has been used in to detect quantum oscillations in a tiny sample of $CeIn_3$ in a plastic high pressure cell in pulsed field measurements up to 60 T [22].

De Haas-van Alphen oscillations in pulsed fields can be observed using miniature piezo-resistive cantilevers [47], but more commonly the sample is placed in a pickup coil. The extremely high sweep rate of the field, covering 10's of tesla in micro- to milliseconds, is sufficient to give a strong oscillatory dM/dT signal without field modulation. In a recent measurement, for example [20], a sample with volume $0.1 \times 0.2 \times 3\,\mathrm{mm}^3$, was placed in a pickup coil having 450 turns of 10 μm copper wire on $\sim$500 μm mandrel, with the compensation coil wound coaxially around the pickup coil. The coil and sample were mounted on a plastic dilution refrigerator and measurements could be carried out between 600 mK and 4 K.

5.3.5 Analysis of the dHvA Signal

As we shall see below for Sr_2RuO_4 (Fig. 5.11) in general a dHvA measurement will consist of a superposition of oscillations arising on different extremal orbits of the Fermi surface. The different oscillations are separated by taking a Fourier transform, with a result such as Fig. 5.12. In order to do this, the data as a function of B are interpolated to give evenly spaced points in $1/B$, and then the fast-Fourier-transform is taken. It is generally helpful to pad the $1/B$ data with extra zeros to give a smoother FFT spectrum. From the FFT the frequency of each peak can be obtained by fitting.

In order to map the Fermi surface the crystal is rotated around its major symmetry axes, and the resultant F vs. θ data is compared with extremal orbits calculated by LDA or other electronic-structure programs. For example one can use the wien-2k package and analyze the output using the extremal-area finder SKEAF [8, 54].

By taking data at different temperatures a plot of dHvA amplitude vs. temperature can be constructed, as in Fig. 5.16, and the data fitted with the Lifshitz-Kosevich (LK) formula, (5.18), to extract the quasiparticle effective mass m^* associated with that extremal orbit.

Similarly, by analyzing a long sweep over several consecutive short field ranges one can, in principle, extract the the Dingle factor, (5.19), but care must be taken because long-period beats can arise from nearly degenerate extremal orbits or field-dependent spin-damping factors, and these can lead to incorrect Dingle analyses, if they are not recognized.

If only a few oscillations are available then the FFT doesn't work well, and in this case the oscillations can be fitted directly using the LK formula. An interesting

recent example is Ramshaw et al., who used a genetic algorithm to simultaneously fit many sweeps at different angles in underdoped YBCO [48], allowing them to separate contributions from nearly degenerate extremal orbits, the Dingle factor, and spin-splitting.

5.4 Case Study: Sr_2RuO_4

Sr_2RuO_4 initially attracted attention as the only layered perovskite oxide that superconducts without copper-oxide planes [37]. It has continued to be of interest as it gradually emerged that Sr_2RuO_4 is a chiral p-wave superconductor, with potential uses in quantum computation [27]. For our purposes, Sr_2RuO_4 offers a superb demonstration of the power of quantum oscillation measurements: it was possible through careful measurements and insightful analysis to build up a very detailed picture of the topography of the Fermi surface and the many-body enhancements of the quasiparticles on the Fermi surface. From this, a detailed correspondence was established between the properties of electron quasiparticles at the Fermi surface, and bulk properties such as specific heat and transport that average over all sheets of the Fermi surface. More importantly, detailed Fermi-surface-specific information from quantum oscillations provides important starting points for theories of p-wave superconductivity in this material.

In this section we will use Sr_2RuO_4 to illustrate how quantum oscillation measurements are analyzed. This exercise is doubly useful because Sr_2RuO_4 is layered and highly anisotropic, like many other materials of current interest such as cuprate and iron-pnictide superconductors, so many of the ideas that emerge in our discussion can be applied elsewhere.

Finally, we note that a number of reviews of Sr_2RuO_4 exist, so that the reader who wishes for more detail, or clarification, can easily find it [7, 27, 36].

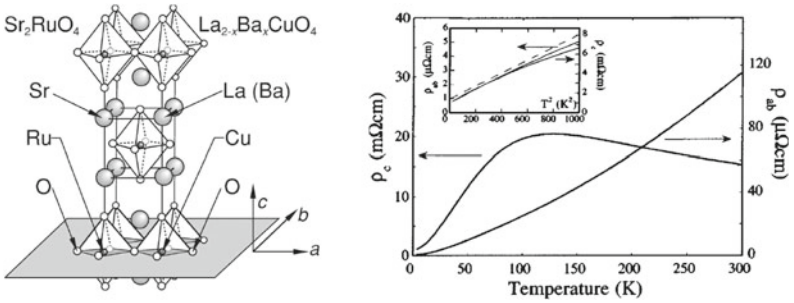

Fig. 5.9 *Left* The crystal structure of single-layer strontium ruthenate, from [36]. Sr_2RuO_4 is isostructural with the cuprate superconductor La_2RuO_4. *Right* The resistivity of Sr_2RuO_4 versus temperature, from [25]. The main panel shows that the resistivity is highly anisotropic, while the inset shows that both ρ_{ab} and ρ_c have a Fermi-liquid, T^2, temperature dependence at low temperature

5.4.1 Summary of Normal State Properties

The crystal structure of Sr_2RuO_4 is shown in Fig. 5.9. Sr_2RuO_4 crystallizes in this base-centered tetragonal crystal structure, identical to the tetragonal form of the layered cuprate La_2CuO_4. Unlike La_2CuO_4, however, Sr_2RuO_4 retains this crystal structure down to low temperature, with no orthorhombic distortion. The ruthenium-oxide ab-planes are highly conducting, while transport between the planes, along the c-axis, is greatly reduced by the insulating strontium-oxide layers, hence electrical transport is highly anisotropic, with low temperature values of ρ_c/ρ_{ab} as high as 4,000 reported [46].

The right-hand panel of Fig. 5.9 shows the temperature dependence of ρ_{ab} and ρ_c, from [25]. Below about 20 K, both ρ_{ab} and ρ_c follow the $\rho(T) = \rho_\circ + AT^2$ dependence expected of a Fermi liquid, and although the A coefficients are very different in magnitude, the ratio ρ_c/ρ_{ab} is fairly constant over this temperature range. The Hall constant has also been measured, giving a value of -1.15×10^{-10} m^3/C in the low field, low temperature limit [33].

As we show below, these bulk transport properties can be calculated accurately using the Fermi surface topology and properties of the quasiparticles on each Fermi surface, as obtained from quantum oscillation measurements.

Another key property of strongly correlated electron systems is the specific heat, because comparison of the linear specific heat coefficient, γ, with the density of states calculated in band-theory gives an indication of the strength of many-body interactions within a metallic system. As expected for a Fermi liquid, at low temperature in Sr_2RuO_4 $C(T) = \gamma T + \beta T^3$ (see Fig. 5.10), where γT describes the contribution from electrons at the Fermi surface, while βT^3 is the phonon contribution. While a few, slighly scattered values have been reported for γ, the accepted result made on the highest quality crystals is 38 ± 2 mJ/mole K^2 [34, 38]. This will be shown to agree with effective masses derived from quantum oscillation measurements.

The Pauli susceptibility, from Knight shift measurements, is $\chi_s \sim 1.7 \times 10^{-4}$ [26]. Both γ and χ_s are quite enhanced compared with the predictions of LDA calculations. This, plus the fact that the related three-dimensional system $SrRuO_3$ is a ferromagnet with a T_c of $\sim$160 K, led Sigrist and Rice to the quite remarkable suggestion that Sr_2RuO_4 has analogous properties to ^{3}He, and therefore its superconductivity might be p-wave [51].

5.4.2 Summary of Quantum Oscillation Results and Analyses

While Sr_2RuO_4 had been known since the late 1950s [49], the discovery of superconductivity was not made until high-quality single crystals were grown using a floating zone image furnace [37]. Not only were high quality crystals necessary for observation of superconductivity, but their high quality also allowed observation of quantum oscillations. Soon after the discovery of superconductivity, Mackenzie et al.

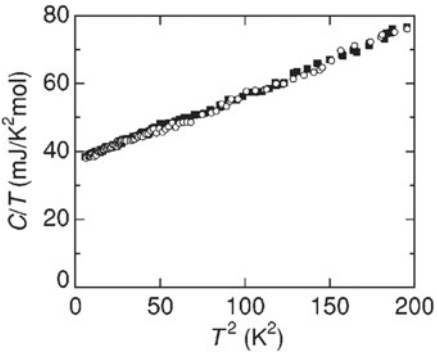

Fig. 5.10 The specific heat of Sr_2RuO_4 at low temperatures, from [34]. $C(T)$ follows the usual $\gamma T + \beta T^3$ behaviour for a metal, however a γ value of $\sim 38 \pm 2$ mJ/mole K^2 is very large for a d-electron metal, suggesting strong correlations

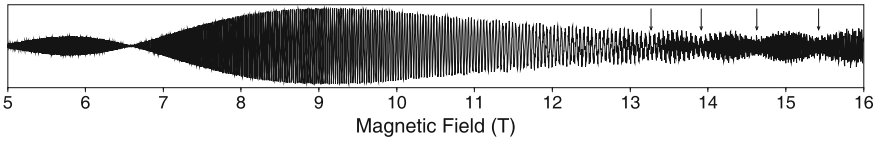

Fig. 5.11 Quantum oscillations in Sr_2RuO_4. The data are de Haas-van Alphen oscillations detected using the field-modulation method, with detection at the second harmonic of the modulation frequency. The temperature was 50 mK, and the modulation field amplitude 54 gauss (5.4 mT). The *arrows* between 13 and 16 T indicate beats of the so-called β frequency. From [6]

[33] published a comprehensive quantum oscillation study, based on both de Haas-van Alphen and Shubnikov-de Haas oscillations. Aside from pioneering work in the 1960s (see e.g. [21, 39]), this was one of the first quantum oscillation studies of an oxide metal.

Typical quantum oscillations from a high quality crystal of Sr_2RuO_4 are shown in Fig. 5.11. There are several frequencies present. Some of these must be close together in frequency, because they produce long-period beat structures, indicated for example by the four arrows between 13 and 16 T. The node in amplitude at about 6.6 T is also due to beating of two nearly degenerate frequencies, whereas the decreasing amplitude below 5 T results from an approaching Bessel-function zero [see (5.38)].

The dHvA spectrum of Sr_2RuO_4 depends, as expected from the earlier discussion, on the field range, field angle, and the temperature. A typical dHvA spectrum of a high-quality sample is shown in Fig. 5.12 [34]. Several peaks are observed. The peak labeled α is a fundamental oscillation, but 2α and 3α can be indentified as harmonics of α (i.e. terms with $p > 1$ in (5.33)), because their frequency is an integer multiple of the frequency of the α peak, and their mass is an integer multiple of the mass derived for the α oscillation, as expected from (5.18). The pair of peaks labeled β could, on the basis of this trace alone, arise from distinct sheets of the Fermi surface, however when the crystal is rotated in the field these two peaks merge, as expected for the maximum and minimum extremal areas for a tube with c-axis warping (Fig. 5.6). The peak labeled $\beta + \alpha$ is seen only in high quality samples, and it arises from mixing of these two frequencies as the chemical potential is modulated.

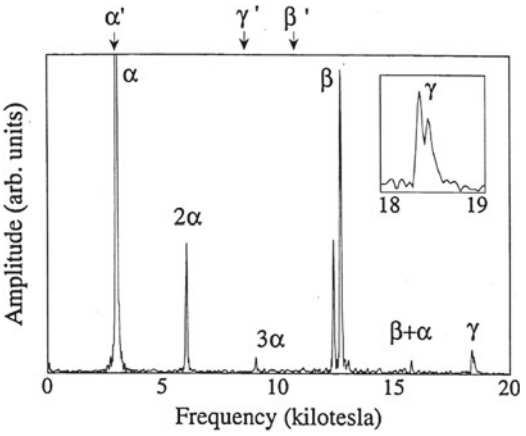

Fig. 5.12 Quantum oscillation spectrum of Sr_2RuO_4, from [34]. The oscillations arise from three sheets of the Fermi surface, α, β and γ. Three harmonics, $p = 1, 2$ and 3 [see (5.33), (5.13)] of the α frequency are visible. The β frequency is split, and the beating of these two fequencies produces the nodes, marked by arrows, in Fig. 5.11. The γ frequency is also weakly split. The labels α', γ' and β' show where the oscillation frequencies are predicted to be, based on an angle-resolved photoemission study that was later shown to have been wrong due to a reorganization of the electronic states at the surface of the crystal [13]

Finally, the peak γ, which is weakly split as can be seen in the inset, can be identified as a distinct quantum oscillation: it is obviously not an integer multiple of β; it is not far from the 6th multiple of α, however it's mass, as discussed below, is not 6 times the mass of α, and it would be peculiar for the 6th harmonic to show up, when the 4th and 5th do not.

No fundamental oscillations are found above 20 kT, and indeed the γ orbit fills a substantial fraction of the Brillouin zone. Rotation of the crystal shows that all of the dHvA frequencies vary as $1/\cos(\theta)$ [35], which is the signature of a tubular Fermi surface, as expected in a quasi-two-dimensional metal.

From a dHvA measurement we can obtain detailed information about the size and shape of each Fermi surface, but not about where it is located in the Brillouin zone. For this, comparison must be made with band structure calculations, and in the case of Sr_2RuO_4 there was excellent agreement with LDA calcuations [35], which predict that three bands cross the Fermi energy to produce the Fermi surfaces shown in Fig. 5.13.

These three bands originate in a simple way from the underlying $3d$ crystal-field levels of ruthenium in an octahedral environment, as illustrated in Fig. 5.14. The β and α sheets of the Fermi surface both arise from quasi-one-dimensional d_{xz} and d_{yz} bands antibonding with O p_z orbitals. These bands are quasi-one-dimensional because d_{xz} has very little hybridization along y, as can be seen, and similarly d_{yz} has little hybridization along x, and they both hybridize weakly in the z direction because of the insulating strontium-oxide layers. Where these two bands cross, spin-

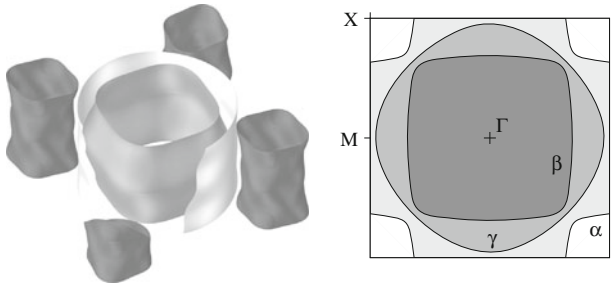

Fig. 5.13 Three-dimensional cartoon of the Fermi surface of Sr_2RuO_4 [7], in which the warpings have been exaggerated by a factor of 15. The right-hand figure shows the cross-section in the *ab*-plane, together with the labels of the Fermi surfaces

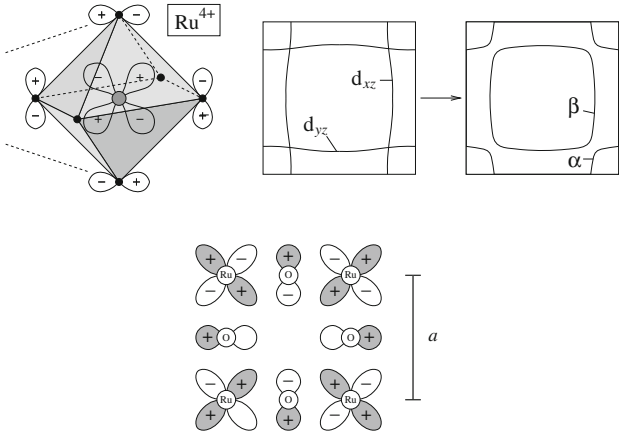

Fig. 5.14 The t_{2g} crystal field levels of Sr_2RuO_4 [7]. *Top left* the d_{xz} orbital of Ru π-bonds to the p_z orbitals of O; *top right* the resulting quasi-one-dimensional bands from the d_{xz} and d_{yz} orbitals hybridize with each other to give rise to the β and α sheets of the Fermi surface; *bottom* the d_{xy} orbital in anti-bonding combination with O p_x and p_y orbitals gives rise to the γ sheet of the Fermi surface

orbit interaction causes them to hybridize with each other, so that the Fermi surface reconstructs into a large electron surface β enclosing occupied states, and a hole pocket α enclosing vacant states, at the corner of the Brillouin zone.

The remaining large electron sheet of the Fermi surface, γ, arises from hybridization of the d_{xy} orbital of ruthenium in antibonding combination with the nearest neighbour O p_x and p_y orbitals.

While there is excellent agreement between the Fermi surface sizes and the predictions of electronic-structure calculations, one can go significantly beyond this analysis and enquire into the detailed warpings of these nearly tubular Fermi surfaces. We expect that the β and α surfaces, arising as they do from orbitals the d_{xz} and d_{yz} that have some extension along the z direction, should have more c-axis warping

(indicative of inter-layer tunneling) than the d_{xy} (γ) Fermi surface, whose orbitals are much more confined to the ab-plane. This is confirmed by Fig. 5.12, in which the β sheet has a much larger splitting between its the maximum and minimum Fermi surface areas, compared with γ, indicating a larger difference between the maximum and minimum extremal areas (Fig. 5.6) as expected for stronger warping.

On the other hand, a very low beat frequency for the α oscillation suggested that this sheet has very little c-axis warping, which would be surprising, given that it too originates on from the d_{xz} and d_{yz} orbitals (Fig. 5.14).

This mystery was solved by more detailed analysis by Bergemann, [6, 7] that illustrates both the power of quantum oscillation measurements and the dangers of overly-simplistic interpretation of dHvA amplitude versus field, when extracting the Dingle factor for example (5.19). Bergemann fitted a three-dimensional data set consisting of dHvA amplitude versus field and rotation angle, using model parameters that included spin-splitting, impurity damping, and warpings described by the series of cylindrical harmonics, shown in Fig. 5.15, of the form

$$k_F(\phi,\kappa) = \sum_{\mu,\nu\geq 0;\mu \text{ even}} k_{\mu\nu}\cos(\nu\kappa)\begin{cases}\cos\mu\phi \text{ if } (\mu \bmod 4) = 0\\ \sin\mu\phi \text{ if } (\mu \bmod 2) = 0,\end{cases} \tag{5.39}$$

where $\kappa \equiv ck_z/2$ and ϕ is the azimuthal angle in the ab-plane. This analysis showed that the k_{01} and k_{02} warpings, which we normally think of when picturing a warped tubular Fermi surface and which would give rise to a beat pattern in the dHvA signal, are indeed small for the α sheet, however the k_{21} warping term is large. This term conserves the Fermi surface cross-sectional area to first order: it can be thought of as a ellipsoidal bulge in the cross-section that first extends in one direction, and then in the perpendicular direction, as we move in the c-direction along this corner of the Brillouin zone [7]. Similarly, the k_{42} term is significant, but this too conserves the area as a function of κ. This analysis shows that a Fermi surface can have substantial warping without a large splitting of the maximum and minimum extremal areas.

In combination with other data such as angle dependent magnetoresistance oscillations [46], a very detailed picture of the Fermi surface and its spin-splitting was built up, from which an accurate tight-binding Hamiltonian can be constructed, and this in turn can be used as the underlying model for theoretical studies of the superconductivity of this compound. Recently, a similar analysis of quantum oscillations was applied to the cuprate superconductor $Tl_2Ba_2CuO_{6+\delta}$ [53].

In addition to obtaining a detailed picture of the Fermi surface, the temperature dependence of the oscillations allowed determination of the effective mass of the quasiparticles, via (5.18). For the measurement, the samples were heat-sunk to the mixing chamber of a dilution refrigerator through a copper wire, attached at the sample by low-resistance silver epoxy, and at the other end clamped by a brass screw to a gold-plated section of the mixing chamber. The temperature dependence of the oscillations was measured by taking spectra such as those in Fig. 5.12 at several temperatures between 20 mK and 2 K. The amplitude versus temperature of each peak was determined by fitting the spectra, and the result fitted to the Fermi liquid

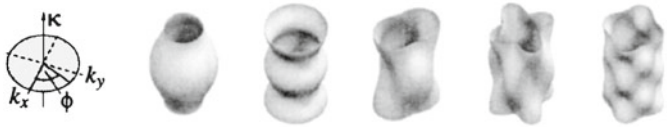

	k_{00}	k_{01}	k_{02}	k_{21}	k_{41}	k_{42}
α	305	—	–0.33	1.3	—	1.0
β	623	3.9	small	—	–1.9	small
γ	754	small	0.5	—	small	0.3

Fig. 5.15 Warping parameters for Sr_2RuO_4, from [6]. The Fermi surfaces are expanded in cylindrical harmonics, (5.39)

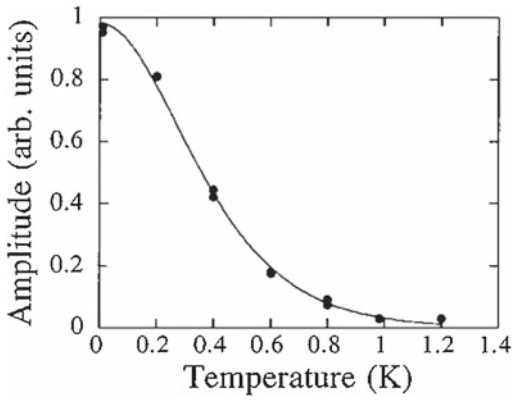

Fig. 5.16 Temperature dependence of the quantum oscillation amplitude for the β frequency [35]. The *solid line* is a fit of $X/\sinh X$ (5.18), the Fermi liquid formula for the temperature dependence of quantum oscillations

form of (5.18). A typical result is shown in Fig. 5.16. From this effective masses for all three sheets of the Fermi surface were obtained.

In Table 5.1 the mass enhancements, m^*/m_{band}, which is the ratio of the measured quasiparticle effective masses to the predictions of LDA band-structure calculations, are given for the three Fermi surfaces. These mass enhancements are all large compared to most d-electron metals, and they vary substantially from one Fermi surface to another, with γ having the largest mass enhancement. The Fermi-surface specific mass enhancement is an important measure of the strength of quasiparticle interactions. For example, models of the pairing interaction for superconductivity in this material ought to be compatible with these mass enhancements, particularly in light of a subsequent study of the pressure dependence of the effective masses and the T^2 coefficient of the resistivity [19], which showed that the superconducting T_c and the many-body enhancements track each other closely.

Table 5.1 Fermi surface and quasiparticle properties obtained from quantum oscillation measurements in Sr_2RuO_4

Fermi-surface sheet	α	β	γ
character	Hole-like	Electron-like	Electron-like
k_F (Å^{-1})	0.304	0.622	0.753
m^*/m_e	3.3	7.0	16.0
m^*/m_{band}	3.0	3.5	5.5
v_F (m s^{-1})	1.0×10^5	1.0×10^5	5.5×10^4
$\langle v_\perp^2 \rangle$ (m^2 s^{-2})	7.4×10^5	3.1×10^6	1.0×10^5
$t_\perp$ (K)	7.3	15.0	2.7

k_F is the average around the orbit, given by $\sqrt{A_e/\pi}$,
A_e is the extremal area,
m_{band} is from [43]; $v_F \equiv \hbar k_F/m^*$; $\langle v_\perp^2 \rangle \equiv (\hbar^2 k_{00}^2 c^2/16 m^{*2})[\sum_{\mu\nu} k_{\mu\nu} v^2 (1 + \delta_{\mu 0})]$, with
c the body-centred tetragonal lattice parameter, comes from the sum over the c-axis warpings of the quasi-tubular Fermi surfaces

5.4.3 Correspondence with Bulk Properties

Table 5.1 summarizes some of the experimentally determined quantities from quantum oscillation measurements. Using these values several bulk properties can be estimated and compared with bulk measurements.

Knowledge of the effective mass and the size of a Fermi surface allows the expected linear coefficient of specific heat to be estimated. In a two-dimensional metal, each cylindrical Fermi surface contributes $\pi k_B^2 \mathcal{N}_A a^2 m_i^*/3\hbar^2$ J mol^{-1} K^{-2} to the specific heat, where a is the in-plane lattice parameter, $\mathcal{N}_A$ is Avogadro's number and k_B is Boltzmann's constant. For Sr_2RuO_4 this gives 1.48 mJ/mol/K^2 $\times$ (3.3 + 7.0 + 16.0) = 38.9 mJ/mol/K^2, which agrees within the error with the measured value of 38 mJ mol^{-1} K^{-2} [34, 38].

Note that in general it can be dangerous to assume that the effective mass is uniform over the whole Fermi surface. For example, in the heavy fermion system $CeIn_3$ at high magnetic field the effective mass is found to vary by a factor of around 15, from $2m_e$ to $\sim 32m_e$, on a single sheet of the Fermi surface [16]. It is good practice, therefore, to measure m^* at several different field angles, to check for such "hot spots". Even if hot-spots are not present, it is good practice to use an LDA band structure to calculate the unrenormalized contribution to γ for a particular orbit (this can be done using available software [54]), and then calculate the enhancement of the effective mass on this orbit, to get m^*/m_{band}. Then, assuming that the density of states for the entire Fermi surface is enhanced by the same amount, the expected value of γ can be calculated. Such a calculation [33], found that the α, β and γ surfaces respectively contribute approximately 1.55, 3.14 and 4.19 mJ mole^{-1} K^{-2} to γ. Enhancing these values by the mass enhancements given in Table 5.1, again gave $\gamma \sim 39$ mJ mol^{-1} K^{-2}.

Next we turn to transport properties.

Within the relaxation time approximation [3] the electrical conductivity tensor for a sheet n of the band structure is given at $T = 0$ by

$$\sigma_{ij}^{(n)} = \frac{e^2}{4\pi^3}\tau \oint\limits_{FS} d^2k\, v_i^{(n)}(\mathbf{k}) v_j^{(n)}(\mathbf{k}).$$

This assumes a constant relaxation time τ over the Fermi surface, and $v_i^{(n)}(\mathbf{k})$ is the Fermi velocity in the $\hat{i}$ direction at $\mathbf{k}$.

Assuming that this approximation holds, the resistivity anisotropy for each Fermi surface is

$$\frac{\rho_{ab}}{\rho_c} = \frac{\sigma_{cc}}{\sigma_{ab}} = \frac{\oint\limits_{FS} d^2k\, v_z(\mathbf{k}) v_z(\mathbf{k})}{\oint\limits_{FS} d^2k\, v_x(\mathbf{k}) v_x(\mathbf{k})} = \frac{\oint\limits_{FS} d^2k \hat{v}_z(\mathbf{k}) \hat{v}_z(\mathbf{k})}{\oint\limits_{FS} dk_c\, k(\phi)\, d\phi \cos^2(\phi)} \tag{5.40}$$

$$= \frac{2}{A_{FS}} \oint\limits_{FS} d^2k \hat{v}_z(\mathbf{k}) \hat{v}_z(\mathbf{k}), \tag{5.41}$$

where $\hat{v}_z$ is the z-component of the unit vector that is parallel to the Fermi velocity at a given point on the Fermi surface. Bergemann et al. [7], using the detailed warpings of the Fermi surfaces extracted from the envelope analysis described above, carried out the integral numerically, and obtained an anisotropy of 3,700, compared with a measured anisotropy of 4,000.

A final consistency check is possible with the Hall effect and the carrier density [33]. The three cylindrical Fermi surfaces enclose fractional volumes of the Brillouin zone of 0.108, 0.457 and 0.667. This corresponds to $2.0 * (0.667 + 0.457 + (1 - 0.108)) = 4.032$ electrons, compared with the expected value of 4.0 conduction electrons per formula unit, with one formula unit per unit cell [33]. Note that because the α surface is a hole surface it encloses empty states, so it contributes $(1 - 0.108)$ electrons per spin-direction.

These checks on the consistency between measured bulk properties and those calculated from Fermi surface parameters and mass enhancements are very important. In Sr_2RuO_4 the agreement is very impressive. In other cases there may be disagreements that could reveal that there are Fermi surfaces that have not been observed in the dHvA measurement. Sometimes, such as in the recent quantum oscillation measurements on underdoped cuprates [15], one is not sure how many copies of an observed Fermi surface there are in the Brillouin zone, and the requirment that the electronic specific heat summed over Fermi surfaces cannot exceed the measured specific heat, and that the carrier density should add up to the known number of carriers per formula unit, can rigorously constrain this.

5.5 Conclusions

In this article we have reviewed the theory of the de Haas-van Alphen effect, emphasizing less-well-known aspects of the theory that are of particular relevance to strongly correlated electron systems. We have briefly discussed the main measurement techniques, and shown an exemplary application, to the p-wave superconductor Sr_2RuO_4, in which comprehensive quantum oscillation measurements lead to measured Fermi-surface-specific properties that can be used to calculate bulk properties that are in excellent agreement with bulk measurements, and that can therefore be used with confidence to help construct models of the exotic superconductivity of this material.

References

1. M.M. Altarawneh, N. Harrison, S.E. Sebastian, L. Balicas, P.H. Tobash, J.D. Thompson, F. Ronning, E.D. Bauer, Sequential spin polarization of the Fermi surface pockets in URu_2Si_2 and its implications for the hidden order. Phys. Rev. Lett. **106**, 146403 (2011)
2. H. Aoki, S. Uji, A.K. Albessard, K. Motoki, H. Ikezawa, T. Ebihara, R. Settai, Y. Onuki, Transition of f-electron nature from itinerant to localized - metamagnetic transition in $CeRu_2Si_2$ studied via the de Haas-van Alphen effect. Phy. Rev. Lett. **71**, 2110 (1993)
3. N.W. Ashcroft, N.D. Mermin, *Solid State Physics* (Holt, Reinhart and Winston, 1976)
4. A.F. Bangura, J.D. Fletcher, A. Carrington, J. Levallois, M. Nardone, B. Vignolle, P.J. Heard, N. Doiron-Leyraud, D. LeBoef, L. Taillefer, S. Adachi, C. Proust, N.E. Hussey, Small Fermi surface pockets in underdoped high temperature superconductors: observation of Shubnikov-de Haas oscillations in $YBa_2Cu_4O_8$. Phys. Rev. Lett. **100**, 047004 (2008)
5. K. Behnia, M.A. Measson, Y. Kopelevich, Oscillating Nernst-Ettingshausen effect in bismuth across the quantum limit. Phys. Rev. Lett. **98**, 166602 (2007)
6. C. Bergemann, S.R. Julian, A.P. Mackenzie, S. NishiZaki, Y. Maeno, Detailed topography of the Fermi surface of Sr_2RuO_4. Phys. Rev. Lett. **84**, 2662–2665 (2000)
7. C. Bergemann, A.P. Mackenzie, S.R. Julian, D. Forsythe, E. Ohmichi, Quasi-two-dimensional Fermi liquid properties of the unconventional superconductor Sr_2RuO_4. Adv. Phys. **52**, 639–725 (2003)
8. P. Blaha, K. Schwarz, G. Madsen, D. Kvasnicka, J. Luitz, *WIEN2K: An Augmented PlaneWave + Local Orbitals Program for Calculating Crystal Properties* (Karlheinz Schwarz, Techn. Universität Wien, Austria, 2001)
9. YuA Bychkov, L.P. Gor'kov, Quantum oscillations of the thermodynamic quantities of a metal in a magnetic field according to the Fermi-liquid model. JETP **14**, 1132 (1962)
10. A. Carrington, Quantum oscillation studies of the Fermi surface of iron-pnictide superconductors. Rep. Prog. Phys. **74**, 124507 (2011)
11. R.G. Chambers, Wave function of a Bloch electron in a magnetic field. Proc. Phys. Soc. **89**, 695 (1966)
12. T. Coffey, Z. Bayindir, J.F. DeCrolis, G. Esper, C.C. Agosta, Measuring radio frequency properties of materials in pulsed magnetic fields with a tunnel diode oscillator. Rev. Sci. Inst. **71**, 4600 (2000)
13. A. Damascelli, D.H. Lu, K.M. Shen, N.P. Armitage, F. Ronning, D.L. Feng, C. Kim, Z.X. Shen, T. Kimura, Y. Tokura, Z.Q. Mao, Y. Maeno, Fermi surface, surface states, and surface reconstruction in Sr_2RuO_4. Phys. Rev. Lett. **84**, 5194–5197 (2000)
14. W.J. de Haas, P.M. van Alphen, The dependence of the susceptibility of diamagnetic metals upon the field. Proc. Netherlands Roy. Acad. Sci. **33**, 1106 (1930)

15. N. Doiron-Leyraud, C. Proust, D. LeBoeuf, J. Levallois, J.B. Bonnemaison, R.X. Liang, D.A. Bonn, W.N. Hardy, L. Taillefer, Quantum oscillations and the Fermi surface in an underdoped high-T-c superconductor. Nature **447**, 565–568 (2007)
16. T. Ebihara, N. Harrison, M. Jaime, S. Uji, J.C. Lashley, Emergent fluctuation hot spots on the Fermi surface of $CeIn_3$ in strong magnetic fields. Phys. Rev. Lett. **93**, 246401 (2004)
17. M. Endo, N. Kimura, H. Aoki, T. Terashima, S. Uji, T. Matsumoto, T. Ebihara, Evolution of spin and field dependences of the effective mass with pressure in $CeIn_3$. Phys. Rev. Lett. **93**, 247003 (2004)
18. S. Engelsberg, G. Simpson, Influence of electron-phonon interactions on de Haas-van Alphen effects. Phys. Rev. B **2**, 1657 (1970)
19. D. Forsythe, S.R. Julian, C. Bergemann, E. Pugh, M.J. Steiner, P.L. Alireza, G.J. McMullan, F. Nakamura, R.K.W. Haselwimmer, I.R. Walker, S.S. Saxena, G.G. Lonzarich, A.P. Mackenzie, Z.Q. Mao, Y. Maeno, Evolution of Fermi-liquid interactions in Sr_2RuO_4 under pressure. Phys. Rev. Lett. **89**, 166402 (2002)
20. R.G. Goodrich, N. Harrison, Z. Fisk, Fermi surface changes across the Néel phase boundary of NdB_6. Phys. Rev. Lett. **97**, 146404 (2006)
21. J.E. Graebner, E.S. Greiner, W.D. Ryden, Magnetothermal oscillations in RuO_2, OsO_2 and IrO_2. Phys. Rev. B **13**, 2426–2432 (1976)
22. D.E. Graf, R.L. Stillwell, K.M. Purcell, S.W. Tozer, Nonmetallic gasket and miniature plastic turnbuckle diamond anvil cell for pulsed magnetic field studies at cryogenic temperatures. High Pressure Res. **31**, 533 (2011)
23. T. Helm, M.V. Kartsovnik, M. Bartkowiak, M. Bittner, M. Lambacher, A. Erb, J. Wosnitza, R. Gross, Evolution of the Fermi surface of the electron-doped high-temperature superconductor $Nd_{2-x}Ce_xCuO_4$ revealed by Shubnikov-de Haas oscillations. Phys. Rev. Lett. **103**, 157002 (2009)
24. R.J. Higgins, D.H. Lowndes, Electrons at the Fermi surface, in *Waveshape Analysis in the dHvA Effect*, ed. by M. Springford (Cambridge University Press, Cambridge, 1980)
25. N.E. Hussey, A.P. Mackenzie, J.R. Cooper, S. Nishizaki, Y. Maeno, T. Fujita, Normal state magnetoresistance of Sr_2RuO_4. Phys. Rev. B **57**, 5505 (1998)
26. K. Ishida, Y. Kitaoka, K. Asayama, S. Ikeda, S. Nishizaki, Y. Maeno, K. Yoshida, T. Fujita, Anisotropic pairing in superconducting Sr_2RuO_4: Ru NMR and NQR studies. Phys. Rev. B. **56**, R505 (1997)
27. C. Kallin, Chiral p-wave order in Sr_2RuO_4. Rep. Prog. Phys. **75**, 042501 (2012)
28. G. Knebel, R. Boursier, E. Hassinger, G. Lapertot, P.G. Nicklowitz, A. Pourret, B. Salce, J.P. Sanchez, I. Sheikin, P. Ponville, H. Harima, J. Flouquet, Localization of 4f State in $YbRh_2Si_2$ under magnetic field and high pressure: comparison with $CeRh_2Si_2$. J. Phys. Soc. Jpn. **75**, 114709 (2006)
29. L. Landau, Diamagnetism of metals. Z. Phys. **64**, 629 (1930)
30. L.D. Landau, E.M. Lifshitz, Motion in a magnetic field, *Quantum Mechanics, Course of Theoretical Physics* (Pergamon Press, UK, 1977), pp. 456–461
31. I.M. Lifshitz, L.M. Kosevich, On the theory of the Shubnikov-de Haas effect. Soviet Physics JETP **2**, 636–645 (1956)
32. G.G. Lonzarich, Magnetic oscillations and the quasiparticle bands of heavy electron systems. J. Magn. Magn. Mater. **76&77**, 1–10 (1988)
33. A.P. Mackenzie, N.E. Hussey, A.J. Diver, S.R. Julian, Y. Maeno, S. Nishizaki, T. Fujita, Hall effect in the two-dimensional metal Sr_2RuO_4. Phys. Rev. B **54**, 7425–7429 (1996)
34. A.P. Mackenzie, S. Ikeda, Y. Maeno, T. Fujita, S.R. Julian, G.G. Lonzarich, The Fermi surface topography of Sr_2RuO_4. J. Phys. Soc. Jpn. **67**, 385 (1998)
35. A.P. Mackenzie, S.R. Julian, A.J. Diver, G.J. McMullan, M.P. Ray, G.G. Lonzarich, Y. Maeno, S. Nishizaki, T. Fujita, Quantum oscillations in the layered perovskite superconductor Sr_2RuO_4. Phys. Rev. Lett. **76**, 3786 (1996)
36. A.P. Mackenzie, Y. Maeno, Superconductivity of Sr_2RuO_4 and the physics of spin-triplet pairing. Rev. Mod. Phys. **75**, 657–712 (2003)

37. Y. Maeno, H. Hashimoto, K. Yoshida, S. Nishizaki, T. Fujita, J.G. Bednorz, F. Lichtenberg, Superconductivity in a layered perovskite without copper. Nature **372**, 532–534 (1995)
38. Y. Maeno, K. Yoshida, H. Hashimoto, S. Nishizaki, S. Ikda, M. Nohara, T. Fujita, A.P. Mackenzie, N.E. Hussey, J.G. Bednorz, F. Lichtenberg, Two-dimensional Fermi liquid behaviour of the superconductor Sr_2RuO_4. J. Phys. Soc. Jpn. **66**, 1405 (1997)
39. S.M. Markus, S.R. Butler, Measurement of de Haas-van Alphen effect in rutile structure RuO_2. Phys. Lett. A **26A**, 518–519 (1968)
40. A. McCollam, R. Daou, S.R. Julian, C. Bergemann, J. Flouquet, D. Aoki, Spin-dependent masses and field-induced quantum critical points. Physica B **359**, 1–8 (2005)
41. A. McCollam, S.R. Julian, P.M.C. Rourke, D. Aoki, J. Flouquet, Anomalous de Haas-van Alphen oscillations in $CeCoIn_5$. Phys. Rev. Lett. **94**, 186401 (2005)
42. A. McCollam, J.S. Xia, J. Flouquet, D. Aoki, S.R. Julian, De Haas-van Alphen effect in heavy fermion compounds - effective mass and non-Fermi-liquid behaviour. Physica B **403**, 717–720 (2008)
43. G.J. McMullan, M.P. Ray, R.J. Needs, Comparison of the calculated and observed Fermi surfaces of Sr_2RuO_4. Physica B **223–24**, 529–531 (1996)
44. G.J. McMullan, P.M.C. Rourke, M.R. Norman, A.D. Huxley, N. Doiron-Leyraud, J. Flouquet, G.G. Lonzarich, A. McCollam, S.R. Julian, The Fermi surface and f-valence electron count of UPt_3. New J. Phys. **10**, 053029 (2008)
45. H. Ohkuni, Y. Inada, Y. Tokiwa, K. Sakurai, R. Settai, T. Honma, Y. Haga, E. Yamamoto, Y. Onuki, H. Yamagami, S. Takahashi, T. Yanagisawa, Fermi surface properties and de Haas-van Alphen oscillation in both the normal and superconducting mixed states of URu_2Si_2. Phil. Mag. B **79**, 1045–1077 (1999)
46. E. Ohmichi, Y. Maeno, S. Nagai, Z.Q. Mao, M.A. Tanatar, T. Ishiguro, Magnetoresistance of Sr_2RuO_4 under high magnetic fields parallel to the conducting plane. Phys. Rev. B **61**, 7101 (2000)
47. E. Ohmichi, T. Osada, Torque magnetometry in pulsed magnetic fields with use of a commercial microcantilever. Rev. Sci. Inst. **73**, 3022 (1999)
48. B.J. Ramshaw, B. Vignolle, J. Day, R.X. Liang, W.N. Hardy, C. Proust, D.A. Bonn, Angle dependence of quantum oscillations in $YBa_2Cu_3O_{6.59}$ shows free-spin behaviour of quasiparticles. Nat. Phys. **7**, 234–238 (2011)
49. J.J. Randall, R. Ward, The preparation of some ternary oxides of the platinum metals. J. Am. Chem. Soc. **81**, 2629–2631 (1959)
50. P.H.P. Reinders, M. Springford, de Haas-van Alphen effect in the Kondo lattice $CeAl_2$. J. Magn. Magn. Mater. **79**, 295–302 (1989)
51. T.M. Rice, M. Sigrist, Sr_2RuO_4: and electronic analogue of ^{3}He? J. Phys.: Condens. Matter **7**, L643–L648 (1995)
52. S.C. Riggs, O. Vafek, J.B. Kemper, J.B. Betts, A. Migliori, F.F. Balakirev, W.N. Hardy, R.X. Liang, D.A. Bonn, G.S. Boebinger, Heat capacity through the magnetic-field-induced resistive transition in an underdoped high-temperature superconductor. Nature Phys. **7**, 332–335 (2011)
53. P.M.C. Rourke, A.F. Bangura, T.M. Benseman, M. Matusiak, J.R. Cooper, A. Carrington, N.E. Hussey, A detailed de Haas-van Alphen effect study of the overdoped cuprate $Tl_2Ba_2CuO_{6+\delta}$. New J. Phys. **12**, 105009 (2010)
54. P.M.C. Rourke, S.R. Julian, Numerical extraction of de Haas-van Alphen frequencies from calculated band energies. Comput. Phys. Commun. **183**, 324–332 (2012)
55. I. Sheikin, A. Groger, S. Raymond, D. Jaccard, D. Aoki, H. Harima, J. Flouquet, High magnetic field study of $CePd_2Si_2$. Phys. Rev. B **67**, 094420 (2003)
56. H. Shishido, R. Settai, H. Harima, Y. Onuki, A drastic change of the Fermi surface at a critical pressure in $CeRhIn_5$: dHvA study under pressure. J. Phys. Soc. Jpn. **74**, 1103–1106 (2005)
57. D.S. Shoenberg, *Quantum Oscillations in Metals* (Cambridge University Press, Cambridge, 1984)
58. F. Steglich, J. Aaarts, C.D. Bredl, W. Lieke, D. Meschede, W. Franz, H. Schafer, Superconductivity in the presence of strong Pauli paramagnetism - $CeCu_2Si_2$. Phys. Rev. Lett. **43**, 1892–1896 (1979)

59. L. Taillefer, G.G. Lonzarich, Heavy-fermion quasiparticles in UPt_3. Phys. Rev. Lett. **60**, 1570–1573 (1987)
60. M. Takashita, H. Aoki, S. Terashima, S. Uji, K. Maezawa, R. Settai, Y. Onuki, dHvA Effect study of metamagnetic transition in $CeRu_2Si_2$ II - The state above the metamagnetic transition. J. Phys. Soc. Jpn. **65**, 515 (1996)
61. B. Vignolle, A. Carrington, R.A. Cooper, M.M.J. French, A.P. Mackenzie, C. Jaudet, D. Vignolles, C. Proust, N.E. Hussey, Quantum oscillations in an overdoped high-T_c superconductor. Nature **455**, 952–955 (2008)
62. A. Wasserman, M. Springford, The influence of many-body interactions on the de Haas-van Alphen effect. Adv. Phys. **45**, 471 (1996)
63. S.A.J. Wiegers, A.S. van Steenbergen, M.E. Jeuken, M. Bravin, P.E. Wolf, G. Remenyi, J.A.A.J. Perenboom, J.C. Maan, A sensitive and versatile torque magnetometer for use in high magnetic fields. Rev. Sci. Inst. **69**, 2369 (1998)
64. K. Yamaji, On the angle dependence of the magnetoresistance in quasi-2-dimensional organic superconductors. J. Phys. Soc. Jpn. **58**, 1520–1523 (1989)
65. E.A. Yelland, J. Singleton, C.H. Milke, N. Harrison, F.F. Balakirev, B. Dabrowski, J.R. Cooper, Quantum oscillations in the underdoped cuprate $YBa_2Cu_4O_8$. Phys. Rev. Lett. **100**, 047003 (2008)
66. Y.B. Zhang, Y.W. Tan, H.L. Stormer, P. Kim, Experimental observation of the quantum Hall effect and Berry's phase in graphene. Nature **438**, 201–204 (2005)

Chapter 6
Pressure Probes

Michael Nicklas

Abstract The physical properties of correlated materials, like low-dimensional organic conductors, cuprate superconductors, heavy-fermion metals, or the recently discovered iron-based superconductors, depend on a delicate interplay of different physical effects. External pressure is an ideal tool to tune this interplay. The resulting phase diagrams and their study is essential for the understanding of the underlying physical principles. This chapter is intended to give an introduction to modern pressure techniques which are used for investigations of strongly correlated materials. We provide a short overview of the different types of pressure cells. Thereby, we focus on the experimental capabilities and point at limits and problems which might occur in a pressure experiment. In a survey of experimental probes we outline the specifics of the experimental setup for pressure studies in comparison with the setup used at ambient pressure. We further address the particular restrictions on the experimental resolution in the pressure study and discuss the accessible parameter range in pressure, temperature and magnetic field. The covered physical probes include, electrical- and thermal-transport measurements, thermodynamic and magnetic studies, magnetic-resonance experiments, and structural and spectroscopic investigations. On the example of heavy-fermion superconductors we elucidate the contributions of pressure experiments on the discovery and understanding of new emerging physical phenomena in correlated electron materials.

6.1 Introduction

External pressure is an excellent tool to tune the interplay of different energy scales in strongly correlated materials in a clean and controlled way. One notable example for competing interactions is the magnetic Ruderman-Kittel-Kasuya-Yoshida (RKKY) exchange interaction and the Kondo effect in heavy-fermion metals. The major drawback of *pressure probes* is the additional complexity of the experiments due to the

M. Nicklas (✉)
Max Planck Institute for Chemical Physics of Solids,
Nöthnitzer Str. 40, 01187, Dresden, Germany
e-mail: nicklas@cpfs.mpg.de

A. Avella and F. Mancini (eds.), *Strongly Correlated Systems*,
Springer Series in Solid-State Sciences 180, DOI 10.1007/978-3-662-44133-6_6

pressure cells needed to generate the high pressure. Today, many physical quantities are accessible at high pressures. Available probes comprise, for example, electrical transport, thermodynamic and magnetic properties, but also magnetic resonance and scattering techniques. Compared to ambient-pressure measurements, the accessible temperature range might be limited and the sensitivity of the experiment reduced.

In this chapter we will concentrate on the experimental techniques adapted to high-pressure environments. In Sect. 6.2 we give an overview on different types of pressure cells with a focus on pressure cells which are currently used in the laboratories. In the following section (Sect. 6.3) we describe the different ways to determine the actual pressure inside the pressure cell and discuss the importance of the pressure transmitting medium in carrying out a successful experiment. In Sect. 6.4 we provide a survey of the implementation of the measurement of different physical quantities in pressure cells. We put our special attention on the particular requirements in the study of correlated electron materials. Our aim is to point out the modifications of experimental setups and the limitations and problems which can occur while performing pressure experiments. A discussion of technical details is beyond this introductory text, therefore, we refer to the literature at the appropriate places. In the final section (Sect. 6.5) we highlight the importance of pressure studies on the example of heavy-fermion materials.

6.2 Pressure Generation

The target of a pressure study is to measure a physical quantity at high pressures with the same sensitivity as at ambient pressure. This is usually difficult due to the fact that the sample and eventually the experimental setup have to be placed inside the pressure cell, which provides only a limited space. The size of the pressure chamber can be of the order of a few hundred micrometers up to several millimeters in diameter depending on the type of pressure cell. There are additional restrictions connected to the specific type of a physical investigation, for example, it might be difficult to reach low temperatures ($T \ll 1\,\mathrm{K}$) and high magnetic fields with a pressure setup.

6.2.1 Pressure Cells

In the following, we give an introduction to high-pressure techniques and present the different types of pressure cells which are used to investigate strongly correlated materials. The main challenge of pressure experiments becomes evident when we write pressure (p) as:

$$p = \frac{F}{A}, \tag{6.1}$$

where F is the force acting on the area A. To increase the maximum achievable pressure of a pressure setup, we can follow two routes: (i) generate larger and larger forces or (ii) reduce the size of the sample chamber further and further. The first route, which is, for example, followed in the field of earth sciences or high-pressure materials synthesis, requires the use of a large hydraulic press and corresponding pressure apparatus. Due to the size of the whole setup this route is not appropriate for low-temperature experiments, which require small pressure cells fitting in a cryostat. On the other hand, going to smaller and smaller dimensions is also no ideal solution, since it becomes more and more challenging to set up an experiment due to the reduced size of the sample chamber. Despite of these challenges, usually the second route is followed to study the physical properties of materials at high pressures.

In general, pressure cells can be divided into different groups depending on their mechanism adapted to generate the pressure [1]. Most commonly used in laboratories are the piston-cylinder type and opposed-anvil type pressure cells. While the maximum pressure in piston-cylinder type cells is limited to about 4 GPa, in diamond-anvil cells (DAC's) pressures well above 100 GPa can be reached. The interesting physics in strongly correlated materials, like pressure-induced superconductivity or quantum critical phenomena, is in most cases observed in the pressure range below 10 GPa.

6.2.2 Piston-Cylinder Type Pressure Cells

Piston-cylinder type pressure cells have the advantage of a reasonably large volume sample chamber and a relatively small size. This enables pressure studies of a large number of physical properties, like electrical transport, heat capacity, magnetic probes, neutron scattering, etc., down to very low temperatures and in high magnetic fields. This type of cell is easy to handle and, therefore, in use in many laboratories. The name *piston-cylinder* type pressure cell comes from the moving piston inside the pressure cylinder, on which the force is applied to compress the sample chamber. To apply the force a hydraulic press is used. After application of the desired force, the pressure inside the cell is clamped with a locking nut. For this reason, also the term *clamp-type* pressure cell is used. Afterwards, the cell can be placed inside the cryostat. For measurements in magnetic fields pressure cells machined from magnetic materials are not suitable. Therefore, a nonmagnetic Cu:Be alloy with about 2.5 % Be is used as material for the cell body. Compared with maraging steel, also used as a material for constructing pressure cells, Cu:Be has the advantage that it is nonmagnetic and still has a reasonably high tensile strength ($\sim$1.3 GPa). Considering the hassles accompanying the usage and machining of alloys containing beryllium, Cu:Ti may become an alternative material for pressure cells [2].

The maximum pressure generated using a Cu:Be piston-cylinder type pressure cell is limited to about 1.5 GPa. Above this pressure plastic deformations take place. In Cu:Be cells with a particular small volume sample chamber higher pressures can be achieved on the expense of a plastic deformation of the pressure chamber. Double-layer piston-cylinder type cells have been invented to reach higher pressures and to

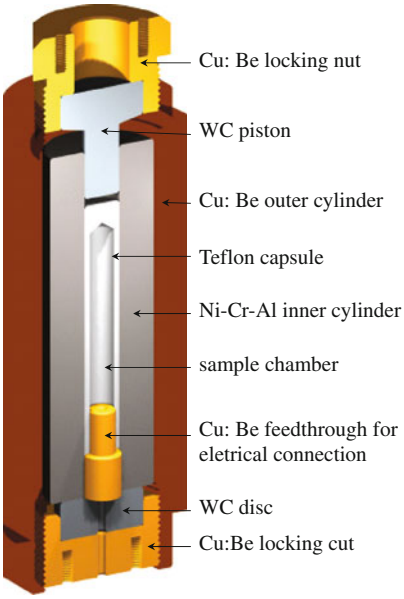

Fig. 6.1 Schematic drawing of a double-layer piston-cylinder type pressure cell. The outer diameter of this cell is about 25 mm. Using this or similar designs pressures between 3 and 4 GPa can be reached

maintain a large volume sample chamber [3]. In a double-layer piston-cylinder type cell pressures between 3 and 4 GPa can be reached [3–6]. Furthermore, this type of cell is extremely versatile and can be used for different kinds of experiments. A schematic drawing of a typical design is displayed in Fig. 6.1. The cell consists of an outer cylinder machined of Cu:Be and an inner cylinder of Ni-Cr-Al, which has a higher tensile strength than Cu:Be [2]. Instead of Ni-Cr-Al also MP35N, a Co-Ni-Cr-Mo alloy, is often used as material for the inner cylinder [2]. Its magnetic properties due to the Co content make its use less favorable.

6.2.3 Opposed-Anvil Type Pressure Cells

The class of opposed-anvil pressure cells comprises many different types of cells. The highest pressures can be reached with the diamond-anvil cell (DAC), but this offers the smallest available sample space. Other types of opposed-anvil cells, like the Bridgman-type cell or the toroidal-anvil cell, have a larger available space for the sample, but do by far not reach the maximum pressures of DAC's.

The general principle of an opposed-anvil type pressure cell is illustrated in Fig. 6.2. One of the anvils is usually fixed in place and the force is applied to the movable anvil. The gasket sits in between the anvils and seals the pressure inside the

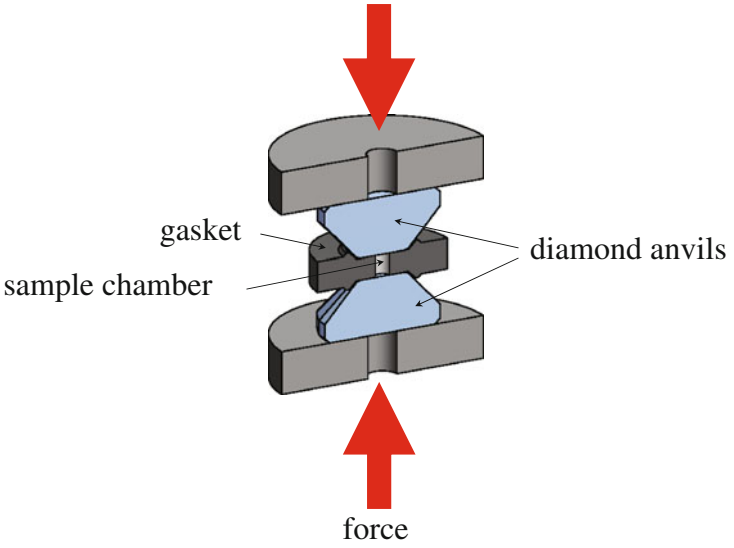

Fig. 6.2 Schematic representation of the principle of an opposed-anvil cell illustrated on the example of a diamond-anvil pressure cell (DAC)

sample chamber filled with the pressure transmitting medium and the sample(s). Next to the sample(s) a pressure gauge is placed in order to determine the pressure inside the sample chamber (see Sect. 6.3). In most setups, the pressure is changed at room temperature using a hydraulic press and then clamped by one or more screws (nuts). In addition to the application of pressure at room temperature, in some experimental setups the pressure can be changed at low temperatures using a bellow system [7, 8].

The clamped Bridgman-type anvil technique has the most simple setup. Usually tungsten carbide (WC) serves as material for the anvils, but sometimes sintered synthetic diamond is used to reach higher pressures. While WC starts to deform above 11 GPa, limiting the maximum pressure which can be obtained with these anvils, sintered synthetic diamond allows to reach pressures up to 30 GPa. The sintered synthetic diamond anvils are magnetic which limits their usability in some experiments. In contrast to sintered synthetic diamond, non-magnetic WC is available. The remnant field of a magnetic anvil after an experiment in magnetic fields can, for example, shift the superconducting transition of lead used as manometer to lower temperatures leading to an overestimation of the pressure inside the cell (see Sect. 6.3.1). Figure 6.3 shows an electrical-resistivity setup in a Bridgman-type pressure cell. The gasket consists of pyrophyllite (a sheet silicate) and the samples sit in between two sheets of the soft mineral steatite, which is in this case the pressure transmitting medium (see Sect. 6.3.2). With this experimental setup the resistivity of two samples and lead, which serves as pressure gauge, can be measured at the same time (see also Sects. 6.3.1 and 6.4.1).

The solid pressure transmitting medium causes non-isotropic pressure distributions in the sample chamber. To obtain more isotropic pressure conditions in

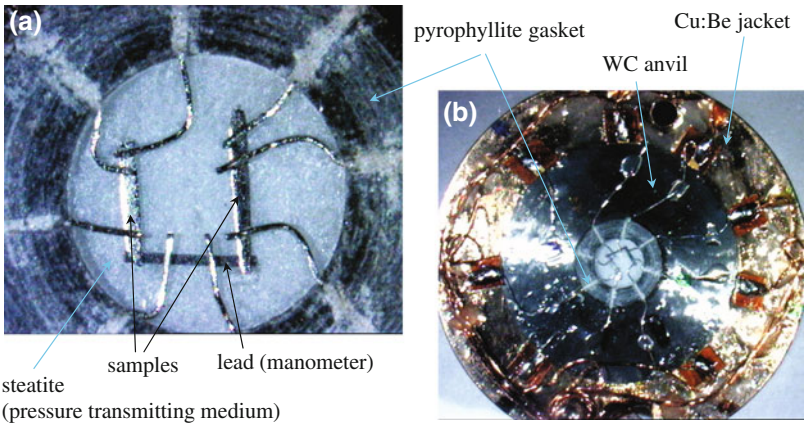

Fig. 6.3 **a** Setup for electrical-resistivity measurements in a Bridgman-type pressure cell. The sample chamber has a diameter of 2 mm. Before closing the cell a second steatite disc will be placed on top of the samples. **b** WC anvil enclosed in a Cu:Be jacket. Pyrophyllite serves as material for the gasket [9]

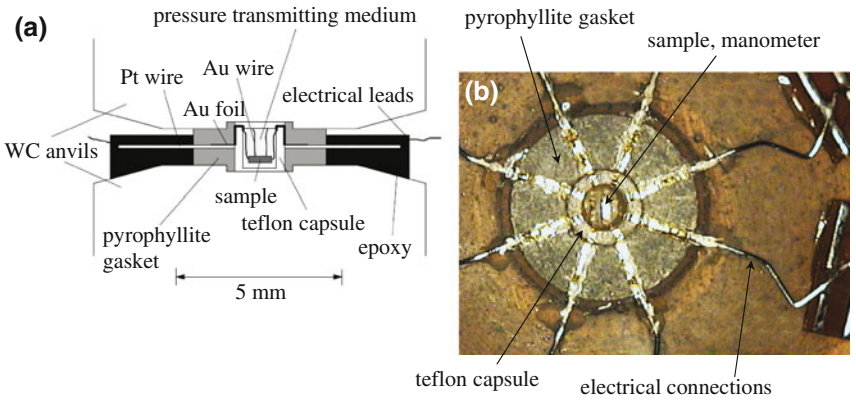

Fig. 6.4 Schematic drawing (**a**) and photograph (**b**) of modified Bridgman anvils with an experimental setup for electrical-resistivity studies. A liquid is used as pressure transmitting medium (see also [10–12])

Bridgman-type pressure cells different attempts have been made to replace steatite by a liquid pressure transmitting medium. One procedure is to impregnate the inner wall of the gasket with epoxy [13]. Another one uses teflon rings as sealing in a classical Bridgman setup [14]. A completely different approach uses modified anvils and a teflon capsule as pressure chamber [10–12]. An example for such a setup is shown in Fig. 6.4. In this cell pressures of about 8 GPa can be reached using a liquid pressure transmitting medium. A similar design has been realized in toroidal-anvil cells [15–17]. The maximum achievable pressure and the available sample space are comparable in both types of pressure cells.

In a diamond-anvil cell the highest possible static pressure can be achieved. This requires a very high precision of the alignment of the opposed diamond anvils. The major drawback of the DAC technique is the limited experimental space of the order of only a few 100 μm in diameter and several 10 μm in height, depending on the size of the diamonds used. A brief history of the DAC, which was invented more than 50 years ago, is given in an article by Basset [18]. Further useful information on technical aspects can be found in [19–21].

Even though, pressures far beyond 100 GPa can be obtained in DAC's, the experimental methods for pressures larger than 50 GPa are typically limited to physical probes which do not need electrical connections inside the pressure chamber, but take advantage of the transparency of diamonds in a large frequency range. These methods include optical spectroscopy, X-ray scattering/spectroscopy, or Mössbauer spectroscopy. For other probes, like electrical transport or specific heat, the main challenge is to bring electrical connections into the high-pressure region. Today, DAC's have been miniaturized so far that they can be used in most standard laboratory cryogenic systems. Examples for different DAC designs can be found in [22–25].

6.2.4 *Indenter-type Pressure Cells*

With indenter-type pressure cells pressures up to 4.5 GPa at low temperatures have been reached using a liquid pressure transmitting medium [26]. This pressure is above the limit of piston-cylinder type cells. Furthermore, the indenter type cell still provides a reasonably sized sample space of about 1.6 mm in diameter and 1.4 mm in depth, which is reduced to 0.7 mm at the maximum pressure. A schematic drawing is shown in Fig. 6.5. In some respects, this pressure cell can be considered

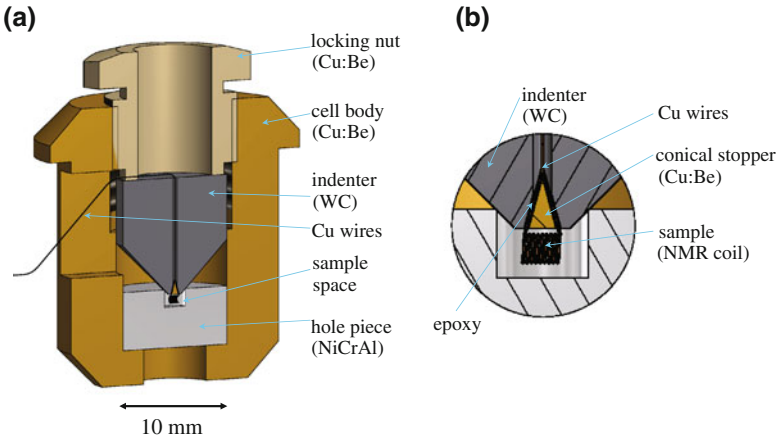

Fig. 6.5 *left* Cross-sectional view of the indenter pressure cell. *right* Arrangement for nuclear magnetic resonance (NMR) measurements in the indenter cell (after [26])

as the upper part of an opposed-anvil cell, just the lower anvil and the gasket are missing and replaced by a piece of Ni-Cr-Al with a hole serving as sample chamber. A main advantage compared to modified Bridgman or toroidal-anvil cells is that the feedthrough for the electrical wires can be reused. However, the piece with the hole is deformed in the experiment and has to be replaced each time.

6.2.5 Other Types of Pressure Cells

We briefly want to mention two further types of pressure cells. The multi-anvil pressure cells are fairly complicated to operate, since the whole setup, including a custom-made cryostat, is placed inside a large hydraulic press [27, 28]. Due to the construction the temperature is limited to the range of a ^{4}He cryostat. The helium gas pressure cells are the second type of pressure cells we want to refer to. In them pressures up to about 1.7 GPa can be reached. However, practically the pressure is limited to 1 GPa because of the safety limits of the available pressure fittings. Due to the usage of helium gas as pressure transmitting medium the helium gas pressure cells offer excellent hydrostatic pressure conditions and a very good pressure control especially at small pressures [29, 30].

6.2.6 Electrical Connections

Several experimental probes require electrical connections inside the pressure chamber. This provides an additional challenge for the experimentalists. The electrical connections are usually the first place where a pressure experiment fails, e.g. due to a short circuit to the ground. For piston-cylinder type pressure cells quite reliable electrical feedthroughs can be prepared using glass or sapphire filled epoxies [3]. To prepare reliable electrical connections for anvil cells using metallic gaskets is more difficult. The wires have to be electrically insulated from the gasket. This can be done by covering the gasket by sapphire (Al_2O_3) or cubic boron nitride (CBN) powder mixed with epoxy. However, there is a high risk of an electrical short circuit while closing the cell and applying pressure, e.g. at the edges of the gasket. A promising way to overcome this obstacle of the anvil cells, are patterned anvils [31–33]. Here, electrical leads or even more complicated structures like multilayered coils for magnetic measurements are deposited on the anvil and consecutively covered by an additional layer of the anvil material. One problem in experiments can arise from the poor electrical properties of the materials which can be used for depositing the structures. Figure 6.6 shows examples of electrical contact leads and a multilayered coil evaporated on sapphire (Al_2O_3) and moissanite (single-crystalline SiC) anvils [34].

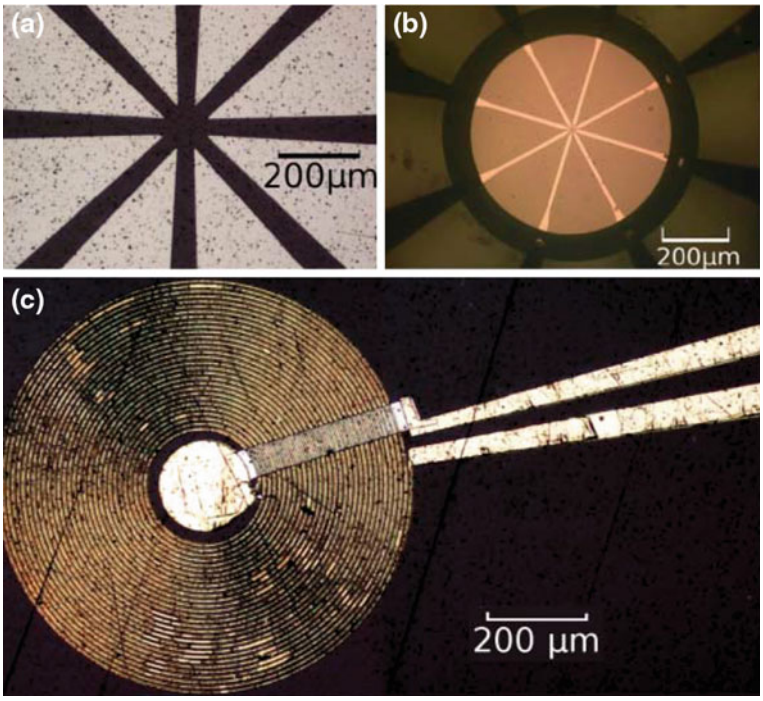

Fig. 6.6 Patterned anvil designs. **a** Al_2O_3 anvil with eight lead probe pattern **b** moissanite (single-crystalline SiC) anvil with eight-lead probe NiCr pattern, and **c** Au on NiCr multilayered coil pattern on an Al_2O_3 anvil [31]. *Reproduced with permission from Review of Scientific Instruments 82, 033901 (2011). Copyright 2011 American Institute of Physics*

6.3 Pressure Determination and Transmitting Media

The exact determination of the pressure and the quality of the pressure conditions inside a pressure cell are very important for any high-pressure experiment.

6.3.1 Pressure Determination

A simple estimation of the pressure inside the pressure cell as applied force per surface area (6.1) is not reliable. Due to friction effects the actual force transmitted to the sample space is not known exactly. Furthermore, the surface area of the pressure chamber can change with pressure, especially, in opposed anvil cells. Therefore, more precise pressure gauges placed next to the sample inside the pressure chamber are needed.

An other important point to consider in a pressure experiment is that due to the different thermal expansions of the materials used in the pressure cell setup, i.e. for the pressure cell body, pistons or anvils, pressure transmitting medium etc., the

pressure inside the pressure cell increases or decreases on cooling. Even though, the design of a pressure cell can compensate this effect partly, it is important to be aware that the pressure inside a pressure cell is never constant on changing temperature. Therefore, it is important at which temperature the pressure inside the pressure cell is determined.

Depending on the type of pressure cell different manometers are available. The pressure dependence of the electrical resistance of Manganin wire can be utilized as pressure gauge [35–38]. Due to the mainly temperature independent resistance, Manganin can be used in a large temperature range. The linear pressure dependence of the electrical resistivity of manganin is very reproducible and can be calibrated using the structural transitions of bismuth under pressure. These are easily detectable in the electrical resistance and serve as reliable fix points for a calibration [39, 40].

Another widely deployed method to determine the pressure at low temperatures uses the strong pressure dependencies of the superconducting transition temperatures (T_c) of lead, tin, or indium [41, 42]. For pressures up to 5 GPa the following relations hold (p in GPa) [41]:

$$\begin{aligned} \text{Pb}: \quad & T_c(p) = T_c(0) - (0.365 \pm 0.003)\,p, \\ \text{Sn}: \quad & T_c(p) = T_c(0) - (0.4823 \pm 0.002)\,p + (0.0207 \pm 0.0005)\,p^2, \\ \text{In}: \quad & T_c(p) = T_c(0) - (0.3812 \pm 0.002)\,p + (0.0122 \pm 0.0004)\,p^2. \end{aligned} \tag{6.2}$$

Here, no additional calibrations are needed and T_c can be determined by electrical resistance or magnetic susceptibility (magnetization). The latter has the advantage that no electrical connections inside the pressure chamber are required. We note, one important drawback of this method is that the T_c of lead, tin, or indium is highly sensitive to a magnetic field. Thus, the remnant field of a superconducting magnet in a typical experimental setup can already lead to a strong shift of T_c to lower temperatures, pretending a much higher pressure inside the cell. Therefore, it is important to remove any remnant field carefully (to less than 0.1 mT) before using this method as pressure gauge. The width of the superconducting transition can also serve as a measure of the pressure gradient inside the pressure chamber by taking the size of the manometer into account.

In diamond-anvil cells, or more generally, in pressure cells with optical access, the pressure shift of the ruby fluoresce line R_1 is used as pressure gauge [43, 44]. This method is not limited to a certain temperature range. Furthermore, the placement of several ruby grains inside the pressure chamber, which can be individually focused by an optics, allows for a detailed study of the pressure gradient. The pressure (p in GPa) can be obtained from the R_1 line-shift [45–47]:

$$p = \frac{1904}{B}\left[\left(1 + \frac{\delta\lambda}{6.9424}\right)^B - 1\right], \tag{6.3}$$

with $\delta\lambda$ the line-shift of the ruby R_1 line in nm and the parameter B as a measure of the hydrostaticity ($B = 7.665$ for hydrostatic conditions).

In addition to the previously described methods, there are further ways to determine the pressure, which are directly related to a particular physical probe. In the case of nuclear quadrupol resonance (NQR) or nuclear magnetic resonance (NMR) experiments the pressure shift of the ^{63}Cu NQR spectrum of Cu_2O is established as pressure gauge [48, 49]. Here, a Cu_2O piece is placed inside the detection coil, next to the sample under investigation (see also 6.4.7.1). Furthermore, X-ray and neutron diffraction experiments allow to utilize the equation of state (EOS), e.g. of NaCl, to determine the pressure [50].

6.3.2 Pressure Transmitting Media

Ideal isotropic pressure conditions cannot be achieved in real pressure experiments. Nevertheless, the quality of the pressure conditions inside the pressure cell can be crucial for the success of an experiment. Non-hydrostatic effects, e.g. uniaxial strain, can strongly influence the physical properties of a sample. Therefore, it is important to carefully choose an appropriate pressure transmitting medium. A gas, like Ar or He, offer the best isotropic pressure conditions. However, we want to point out that even a solid pressure transmitting medium like steatite, AgCl, or NaCl can provide satisfactory pressure conditions depending on the samples and physics investigated. On the other hand, even the solidification of helium can cause anomalies in the data of very strain sensitive materials [51]. Therefore, in case unexpected anomalies appear in the data, it is important to look at the properties of the pressure transmitting medium, e.g. solidification pressure or temperature. A recent study reports on the properties of many commonly used pressure transmitting media [52]. This study covers the pressure range up to 10 GPa in different temperature regions. Further information can be also found in [53–62].

6.4 Physical Probes

6.4.1 Electrical Transport

The electrical resistance is probably the most used probe to investigate the physics of strongly correlated materials under pressure. This is because the electrical resistance, including magnetoresistance and Hall-effect, is the only physical property which can be measured with the same precision, in almost the same temperature and magnetic field range, under pressure like at ambient conditions. All other probes suffer from higher background contributions, reduced sensitivities, or other limiting factors.

In a piston-cylinder type pressure cell several samples can be measured in one experiment. A typical setup for three samples and the pressure gauge is shown in Fig. 6.7. In opposed-anvil cells only one or two samples can be investigated simulta-

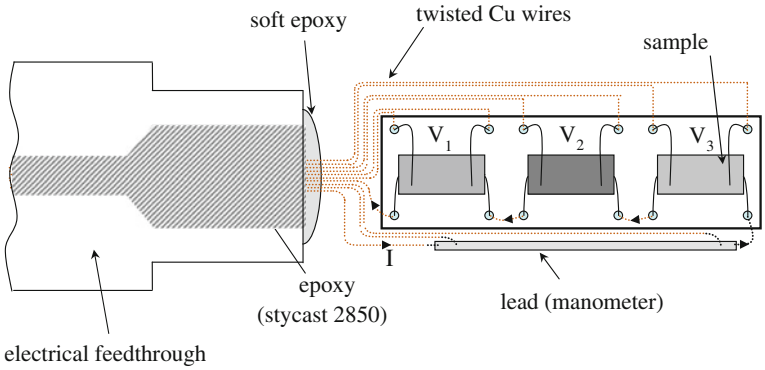

Fig. 6.7 Electrical feedthrough for a piston-cylinder type pressure cell with sample board. The electrical wiring is shown schematically for 3 samples and the pressure gauge (strip of lead). A serial electrical current is used for all samples

neously (see also Fig. 6.3). In electrical-resistance experiments maximum pressures of above 50 GPa can be achieved in DAC's.

6.4.2 Thermal Transport and Thermoelectric Power

6.4.2.1 Thermal Transport

Thermal transport is difficult to measure inside a pressure cell. In contrast to ambient pressure experiments, where the sample sits in vacuum, the heat loss from the sample to the pressure medium is generally significant and makes any measurement of the thermal conductivity using the steady-state method under pressure nearly impossible [63]. To overcome this problem two different methods have been proposed, the transient method [64, 65] and the 3ω method [66]. The latter has the advantage that very small samples can be measured. The small sample size and the high measurement frequencies help to reduce the heat loss from the sample to the pressure medium. However, the losses cannot be neglected. This method is limited to intermediate temperatures ($T \gtrsim 10\,\mathrm{K}$).

6.4.2.2 Thermoelectric Power

In contrast to thermal transport, the measurement of the thermoelectric power (TEP), S, is well established under pressure [67–69]. To measure $S(T)$ a temperature gradient is induced across the sample. S is defined as:

$$S(T, p) = \frac{\Delta T(T, p)}{\Delta V(T, p)}, \tag{6.4}$$

where ΔT is the thermal gradient and ΔV the thermoelectric voltage across the sample. The temperature gradient is usually measured using thermocouples as thermometers. For the determination of S from the experimental data the knowledge of the absolute values of the TEP of the material used for the voltage leads and its pressure dependence is essential [70]. In pressure experiments different setups with one or two thermocouples are used. In the former case it is assumed that the cold end of the sample is at the temperature of the bath [69]. The sensitivity of the available thermocouples limits the experiments to the temperature range above 1 K. TEP experiments have been carried out up to 30 GPa in Bridgman-type pressure cells using steatite as pressure transmitting medium [69, 71]. In DAC's a combination of ZrO_2 and CsI is used as pressure transmitting medium which also serves as a thermal insulation of the sample from the diamond anvils [72]. Piston-cylinder type pressure cells have been also successfully deployed for TEP experiments [68, 73].

6.4.3 Heat Capacity

For studies of the heat capacity under pressure two approaches are followed. The first method provides absolute values of the heat capacity by measuring the heat capacity of the whole pressure cell with the sample inside. A subtraction of the addenda finally yields the heat capacity of the sample. Following the second procedure semi-quantitative data is obtained by using an ac-technique to directly measure the heat capacity of the sample inside the pressure cell.

Using the first technique, the heat capacity of the whole pressure cell with the sample inside is measured [77–79]. To obtain the specific heat of the sample, the addenda, including the contributions of the pressure cell and the pressure trans-

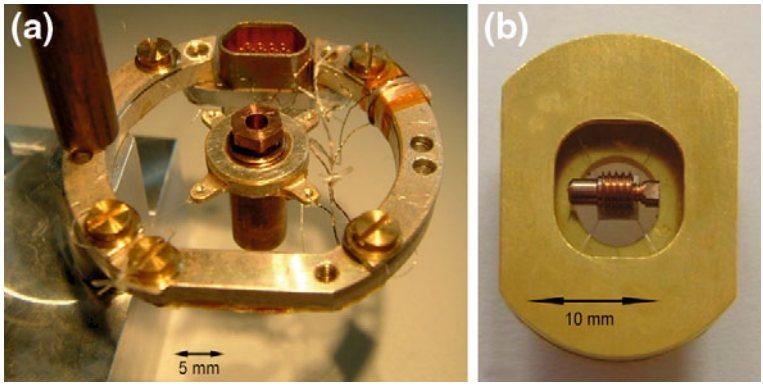

Fig. 6.8 Two different pressure cells for heat-capacity measurements. **a** Setup for a dilution refrigerator, **b** miniature cell on a commercial heat-capacity platform [74–76]

mitting medium, has to be carefully determined and subtracted from the raw data [77–79]. Depending on the size of the pressure cell a customized measurement rig or a standard heat-capacity platform is employed (see Fig. 6.8). The heat capacity is then determined by a quasi-adiabatic heat-pulse technique [80] or a relaxation technique [81, 82]. The main limitation of this method is that only samples with a large heat capacity compared with the heat capacity of the pressure cell can be investigated. Furthermore, only piston-cylinder type pressure cells provide a large enough volume for the sample, but limit the maximum achievable pressures to the 3 GPa range. One class of materials suited for this method are the heavy-fermion materials. In a pressure experiment the heat capacity of a heavy-fermion sample typically reaches between 10 and 120 % of the heat capacity of the pressure cell. At higher temperatures the contribution of the pressure cell to the total heat capacity increases stronger than that of the sample, making measurements above ∼10 K basically impossible. Experiments starting from temperatures below 50 mK can be carried out. However, in the low-temperature range ($T \lesssim 0.5$ K) nuclear Schottky contributions to the heat capacity, e.g. from the Cu in the pressure cell, become substantial in magnetic fields. Since these contribute significantly to the addenda, precise measurement in high magnetic fields and at low temperatures are very challenging.

The second available method, the ac-technique directly measures the heat capacity of the sample and can, therefore, be adapted to different types of pressure cells. It allows to study small crystals since thermometer and resistive heater are usually directly glued to the sample [83, 84]. For diamond-anvil cells also a laser heating method has been developed [85]. For the ac-technique the thermal conduction inside the sample has to be much larger than that from the sample to the surrounding pressure medium. In practice this can be achieved by choosing an appropriate sample geometry and measurement frequency. As thermometer a thermocouple is usually the best choice. Due to its small thermal mass it follows the temperature of the sample immediately. The sensitivity of thermocouples strongly decreases with decreasing temperature. In the low-temperature region (<1 K) AuFe/Au thermocouples give the best sensitivity [70]; at temperatures above 2 K Au/Chromel thermocouples provide a good resolution [70, 85]. Below 300 mK the resolution of the thermocouples decreases rapidly making ac-heat-capacity experiments more and more difficult. The ac-technique has been adapted for different types of pressure cells, e.g. piston-cylinder type pressure cells [86, 87], Bridgman-type cells with solid [70, 88, 89] and liquid pressure medium [71], cubic-anvil setups [90], and diamond-anvil cells [85].

6.4.4 Thermal Expansion and Magnetostriction

The linear thermal expansion, respectively, the volume thermal expansion coefficient,

$$\alpha = \frac{1}{\ell(T)} \cdot \frac{\partial \ell(T)}{\partial T} \text{ and } \beta = \frac{1}{V_s(T)} \cdot \frac{\partial V_s(T)}{\partial T}, \tag{6.5}$$

and the magnetostriction coefficient,

$$\lambda = \frac{1}{\ell(B)} \cdot \frac{\partial \ell(B)}{\partial B}, \tag{6.6}$$

are important thermodynamic properties suitable for studying different types of phase transitions. Here, ℓ is the length and V_s the volume of the sample.

Under pressure there are only two ways to determine the thermal expansion/magnetostriction coefficient: (i) a study of the lattice parameters by X-ray or neutron diffraction (see also Sect. 6.4.8) or (ii) the strain-gauge technique [15, 91, 92]. The first method does not only provide α and β, but also gives structural information, e.g. the pressure dependence of the lattice parameters (see for example [93]). Furthermore, fitting the unit-cell volume, $V(p)$, using the second order Murnaghan's equation of state (EOS),

$$p = \frac{B_0}{B_0'} \left[\left(\frac{V_0}{V(p)} \right)^{B_0'} - 1 \right], \tag{6.7}$$

gives the bulk modulus, B_0, of the material. B_0' is a parameter, which is typically between 3 and 6 in intermetallic compounds, and V_0 is the unit-cell volume at ambient pressure. The second way to study the thermal expansion or magnetostriction is the strain-gauge technique. It is based on a simple electrical resistance measurement. A resistive strain gauge consists ideally of a meander-type resistance structure to enhance the sensitivity. The strain gauge is glued directly on the sample. The expansion, respectively, contraction of the sample gives a change in the length of the strain gauge, which is detectable in the electrical resistance of the strain gauge. This technique has a much better resolution than X-ray or neutron scattering [15], but it does by far not reach the sensitivity of a capacitive dilatometer used at ambient pressure [94]. The limited sensitivity restricts the use of this probe under pressure primarily to the detection of structural phase transitions. X-ray and neutron diffraction experiments can be conducted to pressures above 50 GPa using DAC's. The strain-gauge technique has been adapted to piston-cylinder type pressure cells [91, 92] and toroidal-anvil cells allowing to reach pressures up to 8 GPa [15].

6.4.5 Magnetic Susceptibility and Magnetization

The experimental setups for magnetic susceptibility (χ_{ac}) and magnetization (M) measurements under pressure can be divided in two groups: (i) experiments in which the whole pressure cell including the sample is measured in a conventional magnetometer or susceptometer [97–100], e.g. a commercial SQUID magnetometer and (ii) setups where the sample is placed in a susceptometer which resides inside the pressure cell. The first measurement procedure has the disadvantage of a very small filling factor. In the second type of experimental setup the filling factor can be enhanced by

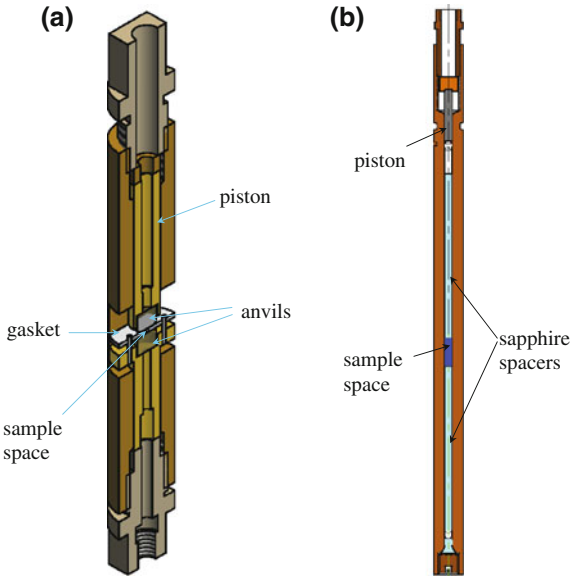

Fig. 6.9 **a** Schematic drawing of a DAC (after [95]) and **b** of a piston-cylinder type pressure cell [96] for a SQUID magnetometer

placing the susceptometer completely or at least its detection coil inside the high-pressure chamber [26, 33, 101–103].

There are several experimental setups belonging to the first group. For measurements in a commercial SQUID magnetometer the whole pressure cell is moved through the detection-coil system. Therefore, it is essential that the pressure cell is nonmagnetic and constructed as homogenous as possible. Ideally only the signal of the sample would be recorded. However, in reality this is not the case. In order to determine the magnetic properties of the sample, the background signal of the pressure cell without sample has to be determined and subtracted from the signal of the pressure cell with sample. Figure 6.9 shows two pressure cells for use in a commercial SQUID system. The DAC is capable of pressures up to 10 GPa [95] and the piston-cylinder type cell reaches about 1.4 GPa [96, 99]. The DAC provides only a very small sample space limiting the resolution of such a setup considerably. In a commercial SQUID magnetometer, e.g. the MPMS from Quantum Design, the lowest achievable temperature is only about 1.8 K and the magnetic field is limited to 7 T. Magnetization studies at lower temperatures and higher magnetic fields are possible with a capacitive Faraday magnetometer in a dilution refrigerator. Using a miniature piston-cylinder type pressure cell in this setup magnetization measurements can be carried out in the millikelvin range and in magnetic fields $B \lesssim 20$ T at pressures up to 1.5 GPa [104]. With the same pressure cell also specific-heat measurements are possible (see Fig. 6.8a and Sect. 6.4.3).

The actual design of the second type of experimental setups depends strongly on the type of pressure cell used and the available space in the sample chamber.

The susceptometer, a coil system, is composed of an excitation (primary) coil and a compensated detection (secondary) coil. The compensated coil consists of two parts wound in opposite direction in order to get a zero signal without sample. At ambient pressure the sample can be moved and measured in both parts of the compensated detection coil. In this way contributions coming from a non-ideal detection coil can be eliminated. This is not possible in pressure experiments. Here, the sample sits always in one part of the compensated detection coil. In piston-cylinder type pressure cells the whole coil system can be placed inside the pressure chamber [101, 103]. So much space is not available in opposed-anvil cells. In recent experimental realizations for opposed-anvil cells one part of the detection coil is placed inside the pressure chamber, while the second part, for the compensation, is placed outside [33, 102]. In earlier setups the whole coil system was fixed outside of the pressure chamber, directly on the anvils in order to obtain an as high as possible filling factor (e.g. [105]).

6.4.6 De Haas–van Alphen Oscillations

The measurement of de Haas–van Alphen oscillations (dHvA) is a powerful tool to study the metallic state. Together with band-structure calculations the Fermi-surface topology can be mapped out. At ambient pressure different methods are available to study dHvA oscillations. For measurements under pressure the field modulation technique is the only one which can be realized [106, 107]. The experimental setup is quite similar to that used for magnetic susceptibility measurements (see Sect. 6.4.5). The excitation coil is usually placed outside of the pressure cell and, to obtain a higher resolution, a compensated detection coil with the sample inside is placed in the pressure chamber. Since dHvA oscillations are typically only visible at very low temperatures and high magnetic fields a dilution refrigerator with a superconducting magnet capable of high magnetic fields is needed. Both, sweeping of the external field for measuring the dHvA oscillations and the modulation of the driving field, can lead to heating effects due to eddy currents induced in the pressure cell. While the former effect can be reduced by choosing a smaller sweeping rate at the expense of a longer duration of the experiment, a reduction of the amplitude of the modulation field reduces the sensitivity. Most of the dHvA experiments under pressure are carried out in the pressure range up to 3 GPa using piston-cylinder type pressure cells [106–109]. Recently, the feasibility to investigate dHvA oscillations at higher pressures has been demonstrated using a moissanite-anvil cell [110].

6.4.7 Magnetic Resonance

Magnetic resonance methods give access to local electronic and magnetic properties of strongly correlated materials, which are not accessible by the methods described above.

6.4.7.1 Nuclear Magnetic Resonance

The nuclear magnetic resonance (NMR) probes the local spin susceptibility at the site of the NMR nucleus and gives information on the local magnetic anisotropy. Furthermore, the spin-lattice relaxation rate can, for example, provide direct information on magnetic fluctuations. The experimental setup is related to the one for ac-susceptibility and dHvA experiments under pressure. A single detection coil as part of the NMR resonant circuit is placed inside the pressure chamber as described in Sect. 6.4.5. Broadband solid-state NMR experiments have been adapted to different types of pressure cells, like piston-cylinder type pressure cells, indenter type cells (see Fig. 6.5 which shows an NMR coil in the sample chamber) [26], opposed-anvil cells [111–113], and cubic-anvil type pressure cells [114].

6.4.7.2 Electron-Spin Resonance

In metallic systems usually an appropriate element (ESR-probe), e.g. Mn or Gd, which does not possess any orbital momentum, has to be doped into the compound under investigation to be able to measure the electron-spin resonance (ESR). ESR investigations under pressure using a classical resonator setup were well established [115], but are generally not in use anymore. With these setups pressures up to 3 GPa and above could be obtained. Only recently the discovery of an ESR signal in the heavy-fermion material $YbRh_2Si_2$ without any ESR probe [116] motivated a renewed interest in ESR measurements under pressure [117]. In addition to the classical ESR experiments, setups for high-field (high-frequency) ESR experiments under pressure have been developed and are used for investigations on quantum-spin systems [118–120].

6.4.7.3 Muon-Spin Rotation/Resonance

μSR stands for both muon-spin rotation and muon-spin resonance. The acronym already draws the attention to the analogy with ESR and NMR. The muons are implanted in the sample and decay after 2.2 μs as $\mu^+ \rightarrow e^+ + \nu_\mu + \nu_e$. The angular distribution of e^+ has a maximum in the muon spin direction. The muon spins precess in a transverse magnetic field, which is equivalent to the free induction decay in pulsed NMR. This is called muon-spin rotation (TF-μSR) in contrast to the muon-spin resonance (RF-μSR). Here, the muon-spin polarization is along the magnetic field and transitions are induced by an RF-field as in conventional NMR. μSR can detect extremely small internal fields. Furthermore, magnetic fluctuations in the range 10^4–10^{12} Hz can be investigated. A comprehensive review on heavy-fermion systems and type-II superconductors studied by μSR techniques can be found in [121] and [122, 123] respectively.

For μSR experiments under pressure a large sample size is essential to obtain a good signal-to-background ratio. Thus, only piston-cylinder type pressure cells are

suitable for μSR measurements under pressure. This limits the achievable pressure to about 3 GPa. Pressure experiments can be carried out at temperatures down to 0.25 K using ^{3}He cryostats (see [124, 125] as an example of a recent study).

6.4.8 Neutron Scattering

Neutron-scattering experiments allow the study of different physical properties. Neutron diffraction is an important tool to investigate crystal (see Sect. 6.4.4) and magnetic structures. Inelastic neutron scattering provides information on different types of excitations. These can include magnetic excitations, which are of special interest in the field of correlated matter, but also crystal-electric field (CEF) and phonon excitations [126].

The biggest challenge for neutron-scattering experiments under pressure is to reduce the additional background signal due to the pressure cell. Crystal-structure investigations need only a relatively small sample size. Using anvil cells pressures up to 50 GPa can be achieved (see for example [127–132]). The investigation of magnetic structures is more challenging due to the low intensity of the magnetic reflections, especially in materials with small magnetic moments. Usually piston-cylinder type cells are utilized in neutron-scattering investigations of magnetic properties under pressure because of their large volume available for the sample [133–137]. A comprehensive introduction to neutron scattering techniques in high-pressure environments can be found in [138].

6.4.9 Mössbauer Spectroscopy

Mössbauer spectroscopy is an effective microscopic tool to investigate magnetic moments and magnetic ordering phenomena. It also reveals the electric-field gradient (EFG) at the site of the Mössbauer active nucleus. Unfortunately, only a very limited number of Mössbauer active nuclei exist. In heavy-fermion materials Mössbauer investigations under pressure have been conducted in Yb-based compounds using ^{170}Yb as Mössbauer active nucleus ([139] and references therein). Mössbauer spectroscopy is also possible on ^{238}U and ^{151}Eu, but no pressure studies are reported. In the iron-based superconductors ^{57}Fe is a Mössbauer active nucleus which allows Mössbauer investigations under pressure directly at the magnetic site (e.g. [140]). Using DAC's Mössbauer experiments can be carried out at cryogenic temperatures at pressures up to 100 GPa [139, 141–143].

6.4.10 Optical Spectroscopy and Related Techniques

Raman scattering, Brillouin scattering, and optical/X-ray spectroscopy are important tools to investigate the effects of electron-phonon coupling and electronic correlations in materials like high-temperature superconductors or transition-metal oxides. Since these techniques require an optical access to the sample, DAC's are regularly utilized. For further details on pressure experiments with these probes we refer to the literature (see for example [144–147] and references therein).

6.5 Pressure Tuning of Strongly Correlated Materials

External pressure has been successfully used to study different classes of strongly correlated materials, like low-dimensional organic conductors (for example [148, 149] and references therein), the recently discovered iron-based superconductors (for example [150] and references therein), or the heavy-fermion materials. In the following we will demonstrate the importance of pressure studies for the understanding of heavy-fermion supeconductors on some selected examples.

$CeCu_2Si_2$, the first heavy-fermion superconductor [151], shows a very broad superconducting region under pressure [152]. Even though this unusual superconducting regime was reported already short after the discovery of $CeCu_2Si_2$ its origin remained puzzling for many years. It was speculated that the low-pressure superconducting region is related to the proximity to antiferromagnetism and that in the high-pressure region valence fluctuations might play an important role [152–154]. A combined pressure and substitution experiment could finally show that indeed two distinct superconducting regions exist in $CeCu_2Si_2$ [155].

Pressure investigations have been highly successful in the discovery of new unconventional Ce-based heavy-fermion superconductors. The heavy-fermion antiferromagnet $CeCu_2Ge_2$ is isoelectronic to $CeCu_2Si_2$, but has a larger unit-cell volume. It was therefore a natural step to apply pressure on $CeCu_2Ge_2$ in order to reduce its unit-cell volume to that of $CeCu_2Si_2$ and look for superconductivity. Application of pressure indeed suppresses the magnetic order and an extended superconducting phase develops above 7.5 GPa [156]. In this way $CeCu_2Ge_2$ was not a completely new heavy-fermion superconductor, since its pressure dependence reproduces that of $CeCu_2Si_2$. Nevertheless, the experimental concept to use pressure to suppress the antiferromagnetic state to induce superconductivity led to the discovery of many Ce-based heavy-fermion pressure-induced superconductors, e.g. $CeRh_2Si_2$ [157], $CePd_2Si_2$ [158], or $CeIn_3$ [158, 159]. Figure 6.10 displays the $T-p$ phase diagram of $CeIn_3$ which is also representative for that of $CeRh_2Si_2$ and $CePd_2Si_2$. In these and several other Ce-based heavy-fermion materials superconductivity develops around the critical pressure where the antiferromagnetic order is suppressed, suggesting that the superconductivity is magnetically mediated.

In the following we will highlight how pressure studies contributed to the understanding of the $CeMIn_5$ heavy-fermion materials (M = Co, Rh, and Ir).

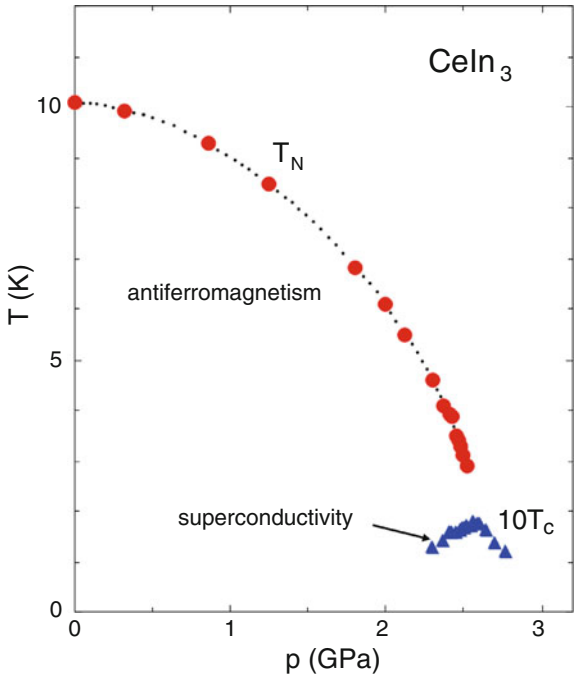

Fig. 6.10 $T-p$ phase diagram of $CeIn_3$. The data were taken from [158]

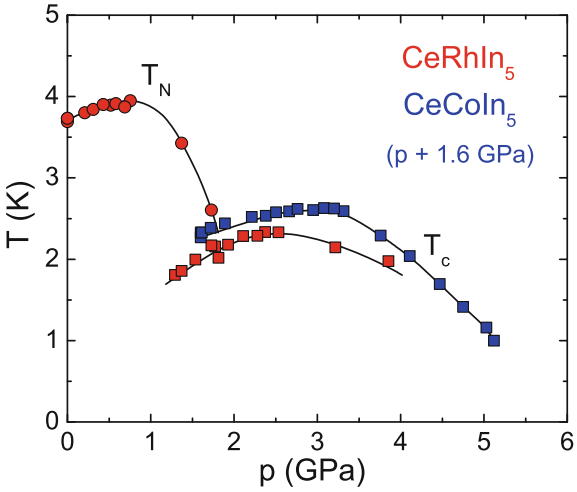

Fig. 6.11 Combined $T-p$ phase diagram of $CeRhIn_5$ and $CeCoIn_5$. The data of $CeCoIn_5$ have been shifted by 1.6 GPa. The data were taken from [161–164]

The CeMIn$_5$ compounds are layered materials which consist of layers of CeIn$_3$ separated by layers of MIn$_2$ [160]. Therefore, CeIn$_3$ can be considered the parent compound of the CeMIn$_5$ family. At ambient pressure CeIn$_3$ orders antiferromagnetically below $T_N \approx 10$ K. Application of pressure suppresses T_N to zero temperature at $p_c \approx 2.5$ GPa [158]. Around p_c superconductivity develops below $T_c \approx 200$ mK (see also Fig. 6.10).

CeRhIn$_5$ orders antiferromagnetically like CeIn$_3$, but has a considerably lower $T_N = 3.8$ K [165]. On application of pressure the antiferromagnetic order is suppressed around 1.9 GPa and superconductivity starts to develop [165]. A broad superconducting dome with a maximum T_c of 2.3 K extends over more than 4 GPa in the T–p phase diagram [161, 163, 165]. While the phase diagram of CeRhIn$_5$ is reminiscent of that of other heavy-fermion superconductors, it shows one important difference, the antiferromagnetic and superconducting ordering temperatures are of the same order. CeCoIn$_5$ and CeIrIn$_5$ are ambient pressure superconductors with $T_c = 2.3$ K [166] and 0.4 K [167], respectively. Detailed experiments confirm the unconventional nature of the superconductivity [168]. The T–p phase diagram of CeCoIn$_5$ displays a broad superconducting dome which extends up to 5 GPa similar to CeRhIn$_5$ [162, 164]. An estimation using the experimental bulk modulus and lattice parameters of CeCoIn$_5$ and CeRhIn$_5$ suggests that CeCoIn$_5$ is under an effective pressure of 1.6 GPa compared with CeRhIn$_5$. Shifting the phase diagram of CeCoIn$_5$ by this value and superimposing it on that of CeRhIn$_5$ leads indeed to a good agreement between the two phase diagrams (see Fig. 6.11). This suggests that at ambient pressure CeCoIn$_5$ is situated in close proximity to antiferromagnetic order.

This finding is supported by studies on Cd substituted CeCoIn$_5$, where In was replaced by a small amount of Cd [169]. For substitution levels of more than $x \approx 0.075$ antiferromagnetism is induced in CeCo(In$_{1-x}$Cd$_x$)$_5$ [169]. In the concentration range $0.075 \lesssim x \lesssim 0.0125$ superconductivity coexists with the antiferromagnetic order at low temperatures [169–171]. Pressure studies on the substituted compounds revealed a T–p phase diagram which can be superimposed on that of CeRhIn$_5$ and CeCoIn$_5$, shown in Fig. 6.11, by considering an appropriate pressure shift [169]. However, there is no direct correspondence of the unit-cell volumes of the different compounds.

CeIrIn$_5$ is the second ambient pressure superconductor in the CeMIn$_5$ family. The superconducting transition temperature of only $T_c = 0.4$ K is rather small compared with the T_c of CeCoIn$_5$ [166, 167]. $T_c(p)$ exhibits also a dome-like shape with a maximum $T_c \approx 1$ K at about 2.5 GPa [173]. In contrast to CeCoIn$_5$ there are no obvious candidates for the superconducting coupling mechanism.

Substituting Rh by Ir in CeRh$_{1-x}$Ir$_x$In$_5$ suppresses the antiferromagnetic order at a critical concentration of about $x_c = 0.65$ (see Fig. 6.12) [174]. A broad superconducting phase covers the $T - x$ phase diagram starting from $x = 0.35$ up to CeIrIn$_5$ [174]. On a first look this might suggest that the superconductivity in CeIrIn$_5$ is related to the pressure-induced superconducting phase in CeRhIn$_5$, similar like in CeCoIn$_5$. However, there is a small dip in $T_c(x)$ around $x = 0.9$ [174]. The dip was taken as a hint for the existence of two distinct superconducting phases in the phase diagram of CeRh$_{1-x}$Ir$_x$In$_5$ [172, 174]. This would imply that the superconductivity in CeIrIn$_5$

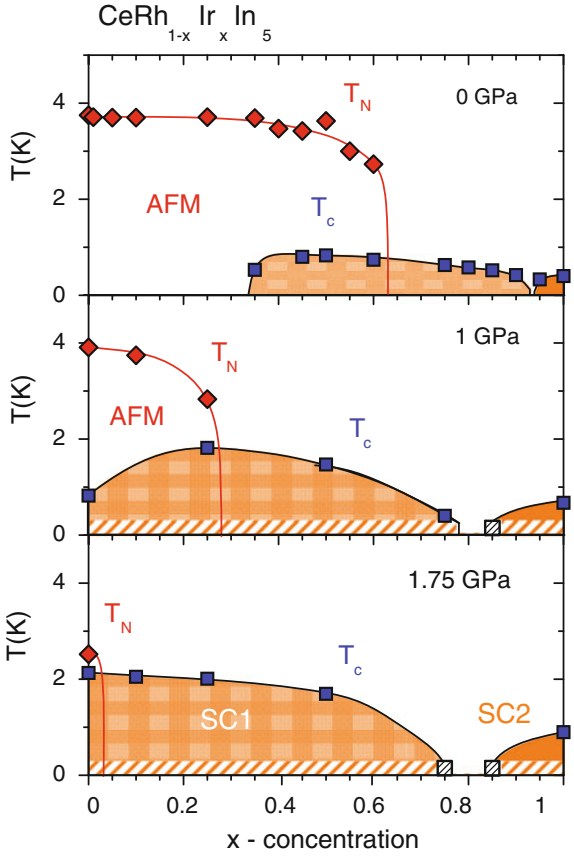

Fig. 6.12 T–x phase diagram of $CeRh_{1-x}Ir_xIn_5$ at ambient pressure, 1 GPa, and 1.75 GPa. The phase diagram evidences the existence of two distinct superconducting phases, SC1 and SC2. The data were taken from [172]

is disconnected from that in $CeRhIn_5$ and, therefore, possibly different in origin. A combined doping and pressure study answered the question and showed that two separated superconducting phases exist in $CeRh_{1-x}Ir_xIn_5$ [172]. The application of pressure slowly removes the antiferromagnetism from the $T - x$ phase diagram. At 1 GPa the critical concentration is only $x_c \approx 0.35$ compared to $x_c \approx 0.65$ at ambient pressure. Finally, at 1.75 GPa only $CeRhIn_5$ exhibits antiferromagnetic order (see Fig. 6.12) [172]. While the antiferromagnetic region becomes narrower upon increasing pressure, the dip in $T_c(x)$ evolves into a range without superconductivity. This result evidences that two distinct superconducting phases, SC1 and SC2, exist in $CeRh_{1-x}Ir_xIn_5$. The position of the maximum of the superconducting dome SC1 is correlated with the critical concentration, x_c, for the disappearance of the antiferromagnetic order. This hints at a magnetic coupling mechanism in the super-

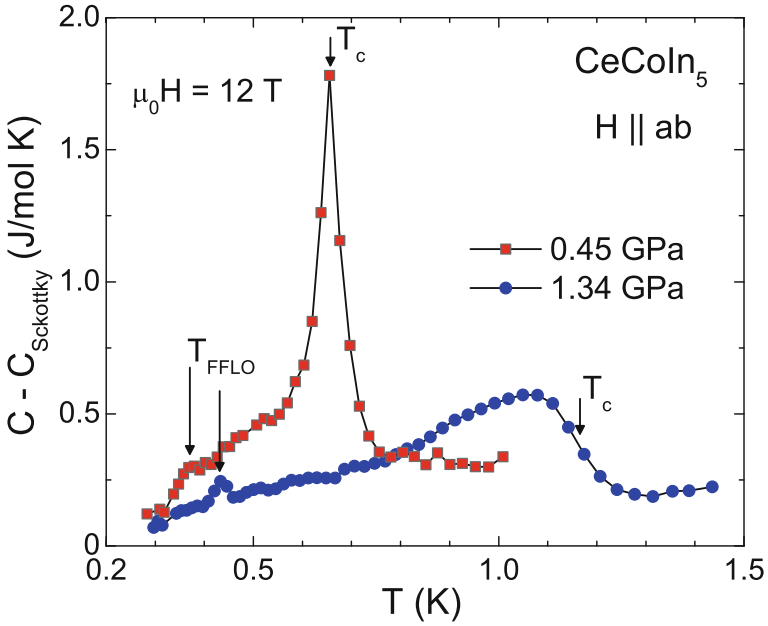

Fig. 6.13 Low-temperature specific heat of $CeCoIn_5$ at 0.45 GPa and 1.34 GPa in a magnetic field of 12 T applied in the *ab* plane. The specific heat at both pressures shows two phase transitions, which are marked by *arrows*. The experiment was carried out using the pressure cell shown in Fig. 6.8b. The data were taken from [76]

conducting phase SC1. The superconducting phase SC2 is disconnected from any magnetic order, thus leaving open the question about the superconducting pairing mechanism in $CeIrIn_5$ [172].

There are more peculiar findings in the $CeMIn_5$ materials. $CeCoIn_5$ shows a second phase-transition anomaly inside the superconducting state close to the upper critical field, $H_{c2}(0)$, for $H \| ab$ [175, 176]. This unusual observation was taken as a strong hint at the realization of the Fulde-Ferrell-Larkin-Ovchinnikov (FFLO) superconducting state [177, 178]. $CeCoIn_5$ does not only show this anomaly, but also fulfills the pre-conditions for the formation of such a state. The FFLO state is an inhomogeneous superconducting state due to competition between superconductivity and Pauli paramagnetism, which had been proposed already in the 1960s [177, 178].

Even though there is strong evidence for the realization of the FFLO phase in $CeCoIn_5$, there remains also the possibility that this phase is magnetic in origin. We have shown before that $CeCoIn_5$ is situated close to a magnetic instability. Furthermore, the observed non-Fermi liquid behavior in thermodynamic and transport properties evidences the presence of strong magnetic fluctuations [166]. Application of external pressure enables us to move $CeCoIn_5$ away from these magnetic fluctuations. Electrical-resistivity and Hall-effect studies under pressure evidence that the mag-

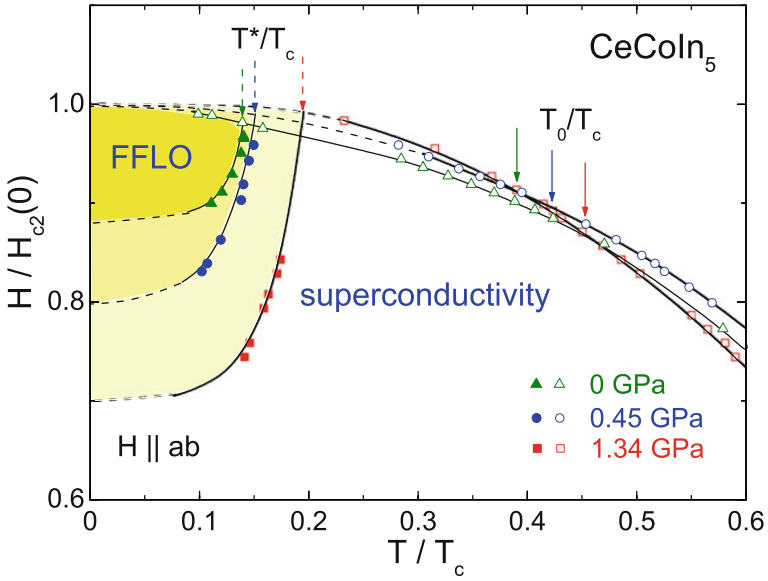

Fig. 6.14 Magnetic field—temperature phase diagram of $CeCoIn_5$ at different pressures. The phase diagram shows the evolution of the low-temperature phase inside the superconducting state. The axes are normalized by the upper-critical field $H_{c2}(0)$ and the superconducting transition temperature T_c, respectively. The data were taken from [76]

netic fluctuations in $CeCoIn_5$ are effectively suppressed around 1.5 GPa [179, 180]. Therefore, a study of the effect of pressure on the low-temperature phase inside the superconducting state in $CeCoIn_5$ can help to clarify the nature of this unusual phase.

Figure 6.13 shows specific-heat data recorded at 12 T at 0.45 and 1.34 GPa [181]. At both pressures the anomaly at the transition into the superconducting state and an additional anomaly inside the superconducting phase are clearly visible. At 12 T the shape of the anomaly at T_c is qualitatively different at 0.45 GPa and 1.34 GPa. At 0.45 GPa it indicates a first-order type phase transition, while at 1.34 GPa the shape of the anomaly is typical for a second-order type transition. At 1.34 GPa the character of the phase transition changes from second- to first-order slightly above 12 T [181, 182]. We note that upon increasing pressure both transitions shift to higher temperatures. The phase diagram in Fig. 6.14 summarizes the results from the specific-heat experiments. The field axis is normalized by the corresponding upper-critical field at zero temperature, $H_{c2}(0)$, and the temperature by T_c at zero field. The low-temperature phase in the superconducting state expands upon increasing pressure. This is generally not expected, if the low-temperature phase would be purely magnetic in nature, since pressure favors a non-magnetic state in Ce-based heavy-fermion metals. Therefore, the pressure studies are in support of a realization of the FFLO state in $CeCoIn_5$. However, neutron scattering experiments find a small field induced magnetic moment at an incommensurate wave-vector inside the low-temperature phase which is not compatible with the FFLO state [183]. The real nature of this phase is still under debate. Several theoretical models have been proposed

to account for this so-far unique relationship between magnetism and superconductivity. Studies of microscopic properties under pressure, e.g. by NMR or by neutron scattering, could help to reveal the true nature of this unusual phase in $CeCoIn_5$.

These examples show that pressure studies do not only contribute to the general understanding of strongly correlated materials. They can lead to the discovery of new unconventional phases or help to answer specific physical questions.

Acknowledgments I would like to thank C. Klausnitzer for the careful preparation of the illustrations. Furthermore, I am indebted to K. Mydeen and E. Lengyel for valuable comments on the manuscript.

References

1. M.I. Eremets, *High Pressure Extperimental Methods* (Oxfrord University Press, Oxford, 1996)
2. T. Matsumoto, Rev. High Press. Sci. Techn. **12**, 280 (2002). doi:10.4131/jshpreview.12.280
3. I.R. Walker, Rev. Sci. Instrum. **70**, 3402 (1999). doi:10.1063/1.1149927
4. Y. Uwatoko, S. Todo, K. Ueda, A. Uchida, M. Kosaka, N. Mori, T. Matsumoto, J. Phys.: Condens. Matter **14**, 11291 (2002). doi:10.1088/0953-89844/44/469
5. Y. Uwatoko, M. Hedo, N. Kurita, M. Kodea, M. Abliz, T. Matsumoto, Phys. B **329—-333**, 1658 (2003). doi:10.1016/s0921-4526(02)02449-3
6. H. Taniguchi, S. Takeda, R. Satoh, A. Taniguchi, H. Komatsu, K. Satoh, Rev. Sci. Instrum. **81**, 033903 (2010). doi:10.1063/1.3310197
7. C. Pfleiderer, E. Bedin, B. Salce, Rev. Sci. Instrum. **68**, 3120 (1997). doi:10.1063/1.1148254
8. B. Salce, J. Thomasson, A. Demuer, J.J. Blanchard, J.M. Martinod, L. Devoille, A. Guillaume, Rev. Sci. Instrum. **71**, 2461 (2000). doi:10.1063/1.1150664
9. M. Nicklas, (2007). Unpublished
10. T. Nakanishi, Rev. High Press. Sci. Techn. **11**, 187 (2001). doi:10.4131/jshpreview.11.187
11. T. Nakanishi, N. Takeshita, N. Mori, Rev. Sci. Instrum. **73**, 1828 (2002). doi:10.1063/1.1458044
12. T. Nakanishi, M. Nicklas, G. Sparn, F. Steglich, J. Phys. Soc. Jpn. **76SA**, 223 (2007). doi:10.1143/JPSJS.76SA.223
13. A.S. Rüetschi, D. Jaccard, Rev. Sci. Instrum. **78**, 123901 (2007). doi:10.1063/1.2818788
14. E. Colombier, D. Braithwaite, Rev. Sci. Instrum. **78**, 1 (2007). doi:10.1063/1.2778629
15. O.B. Tsiok, V.V. Bredikhin, V.A. Sidorov, L.G. Khvostantsev, High Press. Res. **10**, 523 (1992). doi:10.1080/08957959208201471
16. L.G. Khvostantsev, V.A. Sidorov, O.B. Tsiok, High pressure toroid cell: Applications in planetary and material sciences. Geophys. Monogr. Ser. **101**, 89 (1998)
17. A.E. Petrova, V.A. Sidorov, S.M. Stishov, Physica B **359—-361**, 1463 (2005). doi:10.1016/j.physb.2005.01.454
18. W.A. Bassett, High Press. Res. **29**, 163 (2009). doi:10.1080/08957950802597239
19. A. Jayaraman, Rev. Mod. Phys **55**, 65 (1983). doi:10.1103/RevModPhys.55.65
20. D.J. Dunstan, I.L. Spain, J. Phys. E: Sci. Instrum. **22**, 913 (1989). doi:10.1088/0022-3735/221/004
21. I.L. Spain, D.J. Dunstan, J. Phys. E: Sci. Instrum. **22**, 923 (1989). doi:10.1088/0022-3735/221/005
22. G.Y. Machavariani, M.P. Pasternak, G.R. Hearne, Rev. Sci. Instrum. **69**, 1423 (1998). doi:10.1063/1.1148775
23. M. Kano, N. Kurita, M. Hedo, Y. Uwatoko, S.W. Tozer, H.S. Suzuki, T. Onimaru, T. Sakakibara, J. Phys. Soc. Jpn. **76SA**, 56 (2007). doi:10.1143/JPSJS.76SA.56

24. A.G. Gavriliuk, A.A. Mironovich, V.V. Struzhkin, Rev. Sci. Instrum. **80**, 043906 (2009). doi:10.1063/1.3122051
25. G. Giriat, W. Wang, J.P. Attfield, A.D. Huxley, K.V. Kamenev, Rev. Sci. Instrum. **81**, 073905 (2010). doi:10.1063/1.3465311
26. T.C. Kobayashi, H. Hidaka, T. Fujiwara, M. Tanaka, K. Takeda, T. Akazawa, K. Shimizu, S. Kirita, R. Asai, H. Nakawaki, M. Nakashima, R. Settai, Y. Yamamoto, Y. Haga, Y. Ōnuki, J. Phys.: Condens. Matter **19**, 125205 (2007). doi:10.1088/0953-8984/19/12/125205
27. N. Mori, H. Takahashi, N. Takeshita, High Press. Res. **24**, 225 (2004). doi:10.1080/08957950410001661909
28. Y. Uwatoko, K. Matsubayashi, T. Matsumoto, N. Aso, M. Nishi, T. Fujiwara, M. Hedo, S. Tabata, K. Takagi, M. Tado, H. Kagi, Rev. High Press. Sci. Techn. **18**, 230 (2008). doi:10.4131/jshpreview.18.230
29. T. Hikita, T. Maruyama, N. Yamada, Jpn. J. Appl. Phys. **29**, 2519 (1990). doi:10.1143/jjap.29.2519
30. S.M. Stishov, A.E. Petrova, J. Phys. Soc. Jpn. **76SA**, 212 (2007). doi:10.1143/JPSJS.76SA.212
31. O.P. Welzel, F.M. Grosche, Rev. Sci. Instrum. **82**, 033901 (2011). doi:10.1063/1.3541793
32. S.T. Weir, J. Akella, C. Aracne-Ruddle, Y.K. Vohra, S.A. Catledge, Appl. Phys. Lett. **77**, 3400 (2000). doi:10.1063/1.1326838
33. D.D. Jackson, C. Aracne-Ruddle, V. Malba, S.T. Weir, S.A. Catledge, Y.K. Vohra, Rev. Sci. Instrum. **74**, 2467 (2003). doi:10.1063/1.1544084
34. X. Ji-an, M. Ho-kwang, R.J. Hemley, E. Hines, J. Phys.: Condens. Matter **14**, 11543 (2002). doi:10.1088/0953-89844/44/513
35. J.D. Thompson, Rev. Sci. Instrum. **55**, 231 (1984). doi:10.1063/1.1137730
36. O.E. Andersson, B. Sundqvist, Rev. Sci. Instrum. **68**, 1344 (1997). doi:10.1063/1.1147868
37. L.H. Dmowski, E. Litwin-Staszewska, Meas. Sci. Technol. **10**, 343 (1999). doi:10.1088/0957-02330/5/001
38. L.H. Dmowski, J. Przybytek, E. Litwin-Staszewska, High Press. Res. **19**, 743 (2000). doi:10.1080/08957950008202577
39. F.P. Bundy, Phys. Rev. **110**, 314 (1958). doi:10.1103/PhysRev.110.314
40. G. Andersson, B. Sundqvist, G. Bäckström, J. Appl. Phys. **65**, 3943 (1989). doi:10.1063/1.343360
41. A. Eiling, J.S. Schilling, J. Phys. F: Met. Phys. **623**, 11 (1981). doi:10.1088/0305-46081/3/010
42. B. Bireckoven, J. Wittig, J. Phys. E: Sci. Instrum. **21**, 841 (1988). doi:10.1088/0022-3735/21/9/004
43. J.D. Barnett, S. Block, G.J. Piermarini, Rev. Sci. Instrum. **44**, 1 (1973). doi:10.1063/1.1685943
44. G.J. Piermarini, S. Block, Rev. Sci. Instrum. **46**, 973 (1975). doi:10.1063/1.1134381
45. H.K. Mao, J. Xu, P.M. Bell, J. Geophys. Res. **91**, 4673 (1986). doi:10.1029/JB091iB05p04673
46. R.J. Hemley, C.S. Zha, A.P. Jephcoat, H.K. Mao, L.W. Finger, D.E. Cox, Phys. Rev. B **39**, 11820 (1989). doi:10.1103/PhysRevB.39.11820
47. D.D. Ragan, R. Gustavsen, D. Schiferl, J. Appl. Phys. **72**, 5539 (1992). doi:10.1063/1.351951
48. A.P. Reyes, E.T. Ahrens, R.H. Heffner, P.C. Hammel, J.D. Thompson, Rev. Sci. Instrum. **63**, 3120 (1992). doi:10.1063/1.1142564
49. H. Fukazawa, N. Yamatoji, Y. Kohori, C. Terakura, N. Takeshita, Y. Tokura, H. Takagi, Rev. Sci. Instrum. **78**, 015106 (2007). doi:10.1063/1.2426875
50. D.L. Decker, T.G. Worlton, J. Appl. Phys. **43**, 4799 (1972). doi:10.1063/1.1661013
51. w Yu, A.A. Aczel, T.J. Williams, S.L. Budko, N. Ni, P.C. Canfield, G.M. Luke, Phys. Rev. B **79**, 020511 (2009). doi:10.1103/PhysRevB.79.020511
52. N. Tateiwa, S. Ikeda, Y. Haga, T.D. Matsuda, M. Nakashima, D. Aoki, R. Settai, Y. Ōnuki, J. Phys.: Conf. Ser **150**, 042206 (2009). doi:10.1088/1742-6596/150/4/042206
53. D.D. Ragan, D.R. Clarke, D. Schiferl, Rev. Sci. Instrum. **67**, 494 (1996). doi:10.1063/1.1146627

54. T. Varga, A.P. Wilkinson, R.J. Angel, Rev. Sci. Instrum. **74**, 4564 (2003). doi:10.1063/1.1611993
55. Y. Shen, R.S. Kumar, M. Pravica, M.F. Nicol, Rev. Sci. Instrum. **75**, 4450 (2004). doi:10.1063/1.1786355
56. V.A. Sidorov, R.A. Sadykov, J. Phys.: Condens. Matter **17**, S3005 (2005). doi:10.1088/0953-8984/17/40/002
57. A.S. Kirichenko, A.V. Kornilov, V.M. Pudalov, Instrum. Exp. Tech. **48**, 813 (2005). doi:10.1007/s10786-005-0144-5
58. K. Yokogawa, K. Murata, H. Yoshino, S. Aoyama, Jpn. J. Appl. Phys. **46**, 3636 (2007). doi:10.1143/JJAP.46.3636
59. K. Murata, K. Yokogawa, H. Yoshino, S. Klotz, P. Munsch, A. Irizawa, M. Nishiyama, K. Iizuka, T. Nanba, T. Okada, Y. Shiraga, S. Aoyama, Rev. Sci. Instrum. **79**, 085101 (2008). doi:10.1063/1.2964117
60. S. Klotz, J.C. Chervin, P. Munsch, G.L. Marchand, J. Phys. D: Appl. Phys. **42**, 075413 (2009). doi:10.1088/0022-3727/42/7/075413
61. S. Klotz, L. Paumier, G.L. Marchand, P. Munsch, High Press. Res. **29**, 649 (2009). doi:10.1080/08957950903418194
62. Y. Feng, R. Jaramillo, J. Wang, Y. Ren, T.F. Rosenbaum, Rev. Sci. Instrum. **81**, 041301 (2010). doi:10.1063/1.3400212
63. E.S. Itskevich, V.F. Kraidenov, Cryogenics **15**, 552 (1975). doi:10.1016/0011-2275(75)90154-X
64. P. Andersson, G. Bäckström, Rev. Sci. Instrum. **47**, 205 (1976). doi:10.1063/1.1134581
65. S. Andersson, G. Bäckström, Rev. Sci. Instrum. **57**, 1633 (1986). doi:10.1063/1.1138542
66. G.F. Chen, I. Sakamoto, S. Ohara, T. Takami, H. Ikuta, U. Mizutani, Phys. Rev. B **69**, 14420 (2004). doi:10.1103/PhysRevB.69.014420
67. A.K. Singh, G. Ramani, Rev. Sci. Instrum. **49**, 1324 (1978). doi:10.1063/1.1135577
68. P.M. Chaikin, C. Weyl, G. Malfait, D. Jérome, Rev. Sci. Instrum. **52**, 1397 (1981). doi:10.1063/1.1136780
69. D. Jaccard, E. Vargoz, K. Alami-Yadri, H. Wilhelm, Rev. High Press. Sci. Techn. **7**, 412 (1998). doi:10.4131/jshpreview.7.412
70. H. Wilhelm, AC-calorimetry at high pressure and low temperature. Adv. in Solid State Phys. **43**, 889 (2003). doi:10.1007/978-3-540-44838-9_63
71. D. Jaccard, K. Sengupta, Rev. Sci. Instrum. **81**, 041301 (2010). doi:10.1063/1.3360819
72. D.A. Polvani, J.F. Meng, M. Hasegawa, J.V. Badding, Rev. Sci. Instrum. **70**, 3586 (1999). doi:10.1063/1.1149964
73. E.S. Choi, K. Haeyong, Y.J. Jo, W. Kang, Rev. Sci. Instrum. **73**, 2999 (2002). doi:10.1063/1.1489076
74. R. Borth, M. Nicklas, (2012). Unpublished.
75. C.F. Miclea, M. Nicklas, J.L. Sarrao, G. Sparn, F. Steglich, J.D. Thompson, AIP Conf. Proc. 850, 713 (2006). doi:10.1063/1.2354906
76. C.F. Miclea, M. Nicklas, J.L. Sarrao, G. Sparn, F. Steglich, J.D. Thompson, Phys. B **378–380**, 398 (2006). doi:10.1016/j.physb.2006.01.174
77. J.C. Ho, N.E. Phillips, T.F. Smith, Phys. Rev. Lett. **17**, 694 (1966). doi:10.1103/PhysRevLett.17.694
78. A. Berton, J. Chaussy, B. Cornut, J. Odin, J. Paureau, J. Peyrard, Cryogenics **19**, 543 (1979). doi:10.1016/0011-2275(79)90009-2
79. F. Tomioka, I. Umehara, T. Ono, M. Hedo, Y. Uwatoko, N. Kimura, Jpn. J. Appl. Phys. **46**, 3090 (2007). doi:10.1143/jjap.46.3090
80. H. Wilhelm, T. Lühmann, T. Rus, F. Steglich, Rev. Sci. Instrum. **75**, 2700 (2004). doi:10.1063/1.1771486
81. R. Bachmann, J.F.J. DiSalvo, T.H. Geballe, R.L. Greene, R.E. Howard, C.N. King, H.C. Kirsch, K.N. Lee, R.E. Schwall, H.U. Thomas, R.B. Zubeck, Rev. Sci. Instrum. **43**, 205 (1972). doi:10.1063/1.1685596
82. M. Brando, Rev. Sci. Instrum. **80**, 095112 (2009). doi:10.1063/1.3202380

83. P.F. Sullivan, G. Seidel, Phys. Rev. **173**, 679 (1968). doi:10.1103/PhysRev.173.679
84. E. Gmelin, Thermochim. Acta **305**, 1 (1997). doi:10.1016/S0040-6031(97)00126-3
85. A. Demuer, C. Marcenat, J. Thomasson, R. Calemczuk, B. Salce, P. Lejay, D. Braithwaite, J. Flouquet, J. Low Temp. Phys. **120**, 245 (2000). doi:10.1023/a:1004685711942
86. E.S. Itskevich, V.F. Kraidenov, Instrum. Exp. Tech. **21**, 1640 (1978)
87. A. Eichler, W. Gey, Rev. Sci. Instrum. **50**, 1445 (1979). doi:10.1063/1.1135737
88. F. Bouquet, Y. Wang, H. Wilhelm, D. Jaccard, A. Junod, Solid State Commun. **113**, 367 (2000). doi:10.1016/s0038-1098(99)00505-0
89. H. Wilhelm, D. Jaccard, J. Phys.: Condens. Matter **14**, 10683 (2002). doi:10.1088/0953-89844/44/357
90. K. Matsubayashi, M. Hedo, I. Umehara, N. Katayama, K. Ohgushi, A. Yamada, K. Munakata, T. Matsumoto, Y. Uwatoko, J. Phys.: Conf. Ser. **215**, 012187 (2010). doi:10.1088/1742-6596/215/1/012187
91. G. Oomi, T. Kagayama, Y. Ōnuki, T. Komatsubara, Phys. B **163**, 557 (1990). doi:10.1016/0921-4526(90)90268-Y
92. G. Oomi, T. Kagayama, Phys. B **201**, 235 (1994). doi:10.1016/0921-4526(94)91090-1
93. R.S. Kumar, A.L. Cornelius, J.L. Sarrao, Phys. Rev. B **70**, 214526 (2004). doi:10.1103/PhysRevB.70.214526
94. R. Küchler, T. Bauer, M. Brando, F. Steglich, Rev. Sci. Instrum. **83**, 095102 (2012). doi:10.1063/1.4748864
95. P.L. Alireza, G.G. Lonzarich, Rev. Sci. Instrum. **80**, 023906 (2009). doi:10.1063/1.3077303
96. M. Nicklas, (2009). Unpublished.
97. D. Wohlleben, M.B. Maple, Rev. Sci. Instrum. **42**, 1573 (1971). doi:10.1063/1.1684942
98. K. Koyama, S. Hane, K. Kamishima, T. Goto, Rev. Sci. Instrum. **69**, 3009 (1998). doi:10.1063/1.1149048
99. K.V. Kamenev, S. Tancharakorn, A. Robertson, A. Harrison, Rev. Sci. Instrum. **77**, 73905 (2006). doi:10.1063/1.2221537
100. P.L. Alireza, S. Barakat, A.M. Cumberlidge, G. Lonzarich, F. Nakamura, J. Phys. Soc. Jpn. **76SA**, 216 (2007). doi:10.1143/JPSJS.76SA.216
101. C. Pfleiderer, Rev. Sci. Instrum. **68**, 1532 (1997). doi:10.1063/1.1147642
102. P.L. Alireza, S.R. Julian, Rev. Sci. Instrum. **74**, 4728 (2003). doi:10.1063/1.1614861
103. M. Ohashi, G. Oomi, J. Phys. Soc. Jpn. **76SA**, 226 (2007). doi:10.1143/JPSJS.76SA.226
104. Y. Tokiwa, P. Gegenwart, T. Radu, J. Ferstl, G. Sparn, C. Geibel, F. Steglich, Phys. Rev. Lett. **94**, 226402 (2005). doi:10.1103/PhysRevLett.94.226402
105. C.C. Kim, M.E. Reeves, M.S. Osofsky, E.F. Skelton, D.H. Liebenberg, Rev. Sci. Instrum. **65**, 992 (1994). doi:10.1063/1.1144878
106. M. Takashita, H. Aoki, T. Matsumoto, C.J. Haworth, T. Terashima, A. Uesawa, T. Suzuki, Phys. Rev. Lett. **78**, 1948 (1997). doi:10.1103/PhysRevLett.78.1948
107. M.S. Nam, J. Singleton, A.K. Klehe, W. Hayes, M. Kurmoo, P. Day, Synth. Met. **103**, 2259 (1999). doi:10.1016/s0379-6779(98)00444-5
108. H. Shishido, R. Settai, D. Aoki, S. Ikeda, H. Nakawaki, N. Nakamura, T. Iizuka, Y. Inada, K. Sugiyama, T. Takeuchi, K. Kindo, C. Kobayashi, Y. Haga, H. Harima, Y. Aoki, T. Namiki, H. Sato, Y. Ōnuki, Phys. Soc. Jpn. **71**, 162 (2002). doi:10.1143/jpsj.71.162
109. Y. Ōnuki, R. Settai, Low Temp. Phys. **38**, 89 (2012). doi:10.1063/1.3683408
110. S.K. Goh, P.L. Alireza, P.D.A. Mann, A.M. Cumberlidge, C. Bergemann, M. Sutherland, Y. Maeno, Cur. Appl. Phys. **8**, 304 (2008). doi:10.1016/j.cap.2007.10.020
111. K. Kitagawa, H. Gotou, Y. Yagi, A. Yamada, T. Matsumoto, Y. Uwatoko, M. Takigawa, J. Phys. Soc. Jpn. **79**, 024001 (2010). doi:10.1143/jpsj.79.024001
112. J. Haase, S.K. Goh, T. Meissner, P.L. Alireza, D. Rybicki, Rev. Sci. Instrum. **80**, 073905 (2009). doi:10.1063/1.3183504
113. T. Meissner, S.K. Goh, J. Haase, B. Meier, D. Rybicki, P.L. Alireza, J. Low Temp. Phys. **159**, 284 (2010). doi:10.1007/s10909-009-0131-5
114. K. Hirayama, T. Yamazaki, H. Fukazawa, Y. Kohori, N. Takeshita, J. Phys. Soc. Jpn. **77**, 075001 (2008). doi:10.1143/jpsj.77.075001

115. C.P. Poole, *Electron spin resonance a comprehensive treatise on experimental techniques* (Dover, NY, 1996)
116. J. Sichelschmidt, V.A. Ivanshin, J. Ferstl, C. Geibel, F. Steglich, Phys. Rev. Lett. **91**, 156401 (2003). doi:10.1103/PhysRevLett.91.156401
117. J. Sichelschmidt, J. Wykhoff, T. Gruner, C. Krellner, C. Klingner, C. Geibel, F. Steglich, H.A. Krug von Nidda, D.V. Zakharov, A. Loidl, I. Fazlizhanov, Phys. Rev. B **81**, 205116 (2010). doi:10.1103/PhysRevB.81.205116
118. H. Ohta, T. Sakurai, S. Okubo, M. Saruhashi, T. Kunimoto, Y. Uwatoko, J. Akimitsu, J. Phys.: Condens. Matter **14**, 10637 (2002). doi:10.1088/0953-89844/44/348
119. T. Sakurai, A. Taketani, T. Tomita, S. Okubo, H. Ohta, Y. Uwatoko, Rev. Sci. Instrum. **78**, 65107 (2007). doi:10.1063/1.2746818
120. T. Sakurai, T. Horie, M. Tomoo, K. Kondo, N. Matsumi, S. Okubo, H. Ohta, Y. Uwatoko, K. Kudo, Y. Koike, H. Tanaka, J. Phys.: Conf. Ser. **215**, 012184 (2010). doi:10.1088/1742-6596/215/1/012184
121. A. Amato, Rev. Mod. Phys. **69**, 1119 (1997). doi:10.1103/RevModPhys.69.1119
122. J.E. Sonier, J.H. Brewer, R.F. Kiefl, Rev. Mod. Phys. **72**, 769 (2000). doi:10.1103/RevModPhys.72.769
123. J.E. Sonier, Rep. Prog. Phys. **70**, 1717 (2007). doi:10.1088/0034-4885/70/11/R01
124. D. Andreica, Magnetic phase diagram in some kondo-lattice compounds: microscopic and macroscopic studies. Phd-thesis, ETH Zürich (2001). doi:10.3929/ethz-a-004171645
125. N. Egetenmeyer, J.L. Gavilano, A. Maisuradze, S. Gerber, D.E. MacLaughlin, G. Seyfarth, D. Andreica, A. Desilets-Benoit, A.D. Bianchi, C. Baines, R. Khasanov, Z. Fisk, M. Kenzelmann, Phys. Rev. Lett. **108**, 177204 (2012). doi:10.1103/PhysRevLett.108.177204
126. S. Klotz, M. Braden, J.M. Besson, Hyperfine Interact. **128**, 245 (2000). doi:10.1023/a:1012691801269
127. D. Bloch, J. Paureau, J. Voiron, G. Parisot, Rev. Sci. Instrum. **47**, 296 (1976). doi:10.1063/1.1134606
128. S.P. Besedin, I.N. Makarenko, S.M. Stishov, V.P. Glazkov, I.N. Goncharenko, V.A. Somenkov, High Press. Res. **14**, 193 (1995). doi:10.1080/08957959508200918
129. S. Klotz, J.M. Besson, G. Hamel, R.J. Nelmes, J.S. Loveday, W.G. Marshall, High Press. Res. **14**, 249 (1996). doi:10.1080/08957959608201409
130. I.N. Goncharenko, High Press. Res. **24**, 193 (2004). doi:10.1080/08957950410001661882
131. C.L. Bull, M. Guthrie, S. Klotz, J. Philippe, T. Strässle, R.J. Nelmes, J.S. Loveday, G. Hamel, High Press. Res. **25**, 229 (2005). doi:10.1080/08957950500452893
132. I.N. Goncharenko, High Press. Res. **27**, 187 (2007). doi:10.1080/08957950601105507
133. J. Paureau, C. Vettier, Rev. Sci. Instrum. **46**, 1484 (1975). doi:10.1063/1.1134083
134. W. Bao, C. Broholm, S.F. Trevino, Rev. Sci. Instrum. **66**, 1260 (1995). doi:10.1063/1.1146019
135. F. Amita, A. Onodera, Rev. Sci. Instrum. **69**, 2738 (1998). doi:10.1063/1.1149008
136. B. Fåk, D.F. McMorrow, P.G. Niklowitz, S. Raymond, E. Ressouche, J. Flouquet, P.C. Canfield, S.L. Budko, Y. Janssen, M.J. Gutmann, J. Phys.: Condens. Matter **17**, 301 (2005). doi:10.1088/0953-89847/2/006
137. W. Wang, D.A. Sokolov, A.D. Huxley, K.V. Kamenev, Rev. Sci. Instrum. **82**, 073903 (2011). doi:10.1063/1.3608112
138. S. Klotz, *Techniques in High Pressure Neutron Scattering* (CRC Press, Boca Raton, 2012)
139. M.M. Abd-Elmeguid, Hyperfine Interact. **113**, 111 (1998). doi:10.1023/A:1012615414512
140. S. Medvedev, T.M. McQueen, I.A. Troyan, T. Palasyuk, M.I. Eremets, R.J. Cava, S. Naghavi, F. Casper, V. Ksenofontov, G. Wortmann, C. Felser, Nature Mater. **8**, 630 (2009). doi:10.1038/nmat2491
141. J.S. Schilling, U.F. Klein, W.B. Holzapfel, Rev. Sci. Instrum. **45**, 1353 (1974). doi:10.1063/1.1686499
142. G.R. Hearne, M.P. Pasternak, R.D. Taylor, Hyperfine Interact. **92**, 1155 (1994). doi:10.1007/bf02065748
143. G.R. Hearne, M.P. Pasternak, R.D. Taylor, Rev. Sci. Instrum. **65**, 3787 (1994). doi:10.1063/1.1144508

144. L. Degiorgi, Rev. Mod. Phys. **71**, 687 (1999). doi:10.1103/RevModPhys.71.687
145. H. Okamura, M. Matsunami, R. Kitamura, S. Ishida, A. Ochiai, T. Nanba, J. Phys.: Conf. Ser. **215**, 012051 (2010). doi:10.1088/1742-6596/215/1/012051
146. L. Degiorgi, New J. Phys. **13**, 023011 (2011). doi:10.1088/1367-2630/13/2/023011
147. A.F. Goncharov, Int. J. Spectr. **2012**, 617528 (2012). doi:10.1155/2012/617528
148. Y. Syuma, M. Keizo, Sci. Technol. Adv. Mater. **10**, 024307 (2009). doi:10.1088/1468-6996/10/2/024307
149. M. Lang, J. Müller, *Organic Superconductors Superconductivity* (Springer, Berlin, 2008), p. 1155. doi:10.1007/978-3-540-73253-2-20
150. G.R. Stewart, Rev. Mod. Phys. **83**, 1589 (2011). doi:10.1103/RevModPhys.83.1589
151. F. Steglich, J. Aarts, C.D. Bredl, W. Lieke, D. Meschede, W. Franz, H. Schäfer, Phys. Rev. Lett. **43**, 1892 (1979). doi:10.1103/PhysRevLett.43.1892
152. B. Bellarbi, D. Jaccard, A. Benoit, J.M. Mignot, H.F. Braun, Phys. Rev. B **30**, 1182 (1984). doi:10.1103/PhysRevB.30.1182
153. F. Thomas, F. Thomasson, C. Ayache, C. Geibel, F. Steglich, Phys. B **303**, 168–188 (1993). doi:10.1016/0921-4526(93)90561-j
154. F. Thomas, C. Ayache, I.A. Fomine, J. Thomasson, C. Geibel, J. Phys.: Condens. Matter **8**, L51 (1996). doi:10.1088/0953-8984/8/4/002
155. H.Q. Yuan, F.M. Grosche, M. Deppe, C. Geibel, G. Sparn, F. Steglich, Science **302**, 2104 (2003). doi:10.1126/science.1091648
156. D. Jaccard, K. Behnia, J. Sierro, Phys. Lett. A **163**, 475 (1992). doi:10.1016/0375-9601(92)90860-o
157. R. Movshovich, T. Graf, D. Mandrus, J.D. Thompson, J.L. Smith, Z. Fisk, Phys. Rev. B **53**, 8241 (1996). doi:10.1103/PhysRevB.53.8241
158. N.D. Mathur, F.M. Grosche, S.R. Julian, I.R. Walker, D.M. Freye, R.K.W. Haselwimmer, G.G. Lonzarich, Nature **394**, 39 (1998). doi:10.1038/27838
159. F.M. Grosche, S.R. Julian, N.D. Mathur, G.G. Lonzarich, Phys. B **50**, 223–224 (1996). doi:10.1016/0921-4526(96)00036-1
160. J.D. Thompson, N. Nicklas, A. Bianchi, R. Movshovich, A. Llobet, W. Bao, A. Malinowski, M.F. Hundley, N.O. Moreno, P.G. Pagliuso, J.L. Sarrao, S. Nakatsuji, Z. Fisk, R. Borth, E. Lengyel, N. Oeschler, G. Sparn, F. Steglich, Phys. B **446**, 329–333 (2003). doi:10.1016/s0921-4526(02)01987-7
161. A. Llobet, J.S. Gardner, E.G. Moshopoulou, J.M. Mignot, M. Nicklas, W. Bao, N.O. Moreno, P.G. Pagliuso, I.N. Goncharenko, J.L. Sarrao, J.D. Thompson, Phys. Rev. B **69**, 24403 (2004). doi:10.1103/PhysRevB.69.024403
162. M. Nicklas, R. Borth, E. Lengyel, P.G. Pagliuso, J.L. Sarrao, V.A. Sidorov, G. Sparn, F. Steglich, J.D. Thompson, J. Phys.: Condens. Matter **13**, L905 (2001). doi:10.1088/0953-89843/4404
163. T. Muramatsu, N. Tateiwa, T.C. Kobayashi, K. Shimizu, K. Amaya, D. Aoki, H. Shishido, Y. Haga, Y. Ōnuki, J. Phys. Soc. Jpn. **70**, 3362 (2001). doi:10.1143/jpsj.70.3362
164. V.A. Sidorov, M. Nicklas, P.G. Pagliuso, J.L. Sarrao, Y. Bang, A.V. Balatsky, J.D. Thompson, Phys. Rev. Lett. **89**, 157004 (2009). doi:10.1103/PhysRevLett.89.157004
165. H. Hegger, H.G. Moshopoulou, M.F. Hundley, J.L. Sarrao, Z. Fisk, J.D. Thompson, Phys. Rev. Lett. **84**, 4986 (2000). doi:10.1103/PhysRevLett.84.4986
166. C. Petrovic, P.G. Pagliuso, M.F. Hundley, R. Movshovich, J.L. Sarrao, J.D. Thompson, Z. Fisk, P. Monthoux, J. Phys.: Condens. Matter **13**, L337 (2001). doi:10.1088/0953-89843703
167. C. Petrovic, R. Movshovich, M. Jaime, P.G. Pagliuso, M.F. Hundley, J.L. Sarrao, J.D. Thompson, Z. Fisk, Europhys. Lett. **53**, 354 (2001). doi:10.1209/epl/i2001-00161-8
168. R. Movshovich, M. Jaime, J.D. Thompson, C. Petrovic, Z. Fisk, P.G. Pagliuso, J.L. Sarrao, Phys. Rev. Lett. **86**, 5152 (2001). doi:10.1103/PhysRevLett.86.5152
169. L.D. Pham, T. Park, S. Maquilon, J.D. Thompson, Z. Fisk, Phys. Rev. Lett. **97**, 056404 (2006). doi:10.1103/PhysRevLett.97.056404

170. M. Nicklas, O. Stockert, P. Tuson, K. Habicht, K. Kiefer, L.D. Pham, J.D. Thompson, Z. Fisk, F. Steglich, Phys. Rev. B **76**, 052401 (2007). doi:10.1103/PhysRevB.76.052401
171. S. Nair, O. Stockert, U. Witte, M. Nicklas, R. Schedler, K. Kiefer, J.D. Thompson, A.D. Bianchi, Z. Fisk, S. Wirth, F. Steglich, Proc. Natl. Acad. Sci. USA 107, 9537 (2010). doi:10.1073/pnas.1004958107
172. M. Nicklas, V.A. Sidorov, H.A. Borges, P.G. Pagliuso, J.L. Sarrao, J.D. Thompson, Phys. Rev. B **70**, 20505 (2004). doi:10.1103/PhysRevB.70.020505
173. T. Muramatsu, T.C. Kobayashi, K. Shimizu, K. Amaya, D. Aoki, Y. Haga, Y. Ōnuki, Phys. C **539**, 388–389 (2003). doi:10.1016/s0921-4534(02)02731-4
174. P.G. Pagliuso, C. Petrovic, R. Movshovich, D. Hall, M.F. Hundley, J.L. Sarrao, J.D. Thompson, K. Fisk, Phys. Rev. B **64**, 100503 (2001). doi:10.1103/PhysRevB.64.100503
175. A. Bianchi, R. Movshovich, C. Capan, P.G. Pagliuso, J.L. Sarrao, Phys. Rev. Lett. **91**, 187004 (2003). doi:10.1103/PhysRevLett.91.187004
176. H.A. Radovan, N.A. Fortune, T.P. Murphy, S.T. Hannahs, E.C. Palm, S.W. Tozer, D. Hall, Nature **425**, 51 (2003). doi:10.1038/nature01842
177. P. Fulde, R.A. Ferrell, Phys. Rev. **135**, A550 (1964). doi:10.1103/PhysRev.135.A550
178. A.I. Larkin, Y.N. Ovchinnikov, Zh Eksp, Teor. Fiz. **47**, 1136 (1964)
179. F. Ronning, C. Capan, E.D. Bauer, J.D. Thompson, J.L. Sarrao, R. Movshovich, Phys. Rev. B **73**, 64519 (2006). doi:10.1103/PhysRevB.73.064519
180. S. Singh, C. Capan, M. Nicklas, M. Rams, A. Gladun, H. Lee, J.F. DiTusa, Z. Fisk, F. Steglich, S. Wirth, Phys. Rev. Lett. **98**, 057001 (2007). doi:10.1103/PhysRevLett.98.057001
181. C.F. Miclea, M. Nicklas, D. Parker, K. Maki, J.L. Sarrao, J.D. Thompson, G. Sparn, F. Steglich, Phys. Rev. Lett. **96**, 117001 (2006). doi:10.1103/PhysRevLett.96.117001
182. M. Nicklas, C.F. Miclea, J.L. Sarrao, J.D. Thompson, G. Sparn, F. Steglich, J. Low Temp. Phys. **146**, 669 (2007). doi:10.1007/s10909-006-9284-7
183. M. Kenzelmann, T. Strässle, C. Niedermayer, M. Sigrist, B. Padmanabhan, M. Zolliker, A.D. Bianchi, R. Movshovich, E.D. Bauer, J.L. Sarrao, J.D. Thompson, Science **321**, 1652 (2008). doi:10.1126/science.1161818

Chapter 7
Neutron Scattering and Its Application to Strongly Correlated Systems

Igor A. Zaliznyak and John M. Tranquada

Abstract Neutron scattering is a powerful probe of strongly correlated systems. It can directly detect common phenomena such as magnetic order, and can be used to determine the coupling between magnetic moments through measurements of the spin-wave dispersions. In the absence of magnetic order, one can detect diffuse scattering and dynamic correlations. Neutrons are also sensitive to the arrangement of atoms in a solid (crystal structure) and lattice dynamics (phonons). In this chapter, we provide an introduction to neutrons and neutron sources. The neutron scattering cross section is described and formulas are given for nuclear diffraction, phonon scattering, magnetic diffraction, and magnon scattering. As an experimental example, we describe measurements of antiferromagnetic order, spin dynamics, and their evolution in the $La_{2-x}Ba_xCuO_4$ family of high-temperature superconductors.

7.1 Introduction

A common symptom of correlated-electron systems is magnetism, and neutron scattering is the premiere technique for measuring magnetic correlations in solids. With a spin angular momentum of $\frac{1}{2}\hbar$, the neutron interacts directly with the magnetization density of the solid. Elastic scattering can directly reveal stic magnetic order; for example, neutron diffraction provided the first experimental evidence for Néel antiferromagnetism [1]. Through inelastic scattering one can probe dynamic spin-spin correlations; in an ordered antiferromagnet, one can measure the precession of the spins about their average orientations, which show up as dispersing spin waves.

Neutrons do not couple to the charge of the electrons, but instead scatter from atomic nuclei via the strong force. Despite the name, the small size of the nucleus compared to the electronic charge cloud of the atom results in a rather weak scattering cross section. The magnetic and nuclear scattering cross sections are comparable, so that neutron scattering is very sensitive to magnetism, in a relative sense.

I.A. Zaliznyak (✉) · J.M. Tranquada
Brookhaven National Laboratory, Upton, NY 11973-5000, USA
e-mail: zaliznyak@bnl.gov

J.M. Tranquada
e-mail: jtran@bnl.gov

A. Avella and F. Mancini (eds.), *Strongly Correlated Systems*,
Springer Series in Solid-State Sciences 180, DOI 10.1007/978-3-662-44133-6_7

A challenge with neutron scattering is that the combination of weak scattering cross section and limited source strength means that one needs a relatively large sample size compared with many other techniques. The value of the information that can be obtained by neutron scattering generally makes worthwhile the effort to grow large samples; nevertheless, in practice it is useful to take advantage of complementary information obtained from techniques such as muon spin rotation spectroscopy and nuclear magnetic resonance. The latter techniques yield less information but often provide greater precision. There have also been continuing developments in resonant X-ray scattering; nevertheless, neutron scattering will remain an essential technique to investigate strongly correlated systems for the foreseeable future.

As we have space only for a concise introduction to the field, we note that there plenty of more extended references available. A good summary of the theory of neutron scattering is given by Squires [2], while a more detailed description is provided by Lovesey [3]. We have contributed to a technique-oriented book [4] and to book chapters on magnetic neutron scattering [5, 6], and new books on the subject continue to appear.

To illustrate some of the concepts and capabilities, we will use examples involving copper-oxide compounds, especially from the family $La_{2-x}Ba_xCuO_4$, which includes phenomena from antiferromagnetic order to high-temperature superconductivity. More details on neutron scattering studies of cuprates are given in recent reviews [7–10].

7.2 Basic Properties of the Neutron and Its Interaction with Matter

The neutron is an elementary spin-1/2 particle, which, together with its charged relative, the proton, is a building block of the atomic nucleus. According to the "standard model" of the elementary particles, the neutron and proton are fermionic hadrons, or baryons, composed of one "up" and two "down" quarks, and two "up" and one "down" quarks, respectively. The basic properties of a neutron are summarized in Table 7.1.

Although the neutron is electrically neutral, it has a non-zero magnetic moment, similar in magnitude to that of a proton ($\mu_n = 0.684979\,\mu_p$), but directed opposite

Table 7.1 Basic properties of a neutron

Charge	Mass (kg)	Lifetime (s)	Magnetic moment μ_n (J/T)	Gyromagnetic ratio γ_n (s^{-1}/T)	g-factor (g_n)
0	1.67492×10^{-27}	882 ± 2	-0.96623×10^{-26}	-1.83247×10^{8}	3.82609

The gyromagnetic ratio, γ_n, and the g-factor, g_n, are defined by $\boldsymbol{\mu}_n = \gamma_n \boldsymbol{\sigma}_n = -g_n \mu_N \mathbf{S}_n$, where $\boldsymbol{\sigma}_n$ is the neutron's angular momentum, $\mathbf{S}_n = \boldsymbol{\sigma}_n/\hbar$ is the neutron's spin ($S_n = 1/2$), $\mu_N = e\hbar/(2m_p c) = 5.05078 \times 10^{-27}$ J/T $= 5.05078 \times 10^{-24}$ erg/G s is the nuclear magneton [11, 12]

to the angular momentum, so that the neutron's gyromagnetic ratio is negative. The neutron's mass, $m_n = 1.00866\,\text{Da}$ (atomic mass units) is slightly larger than that of the proton, $m_n = 1.00728\,\text{Da}$, and that of the hydrogen atom $m_H = 1.00782\,\text{Da}$. Therefore, outside the nucleus the free neutron is unstable and undergoes β-decay into a proton, an electron, and an antineutrino. Although the free neutron's lifetime is only about 15 mins, this is long enough for neutron-scattering experiments. For example, a neutron extracted through the beam-tube in a nuclear reactor has typically reached thermal equilibrium with the water that cools the reactor in a number of collisions on its way out (such neutrons usually are called thermal neutrons). Assuming the water has "standard" temperature of 293 K, the neutron's most probable velocity would be about 2200 m/s. It would spend only a fraction of a second while it travels along the $<100\,\text{m}$ beam path in the spectrometer to be scattered by the sample and arrive in the detector.

Neutrons used in scattering experiments are non-relativistic. Therefore, the neutron's energy, E_n, is related to its velocity, $\boldsymbol{v}_n$, wave vector, $\boldsymbol{\kappa}_n = m_n \boldsymbol{v}_n/\hbar$, and the (de Broglie) wavelength, $\lambda_n = 2\pi/\kappa_n$, through

$$E_n = \frac{1}{2} m_n \boldsymbol{v}_n^2 = \frac{\hbar^2 \boldsymbol{\kappa}_n^2}{2m_n} = \frac{h^2}{2m_n \lambda_n^2}. \tag{7.1}$$

Following the notation accepted in particle physics, the neutron's energy is measured in millielectronvolts (meV). The neutron's wavelength and its wave vector are usually measured in Å ($1\,\text{Å} = 0.1\,\text{nm} = 10^{-8}\,\text{cm}$) and Å^{-1}, respectively. Using these units, we can rewrite the (7.1) in the following, practical fashion:

$$E_n = 5.22704 \times 10^{-6} \cdot v_n^2 = 2.07212 \cdot \kappa_n^2 = \frac{81.8042}{\lambda_n^2}, \tag{7.2}$$

where E_n is in meV, v_n in m/s, κ_n in Å^{-1}, and λ_n in Å.

For the sake of comparison with the notations used in other techniques and in theoretical calculations, we list several different ways of representing typical neutron energies in Table 7.2. The different energy equivalents shown in the Table can be used interchangeably, as a matter of convenience.

7.3 Neutron Sources

Neutrons are especially abundant in nuclei of high atomic number, where they can significantly exceed the number of protons. To create a neutron beam, the first challenge is to extract neutrons from the nuclei. The first practical source was the nuclear reactor, in which neutron bombardment of ^{235}U nuclei induces fission, a process that releases several neutrons per incident neutron, thus allowing for a self-sustaining chain reaction. The neutrons that are released have a very large energy,

Table 7.2 Different notations used to represent the neutron's energy

E_n (10^{-19} J)	E_n/e (meV)	E_n/h (THz)	$E_n/(hc)$ (cm^{-1})	$E_n/(2\mu_B)$ (T)	E_n/k_B (K)	k_n ($Å^{-1}$)	λ_n (Å)
1.60218	1000	241.799	8065.54	8637.99	11604.5	21.968	0.2860
0.160218	100	24.1799	806.554	863.799	1160.45	6.9469	0.9044
0.0801088	50	12.0899	403.277	431.900	580.225	4.9122	1.27909
0.0240326	15	3.62698	120.983	129.570	174.068	2.6905	2.3353
0.00160218	1	0.241799	8.06554	8.63799	11.6045	0.69469	9.0445

e is the electron charge, h is the Plank's constant, c is the velocity of light, $\mu_B = e^2/2m_e c = 0.92740 \times 10^{-29}$ J/T is the Bohr's magneton, k_B is Boltzman's constant [11]. Also shown are the corresponding neutron wave vector k_n and the deBroglie wavelength λ_n

whereas the fission cross section is enhanced by slower neutrons. The slowing of neutrons can be achieved quite effectively by scattering from hydrogen, especially in the form of H_2O, which can also act to cool the reactor core. In a research reactor, where one would like to extract some of the neutrons, the reactor moderator can be made more transparent to neutrons by replacing H_2O with D_2O (heavy water, with D representing deuterium). Cylindrical thimbles poking into the water moderator provide an escape path for neutrons, which form the beams that supply neutron spectrometers.

Another approach is to knock the neutrons out of heavy nuclei with high-energy protons from an accelerator. Again, the neutrons that can escape the nuclei have very high energies that must be reduced by multiple scattering in a moderator. In contrast to a reactor, which produces neutron beams that are continuous in time, the proton beam provided by an accelerator can be pulsed, so that a spallation source typically has pulsed beams of neutrons. Targets can be made of a heavy metal such as tungsten, but newer sources with higher power tend to use liquid mercury in order to allow adequate heat removal.

A list of the major operating spallation sources in the world is given in the upper portion of Table 7.3. Information on the available instrumentation and capabilities can be obtained from the listed web sites. With a pulsed neutron source, each burst of neutrons is produced in a narrow time window, so that one can distinguish between neutrons of different velocities by their travel time, or "time of flight". Using a rotating shutter, one can select incident neutrons of a desired energy; the energy of scattered neutrons can then be determined by their time of arrival at a detector.

The spallation source SINQ at the Paul Scherrer Institut provides a continuous, rather than pulsed, beam, so its instrumentation has more in common with reactor facilities, which are listed in the lower portion of Table 7.3. With a continuous source, it is common to select the desired energy of incident neutrons by Bragg diffraction from a crystal (or array of crystals). In a triple-axis spectrometer [4], one also uses Bragg diffraction to analyze the energy and momentum of neutrons scattered by a sample. Again, many of the facility web sites provide a wealth of information on spectrometers and capabilities.

Table 7.3 Major neutron user facilities presently in operation

Facility	Laboratory	Location	Web address
Spallation sources			
Spallation neutron source	Oak Ridge National Lab	Oak Ridge, TN, USA	http://neutrons.ornl.gov/
Lujan neutron scattering center	Los Alamos National Lab	Los Alamos, NM, USA	http://lansce.lanl.gov/lujan/
ISIS	Rutherford Appleton lab	Didcot, UK	http://www.isis.stfc.ac.uk/
J-PARC	Japan Atomic Energy Agency	Tokai, Japan	http://j-parc.jp/MatLife/en/
SINQ	Paul Scherrer Institut	Villigen, Switzerland	http://www.psi.ch/sinq/
Reactor facilities			
High flux isotope reactor	Oak Ridge National Lab	Oak Ridge, TN, USA	http://neutrons.ornl.gov/
NIST center for neutron research	NIST	Gaithersburg, MD, USA	http://www.ncnr.nist.gov/
Institut Laue Langevin	ILL	Grenoble, France	http://www.ill.eu/
FRM-II	Technische Universität München	Munich, Germany	http://www.frm2.tum.de/en/
Laboratoire Léon Brillouin	CEA Saclay	Saclay, France	http://www-llb.cea.fr/en/
JRR-3	Japan atomic energy agency	Tokai, Japan	http://qubs.jaea.go.jp/en_index.html
OPAL	ANSTO	Lucas Heights, NSW, Australia	http://www.ansto.gov.au/
HANARO	KAERI	Daejeon, South Korea	http://hanaro4u.kaeri.re.kr/

7.4 Neutron Interactions and Scattering Lengths

Many of the fundamental advantages of neutron scattering techniques arise from the fact that the neutron's interactions with matter are usually weak and are extremely well understood. Hence, neutrons afford direct experimental insight into dynamical properties of the material system of interest, unperturbed by the probe and essentially undistorted by the details of its interaction with matter. These properties contrast favorably with X-ray or charged-particle (electron, muon) techniques, where the probe could significantly perturb the system, and the interaction matrix elements between the system and the probe are often very complicated and profoundly impact the physics measured in the experiment.

The scattering of neutrons by an atomic system is governed by two fundamental interactions. The residual strong interaction (nuclear force) gives rise to scattering by the atomic nuclei (nuclear scattering). The electromagnetic interaction of the neutron's magnetic moment with the sample's internal magnetic fields, mainly originating from the unpaired electrons in the atomic shells, gives rise to magnetic scattering [2, 3, 13–15].

Magnetic interaction of a neutron with a single atom is of relativistic origin and is very weak, so that magnetic neutron scattering can be treated using the Born approximation. The interaction potential consists of the dipole-dipole interaction with the magnetic moment associated with the electronic spin, $\boldsymbol{\mu}_{se} = g_s \boldsymbol{s}_e \approx -2\boldsymbol{s}_e$ ($g_s \approx -2.002319$ is the Landé g-factor),

$$\hat{V}_{se}(\boldsymbol{r}) = -\frac{8\pi}{3}(\boldsymbol{\mu}_n \cdot \boldsymbol{\mu}_{se})\delta(\boldsymbol{r}) - \frac{(\boldsymbol{\mu}_n \cdot \boldsymbol{\mu}_{se})}{r^3} + \frac{3(\boldsymbol{\mu}_n \cdot \boldsymbol{r})(\boldsymbol{\mu}_{se} \cdot \boldsymbol{r})}{r^5}, \tag{7.3}$$

and the interaction with the electric current associated with the electron's orbital motion

$$\hat{V}_{sl}(\boldsymbol{r}) = 2\mu_B \frac{(\boldsymbol{\mu}_n \cdot \boldsymbol{l}_e)}{r^3}. \tag{7.4}$$

Here $\hbar \boldsymbol{l}_e = \boldsymbol{r} \times \boldsymbol{p}_e$ is the electron's orbital angular momentum, and $\boldsymbol{r} = \boldsymbol{r}_e - \boldsymbol{r}_n$ its coordinate in the neutron's rest frame.

While the neutron's interaction with the atomic nucleus is strong—the nuclear force is responsible for holding together protons and neutrons in the nucleus—it has extremely short range, $<10^{-12}$ cm, comparable to the size of the nuclei, and is much smaller than the typical neutron's wavelength. Hence, to describe the neutron's interaction with the system of atomic nuclei in which the typical distances are about $1\,\text{Å} = 10^{-10}$ cm, a highly accurate approximation is obtained by using a delta-function for the nuclear scattering length operator in the coordinate representation,

$$\hat{b}_N(\boldsymbol{r}) = b\,\delta(\boldsymbol{r}_n - \boldsymbol{R}_N). \tag{7.5}$$

Here $\boldsymbol{R}_N$ is the position of the nucleus and b is the nuclear scattering length, which is usually treated as a phenomenological parameter [16, 17] that has been determined

experimentally and tabulated [18–20]. In the Born approximation, the scattering length would correspond to the neutron-nucleus interaction described by the Fermi's *pseudo-potential* [21],

$$\hat{V}_N(\boldsymbol{r}_n, \boldsymbol{R}_N) = -\frac{2\pi\hbar^2}{m_n} b\,\delta(\boldsymbol{r}_n - \boldsymbol{R}_N). \tag{7.6}$$

In general, the bound scattering length (that is, for a nucleus fixed in space) is a complex quantity [2, 13], $b = b' - ib''$, defining the total scattering cross-section, σ_s, and the absorption cross-section far from the nuclear resonance capture, σ_a, through

$$\sigma_s = 4\pi|b'|^2 \quad \sigma_a = \frac{4\pi}{\kappa_i}|b''|^2. \tag{7.7}$$

For the majority of natural elements b' is close in magnitude to the characteristic magnetic scattering length, $r_m = -(g_n/2)r_e = -5.391\,\text{fm}$ ($1\,\text{fm} = 10^{-13}\,\text{cm}$ and $r_e = e^2/(m_e c^2)$ is the classical electron radius).

7.5 Cross-Section Measured in a Neutron Scattering Experiment

In a scattering experiment, the sample is placed in the neutron beam having a well-defined wave vector $\boldsymbol{\kappa}_i$ and known incident flux density $\Phi_i(\boldsymbol{\kappa}_i)$, and the detector measures the partial current, $\delta J_f(\boldsymbol{\kappa}_f)$, scattered into a small (ideally infinitesimal) volume of the phase space, $d^3\boldsymbol{\kappa}_f = k_f^2 d\kappa_f d\Omega_f = (m_n\kappa_f/\hbar^2)dE_f d\Omega_f$, near the wave vector $\boldsymbol{\kappa}_f$, as indicated in Fig. 7.1.This measured partial current, normalized to the appropriate phase space element covered by the detector, yields the scattered current density. The double differential scattering cross-section, which is thus measured, is then defined by the ratio of this scattered current density to the incident neutron flux density, e.g.,

$$\frac{d^2\sigma(\boldsymbol{Q}, E)}{dEd\Omega} = \frac{1}{\Phi_i(\boldsymbol{\kappa}_i)}\frac{\delta J_f(\boldsymbol{\kappa}_f)}{dEd\Omega}. \tag{7.8}$$

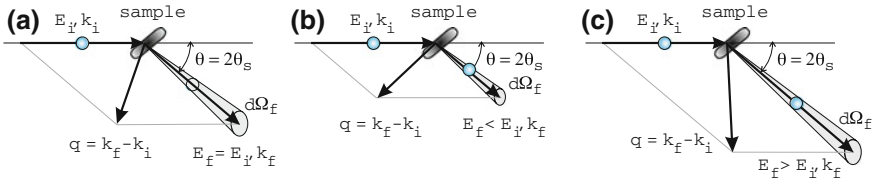

Fig. 7.1 Schematics of the scattering process in a neutron scattering experiment, **a** elastic, **b** inelastic, neutron energy loss, **c** inelastic, neutron energy gain

For each incident neutron in the plane wave state $e^{i\boldsymbol{\kappa}_i\cdot\boldsymbol{r}_n}$, the incident flux density is $\Phi_i(\boldsymbol{\kappa}_i) = \hbar\kappa_i/m_n$. The scattered current density is determined by the transition rate $\Gamma_{i\to f}$ from the initial state $|\boldsymbol{\kappa}_i, S^z_{n,i}, \eta_i\rangle$, where the neutron is in the plane wave state $e^{i\boldsymbol{\kappa}_i\cdot\boldsymbol{r}_n}$ with the spin $S^z_{n,i}$ and the scattering system is described by the set of variables η_i, to the final state, $|\boldsymbol{\kappa}_f, S^z_{n,f}, \eta_f\rangle$. According to scattering theory [5, 13, 22], the transition rate is determined by the matrix elements of the transition operator (or T-matrix) $\hat{T}$, satisfying certain operator equations, which depend on the scattering system's Hamiltonian, $\hat{H}$, and its interaction with the neutron, $\hat{V}$,

$$\Gamma_{i\to f} = \frac{2\pi}{\hbar}\left|\langle\boldsymbol{\kappa}_f, S^z_{n,f}, \eta_f|\hat{T}|\boldsymbol{\kappa}_i, S^z_{n,i}, \eta_i\rangle\right|^2 \delta\left(\frac{\hbar^2\kappa_i^2}{2m_n} - \frac{\hbar^2\kappa_f^2}{2m_n} - E\right). \tag{7.9}$$

Here $E = E_f(\eta_f) - E_i(\eta_i)$ is the scattering system's energy gain. It is convenient to introduce the scattering length operator, $\hat{b}$, which conveniently absorbs several factors,

$$\hat{b}(\boldsymbol{r}_n, \boldsymbol{S}_n, \eta) = -\frac{m_n}{2\pi\hbar^2}\langle\boldsymbol{\kappa}_f, S^z_{n,f}|\hat{T}|\boldsymbol{\kappa}_i, S^z_{n,i}\rangle, \tag{7.10}$$

and its Fourier transform, $\hat{b}(\boldsymbol{q})$,

$$\hat{b}(\boldsymbol{q}) = \int \mathrm{e}^{-i\boldsymbol{q}\cdot\boldsymbol{r}}\hat{b}(\boldsymbol{r}, \boldsymbol{S}_n, \eta)d^3\boldsymbol{r}, \tag{7.11}$$

Summing over all possible final scattering states, we obtain the double differential scattering cross-section for a given initial state, $|\boldsymbol{\kappa}_i, S^z_{n,i}, \eta_i\rangle$,

$$\frac{d^2\sigma(\boldsymbol{Q}, E)}{dEd\Omega} = \frac{\kappa_f}{\kappa_i}\sum_{S^z_{n,f},\eta_f}\left|\langle\eta_f|\hat{b}(-\boldsymbol{Q})|\eta_i\rangle\right|^2 \delta\left(E_f(\eta_f) - E_i(\eta_i) - E\right), \tag{7.12}$$

where the dependence on the spin-state of the neutron is implicit in $\hat{b}(-\boldsymbol{Q})$. The energy and momentum transfer to the sample are governed by the conservation laws,

$$\boldsymbol{Q} = \boldsymbol{\kappa}_i - \boldsymbol{\kappa}_f, \quad E = E_f(\eta_f) - E_i(\eta_i) = \frac{\hbar^2}{2m_n}(\kappa_i^2 - \kappa_f^2). \tag{7.13}$$

Finally, following Van Hove [23], one can use the integral representation of the delta-function expressing the energy conservation in (7.12), and the time-dependent scattering length operator whose evolution is governed by the system's Hamiltonian,

$$\hat{b}(\boldsymbol{q}, t) = \mathrm{e}^{i\hat{H}t/\hbar}\hat{b}(\boldsymbol{q})\mathrm{e}^{-i\hat{H}t/\hbar}, \tag{7.14}$$

to recast the double differential scattering cross-section in the most useful form of the two-time correlation function,

$$\frac{d^2\sigma}{dEd\Omega} = \frac{\kappa_f}{\kappa_i} \sum_{S^z_{n,f}} \int_{-\infty}^{\infty} \mathrm{e}^{-i\omega t} \langle \eta_i | \hat{b}^\dagger(-\boldsymbol{Q}) \hat{b}(-\boldsymbol{Q}, t) | \eta_i \rangle \frac{dt}{2\pi\hbar}. \tag{7.15}$$

Here the sum is over all possible final spin states of the scattered neutron, $S^z_{n,f}$, since in the general case the scattering length operator, $\hat{b}(-\boldsymbol{Q}, t)$, depends on the neutron spin, $\boldsymbol{S}_n$. The sum over the final states of the sample has been absorbed into the expectation value of the two-time correlation function of the scattering length operator. The minus sign in front of $\boldsymbol{Q}$ in (7.15) follows from the convention adopted in the conservation laws in (7.13), where $\hbar\boldsymbol{Q}$ is the momentum transfer to the sample, which is the opposite of the change in the neutron's momentum. The total measured scattering cross-section is obtained by taking the proper thermal average of (7.15) over all possible initial states, $|\eta_i\rangle$.

While the scattered neutron's wave vector $\boldsymbol{\kappa}_f$ is uniquely determined by $\boldsymbol{\kappa}_i$ and $\boldsymbol{Q}$, by virtue of the conservation laws (7.13), the neutron's spin state can be changed by transferring the angular momentum $\hbar(\Delta S^z_n) = \pm\hbar$ to the sample. In a polarized neutron experiment scattering between different neutron spin states can be measured. In such a case, the scattering length operator in (7.15) is a matrix with respect to different initial and final spin state indices; it determines the various spin-flip and non-spin-flip cross-sections [3, 24]. In the more common case of unpolarized neutron scattering, neutron spin indices should be traced out in (7.15), so that it determines a single unpolarized neutron scattering cross-section.

Finally, we should mention that the double differential cross-sections in (7.12), (7.15) are general expressions obtained from scattering theory and are valid for scattering of any probe particles. The remarkable advantage of neutron scattering is in the fact that scattering length operators are rather simple, very well understood, and are directly related to the fundamental physical properties of the scattering sample.

7.6 Nuclear Scattering in Condensed Matter

For scattering from an individual nucleus, the scattering length operator can be very accurately approximated by a delta-function, (7.5). For a collection of nuclei in a condensed matter system, the total scattering length operator is obtained by adding scattering lengths of all nuclei,

$$\hat{b}_N(\boldsymbol{r}_n) = \sum_j b_j \, \delta(\boldsymbol{r}_n - \boldsymbol{r}_j), \tag{7.16}$$

where j indexes the nucleus at position $\boldsymbol{r}_j$ with scattering length b_j. For a system of identical nuclei, this is just a particle number density operator in the scattering system, times b,

$$\hat{b}_N(\boldsymbol{r}_n) = b \sum_j \delta(\boldsymbol{r}_n - \boldsymbol{r}_j) = b\,\hat{n}(\boldsymbol{r}_n), \quad \hat{b}_N(\boldsymbol{q}) = b\,\hat{n}_{\boldsymbol{q}}. \tag{7.17}$$

Substituting this into (7.15) and summing out the neutron's spin states we obtain,

$$\frac{d^2\sigma}{dEd\Omega} = \frac{\kappa_f}{\kappa_i}|b|^2 \int_{-\infty}^{\infty} \mathrm{e}^{-i\omega t}\langle \eta_i|\hat{n}_{\boldsymbol{Q}}\hat{n}_{-\boldsymbol{Q}}(t)|\eta_i\rangle \frac{dt}{2\pi\hbar}. \tag{7.18}$$

Therefore, the nuclear cross-section measures the space-time correlation of the atom number density in a condensed matter system. This is exactly the quantity of interest in many theories of strongly-correlated quantum systems.

One of the first successes of neutron scattering was the measurement of the phonon-roton dispersion of the elementary excitations in superfluid helium-4. Neutron data have confirmed that the shape of the dispersion is in agreement with that previously postulated by Landau and Feynman, as illustrated in Fig. 7.2. This led to the broad acceptance of the neutron scattering technique as a prime tool for studying quantum systems.

Next we consider the case in which two or more types of nuclear scatterers (with distinct scattering lengths b_j and frequency of occurrence c_j) are present in the sample in a random fashion. For example, an element may have multiple isotopes, each with a distinct b_j, or the nuclei have a spin, so that b_j depends on the nuclear and neutron spin orientations, or we have at least two elements that are randomly distributed among equivalent positions. The average product of the scattering lengths for any two sites can then be written as

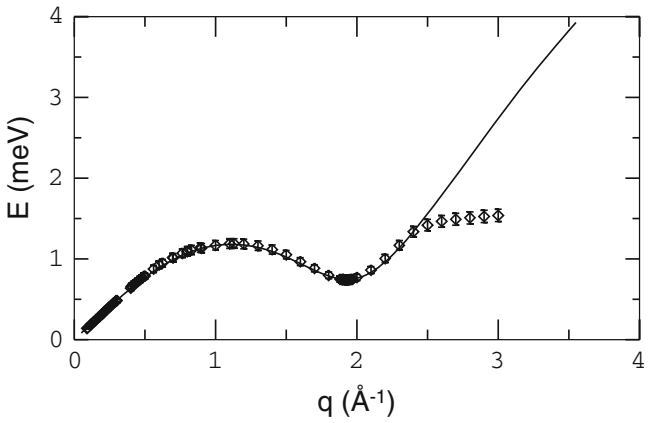

Fig. 7.2 Phonon-roton dispersion of the elementary excitations in the superfluid ^{4}He. The points show the compilation of the experimental neutron data presented in [25]. The *solid line* is the fit of the low-q part of the spectrum to the Bogolyubov quasiparticle dispersion

$$\overline{(b_j b_{j'})} = (\bar{b})^2 \left(1 - \delta_{jj'}\right) + \overline{b^2}\,\delta_{jj'}, \tag{7.19}$$

where

$$\begin{aligned} \bar{b} &= \sum_j c_j b_j, \\ \overline{b^2} &= \sum_j c_j b_j^2. \end{aligned} \tag{7.20}$$

We can then distinguish between coherent scattering,

$$\frac{d^2\sigma_c}{dEd\Omega} = \frac{\kappa_f}{\kappa_i}(\bar{b})^2 \sum_{jj'} \int_{-\infty}^{\infty} \mathrm{e}^{-i\omega t} \langle \mathrm{e}^{-i\boldsymbol{Q}\cdot\boldsymbol{r}_j} \mathrm{e}^{i\boldsymbol{Q}\cdot\boldsymbol{r}_{j'}(t)} \rangle \frac{dt}{2\pi\hbar}, \tag{7.21}$$

which probes the inter-nuclear correlation, and the incoherent scattering,

$$\frac{d^2\sigma_i}{dEd\Omega} = \frac{\kappa_f}{\kappa_i}\left(\overline{b^2} - (\bar{b})^2\right) \sum_j \int_{-\infty}^{\infty} \mathrm{e}^{-i\omega t} \langle \mathrm{e}^{-i\boldsymbol{Q}\cdot\boldsymbol{r}_j} \mathrm{e}^{i\boldsymbol{Q}\cdot\boldsymbol{r}_j(t)} \rangle \frac{dt}{2\pi\hbar}, \tag{7.22}$$

which probes the local autocorrelation of the nuclear position; the angle brackets denote the average over the sample state. In (7.21) and (7.22) we have switched to the co-ordinate representation of nuclear density operator (7.17) and performed the Fourier integration. As a result, nuclear positions $\boldsymbol{r}_j$ and $\boldsymbol{r}_{j'}(t)$ are quantum-mechanical operators and have to be treated appropriately in calculating the cross-section [2, 3, 14].

7.7 Nuclear Scattering in a Crystal: The Bragg Peaks and the Phonons

In a crystal, the equilibrium positions of atomic nuclei are arranged on the sites of a lattice, so that the position of each individual nucleus j can be represented as

$$\boldsymbol{r}_j = \boldsymbol{R}_j + \boldsymbol{u}_j, \tag{7.23}$$

where $\boldsymbol{R}_j$ is the lattice site position, and $\boldsymbol{u}_j$ is a small displacement of the atomic nucleus from its equilibrium position at $\boldsymbol{R}_j$.

Substituting this into (7.21), one can show that the coherent nuclear cross-section of a monoatomic crystal is given by

$$\frac{d^2\sigma_c}{dEd\Omega} = \frac{\kappa_f}{\kappa_i} N(\bar{b})^2 \mathrm{e}^{-\langle(\boldsymbol{Q}\cdot\boldsymbol{u}_0)^2\rangle} \sum_j \mathrm{e}^{-i\,\boldsymbol{Q}\cdot\boldsymbol{R}_j} \int_{-\infty}^{\infty} \mathrm{e}^{-i\omega t} \mathrm{e}^{\langle(\boldsymbol{Q}\cdot\boldsymbol{u}_0)(\boldsymbol{Q}\cdot\boldsymbol{u}_j(t))\rangle} \frac{dt}{2\pi\hbar}, \tag{7.24}$$

Here $\langle(\boldsymbol{Q}\cdot\boldsymbol{u}_0)^2\rangle$ is the time- or lattice-averaged square of the atomic displacement from equilibrium in the direction of $\boldsymbol{Q}$, and we have taken advantage of the fact that the correlation function in (7.21) depends only on relative coordinates, which allows one summation over the N lattice sites to be completed. The integral contains an exponentiated correlation function of atomic displacements. It is useful to consider the series expansion of this term in powers of pair displacement correlations.

In zeroth order, the exponential factor is just 1, and one obtains the expression for the elastic Bragg scattering in a crystal,

$$\frac{d^2\sigma_B}{dEd\Omega} = N(\bar{b})^2 \mathrm{e}^{-2W} \sum_j \mathrm{e}^{-i\,\boldsymbol{Q}\cdot\boldsymbol{R}_j} \delta(\hbar\omega), \tag{7.25}$$

where we used the conventional notation for the Debye-Waller factor, with $W \equiv \frac{1}{2}\langle(\boldsymbol{Q}\cdot\boldsymbol{u}_0)^2\rangle$. Using the lattice Fourier representation, this can be recast in the common form

$$\frac{d^2\sigma_B}{dEd\Omega} = NV^*(\bar{b})^2 \mathrm{e}^{-2W} \sum_{\boldsymbol{\tau}} \delta(\boldsymbol{Q}-\boldsymbol{\tau})\,\delta(\hbar\omega), \tag{7.26}$$

where $V^* = (2\pi)^3/V_0$ is the reciprocal unit cell's volume (V_0 is the volume of the unit cell in real space), and $\boldsymbol{\tau}$ are the vectors of the reciprocal lattice. In a non-Bravais crystal, where the unit cell contains several atoms, the sum in (7.24) has to be split into the intra-unit cell and the inter-unit cell parts, leading to

$$\frac{d^2\sigma_B}{dEd\Omega} = NV^*|F_N(\boldsymbol{Q})|^2 \sum_{\boldsymbol{\tau}} \delta(\boldsymbol{Q}-\boldsymbol{\tau})\,\delta(\hbar\omega), \tag{7.27}$$

where the intra-unit cell summation yields the nuclear unit cell structure factor,

$$F_N(\boldsymbol{Q}) = \sum_{\mu} \mathrm{e}^{-W_\mu} \bar{b}_\mu \mathrm{e}^{-i\,\boldsymbol{Q}\cdot\boldsymbol{r}_\mu}, \tag{7.28}$$

and μ indexes atoms in the unit cell. For some reciprocal lattice points, $F_N(\boldsymbol{\tau})$ can be zero, which gives the Bragg peak extinction rules in a non-Bravais crystal.

Expanding the exponent in (7.24) to the first order, we obtain a contribution to the cross-section that is proportional to the correlation of displacements at two different sites. In cases where static disorder is present in the crystal, such as dislocations or lattice strain, the time-independent correlations of displacements between different sites give rise to elastic diffuse scattering.

Calculation of the time-dependent displacements of atomic nuclei from their equilibrium positions in the lattice is achieved by quantizing their vibrations in terms of quantum oscillators, called phonons. A phonon is a normal mode of atomic vibration, a coherent wave of atomic displacements in the crystal. We distinguish phonons with index s. The polarization vector $\boldsymbol{e}_s$ (direction of atomic displacements) and the dependence of the energy on the wave vector, $\hbar\omega_{\boldsymbol{q}s}$ (dispersion), are determined by the local inter-atomic potentials. The total number of such modes depends on the number of atoms in the unit cell of the crystal. Only three phonons, which are all acoustic, are present for the Bravais lattice, two transverse and one longitudinal. Taking the proper thermal average over the sample's equilibrium state, the contribution to the neutron scattering is given by

$$\begin{aligned}\frac{d^2\sigma_{ph}}{dEd\Omega} &= \frac{\kappa_f}{\kappa_i}(\bar{b})^2 \mathrm{e}^{-2W} \sum_s \frac{(\boldsymbol{Q}\cdot\boldsymbol{e}_s)^2}{2M\omega_{\boldsymbol{q}s}} \\ &\quad \times V^* \sum_{\boldsymbol{\tau}} \big[\delta(\boldsymbol{Q}-\boldsymbol{q}-\boldsymbol{\tau})\delta(\hbar\omega-\hbar\omega_{\boldsymbol{q}s})(n(\omega)+1) \\ &\qquad + \delta(\boldsymbol{Q}+\boldsymbol{q}-\boldsymbol{\tau})\delta(\hbar\omega+\hbar\omega_{\boldsymbol{q}s})n(\omega)\big], \end{aligned} \tag{7.29}$$

where M is the mass of each nucleus. The thermal factor

$$n(\omega) = (\mathrm{e}^{\hbar\omega/\kappa_\mathrm{B}T}-1)^{-1}$$

is the Bose distribution function describing thermal population of the oscillator states for temperature T of the sample. The first term arises from phonon creation and corresponds to the neutron energy loss, while the second term is from an annihilation of a phonon that has been thermally excited in the crystal and results in the neutron energy gain.

For a non-Bravais crystal lattice, there are also optic phonons, arising from the different intra-unit-cell vibrations. The total number of phonons is equal to 3ν, the number of vibrational degrees of freedom of the ν atoms comprising the basis of the unit cell of the lattice. The contribution of each of these phonons to the neutron scattering cross-section is

$$\begin{aligned}\frac{d^2\sigma_{ph}}{dEd\Omega} &= \frac{\kappa_f}{\kappa_i}\left|\sum_\mu \frac{\bar{b}_\mu\,\mathrm{e}^{-W_\mu}}{\sqrt{2M_\mu\omega_{\boldsymbol{q}s}}}(\boldsymbol{\tau}\cdot\boldsymbol{e}_{s\mu})\mathrm{e}^{-i\boldsymbol{\tau}\cdot\boldsymbol{r}_\mu}\right|^2 \\ &\quad \times V^* \sum_{\boldsymbol{\tau}} \big[\delta(\boldsymbol{\tau}-\boldsymbol{q}-\boldsymbol{\tau})\delta(\hbar\omega-\hbar\omega_{\boldsymbol{q}s})(n(\omega)+1) \\ &\qquad + \delta(\boldsymbol{\tau}+\boldsymbol{q}-\boldsymbol{\tau})\delta(\hbar\omega+\hbar\omega_{\boldsymbol{q}s})n(\omega)\big], \end{aligned} \tag{7.30}$$

where $\boldsymbol{e}_{s\mu}$ is the complex polarization vector for site μ in mode s. For an acoustic phonon in the hydrodynamic, long-wavelength (small q) and low-energy limit, this reduces to (7.29), where the total mass of all atoms in the unit cell, $M = \sum_\mu M_\mu$,

should be used and one must multiply by the square of the elastic Bragg structure factor, $|F_N(\boldsymbol{\tau})|^2$.

7.8 Magnetic Scattering in a Crystal: Magnetic Form Factor and Spin Correlations

The magnetic interaction of a neutron with a single atom is very weak, so the Born approximation provides an extremely accurate account for magnetic neutron scattering by the atomic electrons. In this approximation, the transition matrix is given simply by the interaction potential, $\hat{T} = \hat{V}$, where we have to combine the neutron's interaction with the electron's spin and orbital magnetic moment, (7.3) and (7.4). Accurate accounting for the orbital contribution to magnetic scattering presents, in general, a rather difficult and cumbersome task [3]. There are many important cases where the orbital contribution is not significant, such as transition-metal atoms in a crystal, where the local crystal electric field typically quenches the orbital angular momentum, or the case of s-electrons, where $l = 0$. Nevertheless, under some very general assumptions, the neutron's interaction with the electron orbital currents can be recast in the same way as its interaction with the spin magnetic moment, yielding for the total magnetic scattering length,

$$\begin{aligned}\hat{b}_m(\boldsymbol{r}) &= -\frac{m_n}{2\pi\hbar^2}\left(\hat{V}_{se}(\boldsymbol{r}) + \hat{V}_{le}(\boldsymbol{r})\right) \\ &= \frac{m_n}{2\pi\hbar^2}\left(\boldsymbol{\mu}_n \cdot \sum_e \left[\boldsymbol{\nabla} \times \left[\boldsymbol{\nabla} \times \frac{\boldsymbol{\mu}_e(r)}{r}\right]\right]\right),\end{aligned} \tag{7.31}$$

where $\boldsymbol{\mu}_e(r) = \boldsymbol{\mu}_{s,e} + \boldsymbol{\mu}_{l,e}$ is the sum of the spin and the orbital magnetization associated with each electron, e. The Fourier transform of the magnetic scattering length (7.31), which determines the scattering cross-section, is

$$\hat{b}_m(\boldsymbol{Q}) = -\frac{m_n}{2\pi\hbar^2}\frac{4\pi}{Q^2}\left(\boldsymbol{\mu}_n \cdot \left[\boldsymbol{Q} \times \left[\boldsymbol{Q} \times \boldsymbol{m}(\boldsymbol{Q})\right]\right]\right). \tag{7.32}$$

Here $\boldsymbol{m}(\boldsymbol{Q})$ is the Fourier transform of the total magnetization density of the atom,

$$\begin{aligned}\boldsymbol{m}(\boldsymbol{Q}) &= \boldsymbol{m}_S(\boldsymbol{Q}) + \boldsymbol{m}_L(\boldsymbol{Q}) \\ &= \int \mathrm{e}^{-i\,\boldsymbol{Q}\cdot\boldsymbol{r}} \sum_e \left(-2\mu_B \boldsymbol{s}_e \delta(\boldsymbol{r} - \boldsymbol{r}_e) + \boldsymbol{\mu}_{l,e}\right) d^3\boldsymbol{r},\end{aligned}$$

$\boldsymbol{s}_e$ is the spin operator of eth electron, $\boldsymbol{\mu}_{l,e}$ its orbital magnetic moment operator.

The cross product in (7.32) ensures the important property that only magnetization perpendicular to the wave vector transfer, $\boldsymbol{Q}$, contributes to the magnetic neutron scattering. Adding the contributions from all atoms in the crystal and averaging over

the neutron polarizations, we obtain the magnetic neutron scattering cross-section measured in an experiment with unpolarized neutrons ($\alpha, \beta = x, y, z$),

$$\frac{d^2\sigma_m}{dEd\Omega} = \frac{\kappa_f}{\kappa_i}\left(\frac{2m_n}{\hbar^2}\mu_n\right)^2 \sum_{\alpha,\beta}\left(\delta_{\alpha\beta} - \frac{Q_\alpha Q_\beta}{Q^2}\right)\int_{-\infty}^{\infty} \mathrm{e}^{-i\omega t}\langle M^\alpha_{\boldsymbol{Q}} M^\beta_{-\boldsymbol{Q}}(t)\rangle \frac{dt}{2\pi\hbar}. \tag{7.33}$$

Here

$$\begin{aligned} \boldsymbol{M}_{\boldsymbol{Q}} &= \sum_j \mathrm{e}^{-i\boldsymbol{Q}\cdot\boldsymbol{R}_j}\boldsymbol{m}_j(\boldsymbol{Q}) \\ &= \int \mathrm{e}^{-i\boldsymbol{Q}\cdot\boldsymbol{r}}\sum_j \boldsymbol{m}_j(\boldsymbol{r}+\boldsymbol{R}_j)d^3\boldsymbol{r} \end{aligned}$$

is the Fourier transformed magnetization density operator in the crystal. Hence, magnetic neutron scattering measures the time- and space-dependent correlations of the magnetization fluctuations in the sample. Introducing the dynamic correlation function,

$$S^{\alpha\beta}(\boldsymbol{Q},\omega) = \int_{-\infty}^{\infty} \mathrm{e}^{-i\omega t}\langle M^\alpha_{\boldsymbol{Q}} M^\beta_{-\boldsymbol{Q}}(t)\rangle \frac{dt}{2\pi\hbar}, \tag{7.34}$$

we can rewrite (7.33) as

$$\frac{d^2\sigma_m}{dEd\Omega} = \frac{\kappa_f}{\kappa_i} r_m^2 \sum_{\alpha,\beta}\left(\delta_{\alpha\beta} - \frac{Q_\alpha Q_\beta}{Q^2}\right)\frac{1}{(2\mu_B)^2} S^{\alpha\beta}(\boldsymbol{Q},\omega), \tag{7.35}$$

where $r_m = -2\mu_B\mu_n(2m_n/\hbar^2) = -5.391 \times 10^{-13}$ cm is the characteristic magnetic scattering length.

7.8.1 The Detailed Balance Constraint and the FDT

The dynamic correlation function defined above by (7.34) obeys two important relations that are derived in the linear response theory [2, 3, 15]. First, it is the detailed balance constraint, which relates the energy gain and the energy loss scattering at a temperature T,

$$S^{\alpha\beta}(\boldsymbol{Q},\omega) = \mathrm{e}^{\hbar\omega/\kappa_B T} S^{\beta\alpha}(-\boldsymbol{Q},-\omega). \tag{7.36}$$

The second is the fluctuation-dissipation theorem (FDT), which relates the scattering intensity with the imaginary part of the dynamic magnetic susceptibility,

$$\tilde{\chi}''_{\alpha\beta}(\boldsymbol{Q},\omega) = \pi\left(1 - \mathrm{e}^{-\hbar\omega/\kappa_{\mathrm{B}}T}\right)\tilde{S}^{\alpha\beta}(\boldsymbol{Q},\omega). \tag{7.37}$$

Here $\tilde{\chi}''_{\alpha\beta}(\boldsymbol{Q},\omega)$ and $\tilde{S}^{\alpha\beta}(\boldsymbol{Q},\omega)$ denote $\chi''_{\alpha\beta}(\boldsymbol{Q},\omega)$ and $S^{\alpha\beta}(\boldsymbol{Q},\omega)$ symmetrized with respect to $\{\alpha,\beta,\boldsymbol{Q}\} \rightarrow \{\beta,\alpha,-\boldsymbol{Q}\}$. A system with a center of inversion has symmetry with respect to $\{\boldsymbol{Q}\} \rightarrow \{-\boldsymbol{Q}\}$, in which case the tildes can be dropped for the diagonal components in $\{\alpha,\beta\}$ indices. This is the case for which the FDT is most frequently written [5]. The FDT, (7.37), is a consequence of the detailed balance condition (7.36) and the causality relations, which require that $\chi''_{\alpha\beta}(\boldsymbol{Q},\omega)$ is properly asymmetric. The fundamental laws of nature expressed in (7.36) and (7.37) are extremely useful in performing and analyzing neutron scattering experiments.

7.8.2 Elastic and Inelastic Scattering

If there exists a non-zero equilibrium magnetization in the sample, $\langle \boldsymbol{M}_{\boldsymbol{Q}}\rangle = \langle\overline{\boldsymbol{M}_{\boldsymbol{Q}}(t)}\rangle$, where the bar over $\boldsymbol{M}_{\boldsymbol{Q}}(t)$ denotes the time-averaging, we can introduce magnetization fluctuation around this equilibrium, $\boldsymbol{m}_{\boldsymbol{Q}}(t) = \boldsymbol{M}_{\boldsymbol{Q}}(t) - \langle \boldsymbol{M}_{\boldsymbol{Q}}\rangle$, and write

$$S^{\alpha\beta}(\boldsymbol{Q},\omega) = \langle M^{\alpha}_{\boldsymbol{Q}}\rangle\langle M^{\beta}_{-\boldsymbol{Q}}\rangle\delta(\hbar\omega) + S^{\alpha\beta}_{\mathrm{inel}}(\boldsymbol{Q},\omega), \tag{7.38}$$

where the inelastic component $S^{\alpha\beta}_{\mathrm{inel}}(\boldsymbol{Q},\omega)$ is defined similarly to (7.34), but with $\boldsymbol{M}_{\boldsymbol{Q}}$ replaced by $\boldsymbol{m}_{\boldsymbol{Q}}$. The first term here leads to elastic scattering which results from static magnetization in the sample, while the second term describes the inelastic magnetic scattering arising from its motion. Substituting the first term into (7.35) we obtain the unpolarized magnetic elastic cross-section,

$$\frac{d^2\sigma_{m,el}}{dEd\Omega} = \frac{r_m^2}{(2\mu_B)^2}\left|\langle M^{\perp}_{\boldsymbol{Q}}\rangle\right|^2\delta(\hbar\omega), \tag{7.39}$$

where $M^{\perp}_{\boldsymbol{Q}}$ is the Fourier transform of the magnetization component perpendicular to the wave vector transfer, $\boldsymbol{Q}$.

7.8.3 Magnetic Order and Magnetic Bragg Peaks

Equation (7.39) applies equally well to all cases where static magnetism is present in a crystal, whether it is a long-range magnetic order leading to Bragg peaks, or a short-range, e. g. nano-scale magnetic correlation, resulting in an appearance of a broad magnetic diffuse scattering. In the case of a long-range order, the magnetization density in a crystal typically has an equilibrium static component, which is modulated with a wave vector $\boldsymbol{Q}_m$,

$$\langle \boldsymbol{M}(\boldsymbol{r}) \rangle = \boldsymbol{m}_0(\boldsymbol{r}) + \boldsymbol{m}(\boldsymbol{r})\, \mathrm{e}^{i\,\boldsymbol{Q}_m \cdot \boldsymbol{r}} + \boldsymbol{m}^*(\boldsymbol{r})\, \mathrm{e}^{-i\,\boldsymbol{Q}_m \cdot \boldsymbol{r}}, \tag{7.40}$$

where $\boldsymbol{m}_0(\boldsymbol{r})$ is a real vector function that describes the ferromagnetic component, if present, while $\boldsymbol{m}(\boldsymbol{r})$ can be complex and describes the staggered magnetization. These "Bloch amplitudes" are periodic in the crystal lattice, and therefore can be expanded in the Fourier series,

$$\boldsymbol{m}(\boldsymbol{r}) = \frac{1}{V_0} \sum_{\boldsymbol{\tau}} \boldsymbol{m}_{\boldsymbol{\tau}}\, \mathrm{e}^{i\boldsymbol{\tau}\cdot\boldsymbol{r}}, \quad \boldsymbol{m}_{\boldsymbol{\tau}} = \int\limits_{V_0} \boldsymbol{m}(\boldsymbol{r})\, \mathrm{e}^{-i\boldsymbol{\tau}\cdot\boldsymbol{r}}, \tag{7.41}$$

where the integral is over the unit cell of the nuclear (paramagnetic) crystal lattice.

Substituting (7.40) and (7.41) into (7.39), we obtain the following expression for magnetic Bragg scattering associated with the long-range magnetic order at a wave vector $\boldsymbol{Q}_m$,

$$\frac{d^2\sigma_{m,B}}{dEd\Omega} = Nr_m^2 V^* \sum_{\boldsymbol{\tau}} \left(\left| \frac{\boldsymbol{m}^{\perp}_{0,\boldsymbol{\tau}}}{2\mu_B} \right|^2 \delta(\boldsymbol{Q} - \boldsymbol{\tau}) + \left| \frac{\boldsymbol{m}^{\perp}_{\boldsymbol{\tau}}}{2\mu_B} \right|^2 \left[\delta(\boldsymbol{Q} - \boldsymbol{Q}_m + \boldsymbol{\tau}) + \delta(\boldsymbol{Q} + \boldsymbol{Q}_m + \boldsymbol{\tau}) \right] \right) \delta(\hbar\omega). \tag{7.42}$$

Here the summation is over the paramagnetic crystal lattice. This is the "large Brillouin zone" description, which is the most general one, in that it does not rely on the existence of a commensurate magnetic superlattice with a unit cell containing some integer number of nuclear lattice unit cells, and applies to incommensurate, as well as commensurate magnetic structures. Such a description is most convenient for stripe phases in the cuprates, which are often incommensurate.

The intensities of magnetic satellites, $|\boldsymbol{m}^{\perp}_{\boldsymbol{\tau}}|^2$, are given by the Fourier amplitudes of the magnetization, (7.41), which are obtained by performing the Fourier integrals over the unit cell of the paramagnetic lattice. In the case where the unit cell magnetization could be approximated by a number of point-like magnetic dipoles $\boldsymbol{\mu}_\nu$ located at positions $\boldsymbol{r}_\nu$, these amplitudes become the conventional unit cell magnetic structure factors,

$$\boldsymbol{m}(\boldsymbol{r}) = \sum_{j,\nu} \boldsymbol{\mu}_\nu\, \delta\left(\boldsymbol{r} - \boldsymbol{R}_j - \boldsymbol{r}_\nu\right), \quad \left|\boldsymbol{m}^{\perp}_{\boldsymbol{\tau}}\right|^2 = \left| \sum_{\nu} \boldsymbol{\mu}^{\perp}_{\nu} \mathrm{e}^{-i\boldsymbol{\tau}\cdot\boldsymbol{r}_\nu} \right|^2. \tag{7.43}$$

In discussing magnetic scattering we assume a rigid lattice, neglecting atomic displacements due to disorder and vibrations discussed above. The leading correction to this description is obtained by multiplying expressions for magnetic cross-section with the Debye-Waller factor, e^{-2W}.

7.8.4 Magnetic Form Factor and Spin Correlations

In many important cases the magnetization density in the crystal is carried by electrons localized on atomic-like orbitals, which are specified by the local atomic variables, such as spin and orbital quantum numbers. In such cases, the matrix element of the atomic magnetization in the magnetic neutron scattering cross-section can be factorized into the product of the reduced matrix element (form factor), which does not depend on the direction of the atom's angular momentum quantum numbers, and the Wigner 3j-symbol, which entirely accounts for such dependence. Hence, the cross-section can be expressed in terms of a product of the $\boldsymbol{Q}$-dependent form factor, which accounts for the shape of the magnetization cloud associated with the atomic spin and orbital variables, and a dynamical correlation function between these local angular momentum variables at different lattice sites.

For magnetic ions obeying Hund's rule, neutron scattering usually probes states belonging to the same multiplets of the angular momentum, $\Delta L = 0$, $\Delta S = 0$ for the Russel-Saunders atoms with weak spin-orbit and strong crystal field, or $\Delta J = 0$ for the case of strong spin-orbit coupling, where the total angular momentum $\boldsymbol{J} = \boldsymbol{L}+\boldsymbol{S}$ is a good quantum number, such as in rare earths. Hence, we can write for the Fourier transform of atomic magnetization,

$$\langle \eta_f | \boldsymbol{M}(\boldsymbol{Q}) | \eta_i \rangle = -2\mu_B F_S(\boldsymbol{Q}) \langle \eta_f | \boldsymbol{S} | \eta_i \rangle - \mu_B F_L(\boldsymbol{Q}) \langle \eta_f | \boldsymbol{L} | \eta_i \rangle, \tag{7.44}$$

where the spin and the orbital magnetic form factors are,

$$F_S(\boldsymbol{Q}) = \frac{\langle \eta'_f, L, S | \sum_e \mathrm{e}^{-i\,\boldsymbol{Q}\cdot\boldsymbol{r}_e} \, (\boldsymbol{s}_e \cdot \boldsymbol{S}) \, | \eta'_i, L, S \rangle}{S(S+1)}, \tag{7.45}$$

$$F_L(\boldsymbol{Q}) = \frac{\langle \eta'_f, L, S | \sum_e \mathrm{e}^{-i\,\boldsymbol{Q}\cdot\boldsymbol{r}_e} \left(\boldsymbol{\mu}_{e,l} \cdot \boldsymbol{L}\right) | \eta'_i, L, S \rangle}{\mu_B L(L+1)}, \tag{7.46}$$

where we made explicit that initial and final states of the sample belong to the same L and S multiplet. Similar relations hold for the J multiplet in the strong spin-orbit coupling limit.

Typically it is possible to define an effective spin operator,

$$\langle \eta_f | \boldsymbol{M}(\boldsymbol{Q}) | \eta_i \rangle = -g\mu_B F(\boldsymbol{Q}) \langle \eta_f | \tilde{\boldsymbol{S}} | \eta_i \rangle, \tag{7.47}$$

$$F(\boldsymbol{Q}) = \frac{\langle \eta'_f, L, S | \left(\boldsymbol{M}(\boldsymbol{Q}) \cdot \tilde{\boldsymbol{S}}\right) | \eta'_i, L, S \rangle}{g\mu_B \tilde{S}(\tilde{S}+1)} = \frac{g_S}{g} F_S(\boldsymbol{Q}) + \frac{g-g_S}{g} F_L(\boldsymbol{Q}). \tag{7.48}$$

where g and g_S are the effective $g-$factors, $\langle \eta_f | \boldsymbol{L} + 2\boldsymbol{S} | \eta_i \rangle = g \langle \eta_f | \tilde{\boldsymbol{S}} | \eta_i \rangle$, $\langle \eta_f | 2\boldsymbol{S} | \eta_i \rangle = g_S \langle \eta_f | \tilde{\boldsymbol{S}} | \eta_i \rangle$. These expressions are exact in the cases of a J-multiplet, where $\tilde{\boldsymbol{S}} = \boldsymbol{J}$, $g_S = 2(g-1)$ and $g_L = 2-g$, or a pure spin multiplet, where $g = g_S$

and the orbital contribution is absent. They give the leading-order approximation in other cases. If the orbital moment is nearly quenched, as it is for magnetic d-elements in strong crystal field, then $\tilde{\boldsymbol{S}} \approx \boldsymbol{S}$, $g_S \approx 2$, and the orbital contribution to $F(\boldsymbol{Q})$, is small. Assuming this to be the case, we shall omit tildes and use $\boldsymbol{S}$ for the effective spin.

Using the factorization of atomic magnetization provided by (7.47) and (7.48), the magnetic neutron scattering cross-section (7.33) can be recast as

$$\frac{d^2\sigma_m}{dEd\Omega} = \frac{\kappa_f}{\kappa_i} r_m^2 \sum_{\alpha,\beta} \left(\delta_{\alpha\beta} - \frac{Q_\alpha Q_\beta}{Q^2}\right) \sum_{j,j'} g_{\alpha,j} \frac{F_j^*(\boldsymbol{Q})}{2} g_{\beta,j'} \frac{F_{j'}(\boldsymbol{Q})}{2} \times \int_{-\infty}^{\infty} \mathrm{e}^{-i\omega t} \mathrm{e}^{-i\boldsymbol{Q}\cdot(\boldsymbol{R}_j - \boldsymbol{R}_{j'})} \langle S_j^\alpha S_{j'}^\beta(t)\rangle \frac{dt}{2\pi\hbar}, \tag{7.49}$$

where we allow for the possibility that the $g-$factor is anisotropic, and that both $g_{\alpha,j}$ and $F_j(\boldsymbol{Q})$ could be different for different sites j, j' of the lattice. Equation (7.49) relates the magnetic cross-section to the dynamic spin structure factor, which is the Fourier transform of the time-dependent two-point correlation function of the atomic spin variables on the sites of the lattice,

$$S^{\alpha\beta}(\boldsymbol{Q},\omega) = \int_{-\infty}^{\infty} \mathrm{e}^{-i\omega t} \frac{1}{N} \sum_{j,j'} \mathrm{e}^{-i\boldsymbol{Q}(\boldsymbol{R}_j - \boldsymbol{R}_{j'})} \langle S_j^\alpha S_{j'}^\beta(t)\rangle \frac{dt}{2\pi\hbar}. \tag{7.50}$$

$S^{\alpha\beta}(\boldsymbol{Q},\omega)$ is a quantity which is calculated in theoretical models based on the local spin Hamiltonians. It also obeys a number of important relations, known as sum rules, which are extremely useful in analyzing neutron scattering data. The zero moment sum rule is obtained by integrating (7.50) in $\boldsymbol{Q}$ and ω, providing the direct connection of the integral neutron intensity with the spin value S in the lattice spin Hamiltonian,

$$\sum_{\alpha} \int_{-\infty}^{\infty} S^{\alpha\alpha}(\boldsymbol{Q},\omega) d^3\boldsymbol{q} d(\hbar\omega) = S(S+1). \tag{7.51}$$

The first moment sum rule relates $\sum_\alpha \int_{-\infty}^{\infty} \hbar\omega S^{\alpha\alpha}(\boldsymbol{Q},\omega) d^3\boldsymbol{q} d(\hbar\omega)$, which is the integral oscillator strength of the fluctuation spectrum, with the bond energies in the spin Hamiltonian, and so on.

7.8.5 Spin Waves

Representing the neutron scattering cross-section via two-point dynamical spin correlation function, as in (7.49), is possible in a large number of important magnetic systems, such as cuprates and other $3d$ magnetic insulators. Such a representation is extremely useful, as it allows one to connect the measured magnetic neutron intensity with the theoretically predicted properties of model spin Hamiltonians, such as the Heisenberg spin Hamiltonian,

$$\hat{\mathcal{H}} = \sum_{j,j'} J_{jj'} \boldsymbol{S}_j \boldsymbol{S}_{j'} = \sum_{\boldsymbol{q}} N J_{\boldsymbol{q}} \boldsymbol{S}_{\boldsymbol{q}} \boldsymbol{S}_{-\boldsymbol{q}}. \tag{7.52}$$

Here $J_{jj'} = J(\boldsymbol{r}_{jj'})$ is the exchange coupling between sites j and j', and $J_{\boldsymbol{q}}$ and $\boldsymbol{S}_{\boldsymbol{q}}$ are the lattice Fourier transforms,

$$J_{\boldsymbol{q}} = \sum_{\boldsymbol{r}_{jj'}} J_{jj'} \mathrm{e}^{-i\boldsymbol{q}\cdot\boldsymbol{r}_{jj'}}, \quad \boldsymbol{S}_{\boldsymbol{q}} = \sum_{j} \boldsymbol{S}_j \mathrm{e}^{-i\boldsymbol{q}\cdot\boldsymbol{r}_j}. \tag{7.53}$$

In many systems with magnetic order, the average value of spin at each lattice site in the ground state (GS) is "frozen" at nearly the full saturation value, $\langle S_j^z \rangle \approx S$. In particular, this is a very good approximation for the semi-classical spins, $S \gg 1$, in more than one dimension (1D). For quantum spins, $S = 1/2$, and/or in the low-dimensional, or frustrated systems, the order may be weak, or absent, and such a picture is inadequate. Nevertheless, in a large number of systems magnetic order in the ground state is well developed, and the semiclassical spin-wave picture applies.

Spin excitations in a magnetic system with a well-ordered ground state, such as a ferromagnet, where all spins are parallel, or a semi-classical antiferromagnet, where there are two antiparallel sublattices, can be visualized as small oscillations of classical spin vectors around their equilibrium positions in the GS spin structure. Their wave-like spatial composition results from the translational symmetry of the system. Frequencies of such spin-wave oscillations can be calculated from the spin Hamiltonian, such as (7.52), totally within the classical mechanics, simply by writing the torque equations of motion for the classical spin angular momenta. For example, in the case of the Heisenberg Hamiltonian (7.52) for a magnetically ordered system characterized by the ordering wave vector $\boldsymbol{Q}_0$ (this includes ferromagnetism with $\boldsymbol{Q}_0 = 0$, as well as antiferromagnetism and helimagnetism), one obtains the spin-wave dispersion [26, 27],

$$\hbar\omega_{\boldsymbol{q}} = 2S\sqrt{\left(J_{\boldsymbol{q}} - J_{\boldsymbol{Q}_0}\right)\left(\frac{J_{\boldsymbol{q}+\boldsymbol{Q}_0} + J_{\boldsymbol{q}-\boldsymbol{Q}_0}}{2} - J_{\boldsymbol{Q}_0}\right)}. \tag{7.54}$$

This can be recast as $\omega_{\boldsymbol{q}} = \sqrt{\omega_{\boldsymbol{0}}\omega_{\boldsymbol{Q}_0}}$, where $\hbar\omega_{\boldsymbol{0}} = 2S(J_{\boldsymbol{q}} - J_{\boldsymbol{Q}_0})$.

Spin waves are the normal modes of the linearized equations of motion. They involve small spin deviations that are perpendicular to the equilibrium spin direction.

Hence, spin waves are transversely polarized, with two mutually orthogonal linear polarizations of spin oscillations possible. For a spin system on a Bravais lattice there are two spin-wave modes.

In a quantum-mechanical treatment of spins, the spin-wave calculation proceeds via an approximate mapping of spin operators to Bose creation-annihilation operators, i.e. to local oscillator modes. Hence, the so obtained spin-wave theory (SWT) describes spin excitations as coherent waves of small oscillations around the local equilibrium positions, in many ways similar to phonons. The resulting expression for the spin-wave contribution to the neutron magnetic scattering cross-section in a sample with a spiral spin structure with the propagation vector $\boldsymbol{Q}_0$ is

$$\begin{aligned}\frac{d^2\sigma_{sw}}{dEd\Omega} = &\frac{\kappa_f}{\kappa_i} r_m^2 N \left|\frac{g}{2} F(\boldsymbol{Q})\right|^2 \frac{S}{2} V^* \sum_{\boldsymbol{\tau}} (n(\omega)+1)\delta(\hbar\omega - \hbar\omega_{\boldsymbol{q}}) \\ &\times \left[\frac{1}{4}\left(1+\frac{Q_z^2}{Q^2}\right)\sqrt{\frac{\omega_{\boldsymbol{0}}}{\omega_{\boldsymbol{Q}_0}}}\left(\delta(\boldsymbol{Q}-\boldsymbol{q}-\boldsymbol{\tau}-\boldsymbol{Q}_0)+\delta(\boldsymbol{Q}-\boldsymbol{q}-\boldsymbol{\tau}+\boldsymbol{Q}_0)\right)\right. \\ &\left. + \left(1-\frac{Q_z^2}{Q^2}\right)\sqrt{\frac{\omega_{\boldsymbol{Q}_0}}{\omega_{\boldsymbol{0}}}}\delta(\boldsymbol{Q}-\boldsymbol{q}-\boldsymbol{\tau})\right], \end{aligned} \tag{7.55}$$

where z is the direction normal to the plane of the spiral, and we have restricted consideration to the case of a Bravais lattice and retained only the contribution corresponding to creation of a single spin wave. The contribution arising from the absorption of a spin wave is written similarly to that of a phonon in (7.29). For a ferromagnet, the single spin-wave magnetic cross-section simplifies to [2, 3],

$$\begin{aligned}\frac{d^2\sigma_{sw}}{dEd\Omega} = &\frac{\kappa_f}{\kappa_i} r_m^2 N \left|\frac{g}{2} F(\boldsymbol{Q})\right|^2 \frac{S}{2}\left(1+\frac{Q_\parallel^2}{Q^2}\right) \\ &\times V^* \sum_{\boldsymbol{\tau}} \Big[\, \delta(\boldsymbol{Q}-\boldsymbol{q}-\boldsymbol{\tau})\delta(\hbar\omega - \hbar\omega_{\boldsymbol{q}})(n(\omega)+1) \\ &\qquad + \delta(\boldsymbol{Q}+\boldsymbol{q}-\boldsymbol{\tau})\delta(\hbar\omega + \hbar\omega_{\boldsymbol{q}})n(\omega)\,\Big], \end{aligned} \tag{7.56}$$

where $\boldsymbol{Q}_\parallel$ is the wave vector component along the ferromagnetic ordered moment and we have retained the contributions from both the creation and the absorption of a spin wave.

7.8.6 Anisotropic Magnetic Form Factor and Covalency

It is clear from (7.49) that even the exact knowledge of the dynamical spin structure factor (available from theory in some special cases, such as in one dimension) is insufficient to reproduce the measured magnetic scattering cross-section. One also

has to know the magnetic form factor, which needs to be obtained from an ab initio calculation of the electronic density in the crystal.

In the most common case of a Hund's ion with $2S$ unpaired electrons forming spin $(2S+1)$-multiplet, the spin magnetic form factor (7.45) becomes

$$F_S(\boldsymbol{Q}) = \frac{1}{2S}\sum_{e=1}^{2S}\int \mathrm{e}^{-i\,\boldsymbol{Q}\cdot\boldsymbol{r}}\,|\psi_e(\boldsymbol{r})|^2\,d^3\boldsymbol{r} = \frac{1}{2S}\sum_{e=1}^{2S} F_{S,e}(\boldsymbol{Q}), \tag{7.57}$$

where the sum is only over the unpaired electrons. The single-electron density, $|\psi_e(\boldsymbol{r})|^2$, is determined from the many-electron atomic wave function through $|\psi_e(\boldsymbol{r})|^2 = \langle \eta', L, S|\delta(\boldsymbol{r}-\boldsymbol{r}_e)|\eta', L, S\rangle$. The magnetic form factor for an atom is therefore simply an average of those for each of the unpaired electrons. Similarly, the orbital form factor is the Fourier-transformed average density of the uncompensated orbital currents in the atom.

If the average Hartree-Fock potential acting on an unpaired electron e in the atom is spherically symmetric, then the effective one-electron wave functions in (7.57) are the eigenfunctions of angular momentum and are tagged by the $n, l, m = l^z$ quantum numbers, $\psi_e(\boldsymbol{r}) = \psi_{n,l,m}(\boldsymbol{r})$. The angular and the radial dependencies of the electronic density factorize, $\psi_{n,l,m}(\boldsymbol{r}) = R_{n,l}(r)Y_l^m(\theta,\phi)$, where $Y_l^m(\theta,\phi)$ is the spherical function giving the dependence on the polar angles θ, ϕ. This so-called central field approximation is good when the contribution to the potential from electrons in the incomplete shell is small. However, it also becomes exact for an almost-filled shell, with only a single electron, or a single hole, as in the case of Cu^{2+}, or for a nearly half-filled shell, because the average potential of the closed, or half-filled shell, is spherically symmetric.

In the general case, a single-electron wave function can always be expanded in a series in spherical harmonics. In each term of such an expansion, the radial and the angular parts are again factorized, and the magnetic form factor is a sum of Fourier-transformed terms with different l and m. The same kind of an expansion is encountered in calculating the orbital contribution to the magnetic form factor. This is known as a multipole expansion [3]. The calculations are ion-specific and extremely cumbersome. The general expressions can be obtained only for the leading, isotropic contributions, in the limit of small wave vector transfer, known as the dipole approximation,

$$F_S(\boldsymbol{Q}) = \langle j_0(Q)\rangle \quad F_L(\boldsymbol{Q}) = \frac{1}{2}\left(\langle j_0(Q)\rangle + \langle j_2(Q)\rangle\right), \tag{7.58}$$

where $j_0(Q)$ and $j_2(Q)$ are the l, m dependent radial integrals quantifying the radial wave function [5, 18]. The radial integrals for most known magnetic atoms and ions have been calculated numerically from the appropriate Hartree-Fock or Fock-Dirac wave functions and are tabulated in [18]. The full $F(\boldsymbol{Q})$ is given by (7.48).

Although the dipole approximation (7.58) is the one most commonly used, it is extremely crude. In particular, it does not account for the anisotropy of the magnetic

form factors, which can be very important for ions with only one or two unpaired electrons. The anisotropic magnetic form factor of a single $5d$ hole in a t_{2g} orbital of the magnetic Ir^{4+} ion in the cubic K_2IrCl_6 was studied in [28]. The authors found that the anisotropy of the magnetic form factor is very large, with an additional enhancement coming from the hybridization of the Ir $5d$-orbital with the Cl p-orbitals.

The anisotropy of the magnetic form factor is also very pronounced in La_2CuO_4, $YBa_2Cu_3O_{6+y}$, and related cuprate materials, including the high-T_c superconductors, where in the ionic picture a single unpaired magnetic electron occupies a $3d_{x^2-y^2}$ orbital. In [29] the authors found that properly accounting for the anisotropy of the Cu^{2+} magnetic form factor is essential for understanding the magnetic Bragg intensities measured in $YBa_2Cu_3O_{6+y}$ at large wave vectors, and can also explain the peculiar $\boldsymbol{Q}$-dependence of the inelastic magnetic cross-section in this material. Accounting for the anisotropic Cu^{2+} form factor was also very important in analyzing neutron scattering by high-energy spin waves in La_2CuO_4 [30, 31], and the chain cuprates $SrCuO_2$ and Sr_2CuO_3 [32, 33]. The magnetic excitations in these cuprate materials extend to several hundreds of meV. Consequently, the measurements require very large wave vector transfers, for which the anisotropy of the magnetic form factor is very pronounced.

The ionic magnetic form factors for $3d$ orbitals can be explicitly computed by Fourier transforming the corresponding spherical harmonics. In particular, for the $d_{x^2-y^2}$ orbital relevant for Cu^{2+} one obtains [5],

$$\begin{aligned} F(\boldsymbol{Q}) = \langle j_0(Q)\rangle - \frac{5}{7}\langle j_2(Q)\rangle \left(1-\cos^2\theta_{\boldsymbol{Q}}\right) \\ + \frac{9}{56}\langle j_4(Q)\rangle \left(1 - 10\cos^2\theta_{\boldsymbol{Q}} + \frac{35}{3}\cos^4\theta_{\boldsymbol{Q}}\right) \\ + \frac{15}{8}\langle j_4(Q)\rangle \sin^4\theta_{\boldsymbol{Q}}\cos\left(4\phi_{\boldsymbol{Q}}\right), \end{aligned} \tag{7.59}$$

where $\theta_{\boldsymbol{Q}}, \phi_{\boldsymbol{Q}}$ are the polar angles of the wave vector $\boldsymbol{Q}$ in the local coordinate system used to specify the proper orbital wave functions in the crystal field.

Although using the anisotropic ionic magnetic form factor of Cu^{2+} is much better than using a spherical form factor of the dipole approximation, it is still not sufficient for cuprates, as it neglects the effects of covalency (i.e. charge transfer to the neighboring oxygen) that are expected to be very significant in these materials. In [33] it was discovered that covalent bonding results in a marked modification of the magnetic form factor in the quasi-1D antiferromagnet Sr_2CuO_3. The local structure of the planar Cu–O square plaquettes in this material is essentially identical to that in La_2CuO_4. Making use of a precise theoretical result for the excitation spectrum available in 1D, the authors demonstrated that a good fit to the data requires a form factor that takes account of hybridization between the half-filled Cu $3d_{x^2-y^2}$ orbital and the ligand O $2p_\sigma$ orbitals, as given by a density functional calculation. The hybridization causes the spin density to be extended in real space, resulting in a more

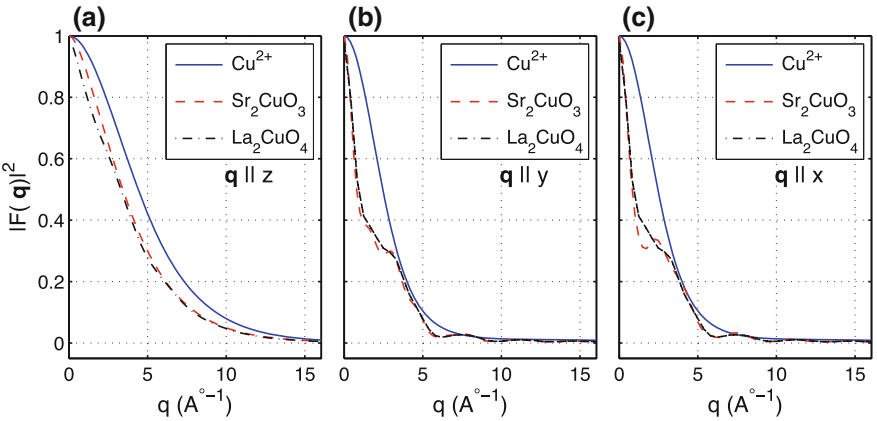

Fig. 7.3 Wave vector dependence of the ionic magnetic form factor of Cu^{2+} given by (7.59) (*solid line*) and the covalent magnetic form factors for Sr_2CuO_3 (*dashed line*) and La_2CuO_4 (*dash-dotted line*) obtained from the ab initio density functional calculations [33]. Panels (**a**–**c**) show the dependence along three principal directions

rapid fall off in reciprocal space compared to a simple Cu^{2+} form factor, as illustrated in Fig. 7.3. Smaller values of magnetic form factor at relatively large wave vectors, where the measurement is performed, lead to the suppression of magnetic intensity, which could be as large as a factor of two or more [33]. Finally, we note that a study of covalent NMR shifts by Walstedt and Cheong [34] found that barely 2/3 of the spin density in La_2CuO_4 resides on the copper sites, in excellent agreement with the Sr_2CuO_3 neutron data of Walters et al. [33].

7.9 Application to Cuprate Superconductors

The discovery of high-temperature superconductivity in $La_{2-x}Ba_xCuO_4$ (LBCO) came as a considerable surprise [35], as ceramic oxides were generally considered to be poor conductors. The structure of LBCO and related cuprates involves CuO_2 layers, with the Cu atoms forming a square lattice with bridging O atoms, as shown in Fig. 7.4a. Anderson [36] predicted that the parent compound, La_2CuO_4, should have strong antiferromagnetic (AF) superexchange interactions between nearest-neighbor Cu atoms. The occurrence of antiferromagnetic order was demonstrated by Vaknin et al. [37] using neutron diffraction on a powder sample of La_2CuO_4. As illustrated in Fig. 7.4b, the antiferromagnetic Néel order doubles the size of the unit cell in real space, which results in magnetic superlattice peaks, as shown in (c). Thus, the antiferromagnetic order can be detected through the appearance of superlattice peaks. The challenge in this case is that one must distinguish from structural superlattice

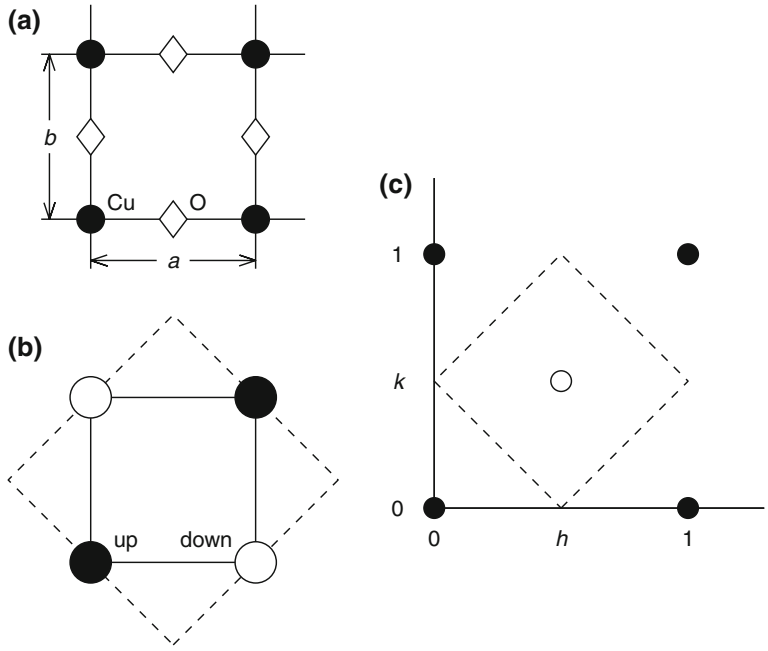

Fig. 7.4 **a** Structure of a CuO_2 plane, with Cu atoms indicated by *filled circles* and O atoms by *open diamonds*. **b** Schematic of antiferromagnetic order, with alternating up (*filled circles*) and down (*open circles*) spins. The *solid line* indicates the chemical unit cell, while the *dashed line* indicates the doubled area of the antiferromagnetic unit cell. **c** *Reciprocal space* showing fundamental Bragg peak positions (*filled circles*) and antiferromagnetic superlattice peak (*open circle*) at $(\frac{1}{2}, \frac{1}{2})$

peaks due to staggered rotations of CuO_6 octahedra [38]. Fortunately, the AF and structural peaks appear at inequivalent positions.

The ordered pattern of the octahedral tilts is associated with an orthorhombic distortion of the crystal structure that makes the diagonal directions of a Cu-O plaquette inequivalent [38], as indicated in Fig. 7.5. By analyzing the $\boldsymbol{Q}$ dependence of the AF Bragg peak intensities, it was possible to determine that the magnetic moments on Cu atoms lie within the CuO_2 planes, pointing along the orthorhombic b axis [37]. Furthermore, it was possible to show that the relative arrangement in neighboring planes is as shown in Fig. 7.5. With the magnetic structure determined, one can evaluate the magnitude of the magnetic moments by normalizing the AF peak intensities to the nuclear intensities and correcting for the magnetic form factor. Early studies yielded a small ordered moment whose magnitude was correlated with the magnetic ordering, or Néel, temperature, T_N [39]. Neutron scattering studies on carefully prepared single-crystal samples eventually demonstrated the impact of interstitial oxygen, within the La_2O_2 layers [40]. Removing the excess oxygen by annealing, one can achieve $T_N = 325\,K$ [41] and a magnetic moment of $0.60 \pm 0.05\ \mu_B$ [39].

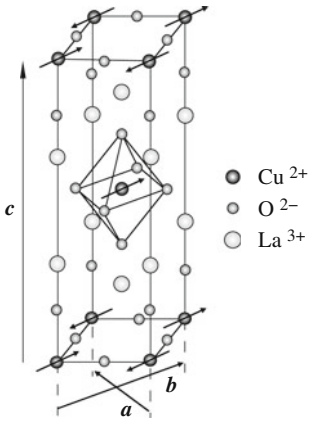

Fig. 7.5 Structure of La_2CuO_4, with arrows indicating the arrangement of the magnetic moments in the antiferromagnetic state. Figure reprinted with permission from Lee et al. [42]. Copyright (1999) by the American Physical Society

If one assumes a g factor of roughly 2, then the ordered moment yields an average ordered spin $\langle S \rangle \approx 0.3$, compared to the expected $S = \frac{1}{2}$ per Cu atom. The reduction results from the strongly anisotropic structure and the low value of the spin. For a two-dimensional magnetic system described by a Heisenberg spin Hamiltonian, long-range order is destroyed at any finite temperature by thermal excitation of spin fluctuations. For La_2CuO_4, weak (nearly-frustrated) couplings between the planes enable the ordering at finite temperature [43]. Nevertheless, the spin correlations have a strongly two-dimensional (2D) character, as demonstrated by neutron scattering studies [44]. The small magnitude of the spin, combined with the enhanced zero-point spin fluctuations in 2D, puts the system close to a quantum critical point [45]. Although the large fluctuations cause problems for perturbation theory, spin-wave theory nonetheless yields a result, $\langle S \rangle = 0.3$, that is very close to the value obtained from experiment [46].

The exchange couplings between the spins can be determined by analyzing the dispersion of the spin excitations, which can be obtained by inelastic scattering measurements on a single-crystal sample. Early studies of La_2CuO_4 with triple-axis spectrometers demonstrated that the superexchange energy J coupling nearest-neighbor spins is greater than 100 meV, and that effects such as exchange anisotropy and interlayer coupling are very small [43]. Time-of-flight techniques were required to measure the highest-energy spin waves [47], and these have been refined over time [30, 31]. The most recent results, from Headings et al. [31], are shown in Fig. 7.6. The line through the data points corresponds to a fit with linear spin-wave theory, which works surprisingly well in light of the large zero-point fluctuations. One impact of the latter is the renormalization factor, with a fitted value of $Z_d = 0.4 \pm 0.04$, that is required to fit the measured intensity. This is somewhat smaller than the value $Z_d \approx 0.6$ that is predicted from quantum corrections to linear spin waves [48]. It should be noted, though, that this analysis did not take account of the hybridization effects on the magnetic form factor, discussed in Sect. 7.8.4, which would account for some of the apparent renormalization. An additional effect is the

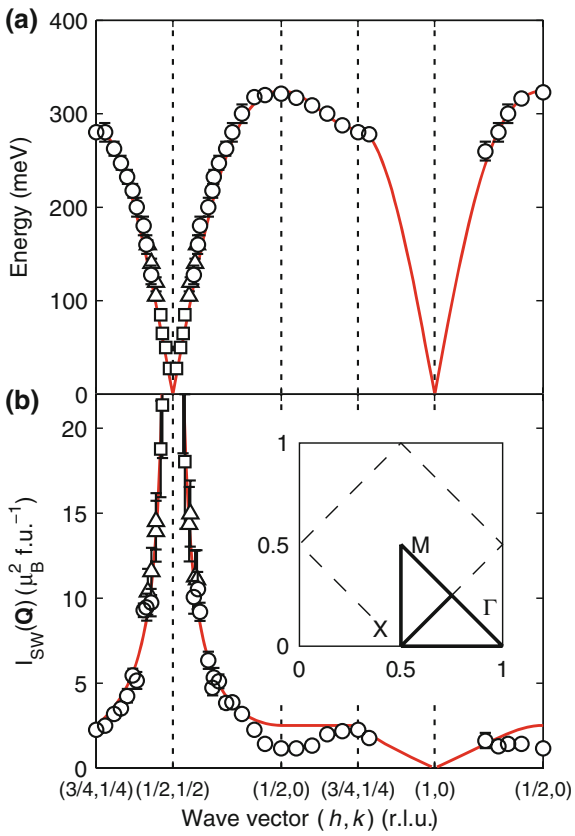

Fig. 7.6 Spin wave **a** dispersion and **b** intensity measured in antiferro magnetic La_2CuO_4 at $T = 10\,\mathrm{K}$. Lines through data correspond to fits with spin-wave theory; the fit to the intensity includes a renormalization factor $Z_d = 0.4 \pm 0.04$. Figure reprinted with permission from Headings et al. [31]. Copyright (2010) by the American Physical Society

damping and broadening of the energy-dependence of the spin-wave line shape at the zone boundary position $\boldsymbol{Q} = (\frac{1}{2}, 0)$. This appears to be the result of interactions with a multi-magnon high-energy continuum [31].

The fitted dispersion corresponds to $J = 143 \pm 2\,\mathrm{meV}$, but also requires longer-range exchange couplings—second and third neighbor couplings J' and J'', which are relatively weak, and a significant 4-spin cyclic exchange term $J_c \approx 0.4\,\mathrm{J}$. The overall bandwidth of the magnetic spectrum is $\sim 2\,\mathrm{J}$. A recent analysis of the couplings, including J_c, in terms of a single-band Hubbard model has been given by Dalla Piazza et al. [49].

To achieve superconductivity, one must dope charge carriers into the CuO_2 planes. Substituting Ba^{2+} or Sr^{2+} for La^{3+} introduces holes. A small density of holes, $p \approx 2\,\%$, is enough to kill the long-range AF order, which is followed by a regime of spin-glass order [7]. Doping beyond $p \sim 0.055$ yields superconductivity. The maximum superconducting transition temperature T_c occurs for $p \sim 0.16$, with T_c heading towards zero for $p > 0.25$. Inelastic neutron scattering studies have been performed on single crystal samples across this entire doping range [7, 9].

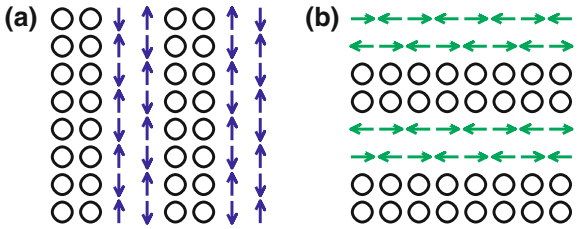

Fig. 7.7 Cartoons of equivalent domains of **a** vertical and **b** horizontal bond-centered stripe order within a CuO_2 plane (only Cu sites shown). Note that the magnetic period is twice that of the charge period. The charge density along a stripe is one hole for every two sites in length. The registry of the stripes with respect to the lattice (for example, site-centered versus bond-centered) has not yet been determined experimentally

A couple of the key features are: (1) the bandwidth of strong spin-fluctuation scattering decreases linearly with doping, being quantitatively similar to the pseudogap energy extracted from various electron spectroscopies [9, 50], and (2) the wave vector characterizing the low-energy spin excitations splits about the AF wave vector, becoming incommensurate [7, 51].

Insight into the cause of the magnetic incommensurability was provided by neutron diffraction measurements on a closely related material, $La_{1.48}Nd_{0.4}Sr_{0.12}CuO_4$ [52]. The impact of the Nd substitution is to modify the tilt pattern of the CuO_6 octahedra such that the in-plane Cu-O bond directions become inequivalent [38]. New superlattice peaks were observed in this low-temperature phase, with in-plane wave vectors $\boldsymbol{Q} = (\frac{1}{2} \pm \epsilon, \frac{1}{2})$ and $(\frac{1}{2}, \frac{1}{2} \pm \epsilon)$ corresponding to spin order and $(\pm 2\epsilon, 0)$ and $(0, \pm 2\epsilon)$ associated with modulations of atomic positions due to charge order, with $\epsilon \approx 0.12$. Such results have been confirmed in the system $La_{2-x}Ba_xCuO_4$ [53, 54]. Analysis of the superlattice peaks indicates that they are evidence for spin and charge stripe order [55, 56], as illustrated in Fig. 7.7. Because of the crystal symmetry, the orientation of the stripes rotates 90° from one layer to the next.

The occurrence of maximum stripe order corresponds to a strong suppression of the bulk T_c at $p \approx \frac{1}{8}$ [54, 57], suggesting that stripe order competes with superconductivity; however, recent studies have demonstrated that 2D superconductivity can coexist with stripe order [58]. It now appears that superconducting order can intertwine with stripe order [59]. Thus, understanding stripe correlations may provide valuable insights into the nature of the superconducting mechanism of cuprates.

Neutron scattering on a time-of-flight instrument has been used to characterize the spin excitation spectrum in $La_{2-x}Ba_xCuO_4$ with $x = 1/8$ [60]. The effective dispersion and the $\boldsymbol{Q}$-integrated spectral weight are shown in Fig. 7.8. Above 50 meV, the excitations disperse upwards like antiferromagnetic spin waves with an energy gap; the solid line through the points in each panel corresponds to a two-leg spin ladder model with $J = 100$ meV. Below 50 meV, the excitations disperse downwards toward the positions of the incommensurate magnetic superlattice peaks. When the sample is warmed to a state with no static stripe order, the spectrum maintains its essential features [53, 61]. It appears that stripes, whether static or dynamic, provide

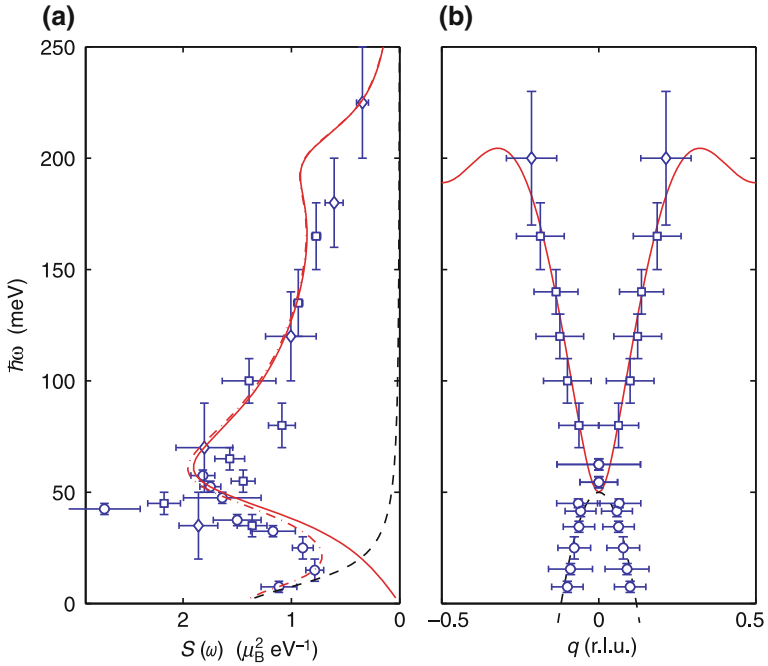

Fig. 7.8 **a** $\boldsymbol{Q}$-integrated spectral weight and **b** effective magnetic dispersion in the stripe-ordered phase of $La_{2-x}Ba_xCuO_4$ with $x = 1/8$, from [60]. The *solid lines* through the data points are described in the text. In **a**, the peak at ∼40 meV is now know to be due to a phonon mode. In **b**, the effective dispersion is plotted for $\boldsymbol{q}$ along a line through the incommensurate magnetic superlattice peaks

a way for the superexchange mechanism to survive when the antiferromagnetic layers are doped with holes.++

The relevance of charge-stripe order is less clear in cuprates families such as $YBa_2Cu_3O_{6+y}$ and $Bi_2Sr_2CaCu_2O_{8+\delta}$; nevertheless, the dispersion of the magnetic excitations in these compounds (measured by neutron scattering) has been shown to be quite similar to that of LBCO [8, 9]. The main difference is that the low-energy excitations tend to be gapped in the superconducting state, with a pile up of weight ("resonance" peak) appearing above the gap for $T < T_c$. The commonality of the dispersions over a broad energy range suggests that the charge and spin correlations in superconducting and striped cuprates are similar.

References

1. C.G. Shull, J.S. Smart, Phys. Rev. **76**, 1256 (1949)
2. G.L. Squires, *Introduction to the Theory of Thermal Neutron Scattering*, 3rd edn. (Cambridge University Press, Cambridge, 2012)
3. S.W. Lovesey, *Theory of Neutron Scattering from Condensed Matter* (Oxford University Press, Oxford, 1984)
4. G. Shirane, S.M. Shapiro, J.M. Tranquada, *Neutron Scattering with a Triple-Axis Spectrometer: Basic Techniques* (Cambridge University Press, Cambridge, 2002)
5. I.A. Zaliznyak, S.H. Lee, in *Magnetic Neutron Scattering*, ed. by Y. Zhu. Modern Techniques for Characterizing Magnetic Materials (Springer, Heidelberg, 2005)
6. I.A. Zaliznyak, in *Handbook for Magnetism and Advanced Magnetic Materials*, ed. by H. Kronmuller, S. Parkin (Wiley, UK, 2007)
7. R.J. Birgeneau, C. Stock, J.M. Tranquada, K. Yamada, J. Phys. Soc. Jpn. **75**, 111003 (2006)
8. J.M. Tranquada, in *Theory and Experiment*, ed. by J.R. Schrieffer, J.S. Brooks. Handbook of High-Temperature Superconductivity (Springer, New York, 2007), pp. 257–298
9. M. Fujita, H. Hiraka, M. Matsuda, M. Matsuura, J.M. Tranquada, S. Wakimoto, G. Xu, K. Yamada, J. Phys. Soc. Jpn. **81**, 011007 (2012)
10. P. Bourges, Y. Sidis, C. R. Phys. **12**, 461 (2011)
11. P.J. Mohr, B.N. Taylor, D.B. Newell. CODATA Recommended Values of the Fundamental Physical Constants: 2010. arXiv:1203.5425
12. F.E. Wietfeldt, G.L. Greene, Rev. Mod. Phys. **83**, 1173 (2011)
13. V.F. Sears, *Neutron Optics* (Oxford University Press, Oxford, 1989)
14. Y.A. Izyumov, R.P. Ozerov, *Magnetic Neutron Diffraction* (Plenum Press, New York, 1970)
15. J. Jensen, A.R. Mackintosh, *Rare Earth Magnetism* (Clarendon Press, Oxford, 1991)
16. E. Fermi, L. Marshall, Phys. Rev. **71**, 666 (1947)
17. E. Fermi, L. Marshall, Phys. Rev. **72**, 408 (1947)
18. A.J.C. Wilson (ed.), *International Tables for Crystallography*, vol. C (Kluwer Academic Publishers, Dordrecht, 1995)
19. V.F. Sears, Neutron News 3(3), 26 (1992). http://www.ncnr.nist.gov/resources/n-lengths/
20. S.F. Mughabghab, *Atlas of Neutron Resonances*, 5th edn. (Elsevier Science, Amsterdam, 2006)
21. E. Fermi, Ric. Sci. **7**, 13 (1936)
22. B.A. Lippmann, J. Schwinger, Phys. Rev. **79**, 469 (1950)
23. L. Van Hove, Phys. Rev. **95**, 1374 (1954)
24. M. Blume, Phys. Rev. **124**, 96 (1961)
25. R.J. Donnelly, J.A. Donnelly, R.N. Hills, J. Low Temp. Phys. **44**, 471 (1981)
26. J. Villain, J. Phys. Chem. Solids **11**, 303 (1959)
27. A. Yoshimori, J. Phys. Soc. Jpn. **14**, 807 (1959)
28. J.W. Lynn, G. Shirane, M. Blume, Phys. Rev. Lett. **37**, 154 (1976)
29. S. Shamoto, M. Sato, J.M. Tranquada, B.J. Sternlieb, G. Shirane, Phys. Rev. B **48**, 13817 (1993)
30. R. Coldea, S.M. Hayden, G. Aeppli, T.G. Perring, C.D. Frost, T.E. Mason, S.W. Cheong, Z. Fisk, Phys. Rev. Lett. **86**, 5377 (2001)
31. N.S. Headings, S.M. Hayden, R. Coldea, T.G. Perring, Phys. Rev. Lett. **105**, 247001 (2010)
32. I.A. Zaliznyak, H. Woo, T.G. Perring, C.L. Broholm, C.D. Frost, H. Takagi, Phys. Rev. Lett. **93**, 087202 (2004)
33. A.C. Walters, T.G. Perring, J.S. Caux, A.T. Savici, G.D. Gu, C.C. Lee, W. Ku, I.A. Zaliznyak, Nat. Phys. **5**, 867 (2009)
34. R.E. Walstedt, S.W. Cheong, Phys. Rev. B **64**, 014404 (2001)
35. J.G. Bednorz, K.A. Müller, Z. Phys. B **64**, 189 (1986)
36. P.W. Anderson, Science **235**, 1196 (1987)
37. D. Vaknin, S.K. Sinha, D.E. Moncton, D.C. Johnston, J.M. Newsam, C.R. Safinya, J.H.E. King, Phys. Rev. Lett. **58**, 2802 (1987)
38. J.D. Axe, M.K. Crawford, J. Low Temp. Phys. **95**, 271 (1994)

39. K. Yamada, E. Kudo, Y. Endoh, Y. Hidaka, M. Oda, M. Suzuki, T. Murakami, Solid State Commun. **64**, 753 (1987)
40. B.O. Wells, Y.S. Lee, M.A. Kastner, R.J. Christianson, R.J. Birgeneau, K. Yamada, Y. Endoh, G. Shirane, Science **277**, 1067 (1997)
41. B. Keimer, A. Aharony, A. Auerbach, R.J. Birgeneau, A. Cassanho, Y. Endoh, R.W. Erwin, M.A. Kastner, G. Shirane, Phys. Rev. B **45**, 7430 (1992)
42. Y.S. Lee, R.J. Birgeneau, M.A. Kastner, Y. Endoh, S. Wakimoto, K. Yamada, R.W. Erwin, S.H. Lee, G. Shirane, Phys. Rev. B **60**, 3643 (1999)
43. M.A. Kastner, R.J. Birgeneau, G. Shirane, Y. Endoh, Rev. Mod. Phys. **70**, 897 (1998)
44. G. Shirane, Y. Endoh, R.J. Birgeneau, M.A. Kastner, Y. Hidaka, M. Oda, M. Suzuki, T. Murakami, Phys. Rev. Lett. **59**, 1613 (1987)
45. S. Chakravarty, B.I. Halperin, D.R. Nelson, Phys. Rev. Lett. **60**, 1057 (1988)
46. E. Manousakis, Rev. Mod. Phys. **63**, 1 (1991)
47. S.M. Hayden, G. Aeppli, R. Osborn, A.D. Taylor, T.G. Perring, S.W. Cheong, Z. Fisk, Phys. Rev. Lett. **67**, 3622 (1991)
48. J. Lorenzana, G. Seibold, R. Coldea, Phys. Rev. B **72**, 224511 (2005)
49. B.D. Piazza, M. Mourigal, M. Guarise, H. Berger, T. Schmitt, K.J. Zhou, M. Grioni, H.M. Rønnow, Phys. Rev. B **85**, 100508 (2012)
50. C. Stock, R.A. Cowley, W.J.L. Buyers, C.D. Frost, J.W. Taylor, D. Peets, R. Liang, D. Bonn, W.N. Hardy, Phys. Rev. B **82**, 174505 (2010)
51. K. Yamada, C.H. Lee, K. Kurahashi, J. Wada, S. Wakimoto, S. Ueki, Y. Kimura, Y. Endoh, S. Hosoya, G. Shirane, R.J. Birgeneau, M. Greven, M.A. Kastner, Y.J. Kim, Phys. Rev. B **57**, 6165 (1998)
52. J.M. Tranquada, B.J. Sternlieb, J.D. Axe, Y. Nakamura, S. Uchida, Nature **375**, 561 (1995)
53. M. Fujita, H. Goka, K. Yamada, J.M. Tranquada, L.P. Regnault, Phys. Rev. B **70**, 104517 (2004)
54. M. Hücker, M.v Zimmermann, G.D. Gu, Z.J. Xu, J.S. Wen, G. Xu, H.J. Kang, A. Zheludev, J.M. Tranquada, Phys. Rev. B **83**, 104506 (2011)
55. S.A. Kivelson, I.P. Bindloss, E. Fradkin, V. Oganesyan, J.M. Tranquada, A. Kapitulnik, C. Howald, Rev. Mod. Phys. **75**, 1201 (2003)
56. J. Zaanen, O.Y. Osman, H.V. Kruis, Z. Nussinov, J. Tworzydło, Phil. Mag. B **81**, 1485 (2001)
57. N. Ichikawa, S. Uchida, J.M. Tranquada, T. Niemöller, P.M. Gehring, S.H. Lee, J.R. Schneider, Phys. Rev. Lett. **85**, 1738 (2000)
58. Q. Jie, S.J. Han, I. Dimitrov, J. Tranquada, Q. Li, Phys. C **481**, 46 (2012)
59. E. Berg, E. Fradkin, S.A. Kivelson, J.M. Tranquada, New J. Phys. **11**, 115004 (2009)
60. J.M. Tranquada, H. Woo, T.G. Perring, H. Goka, G.D. Gu, G. Xu, M. Fujita, K. Yamada, Nature **429**, 534 (2004)
61. G.Y. Xu, J.M. Tranquada, T.G. Perring, G.D. Gu, M. Fujita, K. Yamada, Phys. Rev. B **76**, 014508 (2007)

Chapter 8
Muon Spin Relaxation Studies of Unconventional Superconductors: First-Order Behavior and Comparable Spin-Charge Energy Scales

Yasutomo J. Uemura

Abstract Since the late 1980s, the muon spin rotation and relaxation (μSR) method has been extensively applied to studies of unconventional superconductors, including high-T_c cuprate, ruthenate, FeAs, organic, and heavy-fermion systems. With its unique sensitivity to static magnetic order in both long-range ordered and random spin systems, μSR has played a leading role in determining magnetic phase diagrams and elucidating the evolution from the parent antiferromagnetic state to the superconducting state in these systems. The extremely high sensitivity of μSR to small static magnetic fields allowed studies of time-reversal symmetry breaking in the superconducting state of Sr_2RuO_4 and several other systems and in the pseudogap region of cuprate systems. μSR measurements of the London penetration depth and the superfluid density led to a unique characterization of the pairing symmetry and energy scales of superconducting charges. In this paper, we review the historical developments and recent progress of μSR studies in unconventional superconductors which revealed, among others, scaling of the superfluid density and T_c, comparable spin and charge energy scales, phase separation between superconducting and non-superconducting volumes, and first-order quantum evolution at phase boundaries. We discuss these results in terms of quantum criticality, crossover from Bose Einstein to BCS condensation, and the influence of competing states via inelastic soft modes.

8.1 Brief History and Technical Overview of μSR

In high intensity proton accelerator facilities, such as TRIUMF in Vancouver and Paul Scherrer Intsitut in Switzerland, positive pions are produced by collisions of a proton beam and a meson production target (usually made of carbon or beryllium). Within a very short life time, a positive pion decays into a positive muon and muon neutrino. Since the π^+ is a spin-less particle, the muon spin should be polarized by

Y.J. Uemura (✉)
Department of Physics, Columbia University, New York, NY 10027, USA
e-mail: tomo@lorentz.phys.columbia.edu

A. Avella and F. Mancini (eds.), *Strongly Correlated Systems*,
Springer Series in Solid-State Sciences 180, DOI 10.1007/978-3-662-44133-6_8

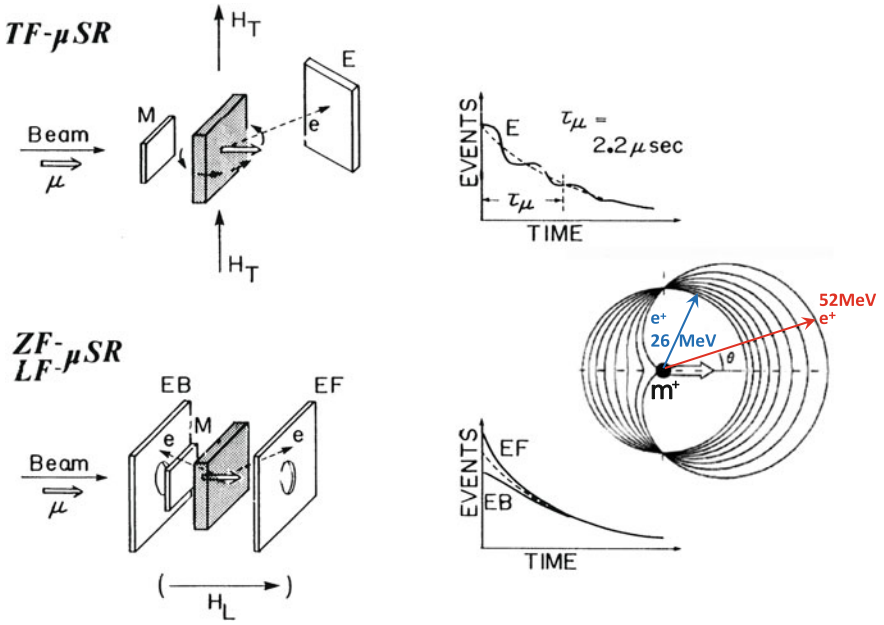

Fig. 8.1 Schematic view of experimental configurations in transeverse-field (TF-), zero-field (ZF) and longitudinal-field (LF) μSR measurements. The specimen is shown as the shaded region, surrounded by the muon-defining (M) and positron-detecting (E, EB, EF) counters. The time spectra of muon decay events are shown in the right figures, together with the angular asymmetry of a decay event of a positive muon, for different positron energies from 26 MeV (without anisotropy) to 52 MeV (with the largest anisotropy). Muon spin precession around the applied external TF can be observed in the TF configuration, in which the amplitude of the oscillatory signal is proportional to population of muons in the para- or non-magnetic environment. Magnetic-field penetration depth in type-II superconductors is measured in the TF-μSR configuration, with the external magnetic field between H_{C1} and H_{C2}. Oscillatory signal is also observed in ZF-μSR when the specimen undergoes static long-range magnetic order. The muon spin-lattice relaxation rate $1/T_1$ can be measured in the ZF and LF configurations. Typical implantation depth (stopping range) of incident muons is about 200 mg/cm^2 (= 0.4 mm from the surface for a material with the density 5) for ordinary surface (Arizona) muons having kinetic energy of 4.1 MeV, while about 200–2000 Åfor low-energy muons with kinetic energy of 5–10 keV. At TRIUMF and PSI, the initial muon spin direction can be rotated to become perpendicular to the beam direction, by the use of a spin–rotator (Wien filter), in which case the TF is applied parallel to the beam direction. For general aspects of μSR, see [5–10, 109]

100 % along its flight direction, if the neutrino generated by the pion decay is to have a full helicity. Therefore, spin polarization of muons is related to the parity violation of weak interaction.

The principle of μSR measurement is illustrated in Fig. 8.1. A positive muon stops in a material of typical thickness of 0.1–1 mm, losing its energy via ionization of atoms composing the material. This energy-loss and stopping process occurs in less than 1 ns, without any change in the μ^+ spin state. After stopping at an interstitial

site in the unit cell, the positive muon often stays localized at that site with its spin precessing around the internal or external magnetic field. After an average life time of 2.2 μs, the positive muon decays in a three-body process into a positron, neutrino and anti-neutrino. In this process, energetic positrons are emitted preferentially along the muon spin direction, due again to parity violation. The arrival time of a given muon is recorded by the "defining counter M" and the emission of the decay positron by the positron counters "EF" or "EB" or "E" shown in Fig. 8.1. The event-rate histograms are obtained as a function of the muon residence time t defined by the interval of the muon arrival and positron emission times. The angular asymmetry, $\{EF(t) - EB(t)\}/\{EF(t) + EB(t)\}$, reflects the time evolution of the muon spin polarization in the specimen.

The first μSR experiment was performed in 1957 at the Nevis Synchro-cyclotron of Columbia University by Garwin et al. [1] to verify parity non-conservation. By using a carbon target as the specimen and applying a transverse external magnetic field, they observed the dependence of the positron intensity on the magnitude of the applied field. Their paper was submitted for publication on January 15, 1957 to Physical Review, which is the same day that the famous beta-decay paper by the group of Wu [2] was submitted to Physical Review. These two experiments, together with another measurement by a group of Telegdi in Europe [3], provided the first experimental confirmation of parity violation in the weak interaction. The historical details of these developments were reviewed by Lee [4].

Figure 8.2 shows a photograph of a modern μSR spectrometer at TRIUMF. We see several sets of Helmholtz coils used for applying external magnetic fields. As shown in Fig. 8.1b, the evolution of the muon spin polarization can be measured in zero field (ZF) as well as in a longitudinal external field (LF) applied parallel to the initial muon spin direction. The spin-lattice relaxation rate $1/T_1$ of muon spin can be measured by LF-μSR. When an internal or external magnetic field is not parallel to the initial polarization, the muon spin will precess around the field and exhibit an oscillation pattern, as illustrated in Fig. 8.1a for transverse-field (TF) μSR measurements in applied external fields.

Oscillation and relaxation of muon spins around a spontaneous internal magnetic field, measured in ZF-μSR, allow the direct observation of the onset of static magnetic order, as can be seen in μSR studies of magnetic phase diagrams. The London penetration depth in type-II superconductors can be determined from the damping rate of muon spin precession around an applied external field in TF-μSR measurements. The asymmetry of muon spin precession observed in a weak external transverse field (WTF) represents signals from muons in para-or non-magnetic environments, which leads to a determination of the volume fraction of magnetically ordered regions near the phase boundary. Details of these μSR techniques can be found in [5–10].

Fig. 8.2 A photograph of a μSR spectrometer at TRIUMF. A large Helmhorz coils are used to generate magnetic field parallel to the muon beam direction, while sets of smaller coils are used to generate magnetic field perpendicular to the muon beam direction. The specimen is placed in the center of these coils within a Helium gas flow cryostat which has horizontal access (shown by the *silver/blue cylindrical* object). *Blue tubes* contain photo-multiplyers connected to *black light* guides and plastic scintillation counters for detecting muons and positrons. In the top-right corner of the picture is shown a part of high-voltage generator of a spin rotator (Wien filter) with which the spin polarization direction of incident muons are rotated from the original direction parallel to the muon flight direction. One sees a part of beamline quadrupole magnets guiding the muon beam to the location of the specimen. This picture was taken at the M15 beamline of TRIUMF. Other instruments for μSR measurements can be seen at web pages of TRIUMF [110], PSI [111] and ISIS [112] muon facilities

8.2 Magnetic Phase Diagrams of Unconventional Superconductors

μSR has played a leading role in studies of static magnetic order in parent systems of unconventional superconductors. For example, μSR provided direct evidence of static magnetic order in La_2CuO_4 [11], the so-called A phase of $CeCu_2Si_2$ [12], and an organic superconductor $(TMTSF)_2PF_6$ [13] prior to any other probes. Figure 8.3 shows magnetic phase diagrams of unconventional superconductors [14]. Among them, the results for LaFeAsO [15], $YBa_2Cu_3O_7$ [16], A_3C_{60} [17] are based on μSR measurements. As listed in Table 8.1, extensive μSR studies have been performed to elucidate static magnetism in parent compounds of FeAs and FeSe superconductors.

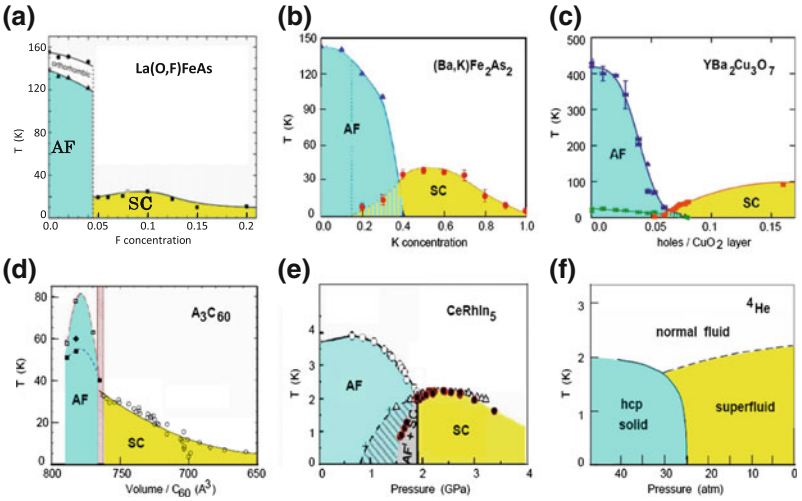

Fig. 8.3 Electronic phase diagrams shown as functions of temperature T and composition, pressure and/or unit-cell volume in different superconductors. **a** La(O,F)FeAs [15]; **b** $(Ba,K)Fe_2As_2$ [113]; **c** $YBa_2Cu_3O_{7-\delta}$ [16]; **d** A_3C_{60} (A = K, Cs, Rb) [17]; **e** $CeRhIn_5$ [114]. ($CeCoIn_5$ at ambient pressure corresponds to $CeRhIn_5$ at the pressure p $\sim$ 2.4 GPa); **f** Phase diagram of superfluid ^{4}He. All these systems show abrupt disappearance of the AF (or hcp solid phase in the case of helium) or coexistence of the AF and the superconducting (SC) phases near the phase boundary. These are features expected in first-order transition in quantum evolution. **a, c** and **d** are based on μSR measurements, while (**b**) on neutron scattering, and (**e**) on transport and NMR studies. Adopted from Fig. 1 of [14] with some revisions

In general, these phase diagrams suggest the importance of magnetic interactions in pairing mechanisms of unconventional superconductors. Implications of these results on possible roles of magnetic quantum criticality are discussed in a subsequent section.

Occasionally, μSR finds static magnetic order in systems which were thought to have a non-magnetic ground state, as in the case of $CeCu_2Si_2$ [12]. The most recent examples of this type of discovery include static magnetic order of $(Sr,Ca)_2RuO_4$ in nearly the entire doping ranges of (Sr,Ca) substitution [18]. For many years, the superconducting phase of Sr_2RuO_4 was thought to be isolated from static magnetism, especially in the Sr-rich region of $(Sr,Ca)_2RuO_4$ [19]. However, the new μSR results revealed the magnetic phase diagram shown in Fig. 8.4, with a part of the results confirmed by subsequent measurements of dc- and ac- magnetic susceptibility.

Since the discovery of Bucky-ball superconductors K_3C_{60} and Rb_3C_{60} in 1991 [20, 21], alkali-doped fulleride superconductors A_3C_{60} were often discussed as belonging to a rather different class of superconductors than the high-T_c cuprates and heavy fermion systems, due to the apparent lack of magnetic parent systems and to the monotonically increasing T_c with increasing lattice constants reminiscent of the effect of increasing density of states at the Fermi level expected in BCS theory. In 2008, by ZF-μSR measurements, Prassides and co-workers [17] reported static

Table 8.1 Muon spin relaxation studies on Fe-based superconductors and relevant magnetic systems

Family	Composition	Tuning	MG or SFD	First author	Journal	Volume	Page	Year	Month	Facility
1111	LaFeAsO		MG	Klauss, H. -H	PRL	101	[077005]	2008	Aug	PSI
1111	LaFeAs(O,F)	(O,F)	SFD	Luetkens, H	PRL	101	[097009]	2008	Aug	PSI
1111	SmFeAs(O,F)	(O,F)	MG SFD	Drew, A. J	PRL	101	[097010]	2008	Aug	ISIS
1111	(Nd,Sm)$FeAsO_{0.82}F_{0.18}$		MG SFD	Dubroka, A	PRL	101	[097001]	2008	Aug	PSI
1111	[Sm/Nd]$FeAsO_{0.85}$		SFD	Khasanov, R	PRB	78	[092506]	2008	Sep	PSI
1111	LaFeAs($O_{0.94}F_{0.06}$)		MG SFD	Takeshita, S	JPSJ	77	[103703]	2008	Oct	TRIUMF
122	$SrFe_2As_2$		MG	Jesche, A	PRB	78	[180504]	2008	Nov	PSI
11	$FeSe_{0.85}$		SFD	Khasanov, R	PRB	78	[220510]	2008	Dec	PSI
	FeAs, $FeAs_2$		MG	Baker, P. J	PRB	78	[212501]	2008	Dec	ISIS
1111, 122	NdFeAsO, (Ba,K)Fe_2As_2	(Ba,K)	MG SFD	Aczel, A. A	PRB	78	[214503]	2008	Dec	TRIUMF
111	NaFeAs		MG	Parker, D. R	Chem.Comm	16	2189-2191	2009		ISIS
122	(Ba,K)Fe_2As_2		MS SFD	Hiraishi, M	JPSJ	78	[023710]	2009	Feb	TRIUMF
1111	SrFeAsF		MG	Baker, P. J	PRB	79	[060402]	2009	Feb	ISIS
1111	LaFeAsO		MG	Carlo, J. P	PRL	102	[087001]	2009	Feb	TRIUMF
111	LiFeAs		SFD MG	Pratt, F. L	PRB	79	[052508]	2009	Feb	PSI
	Review		MG SFC	Takeshita, S	NJP	11	[035006]	2009	Mar	
1111	LaFeAs(O,F)	(O,F)	MG	Luetkens, H	Nat. Mat.	8	305-309	2009	Apr	PSI
1111	SmFeAs(O,F)	(O,F)	MG	Drew, A. J	Nat. Mat.	8	310-314	2009	Apr	PSI, ISIS
	News and views		MG	Uemura, Y J.	Nat. Mat.	8	253-255	2009	Apr	
	Review		MG SFD	Amato, A	Physica C	469	606-613	2009	May	
122, 1111	Ba($Fe,Co)_2As_2$; (Pr,Sr)FeAsO	(Fe, Co), (Pr, Sr)	MG SFD	Bernhard, C	NJP	11	[055050]	2009	May	PSI
122	(Ba,K)Fe_2As_2	(Ba,K)	MG SFD	Khasanov, R	PRL	102	[187005]	2009	May	PSI

(Continued)

Table 8.1 (Continued)

Family	Composition	Tuning	MG or SFD	First author	Journal	Volume	Page	Year	Month	Facility
122	$CaFe_2As_2$; (Ba/Sr,K/Na)Fe_2As_2	pressure, (Ba,K)	MS SFD	Goko, T	PRB	80	[024508]	2009	Jul	TRIUMF
1111	Ca(Fe,Co)AsF		MG SFD	Takeshita, S	PRL	103	[027002]	2009	Jul	TRIUMF
1111	SmFeAs(O,F)	(O,F)	MG	Sanna, S	PRB	80	[052503]	2009	Aug	PSI
122	$Sr(Fe_{1.75}Co_{0.25})As_2$		SFD MG	Khasanov, R	PRL	103	[067010]	2009	Aug	PSI
122	$Ba(Fe_{0.926}Co_{0.074})_2As_2$		SFD	Williams, T. J	PRB	80	[094501]	2009	Sep	TRIUMF
1111	REFeAsO		MG	Maeter, H	PRB	80	[094524]	2009	Sep	PSI
	Review			Uemura, Y J.	Physica B	404	3195-3201	2009	Oct	
11	Fe(Se,Te)	(Se,Te)	MG	Khasanov, R	PRB	80	[140511]	2009	Oct	PSI
11	$FeSe_{1-x}$	Pressure	MG SFD	Bendele, M	PRL	104	[087003]	2010	Feb	PSI
111	Na(Fe,Co/Ni)As	(Fe,Co/Ni)	MG SFD	Parker, D. R	PRL	104	[057007]	2010	Feb	PSI
122	$Ba(Fe,Co)_2As_2$		MG SFD	Marsik, P	PRL	105	[037207]	2010	Feb	PSI
1111	SmFeAs(O,F)		SFD	Weyeneth, S	EPS	91	[47005]	2010	Aug	PSI
1111	CeFeAs(O,F)	(O,F)	MG	Sanna, S	PRB	82	[060508]	2010	Aug	PSI,ISIS
111	Li_x(Fe,Co/Ni)As	(Fe,Co/Ni); Li(x)	SFD	Pitcher, M. J	JACS	132	10467-10476	2010	Aug	PSI, ISIS
122	Ba/Sr$(Fe,Co)_2As_2$	(Fe,Co)	SFD	Williams, T. J	PRB	82	[094512]	2010	Sep	TRIUMF
122	$RbFe_2As_2$		SFD	Shermadini, Z	PRB	82	[144527]	2010	Oct	PSI
11	$Fe_ySe_{0.25}Te_{0.75}$		MG	Bendele, M	PRB	82	[212502]	2010	Dec	PSI
1111	LaFeAs(O,F)	(O,F)	MG	Ohishi, K	JPSJ	80	[024703]	2011	Feb	ISIS
122	$Ba(Fe,Co)_2As_2$		MG SFD	Sonier, J. E	PRL	106	[127002]	2011	Mar	TRIUMF
122FeSe	$Cs_{0.8}(FeSe_{0.98})_2$		MG	Shermadini, Z	PRL	106	[117602]	2011	Mar	PSI
42622	$Sr_4(Sc/V)_2O_6Fe_2As_2$		MG SFD	Munevar, J	PRB	84	[024527]	2011	Jul	TRIUMF
111DMS	Li_x(Zn,Mn)As	Li(x), (Zn,Mn)	MG	Deng, Z	Nat. Comm.	2	[422]	2011	Aug	TRIUMF
1111	$LaFeAsO_{0.945}F_{0.055}$	Pressure	MG	Khasanov, R	PRB	84	[100501]	2011	Sep	PSI
122	(Ba,Rb)Fe_2As_2	(Ba,Rb)	SFD	Guguchia, Z	PRB	84	[094513]	2011	Sep	PSI
1111	SmFe(As,P)O	(As,P)	MG SFD	Zhigadlo, N. D	PRB	84	[134526]	2011	Oct	PSI

Table 8.1 (Continued)

Family	Composition	Tuning	MG or SFD	First author	Journal	Volume	Page	Year	Month	Facility
1111	$Sm(Fe_{1-x}Ru_x)As(O_{0.85}F_{0.15})$	(Fe,Ru)	MG	Sanna, S	PRL	107	[227003]	2011	Nov	PSI, ISIS
1111	CeFeAs(O,F)	(O,F)	MG	Shiroka, T	PRB	84	[195123]	2011	Nov	PSI
122	$(Ba,K)Fe_2As_2$	(Ba,K)	MG	Wiesenmayer, E	PRL	107	[237001]	2011	Nov	PSI
122	$Ba(Fe,Co)_2As_2$		SFD	Ofer, O	PRB	85	[060506]	2012	Feb	PSI-LEM
11	$FeSe_{1-x}$	Pressure	MG	Bendele, M	PRB	85	[064517]	2012	Feb	PSI
1111	La(Fe,Ru)AsO	(Fe,Ru)	MG	Bonfa, P	PRB	85	[054518]	2012	Feb	PSI
111	Na(Fe,Co)As	(Fe,Co)	MG SFD	Wright, J. D	PRB	85	[054503]	2012	Feb	PSI, ISIS
122FeSe	$[Rb/K]_xFe_{2-y}Se_2$		MG SFD	Shermadini, Z	PRB	85	[100501]	2012	Mar	PSI
122FeSe	$K_{0.73}Fe_{1.67}Se_2$		MG SFD	Wang, C.	PRB	85	[214503]	2012	Jun	PSI
122	KFe_2As_2		SFD	Ohishi, K	J.Phys.Conf.Ser.	400	[022087]	2012		TRIUMF,ISIS
1111	LnFeAsO (Ln = La, Ce, Pr, Sm)	Pressure	MG	De Renzi, R	SST	25	[084009]	2012	Aug	PSI
122FeSe	$Rb_xFe_{2-y}Se_2$		MG	Weyeneth, S	PRB	86	[134530]	2012	Oct	PSI
122	$Ba(Fe,Co)_2As_2$	(Fe,Co)	MG SFD	Bernhard, C	PRB	86	[184509]	2012	Nov	PSI
122	$RbFe_2As_2$	Pressure	SFD	Shermadini, Z	PRB	86	[174516]	2012	Nov	PSI
122FeSe	$Li_x(NH_2)_y(NH_3)_{1-y}Fe_2Se_2$		SFD	Burrard-Lucas, M	Nat. Mat.	12	15-19	2013	Jan	ISIS
122DMS	$(Ba,K)(Zn,Mn)_2As_2$	(Ba,K), (Zn,Mn)	MG	Zhao, K	Nat. Comm.	4	[1442]	2013	Feb	PSI
11	$Fe_{1.03}Te$	Pressure	MG	Bendele, M	PRB	87	[060409]	2013	Feb	PSI
1111	$La_{0.7}Y_{0.3}FeAs(O_{1-x}F_x)$	(O,F)	MG	Prando, G	Phys.Stat.Sol.B	250	599-602	2013	Mar	PSI
122FeSe	$Li(C_5H_5N)_{0.2}Fe_2Se_2$		MG SFD	Biswas, P. K	PRL	110	[137003]	2013	Mar	PSI
11	$Fe_{1+y}Se_xTe_{1-x}$	(Se,Te)	MG	Lamura, G	JPCM	25	[156004]	2013	Apr	PSI
1111	L(Fe,Ru)As(O,F) L=La, Nd, Sm	(Fe,Ru)	MG	Sanna, S	PRB	87	[134518]	2013	Apr	PSI
122	$Ba(Fe,Mn)_2As_2$	(Fe,Mn)	MG	Inosov, D. S	PRB	87	[224425]	2013	Jun	PSI
1111DMS	(La,B)(Zn,Mn)AsO	(La,Ba), (Zn,Mn)	MG	Ding, C	PRB	88	[041102]	2013	Jul	TRIUMF.PSI
111DMS	$Li_x(Zn,Mn)P$	Li(x), (Zn,Mn)	MG	Deng, Z	PRB	88	[081203]	2013	Aug	TRIUMF
111	$Li_x(Fe,Co/Ni)As$	(Fe,Co/Ni); Li(x)	MG SFD	Wright, J. D	PRB	88	[060401]	2013	Aug	PSI, ISIS
122FeSe	$Rb_{0.77}Fe_{1.61}Se_2$		MG	Maletz, J	PRB	88	[134501]	2013	Oct	PSI

DMS doped ferromaggntic semiconductor; *MG* magnetic order; *SFD* superfluid density; *LEM* low energy muon facility
PRL Phys. Rev. Lett.; *PRB* Phys. Rev.B; *JACS* J. Am. Chem. Soc.; *JPSJ* J. Phys. Soc. Japan; *JPCM* J. Phys. Condens. Matter
SST superconductor science and technology

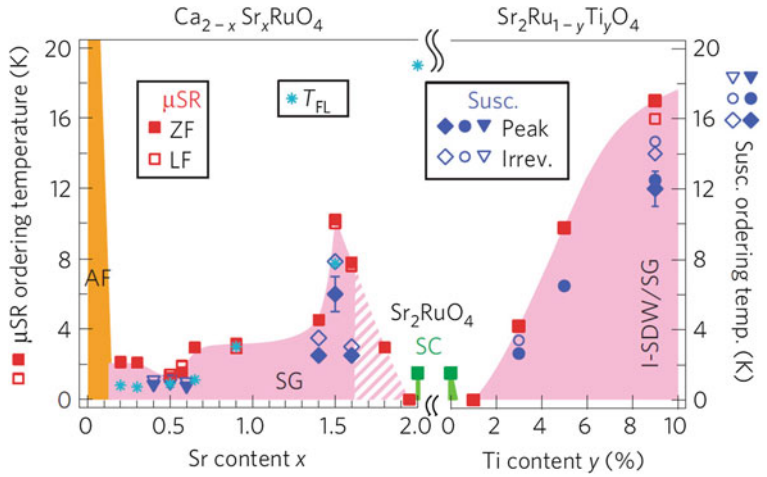

Fig. 8.4 Magnetic phase diagram of $(Ca,Sr)_2RuO_4$ and $Sr_2(Ru,Ti)O_4$ determined by μSR measurements of Carlo et al. [18]. Closed red symbols show transition temperatures determined by the relaxation rate measured in ZF-μSR, open red symbols corresponds to the peak temperature of $1/T_1$ in LF-μSR, and *closed* and *open blue symbols* denote, respectively, the peak temperature and the irreversibility-onset temperature of the dc-magnetic susceptibility. Static magnetic order develops in the colored region. The *blue diamonds* represent the susceptibility results obtained for the present specimens used in μSR, the *blue circles* denote points from Minakata and Maeno [115] and the *blue triangles* are from Nakatsuji and co-workers [19]. The slanted-stripe coloring indicates regions involving phase separation (see Supplementary Information of [18]). SG denotes spin glass and I-SDW indicates incommensurate spin density wave. Static magnetic order of $Ca_{0.5}Sr_{1.5}RuO_4$ has been confirmed by neutron scattering measurements [116]. The in-plane conductivity and specific heat exhibit Fermi liquid behavior below T_{FL} [19, 117, 118]

magnetic order in A_3C_{60} systems with the insertion of NH_3 molecules to further expand the lattice constant. The resulting phase diagram is shown in Fig. 8.3d. By additional μSR and other magnetic measurements, the same group found magnetic parent phases in bcc Cs_3C_{60} [22] and insulating fcc polymorphic Cs_3C_{60} [23], which can be made into superconducting and metallic states by the application of pressure. These discoveries have triggered ongoing studies to re-evaluate possible roles of spin fluctuations in the superconducting pairing of these C_{60}-based systems.

In some cases, μSR studies confirmed the absence of static magnetism in parent systems adjacent to superconducting states, such as in $(Ba,K)BiO_3$ [24] and $BaTi_2(As_{1-x}Sb_x)_2O$ [25, 26]. In these systems and in Cu_xTiSe_2 [27, 28], superconducting pairing may be related to an instability towards charge density wave states.

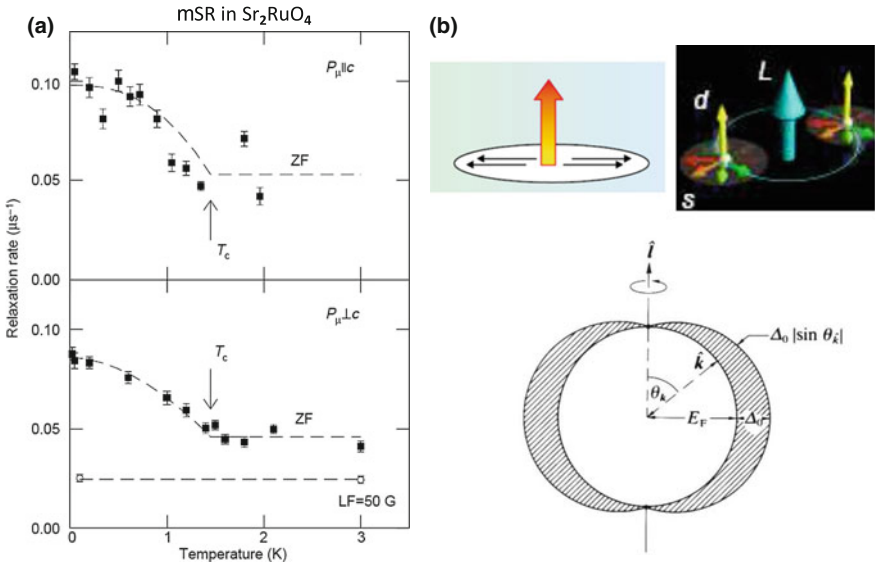

Fig. 8.5 **a** μSR measurements on time reversal symmetry (TRS) breaking in a single crystal of Sr_2RuO_4 from Luke et al. [33]. Zero-field (ZF) relaxation rate Λ for the initial muon spin polarization k parallel to the c-axis (*top*) and perpendicular to the c-axis (*bottom*). T_c from a.c.-susceptibility indicated by *arrows*. *Circles* in *bottom* figure give relaxation rate in LF = 50 G. *Curves* are guides to the eye. **b** Schematic view of configurations of the spin (s) and orbital (L) angular momenta and the d-vector (d) (*top*), and the gap-node structure (*bottom*), expected for the chiral p-wave paring state [36] consistent with the TRS breaking in Sr_2RuO_4. This paring is similar to that of the A-phase of superconducting ^{3}He

8.3 Search for Time-Reversal Symmetry Breaking in the Superconducting and Pseudogap States

The μSR technique has a very high sensitivity to small internal magnetic fields, as demonstrated by ZF-μSR results in systems with nuclear dipolar fields [29]. This feature was used to search for "time-reversal symmetry breaking" phenomena in the superconducting phase, which is due not to static magnetic order in a usual sense but to an emergence of a static magnetic field from superconducting pairs in states different from isotropic s-wave coupling. The first possible example of this phenomenon was found by Heffner and co-workers in (U,Th)Be_{13} [30], followed by UPt_3 [31], both of which may have pairing with high angular momentum.

Soon after the discovery of superconductivity in Sr_2RuO_4 [32], we performed ZF-μSR measurements on single crystal specimens of this system [33], and found a small increase of internal magnetic field below the superconducting T_c shown in Fig. 8.5a, which indicates that time reversal symmetry (TRS) is broken. In this system, NMR Knight shift measurements exhibited no temperature dependence below T_c, suggesting an odd-parity pairing [34, 35]. The most-likely p-wave state has orbital angular momentum $l = 1$ and spin angular momentum $s = 1$, which can lead

to several different states depending on relative directions of l and s. The observation of TRS breaking helps narrow down the ground state to the so-called "chiral p-wave state" [36], illustrated in Fig. 8.5b, which is analogous to the "A-phase" of superfluid ^{3}He. About 10 years after the initial μSR report, Kapitulnick and co-workers reported a corresponding observation using precision measurements of Kerr rotation in Sr_2RuO_4 [37].

Similar TRS breaking has been subsequently detected by μSR in filled Skutteldite systems $PrOs_4Sb_{12}$ [38] and $PrPt_4Ge_{12}$ [39] and non-centrosymmetric superconductors $LaNiC_2$ [40], $LaNiGa_2$ [41], and SrPtAs [42], while TRS is found to be preserved (within experimental limits of detection by μSR) in other non-centrosymmetric superconductors $Mg_{10}Ir_{19}B_{16}$ [43], $LaRhSi_3$ [44] and Re_3W [45]. Recent μSR experiments have found TRS preservation in bulk specimens of candidates for topological superconductors $Cu_xBi_2Se_3$ and (Sn,In)Te [46].

Since 2006, Bourges, Mook, Greven and their collaborators reported [47–49] observations of an increase in elastic neutron scattering intensity corresponding to the build up of antiferromagnetic correlations within the unit cell of YBCO, BISCO, and Hg2201 cuprates below the "pseudogap" temperature T^*. This phenomenon has been often discussed in the context of a theory of Varma [50, 51] which argues that a circulating orbital current within a unit cell can generate such a static magnetism. Much earlier than these neutron studies, searches for static magnetic order in the pseudogap region were conducted with μSR in YBCO and BISCO cuprate systems [52], which found the absence of any signal suggesting an onset of magnetic order below T^*. Similar results were obtained by subsequent μSR studies in LSCO [53, 54]. Sonier et al. [55] initially reported the possibility of a signal corresponding to magnetic order below T^* in YBCO, but later published a more precise study in which no static magnetism was observed in the pseudogap state [56]. Similarly to μSR, no signature of static magnetic order below T^* has been detected by NMR or NQR of various cuprate systems [57, 58]. Static magnetic order below T^* was, however, recently reported from Kerr effect measurements [59, 60]. Thus, the existence of static magnetic order in the pseudogap phase is controversial, and remains to be clarified by further experiments in the future.

8.4 London Penetration Depth and Pairing Symmetry

The superconducting transition is associated with an expulsion of magnetic field known as the Meissner effect. This phenomenon is theoretically described by the London equation, which defines the London penetration depth λ_L as the characteristic length scale for decay of the magnetic field within superconducting materials. Below the superconducting transition temperature, gauge symmetry is broken, and a particular choice of gauge (the London gauge) is required to explain Meissner effect. In this process, photons acquire a mass within superconductors. This phenomenon provided hints to elementary particle physics to explain the acquisition of mass of elementary particles by condensation of the Higgs bosons (corresponding to the condensation of Cooper pairs) with spontaneous gauge symmetry breaking [61].

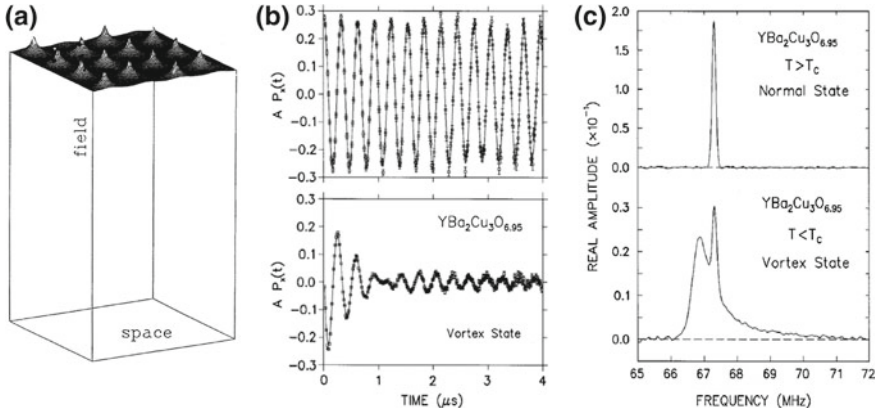

Fig. 8.6 **a** Schematic view of the distribution of the internal magnetic field in the vortex state of type-II superconductors for the case of formation of the triangular Abrikosov vortex lattice. For an external field of 1–2 kG, the distance of adjacent vortex core becomes about 1000–2000 Å. The variation of the magnetic field ΔB within the superconductor is determined by the London penetration depth λ as ΔB scaling with λ^{-2}. **b** Muon spin precession signal observed in a single crystal of $YBa_2Cu_3O_7$ in the normal state above T_c (*top*) and the superconducting state below T_c (*bottom*). From Sonier et al. [62]. **c** Fourier transforms of the time spectra shown in (**b**). The anisotropic field distribution, expected for the Abrikosov vortex lattice, is seen in the *bottom* figure. The *sharp peak* in the *bottom* figure is due to non-relaxing background signal. From Sonier et al. [62]

According to the London equation, the inverse of the penetration depth squared, $(1/\lambda)^2$ is proportional to the superconducting carrier density n_s divided by the effective mass m^* as

$$\lambda^{-2} = \frac{4\pi n_s e^2}{m^* c^2} \times \frac{1}{1 + \xi/l_{mf}} \tag{8.1}$$

where a correction is required in the "dirty limit" when the mean free path l_{mf} is shorter than the superconducting coherence length ξ. The parameter n_s/m^* is often called the "superfluid stiffness" or "superfluid density" and represents the magnitude of the supercurrent screening the external magnetic field. If one replaces the superconducting carrier density n_s with the normal state carrier density n_n, then n/m^* gives a parameter proportional to plasma frequency squared and the Fermi energy in non-interacting two-dimensional Fermion systems.

In type-II superconductors, the external magnetic field penetrates the system by forming a lattice of flux vortices. Since each flux vortex carries a magnetic flux quantum, the density of flux vortices and the resulting distance between adjacent vortices is a material-independent parameter. For an applied field of a few kG, the adjacent vortices are apart by about 1000–2000 Å. After correction for the shape-dependent demagnetizing field, the magnetic field at the core of each flux vortex is

equivalent to the applied field. The field magnitude, however, is reduced in regions between the vortex cores, forming a magnetic field pattern as illustrated in Fig. 8.6a.

In TF-μSR experiments on type-II superconductors, as illustrated in Fig. 8.6b with results from a YBCO cuprate superconductor [62], the muon spin precession around the external magnetic field exhibits clear damping below T_c caused by the inhomogeneous internal magnetic field in the flux vortex lattice. In experiments on polycrystalline ceramic specimens or systems having a rather long penetration depth (slow damping of precession), the damping of the muon spin precession is usually fit with a Gaussian decay envelope $\exp\{-(0.5)\sigma^2 t^2\}$ which defines the muon spin relaxation rate σ. Since the width of the field inhomogeneity is proportional to $1/(\lambda_L)^2$, the relaxation rate σ can be used for deriving the penetration depth and estimating the superfluid density n_s/m^*. In high-quality single crystal specimens, the Fourier transform of the damping pattern exhibits an asymmetric field distribution expected for the triangular Abrikosov vortex lattice, as shown in Fig. 8.6c from μSR in YBCO single crystals [62]. In this case, the second moment of the field distribution, instead of the rate σ, is used to obtain the penetration depth.

The temperature dependence of the relaxation rate σ reflects the reduction of n_s caused by thermal excitations across the energy gap. Thanks to this feature, one can study the structure of gap nodes using TF-μSR results. Initial attempts to apply this to high-T_c cuprate superconductors were made mostly on polycrystalline ceramic specimens, which often exhibited behaviors consistent with an isotropic gap expected for s-wave paring. Measurements on high-quality single crystals were essential for reliable arguments concerning gap nodes. In Fig. 8.7, we depict a few representative results of the temperature dependence of the superfluid density, which have survived various subsequent checks by μSR and other methods. In 2-dimensional organic superconductors (BEDT-TTF)$_2$Cu(NCS)$_2$ and (BEDT-TTF)$_2$Cu[N(CN)$_2$]Br, μSR measurements of Le et al. [63] were among the first to indicate the existence of line nodes in the superconducting gap, from the T-linear variation of the superfluid density at low temperatures as shown in Fig. 8.7a, b. It was later confirmed from the directional dependence of the thermal conductivity [64] that this result is due to d-wave pairing.

Pioneering measurements of the penetration depth in YBCO single crystals were performed by Hardy et al. [65] using microwave methods. They provided the first evidence for d-wave superconducting pairing in high-T_c cuprate superconductors. Soon after that, Sonier et al. [66] performed μSR measurements on the same single crystal specimens and confirmed the T-linear dependence of the superfluid density at low temperatures, as shown in Fig. 8.7c expected for line nodes of d-wave superconductors. By now, the d-wave paring of YBCO has also been confirmed by phase sensitive methods [67, 68], ARPES, STM [69, 70], and many other measurements. More recently, Khasanov et al. [71] performed μSR measurements on de-twinned single crystals of YBCO, and found the signature of an effect arising from the CuO chain which leads to an additional feature of s-wave symmetry, as shown in Fig. 8.7d. This is an example of a multi-band effect seen in the superfluid density measurements. Detailed μSR studies of multi-band effects in FeAs and FeSe superconductors are currently underway [72].

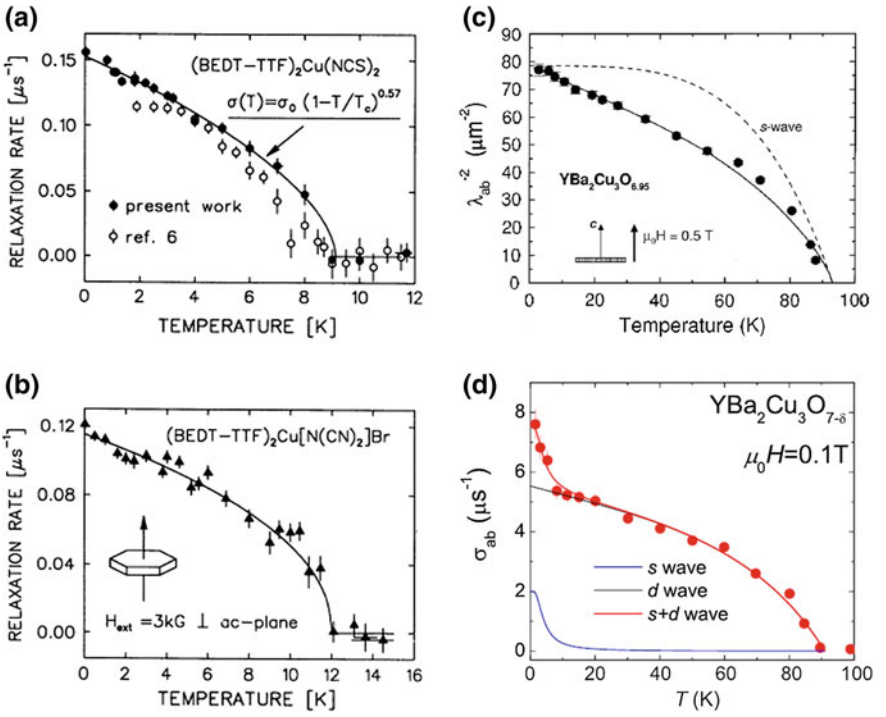

Fig. 8.7 **a, b** Muon spin relaxation rate in quasi 2 dimensional organic superconductor (**a**) κ (BEDT-TTF)$_2$Cu(NCS)$_2$ and (**b**) (BEDT-TTF)$_2$Cu[N(CN)$_2$]Br measured by Le et al. [63] with the external field perpendicular to the conducting ac plane. The T-linear variation of the superfluid density at low temperatures indicates line-nodes in the energy gap. Corresponding d-wave pairing with line-nodes was confirmed by a subsequent study of thermal conductivity [64]. **c** Muon spin relaxation rate in a single crystal of $YBa_2Cu_3O_7$ measured by Sonier et al. [66] with the external field perpendicular to the ab-plane. The *solid line* shows a fit to the variation expected for a d-wave pairing with line nodes, while the *dotted line* shows the behavior expected for an isotropic s-wave pairing. **d** Muon spin relaxation rate in a de-twinned single crystal of $YBa_2Cu_3O_7$ measured by Khasanov et al. [71] with the external field applied perpendicular to the ab-plane. The additional superfluid density seen at low temperatures is due to superconductivity in the CuO chain. This is one of the first results demonstrating the effect of multiple superconducting gaps

8.5 Correlation Between T_c, Superfluid Density, and Superfluid Fermi Energy

Soon after the discovery of high-T_c superconductors, several μSR groups started to measure the London penetration depth. Most of the measurements were performed with poly-crystalline ceramic specimens during the initial several years, due to a lack of high-quality single crystal specimens with sufficient charge doping levels. The observed muon spin relaxation rate was regarded to selectively reflect the in-plane penetration depth assuming the c-axis penetration depth to be much longer. In 1988 [73], we plotted the low temperature relaxation rate $\sigma(T\rightarrow 0)$ versus T_c to

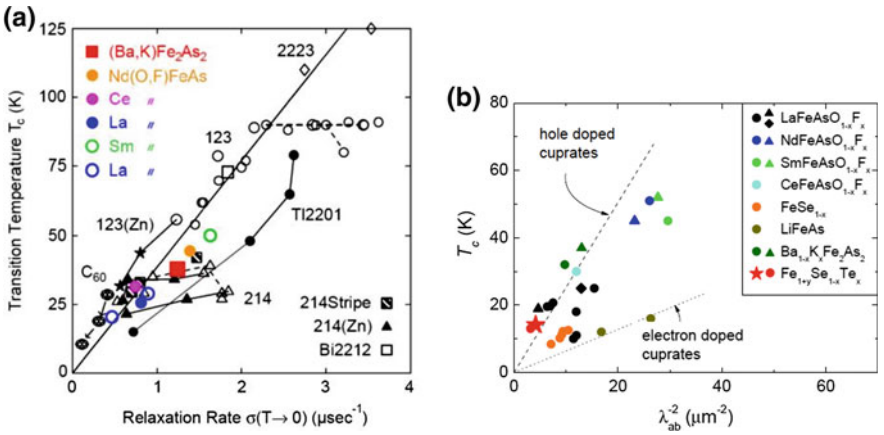

Fig. 8.8 **a** Plot of the superconducting transition temperature T_c versus the muon spin relaxation rate σ(T→0) for various unconventional superconductors (most updated plot from [85]). The horizontal axis represents the superfluid density n_s/m^* in the ground state. Original results were published by Uemura and co-workers for the 214, 123, and 2223 cuprates shown by the *open circle* in [73, 74], Zn-doped $(La,Sr)_2CuO_4$ (214) system in [96], the 214 system with static magnetism in partial volume fraction in [99], overdoped Tl2201 systems in [81], A_3C_{60} systems in [75, 76], and Fe-based superconductor systems in [78, 79]. One finds a general trend that T_c shows nearly linear correlations with the superfluid density, with a common proportionality constant for the 123, 2223, and Tl2201 cuprates, A_3C_{60}, and the 1111 and 122 FeAs superconductors. **b** The correlations between T_c and the superfluid density measured by Khasanov and co-workers in several families of Fe-based superconductors [80], compared with the trends of hole-doped and electron-doped cuprate systems. Although the proportionality constant (slope) varies significantly over different families, nearly linear trends can be seen for the results of each family of unconventional superconductors

study correlations between the superfluid density and T_c. Subsequent accumulation of the results on more than 10 different cuprate systems allowed us to establish [74] nearly linear correlations between T_c and n_s/m^* in the underdoped region of the 214, 123, and 2223 cuprate systems with single, double and triple CuO_2 layers, as shown in Fig. 8.8a.

Since these systems lie in the clean limit where the mean free path l_{mf} is much longer than the superconducting coherence length ξ, this relationship indicates that T_c is controlled by the superfluid density. In BCS theory, T_c is determined by the strength of the superconducting pairing proportional to the energy gap at the Fermi level, and only indirect and weak correlation is expected between T_c and the carrier density. In this sense, the μSR results of nearly linear correlations [74] represent one of the first signatures suggesting that condensation mechanisms for high-T_c cuprate systems may be fundamentally different from that of BCS superconductors.

Stimulated by these results on cuprates, we performed μSR measurements of the superfluid density also in other unconventional superconductors, including A_3C_{60} [75, 76], $(BEDT\text{-}TTF)_2Cu(NCS)_2$ [77], and $(Ba,K)BiO_3$ [77], and found that points from these systems lie close to the linear trend of the cuprates as shown in Fig. 8.8a. Our results on several representative systems of FeAs-based superconductors also

demonstrate a similar trend [78, 79] (see Fig. 8.8a). Accumulated results on FeAs superconductors, plotted by Bendele et al. [80] in Fig. 8.8b, exhibit a wider range of slopes, but still suggest the existence of a linear trend between T_c and the superfluid density.

In 1993, our research team [81] and a European μSR team [82] discovered that the points for overdoped Tl2201 and Tl2212 systems also lie along the monotonic relationship between T_c and the superfluid density (see Fig. 8.8a). This surprising signature indicates that the increase in normal state carrier density does not contribute to an increase in the superfluid density, contrary to the expectation of BCS condensation where all the conducting carriers participate in the superfluid regardless of the magnitude of the superconducting energy gap at the Fermi level. By now, a similar trend has been found in overdoped regions of the 214 cuprates, $CeCoIn_5$, $Ba(Fe,Co)_2As_2$ [83], and $Ba(Fe,Ni)_2As_2$ [84].

In a non-interacting 2-dimensional electron gas, the Fermi energy is proportional to the (areal) carrier density divided by the effective mass. This feature suggests that the superfluid density represents an energy scale of superconducting carriers. It is also useful to remember that n_s/m^* corresponds to the spectral weight of the "Drude" component which condenses into a delta function at zero frequency $\omega = 0$ below T_c. For highly 2-dimensional systems with strong anisotropy, such as cuprate superconductors, one can calculate the "effective Fermi energy" T_F by deriving the 2-d values of n_s/m^* from the μSR relaxation rate multiplied by the average distance between the conducting layers. For nearly isotropic 3-d systems, one can obtain the effective Fermi energy, proportional to $n^{2/3}/m^*$, by combining n_s/m^* with the Pauli susceptibility or the Sommerfeld constant which scales with $n^{1/3}$ times m^*. T_F may also be called the effective "Drude energy" or "superfluid energy".

We converted the superfluid density into such an "effective Fermi energy" T_F [77] and plotted it versus T_c in Fig. 8.9a [85]. For a given carrier density and mass, one can calculate the "idealized Bose Einstein condensation (BEC) temperature" T_B for the case that pairs two fermions with mass $2m^*$ form a tightly bound non-interacting boson gas (in the strong coupling limit) with the boson density $n/2$. As shown in Fig. 8.9a, the points for the cuprates, FeAs, A_3C_{60} and some of the heavy-fermion superconductors are parallel to the T_B line (dotted line). This feature indicates that the linear relationship may be originating from BEC. Figure 8.9a serves as an experimentalist's way to classify various existing superconductors and superfluids in the evolution from the BEC limit (close to T_B) to the BCS limit (with low T_c and high T_F with no correlations).

The actual transition temperatures of all the existing superconductors are reduced by at least a factor of 4–5 from the T_B line. It is also interesting to note that the point for superfluid ^{4}He lies closer to the T_B line but with about 50 % reduction, as the lambda point temperature 2.2 K in ambient pressure is reduced from $T_B = 3.2$ K calculated by the density and mass of liquid He. The point for cold atoms of ^{40}K, which exhibit BEC-BCS crossover [86], lies very close to the T_B line, as shown by a factor 10^8 multiplication for both horizontal and vertical axes. We will discuss the possible origin of the reduction of actual T_c from the T_B line in the subsequent sections.

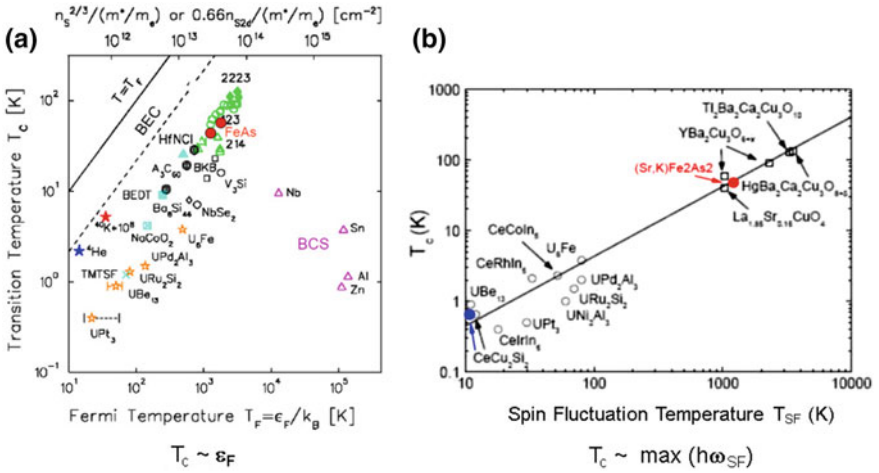

Fig. 8.9 **a** A plot of T_c versus the effective Fermi temperature T_F obtained from the superfluid density n_s/m^* of various superconducting systems, first attempted in [77] in 1991, and updated to include results from [63, 75, 76, 78, 79, 81] (adopted from Fig. 8.2b of [85]). We see an empirical upper limit $T_c/T_F \sim 0.05$ for superconducting systems. Also included are the corresponding points for the superfluid ^{4}He (blue star) and the ultracold ^{40}K [86] in the BEC–BCS crossover region (red star; with T_c and T_F both multiplied by 10^8). The T_B line shows the BE condensation temperature for the ideal non-interacting Bose gas of boson density $n_s/2$ and mass $2m^*$. This plot can be used to classify various unconventional superconductors in the evolution from BEC to BCS condensation. **b** A plot of T_c versus the spin-fluctuation energy scale T_{SF}, estimated theoretically based on the normal-state transport, susceptibility and specific-heat results for cuprates and heavy fermion systems made by Moriya and Ueda [87, 88]. Also included are points for $CeCu_2Si_2$ (*blue solid circle*) based on inelastic neutron scattering results [89, 90] and for (Sr,K)Fe_2As_2 (*red solid circle*) based on neutron scattering results of spin waves in [91]

8.6 Comparisons of Charge and Spin Energy Scales and BEC-BCS Crossover Picture

In an effort to understand the mechanisms of unconventional superconductors, various plots have been generated to see correlations between some key parameters and T_c, in a spirit similar to the development of Fig. 8.9a. One of them is the "Moriya-Ueda plot" [87, 88] shown in Fig. 8.9b for correlations between T_c and the "spin fluctuation energy scale T_{SF}", which is the energy of spin waves or paramagnetic spin fluctuations at the antiferromagnetic zone boundary. Moriya and Ueda derived T_{SF} from the normal state resistivity using their theory [87, 88], but the estimated energy is close to direct results from neutron scattering shown by colored points in Fig. 8.9b [89–91]. In BCS theory for weak-coupling superconductors, T_c is linearly proportional to the Debye frequency, or to the energy scale of pair-mediating bosons $\hbar\omega_B$ in a more general sense, which represents the range of energy integration in the gap equation. If spin fluctuations are playing the role of mediating bosons, and if the BCS theory is applicable to condensation, one would expect correlations

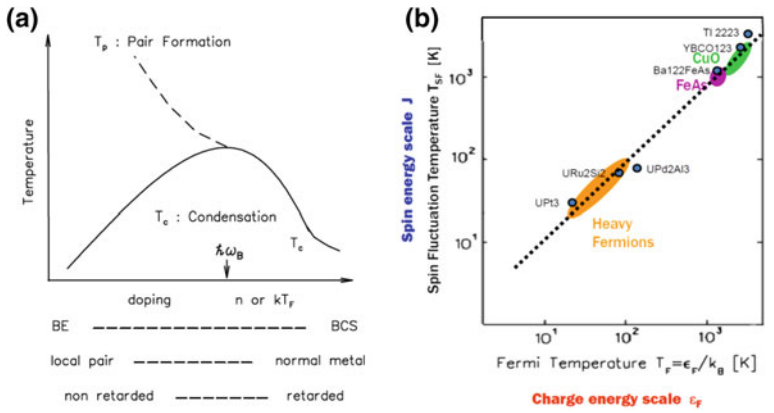

Fig. 8.10 **a** Schematic view of a crossover from Bose Einstein (BE) condensation to BCS condensation caused by increasing carrier density n, proposed by the present author in two conferences for unconventional superconductors held in 1994 [93, 94]. The T_p line represents an energy scale for pair formation (attractive interaction). By identifying T_p as the temperature T^* for the opening of the "pseudo-gap", this model can be mapped to the doping evolution of high-T_c cuprate superconductors. The normal state of the low-doping (underdoped) BEC side at $T_c < T < T_p$ is characterized by the co-existence of paired (2e) and unpaired (e) charges, while the condensation and pair formation occur at the same temperature in the BCS region. It is conjectured that the crossover region with maximum T_c is characterized by the comparable energy scales of charges (kT_F) and of the pairing-mediating bosons $\hbar\omega_B$, which would divide between the non-retarded and retarded interactions. **b** A plot of the charge energy scale T_F versus spin-fluctuation energy scale T_{SF} for selected superconductors based on the results shown in Fig. 8.9a, b. For superconducting pairing mediated by spin fluctuations, $k_B T_{SF}$ corresponds to the pair-mediating boson energy $\hbar\omega_B$. This figure shows that spin and charge energy scales are comparable in several prototypical cuprate, FeAs and heavy-fermion superconductors. A pairing mechanism based on resonance of the spin and charge energy scales was proposed by the present author in [85, 94]

between T_c and T_{SF}. The Moriya-Ueda plot Fig. 8.9b seems to support this scaling, and it is therefore often discussed as a main signature for pairing mediated by spin fluctuations in various unconventional superconductors.

By the early 1990s, the correlations between T_c and the superfluid density were recognized, and the pseudogap behaviors of underdoped cuprates were emerging in NMR, dc- and optical conductivity and ARPES measurements. Based on these observations, the present author proposed a model in 1994 [92, 93] to map the doping evolution of cuprate systems to a general concept of crossover from BEC to BCS condensation, as illustrated in Fig. 8.10a. The "pseudogap" temperature T^* can be identified as the pair formation temperature T_p. In the "BEC side" characterized by low carrier density, fermions (e) start to form bosonic pairs (2e) upon cooling below T_p, the temperature corresponding to energy of the attractive interaction. This energy scale represents a "two-body problem" irrelevant in principle to the particle density. The normal state below T_p is composed of a mixture of fermions (e) and pre-formed bosons (2e).

Upon further cooling, the system will come to a point where the thermal wavelength of a boson becomes comparable to the inter-boson distance. At this point, local superconducting phase coherence develops. In absence of restrictions from competing ground states and dimensionality, global phase coherence can prevail at this point, leading to superconducting BEC condensation. In this case, the condensation temperature T_c scales with the boson density as $T_c \propto n_B^{2/3}/m_B^*$. This process represents a "many body problem" related to the density of condensing bosons.

On the "BCS" side characterized by high particle density, the normal state contains fermions, while the condensation occurs simultaneously with the pair formation, as the particle-density restriction for condensation is readily satisfied. On the high density side, the characteristic energy scale of the system, the Fermi energy, is higher than the energy scale of pair mediating bosons $\hbar\omega_B$, and thus the interaction is "retarded". In the low density and strong-coupling limit, the attractive interaction $k_B T_p$ represents the energy scale of interaction-mediating bosons, similar to how the pion mass represents magnitude of the strong interaction in elementary particle physics, and this energy is larger than the Bose-gas energy scale represented by T_B. Thus the interaction in the BEC side is non-retarded. The present author proposed a conjecture that the crossover region from the BEC to BCS behaviors is characterized by comparable energy scales of particle gas (Fermi energy) and the pair-mediating bosons, i.e., Debye frequency for the case of phonon-mediated pairing and T_{SF} for the case of pairing mediated by spin fluctuations. The transition temperature T_c may exhibit a maximum around this point, as illustrated in Fig. 8.10a.

The T_c versus T_F plot of Fig. 8.9a suggests that T_c is determined by the energy scale of charges, while Fig. 8.9b suggests scaling of T_c with the energy of pair-mediating bosons. Therefore, these two figures are often considered to imply contradicting features. They are, however, both based on experimental data, and furthermore they look very much alike. By further inspection, one realizes that several representative unconventional superconductors have comparable values of the charge energy T_F and the spin energy T_{SF}, as demonstrated by Fig. 8.10b. These systems indeed satisfy the above-mentioned crossover criterion from BEC to BCS condensation.

The coincidence of the charge and spin energy scales in the systems shown in Fig. 8.10b can be accidental. However, it seems to the present author that $T_F \sim T_{SF}$ is the essential condition for having high T_c in given series of superconductors. The comparable energy scales suggests possible resonance of charge and spin behaviors. As we proposed in several papers after 2004 [85, 94, 95], this feature may help charges to move smoothly by "dynamically avoiding" frustration caused by spin patterns, similar to synchronized traffic light alternation (spin fluctuations) helping a smooth flow of cars (charges) in what we call "traffic-light resonance" [85]. Further detailed study of the crossover region of BEC-BCS evolution may possibly lead to a full understanding of unconventional superconductivity.

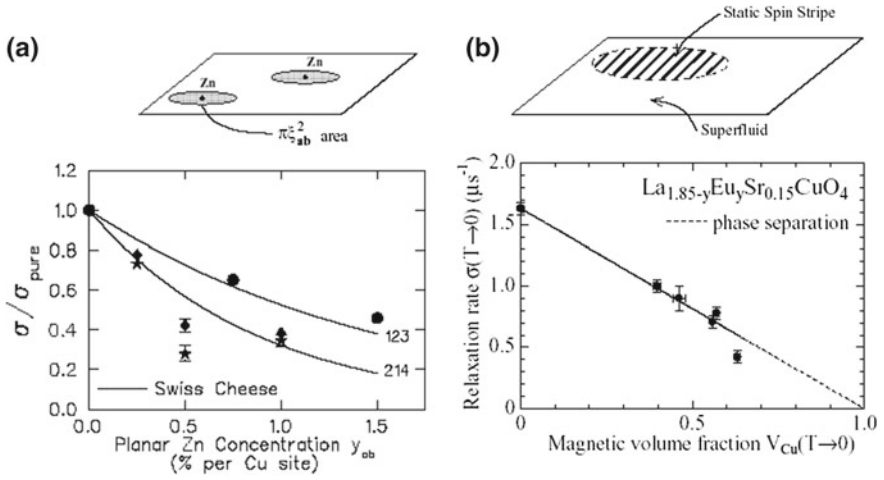

Fig. 8.11 **a** Muon spin relaxation rate $\sigma(T\rightarrow 0)$ measured in $La_{1.85}Sr_{0.15}CuO_4$ (214) and $YBa_2Cu_3O_7$ (123) cuprate systems with a small amount of (Cu,Zn) substitutions measured by Nachumi et al. [96]. The solid line represents the evolution of the superfluid density expected for the "Swiss Cheese model" where each Zn atom generates a normal region around Zn region on the CuO_2 plane with the radius corresponding to the in-plane superconducting coherence length ξ_{ab} as illustrated in the top figure. This situation was subsequently confirmed by an STM study of Davis and co-workers [97]. **b** A plot of the volume fraction of the regions with static magnetic order (horizontal axis) and the muon spin relaxation rate representing the superfluid density (vertical axis) measured by Kojima et al. [98] in $La_{1.85-y}Eu_ySr_{0.15}CuO_4$ with several different Eu concentrations. The trade-off suggests that regions with static magnetism do not carry superfluid, and the magnetic islands are phase separated from the surrounding superconducting regions without static magnetism, as illustrated in the *top* figure. The length scale of the magnetic island was estimated to be comparable to ξ_{ab} by Savici et al. in [99]

8.7 Phase Separation and Overlap of Superconducting and Magnetic States

μSR measurements of the superfluid density also provide unique information on spatial phase separation of superconducting and non-superconducting regions in several cuprate systems. In 214 and 123 cuprate systems with (Cu,Zn) substitutions, we noticed [96] that the reduction of the superfuid density with increasing Zn concentration fits well to a simple model in which each Zn atom generates a small non-superconducting area with a radius equal to the coherence length in the CuO_2 plane, as illustrated in Fig. 8.11a. This "Swiss Cheese Model" was subsequently confirmed by STM measurements of Davis and co-workers [97].

In LSCO cuprate superconductors, (La,Eu) substitution drives the system closer to static magnetic order with "stripe" spin charge correlations. Increasing (La,Eu) substitution in optimally doped LSCO with Sr0.15 reduces the superfluid density at $T \rightarrow 0$ (measured by TF-μSR) while increasing the volume fraction of regions with static magnetism (measured by ZF-μSR), as shown in Fig. 8.11b [98]. The trade-off

between magnetic volume and the superfluid density suggests that there is no superfluid in the volume with static magnetic order and superconductivity is supported by the remaining volume without static magnetism, as illustrated in Fig. 8.11b. In a similar system of over-oxygenated La_2CuO_4 [99], the size of the "magnetic islands" was estimated to be comparable to the coherence length ξ via analyses of the ZF-μSR spectra. Together with a similar study in La_2CuO_4 [100], these μSR results on cuprate systems suggest the tendency of the system towards microscopic and real-space phase separation between regions with and without superconductivity.

In FeAs superconductors, the parent antiferromagnetic (AF) phase is adjacent to the superconducting (SC) phase by a seemingly abrupt phase boundary, as shown in Fig. 8.3a, b. Coexistence of the AF and SC phases has been studied extensively by μSR [101, 102], in combination with optical conductivity in [101], and with six different probes in [102]. These studies generally point towards (1) overlap of the AF and SC orders in real space in the AF-SC border region, and (2) disappearance of the static AF phase with increasing charge doping by means of a reduction of the volume fraction of the AF phase rather than a reduction of the magnitude of the magnetic moment.

8.8 First Order Evolution, Roton-Analogue Resonance Mode, and Quantum Criticality

We have so far reported several signatures found by μSR which indicate heterogeneous behaviors and first-order evolution at quantum phase boundaries. They include: (a) the Swiss Cheese behavior in cuprates with (Cu,Zn) substitutions; (b) the phase separation in the 214 cuprates with (La,Eu) substitutions; (c) the reduction of the superfluid density with charge doping in the overdoped Tl2201; (d) microscopic overlap of the AF and SC phases in FeAs systems; and (e) gradual disappearance of the AF phase with decreasing volume fraction. These features are not expected in mean-field-like second order quantum phase transitions. We note that all the phase diagrams in Fig. 8.3 exhibit first-order evolution at quantum phase boundaries.

The phase diagram of superfluid ^{4}He in Fig. 8.3f has similarities to those of unconventional superconductors shown in Fig. 8.3. The superfluid (lambda) transition temperature 2.2 K of ^{4}He at ambient pressure is reduced from the ideal non-interacting Bose-gas condensation temperature $T_B = 3.2$ K. This is usually explained by the finite size of He atoms and their interaction with neighboring atoms. Another way to explain this reduction is to remember effects of the roton minimum, which provides a thermally excitable mode for the destruction of the superfluid condensate. In Fig. 8.12, we plot correlations between the roton energy and the lambda superfluid temperature measured at ambient and applied pressure [103]. Although data is limited to a small pressure region due to solidification of He, the condensation temperature exhibits a linear correlation with the roton energy. A roton represents short-range and dynamic atomic correlations of hcp He, being a soft mode existing

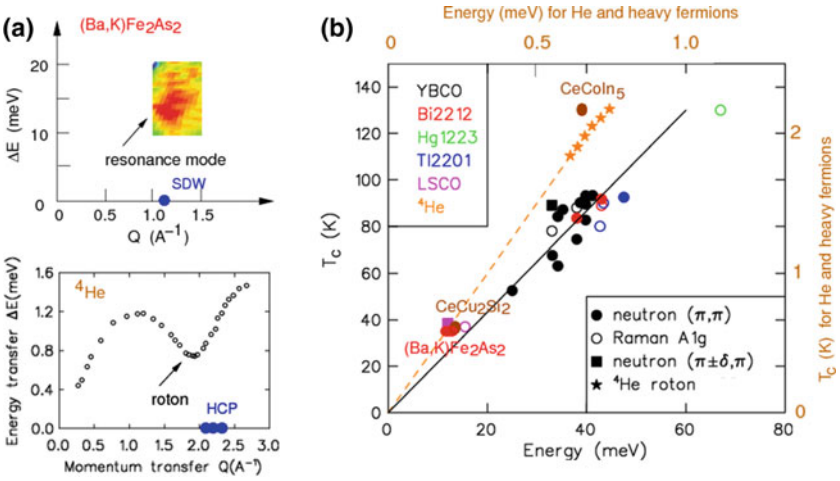

Fig. 8.12 **a** Dispersion relations for inelastic excitations in $(Ba,K)Fe_2As_2$ with the magnetic resonance mode measured by Christianson et al. [119] (*top*), and in superfluid ^{4}He with the roton minimum by Henshaw and Woods [120] (*bottom*). Filled *blue circles* denote the momentum transfer of the 2-dimensional (1/2, 1/2, 0) antiferromagnetic correlations (*top*) and of Bragg points of competing hexagonal closed-packed (HCP) solid phase of ^{4}He (*bottom*). **b** Correlations between the transition temperature T_c and the energy $\hbar\omega$ of the magnetic resonance mode observed in the superconducting state of the high-T_c cuprate systems [121, 122], $(Ba,K)Fe_2As_2$ [119], $CeCoIn_5$ [104], and $CeCu_2Si_2$ [105]. The *closed square* symbols denote the "spin-gap" energy obtained from the low-energy end of the hour-glass dispersion shape [122]. The *star symbols* represent the lambda-point superfluid transition temperature T_c and the roton energies in superfluid ^{4}He at ambient and applied pressure [103]. The *right-vertical* and *top-horizontal* axes for ^{4}He, $CeCoIn_5$ and $CeCu_2Si_2$ are both scaled by a factor 60 with respect to the left and bottom axes for the other systems. The aspect ratio is preserved, however, for direct comparisons of the slope $T_c/\hbar\omega$ of all the different systems. Updated after [94] and adopted from [14]

in momentum space close to the Bragg point of hcp He (see Fig. 8.12). The role played by rotons demonstrates how the competing (hcp solid) state can influence the situation (T_c) of the superfluid state via generating excitable inelastic soft modes [85, 93].

In several different unconventional superconductors, including cuprates, FeAs, and many heavy fermion systems, the SC phase is competing with AF phase. The so-called magnetic resonance mode, which is observed in the SC phase as an inelastic response near the AF wave vector, can be regarded as a soft mode due to the competing state [14, 85, 93–95], analogous to rotons in superfluid He. In Fig. 8.12, we plot the energy of the resonance mode versus T_c for some cuprate and FeAs systems using horizontal and vertical axes both 60 times larger than the ones used in the plot of superfluid He. Points for these superconductors exhibit nearly linear correlations, with the slope very close to that of rotons [14], suggesting similarities of these excitations in thermodynamically determining superconducting / superfluid T_c. We

also find a similar situation for heavy fermion superconductors $CeCoIn_5$ [104] and $CeCu_2Si_2$ [105] (plotted with the axes used for ^{4}He in Fig. 8.12).

Smallness of the soft-mode energy corresponds to closeness of the free energy of the superconducting state to that of the competing AF state. Thus, energetic closeness to the competing state can be regarded as an additional factor which controls T_c in unconventional superconductors via the thermodynamic effect of inelastic excitations. The effect of closeness to the magnetic state can be found in cuprate systems close to the stripe spin-charge orders. Comparing the 123 and 214 cuprate systems in Fig. 8.8a, we find that the former has higher T_c for the same value of the superfluid density, due to closeness of the latter system to AF order. The effect of the competing state can also be appreciated as the origin of the apparent upper-limit of T_c being 20–25 % of T_B as shown in Fig. 8.9a. Unconventional superconductors need to compete with AF (or in some cases charge density wave) phases. This reduces the free energy advantage for SC condensation which controls T_c. In contrast, dilute cold atoms do not have to compete with other ground states, and this makes the point for ^{40}K lying close to the T_B line in Fig. 8.10a.

8.9 Future Outlook

First-order behavior in the quantum phase evolution may be an essential factor in having an inelastic soft mode. Up to now, studies on the roles of quantum criticality have been focused on second order transitions and theoretical considerations. In actual systems, SC phases appear in the process of "avoiding" a quantum critical point. Furthermore, many actual systems exhibit strong indications of first-order like evolution and the intrinsic role of heterogeneity. Recent studies of nanoscale optical responses have revealed real-space images of intrinsic phase separation and history-dependent behaviors in the Mott metal-insulator transition of VO_2 and other systems [106]. Comparisons of first-order transitions in superconducting and non-superconducting systems would be very important for better understanding unconventional superconductors, and μSR can certainly play a major role in this effort.

μSR has a superb and unique sensitivity to static magnetic order even with small ordered moments in random/dilute spin configurations, providing information of volume fractions separately from that of the moment size [99, 107, 108]. Thanks to this feature, μSR results can be nicely complementary to those from other methods obtained on the same specimens, as discussed in Sects. 8.3 and 8.7. We recently performed [102] measurements of $Ba(Fe,Ni)_2As_2$ by μSR, neutron, Moessbauer, specific heat, optical conductivity and STM methods. Such "multiprobe" studies will be highly effective in revealing subtle features near phase boundaries.

The detection of time reversal symmetry breaking by μSR will become a very important activity in elucidating topological systems. Currently, we do not have a good understanding of how the local field at muon sites is generated by the TRS broken state, nor can we provide reliable estimates of the magnitude of that field. Further studies on this point are necessary. In studies of correlations between T_c and

the superfluid density, we notice several systems lying close to "dirty limit", such as BKBO and topological superconductors (Sn,In)Te and $Cu_xBe_2Se_3$. It would be very rewarding to study the effects of carrier scattering in superfluid density and include the results in the phenomenology of BEC-BCS crossover.

The present author has a feeling that the closeness of the spin and charge energy scales demonstrated in Fig. 8.10b, based on results in Fig. 8.9a, b, may be one of the most important elements of the mechanisms for unconventional superconductors. It would be very important to elucidate the crossover region of BEC-BCS evolution and study possible resonance behavior between the charge and mediator-boson energy scales. We can also make further effort to integrate the effects of competing states and quantum criticality in general arguments of BEC-BCS crossover, in view of our findings discussed in Sects. 8.7 and 8.8.

Acknowledgments The author would like to thank Graeme Luke for collaboration on μSR studies continuing since 1988, all the authors of cited μSR references for their important contributions on studies of unconventional superconductors, and to members of Super-PIRE for collaboration on recent multiprobe studies on FeAs superconductors. This work was supported by US NSF with the individual grant DMR-1105961 and PIRE project OISE-0968226, and by JAEA with the Reimei project.

References

1. R.L. Garwin, L.M. Lederman, M. Weinrich, Observation of the failure of conservation of parity and charge conjugation in meson decays: the magnetic moment of the free muon. Phys. Rev. **105**, 1415–1417 (1957)
2. C.S. Wu, E. Ambler, R.W. Hayward, D.D. Hoppes, R.P. Hudson, Experimental test of parity conservation in beta-decay. Phys. Rev. **105**, 1413–1415 (1957)
3. J.I. Friedman, V.L. Telegdi, Nuclear emulsion evidence for parity nonconservation in the decay chain $\pi^+ - \mu^+ - \epsilon^+$. Phys. Rev. **105**, 1681–1682 (1957)
4. T.D. Lee, A brief-history of the muon. Hyperfine Interact. **86**, 439–453 (1994)
5. For general aspects and historical development of μSR, see Proceedings of twelve international conferences on muon spin rotation / relaxation/ resonance in Hyperfine Interact. **6** (1979); **8** (1981); **17–19** (1984); **31** (1986); **63–65** (1990); **85–87** (1994); **104–106** (1997); Physica **B 289–290** (2000); **B 326**(2003); **B 374–375** (2006); **B 404** (2009); Physics Procedia **30** (2012)
6. A. Schenck, *Muon Spin Rotation Spectroscopy* (Hilger, Bristol, 1985)
7. S.L. Lee, S.H. Kilcoyne, and R. Cywinski (ed.), Muon Science: Muons in Physics, Chemistry and Materials, in *Proceedings of the Fifty First Scottish Universities Summer School in Physics*, St. Andrews, 1998, Inst. of Physics Publishing, Bristol, 1999
8. R.H. Heffner and K. Nagamine (ed.), Special Issue on μSR: muon spin rotation, relaxation or resonance, J. Phys.: Condens. Matter **16** (2004) S4403–S4806
9. A. Yaouanc, P. Dalmas de Rotier, *Muon Spin Rotation, Relaxation, and Resonance : Applications to Condensed Matter* (Oxford University Press, Oxford, 2011)
10. J.E. Sonier, MuSR Brochure, http://musr.ca/intro/musr/muSRBrochure.pdf
11. Y.J. Uemura, W.J. Kossler, X.H. Yu, J.R. Kempton, H.S. Chen, D. Opie, C.E. Stronach, D.C. Johnston, M.S. Alvarez, D.P. Goshorn, Antiferromagnetism of La_2CuO_{4-y} studied by muon spin rotation. Phys. Rev. Lett. **59**, 1045–1048 (1987)
12. Y.J. Uemura, W.J. Kossler, X.H. Yu, H.E. Schoene, J.R. Kempton, C.E. Stronach, S. Barth, F.N. Gygax, B. Hitti, A. Schenck, C. Baines, W.F. Lankford, Y. Ooniki, T. Komatsubara,

Coexisting static magnetic order and superconductivity in $CeCu_{2.1}Si_2$ found by muon spin relaxation. Phys. Rev. **B39**, 4726–4729 (1989)
13. L.P. Le, A. Keren, G.M. Luke, B.J. Sternlieb, W.D. Wu, Y.J. Uemura, J.H. Brewer, T.M. Riseman, R.V. Upasani, L.Y. Chiang, W. Kang, P.M. Chaikin, T. Csiba, G. Gruner, Muon spin rotation/relaxation studies in $(TMTSF)_2$-X compounds. Phys. Rev. **B48**, 7284–7296 (1993)
14. Y.J. Uemura, Superconductivity: exotic commonalities in phase and mode. Nat. Mater. **8**, 253–255 (2009)
15. H. Luetkens, H.-H. Klauss, M. Kraken, F.J. Litterst, T. Dellmann, R. Klingeler, C. Hess, R. Khasanov, A. Amato, C. Baines, M. Kosmala, O.J. Schumann, M. Braden, J. Hamann-Borrero, N. Leps, A. Kondrat, G. Behr, J. Werner, B. Buechner, Electronic phase diagram of the $LaO_{1-x}F_xFeAs$ superconductor. Nat. Mater. **8**, 305–309 (2009)
16. S. Sanna, G. Allodi, G. Concas, A.D. Hillier, R. De Renzi, Nanoscopic coexistence of magnetism and superconductivity in $YBa_2Cu_3O_{6+x}$ detected by muon spin rotation. Phys. Rev. Lett. **93**, 207001 (2004)
17. J. Arvanitidis, K. Papagelis, Y. Takabayashi, T. Takenobu, Y. Iwasa, M.J. Rosseinsky, K. Prassides, Magnetic ordering in the ammoniated alkali fullerides $(NH_3)K_{3-x}Rb_xC_{60}$ (x = 2, 3). J. Phys.: Condens. Matter **19**, 386235 (2007)
18. J.P. Carlo, T. Goko, I.M. Gat-Malureanu, P.L. Russo, A.T. Savici, A.A. Aczel, G.J. MacDougall, J.A. Rodriguez, T.J. Williams, G.M. Luke, C.R. Wiebe, Y. Yoshida, S. Nakatsuji, Y. Maeno, T. Taniguchi, Y.J. Uemura, New magnetic phase diagram of $(Sr, Ca)_2RuO_4$. Nat. Mater. **11**, 323–328 (2012)
19. S. Nakatsuji, D. Hall, L. Balicas, Z. Fisk, K. Sugahara, M. Yoshioka, Y. Maeno, Heavy-mass fermi liquid near a ferromagnetic instability in layered ruthenates. Phys. Rev. Lett. **90**, 137202 (2003)
20. A.F. Hebard, M.J. Rosseinsky, R.C. Haddon, D.W. Murphy, S.H. Glarum, T.T.M. Palstra, A.P. Ramirez, A.R. Kortan, Superconductivity at 18 K in potassium-doped C_{60}. Nature **350**, 600–601 (1991)
21. M.J. Rosseinsky, A.P. Ramirez, S.H. Glarum, D.W. Murphy, R.C. Haddon, A.F. Hebard, T.T.M. Palstra, A.R. Kortan, S.M. Zahurak, A.V. Makhija, Superconductivity at 28 K in Rb_xC_{60}. Phys. Rev. Lett. **66**, 2830–2832 (1991)
22. Y. Takabayashi, A.Y. Ganin, P. Jegli, D. Aron, T. Takano, Y. Iwasa, Y. Ohishi, M. Takata, N. Takeshita, K. Prassides, M.J. Rosseinsky, The disorder-free non-BCS superconductor Cs_3C_{60} emerges from an antiferromagnetic insulator parent state. Science **323**, 1585–1590 (2009)
23. A.Y. Ganin, Y. Takabayashi, P. Jeglic, D. Arcon, A. Potocnik, P.J. Baker, Y. Ohishi, M.T. McDonald, M.D. Tzirakis, A. McLennan, G.R. Darling, M. Takata, M.J. Rosseinsky, K. Prassides, Polymorphism control of superconductivity and magnetism in Cs_3C_{60} close to the Mott transition. Nature **466**, 221–225 (2010)
24. Y.J. Uemura, B.J. Sternlieb, D.E. Cox, J.H. Brewer, R. Kadono, J.R. Kempton, R.F. Kiefl, S.R. Kreitzman, G.M. Luke, P. Mulhern, T.M. Riseman, D. Ll Williams, W.J. Kossler, X.H. Yu, C.E. Stronach, M.A. Subramanian, J. Goparakrishnan, A.W. Sleight, Absence of magnetic order in (Ba, K)BiO_3. Nature **335**, 151–152 (1988)
25. F. von Rohr, A. Schilling, R. Nesper, Ch. Baines, M. Bendele, Conventional superconductivity and charge-density-wave ordering in $Ba_{1-x}Na_xTi_2Sb_2O$, Phys. Rev. **B 88** (2013) 140501 (R)
26. Y. Nozaki, K. Nakano, T. Yajima, H. Kageyama, B. Frandsen, L. Liu, S. Cheung, T. Goko, Y.J. Uemura, T.S.J. Munsie, T. Medina, G.M. Luke, J. Munevar, D. Nishio-Hamane, C.M. Brown, Muon spin relaxation and electron/neutron diffraction studies of $BaTi_2(As_{1-x}Sb_x)_2O$: Absence of static magnetism and superlattice reflections. Phys. Rev. B **88**, 214506 (2013)
27. E. Morosan, H.W. Zandbergen, B.S. Dennis, J.W.G. Bos, Y. Onose, T. Klimczuc, A.P. Ramirez, N.P. Ong, R.J. Cava, Superconductivity in Cu_xTiSe_2. Nat. Phys. **2**, 544–550 (2006)
28. M. Zaberchik, K. Chashka, L. Patlgan, A. Maniv, Ch. Baines, P. King, A. Kanigel, Possible evidence of a two-gap structure for the Cu_xTiSe_2 superconductor, Phys. Rev. **B 81** (2010) 220505 (R)
29. R.S. Hayano, Y.J. Uemura, J. Imazato, N. Nishida, T. Yamazaki, R. Kubo, Zero- and low-field spin relaxation studied by positive muon. Phys. Rev. **B20**, 850–859 (1979)

30. R.H. Heffner, J.L. Smith, J.O. Willis, P. Birrer, C. Baines, F.N. Gygax, B. Hitti, E. Lippelt, H.R. Ott, A. Schenck, E.A. Knetsch, J.A. Mydosh, D.E. MacLaughlin, New phase diagram for (U, Th)Be_{13}: a muon-spin-resonance and H_{C1} study. Phys. Rev. Lett. **65**, 2816–2819 (1990)
31. G.M. Luke, A. Keren, L.P. Le, W.D. Wu, Y.J. Uemura, D.A. Bonn, L. Taillefer, J.D. Garrett, Muon spin relaxation in UPt_3. Phys. Rev. Lett. **71**, 1466–1469 (1993)
32. Y. Maeno, H. Hashimoto, K. Yoshida, S. Nishizaki, T. Fujita, J.G. Bednorz, F. Lichtenberg, Superconductivity in a layered perovskite without copper. Nature **372**, 532–534 (1994)
33. G.M. Luke, Y. Fudamoto, K.M. Kojima, M.L. Larkin, J. Merrin, B. Nachumi, Y.J. Uemura, Y. Maeno, Z.Q. Mao, Y. Mori, H. Nakamura, M. Sigrist, Time-reversal symmetry breaking superconductivity in Sr_2RuO_4. Nature **394**, 558–561 (1998)
34. K. Ishida, H. Mukuda, Y. Kitaoka, K. Asayama, Z.Q. Mao, Y. Mori, Y. Maeno, Spin-triplet superconductivity in Sr_2RuO_4 identified by O-17 Knight shift, Nature **394** 658–660 (1998)
35. K. Ishida, Y. Kitaoka, K. Asayama, S. Ikeda, S. Nishizaki, Y. Maeno, K. Yoshida, T. Fujita, Anisotropic pairing in superconducting Sr_2RuO_4: Ru NMR and NQR studies. Phys. Rev. B **56**, R505–R508 (1997)
36. A.P. Mackenzie, Y. Maeno, The superconductivity of Sr_2RuO_4 and the physics of spin-triplet pairing. Rev. Mod. Phys. **75**, 657–712 (2003)
37. J. Xia, Y. Maeno, P.T. Beyersdorf, M.M. Fejer, A. Kapitulnik, High resolution polar kerr effect measurements of Sr_2RuO_4: evidence for broken time-reversal symmetry in the superconducting state. Phys. Rev. Lett. **97**, 167002 (2006)
38. Y. Aoki, A. Tsuchiya, T. Kanayama, S.R. Saha, H. Sugawara, H. Sato, W. Higemoto, A. Koda, K. Ohishi, K. Nishiyama, R. Kadono, Time-reversal symmetry-breaking superconductivity in heavy-fermion $PrOs_4Sb_{12}$ detected by muon-spin relaxation. Phys. Rev. Lett. **91**, 067003 (2003)
39. A. Maisuradze, W. Schnelle, R. Khasanov, R. Gumeniuk, M. Nicklas, H. Rosner, A. Leithe-Jasper, Yu. Grin, A. Amato, P. Thalmeier, Evidence for time-reversal symmetry breaking in superconducting $PrPt_4Ge_{12}$. Phys. Rev. B **82**, 024524 (2010)
40. A.D. Hillier, J. Quintanilla, R. Cywinski, Evidence for time-reversal symmetry breaking in the noncentrosymmetric superconductor $LaNiC_2$. Phys. Rev. Lett. **102**, 117007 (2009)
41. A.D. Hillier, J. Quintanilla, B. Mazidian, J.F. Annett, R. Cywinski, Nonunitary triplet pairing in the centrosymmetric superconductor $LaNiGa_2$. Phys. Rev. Lett. **109**, 097001 (2012)
42. P.K. Biswas, H. Luetkens, 1, T. Neupert, T. Sturzer, C. Baines, G. Pascua, A.P. Schnyder, M.H. Fischer, J. Goryo, M. R. Lees, H. Maeter, F. Bruckner, H.-H. Klauss, M. Nicklas, P.J. Baker, A.D. Hillier, M. Sigrist, A. Amato, D. Johrendt, *Evidence for superconductivity with broken time-reversal symmetry in locally noncentrosymmetric SrPtAs*. Phys. Rev. B **87**, 180503(R) (2013)
43. A.A. Aczel, T.J. Williams, T. Goko, J.P. Carlo, W. Yu, Y.J. Uemura, T. Klimczuk, J.D. Thompson, R.J. Cava, G.M. Luke, Muon spin rotation/relaxation measurements of the noncentrosymmetric superconductor $Mg_{10}Ir_{19}B_{16}$. Phys. Rev. B **82**, 024520 (2010)
44. V.K. Anand, A.D. Hillier, D.T. Adroja, A.M. Strydom, H. Michor, K.A. McEwen, B.D. Rainford, Specific heat and μSR study on the noncentrosymmetric superconductor $LaRhSi_3$. Phys. Rev. B **83**, 064522 (2011)
45. P.K. Biswas, A.D. Hillier, M.R. Lees, DMcK Paul, Comparative study of the centrosymmetric and noncentrosymmetric superconducting phases of Re_3W using muon spin spectroscopy and heat capacity measurements. Phys. Rev. B **85**, 134505 (2012)
46. T. Goko, Y. Ando, M. Kriener, G. Gu, B. Frandsen, Y.J. Uemura et al., unpublished work
47. B. Fauque, Y. Sidis, V. Hinkov, S. Pailhes, C.T. Lin, X. Chaud, P. Bourges, Magnetic order in the pseudogap phase of high-T_c superconductors. Phys. Rev. Lett. **96**, 197001 (2006)
48. H.A. Mook, Y. Sidis, B. Fauqu, V. Baldent, P. Bourges, Observation of magnetic order in a superconducting $YBa_2Cu_3O_{6.6}$ single crystal using polarized neutron scattering, Phys. Rev. B **78** (2008) 020506 (R)
49. Y. Li, V. Baledent, N. Barisic, Y. Cho, B. Fauque, Y. Sidis, G. Yu, X. Zhao, P. Bourges, M. Greven, Unusual magnetic order in the pseudogap region of the superconductor $HgBa_2CuO_{4+\delta}$. Nature **455**, 372–375 (2008)

50. C.M. Varma, Non-fermi-liquid states and pairing instability of a general model of copper oxide metals. Phys. Rev. B **55**, 14554–14580 (1997)
51. C.M. Varma, Theory of the pseudogap state of the cuprates. Phys. Rev. B **73**, 155113 (2006)
52. R.F. Kiefl, J.H. Brewer, I. Affleck, J.F. Carolan, P. Dosanjh, W.N. Hardy, T. Hsu, R. Kadono, J.R. Kempton, S.R. Kreitzman, Q. Li, A.H. O'Reilly, T.M. Riseman, P.W. Schleger, P. Stamp, Hu Zhou, L.P. Le, G.M. Luke, B.J. Sternlieb, Y.J. Uemura, H.R. Hart, K.W. Ley, Search for anomalous internal magnetic fields in high-T_c superconductors as evidence for broken time reversal symmetry. Phys. Rev. Lett. **64**, 2082–2085 (1990)
53. G.J. MacDougall, A.A. Aczel, J.P. Carlo, T. Ito, J. Rodriguez, P.L. Russo, Y.J. Uemura, S. Wakimoto, G.M. Luke, Absence of time reversal symmetry breaking in $La_{2-x}Sr_xCuO_4$. Phys. Rev. Lett. **101**, 017001 (2008)
54. W. Huang, V. Pacradouni, M.P. Kennett, S. Komiya, J.E. Sonier, Precision search for magnetic order in the pseudogap regime of $La_{2-x}Sr_xCuO_4$ by muon spin relaxation. Phys. Rev. B **85**, 104527 (2012)
55. J.E. Sonier, J.H. Brewer, R.F. Kiefl, R.I. Miller, G.D. Morris, C.E. Stronach, J.S. Gardner, S.R. Dunsiger, D.A. Bonn, W.N. Hardy, R. Liang, R.H. Heffner, Anomalous weak magnetism in superconducting $YBa_2Cu_3O_{6+x}$. Science **292**, 1692–1695 (2001)
56. J.E. Sonier, V. Pacradouni, S.A. Sabok-Sayr, W.N. Hardy, D.A. Bonn, R. Liang, H.A. Mook, Detection of the unusual magnetic orders in the pseudogap region of a high-temperature superconducting $YBa_2Cu3O_{6.6}$ crystal by muon-spin relaxation. Phys. Rev. Lett. **103**, 167002 (2009)
57. S. Strassle, J. Roos, M. Mali, H. Keller, T. Ohno, Lack of evidence for orbital-current effects in the high-temperature $Y_2Ba_4Cu_7O_{15-\delta}$ superconductor using ^{89}Y nuclear magnetic resonance. Phys. Rev. Lett. **101**, 237001 (2008)
58. S. Strassle, B. Graneli, M. Mali, J. Roos, H. Keller, Absence of orbital currents in superconducting $YBa_2Cu_4O_8$ using a Zeeman-perturbed nuclear-quadrupole-resonance technique. Phys. Rev. Lett. **106**, 097003 (2011)
59. J. Xia, E. Schemm, G. Deutscher, S.A. Kivelson, D.A. Bonn, W.N. Hardy, R. Liang, W. Siemons, G. Koster, M.M. Fejer, A. Kapitulnik, Polar Kerr-effect measurements of the high-temperature YBa_2Cu3O_{6+x} superconductor: evidence for broken symmetry near the pseudogap temperature. Phys. Rev. Lett. **100**, 127002 (2008)
60. H. Karapetyan, M. Hucker, G.D. Gu, J.M. Tranquada, M.M. Fejer, J. Xia, A. Kapitulnik, Magneto-optical measurements of a cascade of transitions in superconducting $La_{1.875}Ba_{0.125}CuO_4$ single crystals. Phys. Rev. Lett. **109**, 147001 (2012)
61. R.E. Allen, *The London-Anderson-Englert-Brout-Higgs-Guralnik-Hagen-Kibble-Weinberg mechanism and Higgs boson reveal the unity and future excitement of physics*, arXiv:1306.4061 [hep-ph]
62. J.E. Sonier, J.H. Brewer, R.F. Kiefl, μSR studies of the vortex state in type-II superconductors. Rev. Mod. Phys. **72**, 769–811 (2000)
63. L.P. Le, G.M. Luke, B.J. Sternlieb, W.D. Wu, Y.J. Uemura, J.H. Brewer, T.M. Riseman, C.E. Stronach, G. Saito, H. Yamochi, H.H. Wang, A.M. Kini, K.D. Carlson, J.M. Williams, μSR measurement of magnetic penetration depth in organic superconductors (BEDT-TTF)$_2$-X: X=Cu(NCS)$_2$ and Cu[N(CN)$_2$]Br. Phys. Rev. Lett. **68**, 1923–1926 (1992)
64. K. Izawa, H. Yamaguchi, T. Sasaki, Y. Matsuda, Superconducting gap structure of κ-(BEDT-TTF)$_2$Cu(NCS)$_2$ probed by thermal conductivity tensor. Phys. Rev. Lett. **88**, 027002 (2002)
65. W.N. Hardy, D.A. Bonn, D.C. Morgan, R.X. Liang, K. Zhang, Precision measurements of the temperature dependence of λ in $YBa_2Cu_3O_{6.95}$: Strong evidence for nodes in the gap function. Phys. Rev. Lett. **70**, 3999–4002 (1993)
66. J.E. Sonier, R.F. Kiefl, J.H. Brewer, D.A. Bonn, J.F. Carolan, K.H. Chow, P. Dosanjh, N. Hardy, R.X. Liang, W.A. MacFarlane, P. Mendels, G.D. Morris, T.M. Riseman, J.W. Schneider, New muon-spin-rotation measurement of the temperature dependence of the magnetic penetration depth in $YBa_2Cu_30_{6.95}$. Phys. Rev. Lett. **72**, 744–747 (1994)
67. C.C. Tsuei, J.R. Kirtley, Pairing symmetry in cuprate superconductors. Rev. Mod. Phys. **72**, 969–1016 (2000)

68. D.J. Van Harlingen, Phase-sensitive tests of the symmetry of the pairing state in the high-temperature superconductors: evidence for $d_{x^2-y^2}$ symmetry. Rev. Mod. Phys. **67**, 515–535 (1995)
69. A. Damascelli, Z. Hussain, Z.-X. Shen, Angle-resolved photoemission studies of the cuprate superconductors. Rev. Mod. Phys. **75**, 473–541 (2003)
70. K. McElroy, R.W. Simmonds, J.E. Hoffman, D.-H. Lee, J. Orenstein, H. Eisaki, S. Uchida, J.C. Davis, Relating atomic-scale electronic phenomena to wave-like quasiparticle states in superconducting $Bi_2Sr_2CaCu_2O_{8+\delta}$. Nature **422**, 592–596 (2003)
71. R. Khasanov, S. Strassle, D. Di Castro, T. Masui, S. Miyasaka, S. Tajima, A. Bussmann-Holder, H. Keller, Multiple gap symmetries for the order parameter of Cuprate superconductors from penetration depth measurements. Phys. Rev. Lett. **99**, 237601 (2007)
72. see, for example, R. Khasanov, D.V. Evtushinsky, A. Amato, H.-H. Klauss, H. Luetkens, Ch. Niedermayer, B. Buchner, G.L. Sun, C.T. Lin, J.T. Park, D.S. Inosov, V. Hinkov,*Two-Gap Superconductivity in* $Ba_{1-x}K_xFe_2As_2$ *: A Complementary Study of the Magnetic Penetration Depth by Muon-Spin Rotation and Angle-Resolved Photoemission,* Phys. Rev. Lett. **102** (2009) 187005.
73. Y.J. Uemura, V.J. Emery, A.R. Moodenbaugh, M. Suenaga, D.C. Johnston, A.J. Jacobson, J.T. Lewandowski, J.H. Brewer, R.F. Kiefl, S.R. Kreitzman, G.M. Luke, T.M. Riseman, C.E. Stronach, W.J. Kossler, J.R. Kempton, X.H. Yu, D. Opie, H.E. Schone, Systematic variation of magnetic-field penetration depth in high-T_c superconductors studied by muon spin relaxation. Phys. Rev. **B38**, 909–912 (1988)
74. Y.J. Uemura, G.M. Luke, B.J. Sternlieb, J.H. Brewer, J.F. Carolan, W.N. Hardy, R. Kadono, J.R. Kempton, R.F. Kiefl, S.R. Kreitzman, P. Mulhern, T.M. Riseman, D. LI Williams, B.X. Yang, S. Uchida, H. Takagi, J. Goparakrishnan, A.W. Sleight, M.A. Subramanian, C.L. Chien, M.Z. Cieplak, G. Xiao, V.Y. Lee, B.W. Statt, C.E. Stronach, W.J. Kossler, X.H. Yu, Universal correlations between Tc and n_s/m^* (carrier density over effective mass) in high-T_c Cuprate superconductors. Phys. Rev. Lett. **62**, 2317–2320 (1989)
75. Y.J. Uemura, A. Keren, G.M. Luke, L.P. Le, B.J. Sternlieb, W.D. Wu, J.H. Brewer, R.L. Whetten, S.M. Huang, S. Lin, R.B. Kaner, F. Diederich, S. Donovan, G. Gruner, K. Holczer, Magnetic field penetration depth in K_3C_{60} measured by muon spin relaxation. Nature **352**, 605–607 (1991)
76. Y.J. Uemura, A. Keren, L.P. Le, G.M. Luke, W.D. Wu, J.S. Tsai, K. Tanigaki, K. Holczer, S. Donovan, R.L. Whetten, System dependence of the magnetic-field penetration depth in C_{60} superconductors. Physica **C 235–240**, 2501–2502 (1994)
77. Y.J. Uemura, L.P. Le, G.M. Luke, B.J. Sternlieb, W.D. Wu, J.H. Brewer, T.M. Riseman, C.L. Seaman, M.B. Maple, M. Ishikawa, D.G. Hinks, J.D. Jorgensen, G. Saito, H. Yamochi, Basic similarities among Cuprate, Bismuthate, Organic, Chevrel phase, and heavy-fermion superconductors shown by penetration depth measurements. Phys. Rev. Lett. **66**, 2665–2668 (1991)
78. J.P. Carlo, Y.J. Uemura, T. Goko, G.J. MacDougall, J.A. Rodriguez, W. Yu, G.M. Luke, P. Dai, N. Shannon, S. Miyasaka, S. Suzuki, S. Tajima, G.F. Chen, W.Z. Hu, J.L. Luo, N.L. Wang, Static magnetic order and superfluid density of RFeAs(O, F) (R=La, Nd, Ce) and LaFePO studied by muon spin relaxation: unusual similarities with the behavior of Cuprate superconductors. Phys. Rev. Lett. **102**, 087001 (2009)
79. T. Goko, A.A. Aczel, E. Baggio-Saitovitch, S.L. Bud'ko, P.C. Canfield, J.P. Carlo, G.F. Chen, P. Dai, A.C. Hamann, W.Z. Hu, H. Kageyama, G.M. Luke, J.L. Luo, B. Nachumi, N. Ni, D. Reznik, D.R. Sanchez-Candela, A.T. Savici, K.J. Sikes, N.L. Wang, C.R. Wiebe, T.J. Williams, T. Yamamoto, W. Yu, Y.J. Uemura, Superconductivity coexisting with phase-separated static magnetic order in (Ba, K)Fe_2As_2, (Sr, Na)Fe_2As_2 and $CaFe_2As_2$. Phys. Rev. B **80**, 024508 (2009)
80. M. Bendele, S. Weyeneth, R. Puzniak, A. Maisuradze, E. Pomjakushina, K. Conder, V. Pomjakushin, H. Luetkens, S. Katrych, A. Wisniewski, R. Khasanov, H. Keller, Anisotropic superconducting properties of single-crystalline $FeSe_{0.5}Te_{0.5}$. Phys. Rev. B **81**, 224520 (2010)

81. Y.J. Uemura, A. Keren, L.P. Le, G.M. Luke, W.D. Wu, Y. Kubo, Y. Shimakawa, M. Subramanian, J.L. Cobb, J.T. Markert, Magnetic-field penetration depth in $Tl_2Ba_2CuO_{6+\delta}$ in the overdoped regime. Nature **364**, 605–607 (1993)
82. Ch. Niedermayer, C. Bernhard, U. Binninger, H. Glckler, J.L. Tallon, E.J. Ansaldo, J.I. Budnick, Muon spin rotation study of the correlation between Tc and n_s/m^* in overdoped $Tl_2Ba_2CuO_{6+\delta}$. Phys. Rev. Lett. **71**, 1764–1767 (1993)
83. T.J. Williams, A.A. Aczel, E. Baggio-Saitovitch, S.L. Budko, P.C. Canfield, J.P. Carlo, T. Goko, H. Kageyama, A. Kitada, J. Munevar, N. Ni, S.R. Saha, K. Kirschenbaum, J. Paglione, D.R. Sanchez-Candela, Y.J. Uemura, G.M. Luke, Superfluid density and field-induced magnetism in $Ba(Fe_{1-x}Co_x)_2As_2$ and $Sr(Fe_{1-x}Co_x)_2As_2$ measured with muon spin relaxation. Phys. Rev. **B82**, 094512 (2010)
84. C.J. Arguello, Y.J. Uemura, P.C.Dai, unpublished work
85. Y.J. Uemura, Energy-scale phenomenology and pairing via resonant spin-charge motion in FeAs. CuO, heavy fermion and other exotic superconductors. Physica **B 404**, 3195–3201 (2009)
86. C.A. Regal, M. Greiner, D.S. Jin, Observation of resonance condensation of fermionic atom pairs. Phys. Rev. Lett. **92**, 040403 (2004)
87. T. Moriya, K. Ueda, Antiferromagnetic spin fluctuation and superconductivity. Rep. Prog. Phys. **66**, 1299–1341 (2003)
88. T. Moriya, K. Ueda, Spin fluctuations and high temperature superconductivity. Adv. Phys. **49**, 555–606 (2000)
89. C. Stassis, B. Batlogg, J.P. Remeika, J.D. Axe, G. Shirane, Y.J. Uemura, Polarized neutron study of the paramagnetic scattering from $CeCu_2Si_2$. Phys. Rev. **B33**, 1680–1683 (1986)
90. Y.J. Uemura, C.F. Majkrzak, G. Shirane, C. Stassis, G. Aeppli, B. Batlogg, J.P. Remeika, Polarized neutron scattering from $CeCu_2Si_2$ in applied magnetic fields. Phys. Rev. **B33**, 6508–6511 (1986)
91. M. Wang, C. Zhang, X. Lu, G. Tan, H. Luo, Y. Song, M. Wang, X. Zhang, E.A. Goremychkin, T.G. Perring, T.A. Maier, Z. Yin, K. Haule, G. Kotliar, P. Dai, A magnetic origin for high temperature superconductivity in iron pnictides. Nat. Commun. **4**, 2874 (2013). and references therein
92. Y.J. Uemura, Energy scales of exotic superconductors, in *Polarons and Bipolarons in High-Tc Superconductors and Related Materials*, Proc. Int. Workshop on Polarons and Bipolarons in High-T_c Superconductors and Related Materials (Cambridge, UK,1994) ed E. Salje, A.S. Alexandrov and Y Liang (Cambridge: Cambridge University Press) pp. 453–460 (1995)
93. Y.J. Uemura, *Energy scales of high-T_c cuprates, doped fullerenes, and other exotic superconductors*, in Proc. Int. Symp. Workshop on High-T_c Superconductivity and the C_{60} Family (Beijing, 1994) ed H C Ren New York: Gordon and Breach pp. 113–142 (1995)
94. Y.J. Uemura, Condensation, excitation, pairing, and superfluid density in high-T_c superconductors: the magnetic resonance mode as a roton analogue and a possible spin-mediated pairing. J. Phys.: Condens. Matter **16**, S4515–S4540 (2004)
95. Y.J. Uemura, Twin spin/charge roton mode and superfluid density: primary determining factors of T_c in high-T_c superconductors observed by neutron, ARPES, and μSR. Physica **B 374–375**, 1–8 (2006)
96. B. Nachumi, A. Keren, K. Kojima, M. Larkin, G.M. Luke, J. Merrin, O. Tchernyshyov, W.D. Wu, Y.J. Uemura, N. Ichikawa, M. Goto, S. Uchida, Muon spin relaxation studies of Zn-substitution effects in high-T_c Cuprates. Phys. Rev. Lett. **77**, 5421–5424 (1996)
97. S.H. Pan, E.W. Hudson, K.M. Lang, H. Eisaki, S. Uchida, J.C. Davis, Imaging the effects of individual zinc impurity atoms on superconductivity in $Bi_2Sr_2CaCu_2O_{8+\delta}$. Nature **415**, 746–750 (2000)
98. K.M. Kojima, S. Uchida, Y. Fudamoto, I.M. Gat, M.I. Larkin, Y.J. Uemura, G.M. Luke, Superfluid density and volume fraction of static magnetism in stripe-stabilized $La_{1.85-y}Eu_ySr_{0.15}CuO_4$. Physica **B 36**, 316–320 (2003)

99. A.T. Savici, Y. Fudamoto, I.M. Gat, T. Ito, M.I. Larkin, Y.J. Uemura, G.M. Luke, K.M. Kojima, Y.S. Lee, M.A. Kastner, R.J. Birgeneau, K. Yamada, Muon spin relaxation studies of incommensurate magnetism and superconductivity in stage-4 $La_2CuO_{4.11}$ and $La_{1.88}Sr_{0.12}CuO_4$. Phys. Rev. **B66**, 014524 (2002)
100. H.E. Mohottala, B.O. Wells, J.I. Budnick, W.A. Hines, C. Niedermayer, L. Udby, C. Bernhard, A.R. Moodenbaugh, F.C. Chou, Phase separation in superoxygenated $La_{2-x}Sr_xCuO_{4+y}$. Nat. Mater. **5**, 377–382 (2006)
101. C. Bernhard, C.N. Wang, L. Nuccio, L. Schulz, O. Zaharko, J. Larsen, C. Aristizabal, M. Willis, A.J. Drew, G.D. Varma, T. Wolf, Ch. Niedermayer, Muon spin rotation study of magnetism and superconductivity in $Ba(Fe_{1-x}Co_x)_2As_2$ single crystals. Phys. Rev. B **86**, 184509 (2012)
102. C. J. Arguello, J. Munevar, T. Goko, E. Andrade, B.A. Frandsen, L. Liu, F.L. Ning, A.N. Pasupathy, E. Rosenthal, H. Micklitz, J. Aguero, E. Baggio-Saitovitch, R. dOrtenzio, T. Medina, T.J.S. Munsie, T.J. Williams, G.M. Luke, Pengcheng Dai, H.Q. Luo, X.Y. Lu, S. Carr, F. Ronning, E.D. Bauer, R.M. Fernandes, E. Uykur, S. Miyasaka, S. Tajima, M. Nakajima, S. Uchida, Y.J. Uemura, *Multi-probe characterization of coexisting antiferromagnetic and superconducting orders in* $Ba(Fe, Ni)_2As_2$ *near the phase boundary*, submitted for publication (2013)
103. O.W. Dietrich, E.H. Graf, C.H. Huang, L. Passell, Neutron scattering by rotons in liquid Helium. Phys. Rev. **A5**, 1377–1391 (1972)
104. C. Stock, C. Broholm, J. Hudis, H.J. Kang, C. Petrovic, Spin resonance in the d -wave superconductor $CeCoIn_5$. Phys. Rev. Lett. **100**, 087001 (2008)
105. O. Stockert, J. Arndt, E. Faulhaber, C. Geibel, H.S. Jeevan, S. Kirchner, M. Loewenhaupt, K. Schmalzl, W. Schmidt, Q. Si, F. Steglich, Magnetically driven superconductivity in $CeCu_2Si_2$. Nat. Phys. **7**, 119–124 (2011)
106. M.M. Qazilbash, M. Brehm, B.-G. Chae, P.-C. Ho, G.O. Andreev, B.-J. Kim, S.J. Yun, A.V. Balatsky, M.B. Maple, F. Keilmann, H.-T. Kim, D.N. Basov, Mott transition in VO_2 revealed by Infrared spectroscopy and nano-imaging. Science **318**, 1750 (2007)
107. Y.J. Uemura, T. Goko, I.M. Gat-Malureanu, J.P. Carlo, P.L. Russo, A.T. Savici, A. Aczel, G.J. MacDougall, J.A. Rodriguez, G.M. Luke, S.R. Dunsiger, A. McCollam, J. Arai, Ch. Pfleiderer, P. Boni, K. Yoshimura, E. Baggio-Saitovitch, M.B. Fontes, J.J. Larrea, Y.V. Sushko, J. Sereni, Phase separation and suppression of critical dynamics at quantum phase transitions of MnSi and $(Sr_{1-x}Ca_x)RuO_3$. Nat. Phys. **3**, 29–35 (2007)
108. Y.J. Uemura, A.A. Aczel, Y. Ajiro, J.P. Carlo, T. Goko, D.A. Goldfeld, A. Kitada, G.M. Luke, G.J. MacDougall, I.G. Mihailescu, J.A. Rodriguez, P.L. Russo, Y. Tsujimoto, C.R. Wiebe, T.J. Williams, T. Yamamoto, K. Yoshimura, H. Kageyama, μSR studies of the frustrated quasi-2d square-lattice spin system Cu(Cl, Br)La(Nb, Ta)$_2$O$_7$: evolution from spin-gap to antiferromagnetic state. Phys. Rev. B **80**, 174408 (2009)
109. http://en.wikipedia.org/wiki/Muon_spin_spectroscopy
110. http://musr.ca/
111. http://lmu.web.psi.ch/
112. http://www.isis.stfc.ac.uk/instruments/muon-spectroscopy4762.html
113. H. Chen, Y. Ren, Y. Qiu, W. Bao, R.H. Liu, G. Wu, T. Wu, Y.L. Xie, X.F. Wang, Q. Huang, X.H. Chen, Coexistence of the spin-density-wave and superconductivity in the (Ba, K)Fe_2As_2. Europhys. Lett. **85**, 17006 (2009)
114. G. Knebel, D. Aoki, D. Braithwaite, B. Salce, J. Flouquet, Coexistence of antiferromagnetism and superconductivity in $CeRhIn_5$ under high pressure and magnetic field. Phys. Rev. B **74**, 020501 (2006)
115. M. Minakata, Y. Maeno, Magnetic ordering in Sr_2RuO_4 induced by nonmagnetic impurities. Phys. Rev. B **63**, 180504(R) (2001)
116. S. Kunkemoller, A.A. Nugroho, Y. Sidis, M. Braden, Spin-density-wave ordering in $Ca_{0.5}Sr_{1.5}RuO_4$ studied by neutron scattering. Phys. Rev. B **89**, 045119 (2014)
117. S. Nakatsuji, Y. Maeno, Quasi-two-dimensional Mott transition system $Ca_{2-x}Sr_xRuO_4$. Phys. Rev. Lett. **84**, 2666–2669 (2000)

118. S. Nakatsuji, Y. Maeno, Switching of magnetic coupling by a structural symmetry change near the Mott transition in $Ca_{2-x}Sr_xRuO_4$. Phys. Rev. **B62**, 6458–6466 (2000)
119. A.D. Christianson, E.A. Goremychkin, R. Osborn, S. Rosenkranz, M.D. Lumsden1, C.D. Malliakas, I.S. Todorov, H. Claus, D.Y. Chung, M.G. Kanatzidis, R.I. Bewley, T. Guidi, Unconventional superconductivity in $Ba_{0.6}K_{0.4}Fe_2As_2$ from inelastic neutron scattering. Nature **456**, 930–932 (2008)
120. D.G. Henshaw, A.D.B. Woods, Modes of atomic motions in liquid helium by inelastic scattering of neutrons. Phys. Rev. **121**, 1266–1274 (1961)
121. P. Bourges, B. Keimer, S. Pailhes, L.P. Regnault, Y. Sidis, C. Ulrich, The resonant magnetic mode: A common feature of high-T_c superconductors. Physica **C424**, 45–49 (2005)
122. N.B. Christensen, D.F. McMorrow, H.M. Ronnow, B. Lake, S. Hayden, G. Aeppli, T.G. Perring, M. Mangkorntong, M. Nohara, H. Takagi, Universal dispersive excitations in the high-temperature superconductors. Phys. Rev. Lett. **93**, 147002 (2004)

Chapter 9
Optical Properties of Correlated Electrons

Dirk van der Marel

Abstract Optical spectra provide a versatile tool for studying the electronic properties of matter. In addition, the absolute spectral weight of an optical spectrum reveals optical sum-rules, which are one of the most powerful tools of experimental and theoretical physics providing access to deeply rooted quantities such as the effective mass of the charge carriers and their kinetic energy. The formalism for the optical conductivity of correlated electrons is presented in this chapter for general values of the inverse wavelength q and general band dispersion ϵ_k of the electrons. The corresponding sumrule is found to have a characteristic q-dependence for the nearest-neighbour tight binding model, causing in this case a vanishing of spectral weight for q at the Brillouin-zone boundary, i.e. for $qa = \pi$. These findings are of possible importance for k-resolved infrared spectroscopy, a technique which is in full development at the moment.

In the treasure trove of correlated matter lurk great opportunities for novel phases of matter, including various different forms of quantum magnetism, unconventional- and high-temperature superconductivity, and many other forms of behavior resulting from correlated motion of electrons. The correlated behavior of electrons in the context of quantum many-body systems constitutes one of the remaining challenges of physics. Characterizing and understanding electronic materials requires sophisticated experimental probes [1]. These include advanced optical techniques, including infrared spectroscopy at low frequency and small wavelength [2–4]. Although seemingly contradictory, near-field techniques with nano-scale resolution are emerging and will open the way toward non-local optical spectroscopy, i.e. optical spectroscopy probing $\sigma(\boldsymbol{q}, \omega)$ with finite $\boldsymbol{q}$.

Excellent texts are on the market treating the experimental optical techniques in the long wavelength limit [5] and the optical conductivity of weakly correlated electrons [6]. Also the various aspects optical conductivity of for $q = 0$ has been described in detail in the literature [7–12]. A step-by-step introduction into the optical conductivity of correlated electrons, for general electron dispersion ϵ_k and wavevector $\boldsymbol{q}$ is to our knowledge not presented in the literature. The purpose of this

D. van der Marel (✉)
Département de Physique de la Matière Condensée, Université de Genève,
CH-1211, Genève 4, Switzerland
e-mail: Dirk.vandermarel@unige.ch

A. Avella and F. Mancini (eds.), *Strongly Correlated Systems*,
Springer Series in Solid-State Sciences 180, DOI 10.1007/978-3-662-44133-6_9

book chapter is to provide such a discussion. Since the purpose is only to provide a fairly complete description of the many-body formalism underlying the optical conductivity at finite wavelength and wave-vectors, no attempt is made here to review the vast literature on optical properties of interacting electrons.

9.1 Reflection of Electromagnetic Waves

In this section we discuss the reflection and transmission of electromagnetic (EM) waves at the interface between vacuum and a substance which could be a solid, a liquid or even a gas. With optical spectroscopy one measures the reflection or transmission as a function of frequency ω. A variety of different experimental geometries can be used, depending on the type of sample under investigation, which can be a reflecting surface of a thick crystal, a free standing thin film, or a thin film supported by a substrate. Two frequently used configurations for measuring the optical constants are shown in Fig. 9.1.

Important factors influencing the type of analysis are also the orientation of the crystal or film surface, the angle of incidence of the ray of photons, and the polarization of the light. In most cases only the amplitude of the reflected or refracted light is measured, but sometimes the phase is measured, or the phase difference between two incident rays with different polarization as in ellipsometry. The task of relating the intensity and/or phase of the reflected or refracted light to the dielectric tensor inside

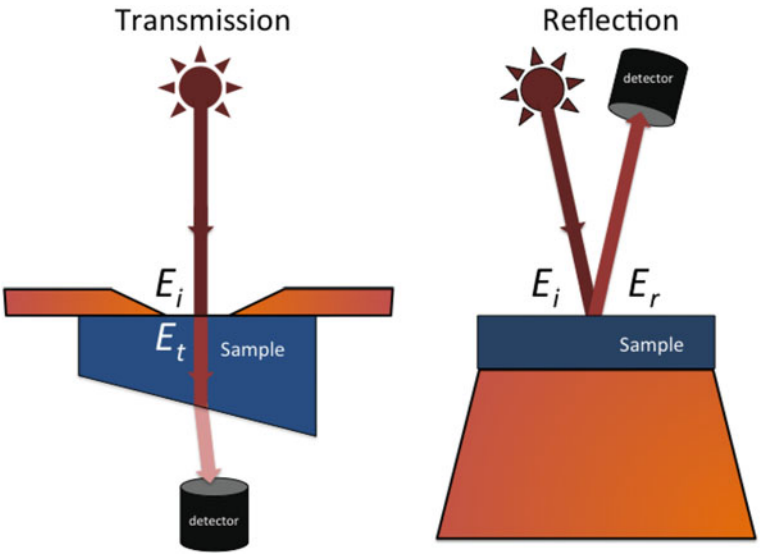

Fig. 9.1 Two commonly used experimental configurations for measuring optical constants

the material boils down to solving the Maxwell equations at the vacuum/sample, sample/substrate interface.

Before attacking the problem of reflection and transmission at an interface, we first give a brief reminder of the macroscopic Maxwell equations inside a medium. The main properties of the medium which controls the propagation of EM-waves are the dielectric constant ϵ, and the magnetic permeability μ

$$\begin{aligned} \boldsymbol{D} &= \epsilon \boldsymbol{E} \\ \boldsymbol{B} &= \mu \boldsymbol{H} \end{aligned} \tag{9.1}$$

We come later in the chapter to the microscopic interpretation of ϵ. We will see among other things, that ϵ depends on $\boldsymbol{q}$ and ω, and that it has a real and imaginary part. The speed of propagation of electromagnetic waves is given by

$$v^2 = \frac{c^2}{\epsilon\mu} \tag{9.2}$$

For $\mathrm{Re}\sqrt{\epsilon\mu} > 1$ the wavelength is compressed compared to what it would be in vacuum for the same frequency, as can be seen from the following expression for the wave-vector inside the medium

$$q^2 = \epsilon\mu \frac{\omega^2}{c^2} \tag{9.3}$$

In vacuum $\mu = \epsilon = 1$. Another consequence of the Maxwell equations is, that the electromagnetic wave has electric and magnetic components, which are given by

$$\begin{aligned} \boldsymbol{E}(z,t) &= \hat{\boldsymbol{x}} E_q e^{i\omega(z\sqrt{\epsilon\mu}/c - t)} \\ \boldsymbol{H}(z,t) &= \hat{\boldsymbol{y}} H_q e^{i\omega(z\sqrt{\epsilon\mu}/c - t)} \\ \mu H_q^2 &= \epsilon E_q^2 \end{aligned} \tag{9.4}$$

We also see now, that the effect of a finite value of $\mathrm{Im}\sqrt{\epsilon\mu}$ is to cause an exponential decay of the wave amplitude from the interface inward to the solid. When one irradiates a perfect interface between the vacuum and a substance with a ray of electromagnetic radiation, part of the light is transmitted to the interior of the substance, and part of the light is reflected. The amplitudes of the incident and reflected rays can measured experimentally. To describe the reflection process one uses the amplitude and phase of the electric field component of the electromagnetic waves just before hitting the sample surface, E_i and just after being reflected E_r, and just after being transmitted inside the solid, E_t. Likewise the corresponding magnetic fields are H_i, H_r and H_t.

In the following table we summarize the consequences of the solution of Maxwell's equations at the interface relevant to this discussion

$$\begin{aligned} E_i + E_r &= E_t \quad \text{(i)} \\ H_i - H_r &= H_t \quad \text{(ii)} \\ H_i &= E_i \quad \text{(iii)} \\ H_r &= E_r \quad \text{(iv)} \\ \mu H_t^2 &= \epsilon E_t^2 \quad \text{(v)} \end{aligned}$$

We divide left and right of (i) and (ii) by E_i and H_i respectively. We then insert (iii), (iv) and (v) in (ii). We furthermore define $r = E_r/E_i$ and $t = E_t/E_i$. The resulting equations are

$$\begin{aligned} 1 + r &= t \quad \text{(i)} \\ 1 - r &= t\sqrt{\epsilon/\mu} \quad \text{(ii)} \end{aligned}$$

Solution of this system of two equations provides

$$r = \frac{1 - \sqrt{\epsilon/\mu}}{1 + \sqrt{\epsilon/\mu}} \tag{9.5}$$

$$t = \frac{2}{1 + \sqrt{\epsilon/\mu}} \tag{9.6}$$

In the following sections we are going to consider the case of *non-magnetic media* where $\mu(\omega) = 1$. Once $r(\omega)$ has been measured, it then suffices to invert 9.5 to obtain the real and imaginary parts of $\epsilon(\omega)$, which is usually the quantity of interest. An example of this is shown in Fig. 9.2. A similar procedure can be followed when measuring the transmission spectrum through a thin film.

9.2 Optical Conductivity, Current and Electric Field

The optical conductivity expresses the current response to an electric field

$$\boldsymbol{J}(\boldsymbol{r}, t) = \int d^3\boldsymbol{r}' \int_{-\infty}^{t} dt' \boldsymbol{\sigma}(\boldsymbol{r}, \boldsymbol{r}', t - t') \boldsymbol{E}(\boldsymbol{r}', t') \tag{9.7}$$

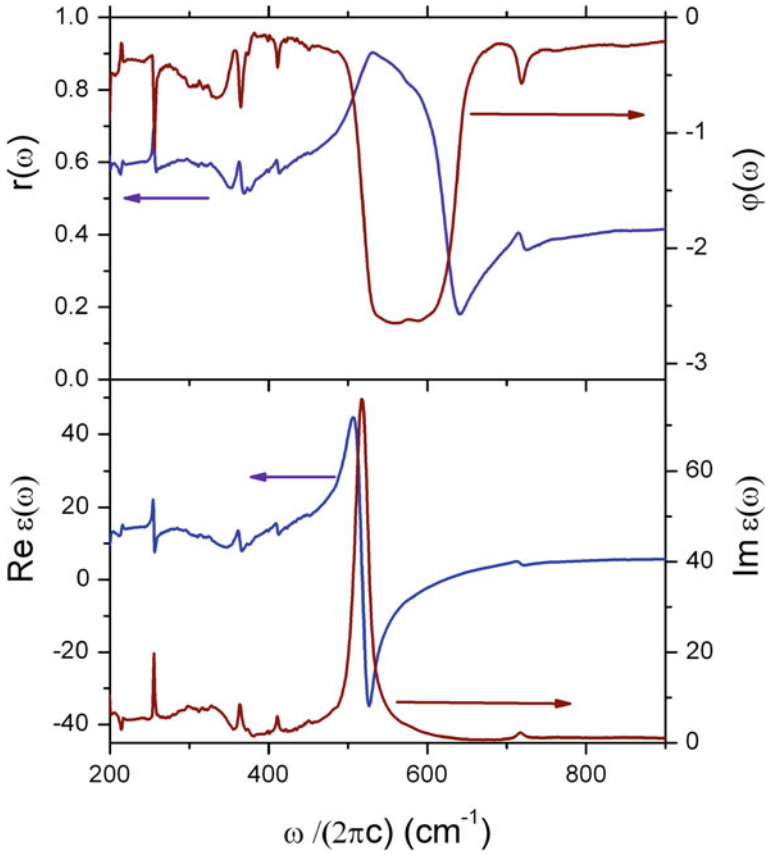

Fig. 9.2 Optical spectrum in the infrared range of the insulating quantum magnet NaV_2O_5. *Top panel* experimental reflectivity and phase. *Lower panel* Real and imaginary parts of the dielectric function $\epsilon(\omega)$. *Source* [13]

We consider the situation where the electric field is described by a plane wave with a wavevector $\boldsymbol{q}$ and a frequency ω, hence $\boldsymbol{E}(r,t) = \boldsymbol{E}_q e^{i(\boldsymbol{q}\cdot\boldsymbol{r}-\omega t)}$, with similar definitions, $\boldsymbol{J}_q$, $\boldsymbol{D}_q$, $\boldsymbol{P}_q$, for the current, displacement field and polarization density. We will assume here, that the fields are sufficiently small, so that we may consider only induced electrical currents which are linearly proportional to the electric fields at each coordinate $\boldsymbol{r}$ of the matter. Consequently the currents oscillate at the same frequency and wavelength as the electric field.

Written in frequency and momentum representation the relation between $\boldsymbol{E}_q$ and $\boldsymbol{J}_q$ is

$$\boldsymbol{J}_q = \boldsymbol{\sigma}(\boldsymbol{q},\omega)\boldsymbol{E}_q \tag{9.8}$$

The electric field of a plane electromagnetic wave is transverse to the photon momentum. The tensor elements of the optical conductivity which can be measured in an optical experiment, are therefore transverse to the direction of propagation of the electromagnetic wave. The component of the dielectric function describing polarization transverse to the propagation of the EM wave can be expressed in terms of the "optical conductivity", which has a real and an imaginary part. The relation linking the optical conductivity to $\boldsymbol{\epsilon}(\boldsymbol{q},\omega)$ is

$$\boldsymbol{\epsilon}(\boldsymbol{q},\omega)=\frac{\boldsymbol{D}_q}{\boldsymbol{E}_q}=1+\frac{4\pi i}{\omega}\boldsymbol{\sigma}(\boldsymbol{q},\omega) \tag{9.9}$$

In a typical optical experiment the photon energy is below 6 eV. In vacuum the photon wave number used in optical experiments is therefore $0.0005\ \text{Å}^{-1}$, or smaller, which is at least three orders of magnitude below the reciprocal lattice constant in a solid. Hence with optical spectroscopy one measures the transverse dielectric function -corresponding to the optical conductivity—in the limit of vanishing wavevector.

9.3 Transverse and Longitudinal Dielectric Function

In the previous sections we have seen that optical experiments measure the transverse dielectric function $\epsilon_t(\boldsymbol{q},\omega)$. This can for example be done by analyzing the reflection coefficient at a sample-vacuum interface. The transverse nature of electromagnetic waves makes that the component of $\epsilon(\boldsymbol{q},\omega)$ relevant for the optical properties, is polarized transverse to $\boldsymbol{q}$, i.e. to the propagation direction of the EM wave. For the purpose of the discussion in the present section we have written the index t specifically as a reminder of that. However, the general definition of $\boldsymbol{\epsilon}(\boldsymbol{q},\omega)$ is

$$\boldsymbol{\epsilon}(\boldsymbol{q},\omega)=\frac{\boldsymbol{D}_q}{\boldsymbol{E}_q} \tag{9.10}$$

where $\boldsymbol{D}(\boldsymbol{r},t)=\boldsymbol{D}_q\exp i(\boldsymbol{q}\cdot\boldsymbol{r}-\omega t)$ and $\boldsymbol{E}(\boldsymbol{r},t)=\boldsymbol{E}_q\exp i(\boldsymbol{q}\cdot\boldsymbol{r}-\omega t)$. For waves traveling in vacuum transverse polarization is the only possibility allowed by Maxwell's equations. Inside a material, on the other hand, longitudinal electromagnetic waves do in fact exist, plasmons for example. Static and dynamic screening of charge inside solids is an important phenomenon which involves the longitudinal component of the dielectric function.

Since we have already seen how to measure $\epsilon_t(\omega)$, we may wonder how one can measure also $\epsilon_l(\boldsymbol{q},\omega)$. The experimental method allowing to do so is called Electron Energy Loss Spectroscopy (EELS). This technique consists of measuring the inelastic decay of fast electrons passing through a sample. Experimentally one creates a monochromatic beam of high energy electrons, typically with an energy of 170 keV. These electrons are fired through a thin slab (100 nm thick) of the material

which one wishes to investigate. Part of the electrons emerge at the other side of the sample with the original energy and momentum, others have lost an amount of their energy, and have transferred momentum to an excitation inside the solid. For each value of transferred momentum, $\boldsymbol{q}$, the number of electrons can be counted for any given value of the energy loss, $\hbar\omega$ by selecting a certain direction in space, and by selecting the energy of the electrons emerging from the sample.

A collision process inside the solid, whereby the momentum changes from $\boldsymbol{p}$ to $\boldsymbol{p}-\boldsymbol{q}$ and the energy from $E_{in} = p^2/(2m)$ to $E_{out} = |\boldsymbol{p}-\boldsymbol{q}|^2/(2m) = p^2/(2m)-\hbar\omega$ generates during the collision process a longitudinal dielectric displacement field, $D(\boldsymbol{r}, t) \propto \exp(i\boldsymbol{q}\cdot\boldsymbol{r} - i\omega t)$. Since inside a material the dielectric displacement is screened by the response of the matter particles, the resulting electric field is

$$\boldsymbol{E}(\boldsymbol{q}, \omega) = \frac{1}{\epsilon(\boldsymbol{q}, \omega)}\boldsymbol{D}(\boldsymbol{q}, \omega) \tag{9.11}$$

The probability per unit time that a fast electron transfers momentum $\boldsymbol{q}$ and energy ω to the electrons was derived by Nozières and Pines for a fluid of interacting electrons

$$P(\boldsymbol{q}, \omega) = \frac{8\pi q_e^2}{|q|^2}\mathrm{Im}\left\{\frac{-1}{\epsilon(\boldsymbol{q}, \omega)}\right\} \tag{9.12}$$

where q_e is the electron charge. Hence this technique provides the longitudinal dielectric function, i.e. the response to a dielectric displacement field which is parallel to the transferred momentum $\boldsymbol{q}$.

Finally we come back to the optical spectroscopy. In the limit $q \to 0$ the distinction between longitudinal and transverse polarization vanishes, and consequently

$$\lim_{q\to 0} \epsilon_t(\boldsymbol{q}, \omega) = \epsilon_l(\boldsymbol{q}, \omega) \tag{9.13}$$

Since optical spectroscopy allows to measure real and imaginary part of $\epsilon_t(\boldsymbol{q}, \omega)$, it is possible to calculate the loss function $\mathrm{Im}(-1/\epsilon(\boldsymbol{q}, \omega))$ for $q \to 0$, and this should correspond exactly to the energy loss spectra measured with EELS. An example where the two techniques are compared for the same material is given in Fig. 9.3. Indeed, we see that the two techniques give the same result for $q \to 0$, as expected.

9.4 Quantum Electrodynamics of Electrons in a Lattice

To keep the notation light, we use Planck units in the remainder of this chapter. In those units $\hbar = 1$, $c = 1$. Since the fine-structure constant is $\alpha = q_e^2/\hbar c$, we automatically have $q_e = -\sqrt{\alpha}$ in these units. We will however continue to use the symbol q_e to indicate the electron charge throughout this chapter. Spin-coordinate plays no role of particular importance in this chapter; we therefore **suppress the spin-labels** in the following subsections in the interest of compactness of notation.

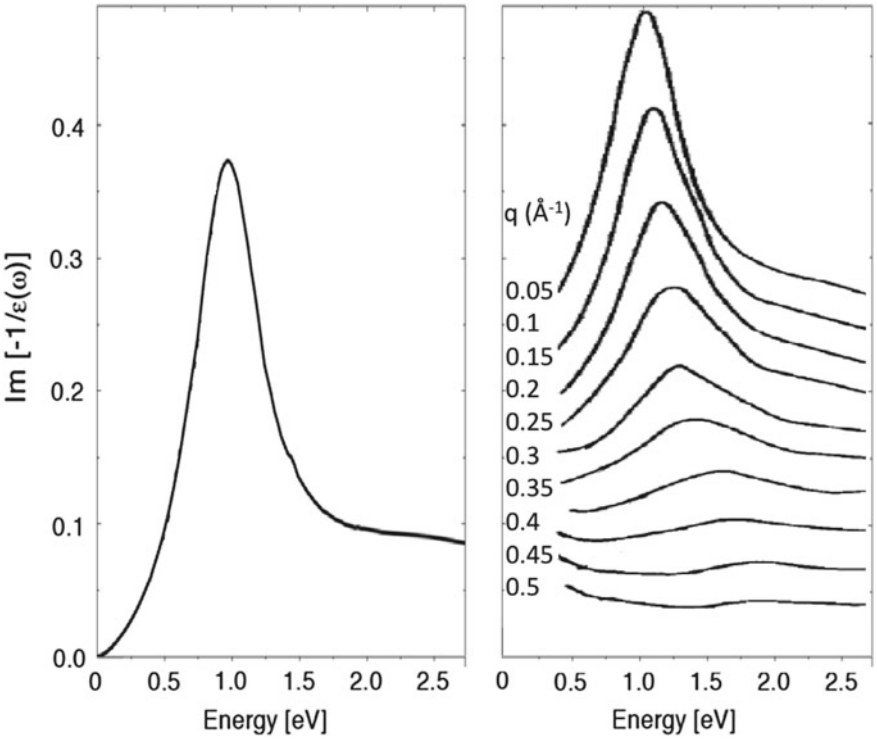

Fig. 9.3 Comparison of the optical data (*left* [14]) and EELS spectra (*right* [15], reproduced from the original figure with permission of the authors.) of $Bi_2Sr_2CaCu_2O_8$, both providing $\mathrm{Im}(-1/\epsilon(\boldsymbol{q},\omega))$. The peak positions in both spectra correspond to the plasma-resonance frequency

9.4.1 Coupling of Interacting Electrons in Solids to an Electromagnetic Field

We begin by defining the system in the absence of an external electromagnetic field. We consider a tight-binding model for the conduction band, where the tunneling of an electron on a given site $\boldsymbol{r}_m$ to surrounding sites $\boldsymbol{r}_{m+j}$ is described by the hopping matrix element t_j. In addition we have to take into account the interaction between the electrons, which in general is a function of their mutual distance. Although the interaction may in principle also depend on the spin, this aspect plays no role in the present discussion. The full matter Hamiltonian including interactions is then

$$\begin{aligned}\hat{H}^0 &= \hat{H}^{kin} + \hat{H}^{int} \\ \hat{H}^{kin} &= -\sum_{m,j} t_j (c^\dagger_{m+j} c_m + c^\dagger_m c_{m+j}) \\ \hat{H}^{int} &= \frac{1}{2} \sum_{m,n} V_{m-n} \hat{\rho}(\boldsymbol{r}_m) \hat{\rho}(\boldsymbol{r}_n)\end{aligned} \tag{9.14}$$

where $\hat{\rho}(\boldsymbol{r_j}) = c^\dagger_j c_j$ is the density operator at lattice site j. For later use we point out, that the first term is diagonal on the basis of Bloch-states represented by the operators

$$c^\dagger_k = \frac{1}{\sqrt{N_s}} \sum_m e^{-i\boldsymbol{k}\cdot\boldsymbol{r}_m} c^\dagger_m$$

In terms of which

$$\begin{aligned}\hat{H}^{kin} &= \sum_k \epsilon_k c^\dagger_k c_k \\ \epsilon_k &= -2 \sum_j t_j e^{i\boldsymbol{k}\cdot\boldsymbol{r}_j} \\ \boldsymbol{v}_k &= \frac{\partial \epsilon_k}{\partial \boldsymbol{k}} = -2i \sum_j t_j \boldsymbol{r}_j e^{i\boldsymbol{k}\cdot\boldsymbol{r}_j}\end{aligned} \tag{9.15}$$

Let us now turn to the microscopic quantum mechanical expression for the optical conductivity. We will follow closely the treatment of Mahan [9], and by Nozières and Pines [7]. We consider the effect of a time-varying electric field, which is the time derivative of the vector potential, i.e. the relation between $\boldsymbol{A} = \boldsymbol{A}_q e^{-i\omega t}$ and $\boldsymbol{E} = \boldsymbol{E}_q e^{-i\omega t}$ is

$$\boldsymbol{E}(t) = -\frac{\partial \boldsymbol{A}(t)}{\partial t} = i\omega \boldsymbol{A}(t). \tag{9.16}$$

In quantum electrodynamics the coupling between the electromagnetic field and the electrons is introduced by making the "minimal substitution" $\boldsymbol{p} \to \boldsymbol{p} - q_e \boldsymbol{A}$ in the kinetic energy term of the Hamiltonian. Since here we are concerned with the tight-binding model on a lattice, we need some form of "course graining" of the vector potential. The relation between direct- and reciprocal space representations is then

$$\boldsymbol{A}_q = \frac{1}{\sqrt{N_s}} \sum_m e^{-i\boldsymbol{q}\cdot\boldsymbol{r}_m} \boldsymbol{A}_m \tag{9.17}$$

If an electron is transferred from lattice coordinate $\boldsymbol{r}_m$ to $\boldsymbol{r}_n$, the wavefunction picks up a phase due to the vector potential, described by the integral $(q_e/\hbar)\int_m^{m+j} \boldsymbol{A}(\boldsymbol{s})\cdot d\boldsymbol{s}$, which depends on the path if $\nabla \times \boldsymbol{A} \neq 0$. A difficulty is, that with the course-graining procedure we have introduced some ambiguity regarding the path followed by the electron. Since the path of a hopping term t_j in the tight-binding Hamiltonian is of the order of a lattice constant, the variation of $\boldsymbol{A}(\boldsymbol{s})$ along the path is very small. We follow the Peierls coupling scheme, and substitute a constant value in the integral, $\boldsymbol{A}_{m,j} = (\boldsymbol{A}_m + \boldsymbol{A}_{m+j})/2$, corresponding to the average over the tunneling path. The integral than becomes $\int_m^{m+j} \boldsymbol{A}(\boldsymbol{s}) \cdot d\boldsymbol{s} = \boldsymbol{A}_{m,j} \cdot \boldsymbol{r}_j$. The corresponding Peierls substitution

$$t_j \rightarrow t_j e^{-iq_e \boldsymbol{A}_{m,j}\cdot \boldsymbol{r}} \tag{9.18}$$

does not affect the interaction part of the Hamiltonian (9.14), but the kinetic energy term picks up the extra phase. The Hamiltonian in the presence of $\boldsymbol{A}_{m,j}$ is, according to the "Peierls coupling" scheme

$$\hat{H} = -\sum_{m,j} t_j (e^{-iq_e \boldsymbol{A}_{m,j}\cdot \boldsymbol{r}} c^\dagger_{m+j} c_m + e^{iq_e \boldsymbol{A}_{m,j}\cdot \boldsymbol{r}} c^\dagger_m c_{m+j}) + \hat{H}^{int} \tag{9.19}$$

9.4.2 General Consideration About the Calculation of the Linear Response

We are interested to calculate the linear response of the current density $\boldsymbol{J}_q$ to the electric field $\boldsymbol{E}_q$, which is related to the vector potential $\boldsymbol{A}_q$ through $\boldsymbol{E}_q = i\omega \boldsymbol{A}_q$. The current density is related to the local velocities of all electrons, described by the expectation value of the current operator $\hat{\boldsymbol{j}}(\boldsymbol{r})$ through $\boldsymbol{J}(\boldsymbol{r}) = \langle \hat{\boldsymbol{j}}(\boldsymbol{r})\rangle$. Note, that $\boldsymbol{J}(\boldsymbol{r})$ refers to the amount charge passing per unit of time per unit area perpendicular to $\boldsymbol{J}(\boldsymbol{r})$. The optical conductivity is then

$$\boldsymbol{\sigma}(\boldsymbol{q},\omega) = \frac{\boldsymbol{J}_q}{\boldsymbol{E}_q} = \frac{\langle \hat{\boldsymbol{j}}_q \rangle}{i\omega \boldsymbol{A}_q} \qquad (\lim \boldsymbol{A}_q \rightarrow 0) \tag{9.20}$$

In general terms our task is to compute the time-dependent expectation value of the current operator in the presence of the vector potential. The vector potential enters the problem on two levels: First, the time-independent current operator in the presence of the vector potential is already different from the current operator without vector potential. Secondly the time evolution of the current operator is described by the Hamiltonian (9.19), which also contains the vector potential. Taken together

$$\boldsymbol{\sigma}(\boldsymbol{q},\omega) = \frac{1}{i\omega \boldsymbol{A}_q} \left\langle e^{i\hat{H}(A_q)t} \hat{\boldsymbol{j}}_q(A_q) e^{-i\hat{H}(A_q)t} \right\rangle \qquad (\lim \boldsymbol{A}_q \rightarrow 0) \tag{9.21}$$

We see, that the vector potential enters in various different positions in the expression. One can proceed by making Taylor series expansions of all terms, and collect at the end all terms linear in $\boldsymbol{A}_q$. Each step takes care and precision, since the operators in this expression don't commute. These steps are treated in the following three subsections.

9.4.3 Expansion of the Current Operator in Powers of the Vector Potential

In quantum electrodynamics the current density is obtained from the relation $\boldsymbol{J} = -\Omega^{-1}\partial\hat{H}/\partial\boldsymbol{A}$. For our tight-binding Hamiltonian (9.14) this implies

$$\begin{aligned}\hat{\boldsymbol{j}}(\boldsymbol{r}_m) &= -\frac{1}{\Omega}\left[\frac{\partial\hat{H}}{\partial\boldsymbol{A}_m}\right] \\ &= \frac{1}{\Omega}\sum_j t_j\boldsymbol{r}_j(-iq_e e^{-iq_e\boldsymbol{A}_{m,j}\cdot\boldsymbol{r}_j}c^\dagger_{m+j}c_m + iq_e e^{iq_e\boldsymbol{A}_{m,j}\cdot\boldsymbol{r}_j}c^\dagger_m c_{m+j})\end{aligned} \tag{9.22}$$

which we expand in powers of $\boldsymbol{A}_{m,j}$, retaining only terms up to first order

$$\begin{aligned}\hat{\boldsymbol{j}}(\boldsymbol{r}_m) &= \hat{\boldsymbol{j}}^r(\boldsymbol{r}_m) + \hat{\boldsymbol{j}}^d(\boldsymbol{r}_m) \\ \hat{\boldsymbol{j}}^r(\boldsymbol{r}_m) &= -i\frac{q_e}{\Omega}\sum_j t_j\boldsymbol{r}_j(c^\dagger_{m+j}c_m - c^\dagger_m c_{m+j}) \\ \hat{\boldsymbol{j}}^d(\boldsymbol{r}_m) &= -\frac{q_e^2}{\Omega}\sum_j t_j\boldsymbol{r}_j(\boldsymbol{r}_j\cdot\boldsymbol{A}_{m,j})(c^\dagger_{m+j}c_m + c^\dagger_m c_{m+j})\end{aligned} \tag{9.23}$$

The first term in (9.23) is the so-called "regular" term of the current operator, since it is independent of the vector potential. We draw attention to the physical interpretation of the velocity operator. The matrix element $\left\langle -iq_e t_j\boldsymbol{r}_j c^\dagger_{m+j}c_m\right\rangle$ describes a process whereby an electron tunnels from position $\boldsymbol{r}_m$ to $\boldsymbol{r}_{m+j}$. The tunneling time of this process is $1/t_j$, and the displacement is $\boldsymbol{r}_j$. The effective velocity of this process is therefore $\boldsymbol{r}_j t_j$. The second term proportional to $< c^\dagger_m c_{m+j} >$ describes the same event, except that it occurs in the opposite direction. The operator $\hat{\boldsymbol{j}}^r(\boldsymbol{r}_m)$ therefore describes exactly the current passing through lattice position $\boldsymbol{r}_m$. While the Peierls substitution is burdened by ambiguities (except if $\boldsymbol{A}(r)$ is uniform), the regular part of the current operator in (9.23) is a robust result, which satisfies our intuitive understanding of a local current. Its momentum-space representation is

$$\hat{\boldsymbol{j}}_q^r = \frac{1}{\sqrt{N_s}} \sum_m e^{-i\boldsymbol{q}\cdot\boldsymbol{r}_m} \hat{\boldsymbol{j}}^r(\boldsymbol{r}_m) = \frac{q_e}{\Omega} \sum_k \frac{\boldsymbol{v}_k + \boldsymbol{v}_{k-q}}{2} c_k^\dagger c_{k-q} \tag{9.24}$$

where $\boldsymbol{v}_k = \partial\epsilon_k/\partial\boldsymbol{k}$ is the group velocity.

The "diamagnetic part" of the current, $\hat{\boldsymbol{j}}^d$, is the term which is proportional to A_m. Its Fourier transform is

$$\hat{\boldsymbol{j}}_q^d = -q_e^2 \sum_{q'} \boldsymbol{A}_{q'} \cdot \hat{\boldsymbol{K}}_{q,q'} \tag{9.25}$$

$$\hat{\boldsymbol{K}}_{q,q'} \equiv \frac{1}{2\Omega} \sum_{j,k} t_j \boldsymbol{r}_j \boldsymbol{r}_j (2e^{i\boldsymbol{q}'\cdot\boldsymbol{r}_j} \cos\boldsymbol{k}\cdot\boldsymbol{r}_j + e^{i\boldsymbol{k}\cdot\boldsymbol{r}_j} + e^{i(\boldsymbol{k}+\boldsymbol{q}-\boldsymbol{q}')\cdot\boldsymbol{r}_j}) c_k^\dagger c_{k+q-q'}$$

The expectation value has finite contributions only from $q = q'$ in the above expression, hence

$$\boldsymbol{J}_q^d = \left\langle \hat{\boldsymbol{j}}_q^d \right\rangle = -q_e^2 \boldsymbol{A}_q \cdot \boldsymbol{K}(\boldsymbol{q}) \tag{9.26}$$

where the tensor $\boldsymbol{K}(\boldsymbol{q})$ is proportional to the spectral weight in the optical conductivity function

$$\boldsymbol{K}(\boldsymbol{q}) = \frac{2}{\Omega} \sum_{k,j} t_j \boldsymbol{r}_j \boldsymbol{r}_j e^{i\boldsymbol{k}\cdot\boldsymbol{r}_j} \cos^2\left(\frac{\boldsymbol{q}\cdot\boldsymbol{r}_j}{2}\right) \left\langle c_k^\dagger c_k \right\rangle \tag{9.27}$$

We see, that (9.27) indicates that $\boldsymbol{K}(\boldsymbol{q})$ depends on the wavevector $\boldsymbol{q}$ of the perturbing field. For the special case of the nearest-neighbour tight-binding model we will find confirmation of exactly this $\boldsymbol{q}$-dependence from a different approach in subsection 9.5.4. Nevertheless, we have to keep in mind that the course-graining procedure used in the Peierls substitution is only fully accurate for a uniform vector potential, i.e. $q = 0$. For a general type of dispersion $\epsilon(k)$ non-negligible corrections of order q^2 to (9.27) are to be expected. The limit for $q \to 0$ of (9.27) gives

$$\boldsymbol{K} = \frac{1}{\Omega} \sum_k \frac{\partial^2\epsilon_k}{\partial\boldsymbol{k}^2} \left\langle c_k^\dagger c_k \right\rangle \tag{9.28}$$

The only exception where $\boldsymbol{K}(\boldsymbol{q})$ is $\boldsymbol{q}$-independent occurs for a parabolic energy-momentum dispersion relation of the electrons, $\epsilon_k = k^2/2m$. We then obtain the result

$$K(q) = K = \frac{n}{m} \tag{9.29}$$

For an entirely filled band at zero temperature

$$\frac{(2\pi)^3}{\Omega}\sum_k \frac{\partial^2 \epsilon_k}{\partial \boldsymbol{k}^2} n_k = \int\limits_{1^t BZ} \frac{\partial \epsilon_k}{\partial \boldsymbol{k}} d\boldsymbol{s}_k = 0 \tag{9.30}$$

where the integral is over the surface of the first Brillouin zone. Since $\partial\epsilon_k/\partial \boldsymbol{k} = 0$ on the BZ surface, this integral is zero, and consequently $K = 0$ in this case.

Combining (9.24) and (9.26) we obtain the full expression for the current operator

$$\hat{\boldsymbol{j}}_q = \hat{\boldsymbol{j}}_q^d + \hat{\boldsymbol{j}}_q^r = -q_e^2 \sum_{q'} \boldsymbol{A}_{q'} \cdot \hat{\boldsymbol{K}}_{q,q'} + \frac{q_e}{\Omega}\sum_k \frac{\boldsymbol{v}_k + \boldsymbol{v}_{k-q}}{2} c_k^\dagger c_{k-q} \tag{9.31}$$

9.4.4 Expansion of the Hamiltonian in Leading Order of the Vector Potential

We now turn to the Hamiltonian in (9.19). Since we are interested in the linear response to the vector potential, we use a Taylor expansion in powers of A_m

$$\hat{H}^{kin}(\boldsymbol{A}_q) = \hat{H}^{kin} + iq_e \sum_{m,j} t_j \boldsymbol{A}_{m,j} \cdot \boldsymbol{r}_j (c_{m+j}^\dagger c_m - c_m^\dagger c_{m+j} + \cdots) \tag{9.32}$$

The terms proportional to $\boldsymbol{A}_{m,j}$ can be worked out as follows:

$$\begin{aligned} & iq_e \sum_{m,j} t_j \boldsymbol{A}_{m,j} \cdot \boldsymbol{r}_j (c_{m+j}^\dagger c_m - c_m^\dagger c_{m+j}) \\ & = iq_e \sum_{k,q,j} t_j \boldsymbol{A}_q \cdot \boldsymbol{r}_j (e^{i\boldsymbol{k}\cdot\boldsymbol{r}_j} - e^{-i(\boldsymbol{k}+\boldsymbol{q})\cdot\boldsymbol{r}_j}) c_k^\dagger c_{k+q} \\ & = -q_e \sum_{k,q,j} \boldsymbol{A}_q \cdot \frac{\boldsymbol{v}_k + \boldsymbol{v}_{k+q}}{2} c_k^\dagger c_{k+q} = -\Omega \sum_q \boldsymbol{A}_q \cdot \hat{\boldsymbol{j}}_{-q}^r \end{aligned}$$

where, in order to write the last equation, we use the result for the regular term of the current operator, (9.24). In leading order of $\boldsymbol{A}_q$ the Hamiltonian can then be written as the sum of two terms, $\hat{H}^0$ representing the full matter Hamiltonian including interactions (9.14), and $\hat{H}^p$ representing the perturbation due to a time-varying vector potential

$$\begin{aligned} \hat{H} &= \hat{H}^0 + \hat{H}^p \\ \hat{H}^p &= -\Omega \sum_q \boldsymbol{A}_q \cdot \hat{\boldsymbol{j}}_{-q}^r \end{aligned} \tag{9.33}$$

9.4.5 Current Response to an Applied Field

The response to the vector potential is described by expectation value of the Heisenberg representation of the current operator, taking the full Hamiltonion including the vector potential

$$\boldsymbol{J}_q(t) = \left\langle e^{i\hat{H}t}\hat{\boldsymbol{j}}_q e^{-i\hat{H}t}\right\rangle = \left\langle \hat{\boldsymbol{j}}_q^d(t)\right\rangle + \left\langle \hat{\boldsymbol{j}}_q^r(t)\right\rangle = -q_e^2\boldsymbol{A}_q\cdot\boldsymbol{K}(\boldsymbol{q}) + \boldsymbol{J}_q^r(t) \quad (9.34)$$

The diamagnetic contribution to the conductivity is now easily obtained using the definition (9.20)

$$\boldsymbol{\sigma}^d(\omega,q) = \frac{\boldsymbol{J}_q^d}{i\omega\boldsymbol{A}_q} = \frac{iq_e^2\boldsymbol{K}(\boldsymbol{q})}{\omega} \quad (9.35)$$

This term expresses that in the absence of a potential binding the electrons to the lattice, the response will be that of a plasma of freely moving charged particles with mass m, charge q_e, and density $n = N/\Omega$.

The second contribution to the current in (9.34) represents the combined effect of the crystal potential in which the electrons move, and their mutual interactions. The corresponding "regular" contribution to the optical conductivity is

$$\boldsymbol{\sigma}^r(\omega,q) = \frac{\boldsymbol{J}_q^r}{i\omega\boldsymbol{A}_q} \quad (9.36)$$

At this point it will be useful to introduce the Heisenberg representation of the current operator *in the absence* of the external field described by the term $\hat{H}^p$ in the hamiltonian.

$$\hat{\boldsymbol{j}}_q^0(t) = e^{i\hat{H}^0t}\hat{\boldsymbol{j}}_q e^{-i\hat{H}^0t} \quad (9.37)$$

The vector potential $\boldsymbol{A}(t)$ has been switched on at a certain time t_0. Without loss of generality we can choose this time to be $t_0 = 0$. To describe the time-evolution of the current operator caused by $\boldsymbol{A}(t)$, we introduce the time-evolution operator

$$\begin{aligned} \hat{U}(t) &= e^{i\hat{H}^0t}e^{-i\hat{H}t} \quad t \geq 0 \\ \hat{U}(t) &= 1 \qquad\qquad\qquad t < 0 \end{aligned} \quad (9.38)$$

With the help of (9.37), (9.38) we can rewrite $\hat{\boldsymbol{j}}_q^r(t)$ in the expression of $\boldsymbol{J}_q^r(t)$

$$\hat{\boldsymbol{j}}_q^r(t) = e^{i\hat{H}t}\hat{\boldsymbol{j}}_q e^{-i\hat{H}t} = \hat{U}^\dagger(t)\hat{\boldsymbol{j}}_q^0(t)\hat{U}(t) \quad (9.39)$$

With the help of this we obtain

$$\boldsymbol{J}_q^r(t) = \left\langle \hat{U}^\dagger(t)\hat{\boldsymbol{j}}_q^0(t)\hat{U}(t)\right\rangle \tag{9.40}$$

We like to expand the expression for the current as a function of $\hat{H}^p$ and look for the leading terms for the linear response. Since the definition of $\hat{\boldsymbol{j}}^0(\boldsymbol{r},t)$ contains $\hat{H}^0$ instead of $\hat{H}$, it does not depend on the vector potential $\hat{H}^p$. It is therefor only necessary to expand $U(t)$ as a function of $\hat{H}^p$. To do so we need to know the properties of $\hat{U}(t)$. First of all, according to (9.38) we have $\hat{U}(-\infty) = 1$. In addition, $\hat{U}(t)$ satisfies the following expression for the derivative with respect to time

$$\begin{aligned}\frac{\partial\hat{U}}{\partial t} &= i\hat{H}^0 e^{i\hat{H}^0 t}e^{-i\hat{H}t} - ie^{i\hat{H}^0 t}\hat{H}e^{-i\hat{H}t} = e^{i\hat{H}^0 t}\hat{H}^p e^{-i\hat{H}t}\\ &= ie^{i\hat{H}^0 t}\hat{H}^p e^{i\hat{H}^0 t}e^{-i\hat{H}^0 t}e^{-i\hat{H}t} = -i\hat{H}^p(t)\hat{U}(t)\end{aligned}$$

To solve this equation, we integrate from the lower limit $\hat{U}(-\infty) = 1$ to finite time t:

$$\hat{U}(t) = 1 - i\int_{-\infty}^{t} dt'\hat{H}^p(t')\hat{U}(t')$$

Iterative solution yields

$$\hat{U}(t) = 1 - i\int_{-\infty}^{t} dt'\hat{H}^p(t') + \frac{1}{2}\int_{-\infty}^{t} dt'\int_{-\infty}^{t'} dt''\hat{H}^p(t')\hat{H}^p(t'') + \cdots$$

Since we restrict the discussion here to linear response, we need only the first two terms. Substituting those in (9.40) yields

$$\boldsymbol{J}_q^r(t) = \left\langle \left(1 + i\int_{-\infty}^{t} dt'\hat{H}^p(t')\right)\hat{\boldsymbol{j}}_q^0(t)\left(1 - i\int_{-\infty}^{t} dt'\hat{H}^p(t')\right)\right\rangle \tag{9.41}$$

The matrix element $\left\langle\hat{\boldsymbol{j}}^0(\boldsymbol{r},t)\right\rangle = 0$ for a system in equilibrium. Furthermore terms proportional to $(\hat{H}^p)^2$ contribute to the quadratic response. We now substitute $\hat{H}^p = -\Omega\sum_q \boldsymbol{A}_q\cdot\hat{\boldsymbol{j}}^r_{-q}$ (9.33). Retaining only the linear terms gives

$$\boldsymbol{J}_q^r(t) = i\Omega \int_{-\infty}^{t} \left\langle \left[\hat{\boldsymbol{j}}_q^0(t), \hat{\boldsymbol{j}}_{-q}^0(t') \cdot \boldsymbol{A}_q(t') \right] \right\rangle dt'$$

We substitute $\boldsymbol{J}_q^r(t) = \boldsymbol{J}_q^r e^{-i\omega t}$ and $\boldsymbol{A}_q(t) = \boldsymbol{A}_q e^{-i\omega t}$ and multiply both sides with $e^{i\omega t}$

$$\boldsymbol{J}_q^r = i\Omega \int_{-\infty}^{t} \left\langle \left[\hat{\boldsymbol{j}}_q^0(t), \hat{\boldsymbol{j}}_{-q}^0(t') \cdot \boldsymbol{A}_q \right] \right\rangle e^{i\omega(t-t')} dt'$$

Due to time-invariance, we have

$$\left[\hat{\boldsymbol{j}}_q^0(t), \hat{\boldsymbol{j}}_{-q}^0(t') \right] = \left[\hat{\boldsymbol{j}}_q^0(t-t'), \hat{\boldsymbol{j}}_{-q}^0(0) \right] \tag{9.42}$$

We substitute $t - t' \rightarrow t''$, so that

$$\boldsymbol{J}_q^r = i\Omega \int_{0}^{\infty} \left\langle \left[\hat{\boldsymbol{j}}_q^0(t''), \hat{\boldsymbol{j}}_{-q}^0(0) \cdot \boldsymbol{A}_q \right] \right\rangle e^{i\omega t''} dt''$$

We now divide both sides by $\boldsymbol{A}_q$

$$\frac{\boldsymbol{J}_q^r}{\boldsymbol{A}_q} = -\chi_{jj}(\boldsymbol{q}, \omega) \tag{9.43}$$

where $\chi_{jj}(\boldsymbol{q}, t)$ is the current-current correlation function defined as

$$\chi_{jj}(\boldsymbol{q}, t) = -i\theta(t)\Omega \left\langle \left[\hat{\boldsymbol{j}}_q(t), \hat{\boldsymbol{j}}_{-q}(0) \right] \right\rangle \tag{9.44}$$

and

$$\chi_{jj}(\boldsymbol{q}, \omega) = \int_{-\infty}^{\infty} \chi_{jj}(\boldsymbol{q}, t) e^{i\omega t} dt \tag{9.45}$$

Comparing this to (9.36) we see, that the regular part of the optical conductivity is

$$\boldsymbol{\sigma}^r(\omega, q) = \frac{i}{\omega + i\eta} \chi_{jj}(\boldsymbol{q}, \omega) \tag{9.46}$$

where $i\eta = i0^+$ moves the pole infinitesimally away from the real axis, such as to assure causality in the time-dependence of the relation between current and electric field.

9.4.6 Frequency and Temperature Dependent Optical Conductivity

We see, that the regular par of the optical conductivity is proportional to the current-current correlation function, divided by the frequency. We continue the discussion by considering a well-defined many-particle state $|n\rangle$, for which we calculate the optical conductivity

$$\boldsymbol{\sigma}^r(\boldsymbol{q},\omega) = \frac{\Omega}{\omega + i\eta}\int_0^\infty \left\langle n \left| \left\{ e^{i\hat{H}^0 t}\hat{\boldsymbol{j}}_q e^{-i\hat{H}^0 t}\hat{\boldsymbol{j}}_{-q} - \hat{\boldsymbol{j}}_{-q} e^{i\hat{H}^0 t}\hat{\boldsymbol{j}}_q e^{-i\hat{H}^0 t} \right\} \right| n \right\rangle e^{i\omega t} dt$$

After some manipulation with the operators $e^{i\hat{H}^0 t}$ and $e^{-i\hat{H}^0 t}$ we obtain

$$\boldsymbol{\sigma}^r(\omega, q) = \frac{\Omega}{\omega + i\eta}\int_0^\infty \sum_{m\neq n} \left\{ \boldsymbol{j}_q^{nm}\boldsymbol{j}_{-q}^{mn} e^{i(\omega + E_n - E_m)t} - \boldsymbol{j}_{-q}^{nm}\boldsymbol{j}_q^{mn} e^{i(\omega + E_m - E_n)t} \right\} dt$$

where for compactness of notation we represent the matrix elements of the current operators as

$$\boldsymbol{j}_q^{nm} \equiv \langle n|\hat{\boldsymbol{j}}_q^r|m\rangle \tag{9.47}$$

In the remainder we will assume a basis on which the conductivity tensor is diagonal, so that $\boldsymbol{j}_q^{nm} // \boldsymbol{j}_{-q}^{mn}$. We can than drop the tensor notation and replace $\boldsymbol{j}_q^{nm}\boldsymbol{j}_{-q}^{mn}$ with $|\boldsymbol{j}_q^{nm}|^2$. We also introduce the short-hand notation for the energy differences $E_m - E_n = \omega_{mn}$. Carrying out the integrations over time we obtain

$$\sigma^r(\omega, q) = i\sum_{m\neq n} \frac{\Omega|\boldsymbol{j}_q^{nm}|^2}{\omega + i\eta}\left\{ \frac{1}{\omega - \omega_{mn} + i\eta_1} - \frac{1}{\omega + \omega_{mn} + i\eta_1} \right\} \tag{9.48}$$

Note, that both η and η_1 are to be taken in the limit $\eta \to 0$, but that these limits are independent from one another, i.e. $\eta_1 \neq \eta$.

The expression for the total conductivity (diamagnetic + regular) is obtained by combining this with (9.35).

$$\begin{aligned}\sigma(\boldsymbol{q},\omega) &= \sigma^d(\boldsymbol{q},\omega) + \sigma^r(\boldsymbol{q},\omega) \\ &= \frac{i}{\omega + i\eta}\left\{ q_e^2 K + \sum_{m\neq n}\left[\frac{\Omega|\boldsymbol{j}_q^{nm}|^2}{\omega - \omega_{mn} + i\eta_1} - \frac{\Omega|\boldsymbol{j}_q^{nm}|^2}{\omega + \omega_{mn} + i\eta_1} \right] \right\}\end{aligned} \tag{9.49}$$

In (9.49) $\sigma(\omega)$ is represented by two separate terms, a δ-function for $\omega = 0$ and a summation over excited many-body eigen-states. The δ-function is a diamagnetic contribution of *all* electrons in the system, the presence of which is a consequence of the gauge invariant treatment of the optical conductivity. Note however, that according to (9.30) for an insulator (the bands of which are either fully occupied or entirely empty) we have $K = 0$. The presence of this term is at first glance rather confusing, since left by itself this δ-function would imply that all metals are ideal conductors! However, the second term has, besides a series of poles corresponding to the optical transitions, also a pole for $\omega = 0$, corresponding to a *negative* δ-function of $\mathrm{Re}\sigma(\omega)$. It turns out, that for all materials except ideal conductors this δ-function compensates exactly the first (diamagnetic) term of (9.49). This exact compensation is a consequence of the relation.[1]

$$\text{For every } n\text{: } q_e^2 K = 2 \sum_{m \neq n} \frac{\Omega |\boldsymbol{j}_q^{nm}|^2}{\omega_{mn}} \tag{9.50}$$

Experimentally truly 'ideal' conductivity is only seen in superconductors. In ordinary conducting materials the diamagnetic term broadens to a Lorentzian peak due to elastic and/or inelastic scattering. The width of this peak is the inverse life-time of the charge carriers. Often in the theoretical literature the broadening is not important, and the Drude peak is counted to the Dirac-function in the origin. The infrared properties of superconductors are characterized by the presence of both a purely reactive diamagnetic response, and a regular dissipative conductivity. The sum of these contributions counts the partial intra-band spectral weight which we discussed previously in relation to the "kinetic energy sum rule". With the help of (9.50), the diamagnetic term of (9.49) can now be absorbed in the summation on the right-hand side, so that after combining all terms

$$\sigma(\boldsymbol{q}, \omega) = 2i\omega \sum_{m \neq n} \frac{\Omega |\boldsymbol{j}_q^{nm}|^2}{\omega_{mn}} \frac{1}{\omega(\omega + i\eta) - \omega_{mn}^2} \tag{9.51}$$

where we have to keep in mind, that the equivalence with (9.49) holds under condition that η $(= 2\eta_1)$ is infinitesimally small. Note, that in deriving (9.51) from (9.49), an $\omega + i\eta$ term in the numerator has been replaced by ω since, unlike for the denominators containing $i\eta$, the effect of $i\eta$ vanishes if we consider the limit $\eta \to 0$.

In (9.51) we have calculated the optical conductivity assuming that, under the influence of the external potential, the system evolves as a function of time from an eigenstate $|n\rangle$. In the most common experimental situation the sample is in thermal equilibrium with heat bath with temperature T. Following the approach of Kubo we calculate the conductivity using thermodynamical weight factors $e^{-\beta E_n}/Z$ for each

[1] Equation (9.50) is obtained if one represents the current operators as commutators of the hamiltonian with the dipole operator defined in (9.68). The expectation value of the hamiltonian is used to cancel out the factor ω_{mn} in the denominator of the expression. In the final step the commutator of the dipole operator and the current operator is calculated, which completes the derivation of (9.50).

many-body eigenstate (see [9] for a discussion on the justification of this approach). Here Z is the partition function, and $\beta = 1/k_B T$. The expression for the optical conductivity at finite temperature becomes then

$$\sigma(\boldsymbol{q},\omega) = 2i\omega \sum_{n,m\neq n} \frac{\Omega|\boldsymbol{j}_q^{nm}|^2}{\omega_{mn}} \frac{e^{-\beta E_n}}{Z} \frac{1}{\omega(\omega+i\eta)-\omega_{mn}^2} \tag{9.52}$$

The imaginary parts of the terms are Dirac δ-functions, so that

$$\mathrm{Re}\sigma(\boldsymbol{q},\omega) = \pi \sum_{n,m\neq n} \frac{\Omega|\boldsymbol{j}_q^{nm}|^2}{\omega_{mn}} \frac{e^{-\beta E_n}}{Z} \{\delta(\omega-\omega_{mn})+\delta(\omega+\omega_{mn})\} \tag{9.53}$$

The spectrum thus consists of a series of peaks, each representing an excitation from the ground state $|n\rangle$ to an excited many-body state $|m\rangle$ at an energy cost ω_{mn}. In atoms and molecules one observes indeed a discrete set of lines. In solids the excitations broaden into bands due to the fact that the excitations in different parts of the lattice are coupled, resulting in bands of excited states. The most commonly observed excited states are the creation of one hole in the occupied band and one electron in the states above E_F. The resulting optical spectrum is than something like a joint density of states of the bands below and above the Fermi energy. Examples of this are shown for a metal (MnSi), a semi-comductor (FeSi), a semimetal (CoSi) and a

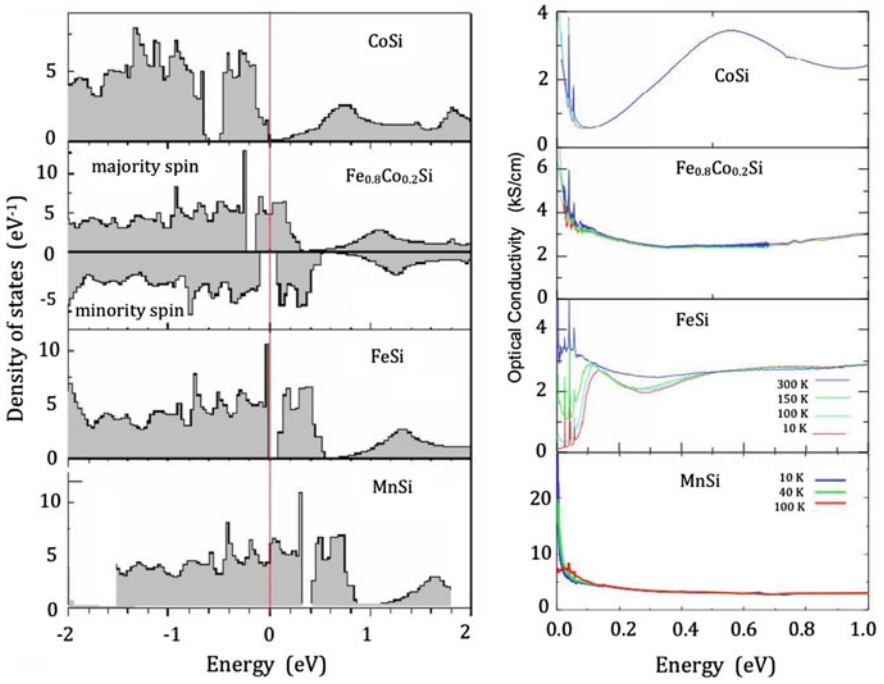

Fig. 9.4 Density of states (*left*) and real part of the optical conductivity (*right*) of a number of transition-metal silicides. *Source* [16]

doped semiconductor (Co-doped FeSi) are shown in Fig. 9.4. The optical conductivity of FeSi reveals the gap around the Fermi energy visible in the density of states of the left panel.

9.4.7 The Drude-Lorentz Expression

It is useful at this stage to relabel the transitions $m, n \rightarrow j$, where j is a generalized index, and to introduce a plasma frequencies for each transition with energy $\omega_{mn} = \omega_j$

$$\Omega_j(\boldsymbol{q})^2 = 8\pi \frac{\Omega |j_q^{nm}|^2}{\omega_{mn}} \frac{e^{-\beta E_n}}{Z} \tag{9.54}$$

with the help of which we obtain the following compact expression for the optical conductivity tensor

$$\sigma(\boldsymbol{q}, \omega) = \frac{i\omega}{4\pi} \sum_j \frac{\Omega_j(\boldsymbol{q})^2}{\omega(\omega + i\gamma_j) - \omega_j^2} \tag{9.55}$$

Although formally $\gamma_j = \eta = 0^+$, a natural modification of (9.55) consists of limiting the summation to a set of oscillators representing the main optical transitions and inserting a finite value for γ_j, which in zero'th approximation represents the inverse lifetime of the corresponding excited state (*e.g.* calculated using Fermi's Golden Rule). With this modification (9.55) is one of the most commonly used phenomenological representations of the optical conductivity, generally known as the Drude-Lorentz expression. An example is shown in Fig. 9.5. In its original incarnation the Drude-Lorentz expression is obtained from a model of classical damped oscillators.

The simple recipe of broadening the δ-functions by a life-time broadening is prone to pitfalls: For example, different line shapes of the oscillators are obtained if we make the substitution $\eta_1 = \eta = \gamma$ in (9.49). Apparently it is important to combine all (positive and negative) δ-functions coming from diamagnetic (σ^d) and regular (σ^r) terms in (9.49), not only in order to cancel out the negative δ-function in the origin, but also to make a connection to the Drude-Lorentz expression.

9.5 Spectral Weight Sum Rules

9.5.1 K-Sum Rule

We define the total spectral weight of the optical conductivity as follows

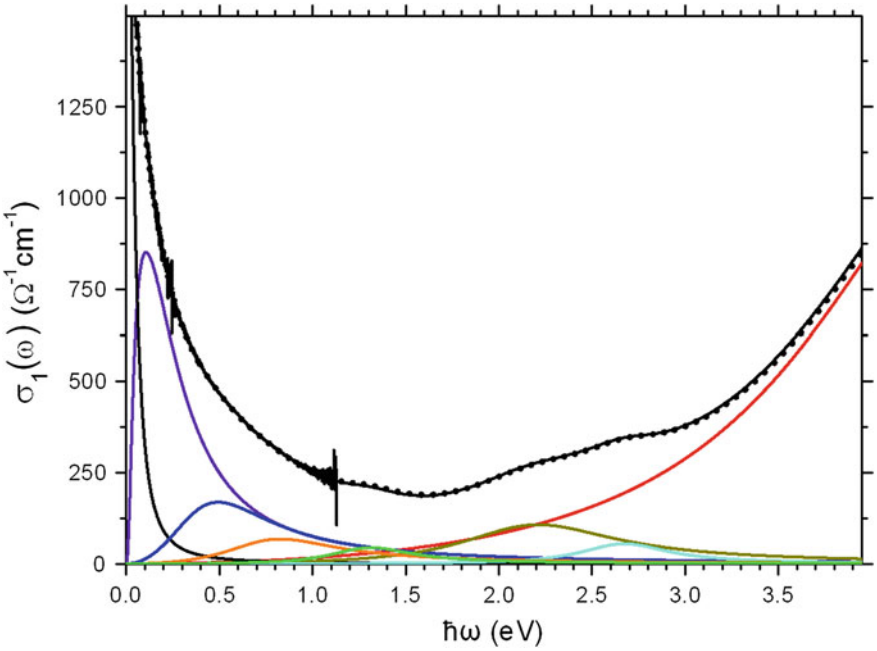

Fig. 9.5 Optical conductivity of $HgBa_2CuO_4$, shown together with a fit to (9.55). Each of the colored curves represents a separate term defined by its position ω_{mn}, strength Ω_{mn}^2 and width γ_{mn}. *Source* [17]

$$W(\boldsymbol{q}) \equiv \mathrm{Re} \int_{-\infty}^{\infty} \sigma(\boldsymbol{q}, \omega) d\omega \tag{9.56}$$

The optical conductivity has, as we have seen in the previous subsection, a diamagnetic part and a regular part. We split up the corresponding contributions to the spectral weight accordingly, i.e.

$$\begin{aligned} W(\boldsymbol{q}) &= W^d(\boldsymbol{q}) + W^r(\boldsymbol{q}) \\ W^d(\boldsymbol{q}) &= \mathrm{Re} \int_{-\infty}^{\infty} \sigma^d(\boldsymbol{q}, \omega) d\omega \\ W^r(\boldsymbol{q}) &= \mathrm{Re} \int_{-\infty}^{\infty} \sigma^r(\boldsymbol{q}, \omega) d\omega \end{aligned} \tag{9.57}$$

To calculate $W^d(\boldsymbol{q})$ we use (9.35)

$$W^d(\boldsymbol{q}) = \mathrm{Re}\int_{-\infty}^{\infty} \frac{iK(\boldsymbol{q})}{\omega + i\eta} d\omega = \pi q_e^2 K(\boldsymbol{q}) \tag{9.58}$$

where $\boldsymbol{K}(\boldsymbol{q})$ is defined in (9.27). The substitution $\omega \to \omega + i\eta$ in the denominator is needed to ensure causality and convergence of the integrals. The same substitution is used in (9.46) from which we calculate $W^r(\boldsymbol{q})$.

$$W^r(\boldsymbol{q}) = \mathrm{Re}\int_{-\infty}^{\infty} d\omega \frac{i}{\omega + i\eta} \int_0^{\infty} \chi_{jj}(\boldsymbol{q}, t) e^{i\omega t} dt \tag{9.59}$$

It is easy to see that the total regular spectral weight is zero. We first interchange the order of integration over frequency and time:

$$W^r(\boldsymbol{q}) = \mathrm{Re}\int_0^{\infty} dt \chi_{jj}(\boldsymbol{q}, t) \int_{-\infty}^{\infty} \frac{i}{\omega + i\eta} e^{i\omega t} d\omega \tag{9.60}$$

We can calculate this by a contour integral. Since $t > 0$ the term $e^{i\omega t}$ converges exponentially to zero for $|\omega| \to \infty$ provided that ω is in the upper half of the complex plane. The contour integral along the half-circle in the upper half of the complex plane than also converges to zero for $|\omega| \to \infty$. The integral along the real axis has the same value as the contour consisting of the integral along the real axis and the half-circle in the upper half plane. To calculate the latter contour, we can apply Cauchy's residue theorem. However, the only pole in the integrand occurs for for $\omega = -i\eta$, and this is in the *lower half* of the complex plane. Since the contour-integral encloses no poles, the integral over ω has a vanishing result. Consequently

$$W^r(\boldsymbol{q}) = 0 \tag{9.61}$$

Apparantly there is an exact compensation going on between positive and negative contributions to the "regular" optical conductivity. In the previous subsection we discussed this in relation to (9.49): The regular optical conductivity has a negative δ-function at zero frequency, which has exactly the same spectral weight as the conductivity integrated over all finite frequencies. Moreover, for all metals except superconductors there is an exact cancellation between the positive δ-function coming from the diamagnetic response, and the negative one from the regular part of the conductivity.

This completes the general discussion of the spectral weight sum rule. Since this is a central theorem of many-body physics, we write here in full glory the limit for $q \to 0$

$$\mathrm{Re}\int_{-\infty}^{\infty}\boldsymbol{\sigma}(0,\omega)d\omega=\frac{\pi q_e^2}{\Omega}\sum_k\frac{\partial^2\epsilon_k}{\partial\boldsymbol{k}^2}\left\langle c_k^\dagger c_k\right\rangle \tag{9.62}$$

Two cases of the spectral weight sumrule, (9.62) are of particular importance, which we detail in the following two subsections.

9.5.2 F-Sum Rule

The free electron dispersion $\epsilon_k = k^2/(2m)$ gives

$$\mathrm{Re}\int_{-\infty}^{\infty}\sigma(\boldsymbol{q},\omega)d\omega=\frac{\pi n q_e^2}{m} \tag{9.63}$$

This is the f-sum rule, or Thomas-Reich-Kuhn rule. It is a cornerstone for optical studies of materials, since it relates the integrated optical conductivity directly to the density of charged objects, and the absolute value of their charge and mass. It reflects the fundamental property that also in strongly correlated matter the number of electrons is conserved.

9.5.3 Kinetic Energy Sum Rule

The nearest-neighbour tight-binding model has a dispersion relation $\epsilon_k = -2t\cos(ka)$, where a is the lattice constant. The implication for the K-sum rule is

$$\mathrm{Re}\int_{-\infty}^{\infty}\sigma(q,\omega)d\omega=\pi q_e^2 K(q) \tag{9.64}$$

$$K(q)=\frac{1}{\Omega}\sum_k 2ta^2\cos(ka)\cos^2\left(\frac{qa}{2}\right)\langle c_k^\dagger c_k\rangle=-\cos^2\left(\frac{qa}{2}\right)\frac{a^2}{\Omega}\langle\hat{H}^{kin}\rangle$$

This is also known as the "kinetic energy sum rule", since the spectral weight is proportional to the minus the average kinetic energy of the electrons. An example of such a measurement is shown in Fig. 9.6 for a high temperature superconductor. Besides a gradual change of the kinetic energy (spectral weight) as a function of temperature, one observes a sudden change at the superconducting phase transition at 110 K.

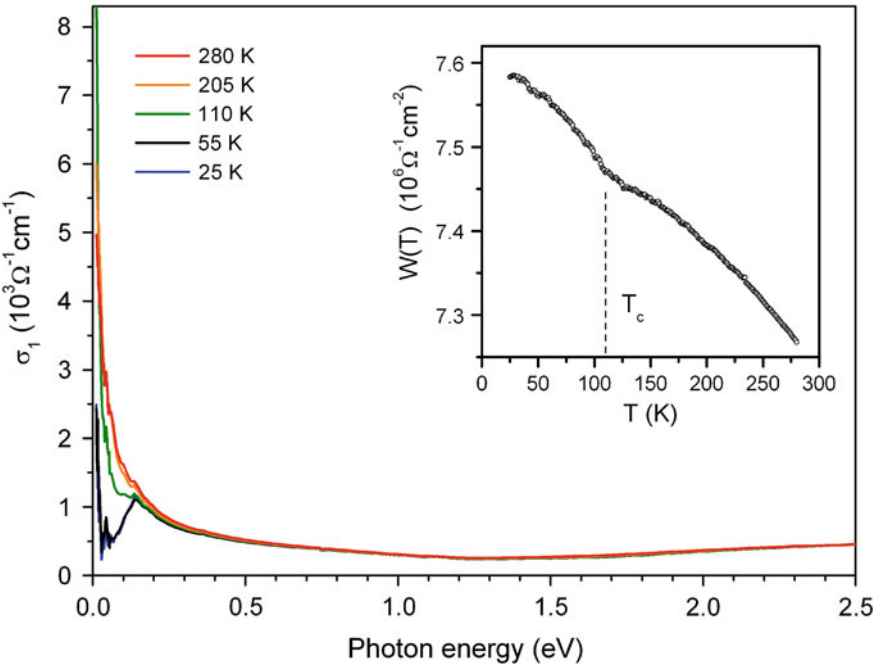

Fig. 9.6 Re$\sigma(\omega)$ of the high T_c superconductor $Bi_2Sr_2Ca_2Cu_3O_{10}$ for some selected temperatures. Inset: Free carrier spectral weight as a function of T. The *dotted line* signals the critical temperature of the sample ($T_c = 110\,\mathrm{K}$). Note that in the superconducting state the optical conductivity has a δ-function at $\omega = 0$. The spectral weight of this δ-function has been experimentally determined from the imaginary part of the optical conductivity (not shown), and it's contribution is taken into account in $W(T)$. *Source* [18]

9.5.4 Regular Part of the Spectral Weight

The exact compensation between the negative *zero*-frequency mode and the finite frequency spectral weight of the regular spectral weight (9.61) deserves some extra attention. It is still interesting to verify the amount present at zero frequency. This is easily obtained. From inspection of (9.59), we notice that the real part of $\frac{i}{\omega+i\eta}$ represents a δ-function $\pi\delta(\omega)$. The spectral weight of the zero-frequency mode is then

$$\boldsymbol{W}^{r,0}(\boldsymbol{q}) = \pi \mathrm{Re} \int_{-\infty}^{\infty} \boldsymbol{\chi}_{jj}(\boldsymbol{q},t)dt = \pi\Omega \mathrm{Im} \int_{0}^{\infty} \left\langle \left[\hat{\boldsymbol{j}}^r_q(t), \hat{\boldsymbol{j}}^r_{-q}(0) \right] \right\rangle dt \qquad (9.65)$$

where (9.44) was substituted to obtain the righthand part of the equation. We first define the "dipole" field operator with the property

$$\frac{\partial \hat{\boldsymbol{p}}_q(t)}{\partial t} = \hat{\boldsymbol{j}}^r_q(t) \tag{9.66}$$

We can now integrate (9.65) and obtain

$$\boldsymbol{W}^{r,0}(\boldsymbol{q}) = \pi\Omega \mathrm{Im}\left(\left\langle\left[\hat{\boldsymbol{p}}_q(\infty), \hat{\boldsymbol{j}}^r_{-q}(0)\right]\right\rangle - \left\langle\left[\hat{\boldsymbol{p}}_q(0), \hat{\boldsymbol{j}}^r_{-q}(0)\right]\right\rangle\right) \tag{9.67}$$

The dipole (current) operator is the position (velocity) operator times the electron charge. Maldague [8] used the position operator for $q = 0$ defined as $\hat{\boldsymbol{x}} = \sum_m \boldsymbol{r}_m c^\dagger_m c_m$, and calculated the commutator with the velocity operator, resulting in the K-sum rule for $q = 0$. Here we generalize this result to $q \neq 0$. It is tempting to use $\hat{\boldsymbol{x}}_q = \sum_m e^{-i\boldsymbol{q}\cdot\boldsymbol{r}_m} \boldsymbol{r}_m c^\dagger_m c_m$. While the time derivative has the required property, that $\partial\hat{\boldsymbol{x}}_q/\partial t = i[\hat{H}^{kin}, \hat{\boldsymbol{x}}_q] = \hat{\boldsymbol{v}}_q$, there are obvious difficulties with this definition due to the divergence of $\boldsymbol{r}_m$ in the thermodynamic limit. However, those difficulties can be avoided. If we consider the following operator

$$\hat{\boldsymbol{p}}_q \equiv -\frac{iq_e}{2\Omega} \sum_k \frac{\boldsymbol{v}_k + \boldsymbol{v}_{k-q}}{\epsilon_k - \epsilon_{k-q}} c^\dagger_k c_{k-q}, \tag{9.68}$$

then we notice that there are no divergencies of the expression in the thermodynamic limit for any $q \neq 0$. Moreover, it is easy to verify, that

$$\partial\hat{\boldsymbol{p}}_q/\partial t = i\left[\hat{H}^0, \hat{\boldsymbol{p}}_q\right] = \hat{\boldsymbol{j}}^r_q \tag{9.69}$$

which implies that $\hat{\boldsymbol{p}}_q$ corresponds to the momentum-space Fourier transform of the dipole operator. The first term in (9.67) represents the response in the $\boldsymbol{p}_q$-channel after an infinite amount of time, which is certainly zero. The second term can be calculated directly from the commutation relations

$$\Omega\left\langle\left[\hat{\boldsymbol{p}}_q, \hat{\boldsymbol{j}}^r_{-q}\right]\right\rangle = iq_e^2 \boldsymbol{K}^r(\boldsymbol{q})$$

where

$$\boldsymbol{K}^r(\boldsymbol{q}) = \frac{1}{4\Omega} \sum_k \left\{ \frac{(\boldsymbol{v}_{k+q} + \boldsymbol{v}_k)^2}{\epsilon_{k+q} - \epsilon_k} + \frac{(\boldsymbol{v}_{k-q} + \boldsymbol{v}_k)^2}{\epsilon_{k-q} - \epsilon_k} \right\} \left\langle c^\dagger_k c_k \right\rangle \tag{9.70}$$

Consequently

$$\boldsymbol{W}^{r,0}(\boldsymbol{q}) = -\pi q_e^2 \boldsymbol{K}^r(\boldsymbol{q}) \tag{9.71}$$

The amount of spectral weight at finite frequencies exactly balances this amount, hence

$$\boldsymbol{W}^{r,+}(\boldsymbol{q}) = \int_{0^+}^{\infty} \mathrm{Re}\boldsymbol{\sigma}(\boldsymbol{q},\omega)d\omega = \frac{\pi q_e^2}{2}\boldsymbol{K}^r(\boldsymbol{q}) \tag{9.72}$$

Let us now consider the properties of $K^r(\boldsymbol{q})$. In the first place it is interesting to look at the limit $q \to 0$. We can use that $\boldsymbol{v}_{k+q} - \boldsymbol{v}_k = \boldsymbol{q} \cdot \partial^2\epsilon_k/\partial\boldsymbol{k}^2$ for the terms in the numerators, and $\epsilon_{k+q} - \epsilon_k = \boldsymbol{q} \cdot \partial\epsilon_k/\partial\boldsymbol{k} + (q^2/2)\partial^2\epsilon_k/\partial k^2$ in the denominators to show that

$$\lim_{q\to 0}\left\{\frac{(\boldsymbol{v}_{k+q}+\boldsymbol{v}_k)^2}{\epsilon_{k+q}-\epsilon_k} + \frac{(\boldsymbol{v}_{k-q}+\boldsymbol{v}_k)^2}{\epsilon_{k-q}-\epsilon_k}\right\} = 4\frac{\partial^2\epsilon_k}{\partial\boldsymbol{k}^2}. \tag{9.73}$$

Consequently by comparing to (9.28) we see, that for $q = 0$ there is a perfect compensation of the zero-frequency spectral weights of the diamagnetic and the regular parts of the conductivity:

$$\boldsymbol{K}^r(0) = \frac{1}{\Omega}\sum_k \frac{\partial^2\epsilon_k}{\partial\boldsymbol{k}^2}\langle c_k^\dagger c_k\rangle = \boldsymbol{K} \tag{9.74}$$

Again we consider the most commonly encountered case: The free electron dispersion $\epsilon_k = k^2/(2m)$ gives

$$\int_{0^+}^{\infty} \mathrm{Re}\sigma(q,\omega)d\omega = \frac{\pi q_e^2}{2m}\sum_k \langle c_k^\dagger c_k\rangle \tag{9.75}$$

which is the same expression as the familiar f-sum rule, (9.63), and we see that in this case $K^r(q) = K$ is independent of q.

With the tightbinding formula $\epsilon_k = -2t\cos(ka)$ one obtains after some goniometric manipulations

$$K^r(q) = \cos^2\left(\frac{qa}{2}\right)\frac{1}{\Omega}\sum_k 2\,T a^2\cos(ka)\left\langle c_k^\dagger c_k\right\rangle = K\cos^2\left(\frac{qa}{2}\right) \tag{9.76}$$

which corresponds exactly to the result in (9.64).

The fact that the same expression for $K(q)$ is found in (9.76) and (9.64) indicates the perfect compensation of the positive (diamagnetic) and negative (regular) zero-frequency delta-functions. This result makes perfect sense physically; the implication is that no dissipation-less DC currents can flow for any wave-vector. Presumably the implementation of the Peierls substitution used here is quite accurate, despite some ambiguity for any $q \neq 0$ due to the course-graining procedure of the tight-binding form.[2]

[2] One can pose the question whether the corresponding expression for the current density satisfies the continuity equation. On a fundamental level this relation expresses the conservation of the number

Following (9.72) the spectral weight of the optical conductivity **decreases as a function of increasing q and vanishes at the Brillouin-zone boundary**. From inspection of (9.68) it is clear why this is the case: for $q = \pi$ there is an exact cancellation of terms in the numerator, i.e. $v_k + v_{k+\pi} = 0$. In other words, all optical matrix elements are zero for $q = \pi$ and consequently the intensity of the optical spectrum vanishes in this limit. While for general $\epsilon(k)$ dispersion such an exact cancellation is not expected, yet this indicates that the trend that $W(q)$ diminishes for increasing q is the rule rather than the exception. With the advent of new experimental techniques which allow the exploration of the optical conductivity at finite $\boldsymbol{q}$ [2–4] the $\boldsymbol{q}$-dependent optical conductivity sumrule in (9.72) provides a lower bound on the intensity of the free carrier optical response of correlated electrons.

Acknowledgments It is a pleasure to thank Adrian Kantian, Christophe Berthod, Alexey Kuzmenko and Gianni Blatter for their comments. This work was supported by the SNSF through Grants No. 200020-140761 and 200020-135085, and the National Center of Competence in Research (NCCR) Materials with Novel Electronic PropertiesMaNEP.

References

1. D.N. Basov, R.D. Averitt, D. van der Marel, M. Dressel, K. Haule, Rev. Mod. Phys. **83**, 471 (2011)
2. F. Keilmann, R. Hillenbrand, Phil. Trans. A **362**, 787 (2004)
3. F. Huth, A. Govyadinov, S. Amarie, W. Nuansing, F. Keilmann, R. Hilenbrand, Nano Lett. **12**, 3973 (2012)
4. J. Chen, M. Badioli, p Alonso-Gonzlez, S. Thongrattanasiri, F. Huth, J. Osmond, M. Spasenović, A. Centeno, A. Pesquera, P. Godignon, A.Z. Elorza, N. Camara, F. Javier Garca de Abajo, R. Hillenbrand, F.H.L. Koppens, Nature **487**, 77 (2012)
5. M. Dressel, G.G. Grüner, *Electrodynamics of Solids: Optical Properties of Electrons in Matter* (Cambridge University Press, Cambridge, 2002)
6. C.F. Klingshirn, *Semiconductor Optics* (Springer, Berlin, 1995)
7. D. Pines, P. Nozières, *The Theory of Quantum Liquids, Part I* (Benjamin, New York, 1966)
8. F.P. Maldague, Phys. Rev. B **16**, 2437 (1977)
9. G.D. Mahan, *Many-Particle Physics*, 2nd edn. (Plenum, New York, 1990), pp. 207–223
10. A. Millis, in *Strong Interactions in Low Dimensions*, Physics and Chemistry of Materials with Low-Dimensions, Vol. 25, (Springer, Dordrecht, 2004)
11. D. van der Marel, in *Strong Interactions in Low Dimensions*, Physics and Chemistry of Materials with Low-Dimensions, Vol. 25, (Springer, Dordrecht, 2004)
12. E. van Heumen, D. van der Marel, in *Lectures on the Physics of Strongly Correlated Systems XI*, ed. by A. Avella, F. Manzini, (American Institute of Physics, New York, 2007)
13. A. Damascelli, D. van der Marel, M. Grueninger, C. Presura, T.T.M. Palstra, J. Jegoudez, A. Revcolevschi, Phys. Rev. Lett. **81**, 918 (1998)

(Footnote 2 continued)
of particles. This condition corresponds to the local constraint $\nabla \cdot \boldsymbol{J} + \partial\rho/\partial t = 0$ in continuous space. Although there is no obvious way to define a quantity equivalent to $\nabla \cdot \boldsymbol{J}$ for a lattice, the situation is in fact somewhat simpler. It is sufficient to verify that removal of an electron from a given site $\boldsymbol{r}_m$ is always compensated by the creation of an electron elsewhere in the lattice. Since the current operator in (9.23) swaps electrons between different sites, the conservation of particle number is therefor built in the definition of the current operator

14. C.N. Presura, Ph.D. thesis, Rijksuniversiteit Groningen, 2003
15. S. Nakai, N. Nuecker, H. Romberg, M. Alexander, J. Fink, Phys. Scripta **41**, 596 (1990)
16. F.P. Mena, J.F. DiTusa, D. van der Marel, G. Aeppli, D.P. Young, A. Damascelli, J.A. Mydosh, Phys. Rev. B **73**, 085205 (2006)
17. S. I. Mirzaei, D. Stricker, J. N. Hancock, C. Berthod, A. Georges, E. van Heumen, M. K. Chan, X. Zhao, Y. Li, M. Greven, N. Barisic, D. van der Marel, Proc. Natl. Acad. Sci. USA **110**, 5774 (2013)
18. F. Carbone, A.B. Kuzmenko, H.J.A. Molegraaf, E. van Heumen, E. Giannini, D. van der Marel, Phys. Rev. B **74**, 024502 (2006)

Index

A. Avella and F. Mancini (eds.), *Strongly Correlated Systems*,
Springer Series in Solid-State Sciences 180, DOI 10.1007/978-3-662-44133-6